

Probing the distribution of pharmaceutical compounds in cells using ToF-SIMS

Carla Newman

Thesis submitted to the University of Nottingham for the degree of Doctor of Philosophy

2018

Statement

This project was written by me, in my own words except for the quotation from published sources that I clearly acknowledge as such. I am aware that the incorporation of any other material without proper acknowledgment is considered plagiarism. All figures and illustrations that do not result from my own research are also indicated as such. This report has been prepared in accordance with the University of Nottingham guidelines for thesis writing.

Abstract

The primary objective of this thesis is to describe the work that I have undertaken during my PhD, evaluating the applicability of Time of Flight Secondary Ion Mass Spectrometry (ToF-SIMS) to study intracellular drug distribution. ToF-SIMS, as a technique has been widely used to characterize inorganic[1] and organic[2] materials, or even unexpected mixtures of both.[3] My objective is to determine if that can be extended to drug discovery, by identifying pharmaceutical drugs in biological matrices such as cells.

In drug discovery, intracellular drug distribution is a subject of profound interest, as scientists need to know if the drug is reaching the target of interest, or if is having adverse off-target activity. However, the techniques currently used to inform on this do not provide a definitive answer to the question, as either spatial resolution or molecular properties are compromised. For example, Matrix Assisted Laser Desorption Ionisation (MALDI) cannot achieve sub-cellular spatial resolution[4] and even the most advance microscopy applications are dependent on labels that might compromise the physical-chemical properties of a drug molecule.

ToF-SIMS bridges the gap, as it has improved spatial resolution and the drug molecules are presented to the in vitro or in vivo system label free with minimal sample preparation. SIMS is also capable of providing three-dimensional information and even potential metabolomics information when OrbiSIMS is employed[3].In this study, I describe the first time a drug molecule, amiodarone, was visualized inside a mammalian cell using ToF-SIMS, this work was published in 2015.[5] I then extend that methodology to other cell lines, and compare the ToF-SIMS data with Liquid-Chromatography tandem Mass Spectrometry data. This study also considers the variability found within cell populations and how different cells have a range of amiodarone intensities, and therefore exhibit different incorporation rates despite being derived from the same clones; this work was published in 2017.[6]

This thesis then focuses on the applicability of ToF-SIMS to the analysis of other drug molecules and investigates if a compound's physical-chemical properties can provide any indication of the ionisation

efficiency of a pharmaceutical drug in ToF-SIMS, this work is currently being written for a peer reviewed publication.

The last chapter concentrates on bacterial imaging using both ToF and Orbi SIMS; the former allows the visualization of a drug molecule inside the bacteria of interest and the latter allows lower resolution imaging but extraction of metabolomic information as a result of the high mass resolution, high mass accuracy data generated by the Orbitrap mass analyser.

List of publications

Single-Cell Analysis: Visualizing Pharmaceutical and Metabolite Uptake in Cells with Label-Free 3D Mass Spectrometry Imaging
Melissa K. Passarelli, Carla F. Newman, Peter S. Marshall, Andrew West, Ian S. Gilmore, Josephine Bunch, Morgan R. Alexander, and Colin T. Dollery
Anal. Chem., 2015, 87 (13), pp 6696–6702
DOI: 10.1021/acs.analchem.5b00842
Publication Date (Web): May 29, 2015

Intracellular Drug Uptake—A Comparison of Single Cell Measurements Using ToF-SIMS Imaging and Quantification from Cell Populations with LC/MS/MS
Carla F. Newman, Rasmus Havelund, Melissa K. Passarelli, Peter S. Marshall, Ian Francis, Andy West, Morgan R. Alexander, Ian S. Gilmore, and Colin T. Dollery
Anal. Chem., 2017, 89 (22), pp 11944–11953
DOI: 10.1021/acs.analchem.7b01436
Publication Date (Web): October 17, 2017

The 3D OrbiSIMS—label-free metabolic imaging with subcellular lateral resolution and high mass-resolving power
Melissa K Passarelli, Alexander Pirkl, Rudolf Moellers, Dmitry Grinfeld, Felix Kollmer, Rasmus Havelund, Carla F Newman, Peter S Marshall, Henrik Arlinghaus, Morgan R Alexander, Andy West, Stevan Horning, Ewald Niehuis, Alexander Makarov, Colin T Dollery and Ian S Gilmore
Nature Methods volume 14, pages 1175–1183 (2017)
DOI:10.1038/nmeth.4504

Acknowledgements

Firstly, I would like to express my sincere gratitude to my PhD supervisors, Dr. Andy West, Prof. Morgan Alexander and Prof. Ian Gilmore for the continuous support during my PhD related research, for their patience, motivation, and knowledge. Their guidance helped me during the time of my research and writing of this thesis. I really appreciate the discussions and their input, even the hard questions during the PhD meetings, and I am very grateful for their continued support.

In addition, I would like to thank Dr. Andy West further, for giving me the opportunity to do a part-time PhD while working in his group at GlaxoSmithKline (GSK), and for being an exceptionally nice person, I sincerely appreciate the opportunity he has given me.

My sincere thanks also goes to Dr. Rasmus Havelund, Dr. Melissa Passarelli, and Dr. David Scurr, for teaching me ToF-SIMS and their insightful comments and discussions.

I would also like to thank my colleagues at GSK for their help, Dr. Andy Nicholls, Dr. Mike Hann, Dr Steve Hood, Dr. Peter Marshall, Mike Lee, Donna Fraser, Satty Borman, Ken Fanton, Dr. Pamela Riester, Tracy Beadle, Ian Francis, Paul McGill, Julia Castro-Pichel, Elena Jimenez-Navarro, Monica Cacho-Izquierdo, Dr. Argyrides Argyrou, Dr. Rob Young, Sir Colin Dollery, Dr. Malcolm Skingle, Dr. Daniel Sevin, Joe Lavelle, Simon Bate, Dr. Jack Euesden, Paul Wilson, Dr. Charles Clifford and probably many more. I would like also to thank all the help for the NiCE-MSI group at the NPL, specially Dr. Jean-Luc Vorng and Dr. Spencer Thomas.

I would also would like to thank my internal examiner Prof. Martyn Davies and external examiner Prof. Alain Brunelle for being kind to a very nervous student.

Last but not the least, I would like to thank my family, specially my husband Richard and my parents, Armando and Fatima for supporting me throughout writing this thesis and my life in general. I am really sorry if I have forgotten anyone, but I suppose it happens when you do a PhD at my age.

List of Figures

1.1: Drug discovery and development diagram. [7] The picture describes both the preclinical and clinical studies workflows. The project team investigates the target and conducts research both in vivo and in vitro before the data is submitted as a New Drug (ND) application to the Federal Drugs Administration (FDA). Once the ND application is approved, the phase I, II and III clinical trial stage can start. If this phase is successful the application for a new drug can be filled, the data is then reviewed by the FDA and the drug is approved for the market. Reproduced with the permission of the publisher, Springer Nature.

1.2: Drug discovery intracellular targets.[8] Most drug targets are intracellular, kinases can be mainly found in the cytoplasm, transporters are mainly found in the mitochondria and there are a multitude of genetic targets in the nucleus. Reproduced with the permission of the publisher, Springer Nature.

2.3: SIMS sputtering schematic by Castner et al. [9] The image shows ions being fired at a substrate. The collision cascade observed is the result of collisions following the impact of the primary ion beam. As a result, a range of molecular and atomic species are ejected from the surface. Only approximately 1% are ions which are then guided to the detector.[9] Reproduced with the permission of the publisher, Springer Nature.

2.4: Computer simulation of the molecular dynamics of different primary ion beams, with a kinetic energy of 15 keV, bombarding an Ag (111) crystal. The different atomic layers are represented with different colours and the grey particles represent a depth of 4.6 nm. The first three rows show a cross-section of the crystal, the first row show the system at 0 ps, the second row shows the system at 3 ps, and the third row at 39 ps. The bottom row shows a top view of the impacted area. The numbers displayed on the third row are the number of atoms ejected upon primary ion impact. Reproduced under Attribution 3.0 Unported, Winograd image from Annual Reviews.

2.5: Simplified schematics of IONTOF's ToF-SIMS. The image represents the basic components of a ToF-SIMS instrument: target plate where the sample is introduced, electron flood gun, the primary ion

gun, the ion optics, the time of flight analyser and finally the detector. Attribution 3.0 Unported, Hofmann and al. image from the Royal Society of Chemistry.

2.6: ION-TOF IV at the School of Pharmacy facilities (The University of Nottingham).

2.7: OrbiSIMS schematics. At the centre of the Orbitrap mass analyser, there is a spindle where the ions orbit around as a result of a dynamic electrostatic field.[3] The two-beam set up is maintained to allow greater flexibility of analysis, most of the ion guiding system to the ToF analyser is similar to the ToF-SIMS 5 except the secondary ion switch which allows the ions to be sent either to the ToF or Orbitrap analyser, the part of the Orbitrap system after the quadrupole is very similar to a QExactive HF. Instrument components not to relative scale. The Orbitrap diagram is included as an insert on the OrbiSIMS schematic. Reproduced with the permission of the publisher, Springer Nature.

2.8: Table of operational methodologies of the OrbiSIMS, and diagram of the different imaging modalities. [3]The table shows the flexibility of the OrbiSIMS, it allows the acquisition of surface spectra only using both the Orbitrap (mode 2) and the ToF analyser (mode 1), spectral depth profile acquisition using the Orbitrap (mode 4), the ToF (mode 3) and the two detectors (mode 5). In imaging mode, it can perform 2D imaging using the ToF (mode 6) or the Orbitrap analyser (mode 7). The 3D imaging capabilities are further illustrated on the diagram, the Orbitrap analyser can be used for imaging by itself (mode 8) or in a dual beam setup, used in conjunction with the ToF analyser (mode 9) on the same scan, or used to analyse the ions that result from the sputter scans (mode 10), in this mode no information is lost, as the imaging is performed using both analysers. The data obtained in this mode has both high spatial resolution (obtained with the focused Bismuth beam and the ToF analyser) and high mass resolution and MS/MS capabilities (obtained with the Argon beam and the Orbitrap analyser).[3] Reproduced with the permission of the publisher, Springer Nature.

2.9: Single NR8383 cell incubated with amiodarone.[3] Top image series shows the total ion image, and the bottom series shows the compound signal (in green) the phosphocholine marker (in grey) and the nuclear marker (in magenta). The spectra on the right shows the difference in peak width between the Orbitrap analyser (blue) and the ToF analyser (black).[3] Reproduced with the permission of the publisher, Springer Nature.

2.10: Freeze-drying theory.[10] The three matter states are a fine balance between temperature and pressure. In case of water, represented on the diagram, white represents the solid state (ice), grey represents the gas state (steam) and blue represents the liquid state (water). As it can be seen the triple point, where the three states coincide, is at 0.006 bar and at a temperature above 0°C. Reproduced with the permission of the publisher, Springer Science Business Media New York

2.11: Piwowar et al. organelle mapping workflow illustration.[11] Here HeLa cells are depicted, but it could be applied to any cell line. Using centrifugation and affinity pull-down, the organelles are separated after cell lysis. These separate organelle enriched fractions could then be analysed using ToF-SIMS and an organelle mass spectral fingerprint created for each of the different organelles. Once these profiles are created, it should be possible to correlate the organelle profile spectra with the spectra per pixel of the cell and therefore a reconstructed cell image based on those profiles. Reproduced with the permission of the publisher, John Wiley and Sons.

2.12: Principal component analysis of the entire dataset in (A) and (B). In this experiment different bacteria can be grouped according to their MS fingerprint profile using PCA. PC-DFA plot of the full data set after the removal of *Enterococci* (C) and (D) shows the separation of the five different *E.coli* strains used in the experiment (the training set is displayed in red and the projected in blue).[12] Reproduced with the permission of the publisher, Elsevier.

2.13: Spatial resolution of biological imaging techniques. The diagram shows the applicability of each technique across a variety of sizes and biological matrices. Reproduced with the permission of the publisher, Elsevier.

2.14: Confocal microscopy and wide-field microscopy.[13] On the left the light path passes through the pinhole, which enhances the z-resolution of confocal microscopy. On the right the normal set-up of wide-field microscopy. Image reproduced under the Creative Commons License (Attribution–Noncommercial–Share Alike 4.0 Unported license.

2.15: Fluorescence microscope basic light path schematics. There are two cubes in a fluorescence microscope an excitation cube and an emission cube. In the excitation cube a dichroic mirror (DM1) directs the light from the source (bulb or laser) to the sample passing the emitted fluorescence to the

indicators in the emission cube. B is a filter that acts as a barrier that prevents the excitation light to reach the detector. DM2 is a beam splitter for the emitted fluorescence light and emission filter (Em1 and Em2) filter out unwanted light. The fluorescence is then detected by cameras or photo multipliers (PMTs).[14] [12] Reproduced with the permission of the publisher, CHS Press.

2.16: Confocal fluorescence microscopy and STED images of 40 nm fluorescent beads.[15] The two images depicted are from the same area, however it can clearly be seen, especially in the area highlighted by the arrows a much cleared imaged with improved spatial resolution. The image on top is quite blurry and undefined whilst the image at the bottom is clearer. Reproduced with the permission of the publisher, Elsevier.

2.17: The Nanolive 3D Cell Explorer Refractive Index microscope principle. Schematics of the microscope, displaying the different components (left). Whole blood spikes with A549 (tumour cells) (right). [16] The middle image shows the light image of a mixed cell population containing both peripheral blood mononuclear cells and circulating tumour cells such as A549 cells. The image on the right depicts the pseudo-stained obtained by the difference in refractive index of the different cellular components. Reproduced with the permission of the publisher, John Wiley and Sons and NanoLive.

2.18: Laser confocal scanning microscopy. On the left is the schematics of the microscope. On the right the same image comparing the non-confocal and the confocal mode. As it can be observed the sharpness of the image increases in the confocal mode, the topology of the sample is much more detailed due to the 10nm z resolution of this microscope.

2.19: Transmission electron microscope schematics (left)[17]. Reproduced with the permission of the publisher, Springer-Verlag. Pancreatic acinar cell fixed in glutaraldehide (x11,000) stained with Osmium Tetroxide.[18] There is a clear contrast between the nucleus and the extra nuclear space. Outside the nucleus a mitochondrion (M), the endoplasmic reticulum (ER) and a zymogen granule (Z) can be observed. Inside the nucleus the nucleolus (nu) can be seen as well as chromatin (ch) and karyoplasm (k). Image reproduced under the Creative Commons License (Attribution–Noncommercial–Share Alike 4.0 Unported license.

2.20: (A) AFM schematics[19]. Reproduced with the permission of the publisher, Royal Society of Chemistry. (B) Bovine red blood cell infected with *Babesia bovis.* (C) higher magnification of image B displaying the ridge morphology of the bacteria. Reproduced with the permission of the publisher, John Wiley and Sons.

2.21: Diagram showing the relationship between omics techniques.[20] The omics techniques refer to the particular type of biological molecule they study. Genomics is the study of DNA (deoxyribonucleic acid), transcriptomics relates to RNA (ribonucleic acid), proteomics relates to the study of proteins and metabolomics is the study of metabolites and their pathways.

A change at the DNA level may, or may not cause a change in the protein expression and metabolic changes, therefore understanding the whole process, and being able to pin-point changes in a disease state helps the drug discovery process. Reproduced with the permission of the publisher, Springer Nature.

2.22: Proteomics workflow [21]. After sample collection, a certain amount is processed (typically protein concentration is determined) the sample is then reduced, alkylated and digested with an enzyme (generally trypsin); once the proteins are converted to peptides the samples are typically analysed using a high mass resolution mass spectrometer in an LC-MS/MS configuration (ordinarily nano-LC). The data can then be proceeds using several different software both freeware and instrument vendor software. Reproduced with the permission of the publisher, Springer Nature.

2.23: Plot represents the summary of all the PubMed indexed articles that mentioned lipidomics between 2000 and October 2017.[22] There is a marked increased number of MS based lipidomics study since the year 2000, which coincides with the introduction of the Orbitrap technology. Reproduced with the permission of the publisher, American Chemical Society.

2.24: Plot describes the lipidomics workflow and the factors that could impact the accuracy of the workflow.[23] This image summarizes the complex procedure required to generate good lipidomics data, along with the caveats associated to each step of the process. In the first step, one needs to pay particular attention to the type of samples and their storage. The extraction step highlights the different extraction methods in existence. The next step relates to sample pre-treatment, such a further purification,

hydrolysis or no treatment at all. The MS part of the process highlights the different types of MS methods that can be used, different ionisation modalities, further separation, targeted and untargeted methods. Finally, the sample processing method, which should account for sample-to-sample and batch-to-batch variability, retention time drift and the use of internal standards. Reproduced with the permission of the publisher, Elsevier.

2.25: Metabolomics full workflow, with pre-analytical, analytical and computational nodes.[24] The pre-analytical steps are arguably more important that the analysis itself, as a well-designed study facilitates both the analysis and the data processing. The analytical step can be quite varied, using both targeted and untargeted methods as well as different sample preparation methodologies. The computational part of the process can be very challenging, and several different data processing procedures need to be undertaken before the metabolic pathway analysis can be performed. Open-access article distributed under the terms of the Creative Commons Attribution License (CC BY).

2.26: Pie chart depicting the reasons why pharmaceutical drugs fail to reach the market.[25,26] Most drugs fail to make it to the market due to adsorption, absorption, distribution, metabolism and excretion issues. Lack of efficacy, animal toxicity and adverse effects on man are also responsible for a pharmaceutical failure to be marketed. Reproduced with the permission of the publisher, Springer Nature.

2.27: The scheme represents the processes of drug interaction for a CNS target. [27] In vitro assays are only affected by non-specific binding, while in vivo assays are affected by the Blood-Brain-barrier and ADME issues. Reproduced with the permission of the publisher, Taylor & Francis.

2.28: Plot showing the relation between decrease in solubility and increase in the number of aromatic rings. The red line indicates 50 µg/mL solubility levels[28] Reproduced with the permission of the publisher, Elsevier.

2.29: This Figure depicts the correlation between Chrom log $D_{pH7.4}$ and number of aromatic rings. The black line depicts PFI=7 which is the threshold that separates what is considered a potentially good drug and a bad one.[29] Reproduced with the permission of the publisher, Elsevier.

2.30: Plot depicting DRUG efficacy Vs affinity.[27] The plots depicts the fine balance between drug efficacy and target affinity, any molecule with a drug efficacy below 0.01 % has an increased risk of

failing. Ideally, lead candidate molecules should move to the green space of the plot, to a higher drug efficacy and affinity beyond at least the 50% Receptor occupancy (RO) line.

2.31: The plot of mean molecular weight and cLogP values of oral drugs .[30] For three different time periods (green), this shows that both molecular weight and cLog P have increased with time. In red, are the values for the patented compounds for 18 pharmaceutical companies between 2000 and 2010. In blue is the single compound patent from the same company. Reproduced with the permission of the publisher, American Chemical Society.

2.32: EMIAT trial profile.[31] This study, involved the treatment of patients with amiodarone and a placebo, the number of patients in each group was the same. The number of deaths was slightly higher on the amiodarone group, particularly due to the non-cardiac related deaths, which is associated with the toxicity associated to this compound. The number of non-cardiac deaths in the placebo group was much lower, 13 versus 18. Despite this, in terms of arrhythmic event associated death the number were much greater in the placebo group when compared to the amiodarone treated group (50 versus 33) which indicates that amiodarone has a positive effect when treating arrhythmic events. Reproduced with the permission of the publisher, Elsevier.

2.33: Amiodarone concentrations measured by LC-MS/MS of fat and plasma of human patients treated with amiodarone. (A) showing a comparison of the concentrations in fat tissue and plasma on a Log scale. (B)Correlative plot of the plasma and fat concentrations.[32] As demonstrated in this two plots, there is a correlation in amiodarone concentration between plasma and fat tissue. However, the amount of amiodarone in fat tissue is 10 to 100 fold more concentrated, which could be expected due to amiodarone lipophilicity. Reproduced with the permission of the publisher, Elsevier.

2.34: Molecular structures of amiodarone, its metabolite, desethylamiuodarone (DEA) and the thyroid regulatory hormones.[33] The similarity between the molecules is known to cause disturbance in T3 productions causing potential thyroid deregulation. Reproduced with the permission of the publisher, Oxford University Press.

2.35: Amiodarone induced pigmentation in patient.[34] This patient suffered from severe blue-grey pigmentation in areas of the skin exposed to the sun caused by long term amiodarone treatment. It is

thought that this hyperpigmentation is caused by dermal lipofuscinosis, as lipofuscin accumulates in dermal macrophages; this was hypothesised as amiodarone is known to cause lysosomal damage. Fitzpatrick's Color Atlas & Synopsis of Clinical Dermatology Klaus Wolff, Richard Allen Johnson, Dick Surmount Copyright 2005, 2001, 1997, 1993 by The McGraw-Hill Companies. All Rights reserved.

2.36: Amiodarone associated pathological finding, arrows point to examples of each event, in (A) two foamy macrophages, in (B) two areas of membrane proliferation and (C) two areas of interstitial fibrosis.[35] Reproduced with the permission of the publisher, Pioneer Bioscience Pub. Co.

2.37: Plots displaying the relative difference in gene expression of ABC transporters (A) and SLC transporters (B) in HeLa, Hek293, HL-6-, K562, Saos-2, Caco-2 and HepG2.[36] Plot a shows that HepG2 have the most ABC transporters from the cells types investigated, while HeLa have the least. For SLC transporters HeLa cells again have the least amount of these transporters on their membrane. Reproduced with the permission of the publisher, American Society for Pharmacology and experimental therapeutics.

2.38: Pie charts depicting the difference in gene expression between HepG2 cells and primary hepatocytes. In (A) the up-regulated genes and (B) the down regulated genes.[37] Genes that are up-regulated, are genes whose expression is increased and down-regulated genes are genes whose expression is decreased. Reproduced with the permission of the publisher, Elsevier.

2.39: Mycobacteria. (A) Morphology of colonies on solid media[38], Reproduced with the permission of the publisher, Elsevier. (B)Acid-fast bacilli (MBT) stained with Ziehl-Neelsen and extracellular material stained with Alcian Blue visualized at x100 magnification, (C) SEM image of an agglomerate of mycobacteria in exponential growth stage[39], (D) TEM of ultra-thin sections of *Mycobacterium tuberculosis* replicating by binary fission, scale bar 200 nm.[40] Images reproduced under the Creative Commons License (Attribution–Noncommercial–Share Alike 4.0 Unported license.

2.40: The lifecycle of *M. tuberculosis*. Within 4 to 6 weeks of expose there is a dendritic cell or T-cell mediated immune response, this will lead to the elimination of the bacteria, infection or the

neutralization of the bacteria not fully killing it (latent TB). After years or decades, a re-infection or re-activation can occur. [41] Reproduced with the permission of the publisher, Springer Nature.

2.41: Mechanics of action of TB treatment. Isoniazid, Rifampin, ethambutol and Pyrazinamide are the first line of treatment against TB. Since some bacteria has become resistant to antibiotics such as Isoniazid and Rifampin other antibiotics have to be used as a second line of treatment. [42] The photo was created by Dr. Ray Butler and Janice Carr, at the CDC. The illustration was created by Krista Townsend, at the National Institute of Allergy and Infectious Diseases.

2.42: MBT cell wall and its constituents. The MBT cell wall is very complex, it is made by an external sugar and protein rich capsule, followed by a layer of mycolic acid which is then followed by an Arabinogalactan layer. The most internal layer is made by peptidoglycan, it displays two types of crosslinking 4-3 and a 3-3.[43]Reproduced with the permission of the publisher, Springer Nature.

2.43: Diagram of the summary of DPA synthesis.[44] The DpRE1 target is part of the DPR complex and is embedded in the plasma membrane, while DpRe2 is part of the DPA complex. Reproduced under the Creative Commons Attribution License.

3.44: Sample preparation diagram of the ToF-SIMS workflow. The cells were plated on 4 well chamber Lab-Tek slides, them incubated with or without Amiodarone, once the incubation was finished they were washed three time with 150mM ammonium formate solution at pH 7.4 and freeze-dried. Once the process was completed, they were kept in the -80°C waiting transport to the National Physical Laboratory or the University of Nottingham for analysis. Once the samples were ready to be used, they were placed in a vacuum chamber to minimize surface condensation on the sample and then mounted and placed inside the instrument.

3.45: Gradient profile used for proteomics nano-HPLC experiment. The plot shows the time in the x – axis and the % of organic on the y-axis. The gradient increases slowly from 5 to 40% organic because the vast majority of peptides elute before 40% organic. Hence, by slowly ramping up the amount of organic phase the peptide peaks will be well separated which also provides the mass spectrometer with more time for the acquisition, resulting in more identifications. Reproduced with the permission of ThermoFisherScientific

3.46: Chemical structures of the compounds used for this study and respective GSK identifiers.

4.47: Light microscopy image of H&E stained NR8383 macrophage cells incubated with the referred compounds at the concentrations of 10 µg/mL Chloroquine, and 12.50 µg/mL of amiodarone and GSK2789899A after 72 hour incubation time at 37ºC. The scale bar is 50 µm.

4.48: Light microscopy image of H&E stained NR8383 cells. The cell morphology varies as a function of time (24, 48 and 72 hours) and amiodarone concentration (0, 3.13, 6.25 and 12.50 µg/mL). The scale bar is 50 µm. As it can be observed the cells increase in size as the amiodarone concentration and incubation time increases.

4.49: Refractive index microscopy NR8383 live cells (A) control and (B) incubated with 3.13 µg/mL amiodarone for 48 hours. The scale bar is 15 µm. As it can be observed in this image the cells are significantly enlarged, as highlighted with the red box, after amiodarone incubations.

4.50: Light microscopy image of H&E stained NR8383 cells doped with amiodarone before and after being freeze-dried. The vertical scale bar is 50 µm. The black arrows demonstrate the increase in the visibility of the cellular attachment filaments under freeze-drying conditions.

4.51: Fluorescent confocal microscopy image of fixed NR8383 cells using lysotracker red to strain the lysosomes and DAPI to strain the nucleus. "foamy" appearance of the macrophage cell model after 72 hours amiodarone incubation at different concentrations, as highlighted by the white arrow. The scale bar is 25 µm

4.52: The number of live cells determined from automated fluorescent wide-field microscopy images of NR8383 cells dosed with amiodarone at 0.78, 1.56, 3.13, 6.25 and 12.50 µg/mL and control. Three wells per performed per condition. The number of live cells was determined by counting the number of nuclei present per condition per well. Each colour/shape represents a different incubation time, the blue diamond represents the 4 hour time-point, the red triangle is the 24 hour time-point, the green circle is the 48 hour time-point and the purple square represents the 72 hour time-point.

4.53: Lysotracker signal per well normalised to the number of living cells in the same well for the different amiodarone concentrations studied (0.78, 1.56, 3.13, 6.25 and 12.50 µg/mL and control). Each colour/shape represents a different incubation time, the blue diamond represents the 4 hour time-point,

the red triangle is the 24 hour time-point, the green circle is the 48 hour time-point and the purple square represents the 72 hour time-point.

4.54: Wide-field microscopy image of high throughput fluorescent microcopy of NR8383 cells incubated for 72 hours at 6.25 µg/mL and stained with Lysotracker red and Hoechst. The images were acquired using a wide-field microscope, the Incell 2000 and a x100 objective. (A) Live cells and in (B) freeze-dried cells.

4.55: Transmission electron microscopy images of freeze-dried HeLa cells. (A) HeLa cells section at a direct magnification of 12000x. (B) HeLa cell mitochondria at 25000x direct magnification. RER indicates the Rough endoplasmatic reticulum feature and M the mitochondria.

4.56: Imaging Flow Cytometry images of NR8383 cell line when incubated with different concentrations of amiodarone for 72 hours. The 2000 cells per condition were fluorescently stained with the nuclear dye Hoescht 33342 (blue) and Lysotracker (red), which stained the lysosomes. The number and size of lysosomes increased with the treatment concentration (white line scale bar is equal to 10 µm).

4.57: 2D ToF-SIMS representation of a depth profile of freeze-dried NR8383 cell dosed with 1.56 µg/mL amiodarone on glass slides (125x125 μm^3 field of view). Signal-to-noise of at least 3:1 throughout the analysis and final ion dose of 2.2 $x10^{12}$ primary ions/cm^2. The lateral resolution of this image was calculated to be 3.4 µm.[5]

4.58: Extrated ion images of a nuclear marker in red, amiodarone in green and a cellular marker in blue of the image shown in Figure 57 with the signal intensity scale on the side of each image. The endogenous markers are $C_5H_5O^+$ (*m/z* 81 Da) in red and phosphatidylcholine fragment from lipids (*m/z* 184 Da) in blue.

4.59: ToF-SIMS from freeze-dried cells incubated with 1.56 µg/mL amiodarone higlighting the amiodarone $[M+H]^+$ ion present in the spectra. This is the total spectra for all the depth profile acquisitions perfomed to produce image 57. There is a rich region at the low molecular weight part of the spectra and at 520 the amiodarone metabolite can be found and well as the isotopic patern of amiodarone on the insert part of the image.

4.60: ToF-SIMS amiodarone signal for five different depth slices of an NR8383 cell incubated with 1.56 µg/mL amiodarone for 72 hours. Laser scanning confocal microscopy results suggest that slice 2 is aproximately 200 nm deep into the cell, slice 5 is 500 nm, slice 10 is 1 µm, slice 20 is 2 µm and slice 30 isaproximately 3 µm. Field of view of 125 x125 μm^3.

4.61: Processed images of the three biological replicates. The green represents the amiodarone signal, and the blue represents one of phosphocholine signal (86 *m/z*). Field of view of 125 x125 μm^3.

4.62: Amiodarone signal intensity for the images shown in Figure 57, which is shown indicating the regions of interest selected, each ROI is a cell. The spectrum shows the intensity of the amiodarone signal in counts for the four selected regions of interest.

4.63: Plot comparing amiodarone signal obtained by ToF-SIMS on the y-axis with amount dosed on the x-axis (dose: 0.78, 1.56, 3.13 and 6.25 µg/mL). One replicate was performed for each concentration, except for 1.56 µg/mL for which three replicates where performed.

4.64: Confocal microscopy (LEXT by Olympus) of amiodarone incubated NR8383 cells. This technique allows the determination of the volume of the cells. These cells were then analysed using ToF-SIMS. (A) Light microscopy image; (B) Image generated by the laser confocal microscope (LEXT, colour scale from 0 to 5 µm) and (C) ToF-SIMS depth profile dataset of the cells seen on the confocal microscopy image, the larger image shows the amiodarone signal and the insert shows the total ion image. Scale bar is 15 µm.

4.65: (A) Correlation between ToF-SIMS amiodarone signal intensity and cell volume for the cells measured using laser confocal microscopy, in Figure 63. (B) Three-dimensional representation of the data shown in Figure 63.

4.66: Amiodarone signal obtained by ToF-SIMS measurement normalized to the cellular volume obtained by confocal laser microscopy plotted against the amiodarone concentration in the incubation media. In this plot three replicates were performed for the following amiodarone concentration 1.56, 3.13 and 6.25 µg/mL. The square in the box plot show the media value, and the whiskers show the upper and lower extremes of the data set

4.67: Chromatogram displaying the total ion count for the NR8383 cell lysate on a C18 column as a function of time.

4.68: Pairwise plots of the numeric data indicate a high degree of correlation within each of the treatment groups. Pairwise plots represent functions pairs of the scatterplots for each column in a matrix. The individual points represent individual proteins

4.69: Principal Component Analysis (PCA) of the data set of the amiodarone incubated NR8383 cells. The samples cluster according to the amiodarone incubation concentration, in pink the control samples cluster together, in red the 0.78 µg/mL amiodarone incubated samples cluster together but away from most of the other concentration points. In olive green the 1.56 µg/mL amiodarone incubated cells cluster with the 3.13 µg/mL incubated cells, green. In blue the higher concentration used, 6.25 µg/mL, clusters separately from the other drug exposure concentrations.

4.70: A distance matrix plot suggests the differences and similarities between sample groups. The different samples and replicates are displayed in a coloured matrix form where the colour indicates abundance as shown in the colour key.

4.71: STRING interactome of the up-regulated and down-regulated proteins identified as having a statistically significant change between the control and the dosed cells. Each sphere represents a protein, and their size is indicative of the information available in STRING. The images shows the interaction of the proteins identified as relevant in the statistical analysis with their closely related proteins that were also identified but whose changes were not deemed statistically significant.

4.72: Lipid class profile distributions (c is the control cells and S1 the amiodarone treated cells) of the lipidome experiment performed in amiodarone incubated NR8383 cells. The lipid classes key on the right hand side relates to the following lipid classes: Ceramides, ChE-Cholesteryl Ester, Co- Coenzyme, DG- diglyceride, LPC-lysophosphatidylcholine, LPE-lysophosphatidylethanolamine, LPG-lysophosphatidylglycerol, MG-Monoglyceride, PC- phosphatidylcholine, PE-phosphatidylethanolamine, PG-phosphatidylglycerol, PI-phosphatidylinositol, PS-phosphatidylserine, SM-sphingomyelin, TG-Triglycerides.

4.73: Data transformation of the lipid profiling analysis performed on amiodarone incubated NR8383 cells to reflect on the data obtained the doubling of the media concentration (A) Log 2 transformation for the amiodarone media concentration. (B) Intensity/ area of the lipid signal, untransformed and (C) Log 10 transformed intensity/ area of the lipid signal.

4.74: Curves for the fifty lipids which have the best fitting dose-response curves/lines for the lipidome profiling experiment in amiodarone incubated NR8383 cells. Each colour represents a lipid, the three points for the three replicates can be visualised for the different concentrations starting from the lowest to the highest (0 µg/mL to 6.25 µg/mL) from left to right

4.75: ANOVA model Manhattan plot of each dose versus the control of the lipid profiling study undertaken using amiodarone dosed NR8383 cells. The orange represents 0.78 µg/mL, green is 1.56 µg/mL, blue is 3.13 µg/mL and purple 6.25 µg/mL. The lipids that the data indicate to be changing the most are labelled on the plot; these are the lipids that could potentially be investigated further using pathway analysis.

5.76: ToF-SIMS 2D images of 3D data acquired from cells entirely consumed by the argon cluster source during analysis and was acquired in high-spatial resolution mode. NR8383 cells were incubated for 2 hours with 6.25 µg amiodarone/ mL. Composite image where red represents Ribose (*m/z* 81), blue shows the signal from the phosphatidylcholine lipid fragment (*m/z* 184) and green shows the amiodarone protonated molecular ion signal (*m/z* 646).

5.77: ToF-SIMS 2D images of 3D data acquired in the same way as Figure 76. The Figure shows HeLa cells incubated for 2 hours with 6.25 µg amiodarone/ mL. Composite image where red represents Ribose (*m/z* 81), blue shows the signal from the phosphatidylcholine lipid fragment (*m/z* 184) and green shows the amiodarone protonated molecular ion signal (*m/z* 646).

5.78: ToF-SIMS 2D images of 3D data analog to Figure 76 and Figure 77. The Figure shows Hek 293 cells incubated for 2 hours with 6.25 µg amiodarone/ mL. Ribose (*m/z* 81) is shown in red, the phosphatidylcholine lipid fragment (*m/z* 184) is shown in blue and the amiodarone protonated molecular ion signal (*m/z* 646) is shown in green.

5.79: ToF-SIMS 2D images of 3D data set acquired in the same way as Figures 76, 77 and 78. In this image the experiment was performed on HepG2 cells (6.25 µg amiodarone/ mL incubation for 2 hours). Composite image where red represents Ribose (*m/z* 81), blue shows the signal from the phosphatidylcholine lipid fragment (*m/z* 184) and green shows the amiodarone protonated molecular ion signal (*m/z* 646).

5.80: ToF-SIMS 2D composite image of secondary ions acquired using the lower spatial resolution mode used to collect the larger number of cell measurements. (A) NR8383 cells, (B) HeLa cells, (C) Hek293 cells, (D) HepG2 cells, incubated for 2 hours with 6.25 µg amiodarone/mL. Composite image with all the three extracted signals. Red represents Ribose *m/z* 81, blue shows the signal from the phosphatidylcholine lipid fragment (*m/z* 184), and green shows the amiodarone protonated molecular ion signal (*m/z* 646).

5.81: Frequency histogram of total amiodarone signal intensity (counts) per cell measured by ToF-SIMS for each of the four cell types, NR8383, HeLa, Hek293 and HepG2. The fitted normal distributions are displayed as a solid red curve.

5.82: (A) box plot showing single cell population measurements for each cell type using the ToF-SIMS integrated amiodarone protonated molecular ion counts for each cell NR8383 $n = 62$; HeLa $n = 86$; Hek 293 $n = 57$; HepG2 $n = 124$ (B) box plot showing cell population measurement using the LC-MS/MS assay, for each sample approximately 4.7×10^6 cells were used.

5.83: Comparison of the average cell associated amiodarone intensity determined by ToF-SIMS from a number of individual cells with the amiodarone cell uptake determined by LC-MS/MS from ensemble measurement of a large cell population (approximately 5000 cells per injection) for all cell lines incubated with 6.25 µg amiodarone/mL for 2 hours. The diamond represents the NR8383 cell line, the square represents HeLa cells, the circle represents HepG2, and the triangle represents Hek293 cells. The error bars represent one standard deviation from the average value. NR8383 $n = 62$; HeLa $n = 86$; Hek 293 $n = 57$; HepG2 $n = 124$

5.84: Amiodarone intensity determined by ToF-SIMS (mean plotted from individual cell measurements) versus the amiodarone cell uptake determine by LC-MS/MS population ensemble

measurement from approximately $4.7x10^6$ cells for all cell lines after incubation with 6.25 µg/mL for 2 hours for the high resolution imaging mode used (this data directly relates to Figure 76, 77, 78 and 79). The diamond represents the NR8383 cell line, the square represents HeLa cells, the circle represents HepG2, and the triangle represents Hek293 cells. The error bars represent one standard deviation from the average value.

6.85: Scatterplot of the multiple variables and replicates. The blue circle represents the neat compound, the red square represents the cell lysate mixture, the green diamond represents the compound spotted on tissue, the pink triangle represents the liver paste method and the black filled circle represents the compound incubated cells. The GSK compounds are identified by the last 3 digits of their designation.

6.86: Pairwise matrix plot comparing the five study conditions: neat, cell lysate, tissue, liver paste method and cell incubation. Each condition is compared with each other to produce a matrix of plots showing that the highest correlation with cells is achieved by the neat application of the compounds.

6.87: Pairwise plot of the correlation between the signal for each of the tested neat compounds and the compound signal in compound incubated cells. The r^2 value and the p-value calculated from that correlation are 0.377 and 0.0256 respectively.

6.88: PCA on the physical-chemical properties of the compounds. This analysis visualises how different the compounds are to each other despite them obeying the physical-chemical properties rules commonly used in drug discovery.

6.89: Scatter plot presenting the relationship between LogD and compound signal in the cell. The p-value is 0.387, and the r^2 value is 0.3614.

7.90: Optical confocal fluorescence microscopy of NR8383 cells co-cultivated with Green Fluorescent Protein (GFP) BCG for 48 hours. (A) Bright field image, (B) 561 nm channel GFP BCG, (C) 488 nm channel, Hoechst nuclear stain, (D) 640 nm channel, cell tracker red, and (E) composite image of the three fluorescence channels.

7.91: Micro-colonies of the tuberculosis model, *Mycobacterium bovis BCG,* overexpressing DprE1 incubated for two days with GSK3338058A at 10x the MIC (30 µM). (A) The location of BCG micro-colonies are depicted by the white arrows. The image shows three technical replicates (different areas

from the same sample), the scale bar is 5 µm (FoV 40x40 µm). (B) Region of the spectrum showing the $[M+H]^+$ of the compound can be seen.

7.92: BCG over-expressing DpRE1 incubated for 48 hours with GSK3338058A at 1x the MIC (3 µM) imaged using ToF-SIMS 5. (A) Total ion image for a larger area were several bacterial micro-colonies can be visualized, and on the right is the analogous image, with compound signal only. (B) Spectral representation of the region of the spectrum showing an ion consistent with the pseudo-molecular ion of the compound which was not observed in the control only experiment.

7.93: ToF-SIMS of BCG incubated with 10xMIC GSK3338058 (30 µM) for 48 hours. (A) Bacteria over-expressing DpRE1, the field of view is 50x50 µm. (B) Non-mutant empty vector control. The main image shows compound molecular ion signal and the smaller images to the side shows the total ion image for the same area as the main image. The field of view is 100x100 µm.

7.94: ToF-SIMS DpRE1 mutant BCG incubated with GSK2620592A at 50x the MIC (250 µM). (A) Shows a pictorial representation of the signal for 324 m/z for potentially two bacteria, with the total ion image on the right side. The scale bar is 5 µm. (B) Shows the spectra associated with the compound's molecular weight region showing the $M+H^+$ 324 of the compound.

7.95: Correlative analysis between AFM (C) and the same bacteria run on the ToF-SIMS (A and B). ToF-SIMS total ion image (B) as well as the compound molecular ion (A). This image shows potentially two bacterial cells side by side, the AFM shows roughness of the sample, this could be associated to the freeze-drying process these samples have undergone.

7.96: BCG DpRE1 incubated for 48 hours with GSK3338058 at 10x the MIC (30 µM) imaged using ToF-SIMS 5. The image shows in (A) the total ion image obtained by ToF-SIMS and the compound region of the spectra (454 m/z) acquired in the high spatial resolution mode. In (B), the AFM data can be observed, and in (C) the compound region of the spectra can be observed (454m/z). The conditions used for the acquisition of the images on Figure 95 were the same as Figure 96.

7.97: Full scan OrbiSIMS spectrum of BCG incubated with 10x the MIC of GSK3338058. Insert of the compound's pseudo-molecular ion. On the insert, the isotopic pattern matches the expected pattern for this compound.

7.98: KEGG obtained BCG metabolite pathways in which at least one metabolite was identified. The red and blue relate to aminoacid metabolism, in yellow the carbohydrate associated metabolite pathways can be seen, in green all the pathways identified associated to lipid metabolism can be identified. The nucleotide metabolism pathways can be found in purple, and vitamin and mineral in sky blue.

List of Tables

3.1: Lysotracker signal as a functions of amiodarone concentration in NR8383 cells using imaging flow cytometry. In this table the lysotracker signal is used as a surrogate for lysosome size, and therefore amiodarone accumulation. The tables show a clear increase of lysotracker signal with the amiodarone dose. However, once it reached 3.13 µg/mL the lysotracker fluorescence plateaus.

3.2: Summary statistics of the fifteen samples (three replicates for each condition, NR8383 cell incubated with 0, 0.78, 1.56, 3.13, and 6.25 µg/mL amiodarone for 72 hours collected in this study suggest no obvious outliers, the different samples and replicates are depicted in each row and in the different columns the statistical results can be found.

3.3: Proteins identified as significantly differentially expressed when comparing the 6.25 µg/mL incubated samples with the control samples from the amiodarone incubated NR8383 cell data set.

3.4. The five lipids whose dose-response curves best fitted the dataset. DC stands for diradylglycerolipids, PC stands for phosphatidylglycerols, and TG refers to triradylglycerolipids.

5.5: Summary table of the compound GSK number, image identifier (usually the last three digits of the whole number), the structure of the compound and in which matrix it was identified. In red are the compounds whose signal was not visible and in green are the compounds whose molecular ion were identified.

Contents

1) Introduction……..….27-30
2) Literature Review……...….31-100
2.1) SIMS overview……..…….31-49
2.1.1) SIMS sputtering……....……34-36
2.1.2) SIMS ionization…….36-37
2.1.3) SIMS instrumentation……....37-42
2.1.4) SIMS biological sample preparation……..…43-45
2.1.5) SIMS of biological samples……...……45-49
2.2) Other cell analysis techniques: Microscopy……49-60
2.2.1) Fluorescence microscopy……..……..51-55
2.2.2) Tomographic microscopy……..…55-56
2.2.3) Confocal laser scanning microscopy……...……...56-57
2.2.4) Electron microscopy……..……..……..…57-58
2.2.5) Atomic force microscopy…….....……..58-60
2.3) Other cell analysis techniques: High Mass Resolution Liquid Chromatography tandem Mass Spectrometry (LC-MS/MS)……...……...……...60-67
2.3.1) Proteomics…….……..…….……..61-63
2.3.2) Lipidomics……..……63-66
2.3.3) Metabolomics……...……..……66-67
2.4) Physical and chemical properties of pharmaceutical compounds and ionization…….....68-79
2.5) Cell lines and amiodarone……79-89
2.5.1) Amiodarone……..……...79-85
2.5.2) NR8383 cell line……....……85-86
2.5.3) HeLa cell line……...……86
2.5.4) Hek293 cell line……...…...……86-88
2.5.5) HepG2 cell line……..……88-89
2.6) Mycobacterium……..…….90-100
2.6.1) Disease pathogenesis……...…92-94
2.6.2) TB treatment……94-96
2.6.3) Mycobacteria cell wall…….……96-98
2.6.4) BCG as a model for TB……..……99-100

3) Experimental……....…..……101-117
3.1) Alveolar macrophage treatment with pharmaceuticals……..….101-103

3.2) Cell lines culture conditions……103
3.3) ToF-SIMS conditions……..……103-104
3.4) Hematoxylin & Eosin…….….104
3.5) Fluorescent microscopy……...…104-105
3.6) Imaging flow cytometry……...…105-106
3.7) Electron microscopy……106
3.8) Refractive Index microscopy……..….……106
3.9) Laser confocal microscopy…….……107
3.10) Proteomics…….……107-110
3.10.1) In-solution digest……...……107-105
3.10.2) MS analysis……..…..……108-109
3.10.3) Data processing analysis……109-110
3.11) Lipidomic profiling……..……..111
3.12) Quantitative LC-MS/MS…….111-112
3.13) Physical-Chemical properties…….……113-114
3.13.1) Materials…….……113
3.13.2) Sample preparation……...…113-114
3.13.3) ToF-SIMS analysis……...…114
3.14) BCG analysis…….115-117
3.14.1) Bacterial culture conditions…….…115-116
3.14.2) Sample preparation……..116
3.14.3) ToF-SIMs analysis conditions……116
3.14.4) OrbiSIMS analysis conditions……..…116-117
3.14.5) AFM analysis conditions……..……117

4) Results I: Visualization of intracellular amiodarone using ToF-SIMS……...……...…118-163
4.1) Bright field microscopy of compound incubated NR8383 cells……119-124
4.2) Fluorescent microscopy of amiodarone incubated NR8383 cells……124-129
4.3) Effect of freeze-drying on mammalian cells……...…129-131
4.4) Imaging flow cytometry of amiodarone incubated NR8383 cells……..…131-134
4.5) ToF-SIMS of amiodarone incubated NR8383 cells……..……134-142
4.6) Correlative ToF-SIMS and scanning laser confocal microscopy of amiodarone incubated NR8383 cells…… …142-146
4.7) Proteomic profiling of amiodarone incubated NR8383 cells……..146-157
4.8) Lipidomic profiling of amiodarone incubated NR8383 cells…….……157-163

5) Results II: Amiodarone ToF-SIMS model applied to other cell lines……...……164-174

6) Results III: Exploring applicability of ToF-SIM to other pharmaceutical compounds……175-187

7) Results IV: Exploring the applicability of SIMS to the analysis of bacteria……..……..188-201

8) Conclusions……..202-206

8.1) Summary……..……202-205

8.2) Future Perspective……...…….205-206

Bibliography…….207-219

Annex……...…….220-333

1. Introduction

The general objective of this thesis is to probe the distribution of pharmaceutical compounds in cultured cells using SIMS. The pharmaceutical industry has struggled to develop reliable and translatable models that are representative of the drug's effect on the patient, hence its absolute reliance on clinical trials. Human clinical trials are always going to be a fundamental part of the drug development process, as only the human body conveys its complexity.[45] However, being able to visualise that the drug is inside cells and tissues can be extremely advantageous for the drug discovery process, as it is the first link on a chain of desired events. Once the internalization of the drug molecule has been established, this provides confidence that one of the requirements of what makes a good drug is met. SIMS has both the spatial resolution and sensitivity to provide this answer, and for this reason it can potentially play a critical role in the drug discovery process.

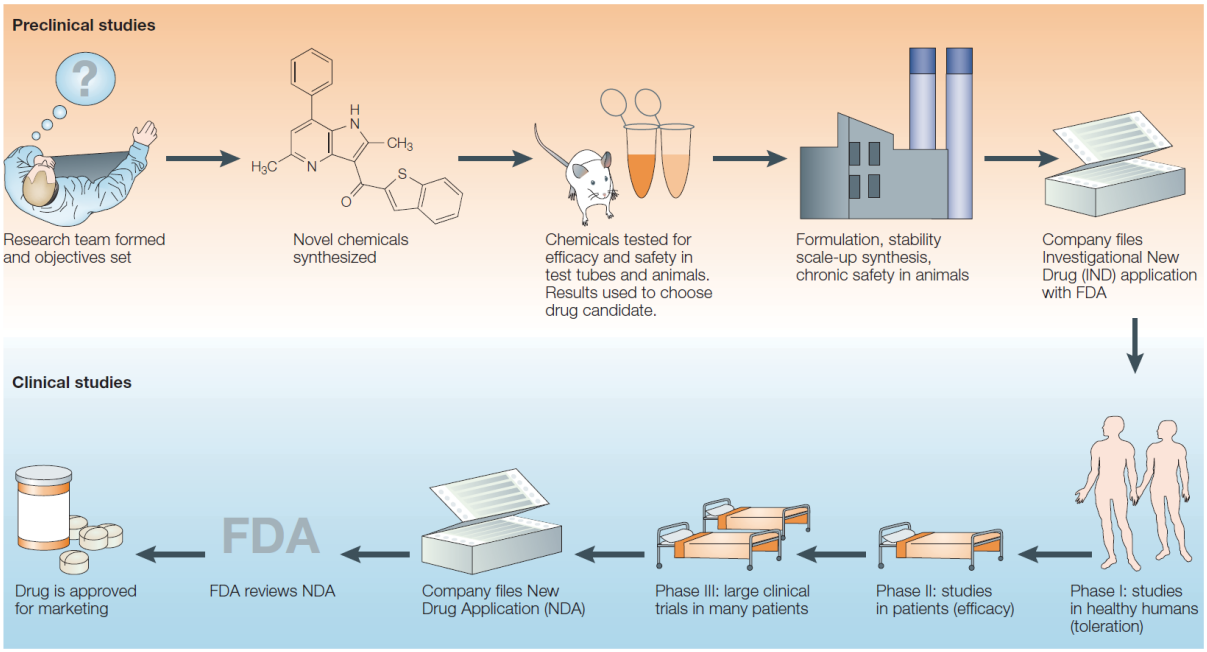


Figure 1: Drug discovery and development diagram.[7] The picture describes both the preclinical and clinical studies workflows. The project team investigates the target and conducts research both in vivo and in vitro before the data is submitted as a New Drug (ND) application to the Federal Drugs Administration (FDA). Once the ND application is approved, the phase I, II and III clinical trial stage can start. If this phase is successful the application for a new drug can be filled, the data is then reviewed by the FDA and the drug is approved for the market. Reproduced with the permission of the publisher, Springer Nature.

The classic drug discovery pipeline comprises several steps, these are fundamental in this process as they always precede human clinical trials steering the direction of *the drug discovery and development process,* which is outlined in Figure 1. The process is divided in two parts, research or discovery phase, a more creative/ less regulation bound environment, while drug development is a much more controlled environment, in which the lead molecule is subjected to a range of tests to ensure compliance with regulatory specifications.[46]

The drug discovery process starts by identifying a disease area and a biological target. *Target identification* is achieved by conducting experiments centred on the biology of the disease target, an endogenous entity responsible for the disease state in question is defined. This step is followed by either designing a range of compounds that are thought to be effective against that target, or embarking on a High Throughput Screening (HTS) campaign to identify molecules that could be useful against the target of interest (*the discovery phase)*.[47] The primary issue with the latter approach, is that it is incredibly complex to design an HTS that has the necessary speed to cover sufficient candidate compounds and is still biologically representative of the disease model studied. Following on from the HTS, which is also commonly referred to as a 1st tier assay, there is a need to develop assays (2nd or 3rd tier assays) that follow these high throughput efforts to interrogate the mechanism behind the drug's effect observed in the HTS and thus validate the compound activity in vivo (*lead validation)*.[47] These assays are either cell or animal-based models, however in many cases, both the cell and the animal are like black boxes, the input and output are known, however the underlying mechanism is unknown, and therefore there is no real understanding of the intricate complexity of the target's biology, and decisions are made based on the phenotypic response observed. [48,49]

Often these campaigns fail to find a suitable drug candidate, this could be due to several different reasons such as reduced compound permeability, off-target activity and target inaccessibility amongst others, illustrated in Figure 2 for cellular targets.[8] The analytical techniques currently available within drug discovery, often merely hint at the reasons why a compound fails to become a drug. Based on these results the compound is often redesigned to try to overcome the issues. An improved understanding of

the reasons why the compound failed would improve success rates in early drug discovery and help reduce the currently high attrition rate in pharmaceutical Research and Development (R&D).[50]

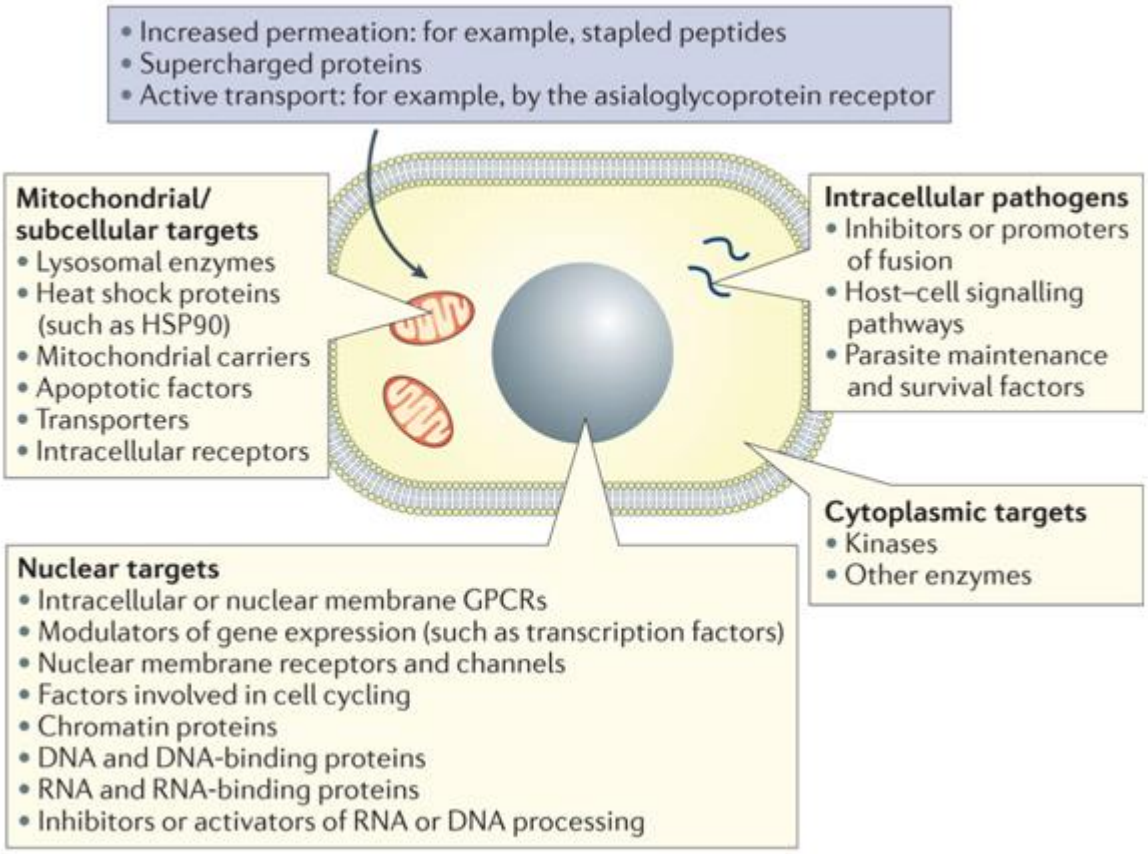


Figure 2: Drug discovery intracellular targets[8] Most drug targets are intracellular, kinases can be mainly found in the cytoplasm, transporters are mainly found in the mitochondria and there are a multitude of genetic targets in the nucleus. Reproduced with the permission of the publisher, Springer Nature.

There are several techniques that are presently used to probe the biology of disease targets, all with advantages and limitations. For instance, Matrix Assisted Laser Desorption Ionisation (MALDI) has shown excellent results in characterising the distribution of drug compounds in tissue.[51] Still, it has limited spatial resolution, therefore it is not suitable for interrogating cells in culture as it cannot resolve sub-cellular distribution. Even the most recent applications from a leader in this field, Richard Caprioli, show only a 5 µm resolution.[52] Other limitations of MALDI are the requirement for deposition of a

matrix on the sample and the fact that it does not produce three-dimensional information. In contrast, electron and light microscopes have a very high spatial resolution, especially the reported cryo-electron microscopes with 2.6 Å resolution that allow structural elucidation of a virus.[53]. In the vast majority of cases, in order for compounds to be observed for both electron and light microsopy, they need to be labelled, a process that might affect their physical-chemical properties, or contain unique moieties that differentiate them from the complex biological background.[54] Liquid- Chromatography -Tandem Mass Spectrometry (LC-MS/MS) can also be used to determine the presence of drug inside the cell[55] as it is very sensitive and can be quantitative, however it contains no localization information since the cells must be destroyed to extract the analyte. In some cases, a controlled destruction protocol can be employed to infer the analyte's localization, such as micro-laser dissection to excise parts of the tissue to then perform LC-MS/MS.[56]

In summary, the current technologies are limited to either label-free at micrometre resolution or sub-micrometre resolution with the addition of tags. Therefore, it is necessary to develop label-free molecular imaging techniques with high spatial resolution (50 nanometres) and sensitivity that allows tracking of intracellular drug distribution. Developing an imaging system to address these issues is where the OrbiSIMS concept comes in. The potential of combining the fast imaging Time-of-Flight analyser (ToF) in most SIMS instruments with the slower, but highly accurate Orbitrap analyser, as proposed by Ian Gilmore et al., increasing the potential applications of this technique which is introduced in the following chapter.[57]

The main objective of this work is to determine if SIMS is suitable to interrogate the presence of pharmaceutical compounds inside cells, both mammalian and bacterial with the aim to provide clear evidence of cellular drug internalization, this is crucial as most drug targets are intracellular. In order to provide further insight on the results obtained using SIMS, other established techniques, such as microscopy and LC-MS/MS were also used in this thesis.

2. Literature review

2.1) SIMS overview

SIMS is an ultra-high vacuum analytical technique in which mass spectrometry is used to analyse ions emitted by a surface after the surface is bombarded with a primary ion beam (including Bi_3^+, $Ar_{2000}^+$and C_{60}^+ amongst others). During surface bombardment by the primary ion beam, a multitude of species are sputtered from the surface, mainly neutral species but also electrons and more importantly ions (Figure 3). These charged species are then able to be extracted using an applied potential into a mass spectrometer (MS) providing a "chemical picture" of the surface.[58]

SIMS was first regarded as a potential characterisation tool in the mid-1970s by the Benninghoven and Vickerman groups but not in its current form. Monoatomic argon ion beams were used along with a quadrupole analyser to characterise the adsorption of carbon monoxide on metal single crystal surfaces.[3,58] In the early 1980s, Briggs et al. published characterisation from a synthetic polymer using argon and xenon ion beams with a quadrupole analyser[59] and this developed to improve lateral resolution using liquid metal ion beams approaching 100 nm spatial resolution.[60] The late 80s saw Briggs and Hearn using a gallium ion beam and a ToF set-up[51] and in the early 90s Vickerman's group collaborated with Winograd's group to develop a SIMS instrument specific for biological samples[60]. According to Vickerman, the first biological experiment performed focused on the analysis of the lipid content of the membrane junction region of protozoa. Since the beginning of the millennium SIMS has been used extensively to determine lipid profiles for several disease states such as Duchenne muscular dystrophy and Fabry disease, amongst others, by the Brunelle lab. This resulted from the detection of lipids and other small biomolecules with high abundance.[61,62]

Metal cluster ion beams, such as Bi_3^+ result in higher ion yields, as the sputter yield increases, however, they still create significant sub-surface damage, so the analysis is constrained to the upper surface. Polyatomic ion beams, with larger cluster sizes such as C_{60}^+ and more recently gas cluster ion beams, such as Ar_{3000}^+, create reduced damage or in the latter case almost no damage to the sample. The

combination of both beams can be beneficial for depth profiling. The old, so called static limit may now be overcome leading the way to improved sensitivity since more material can be analysed.

SIMS has been phrased as a non-destructive technique as it consumes only 1/10 of the uppermost atomic monolayer.[58] A beam of primary or polyatomic ions (between 1 keV to 50 keV) hits the surface resulting in a sequential series of collisions of the sample's constituent atoms and molecules are disturbed, called the collisions cascade, as shown in Figure 3.

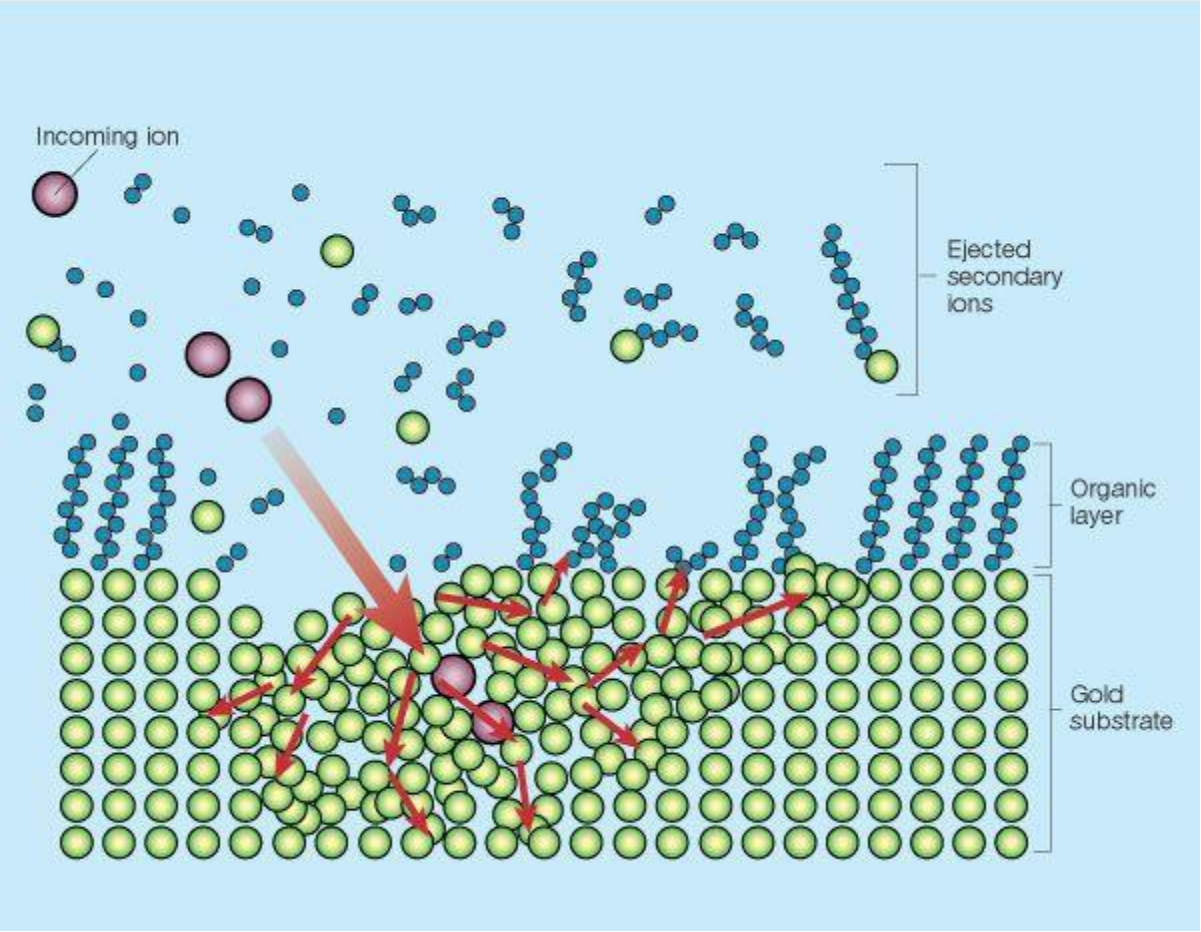


Figure 3: SIMS sputtering schematic by Castner et al.[9] The image shows ions being fired at a substrate. The collision cascade observed is the result of collisions following the impact of the primary ion beam. As a result, a range of molecular and atomic species are ejected from the surface. Only approximately 1% are ions which are then guided to the detector.[9] Reproduced with the permission of the publisher, Springer Nature.

SIMS experiments can be performed in both two (2D) or three (3D) dimensions. A 2D experiment, or surface analysis, provides information from the top 1-2 nm of the sample. In a 3D experiment, also referred to as depth profile, the chemical and spatial information originates both from the surface and from consecutive layers below the surface, as a sputtering beam is used to erode the sample away to provide information as a function of depth.[63] Regardless of the SIMS modality used for any given analysis, SIMS involves the analysis of secondary ions, their ionisation occurs quite close to the surface and the surface's electronic state influences it, this is represented by the following equation[58]:

$$I_m = I_p\, y_m \alpha^+ \theta_m \eta$$

I_m - Secondary ion current of species m
I_p - primary ion particle flux
y_m - sputter yield
α^+ - ionisation probability to positive ions
θ_m - factorial concentration of the chemistry m in the surface layer
η - transmission of the analysis system

The sputter yield (y_m) is dependent on the total number of particles sputtered which depends on the primary particle characteristics, such as mass and energy. There is a fine balance between having a good ion yield and the degree of damage to a surface. Lower molecular weight ion beams cause more damage than higher molecular weight ions beams, where the ion energy is distributed between all the atoms at impact, this introduces the concept of damage cross-section. This can be summarised in the equation below[58]:

$$I_m = I_{mo} \exp(-\sigma I_p)$$

I_m - Secondary ion current of species m
I_p - primary ion particle flux
σ - damage cross-section

Higher molecular weight ion beams have a yield of several hundred molecules per impact and a damage cross-section below 10^{-15}, this accounts for the high sensitivity of this technique.

The Time-of-Flight (ToF) analyser is the most commonly used in SIMS for the analysis of both organic and inorganic molecules, however other mass spectrometers are available and that now currently extends to hybrid instruments with the introduction of the OrbiSIMS in 2016.[3] SIMS has potentially a wide variety of applications and has been used in the analysis of everything from biological cells to smartphone screens and moon rocks.[58]

Most of the data shown in this thesis, was acquired using a dual beam approach with a metal ion gun beam as the analysis beam in most cases, and an argon cluster beam as a sputter beam. The liquid metal ion beam is highly focused and it allows for excellent spatial resolution, however it is quite damaging to the surface of the sample, and for this the gentler polyatomic ion gun can be used to sputter the damaged surface away revealing a new and damage-free surface to be further probed with the metal ion gun, this process occurs recurrently until the end of the experiment is reached. Delayed extraction mode was also used in instances where a high-mass-resolution method is referred, as the mass resolution is improved due to improved ion energy compensation.[64]

At present, SIMS instruments can generate both 2 and 3D chemical images, but further improvements are foreseen for the future. For example, ion beams can be used in direct current (DC) mode which segregates the sputtering from the mass spectrometry; this can potentially allow the use of other analysers and therefore tandem mass spectrometry. In addition to this, DC allows much higher duty cycle, lowering analysis time; the downside is the decrease in transmission.[58]

2.1.1) SIMS Sputtering

SIMS was first regarded as a useful technique for surface analysis towards the end of the 1960s as a consequence of the work performed in Munster by the Benninghoven group. However, the poor ion yield was an issue for detecting and in particular imaging low concentration species.

Big advances in sensitivity came with the use of cluster projectiles such as Bi_3^+, C_{60}^+ and more recently gas clusters ion beams (GCIB) putting forward beams of argon clusters molecules. The nature of a polyatomic beam allows for the energy of the beam to be spread across all atoms that form that beam,

which means that the damage to the surface is reduced, reducing ions fragmentation and therefore allowing the analysis of intact molecules rather than fragments.[58,65]

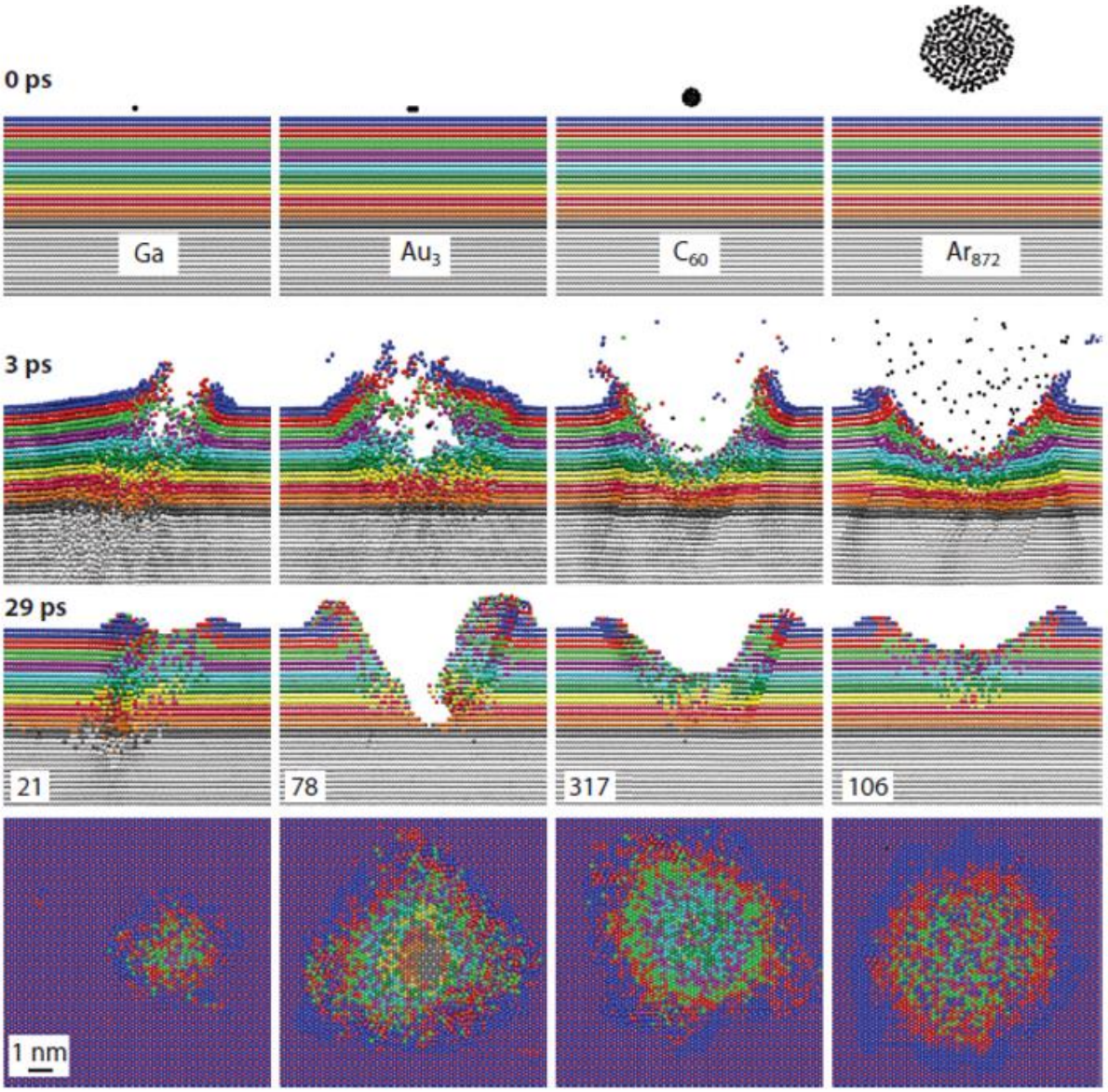


Figure 4: Computer simulation of the molecular dynamics of different primary ion beams, with a kinetic energy of 15 keV, bombarding an Ag (111) crystal. The different atomic layers are represented with different colours and the grey particles represent a depth of 4.6 nm. The first three rows show a cross-section of the crystal, the first row show the system at 0 ps, the second row shows the system at 3 ps, and the third row at 39 ps. The bottom row shows a top view of the impacted area. The numbers displayed on the third row are the number of atoms ejected upon primary ion impact. Reproduced under Attribution 3.0 Unported.

The sputtering yield (Y) is the average number of atoms removed from the target per incident particle (atom per ion). It is dependent on the energy of the primary ion beam and the type of primary ion beam.[58]

In Figure 4, computer simulations of the molecular dynamics that results from the bombardment of a surface with different types of primary ion beams can be observed. The kinetic energy used was 15 keV, which means that the kinetic energy varies between 15 keV for gallium and 17.2 eV for argon. As it can be observed, the ion beams that penetrate deeper into the material are Ga and Au_3, hence causing more damage to the surface, however the number of sputtered atoms is the lowest from the ones observable in Figure 4.

When looking at the craters resulting from the impact of the C_{60} or Ar_{872} primary ion beams their appearance is similar, however the depth-damage caused by the gas cluster ion beam is much lower, and the ion yield is approximately one-third of the ion yield generated using C_{60}, it is thought this is due to the lower kinetic energy per particle in the cluster. This can also have some effects on the ionization probability which tends to be lower for gas cluster metal ion beams.[66]

2.1.2) SIMS ionization

An essential pre-requisite to generating secondary ions is the fact that sputtering results from the incidence on the surface of the primary ion beam. The other requisite is the ionisation of some of the sputtered species. This process is not completely understood, but there is clear evidence of matrix effects where components both enhance and suppress secondary ion yields,[58] and low ion yield are the main factors thought to influence SIMS ionization.[67]

The typical SIMS ionization probability is thought to be below 10^{-5}, therefore, typically the ion yield from a 1 μm^2 pixel area under static conditions is less than 0.01. From Figure 4, it is clear that an increase in the cluster size results in the increase of the ion yield, however if the cluster size increases without the increase of the beam energy, the ion yield will decrease and as the impact energy of the cluster

decreases so does the ionization efficiency. Therefore, increase in sputtering yield does not always result in increased ionization efficiency.[68]

Matrix effects are defined as chemical environment induced changes in the ionization efficiency up to several orders of magnitude, the matrix effect phenomenon is especially prominent in biological samples, as their compositions tends to be highly heterogeneous, composed amongst others, of lipids, proteins, metabolites and nucleic acids.

Jones et al. demonstrated that proton exchange was the most prevalent ionization mechanism in ToF-SIMS, molecules with high ionization efficiency suppress the ionization of the molecules with low ionization efficacy.[69] Several different approaches have been attempted to reduce matrix effects, they range from gold coating of the sample to the use of water polyatomic beams.[70]

Enhancing secondary ion generation can also be performed by using laser post ionisation; a laser illuminates the plume just above the sample and just before the extractor, which potentially ionises the neutrals that are sputtered from the analyte. Unfortunately, the laser beam is not capable of ionising all the species, and the ionisation efficiency is quite variable between samples; therefore the community needs to work on increasing efficiency and robustness of these laser beams.[71]

Currently, the foremost improvement to increase ionisation efficiency lies with primary ion beam improvements. The ideal ion beam needs to produce the highest secondary ion beam with the lowest decline of molecular information.[72]

2.1.3) SIMS Instrumentation

There are many configurations of a SIMS instrument, different primary and sputter ion guns and mass analysers, but in this thesis, the focus will be primarily on ToF-SIMS, or the novel OrbiSIMS.[57] The ToF-SIMS instrument has one or more primary ion guns, once the beam hits the target the ions generated are collected using the extractor electrode. Inside the instrument, the sputtered ions are guided by the ion optics to the mass analyser and their mass to charge can then be determined (Figure 5).

ToF is a mass analyser in which the mass to charge (*m/z*) ratio is determined by the time it takes for the ion to reach the detector. The time of flight is simply proportional to the square root of the mass of the ions.[73]

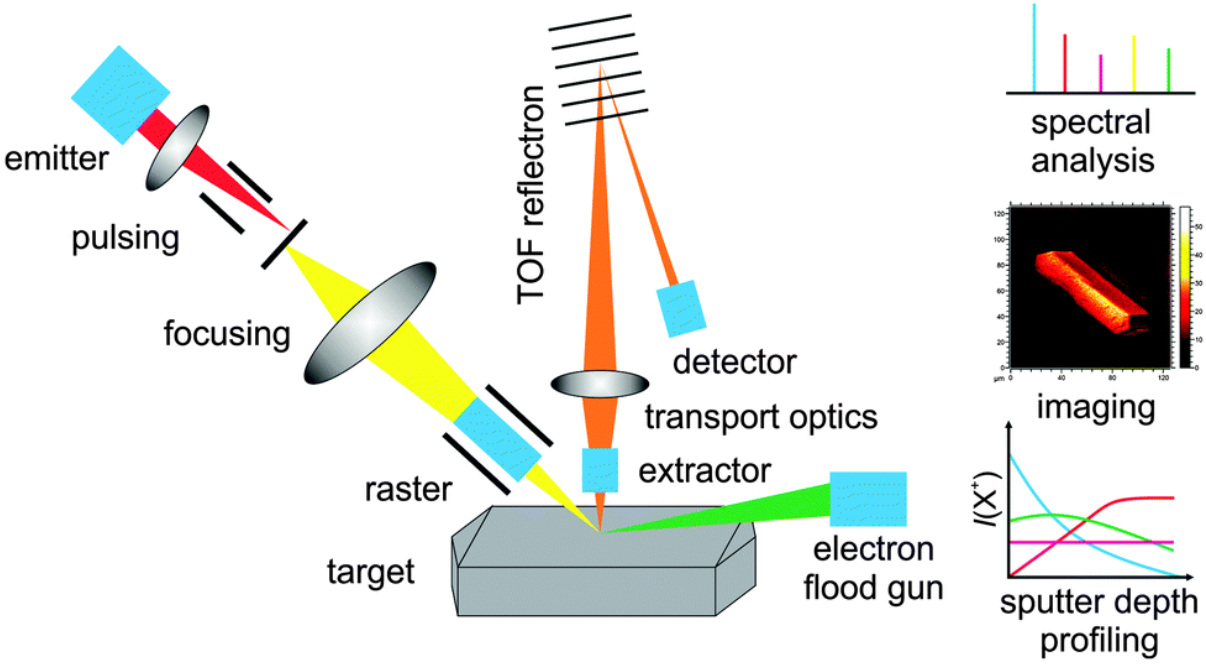


Figure 5: Simplified schematics of IONTOF's ToF-SIMS. The image represents the basic components of a ToF-SIMS instrument: target plate where the sample is introduced, electron flood gun, the primary ion gun, the ion optics, the time of flight analyser and finally the detector. Attribution 3.0 Unported, Hofmann and al. image from the Royal Society of Chemistry

This instrument is equipped with a reflectron mass analyser, which is a low-pass filter, the acceptance of the analyser can be adjusted by adjusting the reflectron voltage; a lower reflectron voltage means fewer ions will be transmitted.[74] The field strength of the electric field above the sample surface is crucial for the extraction of the secondary ions, this is a tuneable parameter that needs to be adjusted as it must be high enough to extract the ions but low enough so the ion beam is not distorted.

The time of flight dispersion of the secondary ions in the analyser is minimised by matching the dynamic emittance when the surface is rastered with the primary ion beam. The reflectron is an energy focusing device meaning that ions with a slight difference in energy have the same time of flight (energy focusing).[74]

To ensure good mass resolution, the primary ion gun has to be operated in bunch mode, where the pulse of ions is sent through a condenser in order to bunch them together to create a below nanosecond ion packet.[75] Mass resolution is strongly influenced by the width of the primary ion pulse, which needs to be below 600 ps for optimum performance.[74]



Figure 6: ION-TOF IV at the School of Pharmacy facilities (The University of Nottingham).

The 50 kHz cycle repetition rate or pixel frequency, as well at a 60 nm spatial resolution on ideal samples, are excellent advantages of the ION-TOF 5, however the mass resoltution is around 10000, for this reason the OrbiSIMS combines the speed of the ToF analyser with the high mass resolution orbitrap analyzer as well as MS/MS capabilities enabling a more accurate identification of the molecules present in the sample.[57]

The Orbitrap is a type of mass analyser that was first introduced in the year 2000 by Alexander Makarov.[76] The Orbitrap technology has made a great contribution towards the MS-based proteomics boom that we are currently experiencing, due to its high mass resolution and accuracy. [77,78,79,80]

The Orbitrap employs orbital trapping in a special electrostatic field. The mass-to-charge ratio is derived from the frequency of the harmonic oscillation of ions along the axis of the field, which is then transformed using Fourier transform algorithms.[76]

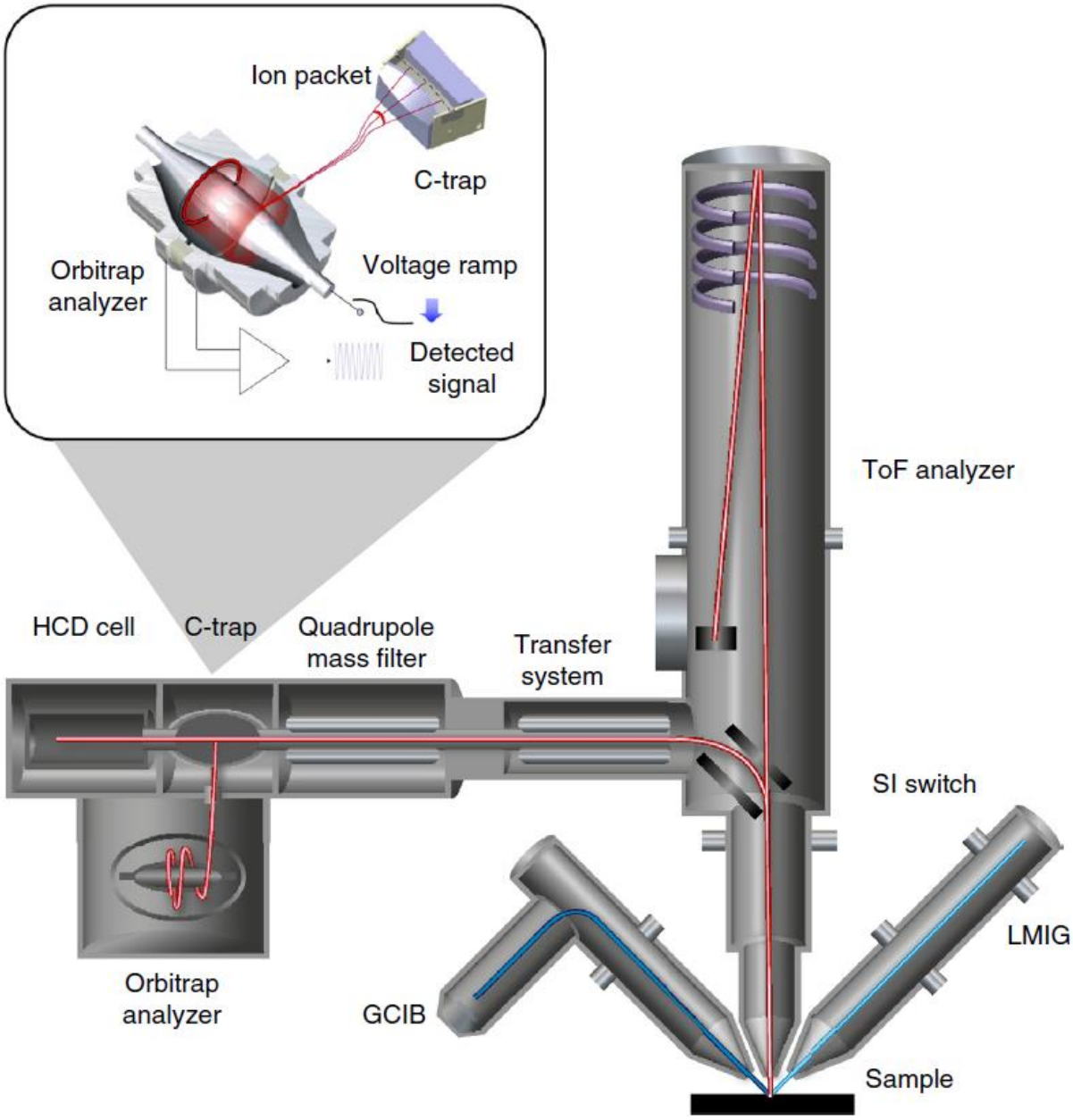
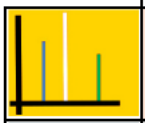
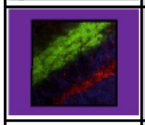


Figure 7: OrbiSIMS schematics. At the centre of the Orbitrap mass analyser, there is a spindle where the ions orbit around as a result of a dynamic electrostatic field.[3] The two-beam set up is maintained to allow greater flexibility of analysis, most of the ion guiding system to the ToF analyser is similar to the ToF-SIMS 5 except the secondary ion switch, which allows the ions to be sent either to the ToF or Orbitrap analyser, the part of the Orbitrap system after the quadrupole is very similar to a QExactive HF. Instrument components not to relative scale. The Orbitrap diagram is included as an insert on the OrbiSIMS schematic. Reproduced with the permission of the publisher, Springer Nature.

As can be observed in Figure 7, the Orbitrap consists of a central spindle-like electrode along the axis and an outer barrel-like electrode.[76] The advantages of the Orbitrap are:

- High mass resolution, currently at 480,000 with the new 18 Hz ultra-high field Orbitrap.
- Increased number of ions are stored in the trap owing to larger trapping volume with reduced space charge effects.
- High mass accuracy (<1ppm with an internal calibration and <3ppm with an external calibration) and high dynamic range (>5000 within a single scan).[76]

	Method	Beam modality	Mass analyzer	Mode
	Surface spectra (1D)	Single beam (Bi_n or Ar_n)	ToF	1
			Orbitrap analyzer	2
	Depth profiling	Single beam (Ar_n)	ToF	3
		Dual beam (Ar_n and Bi_n)	Orbitrap analyzer	4
			Dual analyzer	5
	Imaging (2D)	Single beam (Bi_n or Ar_n)	ToF	6
			Orbitrap analyzer	7
	3D Imaging	Single beam (Ar_n)	Orbitrap analyzer	8
		Dual beam (Ar_n and Bi_n)	ToF	9
			Dual analyzer	10

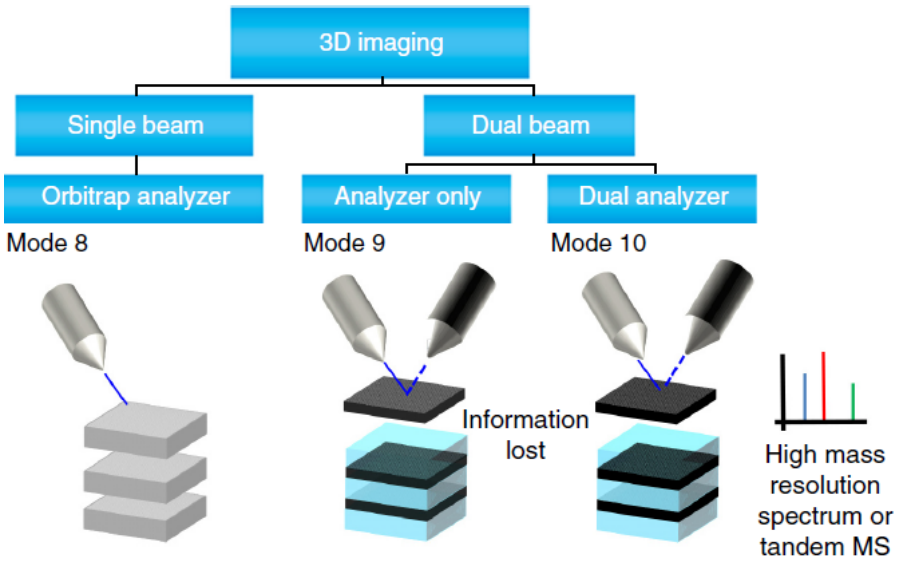


Figure 8: Table of operational methodologies of the OrbiSIMS, and diagram of the different imaging modalities. The table shows the flexibility of the OrbiSIMS, it allows the acquisition of surface spectra only using both the Orbitrap (mode 2) and

the ToF analyser (mode 1), spectral depth profile acquisition using the Orbitrap (mode 4), the ToF (mode 3) and the two detectors (mode 5). In imaging mode, it can perform 2D imaging using the ToF (mode 6) or the Orbitrap analyser (mode 7). The 3D imaging capabilities are further illustrated on the diagram, the Orbitrap analyser can be used for imaging by itself (mode 8) or in a dual beam setup, used in conjunction with the ToF analyser (mode 9) on the same scan, or used to analyse the ions that result from the sputter scans (mode 10), in this mode no information is lost, as the imaging is performed using both analysers. The data obtained in this mode has both high spatial resolution (obtained with the focused Bismuth beam and the ToF analyser) and high mass resolution and MS/MS capabilities (obtained with the Argon beam and the Orbitrap analyser).[3] Reproduced with the permission of the publisher, Springer Nature.

The development of the OrbiSIMS has been a collaboration between the NPL, ION-TOF, ThermoFisherScientific, GSK and the University of Nottingham. This new instrument combines secondary ion ionisation using argon and bismuth guns with two mass analysers, a ToF and an Orbitrap, this allows a number of different imaging modes, as illustrated in Figure 8.

The OrbiSIMS combines the high mass accuracy and mass resolving power of the Orbitrap with the speed of the ToF analyser as shown in Figure 8. We have demonstrated the ability to map the localisation of endogenous and exogenous species in both cells and tissues with a spatial resolution of 1.34 µm for organics and 172 nm for inorganics, and a mass resolving power of 240000@ m/z 200.[3]

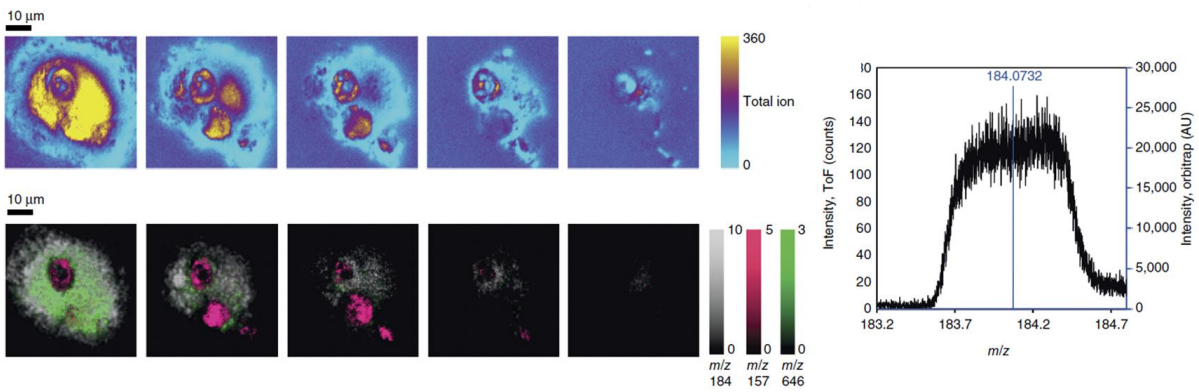


Figure 9: Single NR8383 cell incubated with amiodarone. Top image series shows the total ion image, and the bottom series shows the compound signal (in green) the phosphocholine marker (in grey) and the nuclear marker (in magenta). The spectra on the right shows the difference in peak width between the Orbitrap analyser (blue) and the ToF analyser (black).[3] Reproduced with the permission of the publisher, Springer Nature.

2.1.4) SIMS biological sample preparation

The first step for cell analysis is to establish a suitable method to introduce the cells into the ToF-SIMS instrument. SIMS is an ultra-high vacuum technique and biological samples are abundant in liquid content, as life requires water, this means that biological samples and SIMS are not compatible without any prior sample preparation. For meaningful analysis to be obtained, both chemical and structural integrity of living samples needs to be maintained for analysis in a vaccum environment. Fixing the cells (e.g. with glutaraldehyde), as for optical or electron microscopy, is not possible as the fixing process would most likely change the localisation of small drug-like molecules and the sample chemistry.

One of the methods to analyse cells in ToF-SIMS is freeze-fracturing. The cells are placed between two substrates with beads that are the same height as the cell to protect them from being crushed. They are then placed in a cryogenic liquid, such as liquid ethane and propane, as these liquids are not affected by the Leidenfrost effect as is the case for liquid nitrogen. Therefore, the freezing rate (ideally around -10000ºC/sec) is higher, reducing the potential formation of large crystals that cause cell disruption. The sandwich is then snapped, and the interior of the cells is exposed for analysis.[72,81]

Robinson et al. evaluated three sample preparation methods, frozen-hydrated after cryofixation, lyophilised after cryofixation and chemical fixations. They concluded that the condition that best preserved the structural integrity of the cell was a frozen hydrated preparation, which they proposed can also increase ion yields due to reduced cross-section damage at cryogenic temperatures.[82]

Robinson et al. developed a Z-correction algorithm in Matlab that allowed data sets to be corrected for the 3D/2D issue. They utilised Z-corrected data from fibroblasts that correlated exceptionally well with Atomic Force Microscopy (AFM) data generated on the same samples. Cells are three dimensional, and the data acquired by ToF-SIMS is effectively projected on a 2D image plane, inaccuracies can arise due to topography effects, and therefore the data processing step needs to take this into consideration.[82]

Cryo-preservation has the advantage of better preserving the cells both chemically and structurally than freeze-drying. However, the added time required to analyse cryo-preserved specimens might negate the benefits, especially if the damaged caused by the lyophilisation (freeze-drying) process is on structures

that are below the spatial resolution limit of the instrument. Therefore, for the majority of the analysis performed in this thesis the method of cell preservation used was lyophilisation.

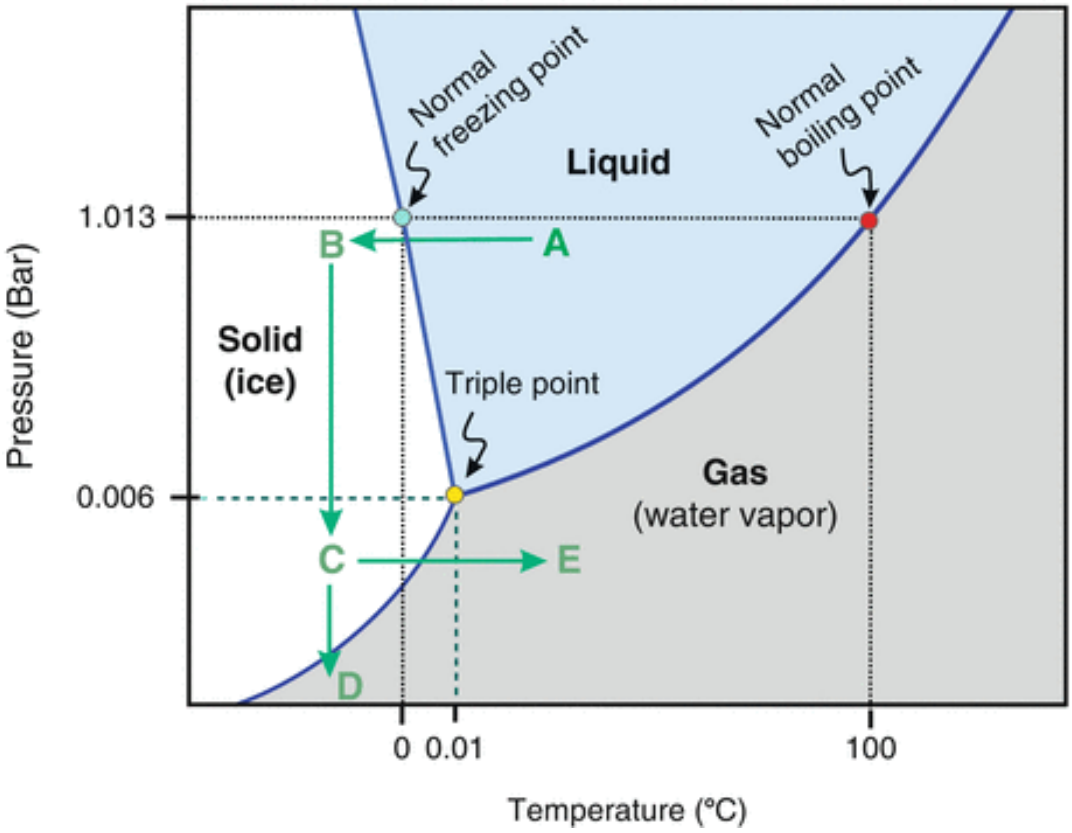


Figure 10: Freeze-drying theory.[10] The three matter states are a fine balance between temperature and pressure. In case of water, represented on the diagram, white represents the solid state (ice), grey represents the gas state (steam) and blue represents the liquid state (water). As it can be seen the triple point, where the three states coincide, is at 0.006 bar and at a temperature above 0°C. Reproduced with the permission of the publisher, Springer Science Business Media New York

The use of lyophilisation has been well studied and documented, Greaves et al.[83] freeze-dried several different biological specimens and concluded that in general it is a suitable method for most biological entities such as mammalian cells and bacteria. However, for mammalian cells formation of crystals and increased concentration of solutes as the water is removed can be damaging to the cells organelle membranes.

The effects caused by freeze-drying will be evaluated in this thesis using microscopy, including electron microscopy. Freeze-drying is characterised by the removal of water under vacuum conditions without defrosting, through sublimation, this process leaves behind the waterless solutes or structures. Lyophilisation is a function of preassure and temperature. therefore, it can be explained by the freeze-drying theory as outlined in the diagram in Figure 10.[84]

2.1.5) SIMS of biological samples

Mass Spectrometry imaging (MSI) has had many developments in the past decade, especially in the MALDI field. Numerous studies have been conducted in tissues and even whole body sections, looking for both pharmaceutical compounds and endogenous molecules.[51]

The number of studies using SIMS to analyse biological matrices has been quite modest compared to MALDI applications. The first single cell imaging publication (Winograd's group) dates from 1997 and describes the optimisation of freeze fracturing in *Paramecium* cells*;* it follows on from detecting intracellular cocaine on cells treated with this compound[85]. *Paramecium* is a large single cell (average 250 µm); however, analysis of more biological relevant mammalian cells (around 20 µm) is more challenging as the spatial resolution needed is higher. This can be achieved by increasing the secondary ion yield, which is possible by using a different metal ion gun such as bismuth.[86]

One of the first examples of cell lipid profiling studies was performed in *Tetrahymena*, a protozoan, which again is a large single cell. Ostrowski et al. managed to prove the proposed hypothesis for the organism's reproduction. It was thought it occurred by passing the nucleic acid material via the membrane when two protozoa were adjacent to each other. By monitoring the difference in lipid signals during the protozoa mating, they observed the phosphocholine signal decreased, and there was an increase in the signal associated with 2-aminoethylphospholipid, which is associated with membrane permeability, supporting the nucleic acid exchange hypothesis[85].

Sjovall et al. used silver deposition, by spin-coating freeze-dried cells with the metal to increase the ionisation efficiency of cholesterol, as silver cationized the cholesterol molecule[87,71]. The downside of

this approach is the artefacts introduced by adding silver onto the surface; in this case, the silver suppresses other signals, which makes it harder to observe masses for endogenous cellular markers. Fletcher et al. used *Xenopus laevis* oocytes to demonstrate the potential of sputter etches an image with a C_{60}^+ at 40 keV with minimal sample preparation. The characteristics of this cell, the size and sturdiness facilitated the depth profiling[88]. However, they encountered some difficulties as it is very challenging to keep the beam focused and maintain enough current to allow the analysis to take place; it would have been beneficial to use a liquid metal ion beam to analyse and a C_{60}^+ to sputter, as liquid ions guns are highy focused. This was precisely what Breinstein et al. attempted by using Bi_3^+ to analyse normal rat kidney cells in 2007. The result was sub-cellular resolution images, which could only be achieved in high spatial resolution mode, sacrificing mass resolution.[89]

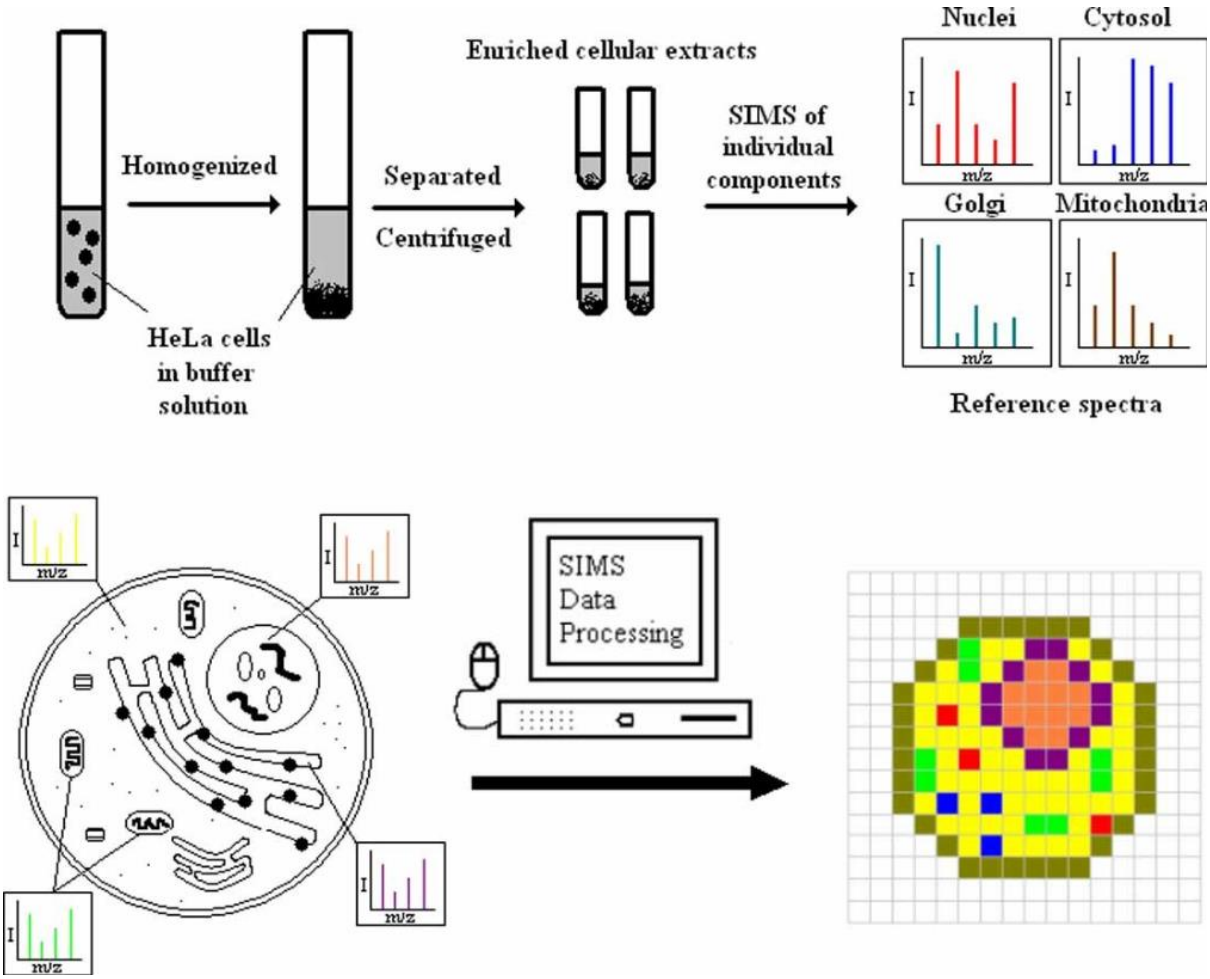


Figure 11: Piwowar et al. organelle mapping workflow illustration.[11] Here HeLa cells are depicted, but it could be applied to any cell line. Using centrifugation and affinity pull-down, the organelles are separated after cell lysis. These separate organelle

enriched fractions could then be analysed using ToF-SIMS and an organelle mass spectral fingerprint created for each of the different organelles. Once these profiles are created, it should be possible to correlate the organelle profile spectra with the spectra per pixel of the cell and therefore a reconstructed cell image based on those profiles. Reproduced with the permission of the publisher, John Wiley and Sons.

In 2010, Piwowar et al. speculated a potential top-down approach to analysing cellular components. The cellular components would be enriched using organelle affinity pull-down techniques, which selectively enrich for the organelle of interest. These could be be analysed using ToF-SIMS, so an organelle MS profile could be generated, this profile could then be matched to some regions of the cell, potentially allowing mapping of cellular components.[11] If one managed to obtain an organelle profile spectra similar to the one generated using this approach with the addition of the compound's mass, one would be able to determine in which organelle the compound was accumulating.

ToF-SIMS has also been used to analyse bacteria. Thompson et al. were able to discriminate between vegetative bacteria and spores based on the phospholipids they identified using their custom –built polyatomic ion guns (Au_n^+, C_{60}^+).[90] This could be invaluable in the food industry where the presence of bacterial spores can have potentially dangerous consequences.

In a diagnostic application, Fletcher et al. used principal component –discriminant function analysis (PC-DFA) to identify different bacteria that are known to cause urinary tract infections.[12] This study was performed using a large dataset, and the principal component analysis (PCA) allowed the bacteria to be grouped according to their species based only on their mass spectral profile as outlined in Figure 12.

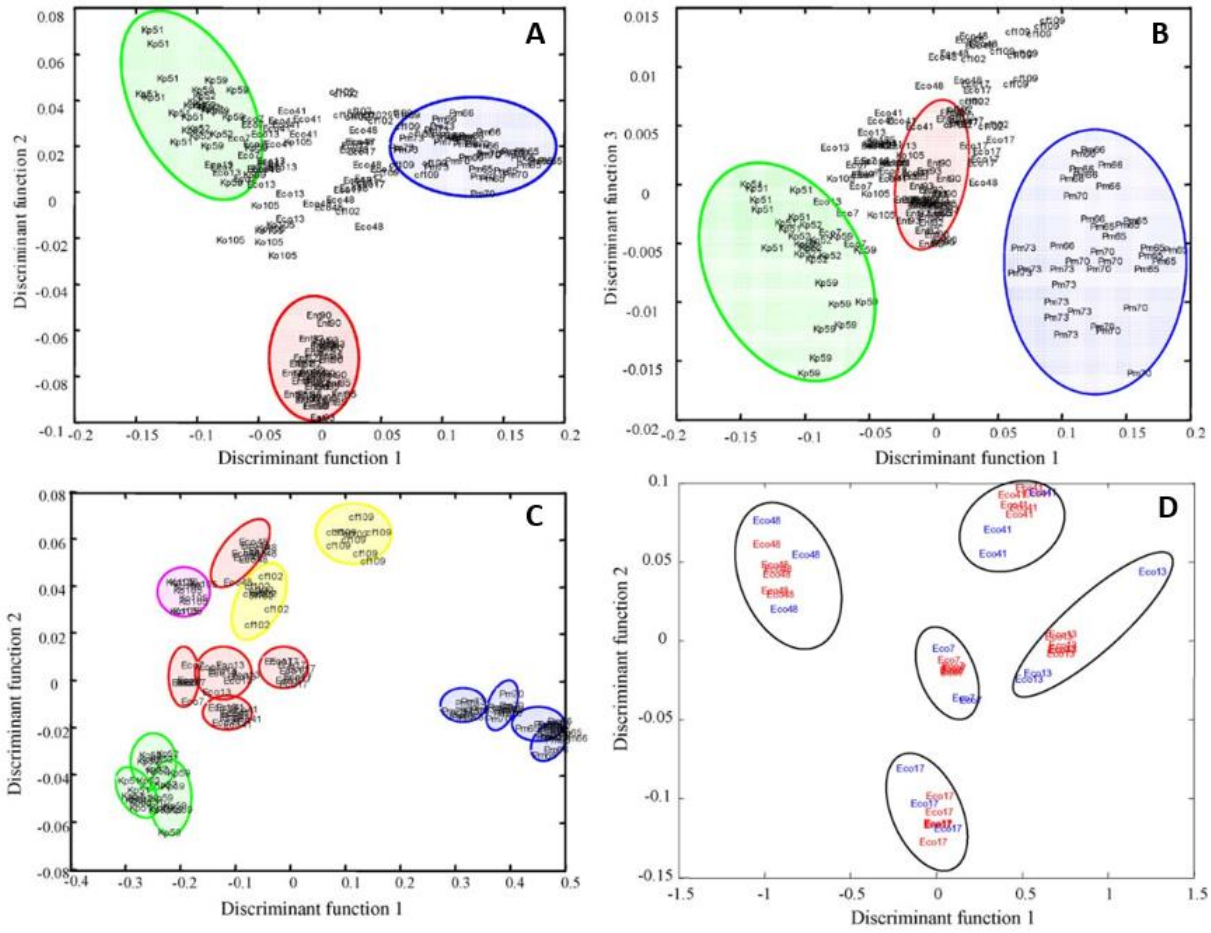


Figure 12: Principal component analysis of the entire dataset in (A) and (B). In this experiment different bacteria can be grouped according to their MS fingerprint profile using PCA. PC-DFA plot of the full data set after the removal of *Enterococci* (C) and (D) shows the separation of the five different *E.coli* strains used in the experiment (the training set is displayed in red and the projected in blue).[12] Reproduced with the permission of the publisher, Elsevier.

It can be clearly seen in Figure 12 that the different bacteria are grouped according to their genus, in Figure 12A is *Enterococcus* and in red in Plot B is for *Escherichia coli*, blue is for *Proteus mirabilis* in both Figures 12A and B, and in green for *Klebsiella pneumoniae* also in both Figures 12A and B. In Figure 12C the *Enterococcus* data was removed to emphasize the separation of the different bacteria, *P. mirabilis* (blue), *K. pneumoniae* (green) are still observed but *Citrobacter Freundii* (yellow) and *Klebsiella Oxytoca* (pink) can also be observed. Figure 11D represents only the *E.coli* and PC-DFA is able to separate the different *E.coli* strains used in the study. This study indicates the potential of ToF-SIMS as a diagnostic tool.

This work clearly shows that ToF-SIMS and multivariate analysis can be a powerful tool when used together, also exemplified in a study performed by Armitage et al.[91] They were able to detect subtle metabolomics profile changes in multicellular tumour spheroids when the spheroids were treated with hypoxia-inducible factor-1 (HIF-1). The changes observed correlated with HIF-1 upstream or downstream metabolism.

ToF-SIMS has been used for biological applications for a relatively short period of time, in fact, as Lockyer points out in an insightful editorial this might only be the beginning and with instruments advances, hopefully, ionization efficiency, speed and mass accuracy can be improved to deliver an improved technique that when associated to powerful computer algorithms for data analysis can provide some insight into the overall biology of the system of interest and not just an answer to a particular question.[92]

All these studies are great examples of how to creatively apply a technique with fundamental limitations to a new field, by using a larger single cell these groups proved that SIMS could be a useful tool to analyse biologics. However, the ultimate goal is still to look at more biologically relevant mammalian cells, requiring sub μm resolution and enhanced secondary ion generation.

2.2) Other cell analysis techniques: Microscopy

Microscopy in its various forms, is a widely used technique and the gold standard for single cell analysis, and is performed using a microscope. A microscope is an instrument that magnifies an object otherwise too small to be observed by the naked eye, generating a larger image of that object. Microscopes can be extremely simple, like the light microscope or complex as the electron microscope, and there is a huge variety of microscopes and microscopy techniques as it can be observed in Figure 13.

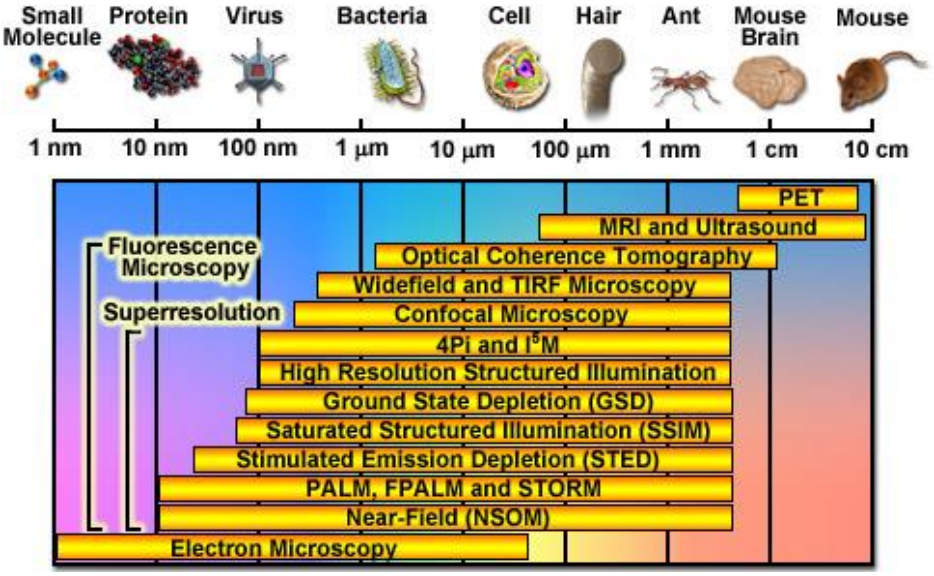


Figure 13: Spatial resolution of biological Imaging techniques. The diagram shows the applicability of each technique across a variety of sizes and biological matrices. Reproduced with the permission of the publisher, Elsevier.

Light or Optical microscopes use light as an illumination source and they can be classified in four different types: bright-field, dark-field, fluorescent and Phase contrast. In bright-field normally the specimen appears darker than the background, in dark-field the opposite happens, a bright specimen can be observed against a black background. In fluorescence microscopy special filters are employed to produce images of fluorescent light emitted from excited molecules in the specimen, this will be discussed further in point 2.2.1). Phase contrast relies on the difference in thickness of the specimen or differences in refractive index within the specimen to visualize the specimen, this is achieved by the phase-contrast condenser and objective.[93]

Electron microscopes use electron beams in order to generate high magnification images while light microscopes use light waves to produce their images. Electron microscopes have a resolving power 200 times greater that light microscopes, magnification of up to x 400000 can be generated, while the magnification of light microscopes is around x 2000.[94]

Electron microscopes can be transmission (TEM), scanning (SEM) or both (STEM). In TEM the electron beam is transmitted through the ultra-thin sample, and the electromagnetic field generates a magnified image, this technique if often used to observed finer details within a mammalian cell such as organelles and bacteria. In SEM the electron beam is used to scan the surface of the sample, generating

an electron dispersion which is collected by the detector generating an image, this technique is often used to observe the surface of the specimen.[94]

Microscopes can also be classified as wide-field and confocal, the main difference between these technique is the resolution in z, the resolution in z for a wide-field system is approximately 3 µm and the resolution of confocal is below 500 nm. Confocal operates on the principle of optical sectioning, or the ability to extract light from a single thin plane in a thicker 3D sample. This is achieved by placing a pinhole to only allows light from a focal plane to reach the detector reducing the noise originating from the light above and below, as it can be observed in Figure 14.[93]

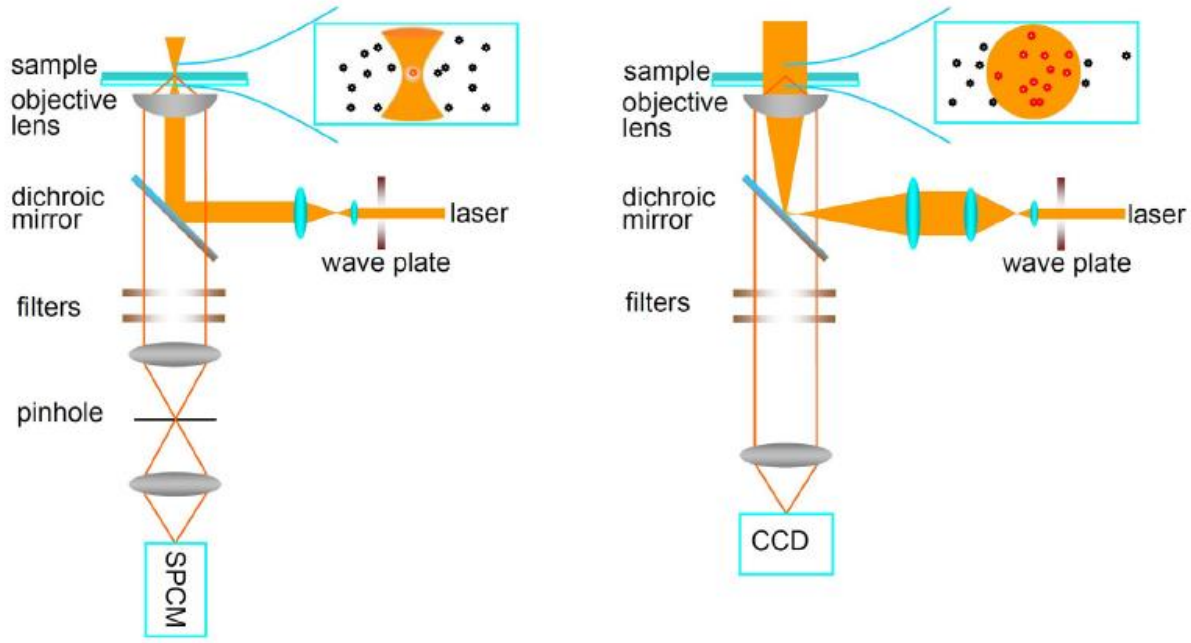


Figure 14: Confocal microscopy and wide-field microscopy.[13] On the left the light path passes through the pinhole, which enhances the z-resolution of confocal microscopy. On the right the normal set-up of wide-field microscopy. Image reproduced under the Creative Commons License (Attribution–Noncommercial–Share Alike 4.0 Unported license.

There are several different microscopy modalities available, however, only the ones used for this thesis are discussed in further detail in this chapter.

2.2.1) Fluorescent microscopy

Fluorescence microscopy is a widely used technique in biology based on the principle of luminescence, and it has been developed by Coons in 1945. In this technique a specimen in stained with a fluorescent dye, this dye absorbs light a one given wavelength (the excitation wavelength) and it emits light at a different wavelength (the emission wavelength).

The labelling of certain aspects of the cell morphology is routinely used in biology in order to obtain insight into biological, functional and structural aspects of the cell. There is a huge variety of fluorophores that can be used in microscopy experiments, as the addition of these tags aids visualization of specimens, however not all the effects fluorescent dyes can have on a cell are known.

Fluorescent dyes are only one part of the equation, microscopes are the other, and currently there is a wide range of microscopes available on the market from a simple light to a custom built multiple laser fluorescent microscope.

The fluorescent tags emit light of a given wavelength when excited by incident light of a different wavelength; the incidence wavelength is usually slightly shorter than the emission wavelength. The excitation can be achieved using specific wavelength lasers or broad emission lamps.

Figure 15 shows the basic components of a fluorescence microscope, overall the essential components are a light source, an objective, detectors and a camera, this can be arranged in several different configurations.

Several improvements have been added over the years including the ability to visualise several sample planes, commonly known as slices, that allows the three-dimensional reconstruction of the image in confocal fluorescence microscopy.[95] The addition of time-resolved fluorescence imaging allowed several different time-points to be acquired, overcoming the issue of only having snapshot data.[96]

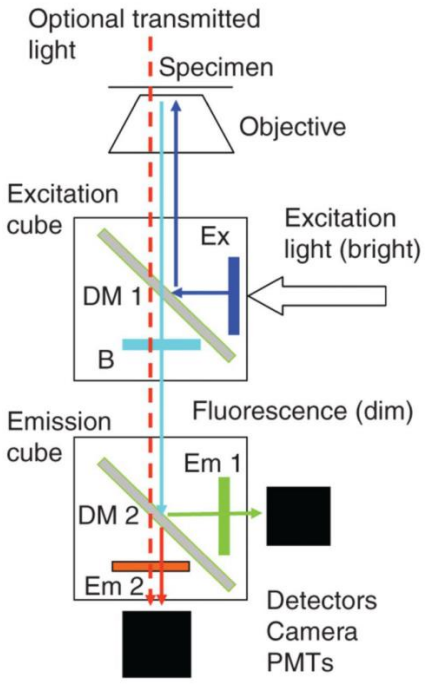


Figure 15: Fluorescence microscope basic light path schematics. There are two cubes in a fluorescence microscope, an excitation cube and an emission cube. In the excitation cube a dichroic mirror (DM1) directs the light from the source (bulb or laser) to the sample passing the emitted fluorescence to the indicators in the emission cube. B is a filter that acts as a barrier that prevents the excitation light to reach the detector. DM2 is a beam splitter for the emitted fluorescence light and emission filter (Em1 and Em2) filter out unwanted light. The fluorescence is then detected by cameras or photo multipliers (PMTs).[14] Reproduced with the permission of the publisher, CHS Press.

More recently, two-photon excitation fluorescence microscopy has allowed deeper imaging in tissue and in some cases in vivo.[97] This nonlinear approach produces images of optical sections by generating a contrast between the second and third harmonica signals, in some instances, it also generates anti-stokes Raman scattering, this technique is able to distinguish molecules based on their vibrational frequency, making it a label free imaging technique.[97]

In 2014 a Nobel prize in chemistry was awarded to the inventors of stimulated emission depletion microscopy (STED). The principle is the use of a point -scanning technique where the fluorescence spot from the first laser is sharpened by the stimulated emission of a second laser. This technique is currently one of the most used super-resolution fluorescence techniques for biological samples.[15]

The main advantage of using STED when compared with fluorescence microscopy is the improved resolution, Figure 16, achieved using the STED beam to scan axially quenching some of the noise generating in routinely used fluorescence confocal microscopy.[15] This application is state of the art and goes beyond the diffraction limit, which was thought to be the limit of conventional microscopy, despite this, conventional microscopy is still widely used due to its simplicity and availability.

Routinely used wide field and confocal fluorescence microscopy have good spatial resolution, which can be calculated as a function of the wavelength divided by twice the numerical aperture of the microscope, which means that at a wavelength of 550 nm the spatial resolution is approximately 0.25 µm.[98]

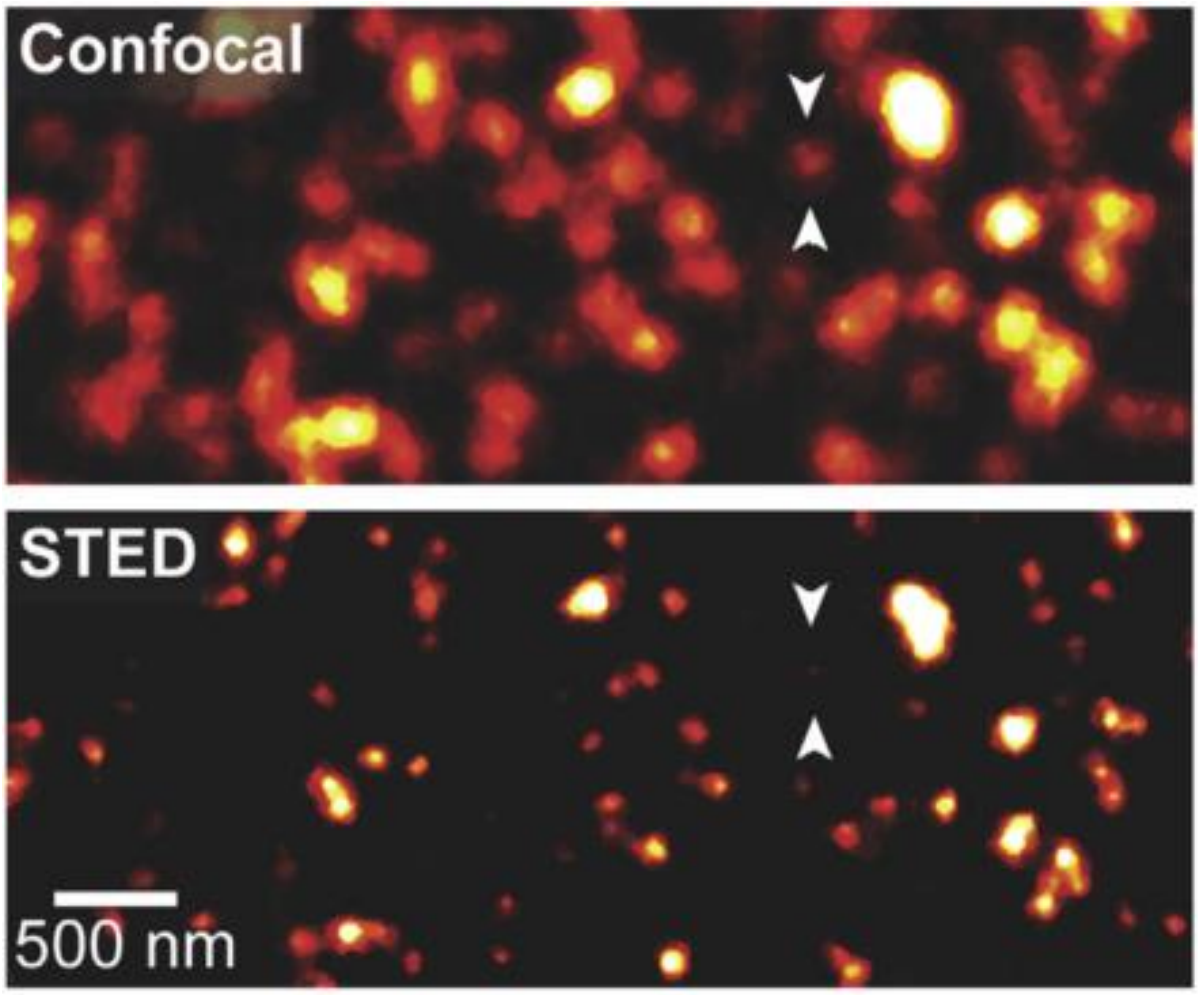


Figure 16: Confocal fluorescence microscopy and STED images of 40 nm fluorescent beads.[15] The two images depicted are from the same area, however it can clearly be seen, especially in the area highlighted by the arrows a much cleared imaged

with improved spatial resolution. The image on top is quite blurry and undefined whilst the image at the bottom is clearer. Reproduced with the permission of the publisher, Elsevier.

This places fluorescence microscopy in the same spatial resolution range as the highest spatial resolution ToF-SIMS applications. Despite this, in most cases, this ToF-SIMS imaging mode cannot be used as it is detrimental to mass resolution and in these situations, fluorescent microscopy can be used as an orthogonal technique to complement ToF-SIMS analyses. There is however, some concern and considerable evidence that the addition of large fluorophores to small molecules interferes with the drug compound absorption into cells since it changes their physical-chemical properties.[99] [100]

2.2.2) Tomographic microscopy

While fluorescence microscopy typically relies on the addition of tags to generate images, label-free tomographic microscopy does not; it uses the difference in refractive index within a cell to create a pseudo-stain that can be used to identify intracellular structures. This technique is fast, label-free, non-destructive and with spatial resolution beyond the optical diffraction limit.

The majority of cells are transparent hence the absence of contrast in classical microscopy techniques. This technique uses the difference in refractive index properties in different cell components to create a tomographic representation on the cell. This is achieved by imaging using a 520 nm laser over a 360º degree rotation of the sample, obtaining a hologram from each illumination direction, therefore creating a 3D representation. [101] As different intracellular organelles have slightly different light propagation properties which result in slightly different refractive indexes, allowing the generation of 3D images in which those slight difference can be observed.[16]

This technique combines holography with a rotational scanning, this associated with high resolution (200 nm) produces images that are superior to other light microscopy techniques.[102]

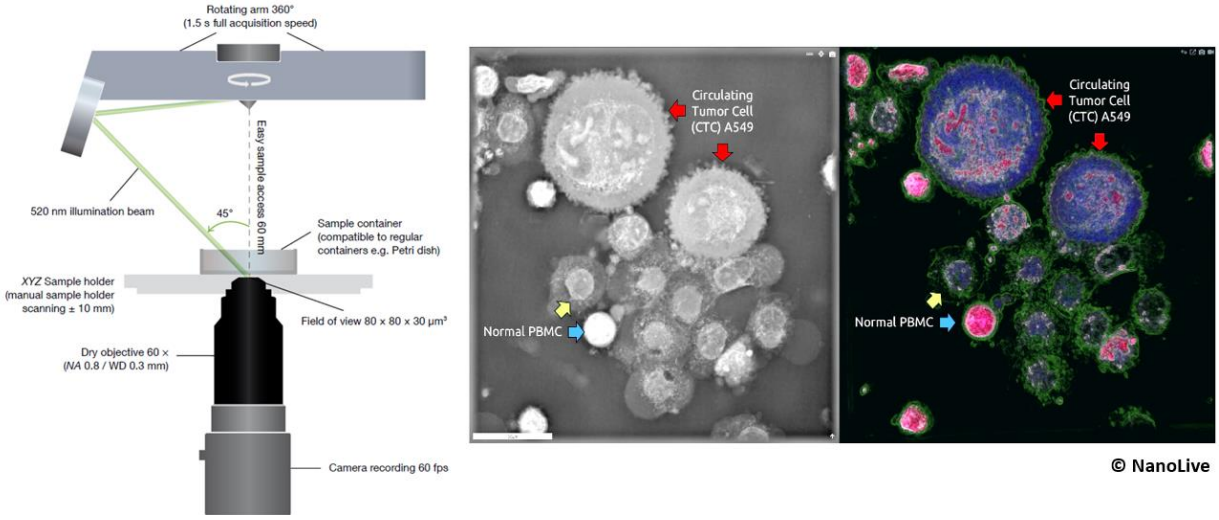


Figure 17: The Nanolive 3D Cell Explorer Refractive Index microscope principle. Schematics of the microscope, displaying the different components (left). Whole blood spikes with A549 (tumour cells) (right). [16] The middle image shows the light image of a mixed cell population containing both peripheral blood mononuclear cells and circulating tumour cells such as A549 cells. The image on the right depicts the pseudo-stained obtained by the difference in refractive index of the different cellular components. Reproduced with the permission of the publisher, John Wiley and Sons and NanoLive.

2.2.3) Confocal Laser scanning microscopy

In wide-field microscopy, achieving high quality images is dependent on the thinness of the sample, despite this, most samples analysed are either too thick or require volume information. Confocal microscopy addresses this issue by applying what is known as optical sectioning. The mechanism is relatively simple, all the signals generated by the sample outside a given focal plane are physically blocked by an aperture. Furthermore, by combining optical sectioning with incremental focusing 3D images of tick specimens can be generated.[103]

Laser confocal microscopy has exceptional spatial resolution in the z plane, hence the reason why it was chosen to determine defences in cell volume, as removal of the water content causes the cell to collapse in the z plane. The resolution of a typical laser scanning microscope is 120 nm in x and y and 10 nm in z. The 405 nm laser and the two-photomultipliers (a standard one and a high sensitivity one) allowed the amplification of the signal, this results in sharper images as it can be observed in Figure 18.

104

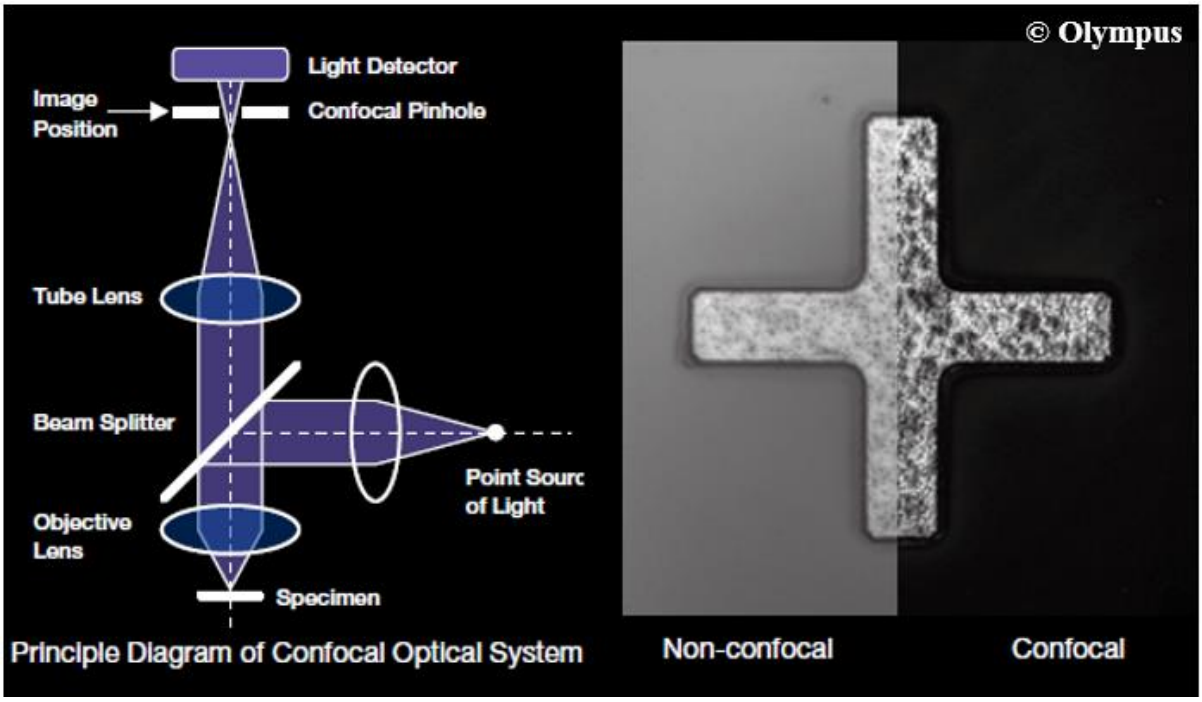


Figure 18: Laser confocal scanning microscopy. On the left is the schematics of the microscope. On the right the same image comparing the non-confocal and the confocal mode. As it can be observed the sharpness of the image increases in the confocal mode, the topology of the sample is much more detailed due to the 10 nm z resolution of this microscope.

2.3.4) Electron microscopy

In light microscopy, photons are the electromagnetic energy used to visualise the sample. If the sample features are smaller than a photon then electrons can be used to image finer subcellular details. There are two types of electron microscope: the transmission EM (TEM) and scanning EM (SEM). TEM is used for thin specimens prepared so that electrons pass through the sample and generate a projection image. SEM is more flexible as it allows thicker specimens to be analysed, less sample preparation is required as it relies on the secondary electrons emitted from the surface of the sample to generate an image as the primary electron gun rasters the specimen. The alternative is back scattered SEM, which uses the electrons that bounce off the specimen to generate an image, however due to their higher energy a different detector, from the one used to detect secondary ion, is required. Back scattered SEM generated images often produce information of the atomic composition of the specimen. [18,105]

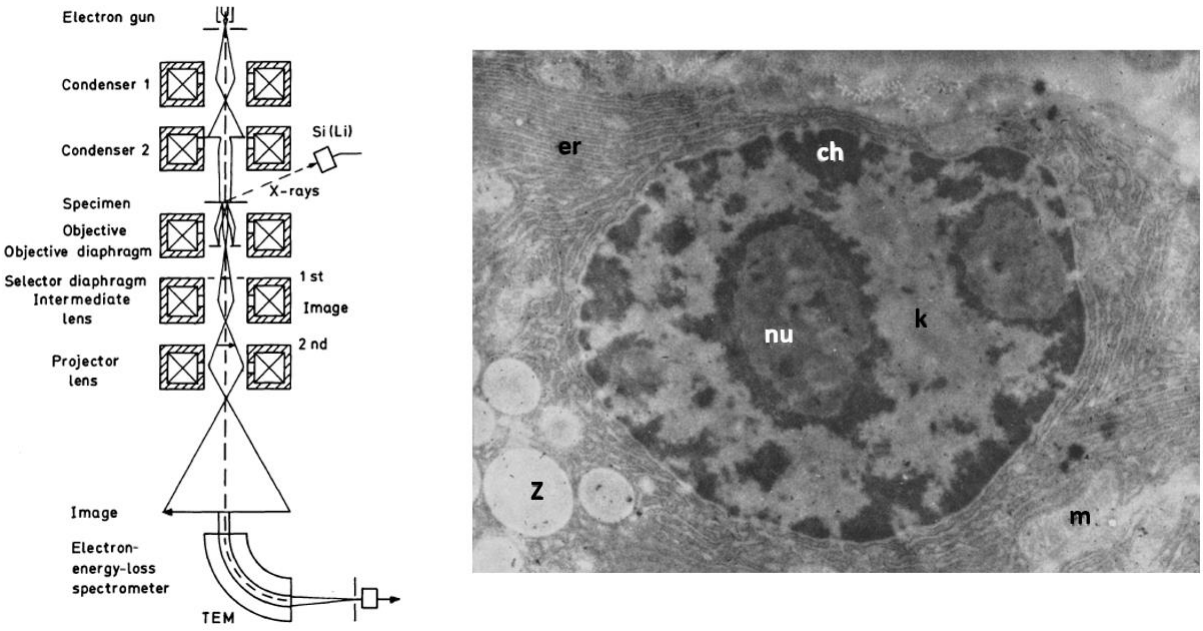


Figure 19: Transmission electron microscope schematics (left)[17]. Reproduced with the permission of the publisher, Springer-Verlag. Pancreatic acinar cell fixed in glutaraldehide (x11,000) stained with Osmium Tetroxide.[18] There is a clear contrast between the nucleus and the extra nuclear space. Outside the nucleus a mitochondrion (M), the endoplasmic reticulum (ER) and a zymogen granule (Z) can be observed. Inside the nucleus the nucleolus (nu) can be seen as well as chromatin (ch) and karyoplasm (k). Image reproduced under the Creative Commons License (Attribution–Noncommercial–Share Alike 4.0 Unported license.

2.2.5) Atomic force microscopy (AFM)

Atomic force microscopy (AFM) is a high spatial resolution microscopy technique that allows imaging with minimal damage to the sample. This is crucial when both microscopy and SIMS are performed on the same sample, it is particularly important when the specimens are extremely small such as bacteria. AFM is a type of scanning probe microscope first described by Binning et al. in 1986, which makes use of an ultra-small probe tip at the end of a cantilever. [106] The image is acquired by scanning the probe over a small area of the sample, measuring the force between the probe and the specimen. The probe is usually a small sharp pyramid shaped tip, 3 to 6 µm tall with a 15 to 40 nm end radius. [107] AFM has

high lateral resolution, approximately 30 nm and at least 0.1 nm in z, this means that it can be severely influenced by surface and environmental conditions.

There two types of atomic interactions at different tip-sample distances, repulsion and attraction (Van der Waals). At very small tip-sample distances a powerful repulsive force is created between the tip and sample atoms due to the overlapping of the electronic orbitals, and in these conditions, the tip and the sample are considered to be in contact.[108]

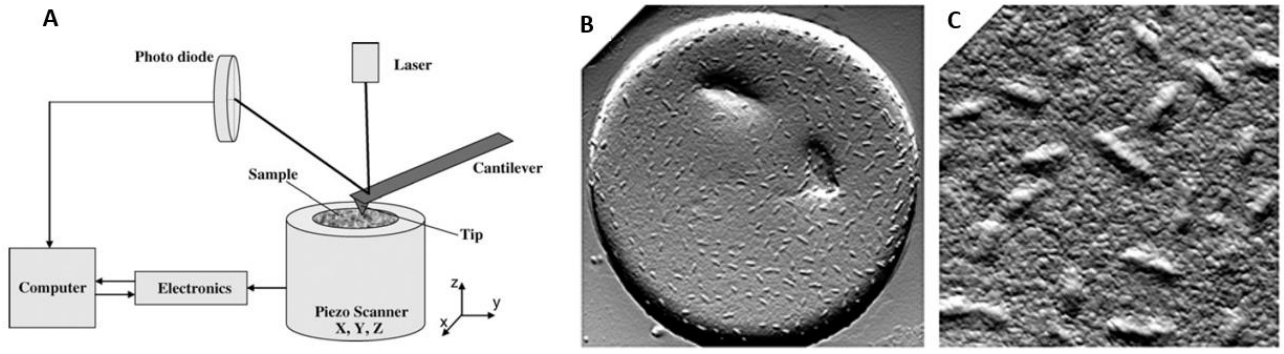


Figure 20: (A) AFM schematics[19]. Reproduced with the permission of the publisher, Royal Society of Chemistry. (B) Bovine red blood cell infected with *Babesia bovis*. (C) higher magnification of image B displaying the ridge morphology of the bacteria. Reproduced with the permission of the publisher, John Wiley and Sons.

AFM can be used in both non-contact and tapping mode; both are based on a feedback mechanism of constant oscillation amplitude. In non-contact, mode the amplitude is set at 100% of free amplitude, and in tapping mode, it is set to 50. Tapping mode provides the best resolution with the least sample damage.[108]

The cantilever is used to scan over the surface and a laser beam is used to detect the cantilevers deflections towards, off or away from the surface, the changes are tracked using, for example, a position-sensitive photodiode (PSPD). As the AFM images the topology of a sample by scanning the cantilever over the region of interest the cantilever detects the raised and lowered area of the sample

surface. A feedback loop controls the height of the tip above the surface, allowing the AFM to generate an accurate topographic map of the sample features.[108]

2.3) Other cell analysis techniques: High Mass resolution liquid chromatography tandem Mass Spectrometry (LC-MS/MS)

Mass spectrometry has long been used to aid structural elucidation[109]. As the mass spectrometers evolved, researchers have realised that they could be used to analyse more complex biological samples[110]. Most disease targets are proteins and therefore having knowledge about the disease target and its interacting proteins is fundamental in drug discovery. In addition to this, understanding how a therapeutic is modulating the disease state by understanding its effects on the proteome enables researchers to create more effective medicines. The study of the proteome and how it changes in a biological system is termed proteomics.

Genomics and transcriptomics are respectively, the study of genetic material and how that material is transcribed, and experiments in these fields are critical to understanding the biology that underpins drug discovery, as summarized in Figure 21. Despite proteomics providing answers at the disease target level, arguably the three combined are a very powerful tool. Technologies to study the proteome have lagged behind the advances in nucleic acid research as proteins are not amplifiable, and therefore sensitivity is an issue.

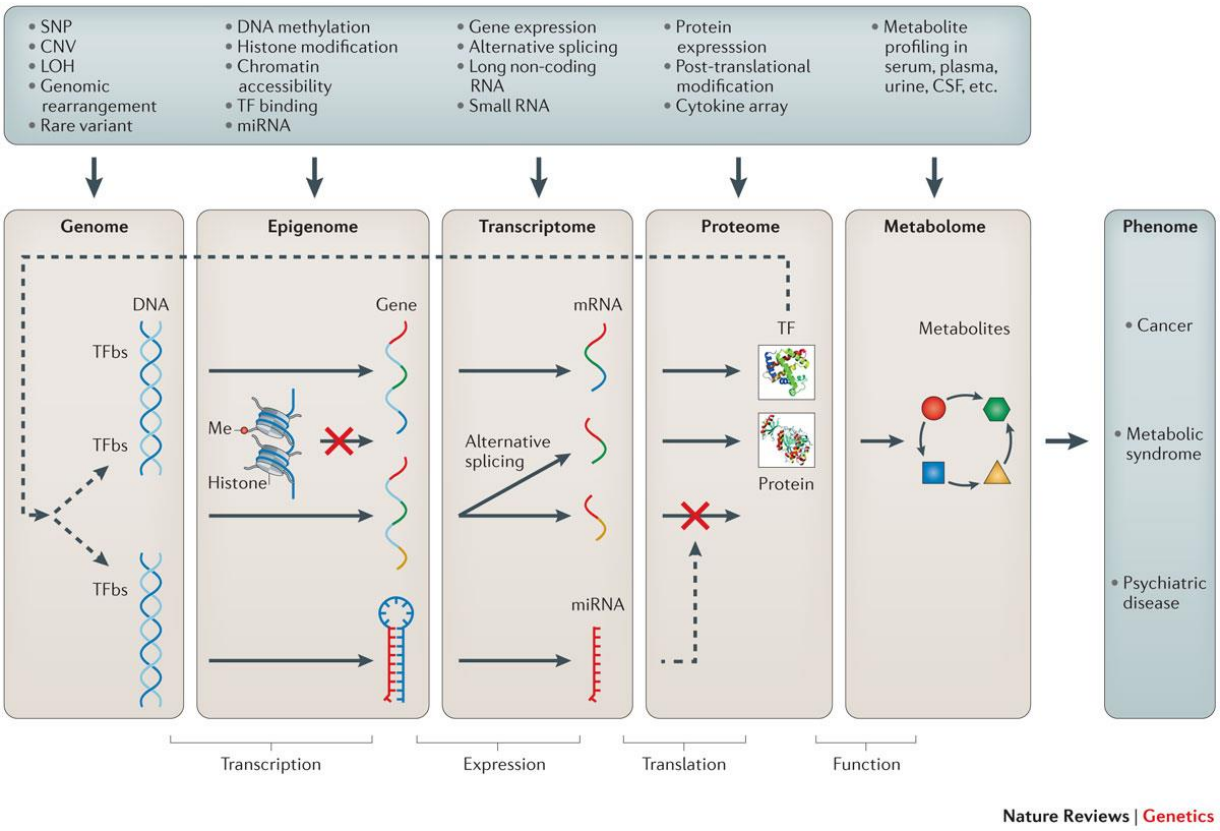


Figure 21: Diagram showing the relationship between omics techniques.[20] The omics techniques refer to the particular type of biological molecule they study. Genomics is the study of DNA (deoxyribonucleic acid), transcriptomics relates to RNA (ribonucleic acid), proteomics relates to the study of proteins and metabolomics is the study of metabolites and their pathways. A change at the DNA level may, or may not cause a change in the protein expression and metabolic changes, therefore understanding the whole process, and being able to pin-point changes in a disease state helps the drug discovery process. Reproduced with the permission of the publisher, Springer Nature.

2.3.1) Proteomics

The introduction of the Orbitrap concept in 2000[76] has truly revolutionized mass spectrometry-based proteomics.[111] Researchers quickly realized the impact that this technology could have on their reasearch,[112] but in order to advance the technology data searching and data mining also needed to be developed further resulting in the appearance of curated databases for MS-based proteomics.[113]

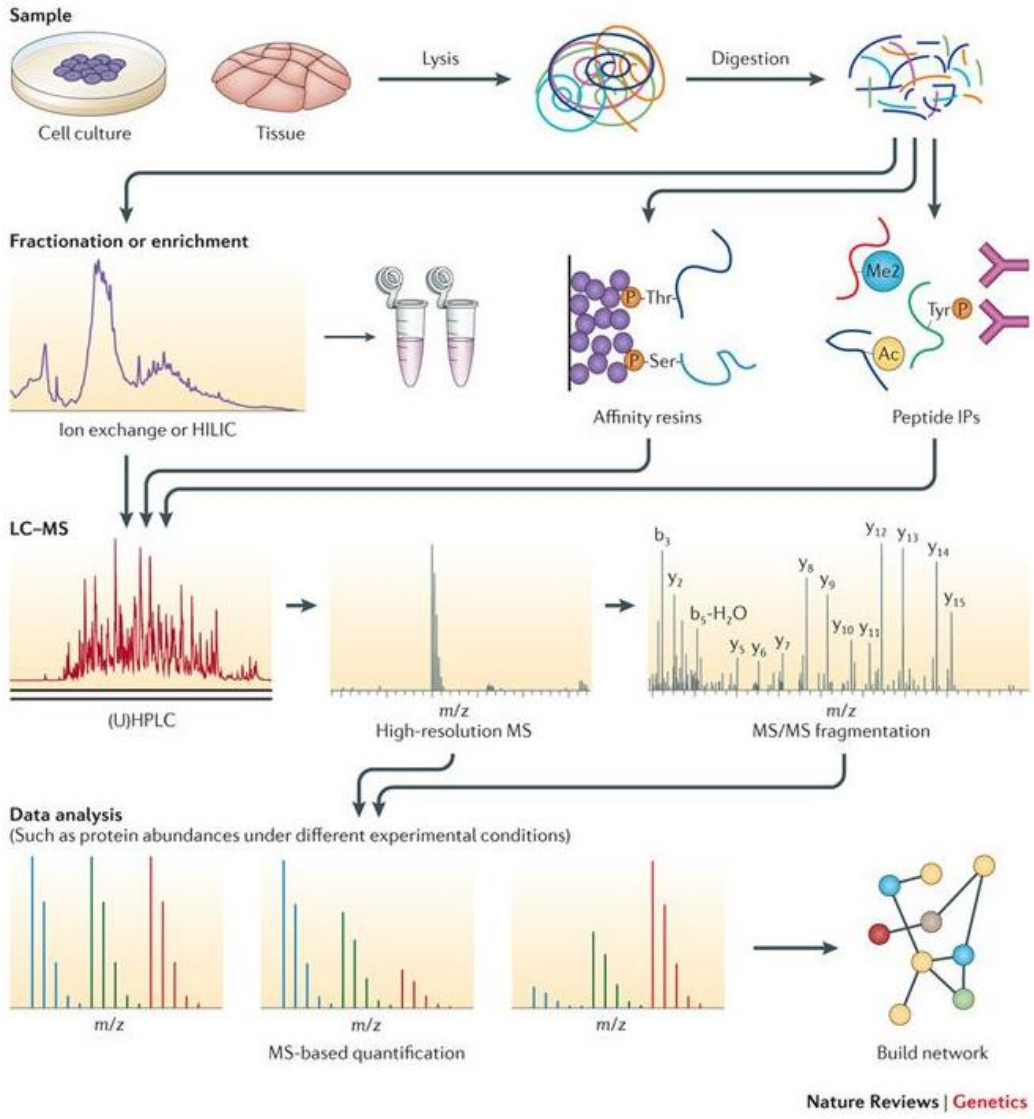


Figure 22: Proteomics workflow [21]. After sample collection, a certain amount is processed (typically protein concentration is determined) the sample is then reduced, alkylated and digested with an enzyme (generally trypsin); once the proteins are converted to peptides the samples are typically analysed using a high mass resolution mass spectrometer in an LC-MS/MS configuration (ordinarily nano-LC). The data can then be proceeds using several different software both freeware and instrument vendor software. Reproduced with the permission of the publisher, Springer Nature.

In the late 2000 the field of proteomics developed significantly, driven forward by groups such as Matthias Mann's in Munich and Reudi Aebersold in Zurich[114], the former developing strategies to increase the number of proteins identified[115] and the latter moving towards absolute quantification of proteins using targeted mass spectrometry[116].

Stable-isotope labelling by amino acids in cell culture (SILAC) has allowed the decrease of false positive in comparative studies, when compared to label-free approaches, by combining the samples in a single run, the run-to-run variability, ionisation suppression and stochastic sampling is reduced.[117] Currently, genomics and proteomics studies are being combined to provide a more global view of the studied models.[118] Furthermore, other Mass Spectrometry based omics, such as metabolomics[119] (study of metabolites) and lipidomics[22] (study of lipids), are also now beginning to be studied with the same agnostic approach as proteomics. Which means that hopefully in the future large metabolomic and lipidomic[120] data sets could be integrated with currently used genomics, transcriptomics and proteomics to provide an even more complete biological understanding. Nonetheless, the processing of both metabolomics and lipidomics[121] data is very challenging as the software and databases are still in their infancy when compared to proteomics.[122]

2.3.2) Lipidomics

In the last few years lipidomics research has experienced a boom as can be observed in Figure 21. Researchers are keen to apply the learnings from proteomics to lipidomics despite significant challenges, as the molecular differences in lipid structure mean that a shotgun approach (as commonly used in proteomics) is unlikely. However, by using several different ionisation modalities, such as electrospray ionisation (ESI), atmospheric pressure chemical ionisation (APCI) and MALDI, a large part of the existing eight lipid categories and twelve lipid classes can be analysed; comprising hundreds of molecular species in total.[123]

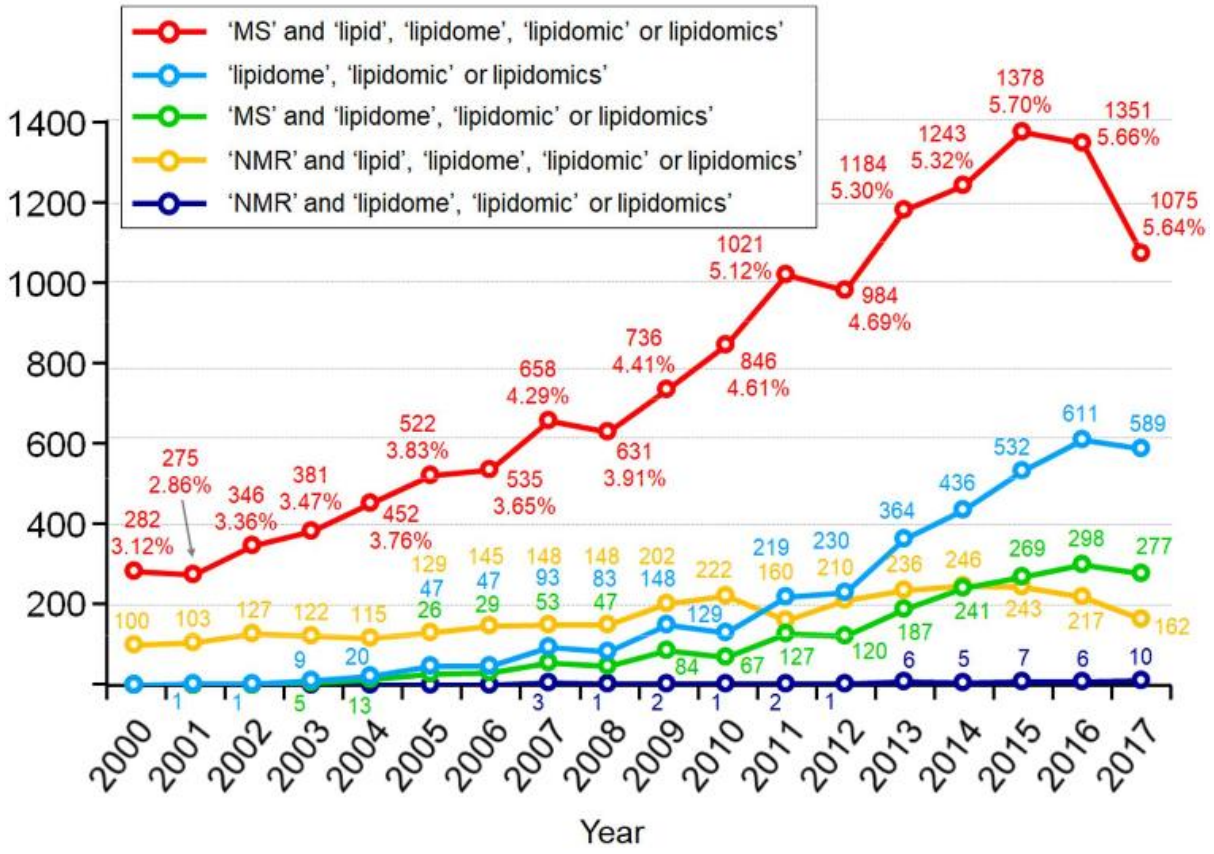


Figure 23: Plot represents the summary of all the PubMed indexed articles that mentioned lipidomics between 2000 and October 2017.[22] There is a marked increased number of MS based lipidomics study since the year 2000, which coincides with the introduction of the Orbitrap technology. Reproduced with the permission of the publisher, American Chemical Society.

In addition to the instrumental and data processing challenges associated with lipidomics, there are also sample preparation obstacles. In the quest to make lipidomics data as relevant as possible, obtaining data that is quantitative or at least semi-quantitative is essential. This requires the evaluation of the lipid extraction method used for the study (several can be used) and the potential sample pre-treatment prior to mass spectrometry analysis to aid detection.

All these methodologies are summarised in Figure 24, which references all methods including the modified Bligh and Dyer, which was the one used in the work presented in this thesis. This method simultaneously extracts and partitions the sample by precipitating the proteins in the liquid layer between the two liquid phases (water and chloroform/methanol).[124] This methodology is commonly used due to its speed and ease.

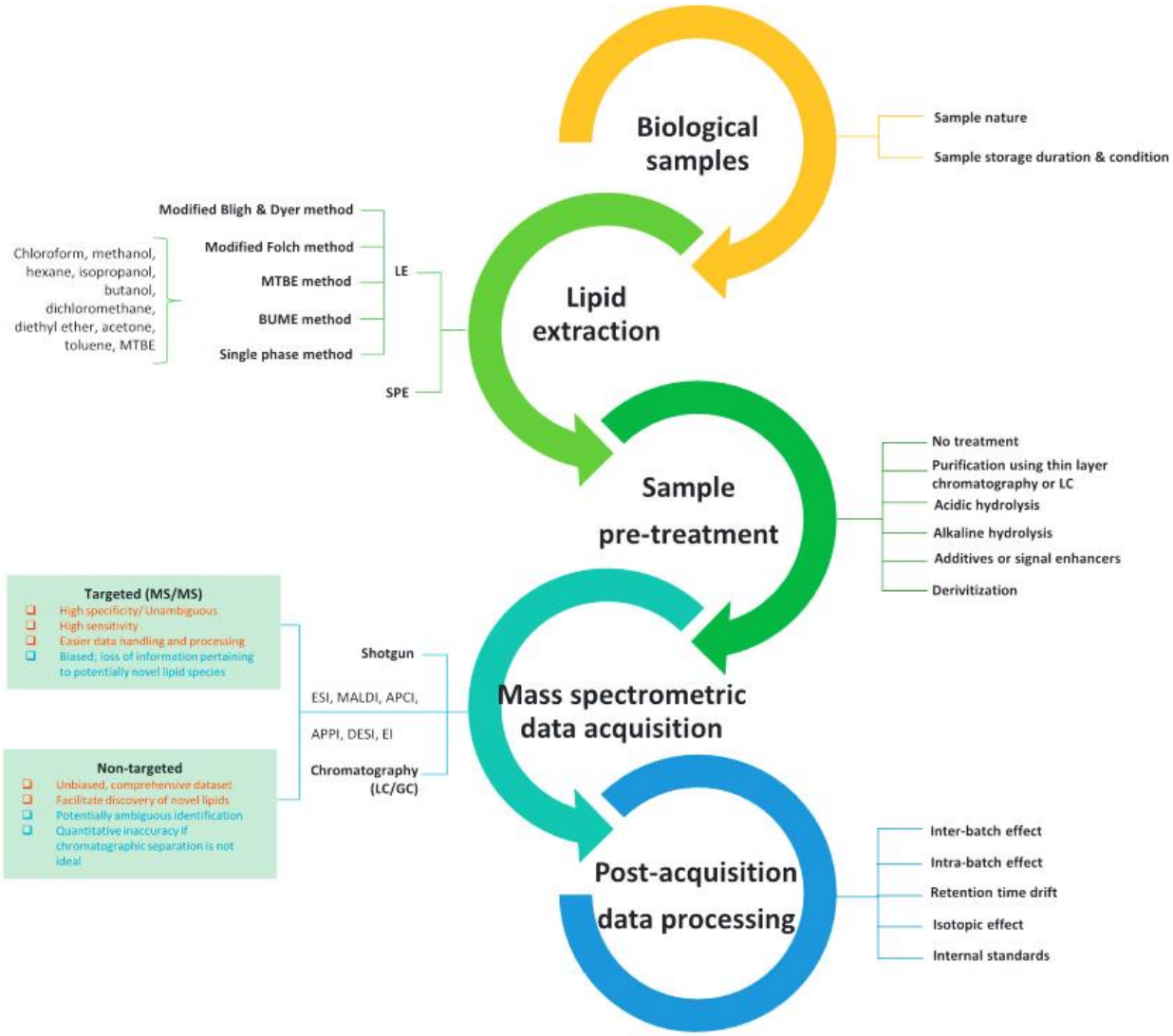


Figure 24: Plot describes the lipidomics workflow and the factors that could impact the accuracy of the workflow.[23] This image summarizes the complex procedure required to generate good lipidomics data, along with the caveats associated to each step of the process. In the first step, one needs to pay particular attention to the type of samples and their storage. The extraction step highlights the different extraction methods in existence. The next step relates to sample pre-treatment, such a further purification, hydrolysis or no treatment at all. The MS part of the process highlights the different types of MS methods that can be used, different ionisation modalities, further separation, targeted and untargeted methods. Finally, the sample processing method, which should account for sample-to-sample and batch-to-batch variability, retention time drift and the use of internal standards. Reproduced with the permission of the publisher, Elsevier.

Other extraction methods include the modified Folch method, in which a salt solution is used to aid the extraction[125] and the Methyl-tert-butyl ether liquid extraction method (MTBE) method that is usually regarded as a faster and cleaner option suited for shotgun lipidomics methodologies.[126] The BUME

method consists of a butanol-methanol extraction followed by as heptane-ethyl acetate extractions, and is especially suited to blood samples[127]. Depending on the samples type and information the researcher wants to obtain from the sample the extraction methodology can be changed as well as the pre-analysis treatment and mass spec acquisition. However, it is crucial to use the correct workflow, so the results are relevant and allow researchers to better understand lipid changes. Lipids have many functions including energy storage, cell signalling and structural integrity. It is known that lipid imbalances can cause disease, therefore the importance of having robust methodologies that allow further insight on the changes of the lipidome are important for drug discovery.[23]

2.3.2) Metabolomics

Metabolomics is the study of metabolites, which are the chemical products resulting from the body's metabolic activities. External stimuli such as injury and stress change the composition and /or concentration of the body's metabolites.[128]

The information obtained from metabolism analysis provides integrative information regarding cellular function. Genetic or environmental changes have profound influences on the phenotype of a cell or tissue. Furthermore, many metabolite molecules are involved in more than one metabolic network, which increases the complexity of the analysis output.[128] Despite this, thousands of metabolites can currently be identified in the region up to 1000 m/z and can provide insight on disease progression, treatment, nutrition and even environmental information.

Metabolomics has been used since the 1970s when there were significant breakthroughs in the metabolomics field, mainly through the application of gas chromatography. However, the analysis was targeted to a few different metabolites. The addition of mass spectrometry in its various forms, ToF and FT-ICR analysers, brought further confidence in the metabolite identification allowing it to evolve to chromatography free analysis such as direct infusion and MALDI. With the addition of heavy labelled internal standards, the targeted MS approaches became accepted within the medical and pharmaceutical field. However, the hypothesis free approached lagged behind due to poor data processing options as

well as mass spectrometry challenges, such as low mass accuracy.[129] With the development of mass spectrometers that routinely provide high mass accuracy, enable multiple stage MS/MS and polarity switching the application to expansive metabolomics studies has increased.

In parallel, new data processing tools have emerged, such as peak alignment and detections scripts, blank and background subtraction, alignment of the data based on retention time, de-isotoping and metabolite extraction using spectral libraries.[129] Regardless of these advances there are still several issues to overcome. This centres on the uncertainty of the metabolite identification, currently the identification of unknowns are made by spectral library matching allowing the probability of the metabolite identification to be scored. However, that score alone has no relevance to the statistical accuracy of the assignment, therefore several different groups are working on ways of making metabolomics identifications more statistically relevant.[119,122]

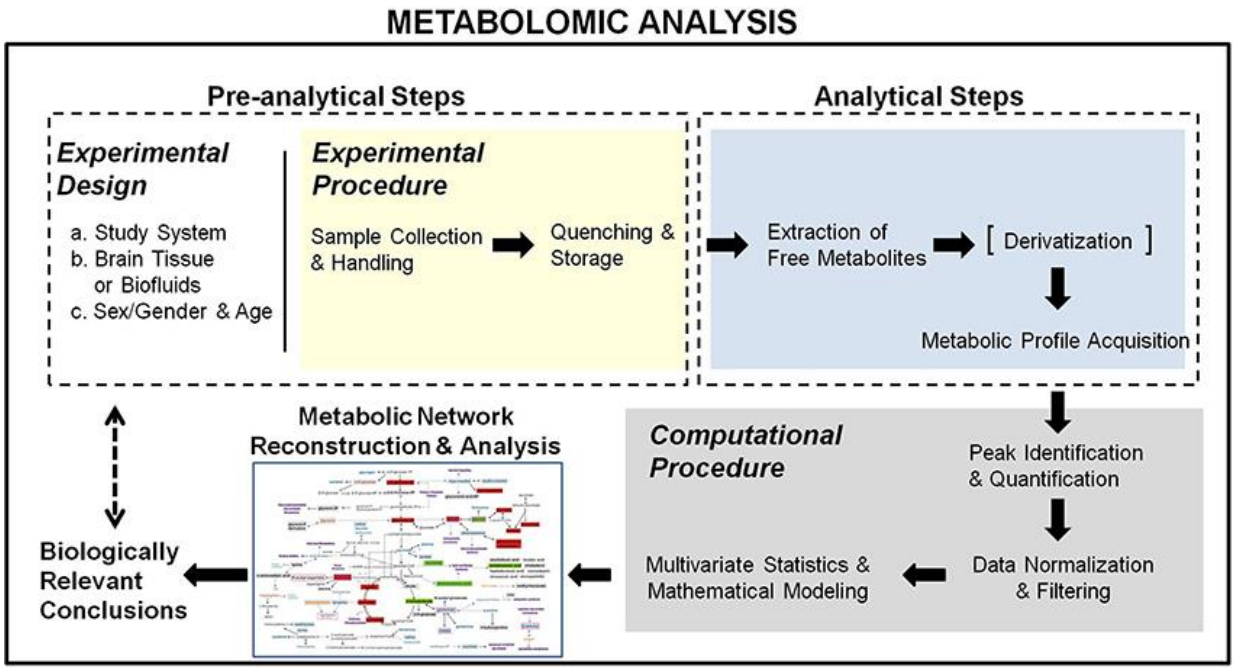


Figure 25: Metabolomics full workflow, with pre-analytical, analytical and computational nodes.[24] The pre-analytical steps are arguably more important that the analysis itself, as a well-designed study facilitates both the analysis and the data processing. The analytical step can be quite varied, using both targeted and untargeted methods as well as different sample preparation methodologies. The computational part of the process can be very challenging, and several different data processing procedures need to be undertaken before the metabolic pathway analysis can be performed. Open-access article distributed under the terms of the Creative Commons Attribution License (CC BY).

2.4) Physical and chemical properties of pharmaceutical compounds and ionization

One of the major problems that the pharmaceutical industry face is drug attrition. If a compound proceeds to the clinical trial stage and fails at any point on that stage that is always associated with the loss of millions of pounds. The reasons why a compound fails at the clinical trials stage are very diverse and some cannot be anticipated, such as species specific toxicity. However, instances where inadequate preclinical target validation is the culprit can be prevented. For this reason, the pharmaceutical industry has devised some preclinical strategies, early in the drug discovery process, those are often referred to as the three pillars of drug discovery. [130]

The three pillars encompass the following concepts:

Pillar 1: Exposure of the compound to the target site of action over a desired period of time.

Pillar 2: Binding of the compound to the target, as expected for its mode of action.

Pillar 3: Expression of the pharmacological activity commensurate with the demonstrated exposure and binding.[131]

Essentially, the three pillars can be summarized as: is the compound getting to the target, is it binding to the target and is it effective? Despite the relative simplicity of the question, the ways to address these problems are rather complex, and in this section the different assays the pharmaceutical industry devised to better answer these questions are explored. One of the strategies devised was to study the compound's physical-chemical properties, and use those properties to predict the behaviour of similar compounds.

Physical-chemical properties are measured in drug discovery to help scientists decide which molecules have the required properties that make drugs efficacious. Lipinski et al. defined in the early 2000s that drug candidates should possess the following physical-chemical properties:

- cLogP below five
- Molecular weight below five hundred
- Less than five hydrogen bond donors

- No more than five hydrogen bond acceptors

This is now known in medicinal chemistry as Lipinski's rule of five.[132] Currently, all pharmaceutical companies use these rules to ensure that their drug candidates have drug-like properties. As a result companies put effort into measuring and calculating physical-chemical properties.

As shown, Figure 26, the main reasons why in 1997 (date of publication) drugs failed to reach market were issues with ADME (adsorption, absorption, distribution, metabolism, excretion). Therefore, pharmaceutical companies started to invest in understanding how these properties affected a drug molecule, and which properties made a compound desirable.

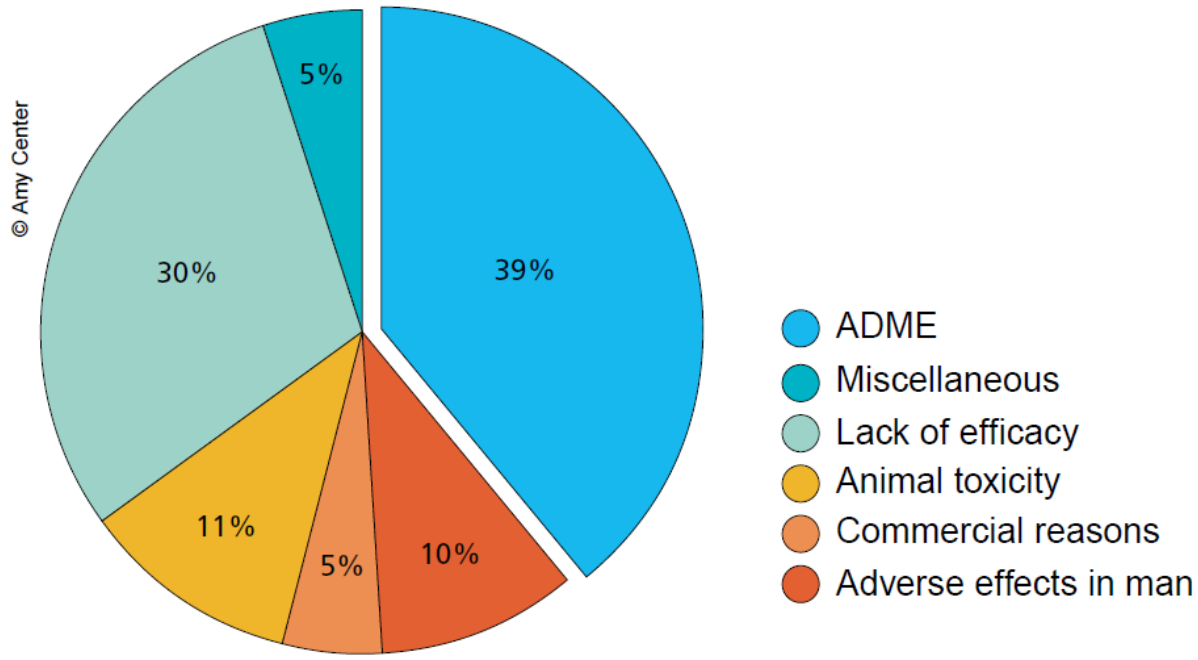


Figure 26: Pie chart depicting the reasons why pharmaceutical drugs fail to reach the market.[25,26] Most drugs fail to make it to the market due to adsorption, absorption, distribution, metabolism and excretion issues. Lack of efficacy, animal toxicity and adverse effects on man are also responsible for a pharmaceutical failure to be marketed. Reproduced with the permission of the publisher, Springer Nature.

Physical-chemical properties are commonly measured or calculated in the pharmaceutical industry to better characterise the compounds and determine if a potential drug candidate has the physical-chemical properties that are desired in a pharmaceutical drug. [50,133]

The properties assessed in this study were both theoretical and empirical and are the ones currently used at GSK to inform drug discovery and development. The properties evaluated were:

- Melting point
- Chromatographic Hydrophobic Index[134] (CHI)
- Properties Forecast Index[30] (PFI)
- Partition coefficient[135] logP
- Chromatographically determined partition coefficient[136] (ChromLogD)
- Acid dissociation constant[137] pKa
- Distribution coefficient[138] (LogD)
- ChemiLuminescence Nitrogen Detector solubility[139](CLND)
- Human Serum Albumin) binding[140] (HSA)
- Retention factor) (LogK) which is the partition coefficient of a compound between the mobile and the stationary phase[141]
- CellConc, the measurement of intracellular compound using LC-MS/MS in HeLa cells[142]
- Molecular weight
- pH

Figure 27 depicts the difference of the in vitro and in vivo processes for a central nervous system (CNS) target. In vitro the only factor to take into consideration is non-specific binding, and the drug's effect can or cannot be seen. On the other hand, *in vivo*, the compound effect is diluted by both ADME and Blood/Brain ratio (BBratio. ADME comprises clearance (Cl), bioavailability (F%), absorption (Abs) and Volume distribution (Vd) and the BBratio is affected PBB (Plasma or blood protein binding), BTB (Brain tissue binding), Perm (permeability across cell membranes), Pgp (P-glycoprotein, or other efflux transporter interaction), all these in vivo parameters have an affect in the mechanism of action (MoA) of a drug and its affinity for its target (pK_b target affinity).[27]

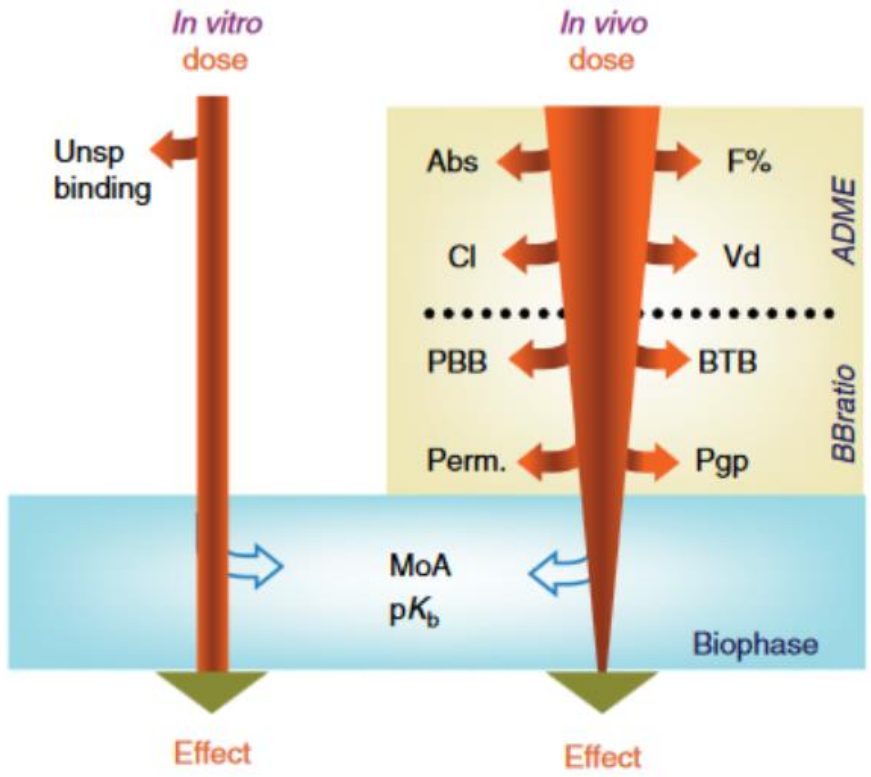


Figure 27: The scheme represents the processes of drug interaction for a CNS target. [27] In vitro assays are only affected by non-specific binding, while in vivo assays are affected by the Blood-Brain-barrier and ADME issues. Reproduced with the permission of the publisher, Taylor & Francis.

Within GSK, as well as in other pharmaceutical companies, several different parameters are measured and calculated to ensure drugs are in the right chemical space.[143]

- pKa is the aqueous ionisation constant, it is defined as the negative base-10 logarithm of the acid dissociation constant (K_a), and it is a measure of acid strength. The lower the pKa the stronger the acid, and this is key to understanding how other properties will be affected by pH. Around 60-70% of drugs undergo acid-base ionisation in solution, and that influences the compound's binding characteristics such as permeability, lipophilicity and solubility.[144]
- Log K is the retention factor; it is determined by chromatographic retention of a given drug and it is affected by temperature.[145]
- The melting point is defined as the temperature in which a compound changes its state from solid to liquid at atmospheric pressure, it commonly used to assess the purity of compounds. It

occurs due to the fact that heat weakens intermolecular force of attraction causing instability in the crystal lattice. There are several different molecular properties that affect the melting point of a molecule, such as molecule size, shape, intermolecular forces, humidity, atmospheric pressure and presence of other molecules.[146] Intermolecular force or types of bonds within a molecule affect the melting point and stronger types of chemical bonds, such as ion-ion interaction, this results in higher melting points. In organic compounds their polarity and presence of hydrogen bonds also results in higher melting points, while molecules that display only weak Van der Waals forces have a relatively low melting point. The size of the molecule also affects its melting point; generally smaller molecules melt at lower temperature than larger molecules. The molecular shape also plays a role in melting point; a molecule with a compact pattern structure usually presents a higher melting point than an oddly shaped molecule.

- LogP is a measurement of hydrophobicity (or by definition lipophilicity), it is defined as the octanol/water partition coefficient and is regarded as a gold standard for measuring partition (logP) or distribution (logD) of molecules.[147]It can be measured in the laboratory or calculated by software packages.[148] LogP refers to intrinsic hydrophobicity, each molecule has an ionisable centre, and logP can only be measured when the compound has no charge. LogD, on the other hand, represents effective hydrophobicity of a given molecule and relates to the distribution of all species at a certain pH, hence it is not constant.[29]

In the early 2000s, software packages for calculating ADMET properties (adsorption, absorption, distribution, metabolism, excretion and toxicology) based upon these principles were an integral part of drug discovery. However, by the mid-2000s pharmaceutical companies started to realise that predictive approaches were not ideal. Mannhold et al. published a study covering approximately 96,000 compounds (206 from a public database and 95,809 from Pfizer's proprietary database) in which they used several different property predictors and they showed that the accuracy of the models declined with the number of non-hydrogen atoms. This study also showed that the majority of the models produced reasonable results for the public database but for the Pfizer database only a few predictors

were better that the arithmetic average of LogP (AAM), for this reason scientists tried to find alternative methodologies.[149]

CHI (chromatographic hydrophobic index) was one of those alternatives developed, it is commonly regarded as a measurement of hydrophobicity. It can be calculated from the retention time observed for a given molecule using a fast reverse-phase HPLC gradient. For the majority of compounds the CHI value will be between 0 and 100, this is roughly the percentage of acetonitrile necessary to achieve an equal distribution of compound between the mobile and stationary phase. This can be performed under acidic, basic and neutral conditions. It can be calculated using the following formula:

$$\log D_{pH} = CHI_{pH} \times 0.0525 - 1.467$$

This formula normally provides a good correlation with clog P (calculated octanol/water partition coefficient). Despite this, it was not widely used due to disconnects between actual values and smaller incremental changes versus the octanol scale.[29] The re-analysis of CHI data originated a new parameter, chromatographic logD, which can be calculated by the following formula:

$$\text{m Chrom log } D_{pH} = CHI_{pH} \times 0.0857 - 2$$

The data obtained by this calculation had a normally distributed dynamic range and good correlation with measured log $D_{pH7.4}$.[134]

Efforts to improve the quality of the physical-chemical predictors resulted in a 31,000 compound study where both the Chrom Log $D_{pH7.4}$ and CLND solubility were measured. The CLND solubility was determined by solubilising the compound for one hour, filtering the solution and assaying the filtrate using chemiluminescent nitrogen detection, this method quickly assessed the solubility of a compound. However, it is likely to overestimate it especially if the compound is highly crystalline and/or has a high melting point.[28]There was a clear correlation between CLND and the number of aromatic rings, Figure 28.

CLND solubility dramatically decreases with increasing number of aromatic rings of the molecule, that effect is clearer in compounds with two or more aromatic rings, as it can be observed in Figure 28.

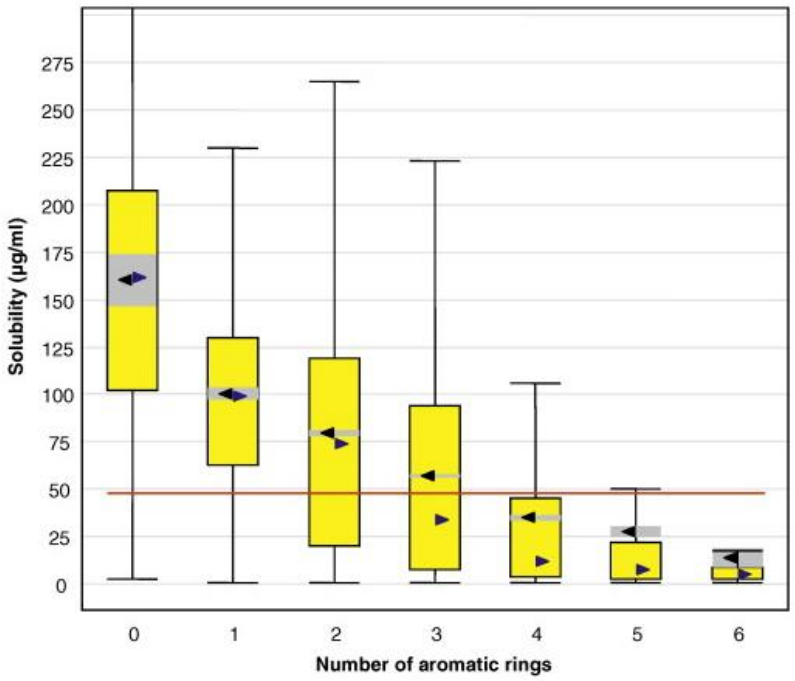


Figure 28: Plot showing the relation between decrease in solubility and increase in the number of aromatic rings. The red line indicates 50 µg/mL solubility levels[28] Reproduced with the permission of the publisher, Elsevier.

One of the other assays devised to study the physical-chemical properties of compounds was the Human Serum Albumin binding assay (HSA). It is often included in the physical-chemical properties assay panel as it is useful to determine if a compound has a high affinity for the protein, which is often an indicator of the drug free fraction, which is the amount of drug available to bind to its target. Young et al. studied the HSA binding of 43700 compounds. In Figure 29, the correlation between Chrom $logD_{pH7.4}$ and number of aromatic rings can be observed, Chrom $logD_{pH7.4}$ in itself does not seem to influence %HSA binding, however when looking at both Chrom $logD_{pH7.4}$ and the number of aromatic rings of a molecule, as it can be seen, as the number of aromatic rings increases so does the %HSA biding. This effect is more visible for compounds with high Chrom $logD_{pH7.4}$. The binding levels were expressed by log K in which K= (%bound / %unbound) and higher binding levels were reported for compounds with high Chrom log $D_{pH7.4}$. In fact, when the number of aromatic rings was included alongside Chrom log $D_{pH7.4}$ a new parameter emerged, the Properties Forecast Index (PFI):

$$PFI = [\log D_{pH7.4} \text{ (or } \log P) + \text{number of Ar}].$$

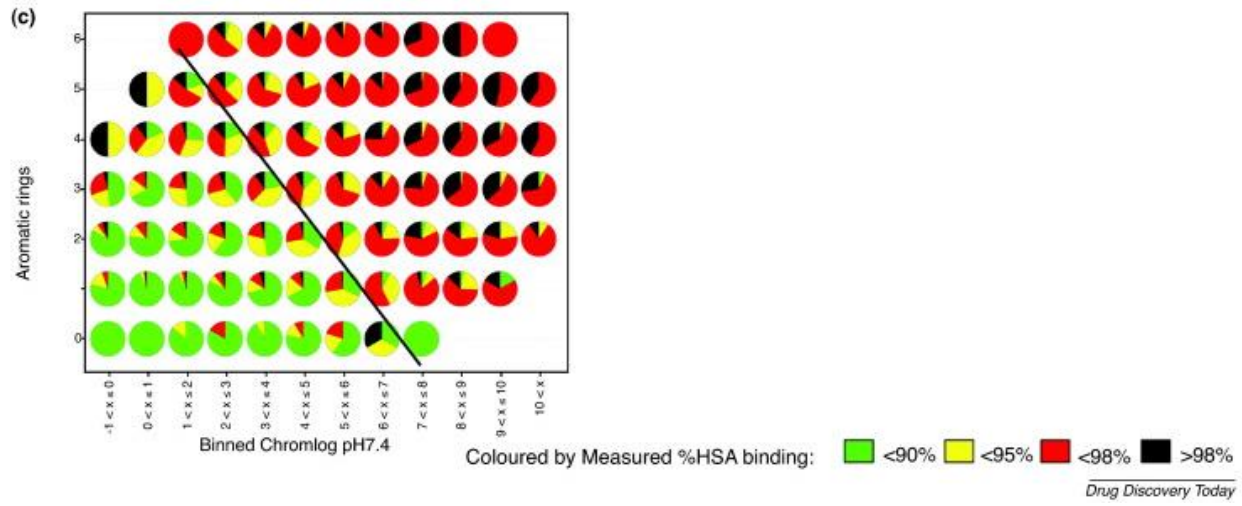


Figure 29: This figure depicts the correlation between Chrom log $D_{pH7.4}$ and number of aromatic rings. The black line depicts PFI=7 which is the threshold that separates what is considered a potentially good drug and a bad one.[29] Reproduced with the permission of the publisher, Elsevier.

As it can be observed in Figure 29, the area above the black line shows PFI values above 7, this equates to high %HSA binding and high Chrom log$D_{pH7.4}$, these compound characteristics are not desirable in drug discovery as they indicate that high protein binding is likely.[29]

Physical-chemical properties, along with in vitro potency measurements, are analysed by experts and used to optimise a given drug's mechanism of action. Drug efficacy is yet another parameter that can be calculated and informs researchers on how drug-like a molecule is and in which direction they should move (Figure 30) in order to place the candidate in the green risk zone. [30]

Drug efficiency is the amount of drug effectively getting to the site of action to bind with its target. It is traditionally measured as the proportion of an oral dose that is free in plasma, and it can be calculated by the equation below.

$$DRUG_{Eff}\ \% = \frac{Biophase Conc\ (\mu g/mL)}{Dose(\mu g/g)} x100$$

Ideally a drug should have high affinity and high drug efficiency. This results in low drug dosage, reducing the probability of unwanted side effects.

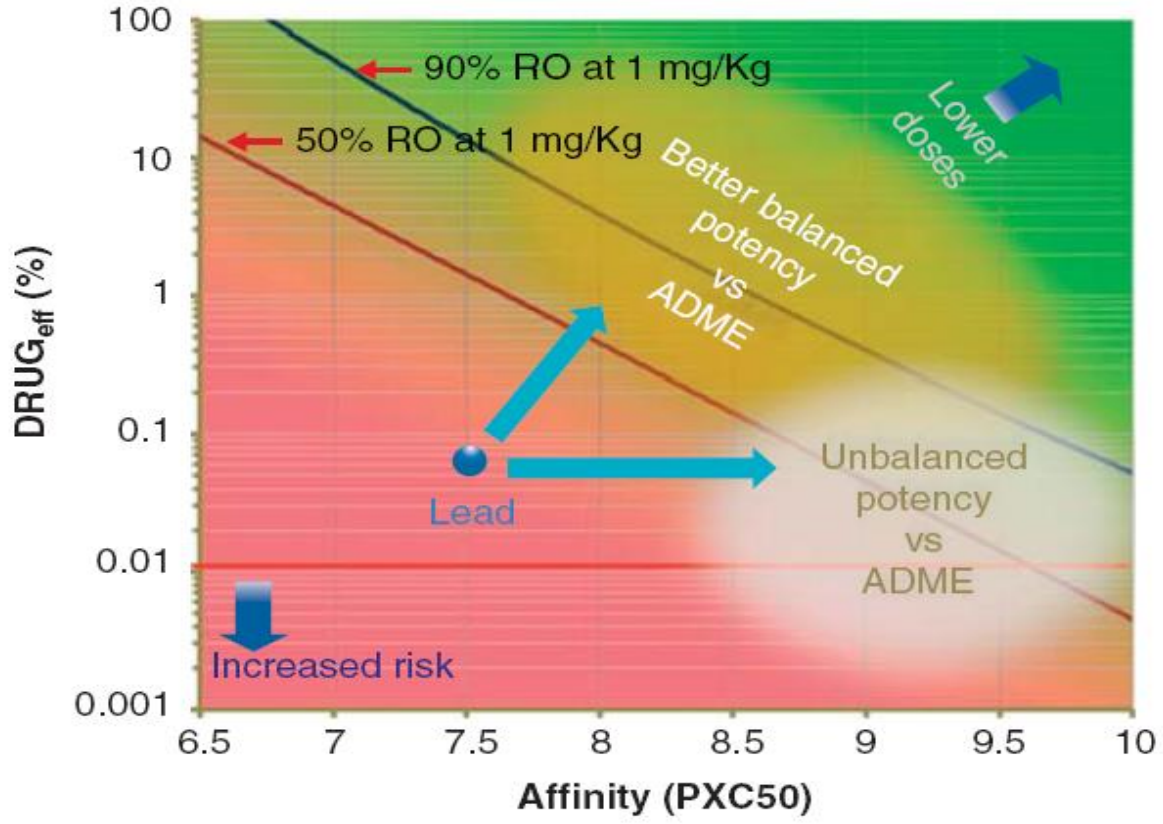


Figure 30: Plot depicting DRUG efficacy Vs affinity.[27] The plots depicts the fine balance between drug efficacy and target affinity, any molecule with a drug efficacy below 0.01 % has an increased risk of failing. Ideally, lead candidate molecules should move to the green space of the plot, to a higher drug efficacy and affinity beyond at least the 50% Receptor occupancy (RO) line.

Despite the efforts of scientists in trying to place their lead drug candidate in the ideal chemical space depicted by the green zone of the plot in Figure 30 it is getting increasingly harder to get drugs into the market. The reasons for this are varied:

- Misinterpretation of the rule of five.
- Missing the drugs that do not follow the rule of five as there are precedents of drugs that do not follow these rules, as shown in Figure 31.
- Harder to identify effective drugs against many of the unmet medical needs
- Disease risk/benefit ratio.
- Hit selection and potency hunting.

- Synthetic disability versus design desirability, often the molecules that fit the drug desirability criteria are hard to synthesize.
- Divergent design practices, physical-chemical properties of marketed drugs have high variability.[30]

In Figure 31, it can be observed that in general, the drugs developed overtime conformed with the first two statements of Lipinski's rule of five. However, drugs developed between 2000 and 2010 (in red in Figure 31) are moving towards the upper limits described by Lipinski for both molecular weight and cLogP. Therefore, a holistic approach that balances attention between activity and physical-chemical properties is more likely to yield candidates that can become good drugs.

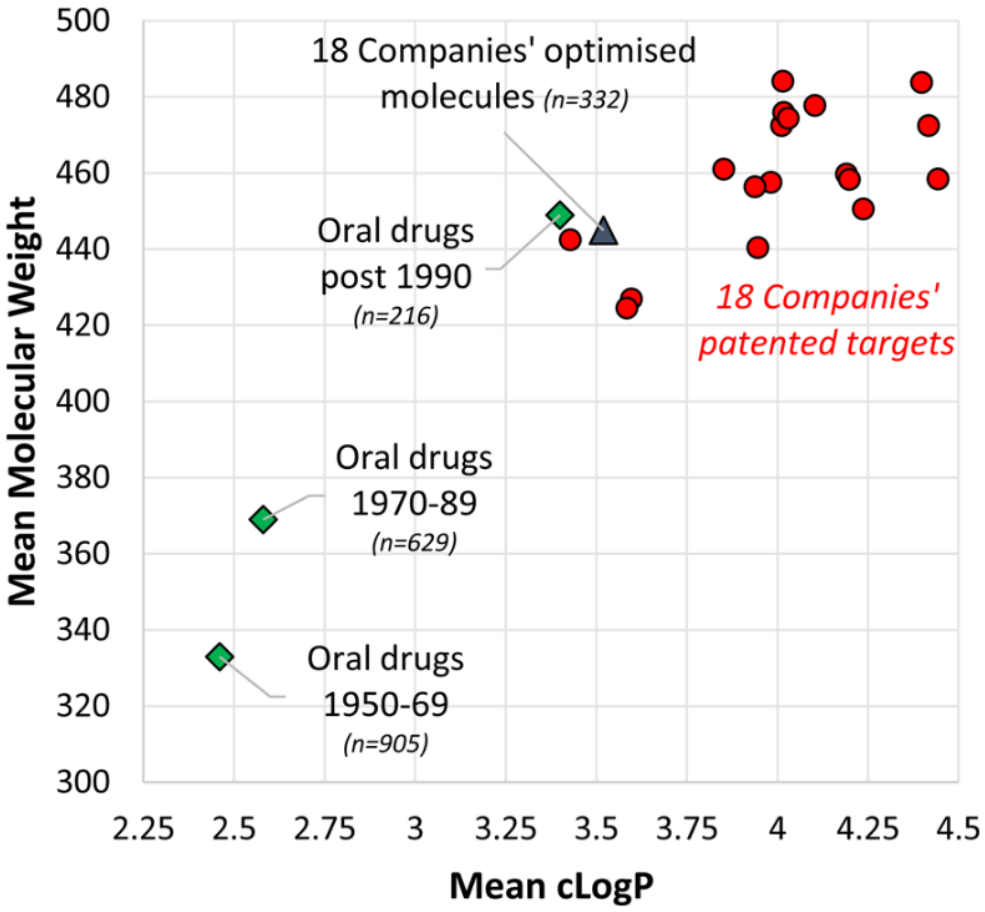


Figure 31: The plot of mean molecular weight and cLogP values of oral drugs .[30] For three different time periods (green), this shows that both molecular weight and cLogP have increased with time. In red, are the values for the patented compounds for

18 pharmaceutical companies between 2000 and 2010. In blue is the single compound patents from the same companies. Reproduced with the permission of the publisher, American Chemical Society.

The physical-chemical properties previously discussed are distributed across the three pillars approach, ToF-SIMS can potentially address the problem of Pillar 1, as intracellular drug can be identified using this technique.[5] However, it is very difficult to predict if a compound is going to be detectable using ToF-SIMS, especially in a complex biological matrix, such as cells and tissues. Here, the different physical-chemical properties of compounds are investigated in order to determine if any of them can be used as a predictor of ToF-SIMS ionization efficiency.

Ionization is crucial in mass spectrometry; there are several types of ionisation, but arguably the best know and well characterised is electrospray ionisation (ESI).[150] A relative ionization efficiency can be determined by comparing the ionization of two compounds, one test and one standard, and then applying a mathematical model to determine how compound**s** rank on a log scale. This was performed for ten organic compounds using an ion trap mass spectrometer, and it was shown that absolute ionization efficiency was strongly dependent on the formation of the sodium adduct. Despite this, the mathematical model was only applied to mono-protonated species.[151] This study was extended to include sixty-two compounds of different chemical nature and a six order of magnitude difference was observed. The authors found that the two most influential parameters are pKa and the molecular volume of the compound.[152] In this study, measurement of hydrophobicity, LogP, was deemed as not statistically significant. However, the value used was LogP determined in hexane, other authors that conducted studies in methanol and acetonitrile have identified a correlation between ionisation efficiency and logP.[153]

These publications start to shed some light on small molecule ionisation; however, this process might be very different for ToF-SIMS ionisation. Unfortunately, the ToF-SIMS ionisation efficiency and process, in general, is not well understood, especially in biological matrices. The most comprehensive study done to date was by Vorng et al., who studied twenty drug molecules with different physical-chemical properties in a biological matrix. It is important to clarify that this work was undertaken using

a biological model, lyophilised bovine liver tissue, and the concentration of compound used was 167 µg/mL which is well above therapeutic doses.[153]

They found that nine of the twenty drugs studied had a protonated signal in positive ion mode and four had a deprotonated signal in negative ion mode, while seven of them provided no signal. Most drugs observed in positive ion mode had a tertiary amine, and a linear correlation was observed between the drug's ion yield and their LogP value. It is noteworthy that when comparing the yield of pure compounds and compound in a biological system, there was a considerable drop in ionization efficiency for drugs in matrix and it varied greatly between positive and negative mode.[153]

In this thesis, it was attempted to determine which test substrate best correlates with the compound signal after the pharmaceutical was up taken by mammalian cells, so the preliminary feasibility study is a good indicator of the propensity for ionisation of a given compound. For this, in addition to the cells incubated with compound, four other samples were prepared: compound solubilised in 50:50 methanol: water (Neat), that solution spotted on a liver tissue section (tissue), same preparation as the Vorng et al. publication (JLV) and on a cell lysate (CL).

2.5) Amiodarone and cell lines

2.5.1) Amiodarone

Amiodarone or 2-butyl, 3-(4-diethylaminoethoxy, 3,5- diiodo, benzoyel) benzofuran hydrochloride, is an anti-arrhythmia drug that came to medical use in 1962.[154] It is used for the treatment of both atrial and ventricular arrhythmia, and it is effective in at least 80% of the patients treated.[155]Amiodarone works by prolonging the durations of the action potential of the cardiac muscle, and it is classified as a class III anti-arrhythmia agent, which means it is a potassium channel blocker and prolongs the depolarisation and repolarisation (QT interval) of the cardiac muscle. However, it also has calcium channel blocking properties (class IV), beta blocking properties (class II), making it also effective at slowing the heart rate and atrioventricular nodal conduction.

In addition, it has sodium blocking properties (class I), which prolongs refractoriness and slows intra-cardiac conduction.[156] Until the late 1990s amiodarone was still prescribed, and in 1998 it accounted for 24.1% of the total antiarrhythmia prescriptions, being especially prevalent in Latin America (73.8%), Europe (34.5%) and North America (32.8%).[157] Currently is is only used in extreme cases, as it has several severe side effects, such as thyroid de-regulation and pulmonary toxicity, the latter was the reason why it was choosen forinclusion in this thesis, as it is known to accumulate in alveolar macrophages in the lung and cause patients breathing difficulties to patients.

Clinical trials, especially the European Myocardial infarct Amiodarone trial (EMIAT), published in the Lancet in 1997, enrolled 1486 patients (743 on the amiodarone group and 743 on the placebo group, Figure 25) for 21 months. Although it did not show an improvement in cardiac mortality in patients on amiodarone it showed that the risk of arrhythmic deaths decreases 35% in the amiodarone group.[31]

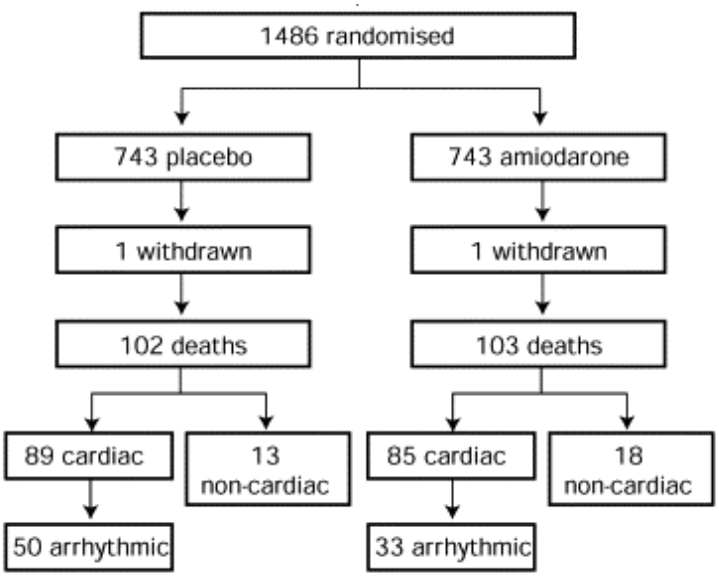


Figure 32: EMIAT trial profile.[31] This study, involved the treatment of patients with amiodarone and a placebo, the number of patients in each group was the same. The number of deaths was slightly higher on the amiodarone group, particularly due to the non-cardiac related deaths, which is associated with the toxicity associated to this compound, the number of non-cardiac deaths in the placebo group was much lower, 13 versus 18. Despite this, in terms of arrhythmic event associated death the number were much greater in the placebo group when compared to the amiodarone treated group (50 versus 33) which indicates that amiodarone has a positive effect when treating arrhythmic events. Reproduced with the permission of the publisher, Elsevier.

This study regards amiodarone as a good treatment for antiarrhythmic conditions; it also starts to provide some clues in regards to amiodarone associated toxicity, as thyroid, skin and liver disorders are reported in the amiodarone group.[31] This data prompted additional studies, and slowly the amiodarone associated toxicity was proved.

Pharmacological studies revealed it has a very large volume of distribution, a low total clearance, and a long half-life, around 40 days.[158] This pharmaceutical generally has poor bioavailability ranging from 22 to 95 percent due to its highly lipophilic nature and the fact that it is stored in high concentration in fat, the liver, lungs, muscle and skin; its absorption can be enhanced when taken simultaneously with food. It can cross the placenta and can be measured in breast milk.[159]

As it can be observed in Figure 33A the amiodarone concentration measured by LC-MS/MS in fat tissue is much greater than in plasma, between 10 to 100 fold. Furthermore, there is a clear correlation between plasma and fat tissue amiodarone concentration, as it can be observed in Figure 33B. Therefore, plasma concentration is an incorrect assessment of drug bioavailability as illustrated in Figure 33.

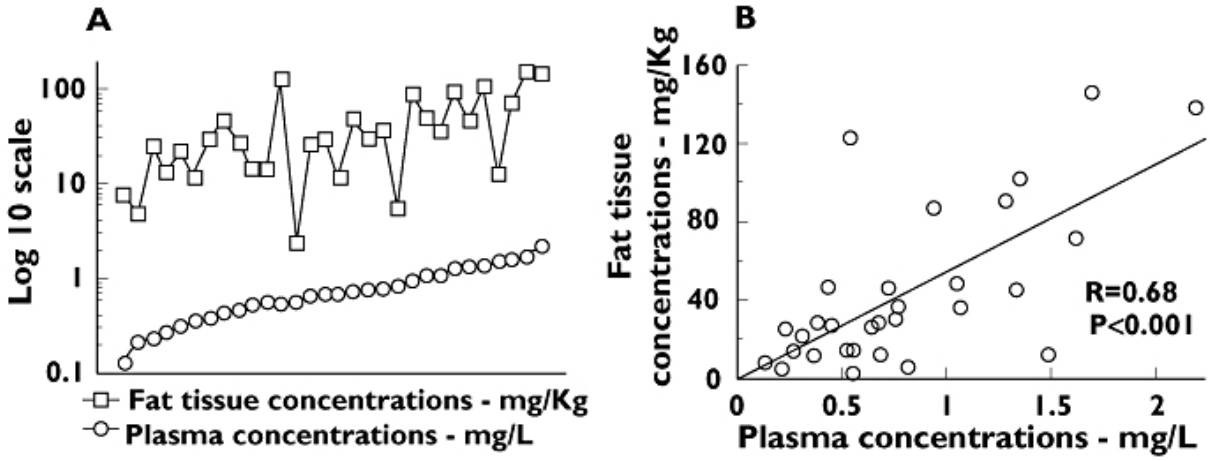


Figure 33: Amiodarone concentrations measured by LC-MS/MS of fat and plasma of human patients treated with amiodarone. (A) showing a comparison of the concentrations in fat tissue and plasma on a Log scale. (B)Correlative plot of the plasma and fat concentrations.[32] As demonstrated in this two plots, there is a correlation in amiodarone concentration between plasma and fat tissue. However, the amount of amiodarone in fat tissue is 10 to 100 fold more concentrated, which could be expected due to amiodarone lipophilicity. Reproduced with the permission of the publisher, Elsevier.

Amiodarone treatment has many side effects: pulmonary and liver toxicity, thyroid deregulation, optic neuropathy, photosensitivity and skin disorders including a blue tinge.[159]One of the many side effects induced by amiodarone is thyroid dysfunction when patients are undergoing amiodarone treatment for an extended period of time. It is estimated that between 14 to 18% of patients undergoing amiodarone treatment will develop thyroid deregulation; this is mainly due to the excess of iodine these patients are subjected to. Approximately 10% of the molecules are de-iodinated daily; a common amiodarone dose ranges from 200 to 600 mg which means there is approximately 7.8 to 23.4 mg of iodine made available each day, that is between 50 to 100 fold the daily recommended dose of iodine.[160]

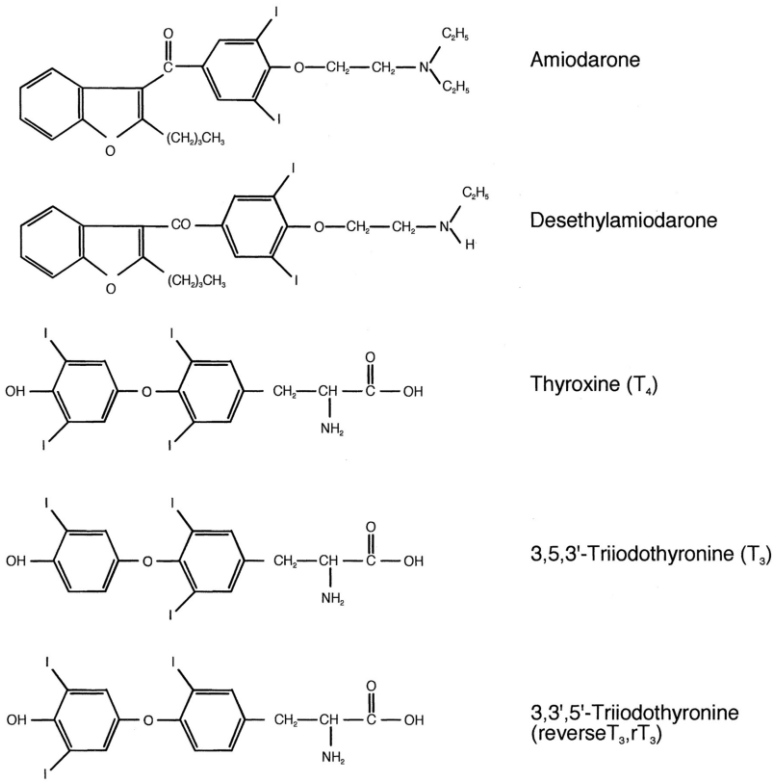


Figure 34: Molecular structures of amiodarone, its metabolite, desethylamiuodarone (DEA) and the thyroid regulatory hormones.[33] The similarity between the molecules is known to cause disturbance in T3 productions causing potential thyroid deregulation. Reproduced with the permission of the publisher, Oxford University Press.

Amiodarone long term exposure is known to decrease the triiodothyronine (T3) production as well as slowing the clearance rate of thyroxine and reverse T3 in serum, causing iodine-induced hyperthyroidism or hypothyroidism.[160] One of the other amiodarone side effects is photosensitivity and

skin pigmentation. Around 75% of the patients on amiodarone develop photosensitivity, this normally happens after four months of treatment when the cumulative amount of amiodarone is approximately 40 g. Microscopy examination of skin from amiodarone treated patients show signs of perivascular inflammation. [161] In severe cases the skin can present blue-grey pigmentation, as shown in Figure 35.



Figure 35: Amiodarone induced pigmentation in patient.[34] This patient suffered from severe blue-grey pigmentation in areas of the skin exposed to the sun caused by long term amiodarone treatment. It is thought that this hyperpigmentation is caused by dermal lipofuscinosis, as lipofuscin accumulates in dermal macrophages; this was hypothesised as amiodarone is known to cause lysosomal damage. Fitzpatrick's Color Atlas & Synopsis of Clinical Dermatology Klaus Wolff, Richard Allen Johnson, Dick Surmount Copyright 2005, 2001, 1997, 1993 by The McGraw-Hill Companies. All Rights reserved.

The drug induced hyper-pigmentation hypothesis was confirmed using LC-MS/MS where the drug and its metabolite were identified at a concentration ten times higher in areas where hyper-pigmentation was observed relative to normal areas of the skin.[34,162] Photosensitivity decreases and ceases 4 to 12 months after the withdrawal of amiodarone.[161]

One of the other side effects of amiodarone therapy, perhaps the most serious of all, is pulmonary toxicity. The clinical features associated with this condition are often cough, dyspnea, hypoxemia, leukocytosis, elevation in the erythrocyte sedimentation rate, accumulation of foamy macrophages in

the alveolar spaces and decreased lung function test results.[163] There are often radiologic findings in these patients, and they are consistent with diffuse interstitial and patchy peripheral alveolar infiltrates mainly associated with the upper lobes. This can then progress into chronic organising pneumonia, acute fibrosis of the lung and acute lung injury associated with acute respiratory distress syndrome.[164]Common pathological findings associated with this condition can be observed in Figure 36.[35]

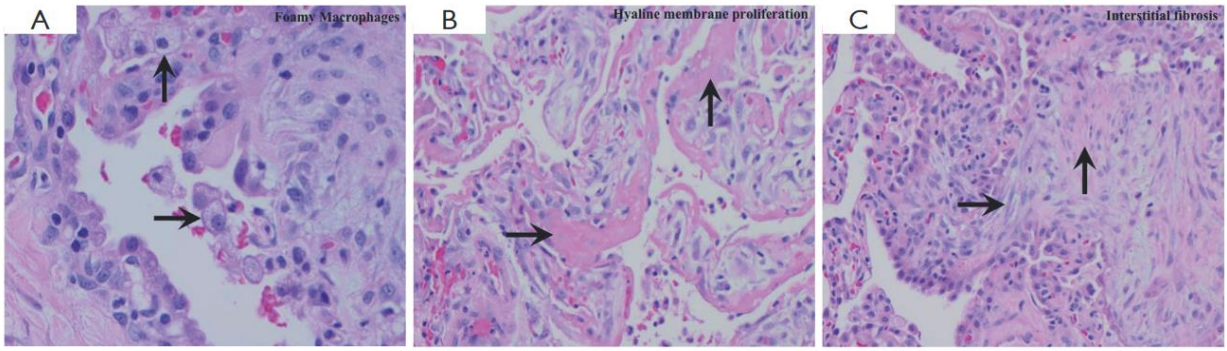


Figure 36: Amiodarone associated pathological finding, arrows point to examples of each event, in (A) two foamy macrophages, in (B) two areas of membrane proliferation and (C) two areas of interstitial fibrosis.[35] Reproduced with the permission of the publisher, Pioneer Bioscience Pub. Co.

Approximately 5% of patients that were treated with amiodarone for long periods of time develop a lung related toxicity.[165] The condition is so common that is now referred as Drug Induced Interstitial Lung Disease (DILD) but its manifestations are extremely varied, ranging from benign infiltrates to life threatening acute respiratory distress syndrome. As it more commonly occurs in older patients these patients are no longer prescribed amiodarone as the negative side effects surpassed the benefits in most cases; DILD is very difficult to diagnose if an accurate medical history was not available. Currently, doctors have other tools at their disposal, and in addition to the classical histology methods they also have serum markers that are commonly associated with these conditions, for example, and increase in KL-6 (Krebs von den Lungen 6) in serum points to a DILD diagnosis.[166]

There is not a clear treatment for DILD; the clinician needs to concentrate on how the DILD manifests and treat that condition. It is noteworthy that amiodarone is only one of 450 drugs known to cause DILD.[167]

In addition to the complications associated with amiodarone therapy, amiodarone is known to cause drug interactions with other pharmaceutical compounds. The main effects are related to the kinetics of other commonly used cardiovascular drugs such as digoxin, quinidine, procainamide and warfarin or dynamic interactions with beta blockers and calcium antagonist.[168,169]In this study, the interest in amiodarone is due to the fact that this compound is known to cause phospholipidosis by inhibiting group XV phospholipase A2[170] in macrophages.

2.5.2) NR8383 cell line

NR8383 are a rat (Sprague-Dawley) derived alveolar macrophage cell line obtained by lung lavage,[171] it is a spontaneously transformed alveolar macrophage cell line that exhibits phagocytosis properties. It is relatively well characterised, and it is known to have Fc receptors, interleuckin-1 secretions, respond to exogenous grow factors, have non-specific esterase activity and also present oxidative burst susceptibility.[172]

The phagocytic properties were evaluated in the first study undertaken using this cell line by Helmke et al., who demonstrated the ability of the cells to ingest Zymosan (between 90 to 98% of the cell population) and phagocyte *pseudomonas aeruginosa* (between 50 to 80% of the cell population). [171,173]

Over the years, many studies have been conducted to determine how similar endogenous macrophages are to the NR8383 cell line. This cell line is commonly used in vitro to determine the pro-inflammatory or anti-inflammatory activity of compounds which is assessed by the secretion of cytokines or macrophage migration inhibitory factors.[174]

NR8383 cells were further characterised by evaluating their mannose receptor expression. Mannose receptor expression is thought to be crucial in macrophage activity, as this transmembrane glycoprotein is known to bind to particulate ligands; these ligands are often pathogens, which means that mannose receptors expression is closely related to functional macrophages. In Lane et al. similar internalisation

of mannose receptor ligand horseradish peroxidise was detected by DNA analysis between NR8383 cells, alveolar macrophages and the isolated protein.[175]Disease relevant interleukins (IL), such as IL-24, are also present both in NR8383 cells and freshly collected rat alveolar macrophages.[176] The NR8383 cell line is also a useful model of macrophages for microorganism infections and was used by Hino et al. to mimic tuberculosis infection in humans.[177]

For the study presented in this thesis the potential use of the NR8383 cell was assessed as a means of investigating the affects amiodarone has in vitro in alveolar macrophages. This was first evaluated using fluorescent dyes, such as lysotracker red, to visualise the increase in cell size and lysosome number. The potential use of this model in ToF-SIMS was investigated as it was hypothesised that the relatively high levels of compound in the macrophage would facilitate compound detection.

2.5.3 HeLa cell line

HeLa cells are arguably the most used immortalised cell line in the history of medical research. These cells revolutionised the medical research field as they were the first cells to be cultured successfully and immortalised; until then researches had to work with cells that did not survive for long in culture and were very heterogeneous, affecting the outcome of the experiments.[178]

There have been numerous studies conducted using HeLa cells, a key one focuses on the ability of HeLa cells to contaminate other cells in culture due to their resilience.[179] Within GSK HeLa cells are extensively used for a variety of assays including an assay that measures the intracellular drug concentration, which informs project teams about the permeability of their compounds as well as its intracellular distribution.[142]

2.5.4 Hek293 cell line

Hek293 cells are one of the most used cell lines in research along with HeLa and CHO (Chinese hamster ovary) cells.[180] They were derived from human embryonic kidneys and are extensively used as a recombinant protein and vaccines expression tool[181] and in electrophysiology.[182] Despite having been generated in 1973 in Alex van der Eb's lab in the Netherlands,[183] and being extensively used in research

there is not much information available on this cell line when it comes to provenance, phenotype, karyotype and tumorigenicity. In fact, gene expression data does not present any tissue specific signature and these cells express markers of renal, neuronal and adrenal glands cells.[184] Nevertheless, this cell line is commonly used in ion channel studies as they display inducible synaptogenesis, and propagate neurotropic viruses, which indicates their potential neuronal lineage. Despite this, there are caveats to the use of these cells, as they do not provide the biochemical complexity, intricate cellular architecture and sub-cellular organisation that neurones provide.[185–187]

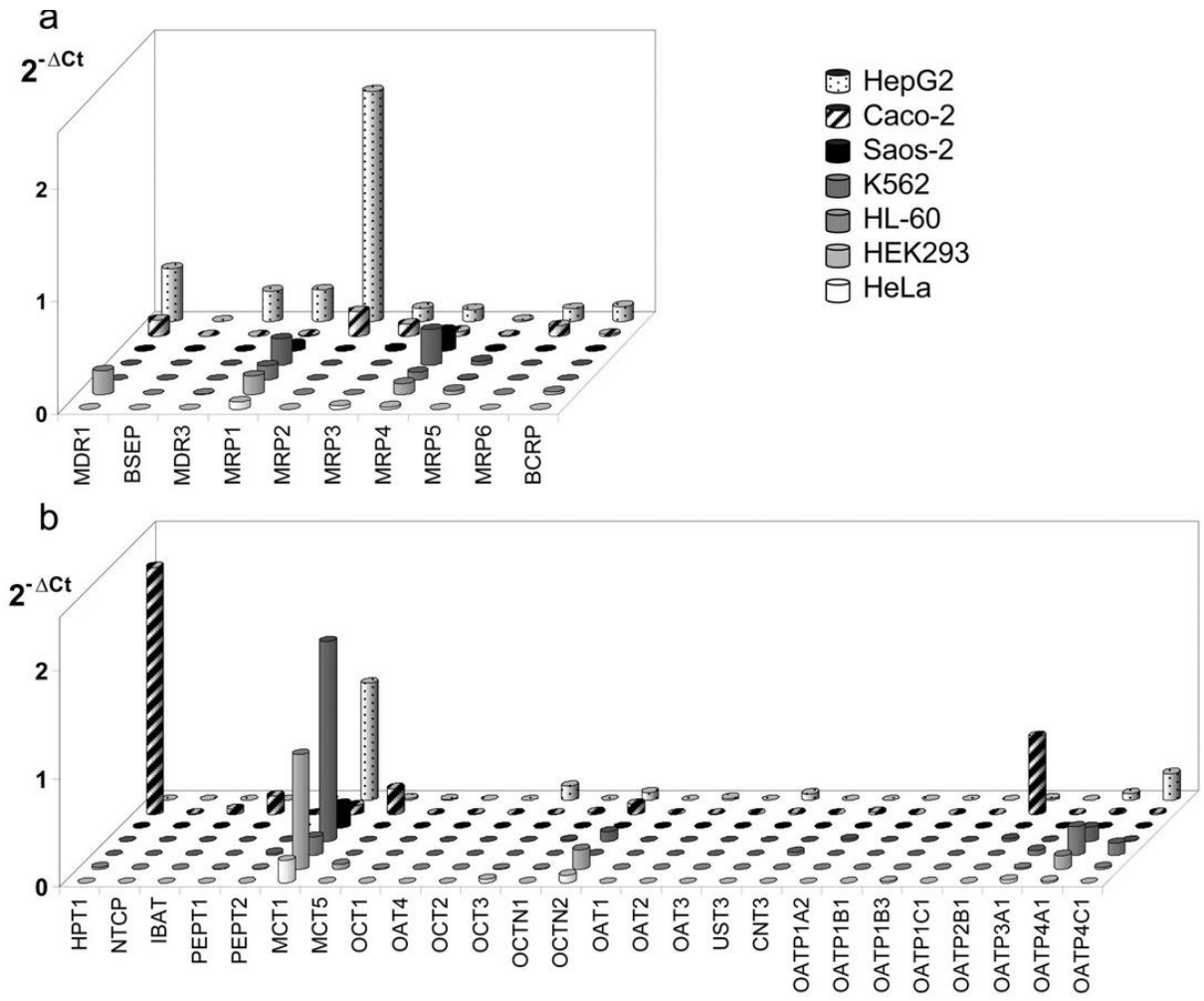


Figure 37: Plots displaying the relative difference in gene expression of ABC transporters (A) and SLC transporters (B) in HeLa, Hek293, HL-6-, K562, Saos-2, Caco-2 and HepG2.[36] Plot a shows that HepG2 have the most ABC transporters from the cells types investigated, while HeLa have the least. For SLC transporters HeLa cells again have the least amount of these

transporters on their membrane. Reproduced with the permission of the publisher, American Society for Pharmacology and experimental therapeutics.

Hek293 cells are extensively used in biotechnology, as these cells are very stable and produce high titres of recombinant proteins. Hek293 cells are particularly useful in instances where the use of CHO cells is inadequate; CHO cells do not perform human glycosylation patterns due to the lack of enzymes such as (2–6) sialyltrans-ferase and (1–3/4) fucosyltransferases, and in addition their murine origin can potentially induce immugenicity due to their own glycosilation moieties.[188]

Hek293 have been used in studies to determine intracellular drug concentrations using LC-MS/MS in a similar assay to the use of HeLa cells.[189,190] These studies have been conducted in Hek293 cells as they are known to have low expression levels of drug transporters and drug-metabolising enzymes. The Per Artursson's group, published extensively on Hek293 intracellular drug penetration, after publishing the study where gene expression of ABC (ATP-binding cassette) and SLC (solute carrier) transporters were studied.[36] In this study, the gene expression levels of 36 transporters were quantified (10 ABC, 25 SLC and one human peptide transporter) in eight commonly used cell lines in research and the results can be observed in Figure 37.

The data (Figure 37) indicates that both HeLa and Hek293 cells present a low expression level of these transporters and this is the reason why there were chosen for the study described in this thesis, as the lack of significant levels of transporters limits their effect on compound uptake into cells.

2.5.5 HepG2 cell line

HepG2 cells, a human hepatocellular carcinoma derived cell line, are commonly used as a liver model in toxicity studies as they are a cost effective alternative to the more biologically relevant primary human hepatocytes. [191] The main characteristics that make these cells an acceptable alternative to human hepatocytes are: stable phenotype, readily available, unlimited lifespan, epithelial-like morphology, fast growing, easy handling and they maintain some hepatic characteristics. The main hepatic functions retained by HepG2 cells relate to secretion and synthesis of plasma proteins,

lipoprotein transport and metabolism, glycogen and bile synthesis, insulin signalling and cholesterol and triglyceride metabolism.[192]

Despite this, there appears to be limited expression of transporters and drug metabolising enzymes when compared with hepatocytes, especially in cytochrome P450 associated enzymes (CYP2D6, CYP2A6, CYP3A4, CYP2C9 and CYP2C19).[192]Costantini et al., performed a comprehensive analysis of the differential gene expression between HepG2 cells and human hepatocytes. Figure 38 illustrates how the genes are grouped according to their functions and the pie chart A depicts the genes that are up regulated in HepG2 cells (2646 genes) while B the down-regulated genes (3586 genes).[37]

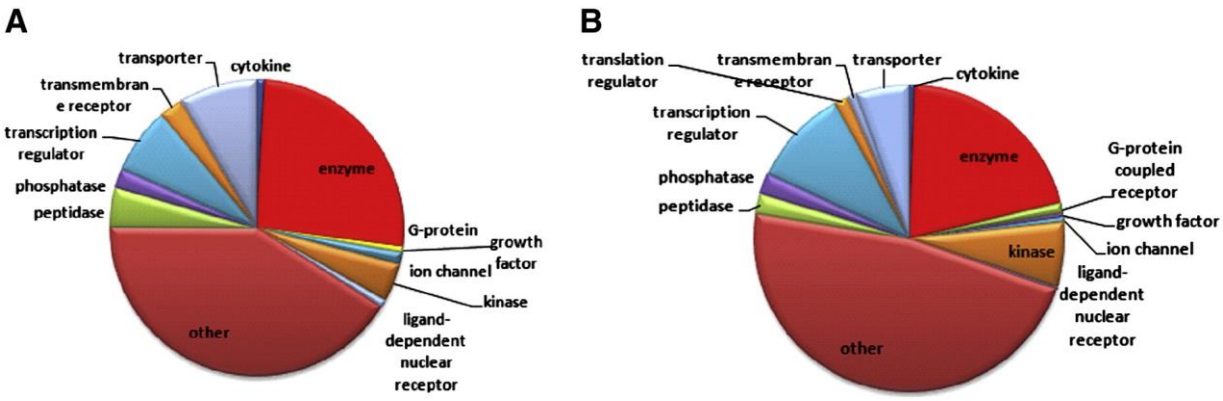


Figure 38: Pie charts depicting the difference in gene expression between HepG2 cells and primary hepatocytes. In (A) the up-regulated genes and (B) the down-regulated genes.[37] Genes that are up-regulated, are genes whose expression is increased and down-regulated genes are genes whose expression is decreased. Reproduced with the permission of the publisher, Elsevier.

In this study ingenuity Pathway Analysis (IPA) was performed to map the differential expressed genes to functional metabolic networks. The up-regulated genes were involved in molecular and cellular functions, hepatotoxicity functions, cell cycle and cell to cell signalling. The down-regulated genes are involved in infectious and immunological disease, lipid metabolism, energy production and small molecule metabolism.[37]Detailed proteomics studies such as the one undertaken by Geiger, et al[193] could be performed to obtain more details about the differences between the four different cell lines chosen as part of this study. However, this is beyond the remit of this PhD thesis.

2.7) *Mycobacterium*

The *Mycobacterium* genus comprises of over 60 species and can be separated into rapid and slow growers. It is characterised by possessing waxy, very thick, lipid-rich hydrophobic cell walls, which grow as fungus-like colonies in liquid media. Taxonomically they belong to the order Actinomycetales and Family Mycobacteriaceae.

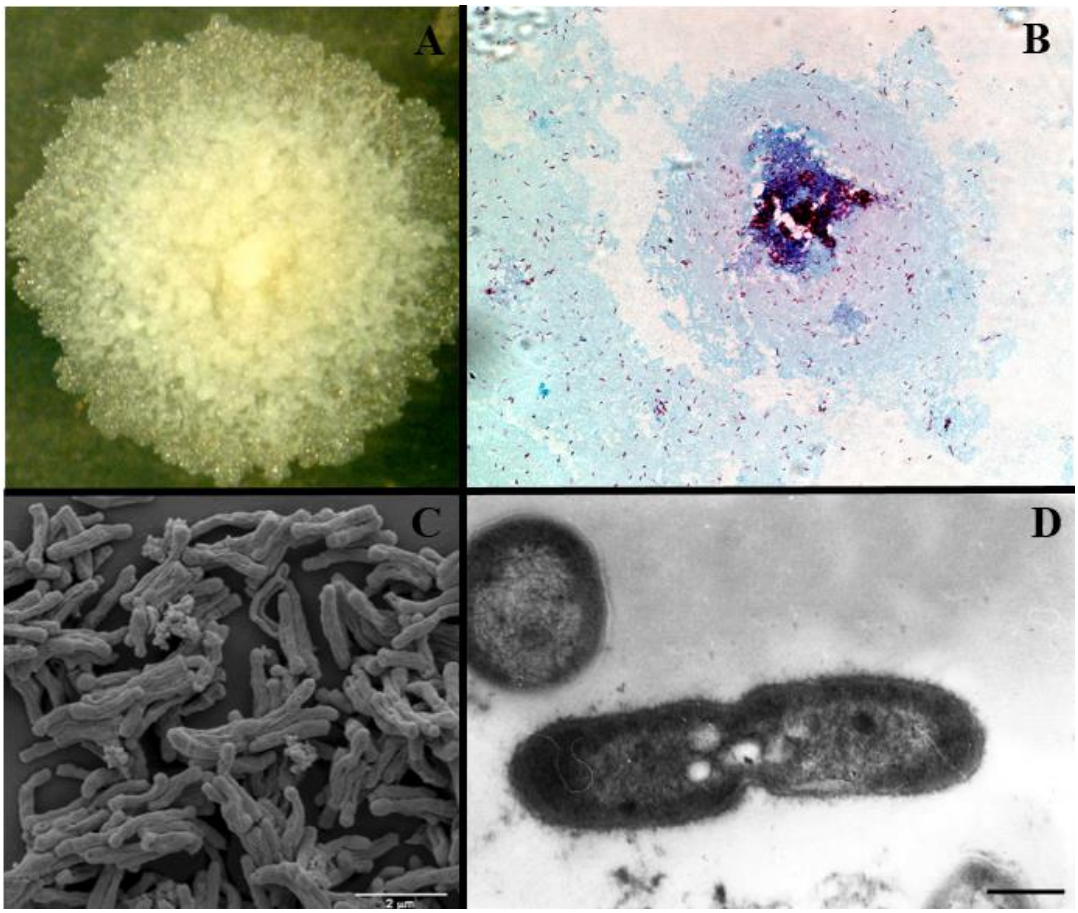


Figure 39: Mycobacteria. (A) Morphology of colonies on solid media[38], Reproduced with the permission of the publisher, Elsevier. (B)Acid-fast bacilli (MBT) stained with Ziehl-Neelsen and extracellular material stained with Alcian Blue visualized at x100 magnification, (C) SEM image of an agglomerate of mycobacteria in exponential growth stag,e,[39] (D) TEM of ultra-thin sections of *Mycobacterium tuberculosis* replicating by binary fission, scale bar 200 nm.[40] Images reproduced under the Creative Commons License (Attribution–Noncommercial–Share Alike 4.0 Unported license.

Mycobacteria are aerobic, non-motile, non-spore-forming acid fast (Ziehl-Neelsen) bacilli, as it can be seen in Figure 39. Their cell wall is made of highly complex mycolic acid-containing long-chain

glycopetidolipids and glycolipids, which confers them low permeability, resulting in their resistance to therapeutics and disinfectants and their ability to survive in different environments.[194]

The most well-known species is *mycobacterium tuberculosis* (MBT or MTB) which was identified by Robert Koch in 1882, for which he received a Nobel Prize in 1905. Tuberculosis (TB) has been claiming lives since around 3 million years ago[195] and throughout history, overcrowding, poor hygiene and poverty were ideal conditions for the spread of disease and TB was endemic in Europe from the 1600s to the 1800s. Several epidemics during the 1800s in Europe and the 1900s in North America claimed thousands of lives, the disease has yet to reach its peak globally as some areas of Africa and Asia present extremely high disease rates.[196,197]

TB is transmitted through aerosols and droplets by the respiratory route with sporadic exceptions such as ingestion, intrauterine and coital.[198]Patients with the active disease can expel MBT during sneezing, coughing or by talking.

The discovery of x-rays in 1895 was crucial for TB diagnosis and the development of a vaccine in 1921, the BCG (Bacille Calmette-Guerin) vaccine, discovered by Albert Calmette and Camille Guerin at the Pasteur Institute, were crucial in controling a disease that until the middle of the 20th century was untreatable. In fact, the treatment of the disease did not occur until the discovery of streptomycin in 1944 and isoniazid, the first mycobacterial drug, in 1952. This and the introduction of rifamycins in 1957 saw the TB rate decrease almost 6% year on year between 1953 and 1985, due both to treatment and prophylactic measures such as vaccination.[199]

However, the decline of the TB dedicated infrastructure, as well as new epidemics as the human immunodeficiency virus infection and acquired immunodeficiency syndrome (HIV/AIDS), combined with increased immigration from counties with high TB rates contributed to a resurgence of TB in the US from 1986 until 2010 and the emergence of drug-resistant TB.[197] The CDC (centre for disease control) reported that in 2016 a total of 9,272 cases (2.9 cases per 100,000 persons), a 3.6% decrease from the number of cases reported in 2015. Despite this, TB is the world's leading infectious cause of death and the biggest infectious killer of all times.[42] It is thought that one third of the world population has latent TB and it is estimated that TB is responsible for approximately 2.5% of all deaths in the

world.[199] In this thesis, we will concentrate on the non-pathogenic model Bacillus Calmette-Guerin (BCG) *M.bovis* as a MBT model.

2.7.1) Disease pathogenesis

Pathogenesis of MBT is divided into four stages once the bacilli are inhaled and taken through the bronchial tree to the alveoli. The deposition of the bacilli triggers a series of immunologic events as it can be observed in Figure 40.

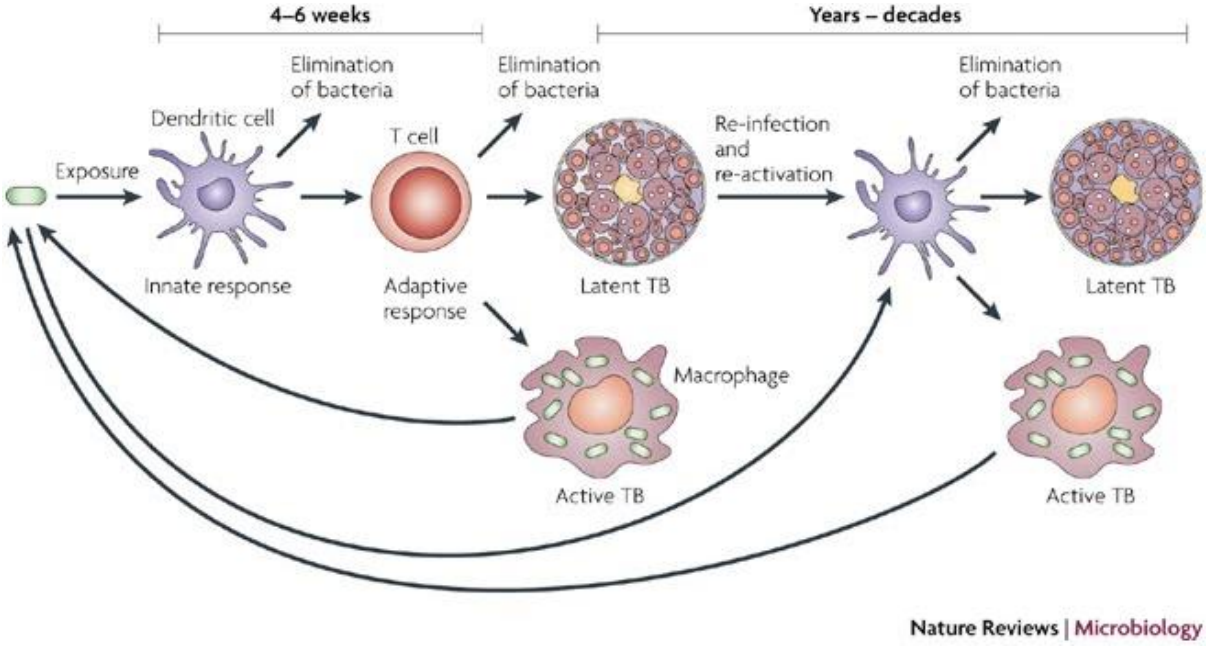


Figure 40: The lifecycle of *M.tuberculosis*. Within 4 to 6 weeks of expose there is a dendritic cell or T-cell mediated immune response, this will lead to the elimination of the bacteria, infection, or the neutralization of the bacteria not fully killing it (latent TB). After years or decades, a re-infection or re-activation can occur. [41] Reproduced with the permission of the publisher, Springer Nature.

The first stage comprises the phagocytosis of bacillus by the alveolar macrophages; if the macrophage is able to destroy the bacillus then no infection occurs; if the mycobacteria manage to overcome the macrophage's response the infection enters the following stage. [200]

Stage two consists of replication of the bacillus inside the macrophage until it lyses and releases the bacilli; this then attracts circulating monocytes to the infection site that differentiate into macrophages and engulf the free bacilli. These macrophages are not activated and cannot destroy the bacteria, this leads to logarithmic replication of the bacilli within the macrophages producing what is called a tubercle. This can then be disseminated to the lymph nodes, kidneys, meningeal areas and posterior apical areas of the lungs via the blood stream.[41]

In the third stage, two to three weeks after the initial infection, the immune system recovers and is able to respond to the infections terminating the unimpeded growth of MBT. The cell mediated immunity is peformed by $CD4^+$ and helper T-cells. The activation of the T-cells occurs when these cells encounter MBT antigens, which allows differentiation into specific T-cells that secrete cytokines, such as tumour necrosis factor and interferon-γ. The release of cytokines attract the monocytes and activates them, so they become macrophages. These cells will then phagocyte and kill the mycobacteria, this is mediated by $CD8^+$ suppressor cells. $CD8^+$ kill the MBT laden, non-activated macrophages, this is associated with the formation of caseating necrotic granulomas; MBT cannot multiply in these acidic, anoxic, extracellular conditions.[41]An immunocompetent host is able to restrict this lesion with layers of epithelial cells to contain the lesion within, arresting the disease. However, MBT can survive dormant in cells for years, and only the host's immune system can determine if it remains dormant or becomes active.[196,201]

Stages one to three are representative of the pathogenesis of primary TB in immunocompetent individuals, and it tends to be self-limited and subclinical. However, in immune compromised individuals, the active primary infection can quickly develop into disease.

In immunocompromised individuals, the cell-mediated immunity is weakened. Therefore, they are more reliant on delayed-type hypersensitivity response. Although the primary lesion is surrounded by non-activated macrophages it is not completely segregated by epithelial cells. which can cause the granuloma to expand damaging lung tissue. If the host's immunity manages to control the infection this will go unnoticed and the only evidence of this condition will be healed parenchymal calcifications of the primary infection in radiography.[202]

If the host's immune system is not able to contain the primary infection that area can develop advanced pneumonia; this is commonly referred to as primary progressive TB. Furthermore, if the lympho-haematogenous infection sites cannot be controlled multiple caseous tubercles will develop, commonly termed disseminated TB. HIV patients are particularly susceptible to this phenomenon due to the fact that HIV specifically targets macrophages and $CD4^+$ cells.[203]

The fourth and final stage of TB infection may occur months to decades after the initial infection and even in immunocompetent individuals TB can progress to this stage due to granuloma reactivation and decreased resistance to MBT. The granuloma is re-activated by its liquefaction releasing the MBT and the extracellular bacilli stimulate delayed-type hypersensitivity once again causes local damage to the surrounding tissues.[41]

2.7.2) TB treatment

TB has been treated since 1952 with the discovery of Isoniazid (INH), since then, several different antibiotics have been used to treat the infection, such as Rifampicin (RIF), Pyrazinamide (PZA), Ethambutol (EMB) and Streptomycin (SM),[204] as it can be observe din Figure 41. MBT is very susceptible to INH, the minimum inhibitory concentration (MIC) is between 0.02- 0.2 µg/mL. It enters the MBT wall by passive diffusion and is highly effective despite some adverse hepa and neurotoxicity. INH is a pro-drug that is activated by a mycobacterial enzyme KatG; drug resistance has often been associated with a loss of catalase and peroxidase activity, which is encoded by *katG.* Ser315Thr is the most widespread katG mutation in clinical isolates. Other genes are also associated with drug resistance such as *ahpC* and *inhA.* Mutations in inhA, or its promoter region(-15C→T), are often associated with low level resistance (MICs between 0.2 and 1 µg/mL) and mono-resistant strains, although some INH resistant MBT can have both *inhA* and *katG* mutations. The *ahpC* gene is commonly associated with an alkyl hydro-peroxidase reductase, which is associated with resistance to reactive oxygen and nitrogen intermediates.[205]

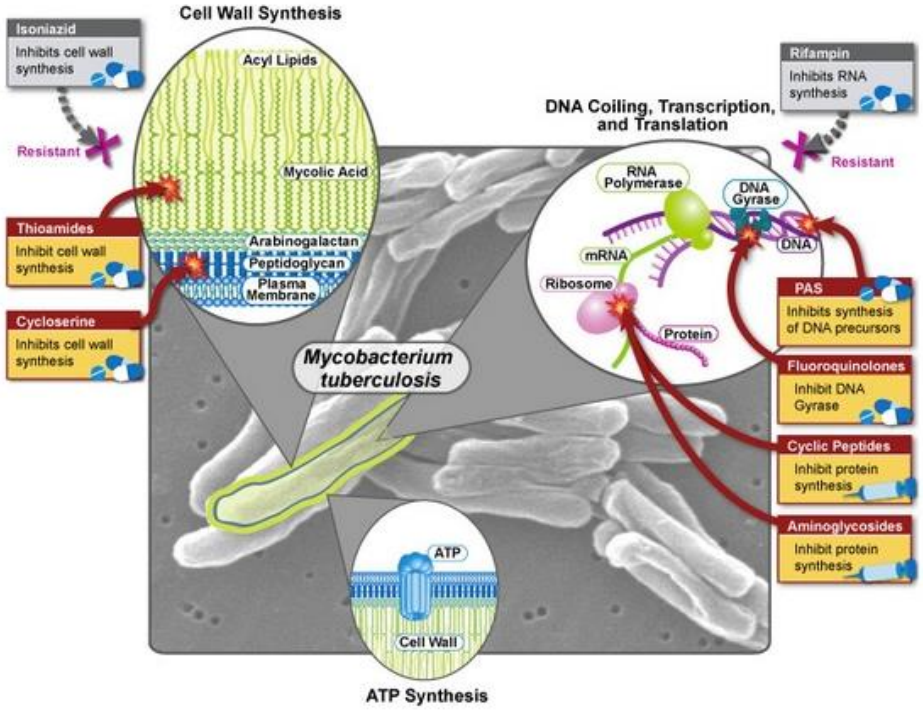


Figure 41: Mechanics of action of TB treatment. Isoniazid, Rifampin, ethambutol and Pyrazinamide are the first line of treatment against TB. Since some bacteria has become resistant to antibiotics such as Isoniazid and Rifampin other antibiotics have to be used as a second line of treatment. [42] The photo was created by Dr. Ray Butler and Janice Carr, at the CDC. The illustration was created by Krista Townsend, at the National Institute of Allergy and Infectious Diseases.

Rifampicin was first used a TB treatment in 1972; it acts by binding to the β-subunit of RNA polymerase (*rpoB*) whose function is the transcription and expression of the MBT genes, inhibiting enzyme transcription resulting in the death of the bacteria. There are very few side effects in RIF therapy; it mainly causes minor gastrointestinal complications.[206] Rifampicin MIC ranges from 0.05 to 1 μg/mL, and RIF resistance is commonly associated with mutations in the *rpoB* gene. This gene encodes the β-subunit of RNA polymerase and the mutation changes the enzyme's molecular conformation, which lowers its affinity for the drug conferring RIF resistance to the bacteria. Studies that tried to pin-point the region of the genome responsible for RIF resistance found that a mutation in the 81bp region of *rpoB* is found in approximately 96% of RIF-resistant MBT.[207]

Pyrazinamide (PZA) is generally used as part of a short-term antibiotic course and its main characteristic is the ability to inhibit semi-dormant MBT that is residing in acidic environments. Chemically, it is an analogue of nicotinamide and, as a pro-drug, it only becomes active after pyrazinamidase/nicotinamidase (PZase) converts it to pyrazinoic acid. PZA is only active at pH 5.5 and even in these conditions its activity is inadequate, putting the MIC range between 6.25 and 50 µg/mL. The side effects associated with PZA therapy are gastrointestinal upset and hypersensitivity reactions.[208] Mutations in the *pncA* gene cause a reduction in PZase activity. Several studies have been conducted demonstrating variations between geographical areas, including missense mutation, the vast majority of the mutations are located in amino acid residues 3–17, 61–85 and 132–142. The mutation profile of the *pncA* gene is very diverse and the origin of this diversity is still not clear. However, it is hypothesised it might be due to a deficiency in DNA mismatch repair mechanisms.[209,210]

Ethambutol (EMB) or [dextro-2,2'-(ethylenediimino)di-1-butanol] is extremely important in TB treatment as it enhances the effect of other TB therapies such as aminoglycosides, rifamycins and quinolones. The most common side effects associated with ethambutol therapy are colour blindness, blurred vison, dizziness, vomiting, nausea, loss of appetite, itching, rash, swelling of the face, lips and eyes, numbness of limbs and breathlessness.[211] EMB is a bacteriostatic agent, which mean it stops MBT proliferation but does not kill the bacteria. The MIC ranges from 0.5 and 2 µg/mL and it works by inhibiting Arabinosyl Transferase, which is responsible for the polymerisation of arabinan in the cell wall.[212]

2.7.3) *Mycobacterium* Cell wall

The *Mycobacterium* cell wall is probably this organism's most remarkable feature. It is unique among prokaryotes and plays a major role in MBT virulence.

The most distinctive feature of the MBT cell wall is its three layers of peptidoglycan, mycolic acids and arabinogalactan, Figure 42. This peculiar arrangement of peptidoglycan and complex lipids provides the microorganism with exceptional resistance to environmental stress due to its low permeability.[213]

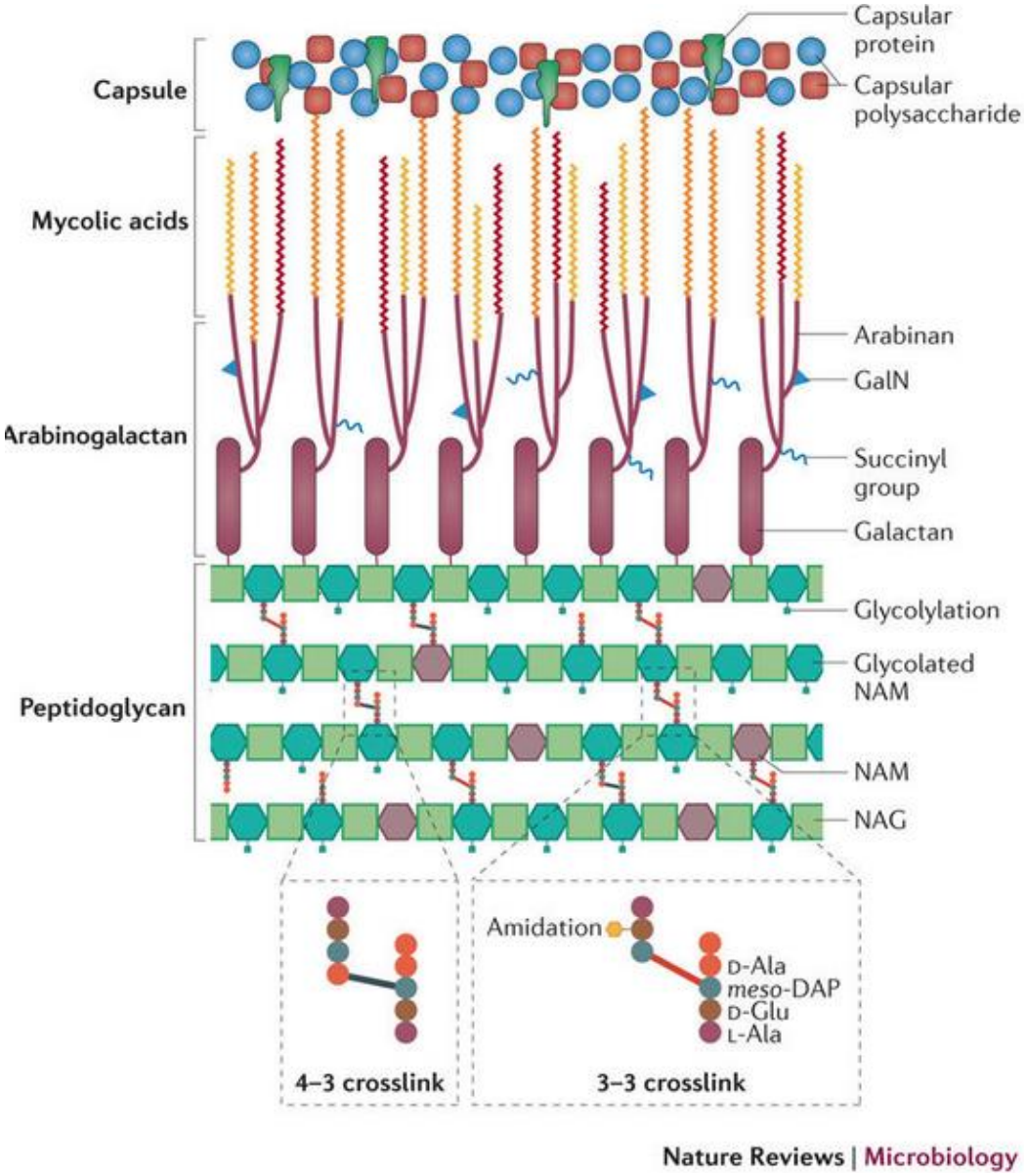


Figure 42: MBT cell wall and its constituents. The MBT cell wall is very complex, it is made by an external sugar and protein rich capsule, followed by a layer of mycolic acid which is then followed by an Arabinogalactan layer. The most internal layer is made by peptidoglycan, it displays two types of crosslinking 4-3 and a 3-3.[43]Reproduced with the permission of the publisher, Springer Nature.

Approximately 60% of the cell wall is made of long chain fatty acids, also known as mycolic acid (MA), they are only found in nature in Mycobacterium and Corynebacterium, and mycolic acids make up approximately 50% of the dry weight of the bacteria cell envelope.[214] MA are strong hydrophobic molecules that significantly reduce the bacteria's permeability conferring resistance to lysozyme and

even the oxygen radicals present in a macrophage granule. Peptidoglycan is made of β-(1,4)-linked alternating sugar units of N-acetylglucosamine and N-acetylmuramic acid, and a peptide provides the cross linking of the N-acetylmuramic molecule.

Mycolic acid is covalently bound to the inner most layer of peptidoglycan and arabinogalactan (AG) and this complex (mycolyl-arabinogalactan-peptidoglycan or PAM) is referred to as the cell wall core.[214] The cell wall composition is complex and the upper most segment is a mixture of long and short fatty acid chain interspersed with proteins, phosphatidylinositol mannosides (PIMs), phthiocerol containing lipids, lipomannan (LM) and lipoarrabinomannan (LAM). These are thought to be signalling effector molecules in the disease process, as they can be solubilised when the cell wall is disrupted. However the PAM complex remains unchanged, which is essential for cell viability.[215]

The inner membrane is more like a cytoplasmatic membrane and is its constituents are phospholipids such as cardiolipin, phosphatidylinositol (PI), phosphatidylethanolam (PE) and diphosphatidylglycerol (DPG). The space between the two membranes resembles the perisplasmic space in gram negative bacteria, nutrients are taken up from the surrounding environments and pass through porins and other channels ensuring a controlled flow between the intracellular and extracellular space.[213]

The other major component of the cell wall is the cord factor, which is responsible for a serpentine like cording around the bacteria that is toxic to mammalian tissues and is abundantly produced in the most virulent strains of MBT. It is thought that cord factor stimulates the host's NADase activity, leading to low levels of NAD in tissues. In addition to this, it is also thought that it has an effect on mitochondrial membranes compromising the mitochondrial respiratory chain and oxidative phosphorylation.[215]

Wolfe et al. studied the MBT cell wall proteome and demonstrated that the cell wall is crucial in MBT survival and remodelling as 35% of all proteins identified are involved in small molecule metabolisms and 25% were responsible for macromolecule synthesis.[216] The fundamental nature of the cell wall means that all its different aspects can be exploited as potential drug targets, illustrated in Figure 42.[217]

2.7.4) BCG an MBT model

Bacillus Calmette-Guerin has been used since the 1930s as a TB vaccine, however, its efficacy has been widely discussed, both for and against. [218–221] In research, BCG has often been used as a model for MBT[222–224] as it is closely related to the virulent *mycobacterium tuberculosis*. MBT is a category III organism and requires special safety measures to conduct research.[225–227] In this study, we follow this approach as the facilities in which this study was conducted do not accommodate category III organisms.

Mahairas et al. performed a study in which subtractive genomic hybridisation was employed to identify the genetic differences between the BCG and MBT. They have found that there are three distinct genomic regions of difference, commonly referred to as RD1, RD2 and RD3 that have been deleted from BCG. RD1 is a 9.5kb DNA segment that was deleted from all BCG sub-strains but conserved in all virulent laboratory strains of both *m. bovis* and *m. tuberculosis*. When RD1 was re-introduced to BCG, it supressed the expression of 10 proteins and resulted in an almost identical expression profile, determined by 2D- gel electrophoresis, to virulent *m. bovis* and *m. tuberculosis* suggesting RD1 regulates virulence in MBT. RD2 is a 10.7 kb DNA segment that contains a novel repetitive element and the previously identified mpt-64 gene, these are conserved in all virulent clinical and laboratory strains but have been deleted from all sub-strains of BCG. RD3 is a 9.3 kb segment that is present in virulent laboratory strains of *m. bovis* and *m. tuberculosis* but were absent from BCG and 84% of virulent clinical isolates.[228]

Further studies suggested that RD1 encoded cell wall proteins such as ESAT-6 and CFP-10 which are T-cells antigens. When RD1 knock-ins were inoculated into immune-deficient mice extensive splenomegaly and granuloma formation was observed. When immunocompetent mice were inoculated an increase persistence and partial reversal of attenuation was observed.[229]

There are some genetic differences between BCG and MBT and, as expected, they are mainly related to MBT virulence. For therapy testing the initial use of BCG is sufficient as cellularly it is believed to be analogous to MBT.

There are several MBT drug targets, in this thesis we will concentrate on decaprenylphosphoryl- β-D-ribose oxidase (DprE1). DprE1 and decaprenylphosphoryl-β-D-ribose-2-epimerase (DprE2) catalyse epimerization of decaprenylphosporyl ribose (DPR) todecaprenylphosporyl arabinose (DPA), which is an arabinose donor in the cell wall and therefore of particular interest as a drug target, as it is critical for the survival of the bacteria and there is no human orthologe.[44] The DPA complex can be observed in Figure 43.

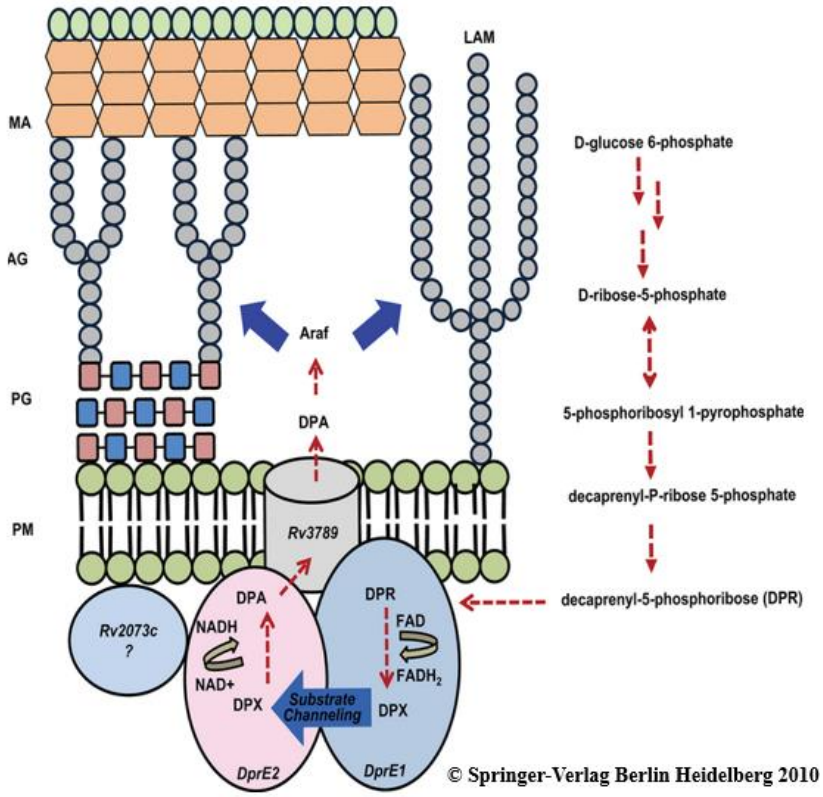


Figure 43: Diagram of the summary of DPA synthesis.[44] The DpRE1 target is part of the DPR complex and is embedded in the plasma membrane, while DpRe2 is part of the DPA complex. Reproduced under the Creative Commons Attribution License.

3. Experimental

3.1) Alveolar macrophages treatment with pharmaceuticals

Rat derived NR8383 cells were grown in F-12K Nutrient Mixture Kaighn's Modification media (21127-022, Gibco) supplemented with 15% Heat inactivated Fetal Bovine Serum (FBS) (10100-147, Gibco) for around 4-5 generations. They were then cultured using Nunc Lab-Tek II Chamber slide system (C6807, Thermo) at a density of 0.5 x 10^5 cells per mL (0.5 mL), which was measured using a Beckman Coulter Vi-Cell-XR (Beckman, USA).[230] The cells were left to settle for 2 hours and an extra 0.5 mL of media was added with one of the three different compounds, so the final concentration of compounds was the following:

Low concentration slide	***High concentration slide***	***Amiodarone conc. gradient***
Control (no compound added)	Control (no compound added)	12.50 µg/mL
5.00 µg/mL Chloroquine	10.00 µg/mL Chloroquine	6.25 µg/mL
3.13 µg/mL GSK2589899A	12.50 µg/mL GSK2589899A	3.13 µg/mL
1.56 µg/mL Amiodarone	12.5µg/mL Amiodarone	0.78 µg/mL

The incubation time was 24, 48 and 72 hours, after this, the cells were washed by gently adding 0.5 mL of 150 mM ammonium formate with a pipette to the side of the chamber of the chambered slide (70222-100G-F, Sigma) three times to remove potential residual compound, so it does not interfere with the measurement, and also to remove salts and media components that can cause ion suppression. To investigate the cell morphology, cells were stained by Hematoxylin and Eosin (H&E) using the method outlined further down in the experimental section. Two replicates were prepared, an H&E stained, and a frozen-dehydrated using an adVantage wizard 2.0 bench top freeze dryer (VirTis, USA). The first to assess if the cells were foamy or not, and the other replicate for SIMS analysis. The compound set-up

displayed above was only performed once as no signal for Chloroquine (C6628, Sigma) and GSK2589899A (from the GSK collection) could be detected by ToF-SIMS. As a result, the following experiments were performed using only amiodarone (A8426-5G, Sigma) so the final concentrations of amiodarone were: 0.78, 1.56, 3.13 and 6.25 µg/mL. The samples used for ToF-SIMS were freeze-dried on the lab-tek glass substrate using a CoolSink XT 96F plate (BioCision, USA) under vacuum in an adVantage wizard 2.0 bench top freeze dryer (VirTis, USA) for approximately one hour, after this they were stored at -80ºC until they were shipped to the National Physical Laboratory or the University of Nottingham, as shown in Figure 44. Once the samples arrived at either of the two locations they were placed in the -80ºC freezer, before the analysis the samples are placed in a vacuum chamber to remove condensation before being placed in the instrument for analysis. All experiments were repeated at least three times to ensure their reproducibility.

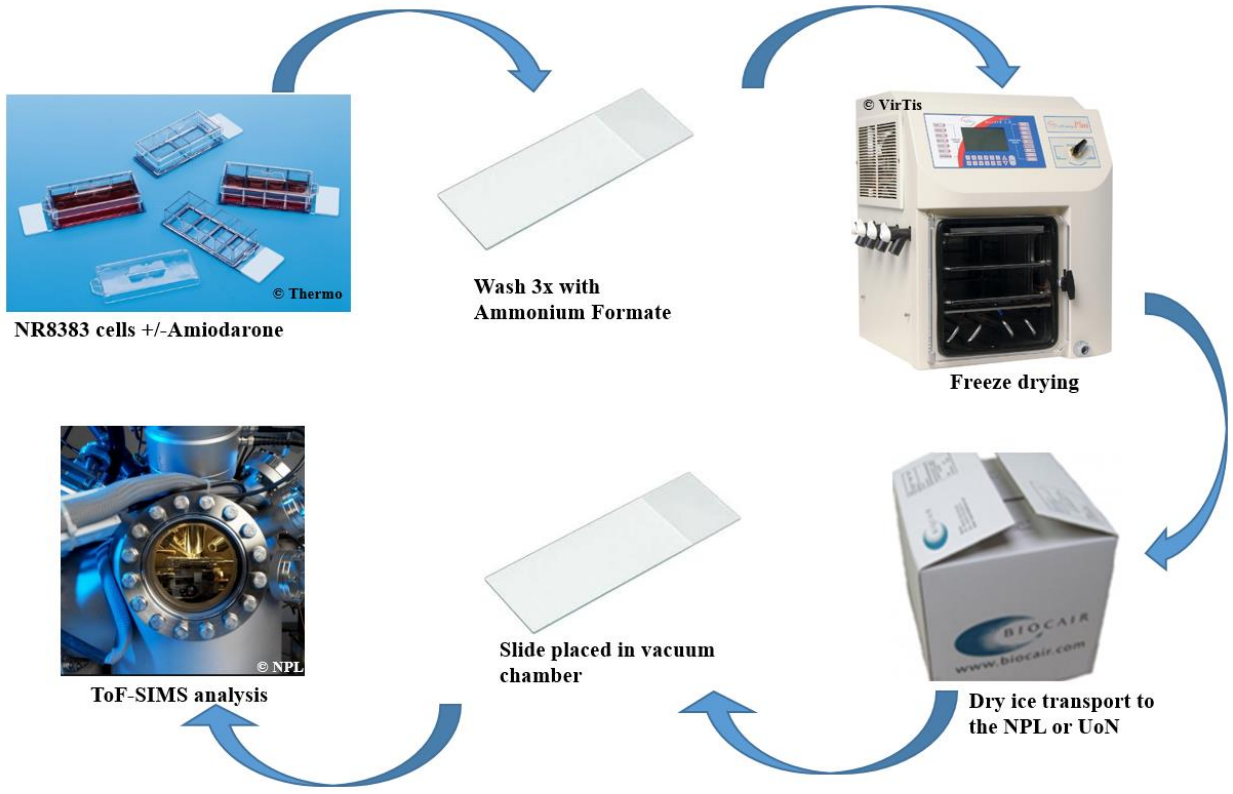


Figure 44: Sample preparation diagram of the ToF-SIMS workflow. The cells were plated on 4 well chamber Lab-Tek slides, them incubated with or without Amiodarone, once the incubation was finished they were washed three time with 150 mM ammonium formate solution at pH 7.4 and freeze-dried. Once the process was complete, they were kept in the -80ºC waiting transport to the National Physical Laboratory of the University or Nottingham for analysis. Once the samples are ready to be

used, they were placed in a vacuum chamber to minimize surface condensation on the sample and then mounted and placed inside the instrument.

3.2) Cell lines culture (HeLa, HepG2 and Hek 293)

Other mammalian cell lines were cultured for the purposes of the work undertaken for this thesis. The other mammalian cell lines studied were HeLa, HepG2 and Hek 293. The cells were cultured from passage one in NunC Easy Flask 175cm^2 (10246131, Thermo), unless stated otherwise. As adherent cells, they needed to be detached with TrypLE (12604013, Gibco), which contains trypsin to facilitate the detachment. After this, the cell density and viability were measured, as described in section 3.1, using a Vi-Cell counter.

HeLa cells (ATCC CCL-2) were grown in Dulbecco's Modified Eagle Medium/Nutrient Mixture F-12 (31331, Gibco) supplemented with 10%. Heat inactivated Fetal Bovine Serum (FBS) (10100-147, Gibco), these cells were grown from 1x10^5 until confluent and passaged every two to three days, up to a maximum of twenty passages. Hek 293 cells were grown in the same media as HeLa cells, each passage up to reaching confluence for the same number of passages as HeLa cells. The same applies to the HepG2 cell line (ATCC HB-8065).

3.3) ToF-SIMS

Experiments were conducted using either a ToF-SIMS 4 or a ToF-SIMS 5 mass spectrometer (ION-TOF, Munster, Germany) in a dual-beam setup with an electron gun used for charge compensation. The instrument was operated in two modes:

(1) High-mass-resolution imaging mode using a Bi_3^{2+} analysis beam at 60 keV, and an Ar_{3000}^+ sputtering beam at 10 keV in a non-interlaced mode. The primary ion beam was in the "Fast Imaging" mode with an approximate spatial resolution of 0.25 µm. Pulsed delayed extraction of secondary ions was employed for improved mass resolving power. The 3D images were collected in positive ion mode over a 150 µm × 150 µm surface area and 256 × 256 pixels. In each analysis phase, the Bi_3^{2+} ion dose was 5.5 × 10^{10} ions/cm^2, and an Ar_{3000}^+ dose of 8.99×10^{13} ions/cm^2 was used to erode the cells between

analysis phases. The cells were fully eroded after a total of 50 analysis-sputter cycles for the images presented in this thesis. Delayed extraction was applied in all instances where high-mass-resolution mode is referred.

(2) Low-mass-resolution "Spectrometry" mode was used with a higher primary ion beam current to increase the number of cells that could be analysed (albeit with poorer but sufficient spatial resolution to be able to visualize the cells and being able to distinguish the nuclear region of the cells). A Bi_3^+ analysis beam set at 30 keV and an Ar_{3000}^+ sputtering beam at 10 keV were used for a total of 20 scans. The Ar_{3000}^+ ion dose in each sputter phase was twice of that above so that the total Ar_{3000}^+ ion dose was similar between the two experiments.

The data analysis was performed using SurfaceLab (ION-TOF, Munster, Germany) (version 6.5). The data processing for the low-resolution mode experiment was performed by defining each individual cell as a region of interest and processing the dataset to obtain the total amiodarone molecular ion intensity.

3.4) Hematoxylin & Eosin (H&E)[231]

H&E is considered as the routine stain in microscopy and uses two separate dyes, hematoxylin stains the nuclear chromatin (dark purple) and eosin stains the collagen in the cytoplasm (red/ pink)[232].

The cells were fixed for five minutes with 4% Parafix solution (PRC/R/38, Pioneer Research Chemicals), rinsed in water, Harris 'modified haematoxylin (HHS32-1L, Sigma) solution was added for thirty seconds and rinsed again with acidic alcohol (56694-100ML-F, Sigma). Following this the samples were rinsed with water and Eosin (HT110232, Sigma) counter stain was added for up to fifteen seconds, sample rinsed with water followed by 100% ethanol (51976, Sigma) and then mounted with DPX mountant for histology (06522-100ML, Sigma), with a drop per well.

3.5) Fluorescence microscopy

The cells were cultured and incubated as described in 3.1. For the higher resolution confocal fluorescence microscopy the staining was performed using Lysotracker red (L7528, Life technologies)

at 75 nM for thirty minutes to stain the lysosomes and 4',6-Diamidino-2-Phenylindole, Dihydrochloride (DAPI) to strain the nucleus using Fluoroshield mounting media with DAPI (F6057, Sigma Aldrich). For the high throughput fluorescent microscopy experiment, the cells were grown using the conditions given in 3.1 with the exception that they were cultured in Greiner 96 well u-clear plate (655090, Greiner Bio-one). The cells were left to settle for two hours, compound added to give the final concentrations: Control (0 µg/mL), 0.78 µg/mL, 1.56 µg/mL, 3.13 µg/mL, 6.25 µg/mL and 12.50 µg/mL and left to incubate for 4, 24, 48 and 72 hours. Hoechst 33342 (H3570, Thermo) and Lysotracker Red DND-99 (L7528, Thermo) were added so the final concentration was 4 µg/mL for Hoechst and 75 µM for Lysotracker red. The cells were imaged using a widefield microscope, the InCell 2000 (GE Healthcare, USA), with a 100x objective and 0.9 numerical aperture (NA) the instrument set up was performed in accordance to the literature [233] using 358 nm excitation and 461 nm emission for Hoechst and 647 nm excitation and 688 nm emission for lysotracker red. At least 50 images were acquired per well and the data processed using Columbus software (Perkin Elmer) (version 2.7.1).[234] For the freeze-dried experiment the samples were analysed before and after freeze-drying. The live images are not shown as focusing was difficult due to the semi-adherence nature of the NR8383 cell line, which means they were not on a single focal plane.

3.6) Imaging flow cytometry

Cells were grown under the same conditions as described in section 3.1 and incubated with amiodarone for 72 hours at amiodarone concentrations of 0 µg/mL (control), 0.78 µg/mL, 1.56 µg/mL, 3.13 µg/mL and 6.25 µg/mL. Hoechst 33342 (H3570, Thermo) and Lysotracket Red DND-99 (L7528, Thermo) were then added, so the final concentrations was 4 µg/mL for Hoechst and 75 µM for Lysotracker red. Cells were incubated for thirty minutes, physically detached from the flask using a cell scraper, washed three times and re-suspended in Phosphate buffered saline (PBS) (10010015, Gibco). Two thousand cells per concentration were sorted using an ImageStream (Millipore, USA)[235] and analysed using IDEAS software[236] (Amnis Corporation, USA) (version 2.0). Images were extracted for the side scatter, light microscopy, and fluorescence of the nucleus and the lysosomes. To determine the degree of

response of the NR8383 cell line the images were segmented using the spots guided analysis wizard, the two thousand acquisitions being filtered by focus and cell size to include only single cells and lysotraker intensity.

3.7) Electron microscopy

The electron microscopy work in this section was performed by Ian Francis at GSK. HeLa cells were grown as described in section 3.2 above and pelleted and freeze-dried in the same manner as the samples prepared for ToF-SIMS, in section 3.1. The samples were processed into Agar 100 epoxy resin (AGR1031, Agar Scientific). The standard EM preparation involved manually processing the sample by dehydrating with a graded series of ethanol followed by immersion into acetone and final epoxy resin infiltration.

The samples were then embedded and polymerised (at 60°C for 24 hours), and the resulting blocks were sectioned at approximately 80 nm; stained with Uranyl Acetate/Lead Citrate (155, Pelco). These were then examined in a Hitachi H7500 (Hitachi, Japan) transmission electron microscope (TEM), operating at 80 kV and representative digital micrographs taken.

3.8) Refractive index microscopy

The cells were seeded at 1x10^{5} cells/mL in 170 µm bottom 35 mm Petri dishes (Ibidi GmbH, Munich, Germany) and incubated with amiodarone at 3.13µg/mL for 72 hours as in section 3.1 and 3.2. The media was then replaced with Phosphate buffer saline for imaging (refractive index 1.337), and the plate was placed under the microscope on the 3D cell explorer (Nanolive SA, Switzerland). The image took approximately two seconds to acquire, and it was visualised in the 3D Cell Explorer software (version 1.3).

3.9) Laser confocal microscopy

Cells were prepared as in point 3.1, placed under the LEXT microscope OLS4000 (Olympus, Japan) and 3D measurements were performed both in bright field mode and in laser scanning confocal microscopy mode using a violet laser (405 nm). A 50x objective was used and 50 x 50 µm field of view was acquired, with 4096 x 4096 pixel, the spatial resolution was 10 nm in z and 100 nm in x-y. The data was analysed using OLS4000 2.1 software, provided by the microscope manufacturer. The same cells were then analysed using ToF-SIMS.

3.10) Proteomics

3.10.1) In-solution digest

The cells were prepared as described in 3.2 in T175cm^2 flasks. As before, three washes with ammonium formate were performed to reduce the salt content. The number of cells was adjusted to 5x10^{6} and re-suspended in 200 µL of lysis buffer: 8 M urea (U5128, Sigma) with complete mini EDTA-free Protease inhibitor (4693159001, Roche). A total protein measurement was performed using a NanoDrop[237] (ThermoScientific), by placing 1.5 µL of the solution on the Nanodrop, the concentration value was determined automatically by the instrument, using the absorbance at 280 nm and the lysis buffer as a background. The samples were reduced using Dithiothreitol (DTT) (D0632, Sigma) at a final concentration of 10 mM for one hour at 37ºC. The resulting free thiols were then alkylated with Iodoacetamide (I1149, Sigma) at a final concentration of 50 mM for one hour at room temperature in the dark. Subsequently, the samples were diluted four-fold in 25 mM ammonium bicarbonate to reduce the urea concentration to allow trypsinisation. The digestion was performed overnight at 37 ºC using a 1:25 trypsin (V5111, Promega) to total protein ratio [238]. After digestion, the samples were desalted using StageTips before MS analysis.[239] The StageTipping procedure consisted on manually cut to measure a Empore C18 phase disk (14-386-2, 3M), to fit a T200 pipette tip, the phase was then pushed into the tip until it reached its extremity. The phase was then wet twice with 100 µL off a 50:50 mixture of acetonitrile (A9551, Thermo) and water (W61, Thermo) and a Technico Mini centrifuge (Thermo, UK)

was used to spin out the liquid. The phase was then washed twice, with 100 µL of 0.1% formic acid (A117010x1Amp, Thermo) in water (equilibration buffer). The sample was then loaded onto the tip and the liquid was spun out, the phase was then washed three times with equilibration buffer. Finally, the sample was eluted using 50 µL of a mixture of 0.1% Formic acid, 80% acetonitrile and 20% water (elution buffer). Using a Speed-Vac (Thermo, USA) the sample was dried down and re-suspended in 20 µL of equilibration buffer.

3.10.2) MS analysis

The samples were analysed using a QExactive mass spectrometer (Thermo, USA) with an EasySpray nanoelectrospray ion source (Thermo, USA) coupled to an easy-nLC 1000 (Thermo, USA) fitted with an Acclaim PepMap 100, 75 µm x 2 cm nanoViper pre-column (164567, Thermo) and an Easy PepMap 75 µm x 15 cm C18 (Octadecylsilane, endcapped), 2 µm, 100 Å chromatography column (ES800, Thermo). In both cases, the mobile phases were 0.1% Formic acid (A117010x1Amp, Thermo) in LC-MS water (W61, Thermo) for the aqueous phase and 0.1% Formic acid in LC-MS acetonitrile (A9551, Thermo) for the organic phase. The injection volume was 2 µL per sample, and it was loaded with 6 µL of 0.1% Formic acid in water, the pre-column and the column were equilibrated with 8 µL and 6 µL respectively to a maximum pressure of 800 bar. The QExactive gradient time was 2.5 hrs, and the column temperature was set to 40°C, further details related to the gradient can be seen in Figure 45. The MS data was acquired using a Top 10 method using higher energy collisional dissociation HCD fragmentation to sequence the top 10 ions per full scan spectrum, and the instrument was set to 2% underfill ratio, and 3 *m/z* isolation window[240].

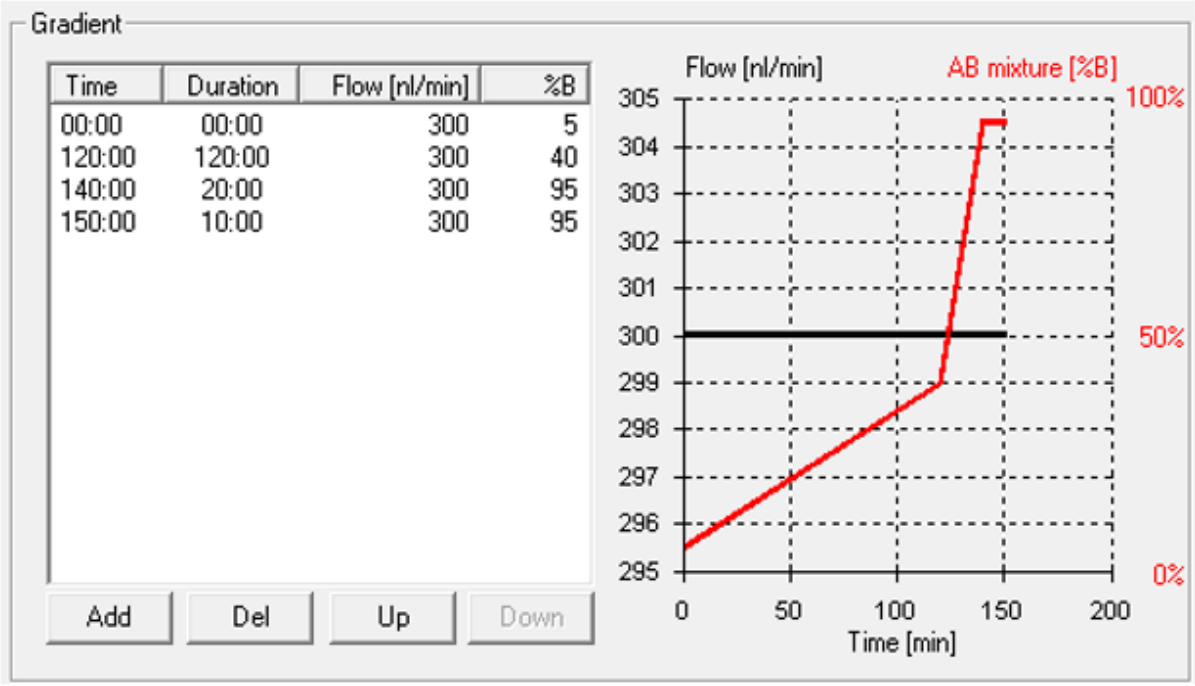


Figure 45: Gradient profile used for proteomics nano-HPLC experiment. The plot shows the time in the x –axis and the % of organic on the y-axis. The gradient increases slowly from 5 to 40% organic because the vast majority of peptides elute before 40% organic. Hence, by slowly ramping up the amount of organic phase the peptide peaks will be well separated which also provides the mass spectrometer with more time for the acquisition, resulting in more identifications. Reproduced with the permission of ThermoFisherScientific.

3.10.3) Data processing and Analysis

Data analysis was performed with Thermo Proteome Discoverer software version 1.4 (Thermo Fisher Scientific) using SEQUEST (Thermo Fisher Scientific) and the Universal Protein Resource (Uniprot) rat database as of January 2016 and its decoy, the false discovery rate was set to 1% (only 1% of the positive test are false positives) and the label free quantification node, as described in Končarević et al.[241] The Benjamini-Hochberg false discovery rate (FDR) is a powerful tool enbedded in most proteomics data processing software packages. It is basically applied to control the proportion of false positives, by adjusting the p-value in a way that limits the number of false positives that are reported as significant, a 1% FDR indicates that 1% of the declared positive results are actually negative.[242]

The dataset was then further processed using Scaffold (Proteome Software Inc., Portland, OR) version 3.6.1 where Proteome Discoverer files were imported and reprocessed using X! Tandem (The GPM, thegpm.org; version CYCLONE (2010.12.01.1)). Protein identifications were accepted if they could be established at higher than 99.9% probability and contained at least two identified peptides. Protein probabilities were assigned using a software endeded in Scaffold called Protein Prophet (SourceForge, USA).[243] The statistical analysis was performed in DESeq2[244], which included Wald test, pairwise plots and Principal Component Analysis (PCA).

The Wald test is a parametric statistical test used to determine whether a certain predictor variable is significant or not. It rejects the null hypothesis of the corresponding coefficient being zero. The test consists of dividing the value of the coefficient by standard error. Pairwise plots compare each channel against each other in a matrix format.[245]

PCA is a statistical procedure that simplifies complex datasets while simultaneously emphasising variation within that dataset. The data is plotted to tease out variations and a new set axis are generated, they are the principal components. This type of analysis is unsupervised and does not require prior knowledge about the samples. Closely related samples cluster together, and different samples are represented further apart on the plot[246].

The interaction network analysis was performed using STRING 10.0[247] (Search Tool for the Retrieval of Interacting Genes/Proteins) which is a protein functional association networks tool developed by the STRING consortium which is composed by the Swiss Institute of Bioinformatics (SIB), the Centre for Protein research (CPR-NNF) and the European molecular biology laboratory (EMBL) that allows the input on protein list and outputs information about the association of those proteins.

3.11) LC-MS/MS lipid analysis (sample preparation, run and data processing)[248]

The cell samples were prepared in the way described in point 3.9.1. Three flasks were prepared one as a control, another two dosed at 1.56 µg/mL amiodarone and left to incubate for 72 hours. The cells were then washed three times with 150 mM ammonium formate pH 7.4 and scraped from the flask using a Nunc cell scraper (179707, Thermo) to form a cell pellet. To perform the lipid extraction 1 mL of a 2:1 mixture of chloroform (1601383, Sigma) and methanol (494291, Sigma) was added to each pellet, they were then left shaking at room temperature for thirty minutes. The mixture was centrifuged at 14000 rpm for fifteen minutes, the liquid fraction collected and dried in a speed vac (Genevac, USA) until it reached a volume of 50 µL. The samples were analysed on a QExactive coupled to an Easy n-LC (Thermo USA) for sixty minutes (for method details, please refer to the annex), and the data was then processed using Lipid Search (Thermo, USA) (for parameters, please refer to annex).

3.12) Quantitative LC-MS/MS

Cells were grown using T175 flasks (Corning, USA), seeded at $1x10^5$ cells/mL, grown until the they reached a density of approximately $4.7x10^6$ and then incubated with amiodarone at a concentration of 6.25 µg/mL for two hours. They were washed three times with ammonium formate pH 7.4 by scraping the cells off the flask with the first wash followed by two washes with centrifugation (five minutes at 1500 rpm) to avoid losing cells in the washing process. They were re-suspended in 10 mL of ammonium formate, and the cell count was determined using a Vi-Cell XR (Beckman Coulter, USA). They were then pelleted and re-suspended in the appropriate volume of ProNet cell lysis buffer Tris pH 7.6 (ESI Source Solution, LLC, Woburn, MA) depending on the cell density. Appropriate dilutions of the cell lysate were performed, so the compound signal fell within the linear portion of the calibration curve and reserpine was used as an internal standard. The samples were analysed using an API4000 triple quadrupole (Sciex, USA) coupled to a Waters UPLC (Waters, UK) system fitted with an Acquity UPLC

BEH C18, 1.7 µm 2.1x50 mm (176000863, Waters) coupled to an Acquity UPLC BEH C18 VanGuard cartridge 1.7 µm 2.1x5 mm (1760003975 Waters). A gradient of 2 to 95% organic (0.1% formic acid in acetonitrile, the aqueous eluent being 0.1% formic acid in water) in 5 minutes, operated at a flow rate of 0.5 mL/min was employed. Multiple reaction monitoring (MRM) methods were created for reserpine and amiodarone with at least three transitions for amiodarone. The amiodarone calibration curve was obtained using the same amount of cell lysate as the samples to account for any ion suppression[249,250]. The assay validation showed very good sensitivity, precision and linearity with correlation efficiencies greater than 0.97.

The amount of compound per cell was calculated by normalising the LC-MS/MS result to the cell count obtained for each sample. Each sample was run eight times and had three biological and three technical replicates. Therefore nine samples were analysed for each cell line in a total of seventy-two LC-MS/MS runs. On average the number of cells analysed per injection was approximately five thousand cells. The data processing was done using Analyst (Sciex). The plots were generated in Statistica 64 (StatSoft).

3.13) Physical-chemical properties study sample preparation and acquisition

HepG2 cells were chosen for the physical-chemical properties study as previous experiment indicated that they were the most appropriate for this type of study, as they appear to have greater ToF-SIMS signal. Furthermore, the model used by Vorng et al. was a liver paste, and the HepG2 cell line is liver derived cell line commonly used for drug metabolism and hepatotoxicity studies.[192]

For this, in addition to the cells incubated with compound, four other samples were prepared: compound solubilised in 50:50 methanol: water (Neat), that solution spotted on a liver tissue section (tissue), same preparation as the Vorng et al. publication (JLV) and on a cell lysate (CL).

The compound set used in chapter 4 of this thesis was a collation of drug like entities with diverse physical-chemical properties, the structures are given in Figure 45.

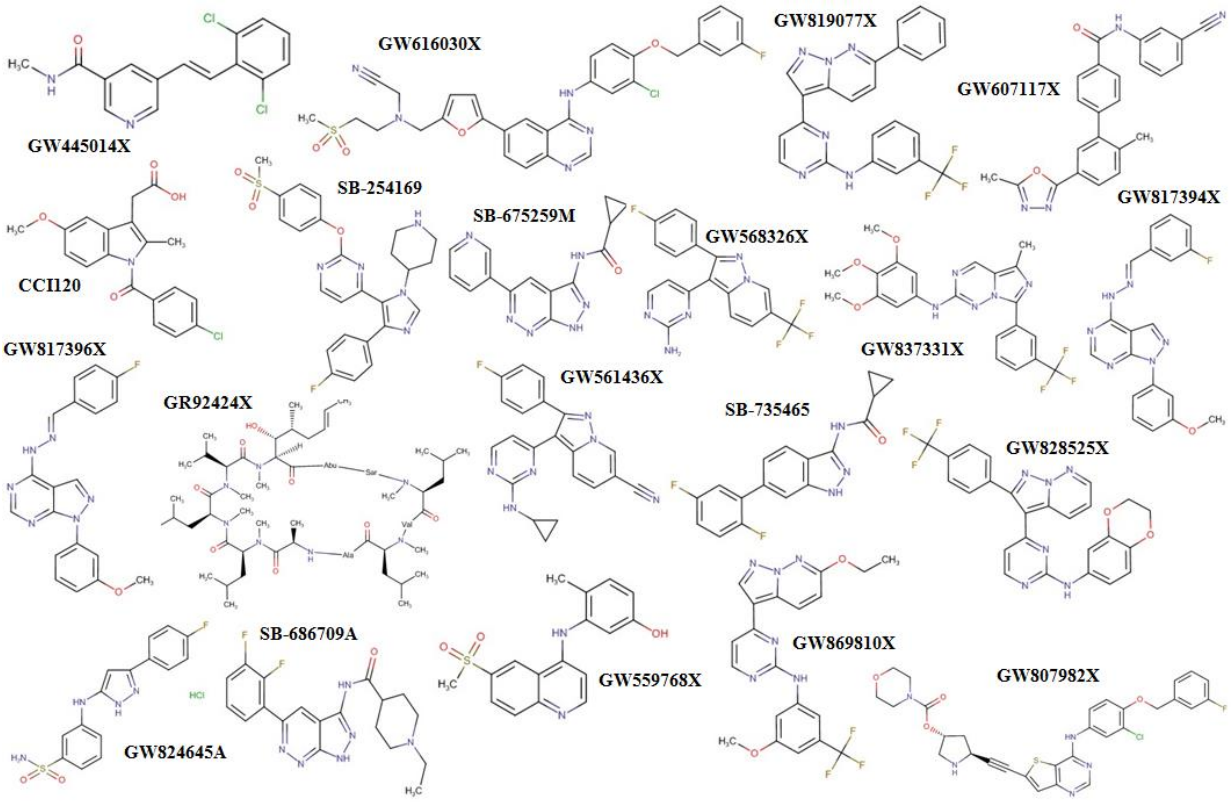


Figure 46: Chemical structures of the compounds used for this study and respective GSK identifiers.

3.13.1) Materials

The compounds were obtained from the GSK compound store. Reagents used were methanol (494291, Sigma), water (W61, Thermo), anhydrous dimethyl sulfoxide (DMSO) (276855, Sigma). All reagents were of MS grade purity.

3.13.2) Sample preparation

Compound stock solutions were made in DMSO to give a final concentration of 10 mM. The neat compound solution was prepared by diluting the stock solutions to 500 µM in 50:50 methanol: water and 1 µL was spotted on a glass slide.

The top of tissue samples were prepared by spotting 1 µL of the neat compound solution on top of rat liver tissue slices. For the cell lysate homogenate, the cells were washed three times with 150 mM ammonium formate, spun down for five minutes at 1500 rpm, suspended in 1000 µL of water and

sonicated for twenty minutes. The sample protein concentration was determined, using the Nanodrop as described in section 3.9.1. The mixture was then concentrated using the SpeedVac as in 3.9.1, so the final protein concentration was 100 µg/mL (as per Vorng publication). The compound was added so the final concentration was 50 µM and 10 µL was spotted onto a chamber slide. The samples were freeze-dried as described in the cell sample preparation section (section 3.1). For the Jean-Luc Vorng (JLV) or liver paste method, this method was described in Vorng et al. Semi-empirical rules to determine drug sensitivity and ionisation efficiency in SIMS using a model tissue sample. [153]

3.13.3) ToF-SIMS

Experiments were conducted using a ToF-SIMS V mass spectrometer (ION-TOF, Munster, Germany) in a dual-beam setup ($Bi_3^{2+}$and Ar_{2642}^{+}) and using delayed extraction. It was run in two slightly different modes: (i) For the neat compounds, compound in tissues, compounds in cell lysate and compounds in the JLV liver paste experiments the instrument was operated in non-interlaced mode using a Bi_3^{2+} analysis beam at 60 keV and an Ar_{2642}^{+} sputtering beam at 10 keV. The data were collected in positive ion mode over a 150 µm × 150 µm surface area and 256 × 256 pixels. In each analysis phase, the Bi_3^{2+} ion dose was 2.73×10^{11} ions/cm^2 (within the static limit) and an Ar_{2642}^{+} dose of 8.28×10^{13} ions/cm^2 was used to erode the layers between analysis phases; three scans were performed. (ii) The instrument was operated in the same conditions as in (i), however 30 scans were performed and the ion dose was 2.73×10^{12} ions/cm^2 for Bi_3^{2+} gun and an Ar_{2642}^{+} dose of 1.37×10^{15} ions/cm^2. The data analysis was performed in SurfaceLab (ION-TOF, Munster, Germany) (version 6.5). Statistical data processing was performed using STATISTICA 64 version 12 (STATSOFT).

3.14) Mycobacterium bovis BCG study[251]

3.14.1) Bacterial culture

The three strains of *m. bovis* BCG, empty vector (EV), overexpressing DpRE1 (DpRE1) and GFP (Green Fluorescent protein) BCG were cultured in Middlebrook 7H9 (M0178, Sigma) medium supplemented with 10% ADC (Albumin, Dextrose, Catalase) supplement (M0553, Sigma) and 0.025% Tween 80 (P8074, Sigma). These cultures were left to incubate at 37ºC for approximately ten days. The inoculum was standardised at approximately $1x10^7$ cfu/ml by measuring the Optical Density (OD) at 600 nm. The culture was then diluted 1 in 100 in Middlebrook 7H9 broth supplemented with 10% ADC and 0.025% Tween, 100 µL of the culture was placed in Eppendorf tubes and the compound was added so that the concentration was 1, 10 and 50 times the Minimum Inhibitory Concentration (MIC), as well as a no compound control, the concentrations were 3 uM, 30 uM and 150 uM for GSK3338058A and 5 uM, 50 uM and 250 uM for GSK2620592A.The cultures were incubated at 37ºC for two days.

For the co-culture experiment NR8383 cells were cultured as described in point 3.1 and plated in 35 mm cell culture dishes (81218, Ibidi) at a cells density of $1x10^5$ the cells were left to grow so the confluence was between 60 and 70%. The OD at 600 nm of the GFP BCG culture was measured and assuming 0.1 OD is equal to 10^7 cfu/mL the culture was concentrated by centrifuging for 10 minutes at 3500 rpm so the OD measured was approximately 1, therefore the density of the culture was 10^8 cfu/mL. The concentrated culture of GFP BCG was added to the plate containing the NR8383 macrophages so the ratio of mammalian cell to bacteria was 1:100. The co-culture was left overnight and thirty minutes prior to imaging Hoechst 33342 (H3570, Thermo) and Cell Tracker red (C10046, Thermo) were then added, so the final concentrations were 4 µg/mL for Hoechst and 3 µg/mL for the Cell Tracker red, after thirty minutes incubation the cells were washed three times with FluoroBrite DMEM (A1896701, Thermo).

The cells were them imaged using a confocal laser microscope (CQ1, Yokogawa) using the 561 nm, 488 nm and 640 nm channels at a laser power of 20% and a 500 milliseconds exposure. A stack was

acquired of 500 nm intervals (40 slices) and the maximum intensity projections image was generated in the CQ1 software.

M. bovis BCG is a Biosafety level 2 organism and therefore any work needs to be performed in a containment class 2 laboratory. The containment level at the NPL is category 1, however as the water was removed from the cells, that renders then no longer active as they die during the freeze-drying process.

3.14.2) Sample preparation

Each sample was centrifuged for 10 minutes at 3500 rpm and washed three times with 150 mM ammonium formate. The pellet was re-suspended in 20 µL of 150 mM ammonium formate, and 2 µL was added to well slides and freeze-dried as per the same preparation conditions described earlier for mammalian cells (section 3.1). Letters were made on the glass slice using the Gallium ion beam (FIB) beam on the ToF-SIMS 5 and used as markers to allow analysis of the same bacteria in Atomic Force Microscopy and ToF-SIMS.

3.14.3) ToF-SIMS

ToF-SIMS V was run in high spatial resolution imaging mode using a Bi_3^{2+} analysis beam at 60 keV (ion dose was 5.5×10^{10} ions/cm^2) and an Ar_{3000}^{+} sputtering beam at 10 keV in a non-interlaced mode (8.99×10^{13} ions/cm^2). Pulsed delayed extraction of secondary ions was employed for improved mass resolving power and an approximate spatial resolution of 0.25 µm.

3.14.4) OrbiSIMS

The instrument was controlled using SurfaceLab 6.7 and the mass calibration was performed using a Bi_3 ion bean with a 20 keV energy and a current of approximately 20 pA. Both positive and negative calibrations were performed on a silver (Ag) sample (ion list in the annex section). For calibrations purposes the OrbiSIMS helium gas pressure was changed from low to high on the instrument tab to

improve the ions transmission. The QE HF tune page was used to control the Orbitrap analyser for the calibration procedure.

To acquire mass spectra only, the argon beam was set at 20 keV, approximately 1 pA and Ar_{5000}^{+}, to minimize fragmentation. The electron flood gun was set to 20 eV to provide charge compensation. The Orbitrap was set to a resolution of 240,000 and the ion dose was approximately 1 x 10^{11} ions / cm^2.

The data were acquired using SurfaceLab 6.7. To facilitate processing using the R pipeline, required to obtain metabolomics elucidation, the two files generated had to be separated using Thermo's Slicer as Surface analysis generates two .raw files within the same file but only one of them contains the required data. The files were analysed using a R Pipeline that performed for each individual sample the following steps: file conversion from .raw to mzml, then scan alignment, followed by scan summing, then it would perform peak detection and modelling and finishing with the recalibration of the spectra using the lock masses acquired. After this step, conducted for each individual sample, other data processing steps were performed across all samples, they evolved global alignment to discard retention time fluctuations, global peak detection and metabolite ID using the accurate mass measurement with up to four decimal places.

3.14.5) Atomic Force Microscopy (AFM)

AFM was performed using an Asylum Cypher AFM under ambient conditions. The cantilevers used were OPUS 240AC-NA with a resonant frequency of 70 kHz and a force constant of 2 N/m.

4. Results I: Visualization of intracellular amiodarone using ToF-SIMS

In this chapter, the results from amiodarone incubated cells experiments are presented with the aim of showing that amiodarone can be detected intracellularly using ToF-SIMS. This was the first time a pharmaceutical drug was shown inside a mammalian cell at a physiological level and label-free using ToF-SIMS. Furthermore, several microscopy techniques were applied to show correlation between cell size, lysosomal activity and intracellular amiodarone accumulation. In order to find evidence of amiodarone induced biological changes in NR8383 cells, a proteomics study was performed in parallel with a lipidomics study to determine the effects of amiodarone on the lipid metabolism and on the protein expression levels.

Three compounds were initially tested, amiodarone, chloroquine and GSK2789899A, however only amiodarone was detected using ToF-SIMS. Therefore, this chapter concentrates essentially on the effects of amiodarone in cells.

The NR8383 cell assay had to be developed within GSK to assess cytotoxicity of the compounds at therapeutic doses; this was done by choosing a range of concentrations based on both the half maximum inhibitory concentration (IC50) and the therapeutic dose. Amiodarone is one of the compounds used in the assay as a positive control due to its known toxicity, which results from compound being trapped and accumulated in the lysosomes, which results in a high intracellular amiodarone concentration which should be easier to detect using ToF-SIMS than a compound that does not accumulate intracellularly.

Amiodarone IC50 is reported to be 3.6 µM[252] and the regular standard dose tends to be between 0.8-1.2 g a day up to 10 g, followed by a maintenance dose of 0.2-0.4 g a day for all patients regardless of body weight or fat mass.[253] However, as a lipophilic drug, amiodarone associates with fats and binds to the serum proteins rather than being free in serum, therefore, the serum measured amiodarone concentration is an inaccurate measurement of the drug in the body, and should not be correlated to therapeutic doses. Furthermore, in some instances amiodarone is given intravenously and the serum availability of

amiodarone in those cases ranges from 8.604 to 19.411 mg/L[254], which makes it even harder to get to an exact therapeutic dose. As a result, in this study a range of concentrations were tested: 0.78 µg/mL, 1.56 µg/mL, 3.13 µg/mL, 6.25 µg/mL and 12.50 µg/mL.

4.1) Bright field microscopy of compound incubated NR8383 cells

Three compounds (amiodarone, chloroquine and GSK2789899) known to accumulate inside cells were tested as it can be observed in Figure 47. The cells were incubated, fixed, H&E stained and light microscopy was used to acquire images of single cells, as the foamy macrophage morphology is more noticeable if the cells were not confluent.

A visually foamy state[255] for the NR8383 cells is exhibited in Figure 47 after being dosed with all three compounds. This may be interpreted as intracellular drug accumulation.[256] This state was observed for the three compounds, however the only compound that was detected using ToF-SIMS was amiodarone, and therefore all consecutive experiments were performed using amiodarone only.

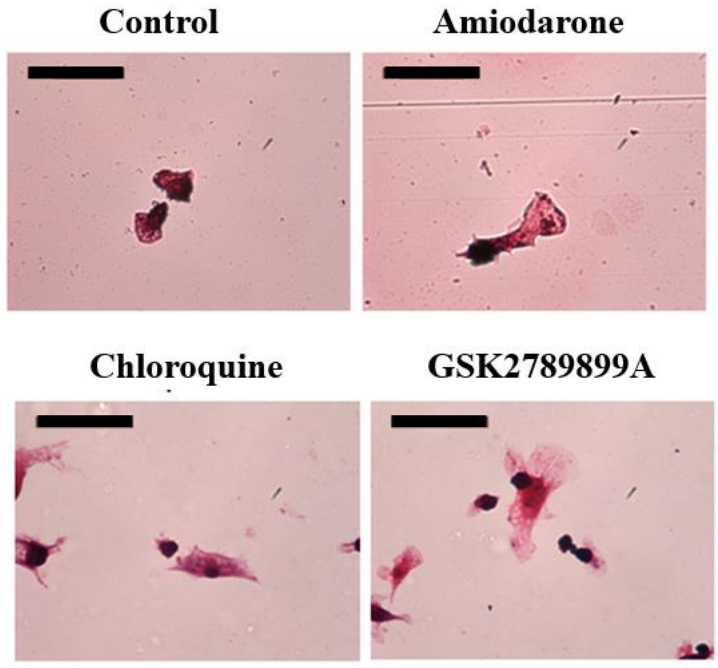


Figure 47: Light microscopy image of H&E stained NR8383 macrophage cells incubated with the referred compounds at the concentration of 10 µg/mL for Chloroquine, and 12.50 µg/mL for amiodarone and GSK2789899A. The cells were incubated for 72 hours at 37ºC. The scale bar is 50 µm.

Despite being well documented in the literature[173] that amiodarone causes phospholipidosis and enlargement of the cell (cell becomes "foamy" in appearance), optical images were essential to determine the effect of various concentrations, as can be seen in Figure 48. Several mechanisms can be responsible for the appearance of foamy macrophages, however, amiodarone is the only study subject in this thesis.

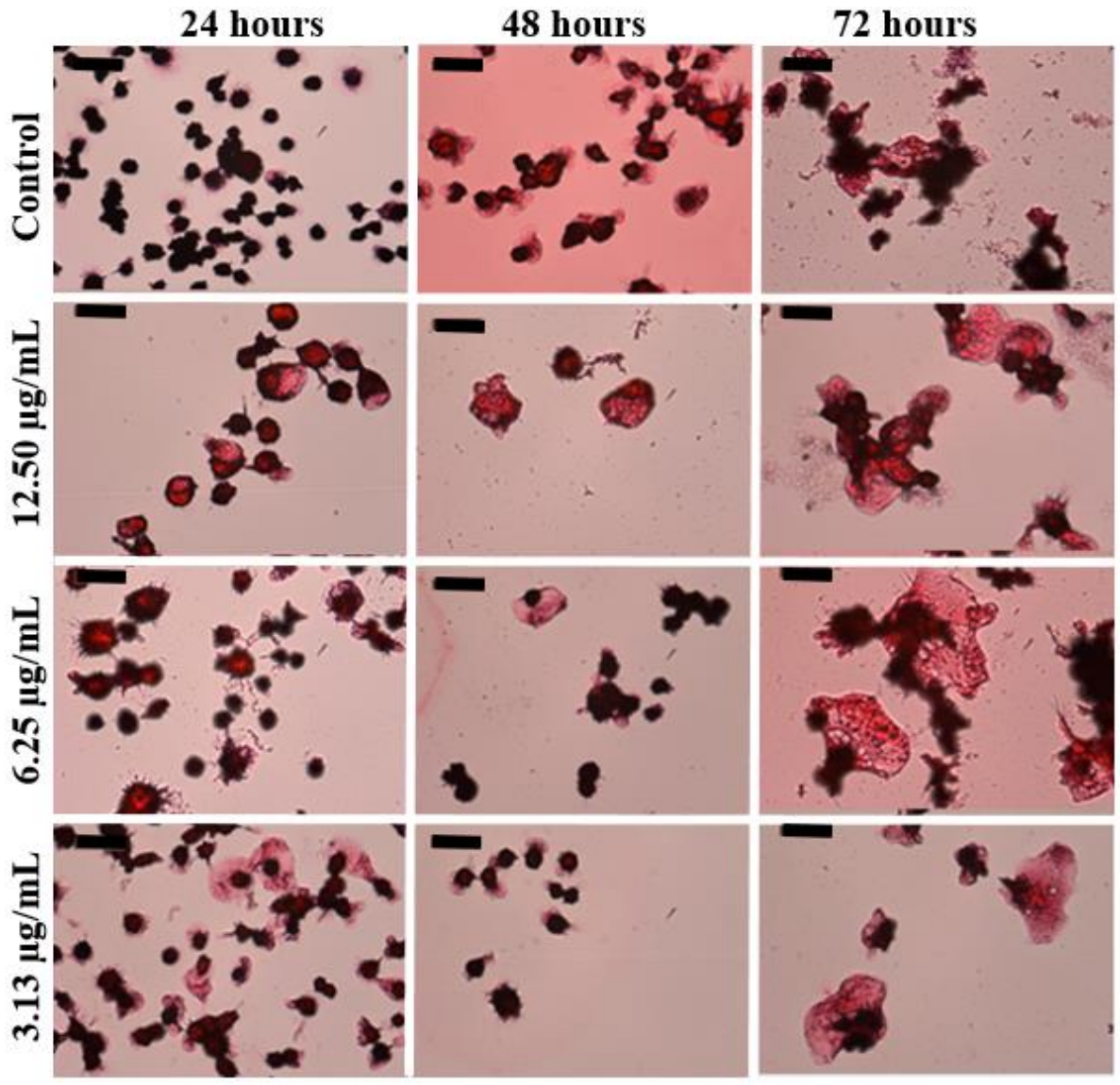


Figure 48: Light microscopy image of H&E stained NR8383 cells. The cell morphology varies as a function of time (24, 48 and 72 hours) and amiodarone concentration (0, 3.13, 6.25 and 12.50 µg/mL). The scale bar is 50 µm. As it can be observed the cells increase in size as the amiodarone concentration and incubation time increases.

A time-course was performed using three different amiodarone concentrations and three time-points. The cells were fixed, H&E stained and imaged after compound incubation, as it can be seen in Figure 48, the nucleus is the dark round structure and the cytoplasm is stained red by eosin.

In Figure 48, the concentration and length of amiodarone incubation is evaluated. The cells have been incubated for 24, 48 and 72 hours, at different amiodarone concentrations: 3.13 µg/mL, 6.25 µg/mL and 12.50 µg/mL. The images clearly show an increase in cell size with the length of treatment as well as amiodarone dose. The amiodarone dose appears to have the greatest effect on cell viability, at it can be observed, especially for the 24 hour time-point the number of cells observed in each field of view decreases with the increase of amiodarone dose. At 12.50 µg/mL amiodarone is potentially cytotoxic to the vast majority of the NR8383 cell population, and here, the first indications of the potential differences in response to drug treatment within the same cell population can be observed, this subject will be discussed at length later in this thesis. The amiodarone effect can also be observed at the 48 hour time-point, as there were substantially less cells in the treated samples than the control.

At the 72 hour time-point, for the amiodarone treated samples, potentially only cells that respond to amiodarone treatment were left, hence the lower variability observed for the different amiodarone concentration. There is a stark difference in phenotype between these cells and the control cells, as they appear much more enlarged and with structures that are similar to vacuoles. This type of phenotype is known to be characteristic of amiodarone laden macrophages, and in pathology they are colloquially referred to as "foamy macrophages", as the cells appear to have foamy holes in their cytoplasmic region, this is however an artefact of H&E staining and live cells do not present these holes, as the lipid that had accumulated in the cells as a result of phospholipidosis and washed away during the H&E procedure only the lysosomal membranes are left behind, and that causes this characteristic appearance of "foamy macrophages".

In order to investigate the appearance of the live cells that had been submitted to the same amiodarone treatment, a refractive index microscopy experiment was performed. Refractive index microscopy produces both bright field images and a tomographic representation of the specimens, however, in Figure 49 only one plane of the bright field is shown, also an increased level of detail can be observed

when compared with a standard light microscopy. The nucleus is clearly visible for the larger cells, and in the cell highlighted in Figure 49B there is a clear difference between organelle dense region of the cell closer to the nucleus and the rest of the cell.

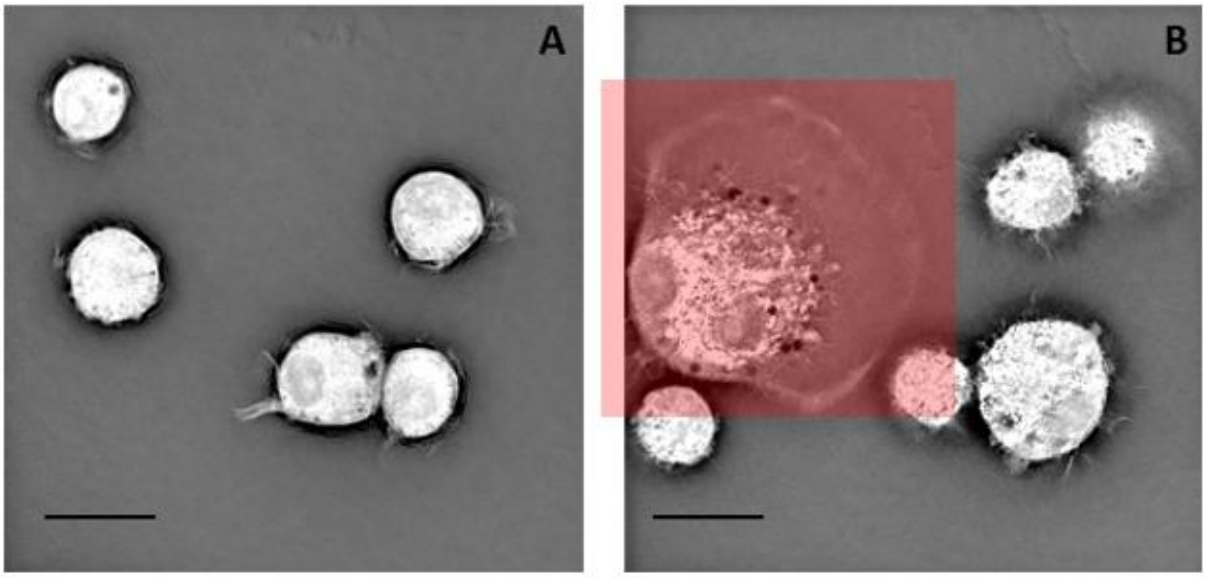


Figure 49: Refractive index microscopy NR8383 live cells (A) control and (B) incubated with 3.13 µg/mL amiodarone for 48 hours. The scale bar is 15 µm. As it can be observed in this image the cells are significantly enlarged, as highlighted with the red box, after amiodarone incubations.

In Figure 49 there is a clear difference between the untreated cells in 49A and the treated cells in 49B, this reinforces what was already observed in H&E stained cells, that the cell size tends to increase with time in amiodarone treated cells. Both Figure 48 and 49, demonstrate that there is a phenotypic variability within this cell population, as only a sub-population appears to respond amiodarone treatment, as it is the case of the cell highlighted in Figure 49, this cell is considerably larger than the cells around it as well as the control cells. This matter is further explained in the high-throughput microscopy section below.

The cytoplasmic region away from the nucleus is thought to be the area where the “holes” are observed in H&E stained samples, however this is not visible in live cells, as it can be observed in Figure 49.

To chemically investigate the same cells imaged using light microscopy, ToF-SIMS was carried out on frozen-dehydrated cells. This condition was chosen because it facilitates the ready handling of the sample in the ToF-SIMS instrument: there is no need for cold stage usage, and the analysis is faster as the vacuum is not affected, as it is when working with frozen-hydrated samples.

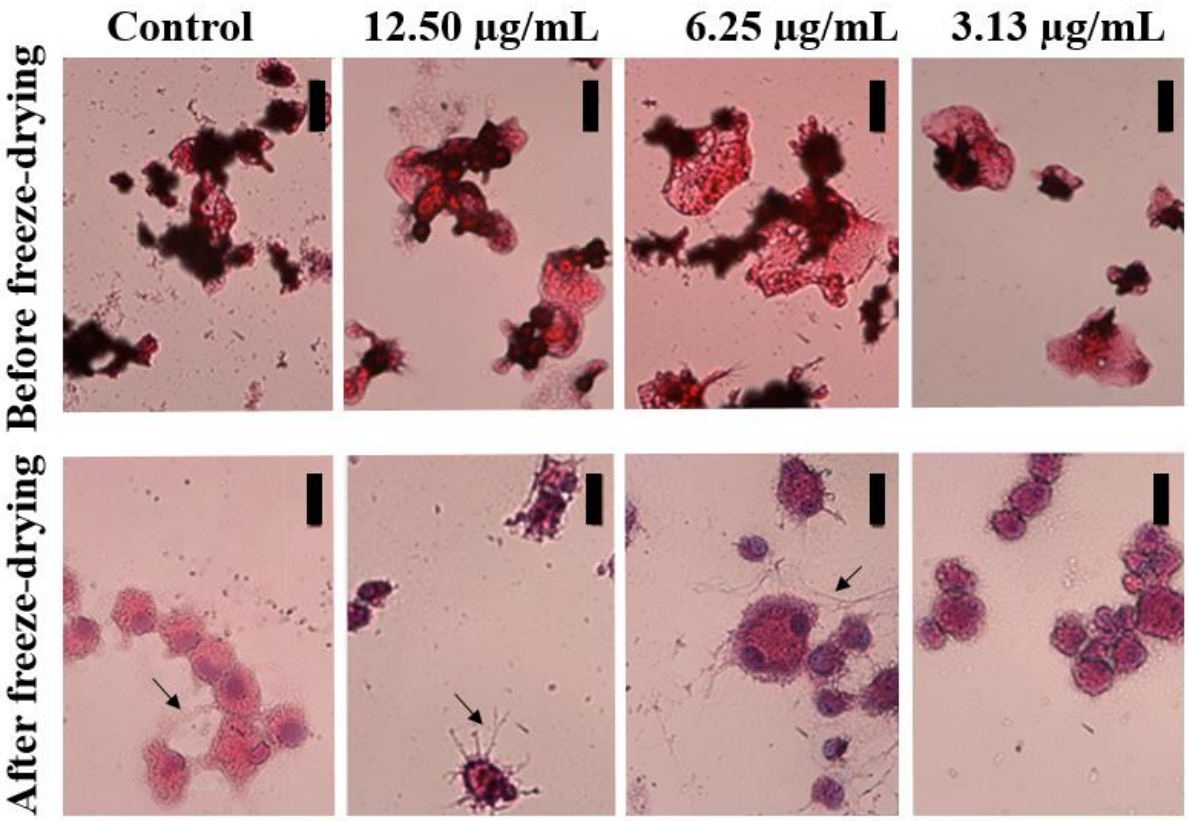


Figure 50: Light microscopy image of H&E stained NR8383 cells doped with amiodarone before and after freeze-drying. The vertical scale bar is 50 µm. The black arrows demonstrate the increase in the visibility of the cellular attachment filaments under freeze-drying conditions.

To evaluate if the process of freeze-drying changed the morphology of the cell an experiment where the cells were H&E stained before and after freeze-drying was conducted. As shown in Figure 50, there are some differences between the before (where fixing was the first stage of the process) and the frozen-dehydrated (when fixing was performed after FD). The degree of cell disruption is not higher in the frozen-dehydrated cells, as the debris left on the slides is not consideraly increased when compared to the non-frozen-dehydrated. However, cell attachment filaments are more visible after freeze-drying

than the non-freeze-dried cells, as demonstrated by the black arrows in Figure 50. In addition, the stain in the nucleus looks less intense, as it can be observed in Figure 50 pointed out by the black arrows. The latter is most likely to be one of three phenomena, either the nuclear membrane has been disrupted, the dye does not concentrate as much, or the basic/acid interaction that happens between the DNA and the hematoxylin dye is somehow disrupted once the liquid content is removed from the cells, the latter is the most likely.

4.2) Fluorescence microscopy of amiodarone incubated NR8383 cells

Fluorescent microscopy was undertaken in order to confirm the results obtained by H&E staining. It was apparent in the H&E shown in Figure 48, that some of the cells presented signs of phospholipidosis, as seen by the increased cell size and "holes" in the cytoplasmic region, however it was necessary to prove that the size increase corresponded to an increase in lysosome formation, as that is the hallmark of amiodarone associated phospholipidosis.

To determine dose dependency in the formation of lysosomes NR8383 cells were dosed with amiodarone at different concentrations and the lysosomes and nuclei of the cells were stained using fluorescent tags after 72 hours incubation. The cells were incubated with amiodarone as before at 0.78, 1.56, 3.13, 6.25 and 12.50 µg/mL and then stained with lysotracker red, and DAPI 4',6-diamidino-2-phenylindole) to show the lysosome and nucleus respectively.

In Figure 51, in the absence of amiodarone, few lysosomes were observed, but with increasing concentration of the compound the lysosomes became larger and occurred in higher numbers up to 3.13 µg/mL amiodarone where the compound concentration started to impact cell viability**.**

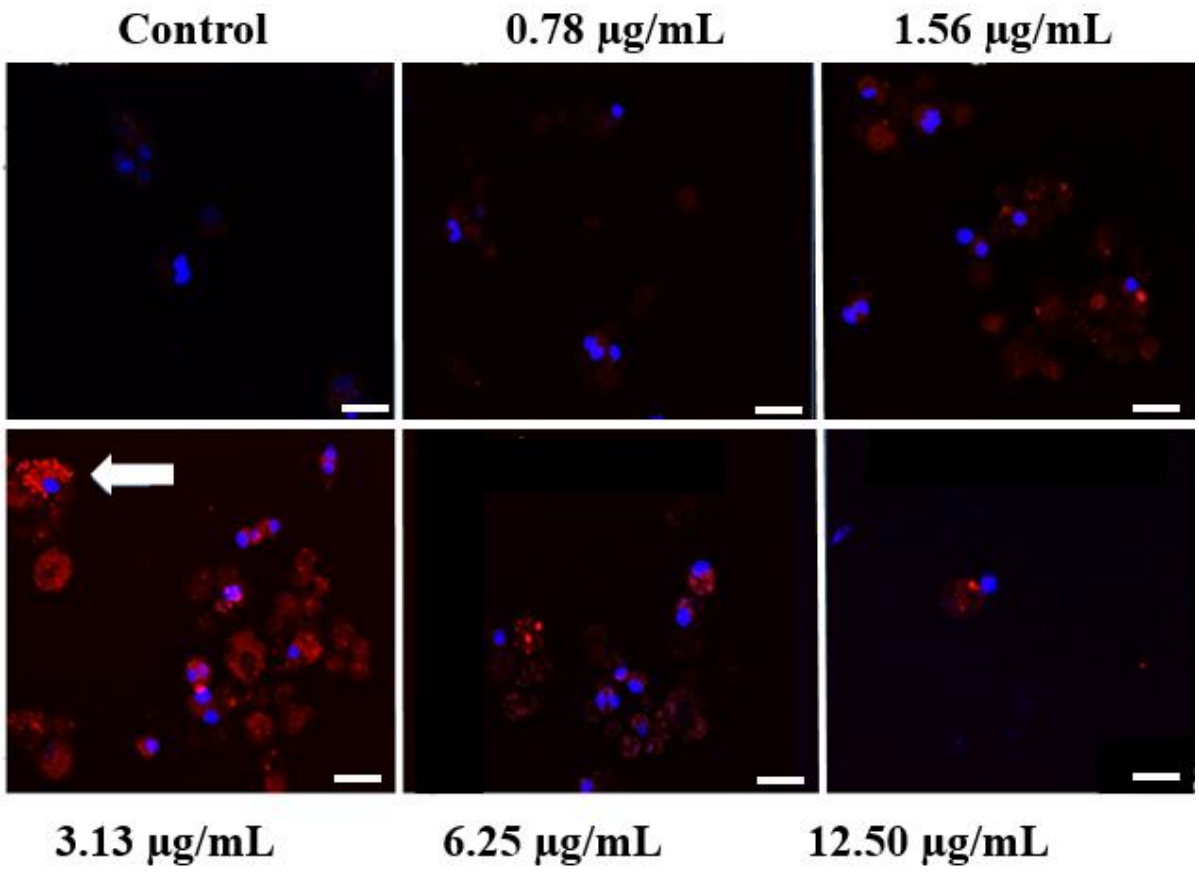


Figure 51: Fluorescent confocal microscopy image of fixed NR8383 cells using lysotracker red to strain the lysosomes and DAPI to strain the nucleus. The "foamy" appearance of the macrophage cell model after 72 hours amiodarone incubation at different concentrations, as highlighted by the white arrow. The scale bar is 25 µm

As it can be observed in Figure 51, the lysotraker signal (in red) increases with the concentration of amiodarone in the media, up until 3.13 µg/mL. Above this concentration, it can be hypothesised that the compound becomes cytotoxic. The cell viability was compromised at the 6.25 µg/mL amiodarone concentration and this was even more evident for the 12.50 µg/mL amiodarone incubated cells where it was quite challenging to find cells that had survived and were still adherent after the treatment, this cell line is a semi-adherent cell line and when the conditions of the cells's environment are not ideal, their adherence becomes compromised.

To confirm or refute this hypothesis, a series of high-throughput (HT) fluorescence microscopy experiments were performed, as the number of cells present in the field of view of the confocal microscope was not enough to make a thorough assessment of cell viability, a HT experiment would

allow the increase of the number of cells imaged and therefore provide a more confident assessment. The parameters were kept the same for the high throughput imaging experiment as for the experiment shown in Figure 51, amiodarone media concentration, number of passages the cells were in culture for and the number of cells per well, to account for the smaller surface area of the 96-well plate used for this experiment. As these cells were semi-adherent and the high throughput imaging focal plane could only be set during the initial set up, this assay only measured the cells adhered to the glass substrate, the increase in cell numbers analysed mitigated the fact that only one focal plane was used for analysis, this was done in the interest of time.

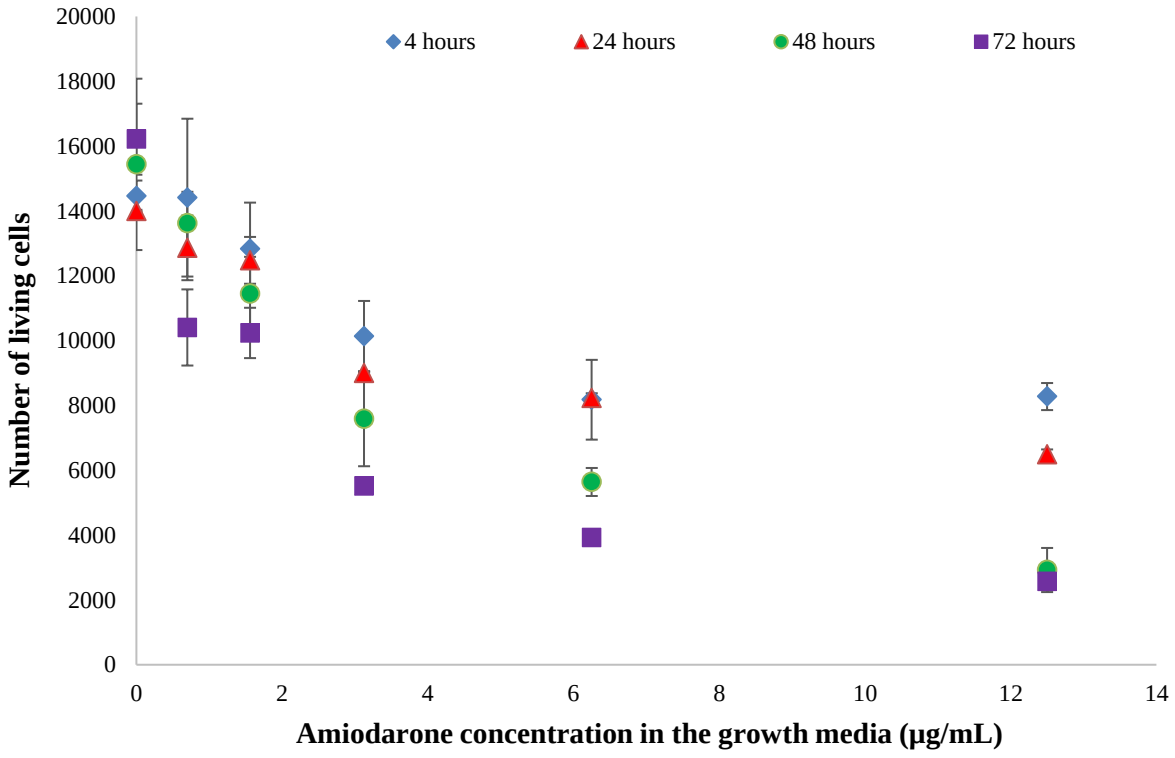


Figure 52: The number of live cells determined from automated fluorescent wide-field microscopy images of NR8383 cells dosed with amiodarone at 0.78, 1.56, 3.13, 6.25 and 12.50 µg/mL and control. Three wells per performed per condition. The number of live cells was determined by counting the number of nuclei present per condition per well. Each colour/shape represents a different incubation time, the blue diamond represents the 4 hour time-point, the red triangle is the 24 hour time-point, the green circle is the 48 hour time-point and the purple square represents the 72 hour time-point.

Figure 52 shows that the number of live cells in culture decreased as the concentration of amiodarone in the media increased. This was also true for the length of the incubation; the longer the cells were dosed with amiodarone the lower their viability was. This confirmed the hypothesis formulated as a result of the observation of the high resolution microscopy data shown in Figure 51, that cell viability decreases with the increase in amiodarone concentration.

The high throughput imaging data allowed the assessment of several parameters due to the flexibility of the image segmentation provided by the analysis software used (Columbus[234]). This software has machine learning capabilities and was taught to pick up features of interest, in this case the lysosomes, by applying the rule that all features displaying fluorescence in the red region of the spectra were lysosomes, as the dye used in this region of the spectra was targeted to stain lysosomes.

The intensity of the red fluorescent dye associated to the lysosomes was also measured to assess phospholipidosis, the larger the lysossome occupied area within a cell the larger the intensity of the dye. A similar plot to the one displayed in Figure 52 was created showing the relationship of lysotracker intensity and the amiodarone concentration in media, showing that the lysotracker intensity increased with amiodarone concentration, and also with incubation duration. However, at 12.50 µg/mL amiodarone becomes cytotoxic and the number of cells decreases, and it can be seen in Figure 52, this needs to be taken into consideration when analysing the total lysotracker intensity per well, as less lysotracker intensity does not necessarily mean less lysosomes, it might only mean less living cells. Therefore, the lysotracker intensity per well was normalized to the number of live cells, as previously it was established that the cell viability was affected by the length of exposure to amiodarone as well as the concentration of compound the cells were subjected to.

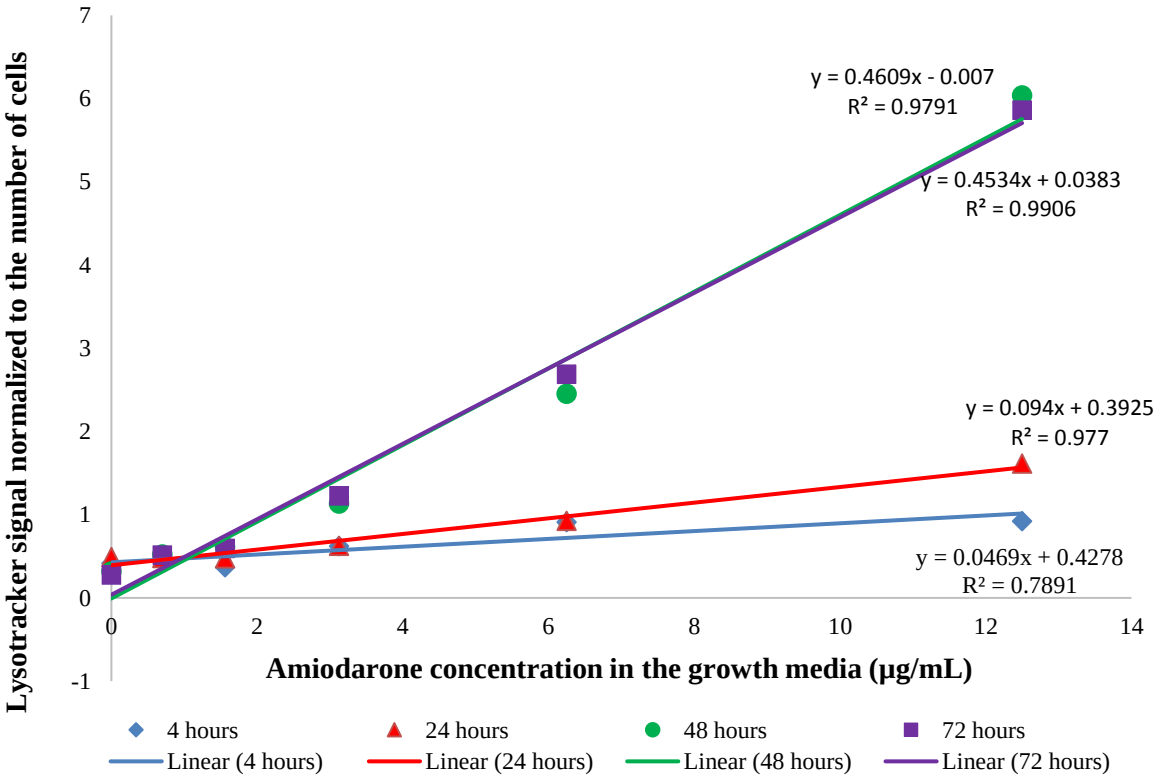


Figure 53: Lysotracker signal per well normalised to the number of living cells in the same well for the different amiodarone concentrations studied (0.78, 1.56, 3.13, 6.25 and 12.50 µg/mL and control). Each colour/shape represents a different incubation time, the blue diamond represents the 4hour time-point, the red triangle is the 24 hour time-point, the green circle is the 48 hour time-point and the purple square represents the 72 hour time-point.

The response for the 4 hour and 24 hour incubation times did not show substantial differences, despite the intensity signal being stronger for the 24 hour drug incubation. In contrast, the 48 hour and 72 hour time-points displayed a much higher signal response, as if incubation time was far more important than the concentration of amiodarone the cells were exposed to. This could be due to two different phenomena. One is just a result of regular macrophage accumulation; the longer the cells are exposed to compound the more they are going to internalise it. The other response is somewhat more complex than that; the hypothesis is that the increased intensity for the later time-points can somehow be mediated by an increasing number of macrophages responding to the treatment. The data in Figure 53, unfortunately, cannot shed light on the latter hypothesis, as the information only relates to intensity and number of cells, not the number of responsive cells, this could be addressed by analysing each cell

individually and determine what percentage of cells developed lysosomes upon amiodarone incubation. This topic is addressed later in this thesis with an imaging flow cytometry experiment.

4.3) Effect of freeze-drying on mammalian cells

One of the fundamental issues in ToF-SIMS sample preparation is that, in the interest of time, the vast majority of the experiments are run at room temperature, and therefore the samples need to be freeze-dried. The removal of water by sublimation might affect cellular structural integrity, due to the formation of crystals at the time of the freezing process and their dissipation at the time of sublimation can cause damage to the cell wall and organelles.

As seen in Figure 50, where H&E stained cells were imaged before and after freeze-drying, cellular structures such as the membrane and nucleus were kept intact, however it was difficult to assess the impact of freeze-drying in other intracellular organelles such as lysosomes. In order to address this concern, a study using fluorescent microscopy was conducted in the NR8383 cell line.

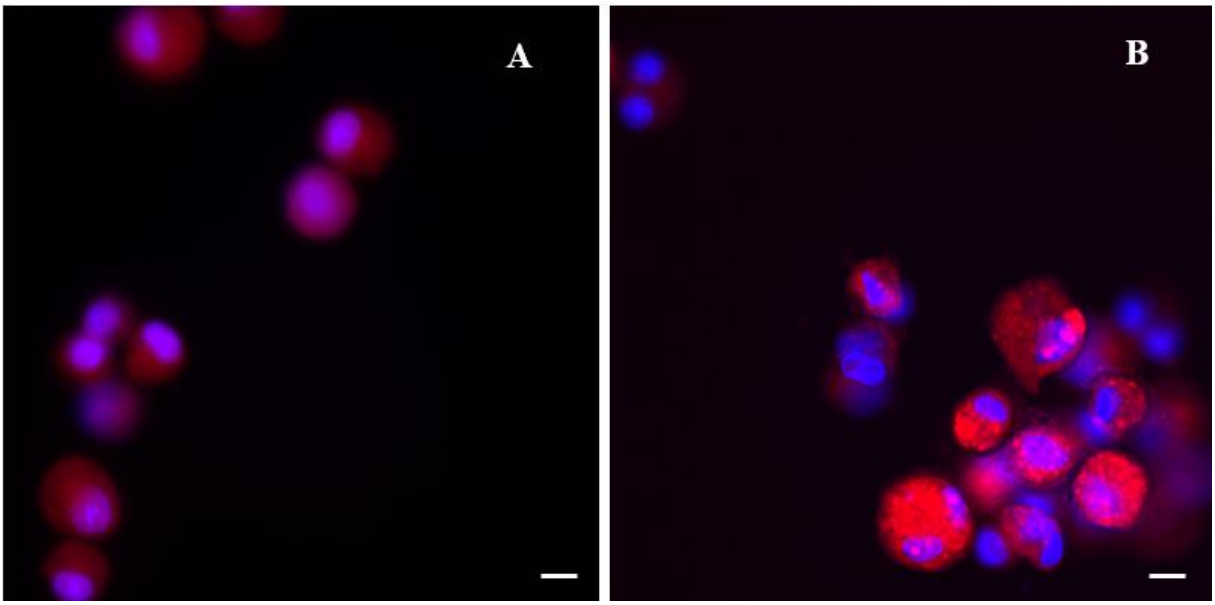


Figure 54: Wide-field microscopy image of high throughput fluorescent microcopy of NR8383 cells incubated for 72 hours at 6.25 µg/mL and stained with Lysotracker red and Hoechst. The images were acquired using a wide-field microscope, the Incell 2000 and a x100 objective. (A) Live cells and in (B) freeze-dried cells.

The before and after freeze-drying images are shown in Figure 54. This data indicated that the cell morphology was not overly disrupted compared to live cells, as can be observed in Figure 54B the lysosomes and the nucleus appear defined, which indicates that they maintain their membranes' integrity.

The main benefit of high throughput fluorescent microscopy is speed, a large number of cells can be imaged even using a high magnification objective in a relative short period of time when compared with confocal microscopy, the downside is the fact that only one focal plane is taken for the whole field of view. This is not a problem for most adherent cell lines, however, as the NR8383 cell line is semi-adherent, the cells appear unfocused on the live cell image, as shown in Figure 54A, however, after freeze-drying which results in the removal of water from the cells, they collapse and the volume decreases which allows the generation of clearer images. The fluorescent microscopy data also indicates that freeze-drying does not affect the lysosomal membrane, nuclear membrane and cell membrane, as disruption of any of these membranes would result in a diffuse appearance of the fluorescent dye and that is not the case.

In addition to the fluorescence microscopy data and in order to check the integrity at the ultra-structural level, electron microscopy was also performed to further confirm the hypothesis that the freeze-drying process was not causing structural damage to the cells. The transmission electron microscopy image, shown in Figure 55, clearly demonstrated ultra-structure consistent with high quality preservation of the freeze-dried cells.[105] The results indicated that around 95% of the cells looked viable with good ultra-structure including mitochondria with visible cristae as well as preserved Golgi complexes, glycogen and endoplasmatic reticulum. Therefore, it can be concluded that the freeze-drying process did not overtly affect the morphology of the cells. This provided confidence in the sample preparation method for ToF-SIMS chemical imaging.

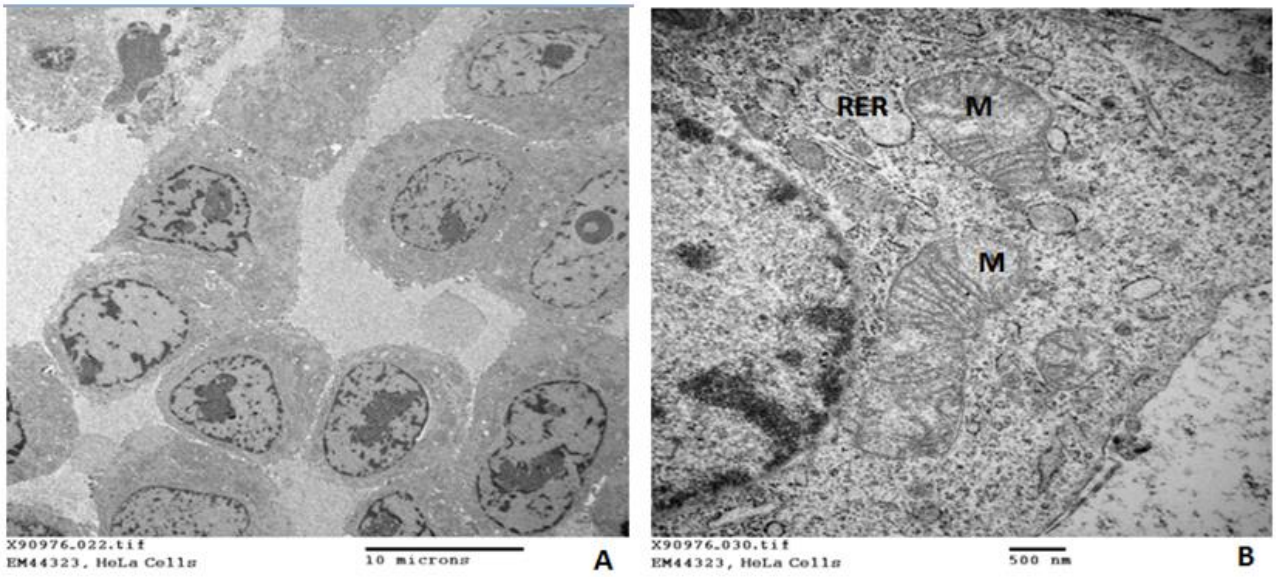


Figure 55: Transmission electron microscopy images of freeze-dried HeLa cells. (A) HeLa cells section at a direct magnification of 12000x. (B) HeLa cell mitochondria at 25000x direct magnification. RER indicates the Rough endoplasmatic reticulum feature and M the mitochondria.

4.4) Imaging flow cytometry of NR8383 cells

Imaging flow cytometry was performed to try to address the issue of amiodarone responding macrophages, from the imaging performed it is clear not all cells respond in the same way to compound treatment, and in this experiment a potential link between amiodarone concentration and biologic activation was investigated. For the imaging flow cytometry experiment the NR8383 cells were prepared as described in section 3.1 apart from the freeze-drying stage. There was little evidence in the literature of NR8383 activation, despite there being a panoply of studies addressing macrophage activation.[257] It is well known and characterised that different types of macrophages and their functions are closely related to their mechanism of activation.[258]

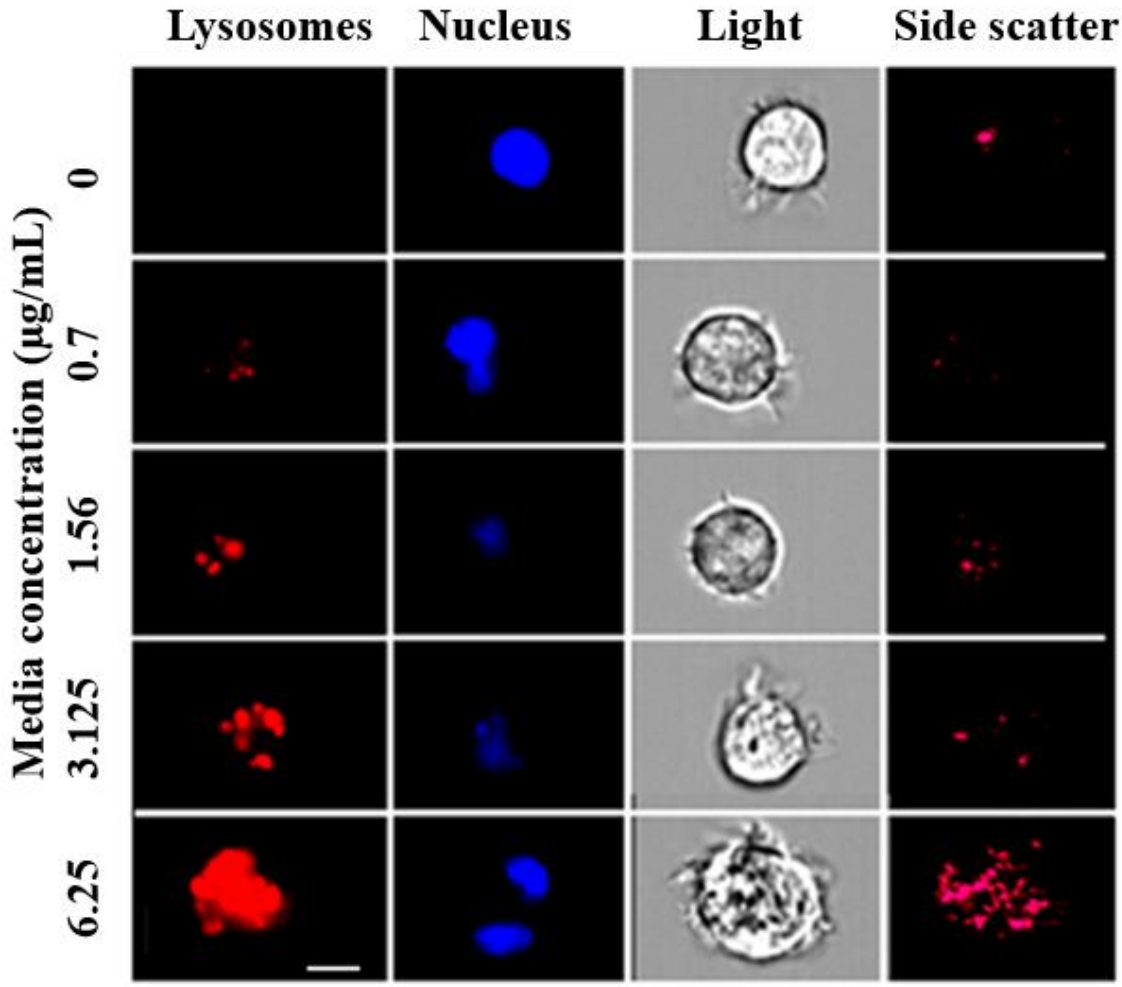


Figure 56: Imaging Flow Cytometry images of NR8383 cell line when incubated with different concentrations of amiodarone for 72 hours. The 2000 cells per condition were fluorescently stained with the nuclear dye Hoescht 33342 (blue) and Lysotracker (red), which stained the lysosomes. The number and size of lysosomes increased with the treatment concentration (white line scale bar is equal to 10 µm).

The high throughput optical microscopy conducted on amiodarone incubated NR8383 cells brought to light a curious observation, not all NR8383 cells accumulated amiodarone. This is illustrated both in Figure 48, where the H&E stains show that only some cells become enlarged and in Figure 51 where the lysotracker signal is not present in every imaged cell. This could be a function of time, as shown in Figure 53 given that there was a clear distinction in signal intensity between the earlier and the later time-points. However, it can be hypothesised that it might also be a function of concentration, for instance, by investigating further the 72 hour incubation time-point with imaging flow cytometry it was

observed that percentage of cells that were accumulating amiodarone for the studied concentrations, as it can be observed in Table 1.

Figure 56 displays the difference in cell morphology at the different concentrations. The top row shows an increase in complexity of the side scatter as the concentration was increased, which is indicative of further complexity in cell morphology due to the increase of the number of lysosomes within the cell as a results of amiodarone incorporation. The lysotracker channel in red indicated an increase in lysosome size and numbers and the bright field images also showed an increase in cell size.

The difference observed in Figure 56 between the different amiodarone concentrations is stark, however 2000 cells were analysed per concentration-point and once those results were interpreted a clearer picture started to emerge as is can be observed in Table 1.

Amiodarone media concentration	Percentage of cells with lysotracker signal (n=2000)
Control (0 µg/mL)	2.5 %
0.78 µg/mL	22.7%
1.56 µg/mL	43.0%
3.13 µg/mL	72.1%
6.25 µg/mL	72.2%

Table 1: Lysotracker signal as a functions of amiodarone concentration in NR8383 cells using imaging flow cytometry. In this table the lysotracker signal is used as a surrogate for lysosome size, and therefore amiodarone accumulation. The tables show a clear increase of lysotracker signal with the amiodarone dose. However, once it reached 3.13 µg/mL the lysotracker fluorescence plateaus.

The percentage of cells responding to amiodarone treatment, for which the lysotracker signal was used as a surrogate, started at 2.5% for the control; it increased to 22.7% for the lowest concentration (0.78 µg/mL), it almost doubled at 43% for the 1.56 µg/mL concentration, and then plateaued for the higher concentrations, 72.10% at 3.13 µg/mL and 72.2% at 6.25 µg/mL.

This data provides further evidence of the dual activation mechanism that the cells underwent, which was depended not only on the duration of the incubation but also on the concentration of amiodarone the cells were incubated with. The biological meaning of this observation could be explored further, however, this is not the remit of the work in this thesis.

4.5) ToF-SIMS of amiodarone incubated NR8383 cells

In order to investigate if pharmaceutical compound used at a physiological dose could be visualised using ToF-SIMS, cells were incubated with amiodarone, chloroquine and GSK2789899A as described in section 3.1. Neither chloroquine nor GSK2789899A could be detected using ToF-SIMS, probably because the intracellular concentration of these compounds was below the limit of detection of the instrument, due to low intracellular concentration or poor ionization efficiency of the compound, hence this report will focus on the analysis of intracellular amiodarone.

Figure 57 is the composite of a two-dimensional representation of the three-dimensional data set; the image was pseudo-coloured for better visulization of the endogenous and exogenous species.

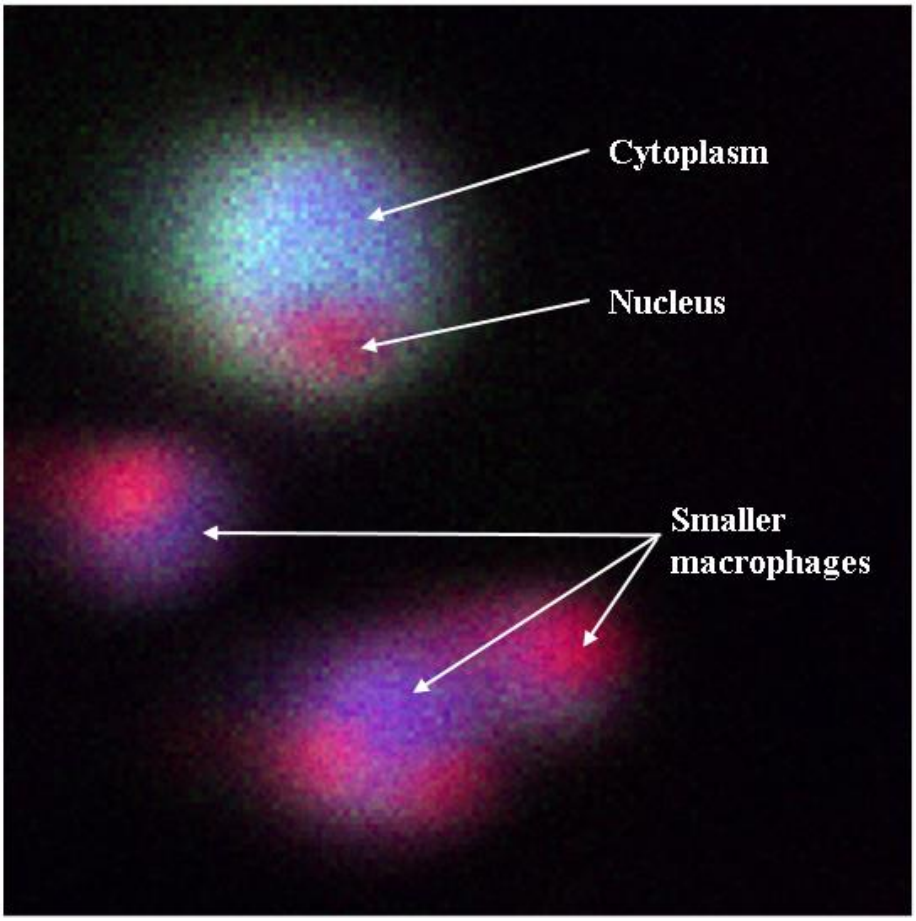


Figure 57: Composite 2D ToF-SIMS representation of a depth profile of freeze-dried NR8383 cell dosed with 1.56 µg/mL amiodarone on glass slides (125x125 μm^3 field of view). Signal-to-noise of at least 3:1 throughout the analysis and final ion dose of 2.2 $x10^{12}$ primary ions/cm^2. The lateral resolution of this image was calculated to be 3.4 μm^5

In order to identify cellular structures, ions associated with molecules abundant in those cellular structures were used as can be observed in Figure 58. A SIMS secondary ion fragment unique in the cell to ribose, $C_5H_5O^+$ (*m/z* 81 Da) was selected as a nuclear marker (in red). Ribose is highly adundant in the nucleus forming part of the backbone of the DNA and RNA structure.[170,259] The blue colouring represents phosphatidylcholine fragment from lipids (*m/z* 184 Da), and it was used as a cellular marker. Green corresponds to the amiodarone signal and shows the distribution of the intact molecular ion from the compound.

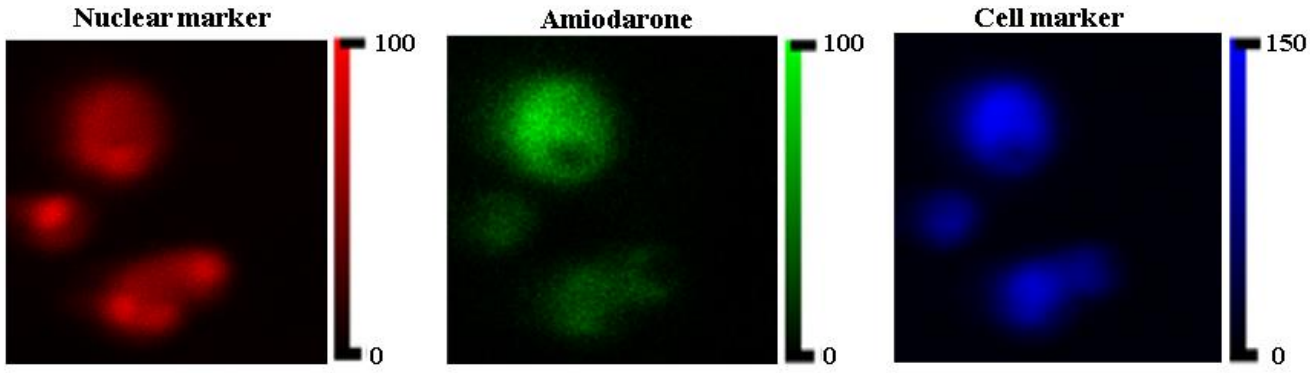


Figure 58: Extrated ion images of a nuclear marker in red, amiodarone in green and a cellular marker in blue of the image shown in Figure 57 with the signal intensity scale on the side of each image. The endogenous markers are $C_5H_5O^+$ (*m/z* 81 Da) in red and phosphatidylcholine fragment from lipids (*m/z* 184 Da) in blue.

The brightness of the colour observed in Figure 58 indicates the signal intensity; the brighter the colour, the more of the selected ion is present per pixel, the pixel size of this experiment was 0.5 μm^2. The data shows that the enlarged macrophage cell has accumulated more of the compound (green), and the compound is present mainly in the cytoplasm. It is also clear that the ribose signal is more concentrated in the nucleus but it is not exclusive to this region, DNA is ribose rich, but this molecule is not exclusive to DNA, ribose is also present in RNA and proteins, which are present in the cytoplasm, hence why a diffuse ribose signal is observed in the cytoplams and a clearer signal is observed in the nucleus.

Figures 57, 58 and 59 show clear evidence of intracellular amiodarone, despite this, the signal was not present in the initial stage of data aquisition, the compound signal signal only became apparent after one sputter cycle. Figure 59 shows the mass spectrum that relates to a full depth profiling experiment performed on cells freeze-dried after being incubated with amiodarone at 1.56 µg/mL.

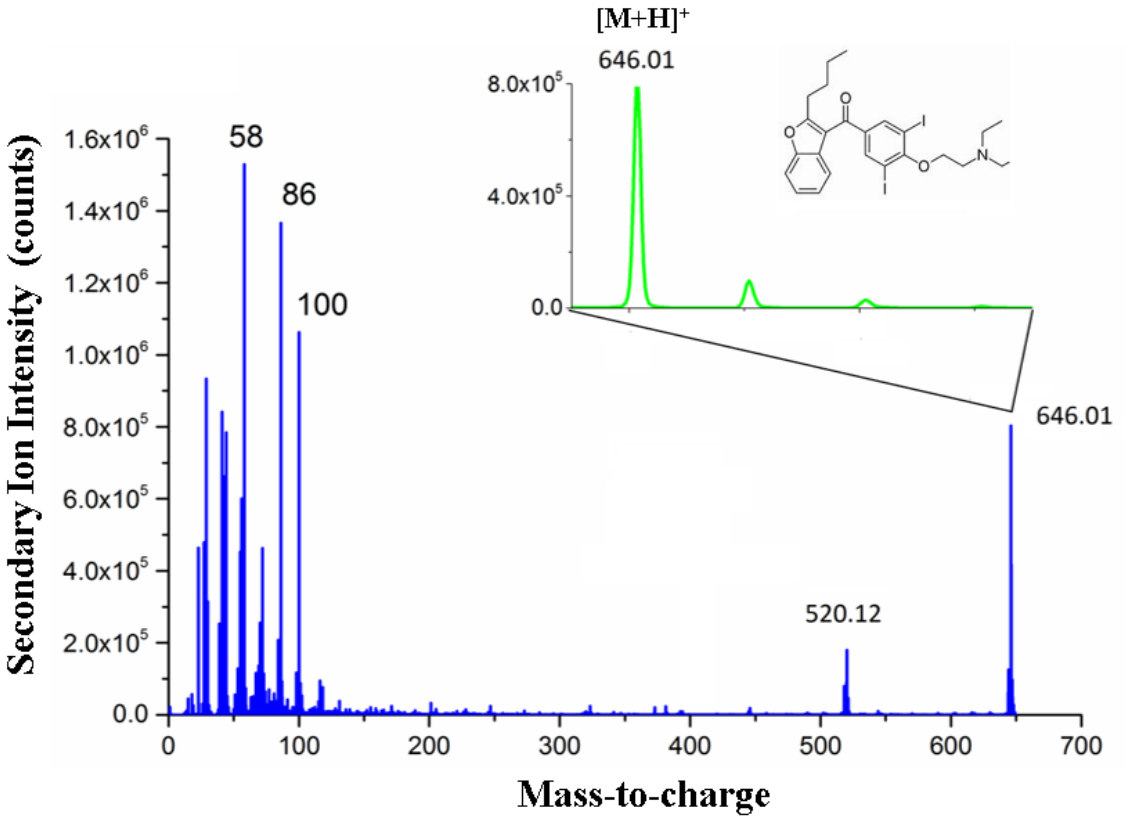


Figure 59: ToF-SIMS from freeze-dried cells incubated at 1.56 µg/mL amiodarone highlighting the amiodarone $[M+H]^+$ ion present in the spectra, and at *m/z* 520 an amiodarone fragment can be found and well as the isotopic patern of amiodarone on the insert part of the image. This is the total spectra for the data in Figure 57.

The lower mass to charge region (m/z) of the spectra is typical of ToF-SIMS, rich in lower mass fragments. Lower abundace fragments appear between 200 and 500 *m/z*, at the higher molecular weight end of the spectra amiodarone related masses can be found, 646 *m/z* (amiodarone $[M+H]^+$) and 520 *m/z* (amiodarone fragment). To ensure that the ions at 646 *m/z* is not cellular artefacts, a cell control with no compound was analysed to verify that there was no signal at the *m/z* of amiodarone, and as expected, no signal could be observed at 646 *m/z*.

To the best of my knowledge, this was the first time an unlabelled pharmaceutical compound has been imaged at physiological doses inside a mammalian cell using ToF-SIMS[45]. There were a few limitations to this experiment, such as the fact that the cells were in the freeze-dried state, which is not entirely ideal as hydrated cells are far more representative of a living cell's natural biological enviroment. Furthermore, the influence of the sample preparation was investigated using the optical and electron

microscopy experiments outlined in section 4.3) and the outcome of both those experiments suggest that freeze-drying does not cause damage to the cell morphology, this is crucial information as SIMS analysis does not have the spatial resolution to visualize such morphology changes.

As Sjövall et al. mention in their publication, the lipid signal intensity varies with the temperature of the sample.[87] They analysed freeze-dried mouse brain sections at different temperatures, from -130 to 60ºC and their findings indicate that the freeze-drying procedure results in lipids moving to the surface of the tissue.[87] Potentially, a similar phenomenon appears to be occurring in these cells, the compound is migrating in the vaccum similarly to the migration of the lipid species decribed in the literature,[87] as most of the compound is observed roughly in the first third of the cell, as Figure 60 illustrates.

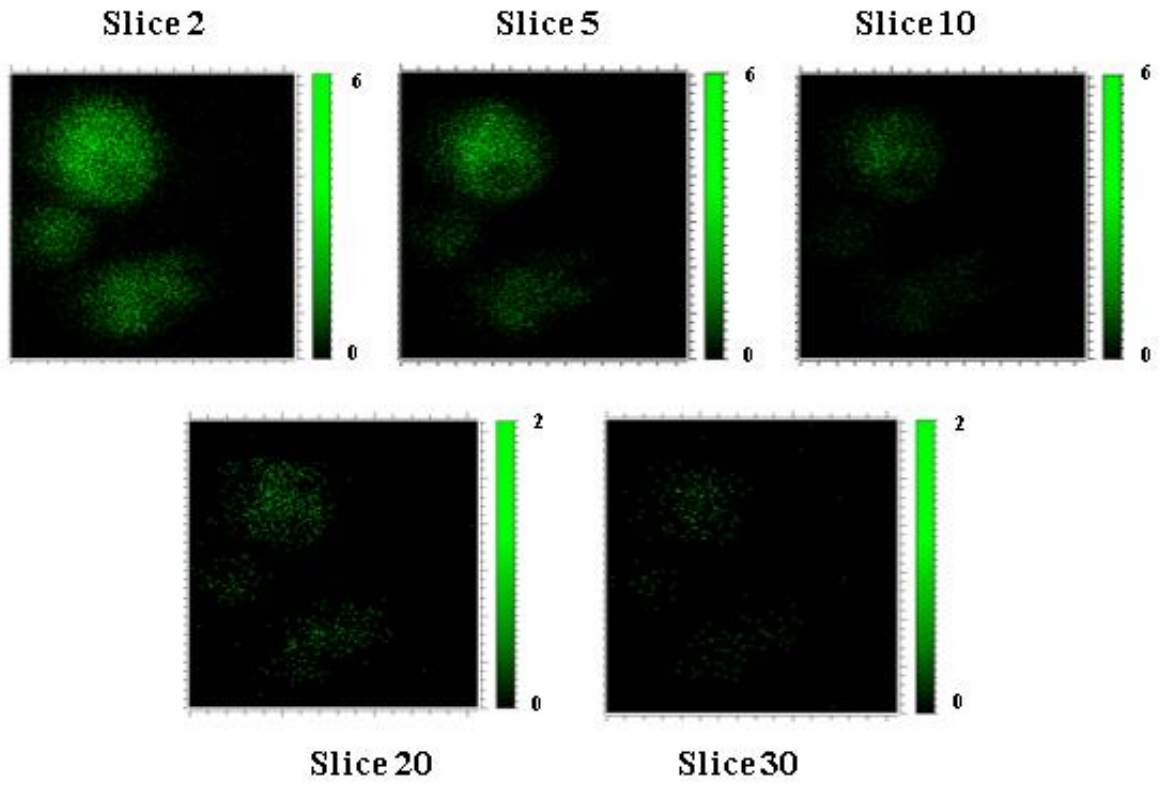


Figure 60: ToF-SIMS amiodarone signal for five different depth slices of an NR8383 cell incubated with 1.56 µg/mL amiodarone for 72 hours. Laser scanning confocal microscopy results suggest that slice 2 is aproximately 200 nm deep into the cell, slice 5 is 500 nm, slice 10 is 1µm, slice 20 is 2 µm and slice 30 isaproximately 3 µm. Field of view of 125 x125 μm^3.

It is noteworthy that when looking at the peak intensity values of the different slices, the second slice (slice 2) seems to have more amiodarone signal followed by slice five which indicates that the drug is inside the cell, but its localisation is probably in the upper part of the cell as previously mentioned. It should also be noted that the cells imaged were all semi-adherent and amiodarone uptake into the cell would, therefore, occur from the top of the cell.

The laser scanning confocal microscopy results presented later in this thesis estimated that the height of a large freeze dried cell is aproximately 3 µm, therefore, each sputter scan is removing aproximatly 100 nm from the sample surface, this could also be calculated based on the ion dose applied to the sample and the sputter rate of biological samples.

To ensure that the experiment could be reproduced, technical and biological replicates were performed in triplicate. Three biological replicates were sampled in three different areas. Figure 61 shows the three biological replicates; the technical replicates are not shown.

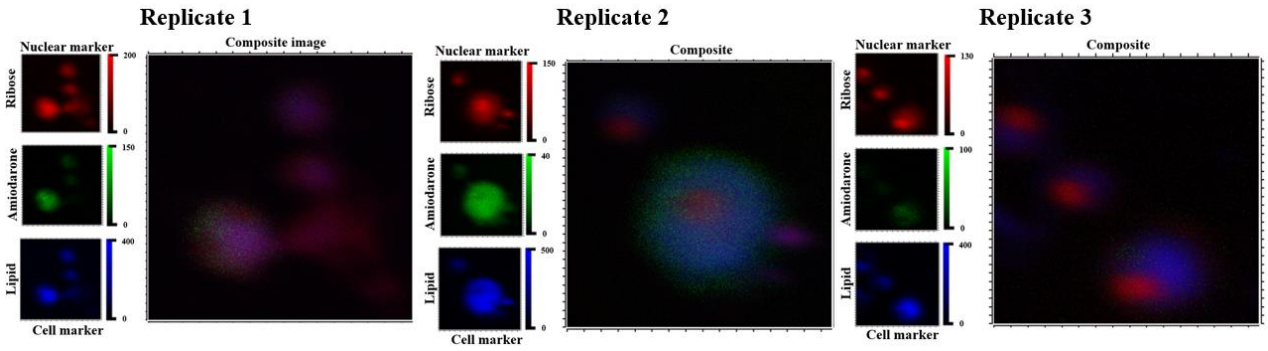


Figure 61: Processed images of the three biological replicates. The green represents the amiodarone signal, and the blue represents one of phosphocholine signal (86 *m/z*). Field of view of 125 x125 µm^3.

As it can be seen by the images in Figure 61, there is a high degree of inter-cell heterogeneity both in terms of morphology and in terms of drug uptake, hence the importance of running replicates.

Until 2013 it was believed that in vivo the generation of new macrophages was done by the development from hematopoietic stem cells via bone marrow-progenitors and blood monocytes, however, now it is believed that they actually can self-renew by local proliferation of mature differentiated cells.[261]

The work in this thesis was performed with rat derived macrophages that have been immortalized, however it was possible that some of these cells are still self-renewing, this associated to the variability of phenotypes that can occur during a cell cycle, can account for the variability of morphology and drug uptake that was observed in this experiment.

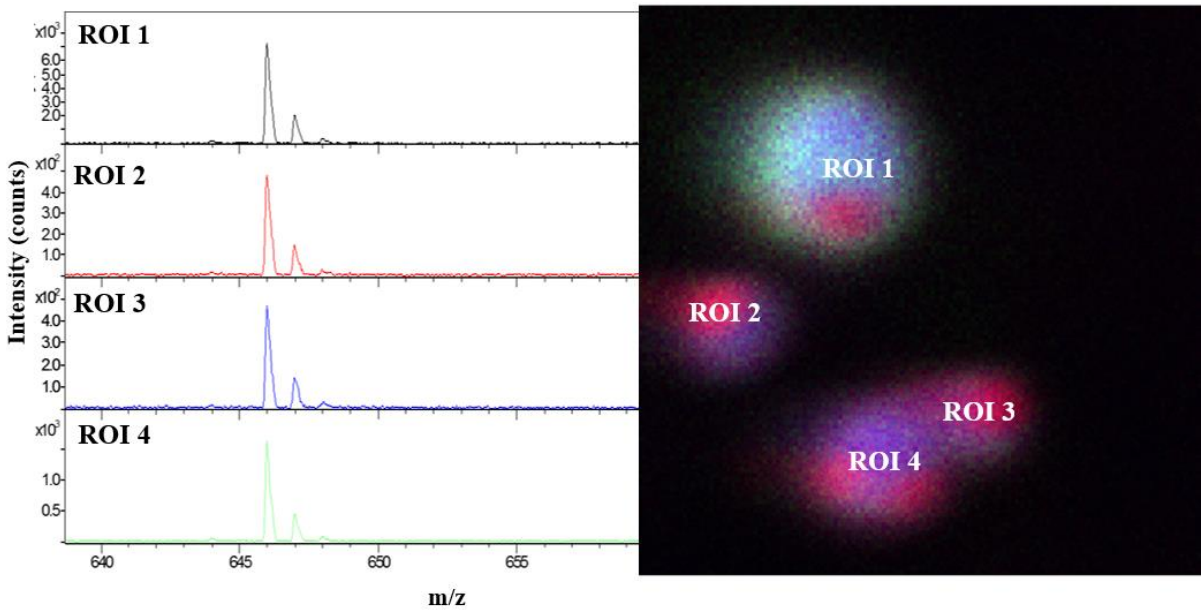


Figure 62: Amiodarone signal intensity for the images shown in Figure 57, which is shown indicating the regions of interest selected, each ROI is a cell. The spectrum shows the intensity of the amiodarone signal in counts for the four selected regions of interest.

Figure 62 shows the difference in compound signal for the four different cells in this image, each cell was defined as a region of interest (ROI) and the amiodarone signal was expressed in the spectral area in counts. The data demonstrates that within the same cell population there are different phenotypes, the cell in ROI 1 is at least four times the size of the other cells present in ROI 2 and 3, these cells appear to be similar in size, and ROI 4 represents a cells that is either dividing or poly-nucleated. Despite this, the amiodarone signal for the cell in ROI 1 is 10 times higher than the signal of the other ROIs, this supports the argument of intracellular compound accumulation.

As previously demonstrated in the imaging flow cytometry section, not all the cells respond to the amiodarone treatment, therefore not all cells start to accumulate amiodarone despite its presence in the

extracellular media, and that can be seen for ROI 2, 3 and 4, despite the amiodarone being present intracellularly the signal is much lower that the signal observed for ROI 1.

The HT fluorescence imaging experiment allowed to ascertain that the lysotracker signal increased with increasing amiodarone concentration and incubation time (Figure 53). The lysotracker signal was used as a surrogate for amiodarone accumulation as the compound is known to accumulate in the lysosome increasing their size as well as the cell's overall size[262]. ToF-SIMS allowed the verification of this hypothesis, if the surrogate measurement was indeed correct, the objective was to determine if an increase in cell size was an indicator of a higher amiodarone signal in ToF-SIMS as hypothesised.

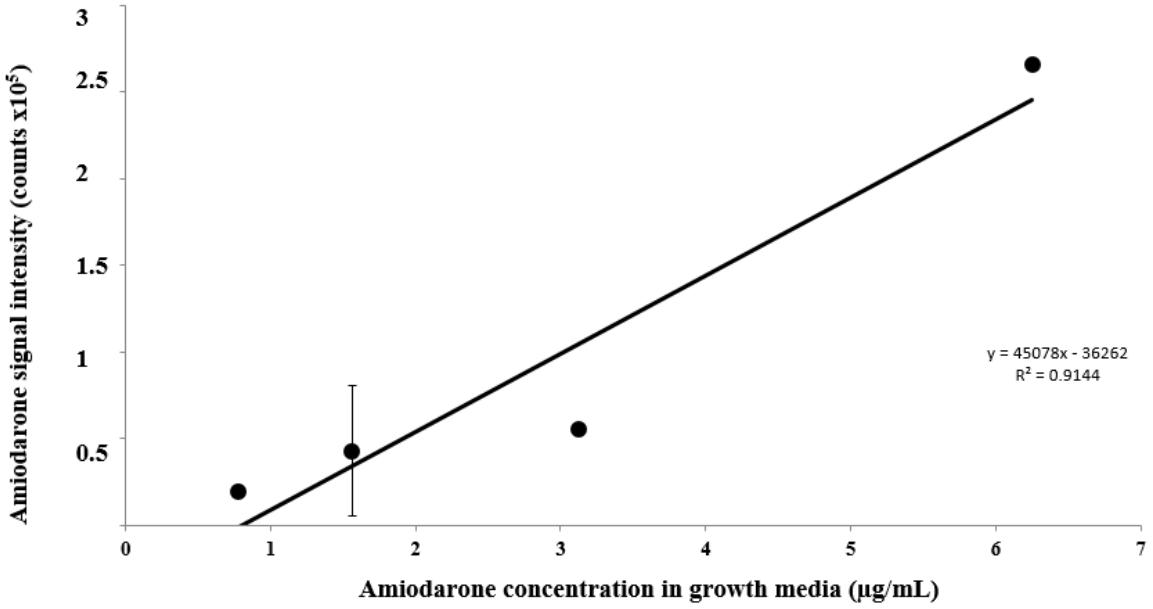


Figure 63: Plot comparing amiodarone signal obtained by ToF-SIMS on the y-axis with amount dosed on the x-axis (dose: 0.78, 1.56, 3.13 and 6.25 µg/mL). One replicate was performed for each concentration, except for 1.56 µg/mL for which three replicates where performed, the compound incubation time was 72 hours.

The correlation between the amiodarone signal observed in counts in the ToF-SIMS measurement and the amiodarone present in the growth media is shown in Figure 63. The data indicates that the higher the compound concentration in the extracellular media the greater the amiodarone uptake by the cells. The response appears to be linear (R^2=0.91), however, replicates were only acquired for one of the concentrations studied and there was some variability between the replicates. This was also made

evident by observing Figure 61 and 62, therefore, the ToF-SIMS signal cannot singularly be an indication of the phospholipidic state of the cell, a correlation of cellular size and amiodarone intensity would be more meaningful. This point will be addressed further in the next chapter, as cell to cell variability and the central limit theorem is discussed.

4.6) Correlative ToF-SIMS and scanning laser confocal microscopy of amiodarone incubated NR8383 cells

In general, an increase in compound concentration and incubation time can cause phenotypic changes to the cell. Hence it can be hypothesised that the larger the cell the greater the level of lysosomal trapping and therefore the higher the concentration of amiodarone inside the cell. This hypothesis can be tested by measuring cell sizes, using a high resolution confocal laser scanning microscope and then analysing those same cells using ToF-SIMS.

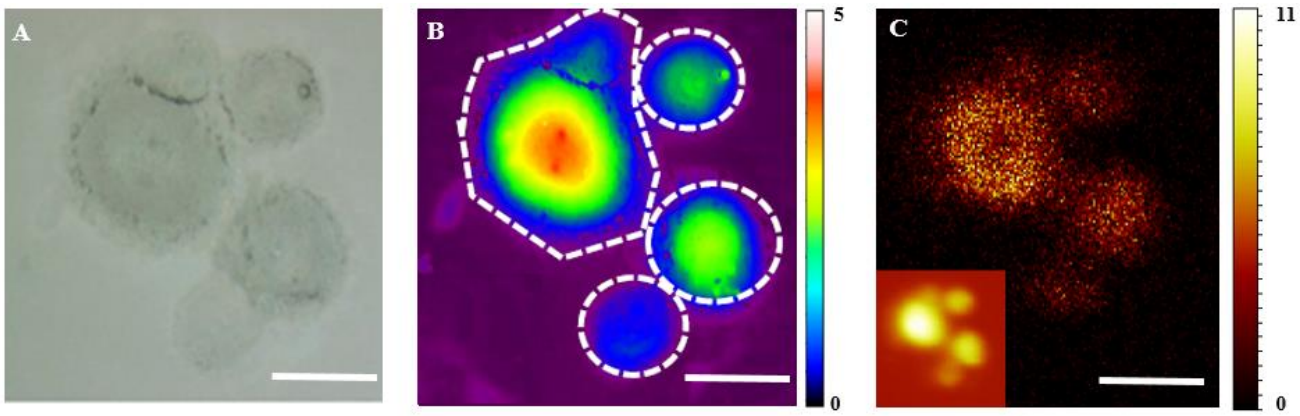


Figure 64: Confocal microscopy (LEXT by Olympus) of NR8383 cells incubated with 1.56µg/mL amiodarone. This technique allows the determination of the volume of the cells, these cells were then analysed using ToF-SIMS. (A) Light microscopy image; (B) Image generated by the laser confocal microscope (LEXT, colour scale from 0 to 5 µm) and (C) ToF-SIMS depth profile dataset of the cells seen on the confocal microscopy image, the larger image shows the amiodarone signal and the insert shows the total ion image. Scale bar is 15 µm.

The frozen-dehydration procedure affects the cell morphology in z; as the water content was removed the cell collapsed and became flattened. The data shown in Figure 64 allows the correlation between cell volume, obtained using the confocal laser microscope and amiodarone intensity obtained from the ToF-SIMS measurement. The data generated by the confocal laser microscope and ToF-SIMS could then be plotted to see if a correlation between the two variables can be determined.

The data in Figure 64 is shown in Figure 65 as a plot, correlating cell volume to ToF-SIMS amiodarone signal, as well as a 3D representation generated by the confocal laser microscope. For this image the cell size and amiodarone signal intensity were well correlated with a r^2=0.99, showing that the higher the amiodarone intensity, the larger the cell.

As it can be observed in Figure 65 there is almost 40-fold variance in cell size within this cell population (the four cells in Figure 65). This variance in cell size was previously observed in the fluorescence microscopy work described earlier in this chapter. This variability in cell size is also evident in the ToF-SIMS data, as it can be observed in Figures 57 and 61.

In order to determine if the uptake of compound into the cell was influenced by the amiodarone concentration in the growth media, and if that effect could be detected by ToF-SIMS, the cells were cultured in triplicate at three amiodarone concentrations (6.25, 3.13 and 1.56 μg/mL) they were then freeze-dried and confocal laser microscopy was performed prior to the ToF-SIMS experiment, the same cells were analysed using both techniques, despite challenges in localizing the same cells for the ToF-SIMS experiment (Figure 64). This was performed in rudimentary fashion, by using a marker pen under the area sampled after confocal laser microscopy, and choosing for analysis areas of the sample where the shapes created by the cells were easily identifiable.

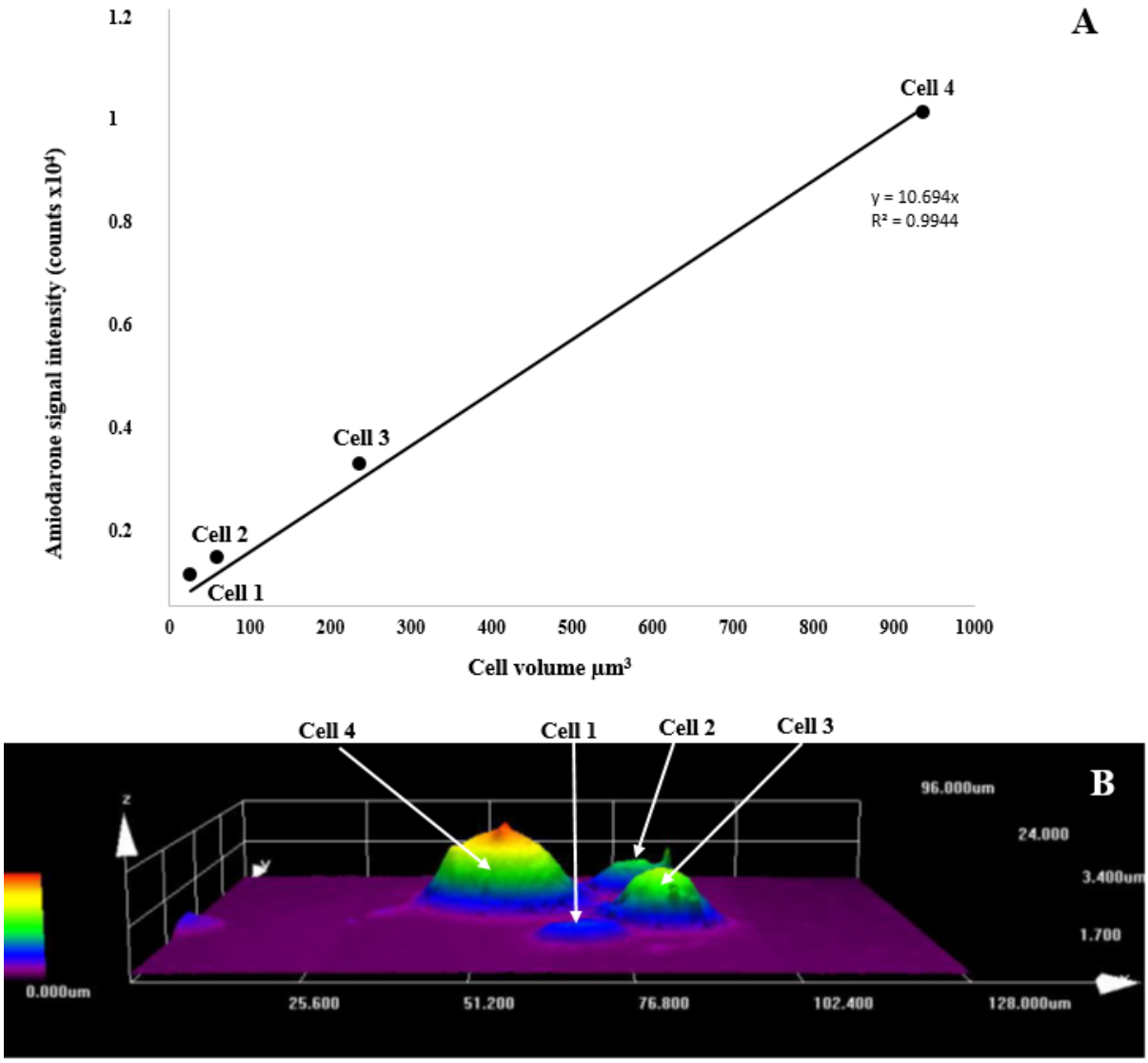


Figure 65: (A) Correlation between ToF-SIMS amiodarone signal intensity and cell volume for the cells, measured using laser confocal microscopy in Figure 64, in NR8383 cells incubated with 1.56µg/mL amiodarone. (B) Three-dimensional representation of the data shown in Figure 64.

In Figure 65 the plot shown relates to a particular replicate, in Figure 66 all replicates and concentrations are plotted. In the plot shown in Figure 65 the ToF-SIMS counts were normalized to the cell volume, and then plotted according to the concentration of amiodarone present in the incubation media, three replicates were performed per amiodarone media concentration. Figure 66 shows that for the 1.56 µg/mL amiodarone incubation concentration the variability observed between the three replicates was

high, up to a 3-fold change within the same cell population, this might be explained by an extremely heterogeneous population size and amiodarone incorporation. This suggests that this cell group was comprised of both small cells with low amiodarone signal and large cell with large amounts of intracellular amiodarone.

The variability in the data for the 3.13 µg/mL amiodarone concentration is much tighter, which probably hints at a more homogeneous population, the relatively low spread in the cell variability suggests that potentially the sampled cells were all around the same size, and no "foamy macrophages" were present in the field of view. Furthermore, the amount of amiodarone per pL of cell was much lower than for the 1.56 µg/mL amiodarone concentration, this data was unexpected the amount of amiodarone per pL of cell (intracellular amiodarone) should in theory tie with the concentration of amiodarone in the media (extracellular amiodarone).

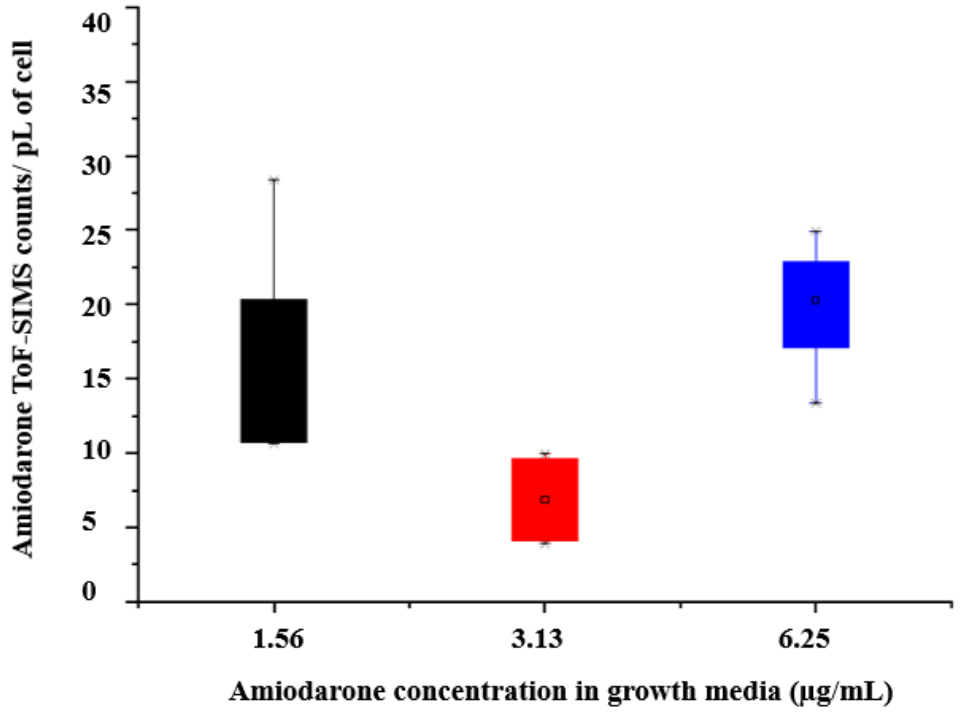


Figure 66: Amiodarone signal obtained by ToF-SIMS measurement normalized to the cellular volume obtained by confocal laser microscopy plotted against the amiodarone concentration in the incubation media. In this plot three replicates were performed for the following amiodarone concentration 1.56, 3.13 and 6.25 µg/mL. The square in the box plot show the media value, and the whiskers show the upper and lower extremes of the data set.

At 6.25 µg/mL amiodarone concentration point there was some variation in the data but not as much as the one observed for the 1.56 µg/mL amiodarone concentration, which means that at this concentration most cells incorporated amiodarone and their size increased due to that incorporation. The data shown in Figure 66 indicates that the variability observed cannot be only related to the cell cycle stage.[261] There is evidence that cells incorporate amiodarone differently and that could be a result of their activation stage, more active cells incorporated more compound and increased in size, and some did not incorporate compound, as they were not as active.

In summary, a high amiodarone signal observed in larger cells may be associated to phospholipidosis, but a low amiodarone concentration in the culture media did not always result in low amiodarone signal measured in ToF-SIMS, as individual cells accumulated relatively high levels of the compound. Despite this, a higher amiodarone concentration in the growth media generally resulted in a higher intensity in the ToF-SIMS signal.

4.7) Proteome profiling of amiodarone incubated NR8383 cells

The fluorescent microscopy data (section 4.2) suggests that between the 24 hour and 48 hour amiodarone incubation time something occurred that significantly increased the number of cells that accumulated amiodarone, as well as showing significant change in cell morphology. From the time scale on which these changes were observed, it is likely that the event was related to protein expression or signalling, as proteins tend to take hours to be produced by the cells; therefore, a proteomic study was conducted to investigate this further.

In the proteomics study described in this thesis the 72 hour time-point was scrutinised and three replicates were performed for each of the different concentrations previously studied for the fluorescent microscopy sections (4.2) and the ToF-SIMS study (section 4.5).

A 2011 study [263] used MALDI to perform a proteomics study in HepG2 cells, one of the compounds used was amiodarone and from the 254 proteins identified most were related to necrosis. After extensive

search, this was the only proteomics study available in the literature that tried to uncover the effects of amiodarone in mammalian cells at the protein level.

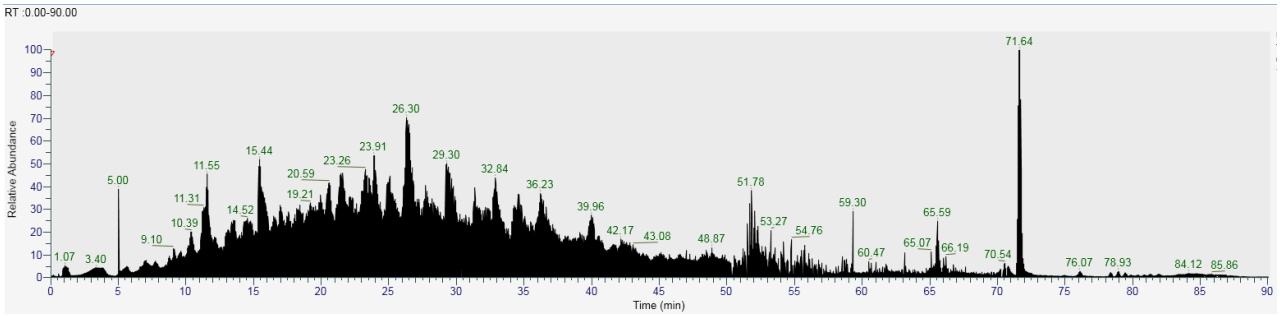


Figure 67: Chromatogram displaying the total ion count for the NR8383 cell lysate on a C18 column as a function of time.

A high resolution Orbitrap instrument (Q Exactive[115]) was used to gather data for proteomic analysis of the three technical replicates, an example of each run can be seen in Figure 67. The samples were prepared as in section 3.1, lysed and digested using trypsin as described in section 3.10.1. In this dataset 1,377 unique proteins were identified using a false discovery rate of 1% (p-value of 0.01). There were a total of 15 runs consisting of three replicate analyses at each of the four amiodarone concentrations plus the non-dosed control. The dataset was filtered to only include those proteins reported in all three replicates. The samples were normalised and compared against the control. Log ratios, with an adjusted p-value of <0.05, were considered significantly differentially expressed and used as input for STRING (functional protein association networks) pathway representation.

The bulk of the statistics was performed using DESeq2, which is a differential analysis method based on a negative binomial model to test differential expression in count type data. It was developed for RNA-seq data and it uses fold changes as shrinkage estimation of dispersions in order to analyse large data sets such as RNA-seq. This tool allows the analysis of data based on the input of a raw count table, which was associated with the experimental group. DESeq2 was used to calculate the geometric mean for each protein across all samples after performing an internal normalisation of the dataset. The

calculated mean was then used to obtain the product between each sample and the mean for each of the proteins identified. This allowed corrections of experimental biases, as for example, if a protein was highly expressed in one condition but not present in the other. The presence of replicates was essential to estimate dispersion of the data and fold-change values; the significance testing was performed using the Wald test. Low count or zero count proteins were considered outliers and removed from the analysis[264].

	Non-zero observations	Mean	Median	Variance	Min	Max
NR8383 cells incubated with 0.78 µg/mL amiodarone for 72hours	813	8.44	1.64	608.41	0	531.04
	729	8.44	1.77	714.94	0	600.87
	708	8.44	1.81	758.28	0	621.71
NR8383 cells incubated with 1.56 µg/mL amiodarone for 72hours	618	8.43	0	809.7	0	652.45
	604	8.42	0	859.41	0	699.67
	589	8.41	0	872.66	0	703.13
NR8383 cells incubated with 3.13 µg/mL amiodarone for 72hours	654	8.43	0	721.91	0	572.98
	645	8.44	0	783.2	0	608.33
	611	8.44	0	853.31	0	648
NR8383 cells incubated with 6.25 µg/mL amiodarone for 72hours	554	8.42	0	915.4	0	603.91
	527	8.41	0	1049.2	0	677.26
	534	8.43	0	980.95	0	633.71
NR8383 cells incubated with vehicle for 72hours (control)	845	8.43	2.62	527.31	0	477.54
	786	8.43	1.72	663.35	0	586.57
	768	8.44	1.75	744.33	0	648.43

Table 2: Summary statistics of the fifteen samples (three replicates for each condition, NR8383 cell incubated with 0, 0.78, 1.56, 3.13, and 6.25 µg/mL amiodarone for 72 hours) collected in this study suggest no obvious outliers, the different samples and replicates are depicted in each row and in the different columns the statistical results can be found.

DESeq2 has been applied to label-free proteomics data by Langley et al. with a few caveats, the authors tested seven different analysis algorithms and suggest that DESeq2 performed very well in detecting true positives as well as identifying false positives, therefore recommending the use of this analysis platform for proteomics data[265]. However, RNA-seq is single count data and protein intensities are continuous, which means that only spectral data can be analysed using this package. However, the low count numbers observed in proteomics data would pose problems to the DESeq2 algorithm, and would

give quite high numbers of rejection of the null hypothesis, therefore Benjamini-Hochberg false discovery rate (FDR) correction was applied[265].

Table 2, shows a summary of the proteomics data with means, variance, median, minimum and maximum values observed. The spread of the data was relatively small; the variance column was below 500 units. This usually indicates that there no apparent outliers, this means that all samples studied were somehow similar. This was expected, as they were samples from the same cell line, the only differences observed on the protein expression levels should have been drug induced changes. The summary of the data presented in Table 2 indicates that there is no evidence of instrumentation or samples preparation issues. In this study of NR8383 cells the cells were incubated with amiodarone for 72 hours at the following concentration: 0.78, 1.56, 3.13 and 6.25 µg/mL, each sample was run in triplicate.

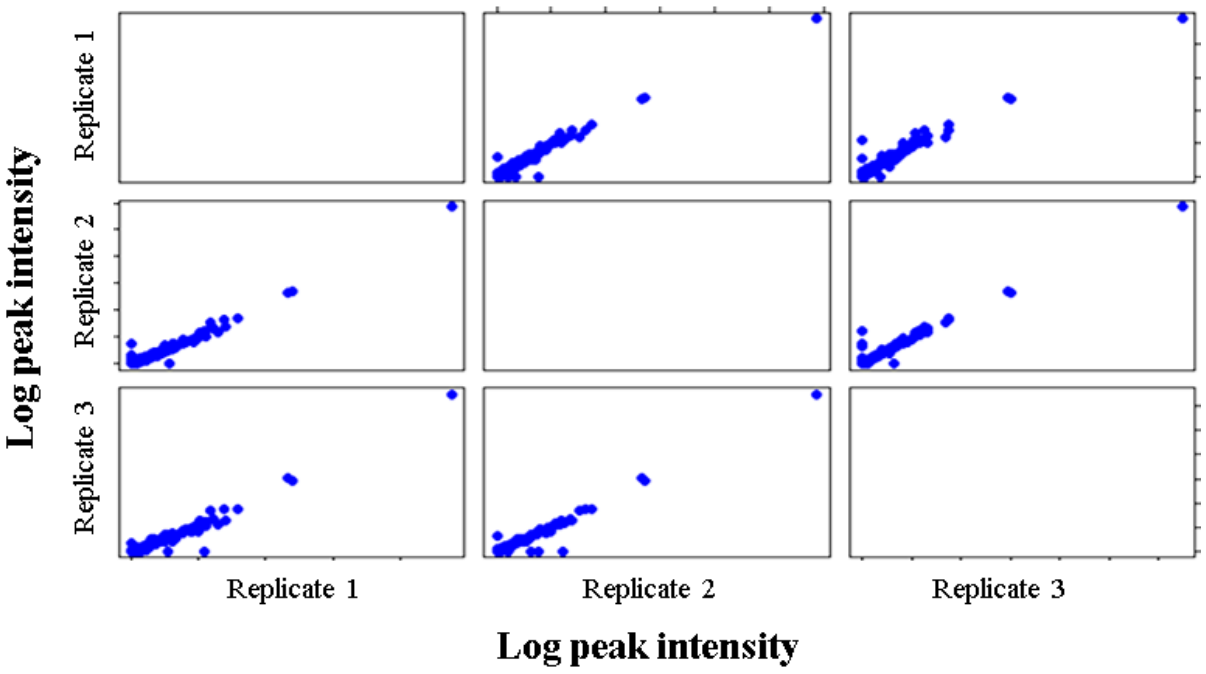


Figure 68: Pairwise plots of the LC-MS/MS replicate runs performed for the control NR8383 cells. The numeric data indicate a high degree of correlation within this treatment group, a similar profile was observed for the other treatment groups (not shown). Pairwise plots represent functions pairs of the scatterplots for each column in a matrix, the individual points represent individual proteins. Only the data for the control is shown, however, pairwise plots were generated for all replicates for each concentration run, this was performed for assay quality control purposes.

The number of non-zero observations, refers to the number of proteins identified per run, the mean value refers to the mean of normalized counts of all samples, and compares the expression of one group to the mean of others, similar values indicate similarity between the samples. The other values are self-explanatory.

Pairwise plots were created for all replicates and all concentrations as a quality control type of exercise, good correlation between replicates indicates no instrument related issues or sample preparation problems. As the representation of the all the created pairwise plots would be unintelligible on paper, only the pairwise plot matrix performed for the control is shown as an example in Figure 68, however a similar profile was observed for all the concentrations analysed.

The pairwise analysis, represented in Figure 68, demonstrated a good correlation between the different replicates, this indicated that the technical replicates were very similar and there were not any issues with the instrumentation. This step was a quality control step and showed evidence that the technical replicates were similar. In order to visualize the whole dataset and determine if the dosing concentrations of amiodarone had an impact in the protein expression, principal component analysis (PCA) was performed.

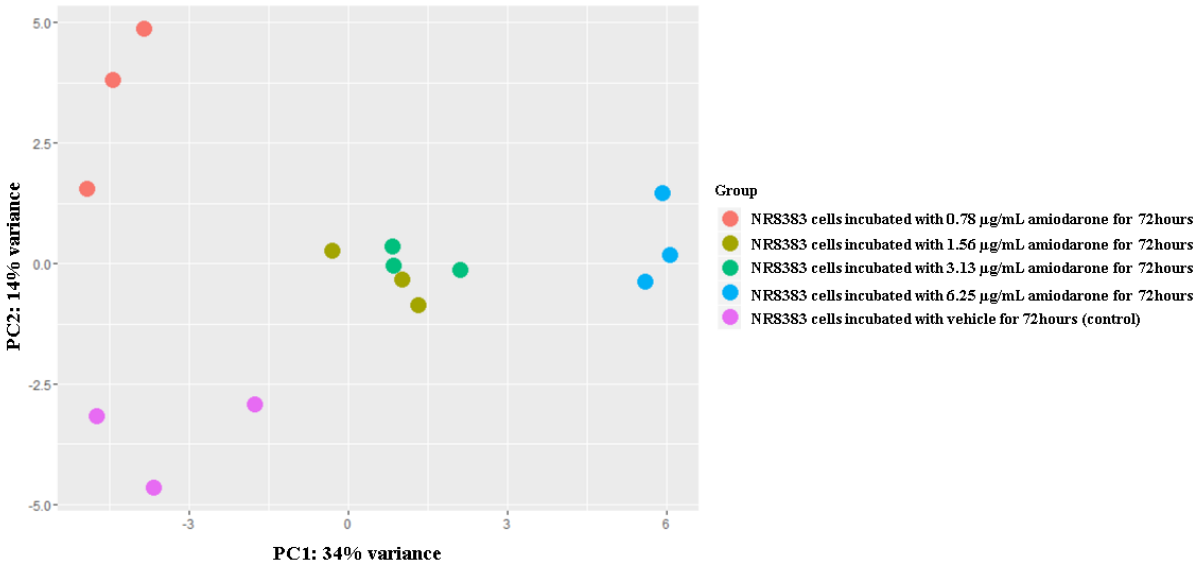


Figure 69: Principal Component Analysis (PCA) of the whole set of the amiodarone incubated NR8383 cells. The samples cluster according to the amiodarone incubation concentration, in pink the control samples cluster together, in red the 0.78 µg/mL amiodarone incubated samples cluster together but away from most of the other concentration points. In olive green

the 1.56 µg/mL amiodarone incubated cells cluster with the 3.13 µg/mL incubated cells, green. In blue the higher concentration used, 6.25 µg/mL, clusters separately from the other drug exposure concentrations.

The PCA analysis in Figure 69 shows PC1 was plotted against PC2, in the x and y-axis respectively. The data indicates a prominent clustering by treatment group, and further suggests that all treatments differ from the control group. It is noteworthy that 3.13 µg/mL and 1.56 µg/mL appear to be very similar to each other and that control and 0.78 µg/mL samples are closer to one another relative to the other three treatment groups, as they appear closer on the PCA plot.

As this data set is rather complex, and as shown by the PCA results, there are considerable differences between the different dose treatments, a different way of visualizing the whole data set can be by heat map representation. This is a two-dimensional representation of a dataset; in which we can assess the variation of each sample against any other sample in the data set. This allows the visualization of how the different samples cluster, as it can be observed in the heat map below.

Figure 70 depicts a heat map that summarizes the dataset after comprehensive analysis it performed and displaying differences between samples. These differences are represented by a colour which represents abundance. Each sample was compared against itself and all the other samples. Deep colours indicate closely related samples and lighter colours indicate difference between the samples. The darkest colour is shown when a sample is compared against itself, as suggested by the embedded colour key histogram in Figure 70. Overall the control samples were the most distinct of all the samples as they have not been incubated with amiodarone.

The heat map also shows that the sample groups that are more closely related are the 3.13 µg/mL and 1.56 µg/mL, suggesting that at these concentrations the effect of amiodarone on the proteins detected was similar. It can be hypothesized that at these concentrations the amiodarone concentration is cytotoxic to the cells, therefore protein expression can potentially differ between the higher and the lower concentrations of amiodarone. In order to investigate the potential amiodarone cytotoxicity at 6.25 µg/mL the proteins that change the most when compared to the control in this condition were investigated.

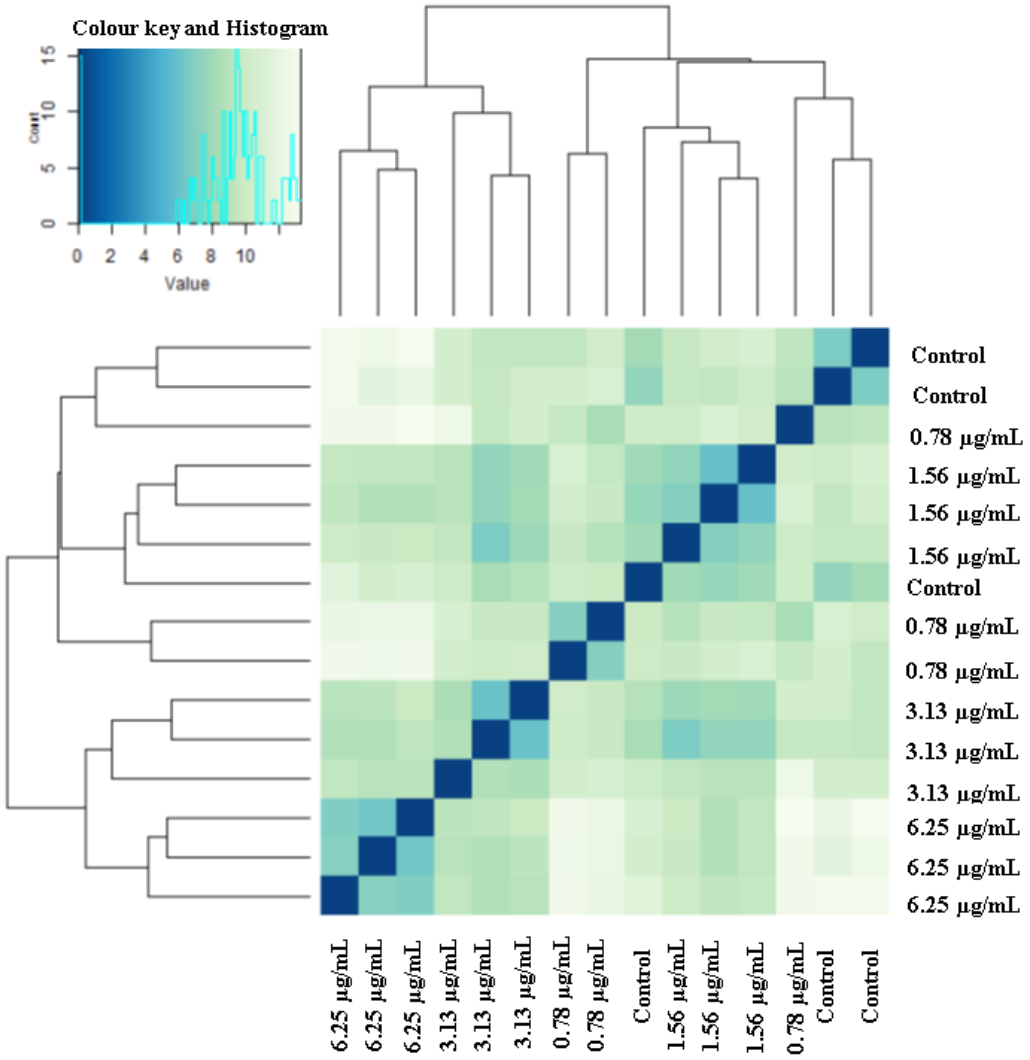


Figure 70: A distance matrix plot suggests the differences and similarities between sample groups. The different samples and replicates are displayed in a coloured matrix form where the colour indicates abundance as shown in the colour key.

At lower amiodarone concentrations the cells are better able to cope with the effects of the compound on their metabolism and therefore the production of proteins that differ from their original phenotype are not expressed.

DESeq2 was also able to provide information on the protein groups that were up-regulated and down-regulated when compared to the control based on their statistical analysis. Table 3 displays the SwissProt identifiers of proteins that were up-regulated and down-regulated in the cells incubated with amiodarone at 6.25 µg/mL when compared to the control. This concentration was chosen as both the

PCA analysis and the heat map suggested this condition was the most different from the control, or their basal state.

In Table 3 several different values are reported, the base mean value is the mean of normalized counts for all samples. The log2Foldchange is the log2 of the ration between the treated and untreated sample, for example, a value of 2 means the expression increased 4-fold.

	baseMean	log2FoldChange	lfcSE	stat	pvalue
A0A0H2UHR7_RAT	9.51	3.55	1.23	2.88	0.00
FABP5_RAT	2.39	3.01	1.37	2.20	0.03
D3ZFL2_RAT	5.16	3.01	1.29	2.33	0.02
Q6P6R6_RAT	0.81	2.56	1.28	1.99	0.05
Q9QZF6_RAT	172.89	2.53	1.00	2.52	0.01
Q5XI77_RAT	9.07	-2.44	1.15	-2.12	0.03
NCPR_RAT	0.79	-2.54	1.28	-1.98	0.05
NIBAN_RAT	3.47	-2.54	1.29	-1.97	0.05
RS28_RAT	2.96	-2.59	1.30	-2.00	0.05
A0A0G2JV31_RAT	2.88	-2.66	1.34	-1.98	0.05
B0BNN4_RAT	2.83	-2.71	1.30	-2.08	0.04
F1LR10_RAT	3.31	-2.76	1.35	-2.04	0.04
Q68FX4_RAT	6.08	-2.89	1.21	-2.38	0.02
RISC_RAT	5.14	-2.93	1.27	-2.31	0.02
GPDA_RAT	3.24	-2.99	1.29	-2.31	0.02
PUR6_RAT	3.49	-2.99	1.29	-2.32	0.02
F1M3H8_RAT	3.42	-3.03	1.29	-2.35	0.02
NOLC1_RAT	4.75	-3.13	1.27	-2.46	0.01
F1LMM5_RAT	7.01	-3.36	1.29	-2.61	0.01
A0A0G2K9A2_RAT	5.30	-3.42	1.30	-2.64	0.01
LDHB_RAT	8.49	-3.45	1.24	-2.78	0.01
A7LAC4_RAT	12.96	-3.54	1.28	-2.77	0.01
H2A1_RAT	78.22	-3.79	1.27	-2.98	0.00

Table 3: Proteins identified as significantly differentially expressed when comparing the 6.25 µg/mL incubated samples with the control samples from the amiodarone incubated NR8383 cell data set.

The IfcSE is the log fold change of the Standard Error, and stat value on the table relates to the Wald statistic value, which is log Fold Change divided by its standard error. The p-value is associated to the significance of a result; it is defined as the probability of finding the observed results (or more extreme) when the null hypothesis is true. As a convention, a p-value below 0.05 is deemed statically significantt.[264]

As it can be observed on Table 3, the log2 fold change provides an indication of the size and direction of the response observed, a positive value indicates the protein expression increases when compared to the control sample, and a negative value indicates that the protein expression decreases when compared to the control.

The p-values were also all below 0.05, which is the cut-off for a result to be considered statically significant, as that was one of the criteria for the protein threshold selection. The significance is defined as passing the null hypothesis test, which means that if the data was removed from the model, it would not affect the results of the experiment. To evaluate if the identified proteins were connected in any way a STRING analysis was performed.

STRING is a molecular biology tool, used to predict protein-protein interactions. The database includes both direct (physical) and indirect (functional) associations. STRING provides visual representation of the association between the proteins present in the input data and also numerical values such as PPS (degree of protein interactions) enrichment value and clustering coeficent. PPS enrichment value is similar to a p-value and the average clustering coefficient, which is the measure of how connected the nodes in the network of proteins are.[247]

STRING analysis of these proteins (Figure 71) showed little interaction between the identified proteins, with a PPS (degree of protein interactions) enrichment value of 0.0987. This value is above what would generally be considered significant (0.05) as a small PPS value indicated that the connections were not random. The average clustering coefficient was 0.04, the closer the clustering coefficient is to 1 the more likely it is for a cluster in a network to be formed. However, this does not necessarily mean the results are not biologically meaningful only that the set of proteins interrogated is small or that the

function of the proteins identified has not been studied. The up-regulated protein set was composed of the following proteins:

- Fatty acid-binding protein
- Transmembrane glycoprotein NMB
- Protein-glutamine gamma-glutamyltransferase 2
- Gene Lce1d non- characterised protein

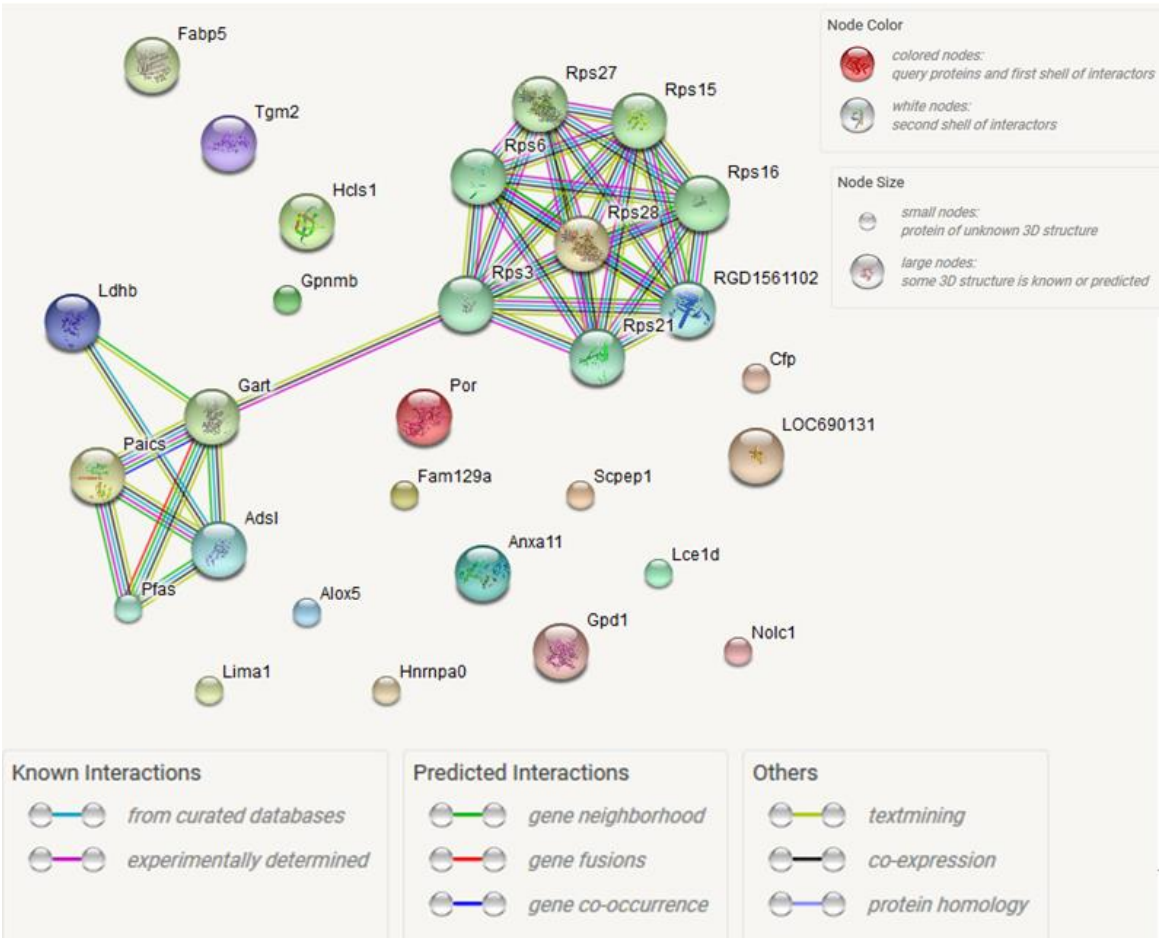


Figure 71: STRING interactome of the up-regulated and down-regulated proteins identified as having a statistically significant change between the control and the dosed cells. Each sphere represents a protein, and their size is indicative of the information available in STRING. The images shows the interaction of the proteins identified as relevant in the statistical analysis with their closely related proteins that were also identified but whose changes were not deemed statistically significant.

Apart from gene Lce1d, which has not been characterised, the other proteins are thought to be involved in apoptosis and cell signalling.[266–268] The transmembrane glycoprotein NMB which is significantly up-regulated is also involved in chemotaxis,[269] or the directed movement of a motile cell towards a higher concentration of a chemical.[270] The fatty acid binding protein is, as the name indicates, involved in lipid binding and lipid metabolism. Protein-glutamine gamma-glutamyltransferase 2 is mainly responsible for apoptotic cell clearance, which is crucial in the cytotoxic environment caused by amiodarone incubation.[271]

The list of down-regulated proteins is greater than the up-regulated proteins; however, in general, the reduced expression of proteins that are not expressed in situations when the cell is under chemical-stress. Several cell death precursors as well as enzyme production were reduced. There was also a reduction in the production of proteins involved in phosphorylation events, ribosomal production and inflammatory response activities. This data, despite not pin-pointing a protein responsible for the increased uptake observed in the 48 hour and 72 hour time-points, provide important clues on what is happening to the cell. Lipid uptake and metabolism are increased, consistent with the known effect of amiodarone on lipid metabolism that results in phospholipidosis[272]. Chemotaxis response is increased as demonstrated by the up-regulation of transmembrane glycoprotein NMB, this was expected following incubation of the cells in a media with a relatively high amiodarone concentration. Furthermore, all non-essential cellular functions that are not necessary for a chemical stress type of environment are down-regulated, such as enzyme production, phosphorylation, ribosome production and inflammatory response. The identification of proteins associated with apoptosis, such as Protein-glutamine gamma-glutamyltransferase 2, provides evidence that the higher concentrations of amiodarone used are cytotoxic. The data indicated that at 6.25 µg/mL proteins associated with cytotoxicity and cell death appear up-regulated, this indicates that this concentration is harmful for the cell.

The data also indicated that some lipid production associated proteins are up-regulated, such as Fatty acid-binding protein, which potentially indicates that the cell is finding alternative lipid production and

disruption pathways, this is to be expected as amiodarone is known to disrupt the lipid metabolism and the cells are trying to adapt to their environment in order to survive.

4.7) Lipidome profiling of amiodarone incubated NR8383 cells

There is extensive literature on phospholipidosis inducing compounds[273,274] such as amiodarone. Microscopy data demonstrate that the cells appear enlarged and have a "foamy" appearance due to the swelling of lysosomes caused by the increased levels of lipid within them. Some examples can be found in the literature of metabolomic studies performed on amiodarone dosed animals.[275,276] However, data for cells was not available in the literature, therefore a lipidomics study in amiodarone dosed NR8383 cells were yet to be undertaken. For this reason, a lipidomics study was designed to investigate the lipid changes in NR8383 cells after amiodarone dosing

The cells were prepared as in section 3.1, for all microscopy, ToF-SIMS and LC-MS/MS data (both proteomic and lipidomic profile). The cells studied were NR8383 and the concentration of amiodarone were the same: 0, 0.78, 1.56, 3.13 and 6.25 µg/mL.

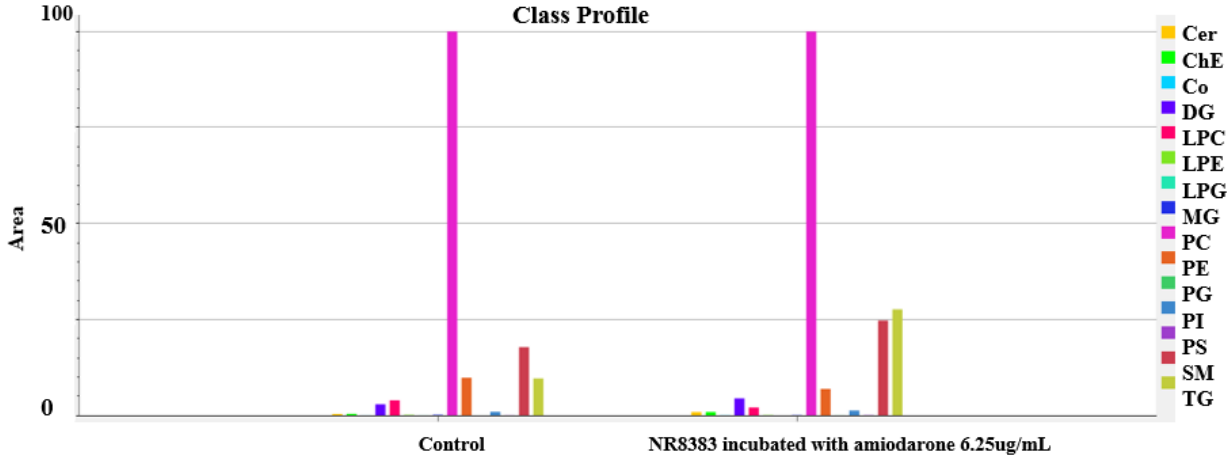


Figure 72: Lipid class profile distributions (c is the control cells and S1 the amiodarone treated cells) of the lipidome experiment performed in amiodarone incubated NR8383 cells. The lipid classes key on the right hand side relates to the following lipid classes: Ceramides, ChE-Cholesteryl Ester, Co- Coenzyme, DG- diglyceride, LPC-lysophosphatidylcholine, LPE-lysophosphatidylethanolamine, LPG- lysophosphatidylglycerol, MG-Monoglyceride, PC- phosphatidylcholine, PE-

phosphatidylethanolamine, PG-phosphatidylglycerol, PI-phosphatidylinositol, PS-phosphatidylserine, SM-sphingomyelin, TG-Triglycerides.

The NR8383 cells, control and treated, were prepared for lipid analysis by extraction of the lipid as described in section 3.11. the samples were run using a nano-LC and a high mass resolution, high mass accuracy mass spectrometer. The data were processed as described in section 3.11 using LipidSearch. The results suggest there are a few differences in the lipid profile of the control group and the cells treated with Amiodarone at 6.25 µg/mL, as illustrated in Figure 72, especially in Diradylglycerolipids, Triradylglycerolipids and Sphingomyelins. The glycerophosphocoline group is, without doubt, the most abundant, and there are a few changes in the lipid profile between treated and untreated cells.

Further statistical work was performed to provide a better understanding of this data, as Figure 72 relates only to lipid classes. The data was exported from LipidSearch as mass, lipid identifier and relative abundance. To perform statistical analysis two approaches were attempted, as there are no clear guidelines in performing statistical analysis on open lipidomics experiments. The first was by attempting to identify the lipids whose signal intensity showed a trend or relationship with the increased dose of amiodarone. The second was based on an ANOVA type approach in which the data for each of the amiodarone doses were compared with the undosed control. All statistical analysis was performed using an R statistical pipeline.

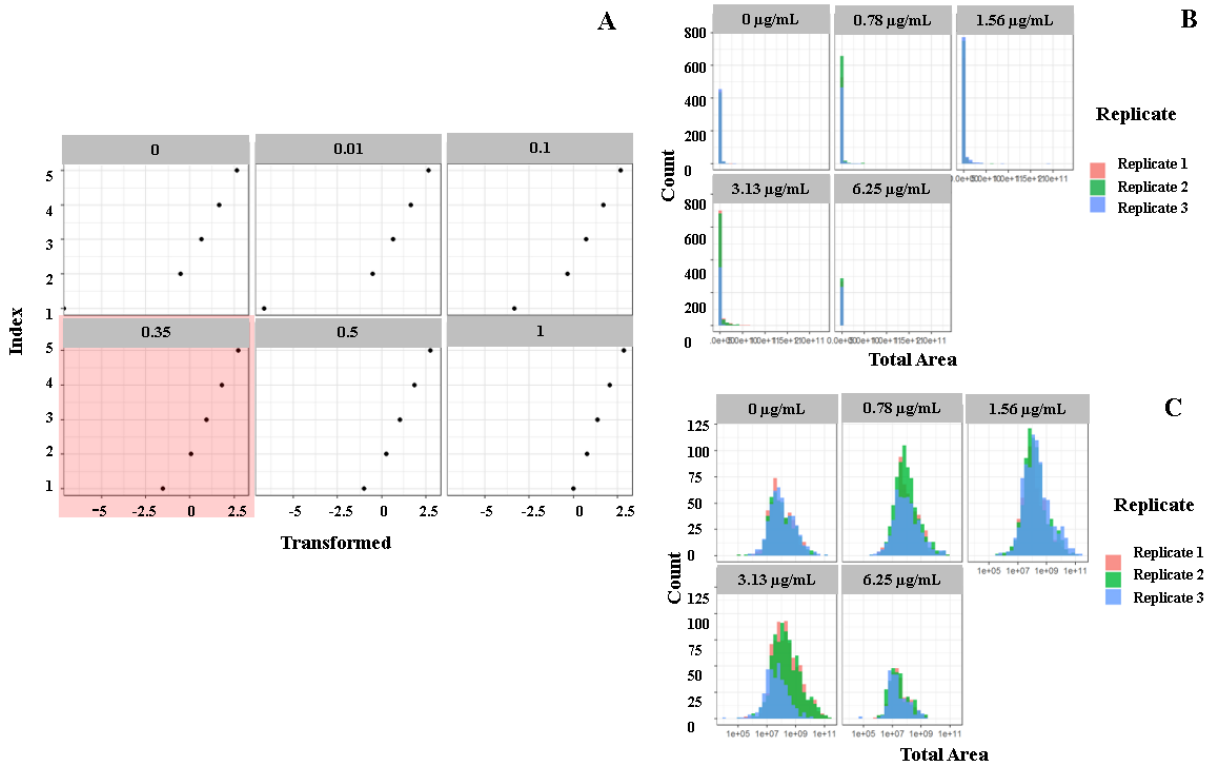


Figure 73: Data transformation of the lipid profiling analysis performed on amiodarone incubated NR8383 cells to reflect on the data obtained the doubling of the media concentration (A) Log 2 transformation for the amiodarone media concentration. (B) Intensity/ area of the lipid signal, untransformed and (C) Log 10 transformed intensity/ area of the lipid signal.

The initial step in both instances was to perform the data transformation to the log scale. Log2 was chosen for the media concentration parameters, as the concentrations of amiodarone in the media double, and Log10 was chosen for the intensity parameter. As it can be observed in Figure 73A a constant had to be added to the Log2 value to reflect the doubling of the concentration. Several different constants were tested but 0.35 was chosen as it was the one the better replicated the doubling of the media concentration. In Figure 73B and C the total area plotted against the peak count is shown, in Figure 73B is the untransformed data and in Figure 73C, the Log10 transformed data. After the log 10 transformation, the data displayed a normal distribution, as demonstrated in the frequency histograms in Figure 73C.

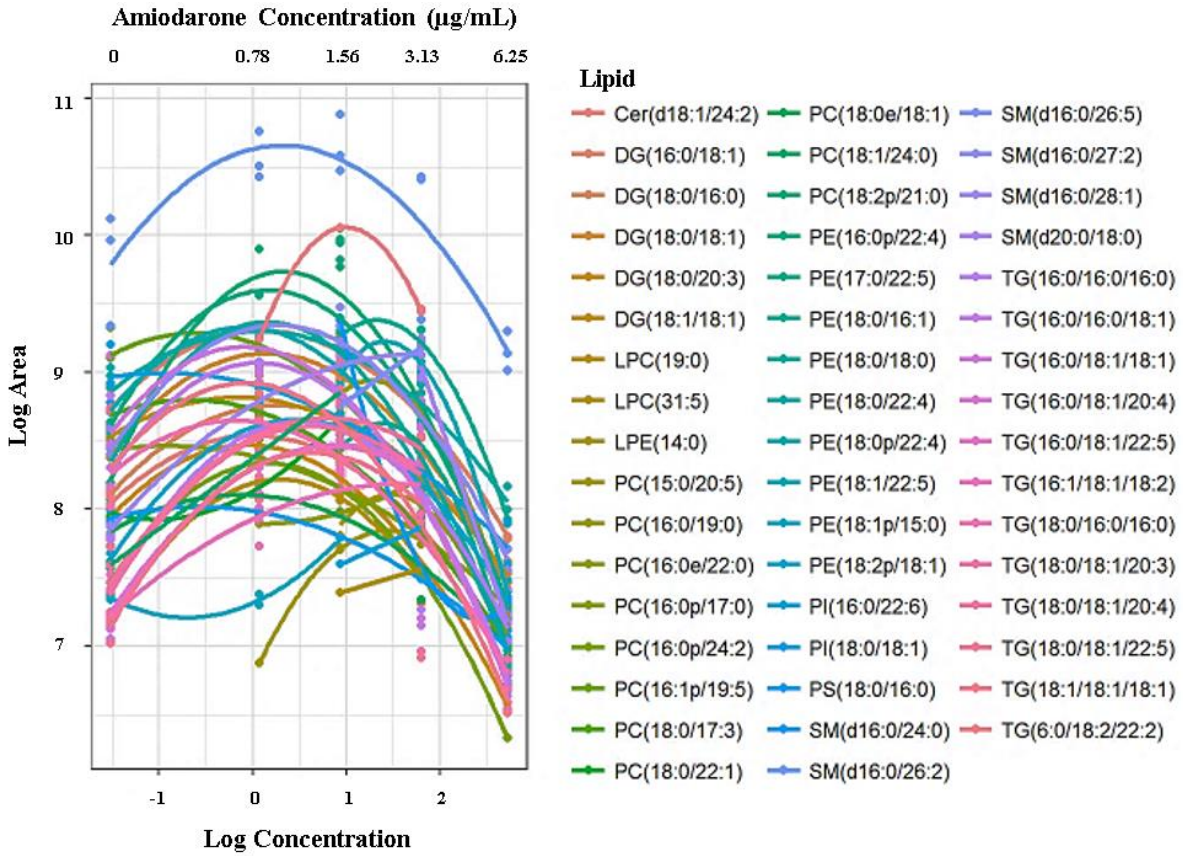


Figure 74: Curves for the fifty lipids which have the best fitting dose-response curves/lines for the lipidome profiling experiment in amiodarone incubated NR8383 cells. Each colour represents a lipid, the three points for the three replicates can be visualised for the different concentrations starting from the lowest to the highest (0 µg/mL to 6.25 µg/mL) from left to right.

In Figure 74, the data for the fifty lipids that best fit a typical drug response curve is displayed. Each lipid is represented by a different colour and the points for the three replicate run can often be seen in close proximity. The concentration of amiodarone increases from left to right starting at 0, followed by 0.78, 1.56, 3.13 and 6.25 µg/mL. The lipids identified are mainly diradylglycerolipids, triradylglycerolipids, sphingomyelins, ceramides, phosphatidylglycerols, lysophosphatidylcholines, lysophosphatidylethanolamines and phosphatidylinositol. Further analysis was performed and the five best fitting lipids to a drug response type of fitting, were analysed and are summarised in Table 4. The table displays the lipid and its lipid class as well as the p-value associated to the statistical analysis performed for each. The curve relevance was assessed using both linear and quadratic line/curve fitting.

Lipid	Lipid Class	P value	Method
DG(18:0/16:0)	DG	1e-07	Linear plus quadratic
DG(18:1/18:1)	DG	0e+00	Linear plus quadratic
PC(16:0/19:0)	PC	0e+00	Linear plus quadratic
PC(16:1p/19:5)	PC	2e-07	Linear plus quadratic
TG(16:0/18:1/22:5)	TG	0e+00	Linear plus quadratic

Table 4. The five lipids whose dose-response curves best fitted the dataset. DC stands for diradylglycerolipids, PC stands for phosphatidylglycerols, and TG refers to triradylglycerolipids.

Table 4 displays the five lipids that best fit the dose-response curve approach chosen for the analysis of the data. This correlates with the preliminary results obtained from the LipidSearch summary that showed the lipid classes that were changing were diradylglycerolipids and triradylglycerolipids. The phosphatidylglycerols group was difficult to assess due to the normalisation of the data, as the data is generally normalised to the highest lipid group, which in this case was the phosphatidylglycerols.

The results shown in Table 4 are somehow surprising, as odd-chain fatty acids are only found in mammalian cells in trace amounts, however odd-chain fatty acids occur in appreciable amounts in ruminants and the cell culture media has been supplemented with Fetal Bovine Serum, which could explain the presence of odd-chain lipids, furthermore the presence of odd-chain lipids could also be an oxidation product of long chain fatty acids, and it is not known if amiodarone-induced lipid accumulation results in lipid oxidation.

The second approach to statistical analysis was an ANOVA type approach, in which each concentration was directly compared to the control sample. This type of data analysis makes fewer assumptions than

the dose-curve approach presented before, however, the interpretation was more difficult, and it can potentially discard a lot of information.

Figure 75 shows the results of ANOVA modelling of each amiodarone concentration versus the control. Close to the x-axis are the lipids that do not change much between the control and the different samples. Samples further away from the x-axis are the most different from the control samples.

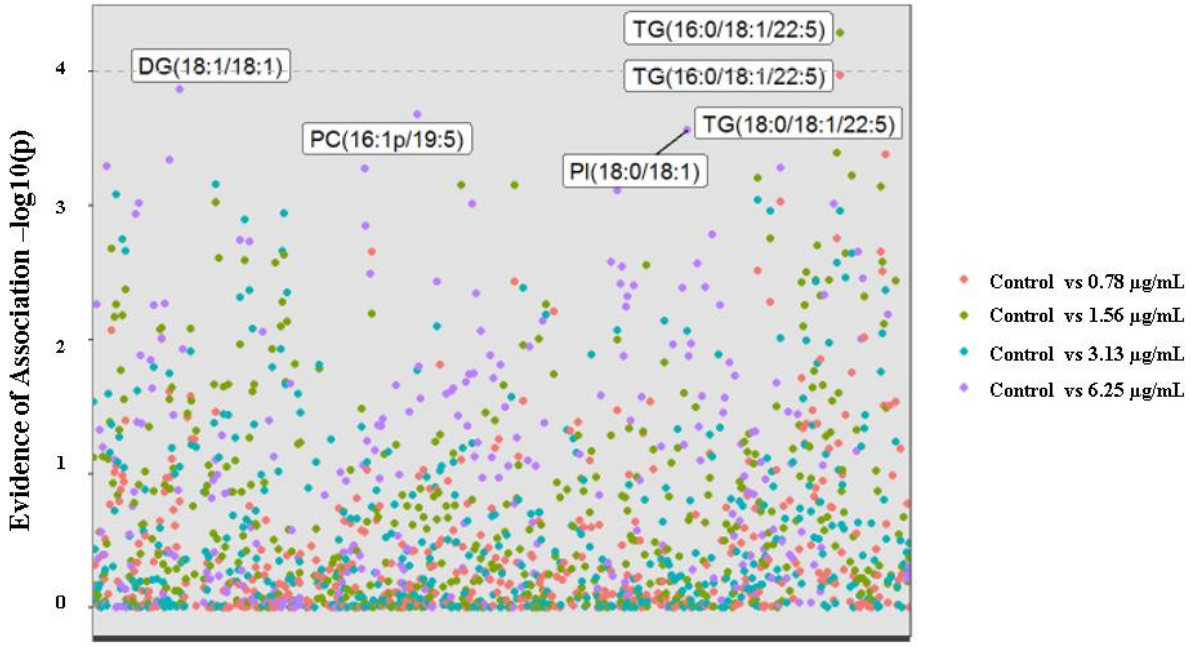


Figure 75: ANOVA model Manhattan plot of each dose versus the control of the lipid profiling study undertaken using amiodarone dosed NR8383 cells. The orange represents 0.78 µg/mL, green is 1.56 µg/mL, blue is 3.13 µg/mL and purple 6.25 µg/mL. The lipids that the data indicate to be changing the most are labelled on the plot; these are the lipids that could potentially be investigated further using pathway analysis.

As in the dose-curve analysis presented above and the preliminary data from LipidSeach, diradylglycerolipids, triradylglycerolipidis, phosphatidylcholines and phosphatidylinositol are the most changed lipid groups. These ANOVA results are also in accordance with the dose-response fitting statistical approach.

In the literature, there is evidence of lipid studies performed in animal tissues that show a similar profile changes to the one observed here for the NR8383 cells, showing up-regulation of PI and PC species.[277]

Commonly lipid studies have a hypothesis, and the MS assays are targeted, which means only the lipids that feature in the hypothesis are analysed, this is a reductionist approach that is commonly used due to the issues in data processing, but data processing software is increasingly improving and allowing lipidomics data to become searchable following the success seen in the proteomics field.

The lipidomics study described in this thesis was performed hypothesis free, all lipid masses present were identified and statistical analysis was performed, and its findings are in accordance with the literature, such as the up-regulation of PI and PC species. However, the TG up-regulation seen in this study is not documented in the literature as a result of amiodarone incubation, this can be a new finding due to the fact that an open lipidomics study was performed rather than a targeted one.

In summary, amiodarone has a marked effect on NR8383 cells, that effect can be observed phenotypically, with an increase in cell size and lysosomal accumulation. This can be observed by H&E staining of the cells, where "foamy" macrophages are clearly visible. The effect is also observed in fluorescence microscopy, as an increase in amiodarone dose results in increased lysosomal size and numbers. The compound can be detected intracellularly, label-free at physiological doses using ToF-SIMS, however there is a very diverse cellular response, especially at higher amiodarone doses. This could potentially be explained by amiodarone cytotoxicity in these conditions, as supported by the proteomics study performed.

5. Results II: Amiodarone ToF-SIMS model applied to other cell lines

The principal objective of this chapter is to determine if ToF-SIMS is cell line agnostic when looking at intracellular compounds. Furthermore, the ToF-SIMS signal was compared to the bulk LC-MS/MS measured intracellular amiodarone concentration to provide a semi-quantitative value to the ToF-SIMS measurement. However, the intracellular variability within the same cell population observed indicated a bulk measurement is unlikely to be representative of the cell population.

In order to determine if the ToF-SIMS analysis method developed for NR8383 cells could be applied to other cell lines such as HEK293, HepG2 and HeLa cells, these cells were incubated using the same cell numbers with the same amiodarone concentrations for direct comparison by ToF-SIMS and LC-MS/MS, NR8383 cells were also studied for comparison with earlier studies. Since ToF-SIMS is a vacuum based technique the samples were freeze-dried for analysis as for the study described in the previous chapter of this thesis; it was important to know the extent of cell damage or morphological changes caused during this process.

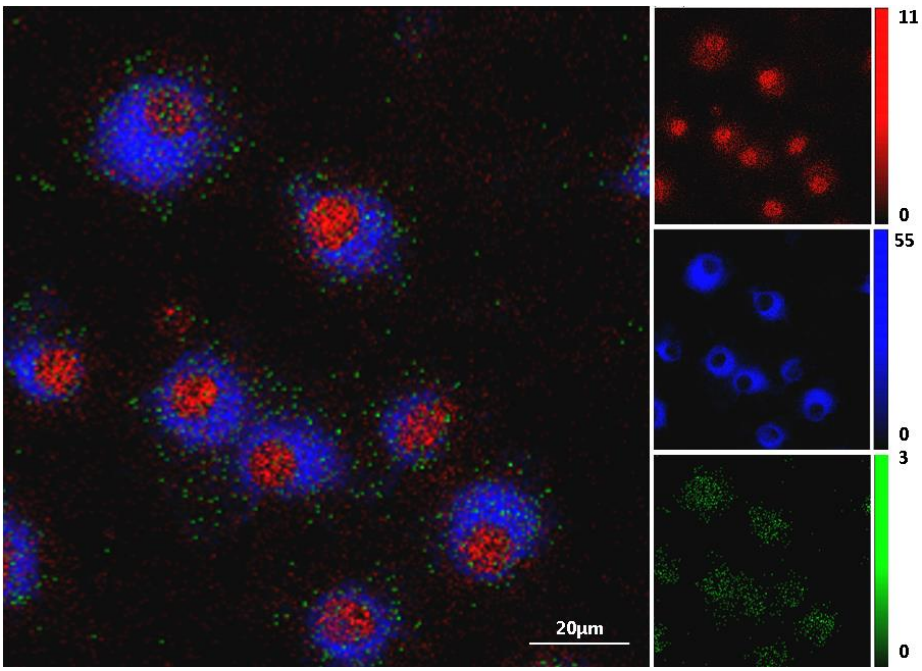


Figure 76: ToF-SIMS 2D images of 3D data acquired from cells entirely consumed by the argon cluster source during analysis and was acquired in high-spatial resolution mode. NR8383 cells were incubated for 2 hours with 6.25 µg amiodarone/ mL. Composite image where red represents Ribose (*m/z* 81), blue shows the signal from the phosphatidylcholine lipid fragment (*m/z* 184) and green shows the amiodarone protonated molecular ion signal (*m/z* 646).

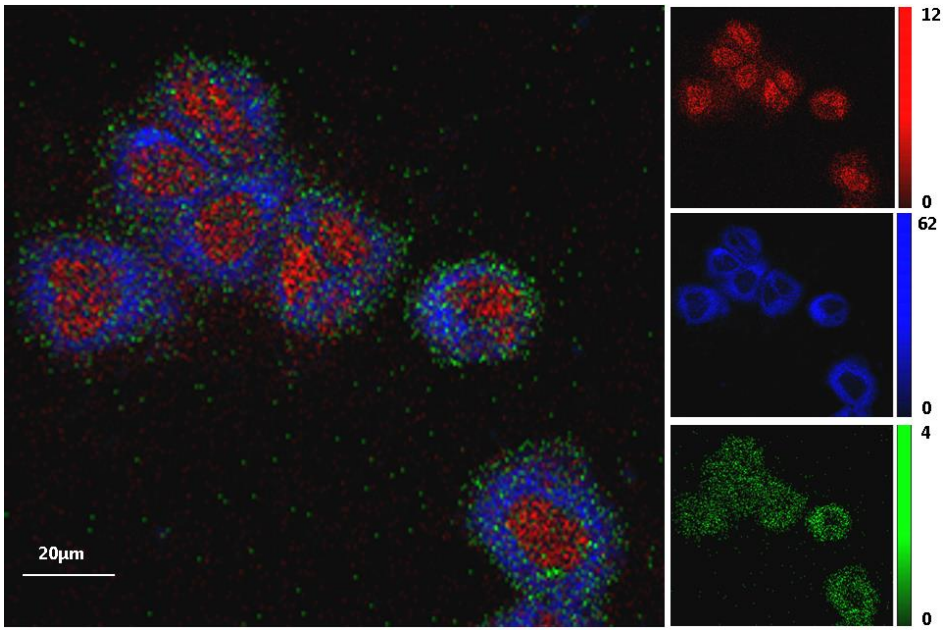


Figure 77: ToF-SIMS 2D images of 3D data acquired in the same way as Figure 76. The Figure shows HeLa cells incubated for 2 hours with 6.25 µg amiodarone/ mL. Composite image where red represents Ribose (*m/z* 81), blue shows the signal from the phosphatidylcholine lipid fragment (*m/z* 184) and green shows the amiodarone protonated molecular ion signal (*m/z* 646).

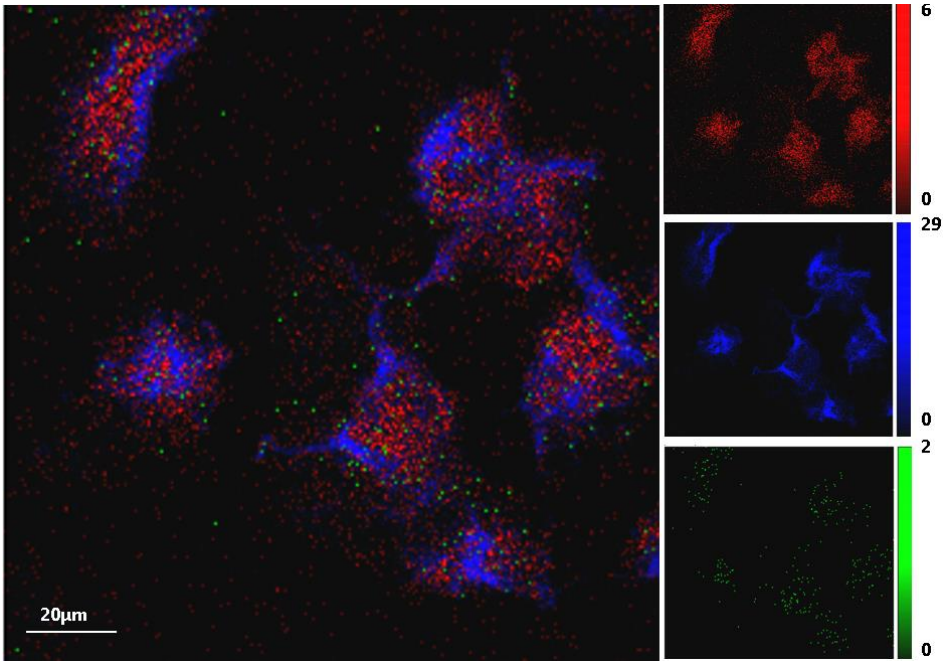


Figure 78: ToF-SIMS 2D images of 3D data analog to Figure 76 and Figure 77. The Figure shows Hek 293 cells incubated for 2 hours with 6.25 µg amiodarone/ mL. Ribose (*m/z* 81) is shown in red, the phosphatidylcholine lipid fragment (*m/z* 184) is shown in blue and the amiodarone protonated molecular ion signal (*m/z* 646) is shown in green.

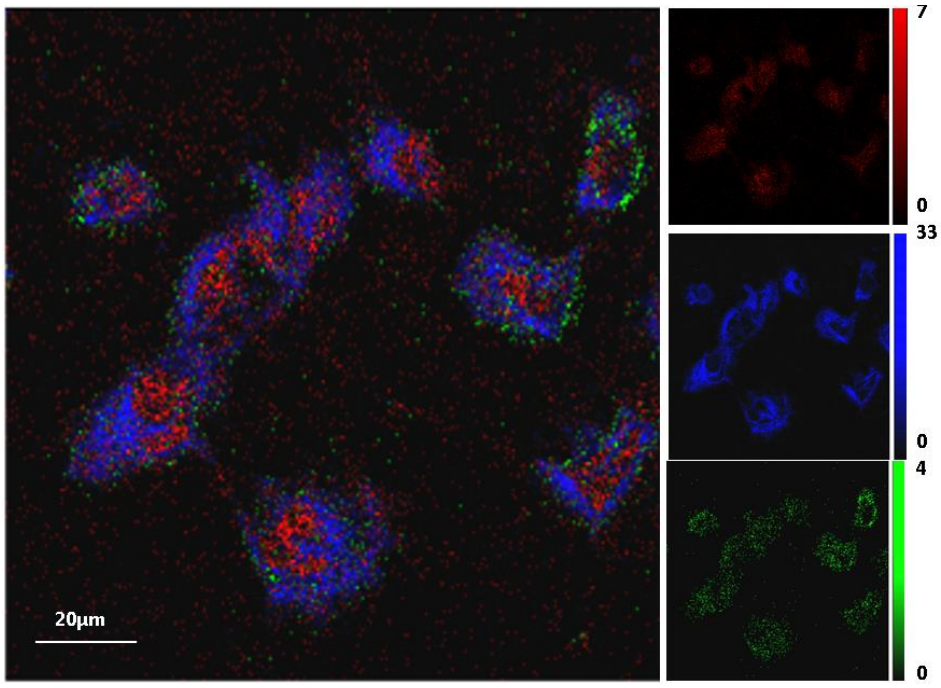


Figure 79: ToF-SIMS 2D images of 3D data set acquired in the same way as Figures 76, 77 and 78. In this image the experiment was performed on HepG2 cells (6.25 µg amiodarone/ mL incubation for 2 hours). Composite image where red represents Ribose (*m/z* 81), blue shows the signal from the phosphatidylcholine lipid fragment (*m/z* 184) and green shows the amiodarone protonated molecular ion signal (*m/z* 646).

The three cell lines (HepG2, Hek293 and HeLa) selected for this study are arguably some of the most used cell lines in drug discovery. The NR8383 cell line was used as a control cell line, as the data shown in the previous chapter clearly demonstrated that amiodarone could be detected using ToF-SIMS. The four cell lines were prepared and incubated with amiodarone in the same way for the ToF-SIMS experiment and the LC-MS/MS experiment.

The ToF-SIMS data in Figures 76, 77, 78 and 79 clearly shows compound and cell co-localization for all the cell lines. The dose chosen was 6.25 µg/mL with two-hour incubation. The relatively short incubation time helped minimise the range in cell size in the NR8383 cell line that resulted from the

disruption of lipid metabolism, this should reduce the variability of the cell sizes observed in the experiment described in the previous chapter of this thesis.

Figures 76 to 79 show 2D representations of the ToF-SIMS 3D data that integrated the entire signal in the vertical direction as the sample was etched away using the gas cluster ion source (i.e. a cumulative plan view) for NR8383 (Figure 76), HeLa (Figure 77), HeK 293 (Figure 78) and HepG2 cells (Figure 79). For each cell type, the large image to the left is a composite colour image with red representing the intensity of the ribose fragment (*m/z* 81), blue representing the intensity of the phosphatidylcholine fragment (m/z 184) and green representing the amiodarone protonated molecular ion intensity (m/z 646). These extracted ion images are shown separately as a panel of small images on the right of each Figure for clarity. The amiodarone was clearly detected for each cell type, and the intensity appeared higher in the HeLa and HepG2 cell lines. For determining the cell associated amiodarone signal the perimeter of the cell was defined by outlining the cell using the Surface Lab 6.5, regions of interest tools and the amiodarone ion intensity was obtained by factoring in the primary ion dose.

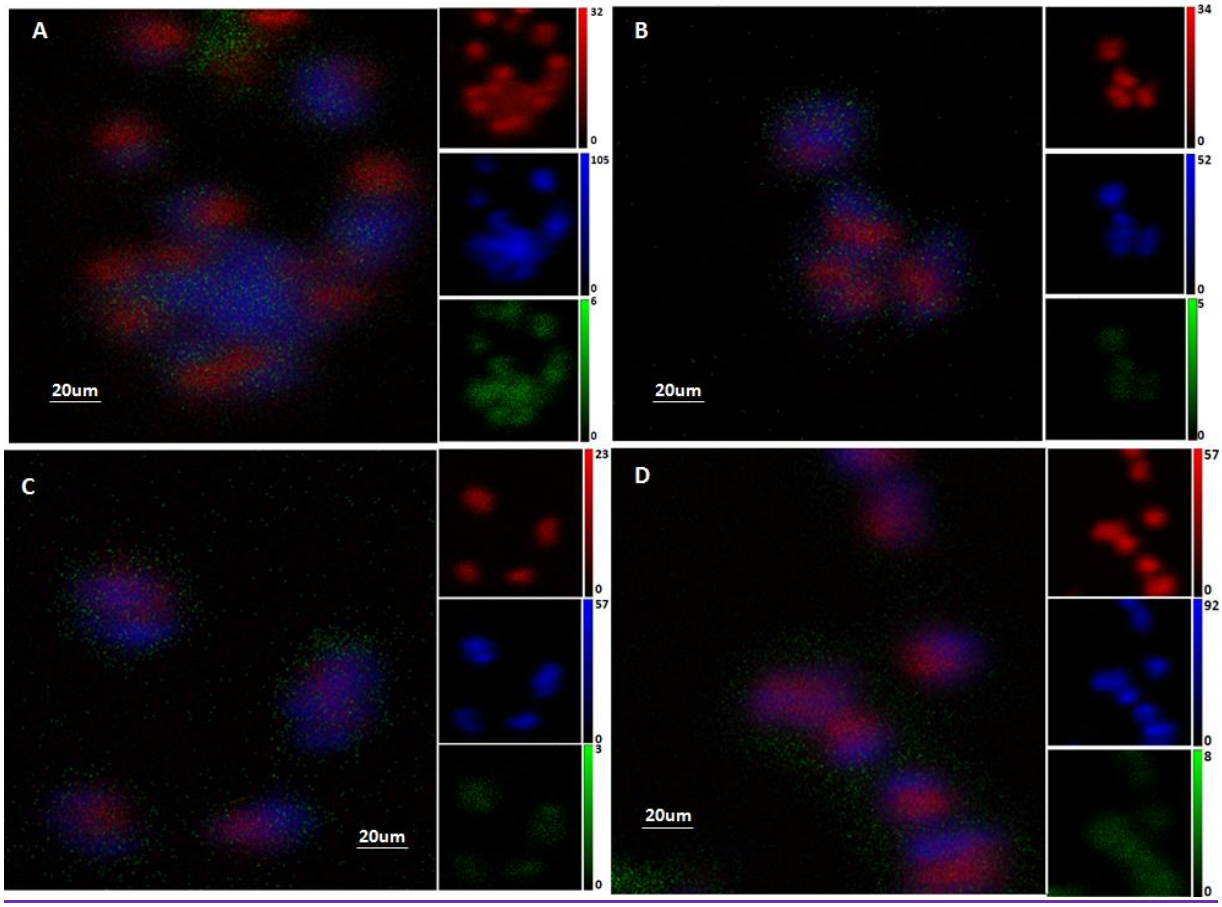


Figure 80: ToF-SIMS 2D composite image of secondary ions acquired using the lower spatial resolution mode used to collect the larger number of cell measurements. (A) NR8383 cells, (B) HeLa cells, (C) Hek 293 cells, (D) HepG2 cells, incubated for two hours with 6.25 µg amiodarone/mL. Composite image with all the three extracted signals. Red represents Ribose (*m/z* 81), blue shows the signal from the phosphatidylcholine lipid fragment (*m/z* 184), and green shows the amiodarone protonated molecular ion signal (*m/z* 646).

To generate sufficient individual cell measurements ($n > 50$) to compare with the average ensemble cell population measurements from LC-MS/MS, a low resolution imaging mode was used to increase throughput since the data acquisition was faster. Therefore, the data generated has been acquired in two different modes, a high spatial resolution mode with lower throughput but higher image quality (Figures 76, 77, 78 and 79) and a low spatial resolution mode, which provided higher throughput but with lower spatial resolution (Figure 80). The spatial resolution of the later method was still sufficienct to discern the cellular contour to define a cell; Figure 76, 77, 78 and 79 are analogues of Figure 80 using different

spatial resolution modes. In instances when the cells could not be resolved, they were not included in the data set. This occurred for approximately 10% of the cells analysed for all cell types.

This data indicates that ToF-SIMS can be used to detect intracellular compound independently of the cell line used.

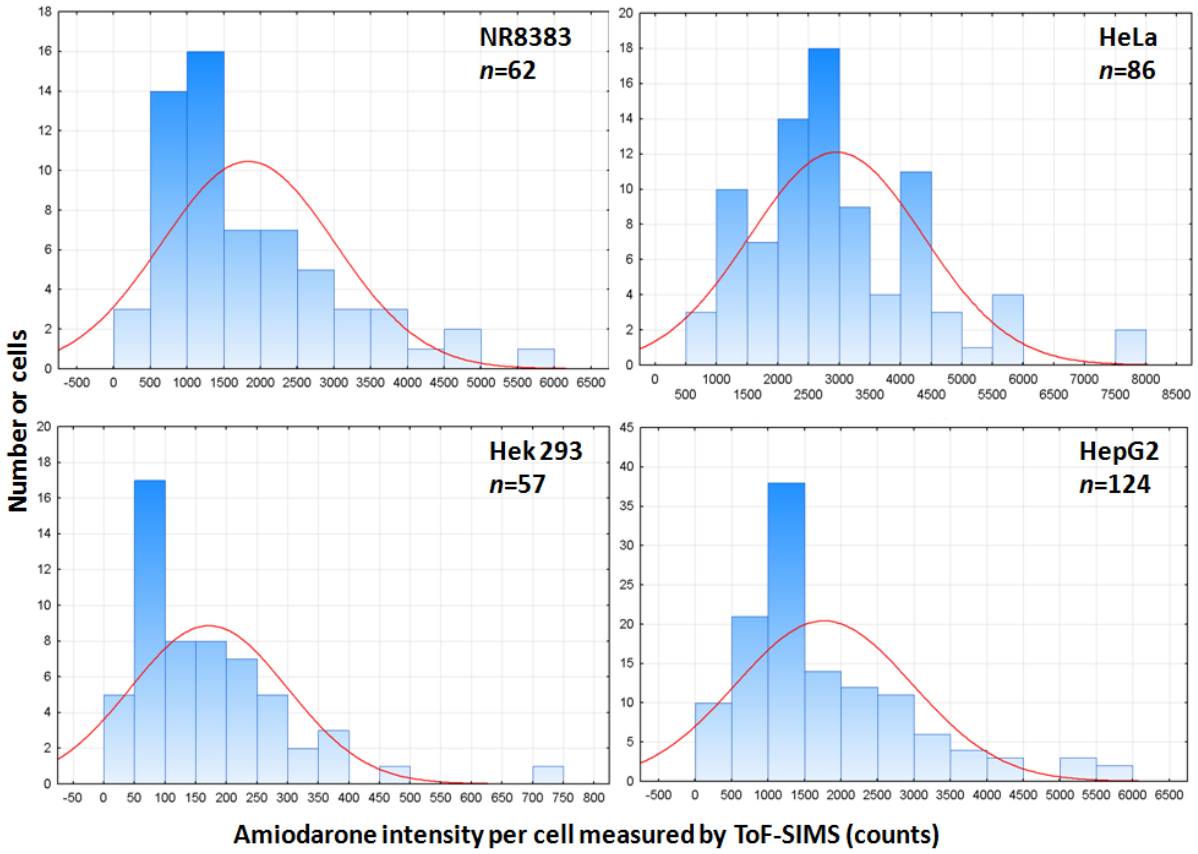


Figure 81: Frequency histogram of total amiodarone signal intensity (counts) per cell measured by ToF-SIMS for each of the four cell types, NR8383, HeLa, Hek293 and HepG2. The fitted normal distributions are displayed as a solid red curve.

In Figure 81 a total of 329 individual cell ToF-SIMS measurements acquired are shown (NR8383 n = 62; HeLa n = 86; Hek 293 n = 57; HepG2 n = 124). Analysis of the frequency histograms of the amiodarone signal intensities in Figure 81 reveals an asymmetric distribution for NR8383, HepG2 and Hek293 cells and a distribution closer to a normal distribution for HeLa cells.

Despite the two-hour time-point used for this study, there was still some variability in the compound incorporation both within the different cell lines and within the same cell population. This variability was not expected, as it can be observed in Figure 81 the majority of the cells for the HepG2, Hek293 and NR8383 cell lines had incorporated a relatively low amount of amiodarone, however, the distribution of incorporation was variable and if an average value was reported that would not be representative of the variability observed in Figure 81.

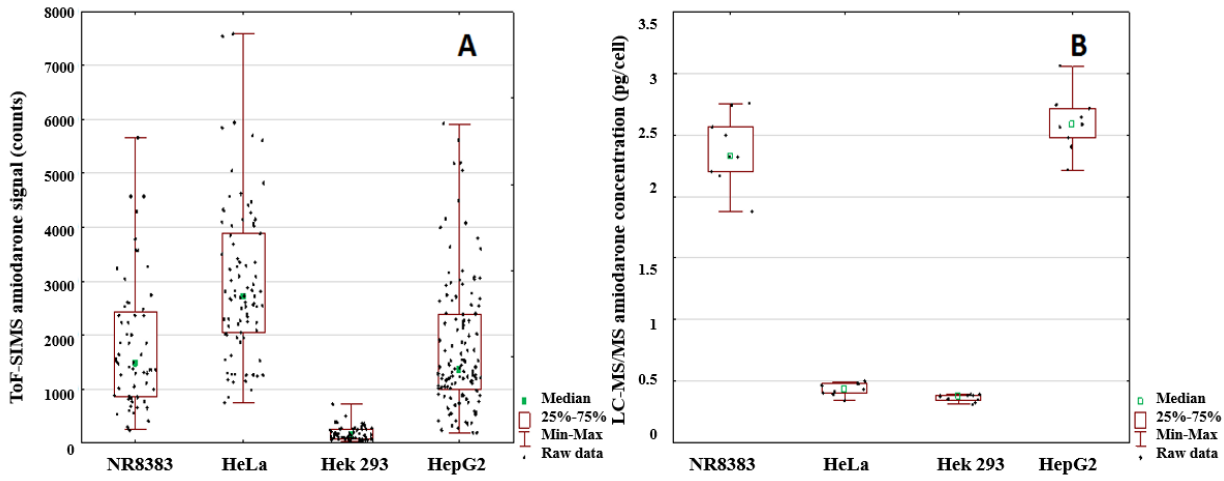


Figure 82: (A) box plot showing single cell population measurements for each cell type using the ToF-SIMS integrated amiodarone protonated molecular ion counts for each cell NR8383 *n* = 62; HeLa *n* = 86; Hek 293 *n* = 57; HepG2 *n* = 124 (B) box plot showing cell population measurement using the LC-MS/MS assay, for each sample approximately 4.7×10^6 cells were used.

LC-MS/MS measurements were performed and in Figure 82 those are shown in parallel with the ToF-SIMS data. In Figure 82A, each data point represents a single cell measurement and reveals considerable cell-to-cell variation. The variability observed for the different cells is above 50% of the mean for all cell lines. The variation between individual cells be due to several reasons including that these cells were not synchronised, this was not undertaken as the effect of the inhibitors required to achieve synchronisation are unknown. Furthermore, having cells within the culture in different phases of the

cell cycle made the model more biologically relevant, as it is more representative of what occurs in vivo.

The LC-MS/MS data in Figure 82B shows that both HeLa and Hek 293 cells have a lower amiodarone uptake. These cells are known to express less of the common ABC (ATP-Binding Cassette) and SLC (solute carrier) transporters, and this might contribute to the lower amount of cell associated compound.[36] Detailed proteomics studies such as the one undertaken by Geiger, et al[193] could be used to provide details on the differences in transporters between the different cell lines, but this is beyond the scope of this thesis.

The higher drug uptake observed for the NR8383 cells can be explained by their biological function, as macrophages possess remarkable endocytosis capabilities[278]. Being an immune system cell they target microorganisms and other potential threats to the host. In this particular case the threat was the compound and as a phagocyte they tried to internalise the compound to minimise the damage the drug could cause to other cells, with the intent to metabolise it or contain it within.[36,278] Since they could not metabolise amiodarone the internal drug concentration increased. Amiodarone disrupted the lipid metabolism in macrophages causing them to become enlarged with lipid and compound laden vesicles. Most intracellular drug determination studies only report ratios of bound versus unbound compound,[189] so it is hard to draw a direct comparison between the intracellular drug concentration values obtained here and other studies. However, previous publications reported intracellular drug concentration of the same order of magnitude as those presented in Figure 83 measured by LC-MS/MS. Furthermore, the intracellular concentration also increased in the same order as the referenced study[189,279] which was around 10 to 50 times higher than the extracellular media concentration[280].

As one of the objectives of this study was to determine if there was any correlation between the single cell measurements by ToF-SIMS and the average cell population measurements quantified using LC-MS/MS, the data from these experiments was compared in Figure 83. It is evident that the HeLa cells do not fit this correlation with a far higher ToF SIMS signal, relative to the LC-MS/MS determined drug content, compared to the trend for the other three cell types. This could be due to a number of factors including, (1) difference in the intrinsic biological diversity in cells (2) some type of matrix

effect may be reducing the signal intensity, (3) the number of single cells (n >60) measured by ToF-SIMS may be insufficient to correctly represent the average of the population measured by LC-MS/MS.

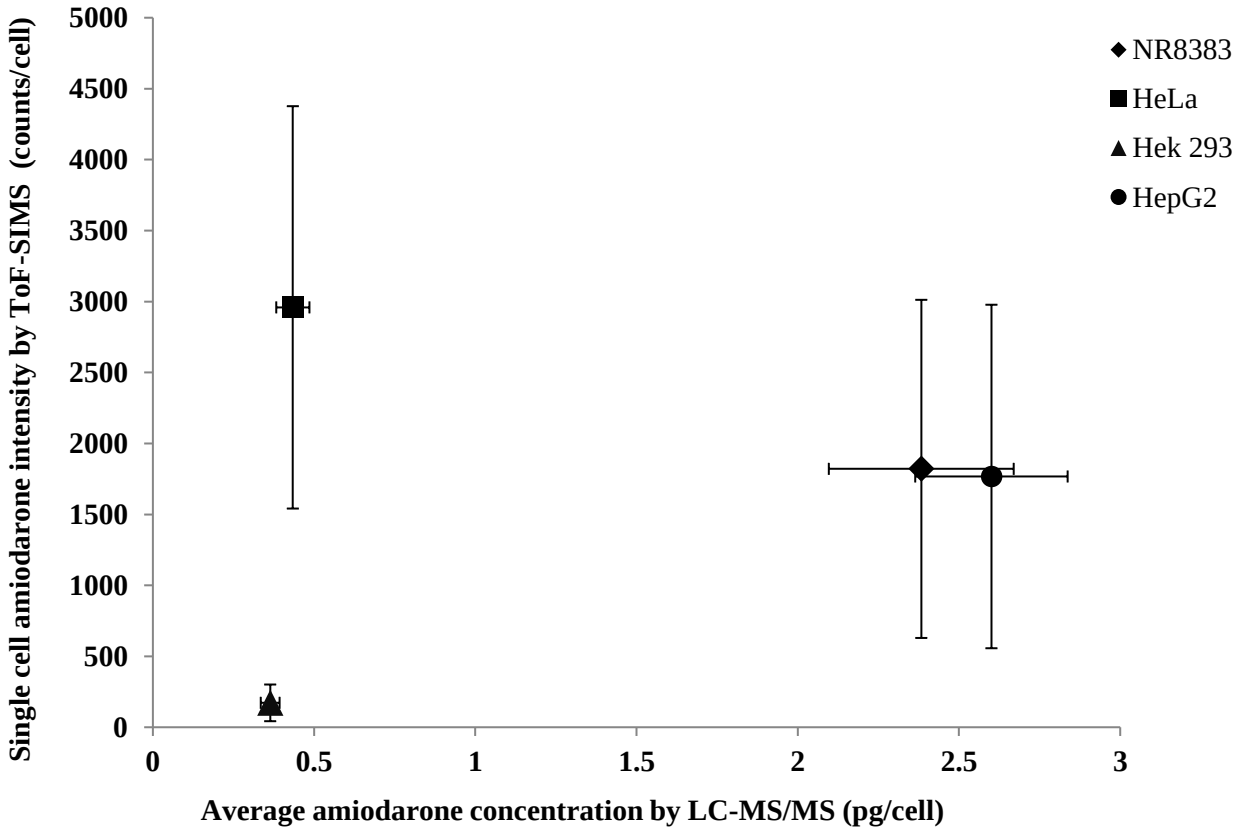


Figure 83: Comparison of the average cell associated amiodarone intensity determined by ToF-SIMS from a number of individual cells with the amiodarone cell uptake determined by LC-MS/MS from ensemble measurement of a large cell population (approximately 5000 cells per injection) for all cell lines incubated with 6.25 µg amiodarone/mL for two hours. The diamond represents the NR8383 cell line, the square represents HeLa cells, the circle represents HepG2, and the triangle represents Hek293 cells. The error bars represent one standard deviation from the average value. NR8383 n = 62; HeLa n = 86; Hek 293 n = 57; HepG2 n = 124

There is no definative explanation for why the HeLa data is inconsistent with the monotonic relationship between ToF-SIMS and LC-MS/MS for the other cells, and consequently it cannot be stated with confidence that there is an overall correlation between amiodarone uptake in individual cell ToF-SIMS measurements and ensemble population LC-MS/MS measurements. The significant variability

associated with the ToF-SIMS measurement is far greater than the reproducibility of the technique despite the relatively high number of cells analysed indicating significant cell-to-cell drug uptake differences.

Elsewhere,[281] we have demonstrate that the SIMS protonated amiodarone molecular ion intensity is approximately linearly proportional to the amiodarone incubation concentration for NR8383 cells. The phenomena observed for HeLa cells could be explained by the biological effect of amiodarone in HeLa cells at the concentration used for the study, which was relatively high and signs of cytotoxity were beginning to be observed, as demonstrated by the proteomics profiling data, shown in the previous chapter of this thesis, in which cell death related proteins were up-regulated at 6.25 µg/mL of amiodarone. This could be addressed in the future using SIMS to investigate changes in endogenous molecules in the biological system or using an orthogonal technique, such as electron microscopy, to investigate changes in lipid structures within HeLa cells with increasing levels of amiodarone.

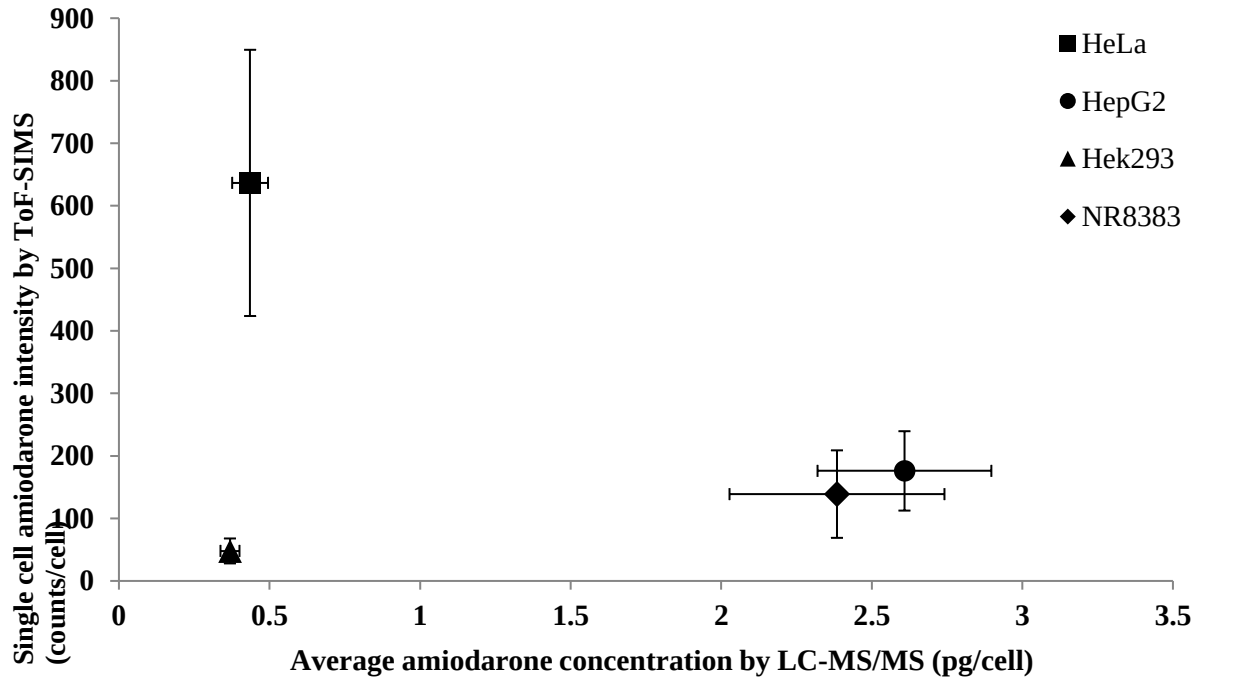


Figure 84: Amiodarone intensity determined by ToF-SIMS (mean plotted from individual cell measurements) versus the amiodarone cell uptake determine by LC-MS/MS population ensemble measurement from approximately $4.7x10^6$ cells for all cell lines after incubation with 6.25 µg/mL for two hours for the high resolution imaging mode used (this data directly relates to Figures 76, 77, 78 and 79) . The diamond represents the NR8383 cell line, the square represents HeLa cells, the circle

represents HepG2, and the triangle represents Hek293 cells. The error bars represent one standard deviation from the average value.

In Figure 84 the high spatial resolution data acquired for image 74 was plotted in relation to the LC-MS/MS data. This is in fact an analogue of Figure 83 but generated with the high spatial resolution ToF-SIMS data, which means the number of cells analyzed was much smaller, nine cells for the HepG2, eight cells for the NR8383 and the HeLa and seven cells for the Hek 293. Despite this, the results are consistent with Figure 83, still showing the HeLa cells as the outlier. The amiodarone count intensity, as expected, was approximately 10-fold lower in this mode than in the high mass resolution mode due to the lower beam current used.

In summary, four different cell lines were subjected to the same treatment with amiodarone for the same time and, as it can be observed, different cell types incorporate amiodarone at different rates. Furthermore, within the same cell population the levels of incorporation were variable. When comparing the amiodarone signal obtained by ToF-SIMS and the intracellular amiodarone concentration measured by LC-MS/MS the two values do not show correlation for the HeLa cells while showing much greater ToF-SIMS signal when compared with the concentration determined by LC-MS/MS. This could potentially be explained by the difference in biological activity between the different cell line, the simplicity of HeLa cells in terms of transporters perhaps decreased the ion suppression in ToF-SIMS or simply not enough cells were analyzed to arrive to an accurate value.

6. Results III: Exploring applicability of ToF-SIMS to detection of a wider range pharmaceutical compounds

In this chapter, it was attempted to determine which test substrate best correlates with the compound signal after the pharmaceutical was up taken by mammalian cells, so the preliminary feasibility study is a good indicator of the propensity for ionisation of a given compound. For this, in addition to the cells incubated with compound, four other samples were prepared: compound solubilised in 50:50 methanol: water (Neat), that solution spotted on a liver tissue section (tissue), same preparation as the Vorng et al. publication (JLV) and on a cell lysate (CL). A library of twenty pharmaceutical compounds curated to be representative of a broad class of pharmaceutical molecules were analysed by ToF SIMS in order to assess its sensitivity in five different matrices.

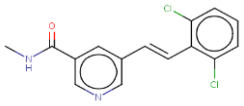
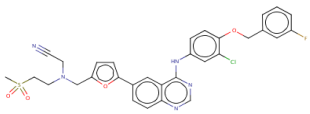
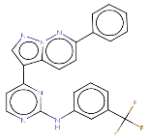
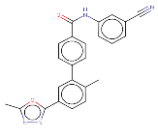
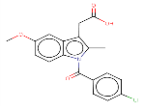
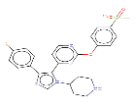
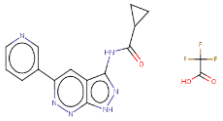
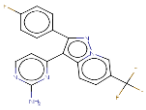
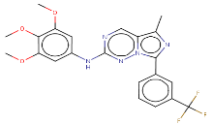
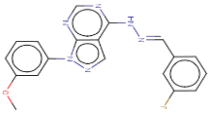
The objective of this work was to better understand if there is a link between ToF-SIMS ionization and any of the physical-chemical properties often measured and calculated as part of the drug discovery process. Furthermore, by looking at five different matrices, a better understanding can potentially be drawn of which medium better correlates with the intracellular ToF-SIMS signal for the compound, so this information can be used with confidence during the feasibility study that occurs prior to the study itself.

The mechanism of secondary ion ionisation in ToF-SIMS is still not very well understood despite some efforts from Vorng et al., in this study they have found that LogP was a good predictor of ToF-SIMS ionisation efficiency in pharmaceutical molecules[153]. The results at the beginning of chapter 4, in which amiodarone, chloroquine and a GSK compound were incubated in cells and analysed using ToF-SIMS, demonstrated that only amiodarone was observable intracellularly using this technique. This is in accordance with Vorng's publication, which indicated a better ion yield for amiodarone than chloroquine. Given that amiodarone's LogP is 7.64 and chloroquine's LogP is 3.93 it is in accordance with the observation that ionization efficiency was correlated with the increase of LogP of a pharmaceutical compound. Despite the valuable information provided to the SIMS community Vorng's

publication has a caveat, it is not known if the liver paste used as a biological background for the compounds is the best test matrix to mimic mammalian cells and tissues. No doubt cells are rich in lipids, but they are also rich in proteins, salts, and multitude of other endogenous metabolites. For this reason, in this chapter, the results obtained for a set of twenty GSK compounds analysed in five different background matrices using ToF-SIMS is discussed.

The twenty compounds (seen in Table 5) were analysed using ToF-SIMS using five different sample preparation methods in triplicate as described in section 3.13. The matrices studied were: neat compound, spotted on tissue, lipid paste (Vorng et al. method), cell lysate and incubated in HepG2 cells. As it can be observed in Table 5, the compound molecular ion could be found for all the compounds in their neat form and the compound could be identified intracellularly in thirteen out of twenty compounds, despite the relatively small number of compounds studied this shows that ToF-SIMS has a 65% success rate of identifying drug molecules intracellularly.

When looking at the biological matrices in which compounds can be tested prior to the cell assay (where cells are incubated with compound): tissue, liver paste and cell lysate, it becomes clear by looking at Table 5 that some compounds would not have progressed to the cell assay stage if these matrices had been used for the compound feasibility study, three compounds in tissue, four in the liver paste method and one in cell lysate. This obviously poses questions regarding the surrogate matrices, indicating that perhaps they are not the most adequate format for testing compounds for ToF-SIMs ionization prior to the actual cell incubation experiment.

GSK compounds	Image identifier	Structure	Neat	Tissue	lipid paste (JLV)	Cell lysate	Incubated cells
GW445014X	14		Yes	Yes	No	Yes	No
GW616030X	30		Yes	Yes	No	Yes	Yes
GW819077X	77		Yes	Yes	Yes	Yes	Yes
GW607117X	117		Yes	Yes	Yes	Yes	Yes
CCI120	120		Yes	No	No	Yes	No
SB-254169	169		Yes	No	No	Yes	No
SB-675259M	259		Yes	No	No	Yes	Yes
GW568326X	326		Yes	Yes	Yes	Yes	Yes
GW837331X	331		Yes	Yes	Yes	Yes	Yes
GW817394X	394		Yes	Yes	Yes	Yes	Yes

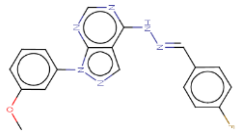
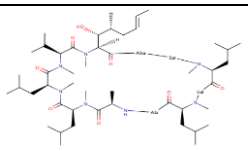
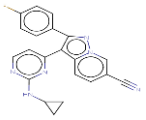
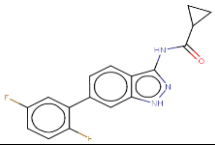
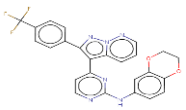
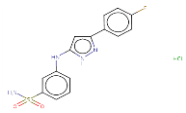
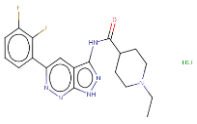
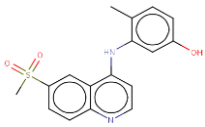
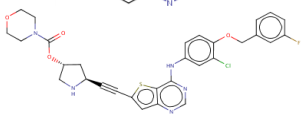
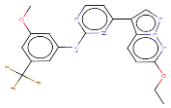
GSK compounds	Image identifier	Structure	Neat	Tissue	lipid paste (JLV)	Cell lysate	Incubated cells
GW817396X	396		Yes	Yes	Yes	Yes	Yes
GR92424X	424		Yes	Yes	Yes	Yes	Yes
GW561436X	436		Yes	No	No	Yes	Yes
SB-735465	465		Yes	Yes	No	Yes	No
GW828525X	525		Yes	Yes	Yes	Yes	Yes
GW824645A	645		Yes	No	No	Yes	No
SB-686709A	709		Yes	No	No	Yes	No
GW559768X	768		Yes	No	No	No	No
GW869810X	810		Yes	No	No	No	Yes
GW807982X	982		Yes	Yes	Yes	Yes	Yes

Table 5: Summary table of the compound GSK number, image identifier (usually the last three digits of the whole number), the structure of the compound and in which matrix it was identified. In red are the compounds whose signal was not visible and in green are the compounds whose molecular ion was identified.

In order to be able to look at this data in greater detail, rather than just in a binary way the data had to be processed. The signal reported relates solely to the molecular ion of each compound and for all instances, with the exception of the cell incubated samples, the total compound signal in the analysed field of view signal is reported and normalised to the number of pixel in that field of view. The criteria for this decision was 2-fold: 1) fragments of the compound might not have sufficient mass resolution to perform the assignment with confidence: 2) most of the compound masses fell in a relatively quiet region of the spectra, therefore there were fewer peaks around and the identification could be performed with more confidence. It is worth noting that for all the five matrices a no-compound control was performed to increase the confidence that the ions seen were compound related, and were absent from the control.

For the compound incubated cells in order to calculate the integrated compound intensity for the cell incubated samples the perimeter of the cell was defined by manually defining a region of interest on the acquired image. In instances where the cells could not be resolved they were not included in the data analysis, furthermore, the defined cells signal was also normalized to the number of pixels.

A logarithm transformation was then applied to the data set so changes within the data set were more perceptible. In additon to this, two other statistical analysis methods were used, PCA and pairwise correlation plots.

The plot in Figure 85 shows the triplicate measurements for each of the individual sample preparation methods. There were several measurements where signal was not obtained, for example, compound GW559768X was only detectable in neat compound conditions.

The signal for neat compound could be seen in blue, and as it can be observed it has consistently the highest intensity values, as no biological matrix is present to cause ion suppression.

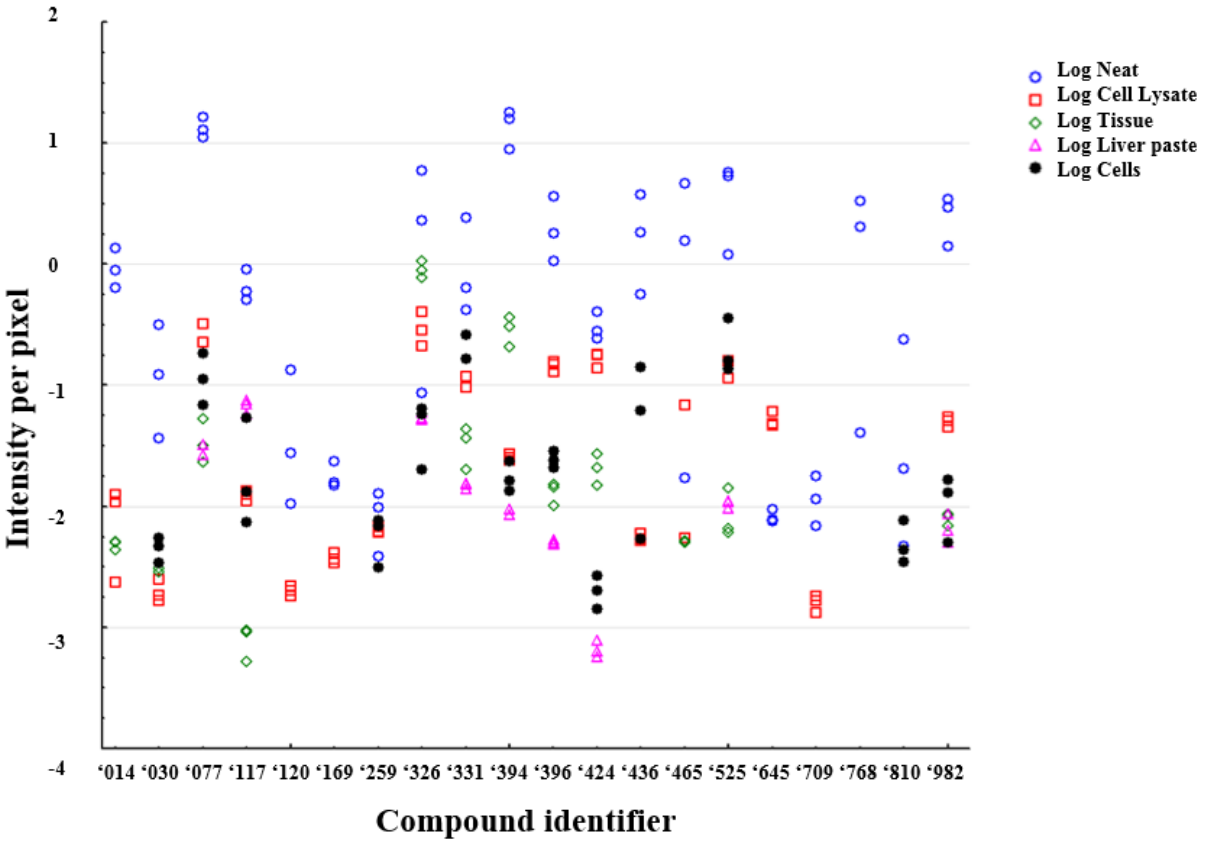


Figure 85: Scatterplot of the multiple variables and replicates. The blue circle represents the neat compound, the red square represents the cell lysate mixture, the green diamond represents the compound spotted on tissue, the pink triangle represents the liver paste method and the black filled circle represents the compound incubated cells. The GSK compounds are identified by the last three digits of their designation.

For the other sample presentation matrices, the intensity is much lower, in these conditions, the complexity associated to the biological matrices suppresses compound ionisation. However, the three replicates performed are quite consistent as it can be observed in Figure 85.

As one of the objectives of the experiment was to determine which methods best correlated with the signal from compound incubated with cells, the focus was on the compounds for which signal was observed in the cells, which were: GW616030X, GW819077X, GW607117X, SB-675259M, GW568326X, GW837331X, GW817394X, GW817396X, GR92424X, GW561436X, GW828525X, GW869810X and GW807982X.

The compounds that appeared to be more consistent across the three replicates and the different sample preparation conditions were GW819077X and SB-675259M. In all instances, the neat compounds had better ToF-SIMS signal than any of the other conditions except for GW824645A, in which the compound signal obtained when mixed with the cell lysate was greater that the compound signal for the neat compound. It can be hypothesised that for this compound something in the cell lysate buffer was enhancing the ionization. This phenomenon has been demonstrated for lipid species[282] whose ionization efficiency increases when comparing the signal of the lipid in the pure form and in a more complex matrix.

The data was then averaged and each of the conditions was compared against each other in a matrix of pairwise plots (Figure 86); this data plotting technique quickly identified which conditions showed better correlations. The data suggests that potentially the best correlation between the different compound conditions and the compound incubated cells is obtained with neat compound. Nevertheless, all pair wise plots were examined and each pair wise plot was fitted with a simple linear regression trend line so an r^2 could be calculated.

It was essential to determine how well the model could be fitted to the dataset as it provided a relation between the trend line and each of the points fitted to the trend line. Furthermore, the p-value or probability value was also calculated, this value indicates the significance of the results, p-values of 0.05 or below indicate that the probability of a result being random is very low, and therefore p-values below 0.05 are desirable.

The matrix plots in Figure 86 compare each matrix conditions against each other in order to identify if there is any correlation between the compound signal in the compound testing matrices and the compound incubated cells.

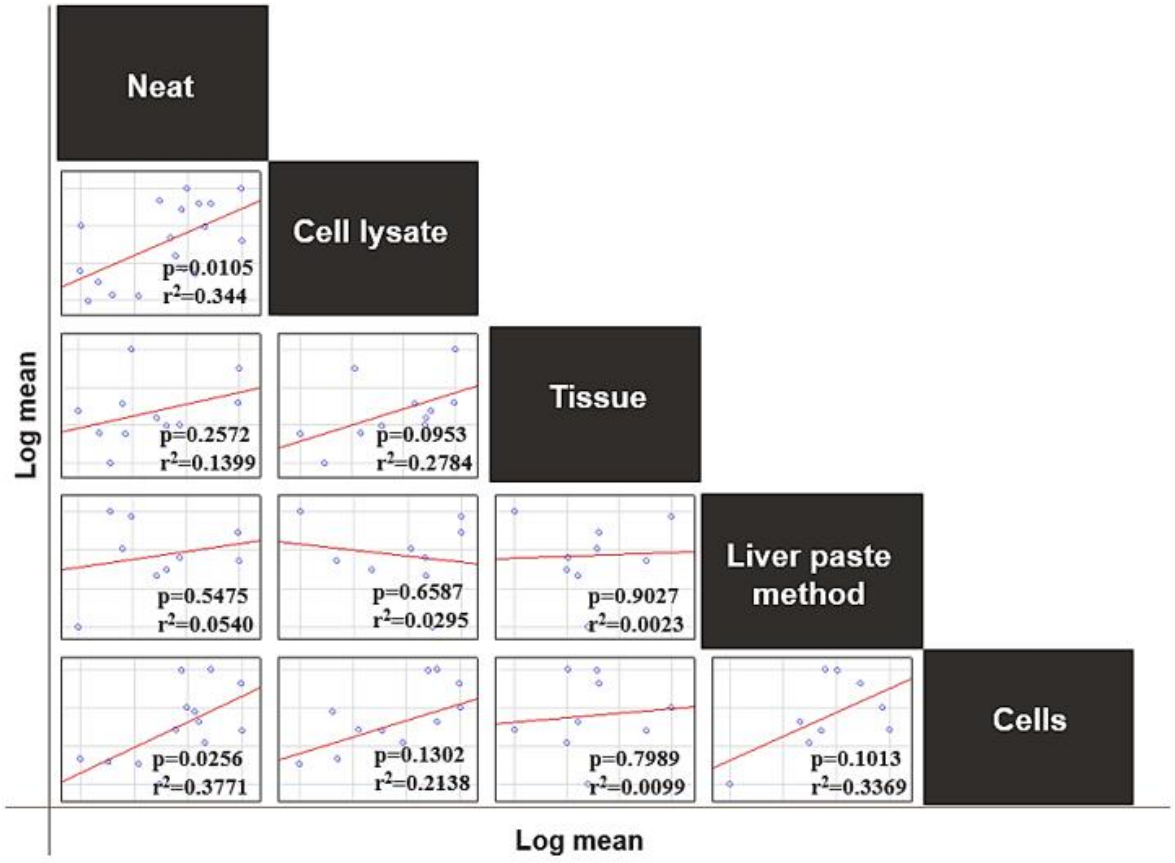


Figure 86: Pairwise matrix plot comparing the five study conditions: neat, cell lysate, tissue, liver paste method and cell incubation. Each condition is compared with each other to produce a matrix of plots showing that the highest correlation with cells is achieved by the neat application of the compounds.

The data in Figure 86 suggest that there is no real correlation between the matrices and the compound incubated cells, and although a correlation would be desirable to better predict the ionization of compound intracellularly, it is not crucial, as what was required was a feasibility method that does not preclude a compound proceeding to the cellular assay, and for this reason the neat condition was the best to use, as it did not discard compounds from being progressed to the cellular assay stage, while the other matrices would have done.

The best r^2 value was observed when the neat compound was plotted against the compound incubated cells, as seen in Figure 87. The plot in Figure 87 depicts the log mean of the three replicates analysed for both neat compound and cells incubated with compound, not all compounds that were detected in

the neat compound analysis were detected in cells incubated with compounds, and therefore there were some zero values associated with this data.

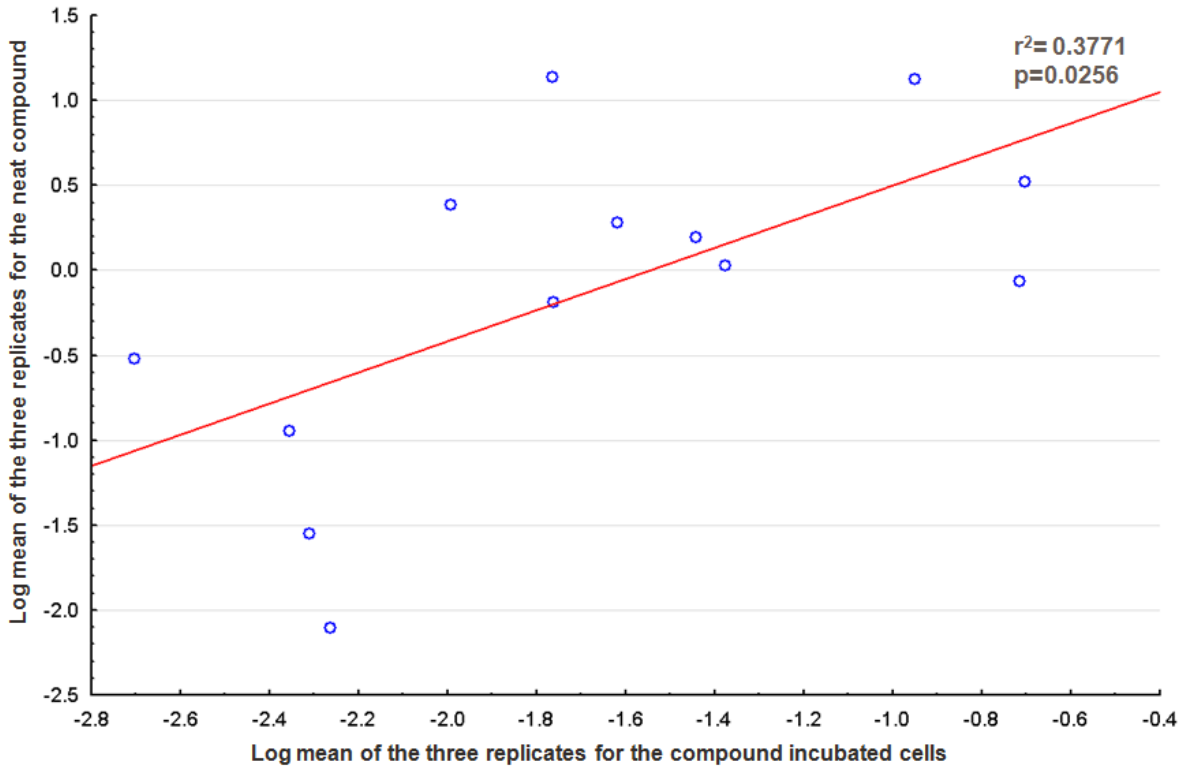


Figure 87: Pairwise plot of the correlation between the signal for each of the tested neat compounds and the compound signal in compound incubated cells. The r^2 value and the p-value calculated from that correlation are 0.377 and 0.0256 respectively.

As it can be observed in Figure 87, the correlation between any of the drug intensities is very weak, this is perhaps due to the variance in the data set in all matrices studied, despite the apparent negative results, it is noteworthy that there was not a clear background matrix that correlated to the signal of the compound when it was incubated in cells. In fact, it can be argued that the best r^2 value observed was between the cells incubated with compound and the neat compound, and the low p-value for these conditions indicates that the likelihood of the correlation being random is relatively low, as the p-value tests for consistency between the data and the null hypothesis.[283] The poor correlation observed can potentially be attributed to the variability of the data generated, unfortunately only three replicates were

performed per condition, perhaps if more replicates were to be performed the data would become tighter and the r^2 would improve.

This data showed that it was acceptable to use the compound alone in a feasibility study, as no better results were observed for any of the other matrices tested; this saves time, effort and materials when it comes to the overall experimental design. The compound ionization assessment neat and in cells is useful information, however, the truly valuable information would be if one could predict if a compound would be amenable to SIMS ionisation. This ionisation process is very low yield and poorly understood[58]. Nevertheless there are some ongoing efforts to overcome this challenge with instrumentation developments.[284]

Using the acquired data, the potential correlation between a pharmaceutical's physical-chemical properties and its ToF-SIMS ionisation ability was explored. The physical-chemical properties of a molecule are a well discussed topic within the pharmaceutical industry, as certain characteristics in physical-chemical properties carry the hallmarks of a good drug.[50]

Figure 88 depicts the score plot of the Principal Component Analysis (PCA) performed on a wide range of physical-chemical properties associated with the compounds studied in this chapter. The physical-chemical properties applied in this analysis were, Melting point, Chromatographic Hydrophobic Index[134] (CHI), Properties Forecast Index[30] (PFI), Partition coefficient[135] logP, Chromatographically determined partition coefficient[136] (ChromLogD), Acid dissociation constant[137] pKa, Distribution coefficient[138] (LogD), ChemiLuminescence Nitrogen Detector solubility[139](CLND), Human Serum Albumin binding[140] (HSA), Retention factor (LogK) which is the partition coefficient of a compound between the mobile and the stationary phase[141], CellConc, the measurement of intracellular compound using LC-MS/MS in HeLa cells[142], molecular weight and pH. Each of these properties has a value associated to it that has been either calculated or empirically determined, in order to assess the diversity of the twenty compound set PCA analysis was performed.

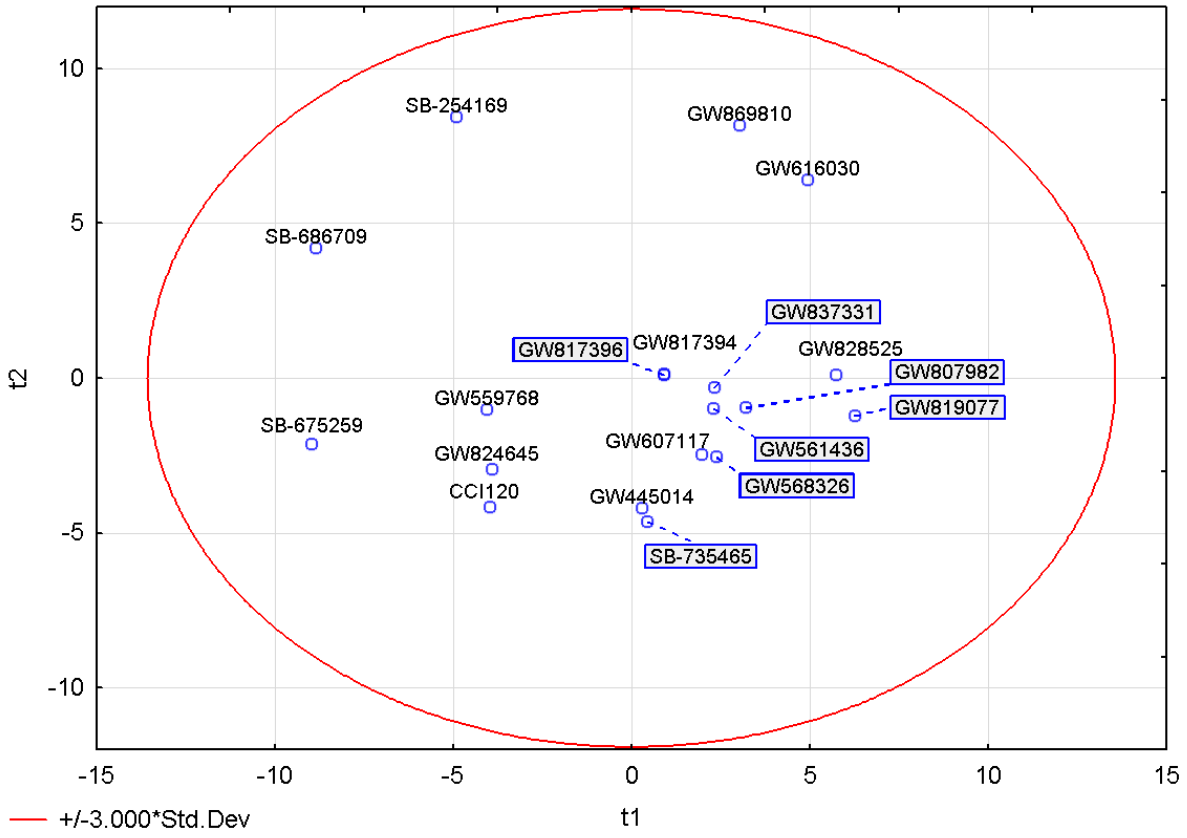


Figure 88: PCA on the physical-chemical properties of the compounds. This analysis visualises how different the compounds are to each other despite them obeying the physical-chemical properties rules commonly used in drug discovery.

All these molecules are drug molecules, so they fall in the same region of the chemical space. However, there are some compounds that present differences, in Figure 88, compounds located closer together tend to be similar to each other than compounds that are located further apart on the plot.

The values of all the different physical-chemical porperties mentioned above where used to perform statistical analysis, to evaluate if a correlation could be found between any of the physcical-chemical properties and the ToF-SIMS ionisation signal. To assess this correlation, scatter plots were gerenated for each of the properties and the compound signal intensity in cells, as the plot generated for this data matrix is very complex and it would not be intelligible on paper, this data is not show. Only the parwise plot with the best p-value and r^2 value from the full matrix pairwise plots is shown in Figure 89, however, matrix plots were generated for each of the physical-chemical properties evaluated. Despite the poor r^2

, logD was the parameters that shows the best correlation and given the low p-value, this correlation is statistically significant.

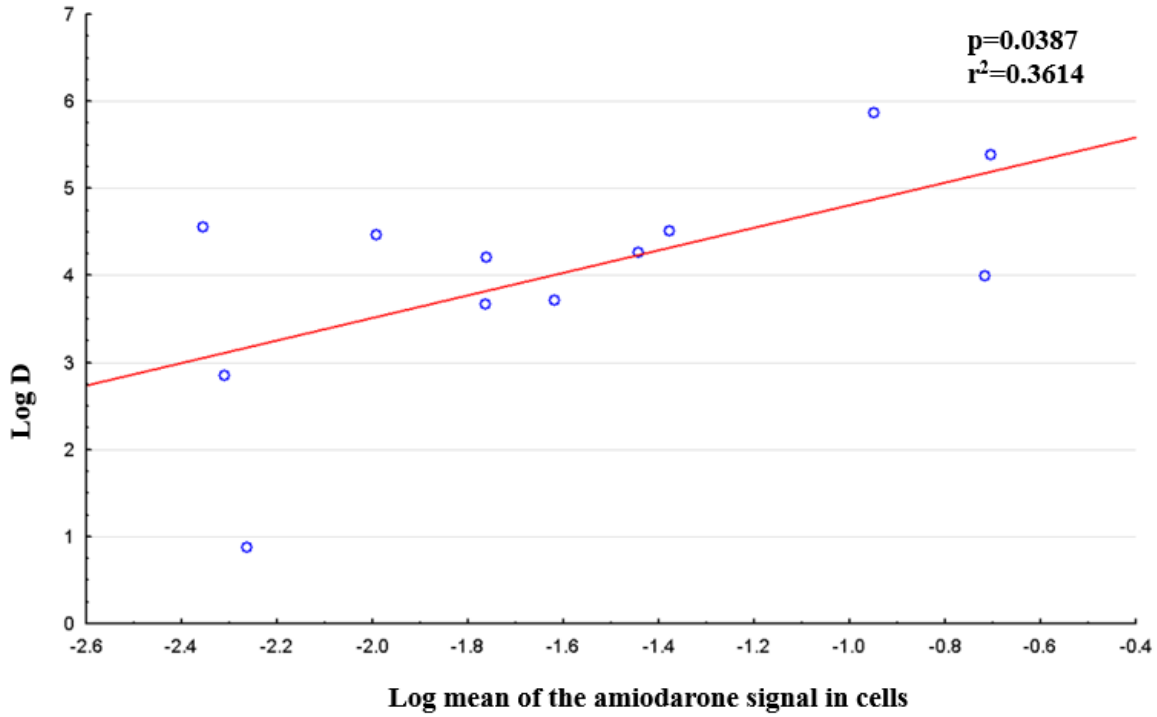


Figure 89: Scatter plot presenting the relationship between LogD and compound signal in the cell. The p value is 0.387, and the r^2 value is 0.3614.

Figure 89 shows the correlation of the distribution constant LogD with the compound SIMS signal in the cell, which was found to be the physical-chemical property that had better r^2 and p-values when correlated with the compound SIMS signal. LogD together with the partition coefficient (LogP) is a measurement of lipophilicity. The partition coefficient (LogP) is defined as a measure of a compound's differential solubility when in two immiscible solvents, those solvents are normally octan-1-ol and water, and it represents the lipophilicity of neutral compounds.[285] Most drug molecules are weak acids or bases, which means that they possess at least one site in which a hydrogen atom can associate or dissociate to form a negatively charged anion or positively charged cation. LogD takes into consideration both neutral and charged forms of the molecule and is thus a better indicator of a good pharmaceutical drug molecules. In a cell, the consensus is that the pH is neutral (between 7.0 and 7.4)[286], several different studies applied different techniques that provided some insight on the matter. Some

studied the use of fluorophores[287] to address that question; others used complementary techniques such as confocal microscopy and electron microscopy.[288] Furthermore, some studies even revealed that pH dysregulation could be responsible for cancer proliferation.[289] However, some organelles have distinct pH windows, such as mitochondria with a pH of around 8 and the secretory and endocytic organelles in which the pH varies from 4.7 to 6.7.[286] This pH variations within the cell, combined with the fact that most drug molecules are weak acids or bases, indicate that perhaps logD rather than logP could provide a better correlation when looking at compound inside cells using ToF-SIMS. Despite this, traditionally LogP is more widely used due to the ease of calculating this property from the greater number of software packages that provide calculation algorithms for this property. For example, it is commonly known that pharmaceutical drug molecules have a LogP between 0 and 5.5, which means that they are lipophilic and therefore more likely to penetrate the cell membrane[290].

In summary, despite not being able to find a true correlation between the feasibly testing matrices and the signal of compound in dosed cells, it is safe to say that the neat compound testing is the preferred method of testing compound ionization, as it did not prevent any of the studied compound from progressing to the cell assay, while if the compounds had only been tested in tissue, cell lysate and liver paste, they would have been precluded from the cell assay, despite having been identified in dosed cells as shown. Furthermore, this method does not require, tissue, cells or liver past, hence it is cheaper and less time consuming.

In regards to the usage of a physical-chemical property to predict SIMS ionization, yet again, no real correlation was found, despite this, LogD was shown to have the best r^2 and p-value, this is in accordance with the literature,[153], as LogD is effectively LogP but taking in consideration the neutrality of the cellular pH.

7. Results IV: *Mycobacterium tuberculosis* study using *mycobacterium bovis (*Bacillus Calmette-Guerin, BCG) as a TB model

In previous chapters of this thesis it was shown that ToF-SIMS is a useful tool to detect pharmaceuticals inside mammalian cells, and thefore, here, the potential application of ToF-SIMS to visualize a pharmaceutical drug inside bacteria is explored. For this, a collaboration with the Disease of the Developing World (DDW) TB group at GSK was established.

According to WHO, Tuberculosis is one of the top 10 causes of death worldwide; they estimate that just under half a million people developed drug-resistant TB and in order to fill the resource gap in the TB field 2.3 billion dollars need to be spent a year on researching new ways of tackling the disease. For these reasons treating TB is extremely important for pharmaceutical companies. In 2011 GSK opened a site in Madrid, Spain, that concentrates on drug development for diseases of the developing world and most of the TB research is focused at this GSK site. Scientists at the Tres Cantos site have developed several different drugs that are traditionally tested using in-vitro cell death assays. In these assays bacterial growth is assessed in a mono baterial culture or as a co-culture with mammalian cells; the success of a drug is often measured by it bacterial killing efficiency. The current standard test used to assess antimicrobial performance determines how well a drug molecule eradicates the bacteria in Mueller-Hinton Broth. Despite this being a crude surrogate for the infection in humans this type of measurement provides the scientists with vital information about the efficacy of the compound.

There are a variety of antibiotics on the market, and their applicability to TB has been discussed in the introduction at length, however, with the rise of multi-resistant TB stains we can also appreciate the need to develop new antibiotics that either explore the flaws in the bacteria's biology or the biological differences between the bacteria and the host. When microbiologists and chemists seek to develop a new antimicrobial they constantly strive to develop a profound knowledge of the target and the

mechanism of action of the drug molecule. Nevertheless, drugs still fail due to a variety of reasons, including lack of microorganism permeability and/or mammalian host cell permeability.

Traditionally, bacterial homogenates were prepared after drug dosing and the compound concentration is measured by LC-MS/MS. However, as for mammalian cells, this type of bulk measurement does not account for extracellular binding, as the drug can potentially bind to the extracellular membrane causing no effect on the bacteria but producing a high compound concentration in the assay. ToF-SIMS can potentially provide the answer to this question, despite the size of the bacteria, by determining if the compound is localised intracellularly.

As a level 3 containment microorganism, *Mycobacterium tuberculosis* cannot be used in the lab category in which the NPL ToF-SIMS is located, therefore, *Mycobacterium bovis* the Calmette-Guerin strain (BCG) was used as a model in this study as it is classified as requiring containment level 2 in the UK. The National Physical Laboratory facility in which these samples were analysed, does not have category 2 containment level, however as the bacteria was freeze-dried, all the water content was removed from the cells, and this renders the bacteria inactive, allowing these samples to be analysed in a category 1 environment.

Initially, it was essential to replicate the growth of the microorganism both mono and in co-culture with macrophage like cells (immortalized macrophages cell line). For this, Green Fluorescent Protein (GFP)-BCG was grown and co-incubated with NR8383 cells to show the incorporation of BCG in macrophages. This was performed by culturing the macrophages as normal and once the cell confluence is between 60 to 70% a GFP BCG is added to the mammalian cell culture media so the ratio between mammalian cells and bacteria is 1:100. The addition of the Cell tracker dye and Hoechst allows the visualization of the mammalian cell, the bacteria were genetically modified to express green fluorescent protein, the image of a co-culture of these two organism can be seen in Figure 90. GFP BCG can be observed in green (B), the nuclear dye staining the nucleus in blue (C) and the cell outline can be visualised by the red dye (D), which was cell tracker. In (A) the bright field image can be seen and in (E) the composite image showing the bacteria in green inside macrophages.

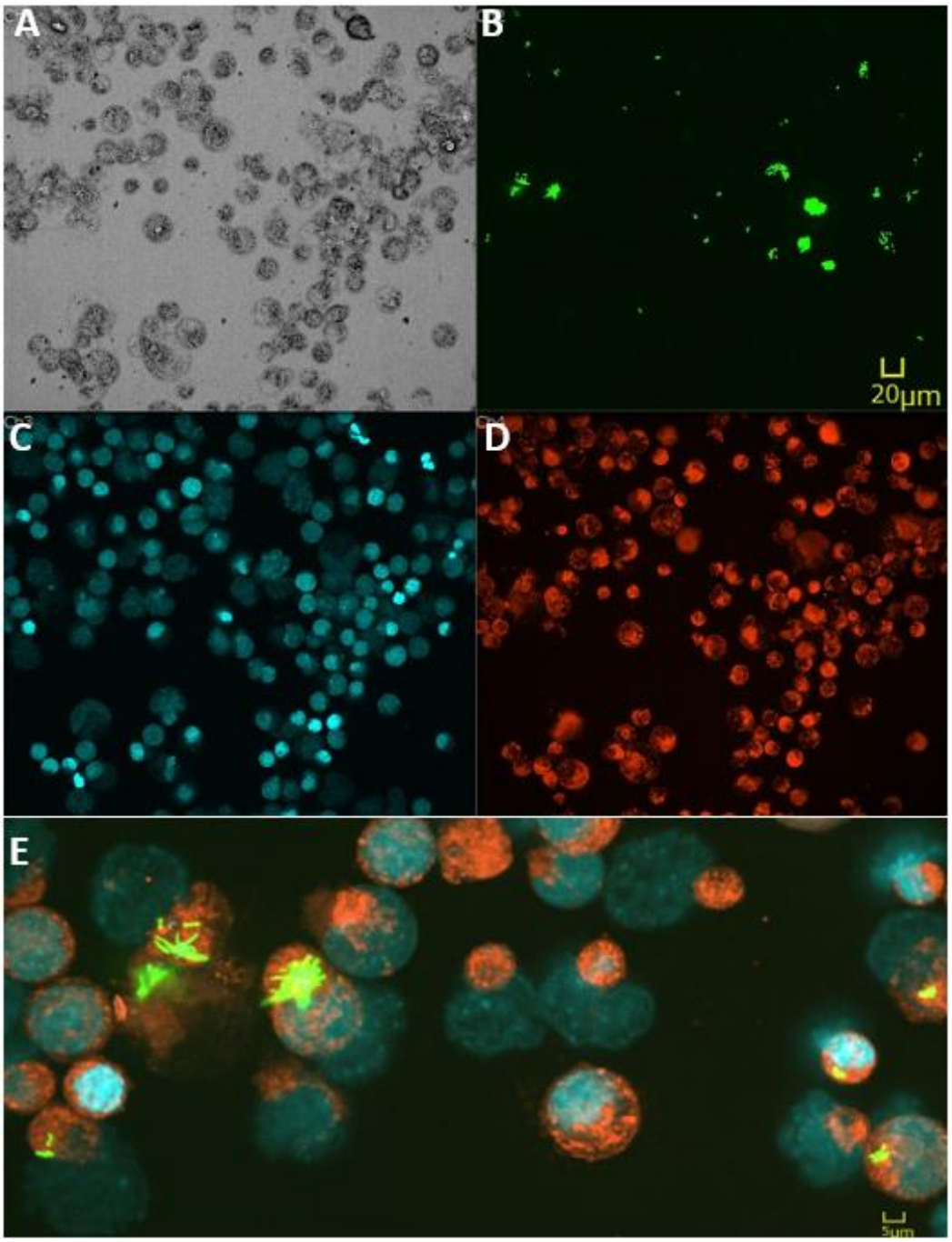


Figure 90: Optical confocal fluorescence microscopy of NR8383 cells co-cultivated with Green Fluorescent Protein (GFP) BCG for 48 hours. (A) bright field image, (B) 561 nm channel GFP BCG, (C) 488 nm channel, Hoechst nuclear stain, (D) 640 nm channel, cell tracker red, and (E) composite image of the three fluorescence channels.

These data indicated that the 1:100 ratio used of bacteria to macrophages provided suitable co-culturing conditions. As it can be observed not all the macrophages are able to incorporate the bacteria, which

means that even within the same cell population there are phenotypical differences between the cells. This point was previously studied in chapter 4, in which it was shown that there were differences in compound incorporation within the same cell population.

The experiment was conducted using both the empty vector (EV) or non-genetically modified and genetically modified to overexpress DpRE1 bacteria. These were incubated with GSK compound at 1, 10 and 50 times the minimum inhibitory concentration (MIC), 3 uM, 30 uM and 150 uM for GSK3338058A and 5 uM, 50 uM and 250 uM for GSK2620592A for 48 hours.

Theoretically, the over-expressing DpRE1 mutant should have an increased accumulation of the compound in the cells, as the compound is designed to bind to the target and the mutant bacteria expresses more of the target. Therefore, the first experiments were conducted using the DpRE1 over-expressing bacteria to maximize the chance of visualizing the compound in bacteria.

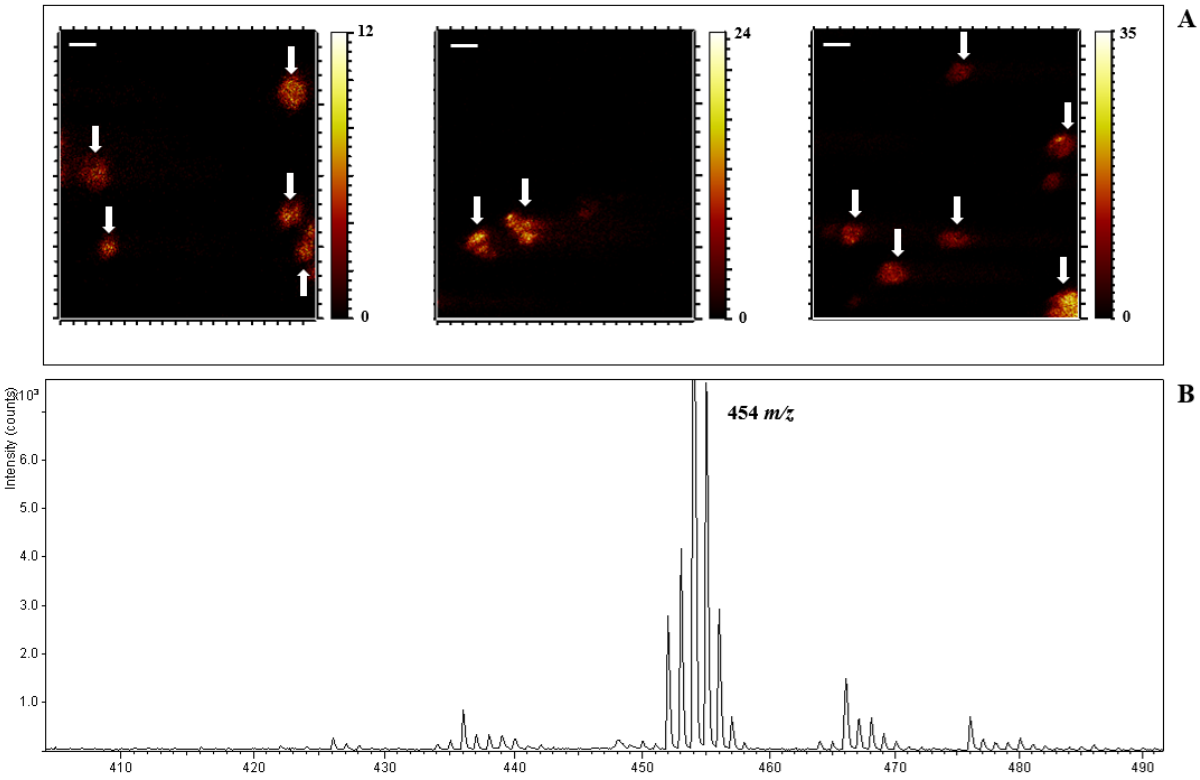


Figure 91: Micro-colonies of the tuberculosis model, *Mycobacterium bovis BCG*, overexpressing DprE1 incubated for two days with GSK3338058A at 10x the MIC (30 µM) grown as a mono-culture. (A)The location of BCG micro-colonies are depicted by the white arrows. The image shows three technical replicates (different areas from the same sample), the scale bar is 5 µm (FoV 40x40 µm). (B) Region of the spectrum showing the $[M+H]^+$ of the compound can be seen.

The results shown in Figure 91 were acquired in high mass resolution mode, the ToF-SIMS generated spectra showed a clear peak consistent with the molecular weight of GSK3338058A, as shown in the spectra in Figure 92B, in 92A micro-colonies of DpRE1 mutant BCG incubated with GSK3338058A at ten times the MIC are shown, as highlighted by the arrows located on the image. For all the samples shown in this thesis the cells were fully consumed during the ToF-SIMS analysis.

The control samples (no compound incubation) do not show the 454 *m/z* peak, which is the compound molecular weight this provided evidence that this mass is compound related. This data indicated that ToF-SIMS could be used to analyse bacteria at the micro-colony level. The size of the micro-colonies observed in the ToF-SIMS experiment were approximately 5 µm, however it is difficult to estimate the number of cells contained in these micro-colonies, as bacteria tend to grow on multiple planes, this is in accordance with the literature on colony formation. [291]

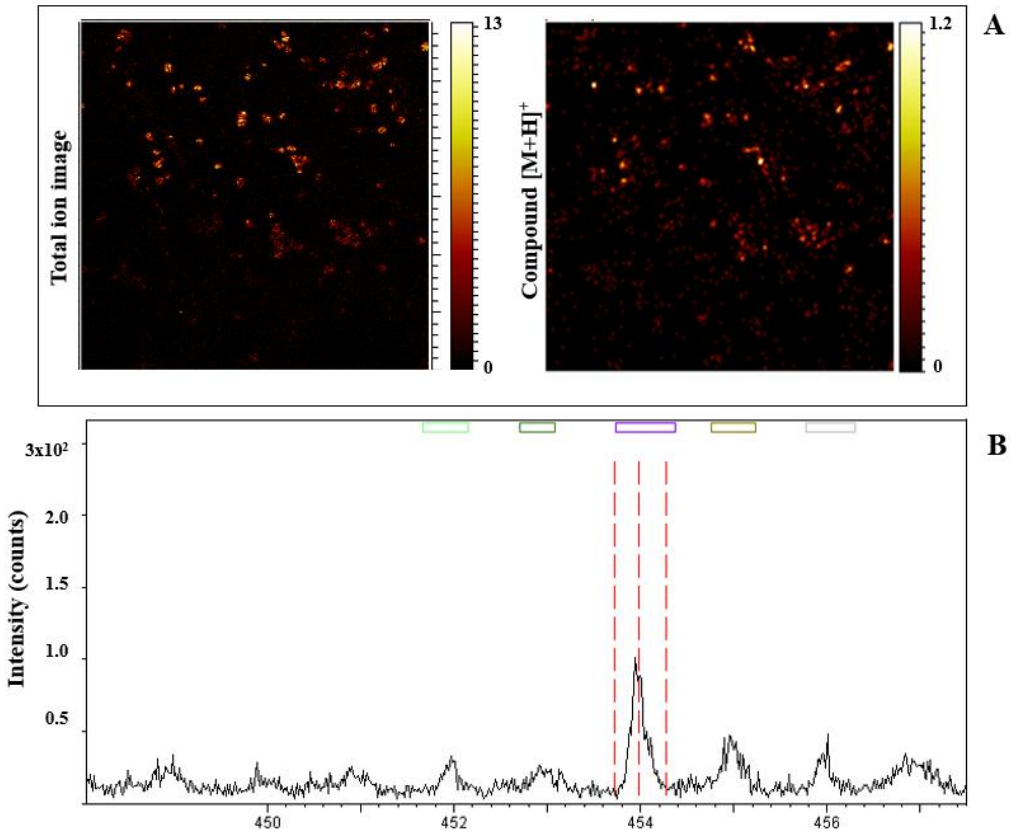


Figure 92: BCG overexpressing DpRE1 incubated for 48 hours with GSK3338058A at 1x the MIC (3 µ M) imaged using ToF-SIMS 5. (A) Total ion image for a larger area were several bacterial micro-colonies can be visualized, and on the right is

the analogous image, with compound signal only. (B) Spectral representation of the region of the spectrum showing an ion consistent with the pseudo-molecular ion of the compound which was not observed in the control only experiment.

Further ToF-SIMS imaging experiments were performed using GSK3338058A at lower compound concentrations, such as 1xMIC. In Figure 92, the spectra for GSK3338058A can be observed after 48 hour incubation at the MIC concentration of approximately 3 μM. As expected, the pseudo-molecular ion was much weaker than that observed for the 10x MIC experiment, however, even at a concentration that is 10 times reduced from the previous experiment the drug compound was still detectable using ToF-SIMS.

This shows evidence that ToF-SIMS can be used to detect a TB therapy at therapeutic levels, however the bacteria shown is DpRE1 mutant and therefore analysis of the unmodified bacteria is crucial to determine if the compound can still be visualized using ToF-SIMS in native conditions.

The main difference between the genetically modified and the empty vector was that the mutant had been genetically engineered to over-express the DpRE1 protein, it was known from data generated at GSK that GSK3338058A binds to DpRE1. Therefore, a higher compound signal would be expected when analysing the mutant when compared to the unmodified bacteria. The data in Figure 93 attempts to show that, however, it was challenging to vizualise differences in signal intensity based only on images. Figure 93 shows in (A) the DpRe1 mutant bacteria incubated with GSK3338058A at 10x the MIC. The main image shows solely the drug related ion while the smaller image besides it shows the total ion image. In (B), the empty vector control BCG can be seen, this terminology is often used when no changes were performed to the genome of the bacteria, in this image the micro-colonies can also be observed. As for (A), the smaller image to the side also shows the corresponding total ion image. As it can be observed in the colour scale in Figure 93, the compound intensity is higher for the DpRE1 image than the empty vector image, and at 1xMIC the compound cannot be detected in the unmodified bacteria, despite being observed in the DpRE1 mutant bacteria, as shown in Figure 92. This indicates that if these samples were patient isolates the compound probably would not be detectable, or it would only be detectable after a few treatment doses, after the compound had time to accumulate in the

bacterial membrane, but before killing the bacteria, at this point it will no longer be observable as the treatment causes the bacteria to die by destruction of their cell membrane.

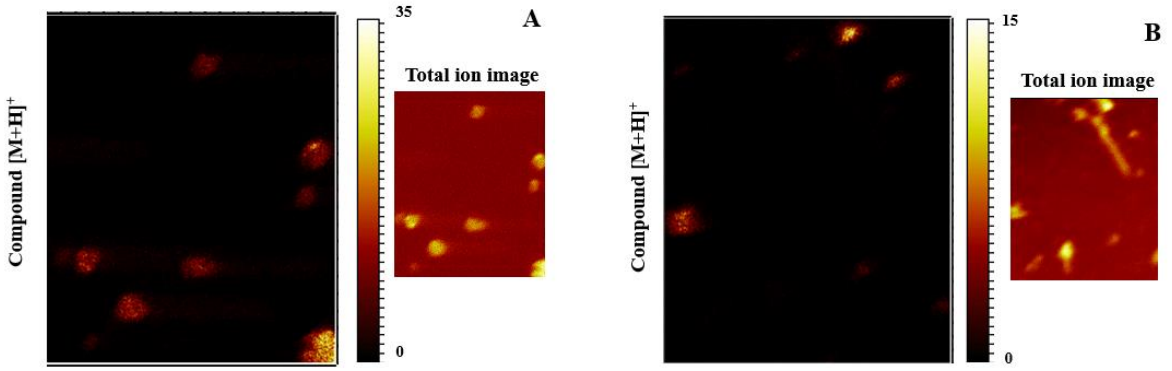


Figure 93: ToF-SIMS of BCG incubated with 10xMIC GSK3338058 (30 µM) for 48 hours. (A) bacteria over-expressing DpRE1, the field of view is 50x50 µm. (B) Non-mutant empty vector control. The main image shows compound molecular ion signal and the smaller images to the side show the total ion image for the same area as the main image. The field of view is 100x100 µm.

The images were acquired in a slightly different way, as the field imaged for the empty vector was bigger than the one acquired for DpRE1 overexpressing bacteria. This was done to observe multiple colonies for both samples, as shown in Figure 92. Choosing the field of view for this type of experiment was quite difficult as the bacteria could not be easily seen in the ToF-SIMS optical camera, mammalian cells on the other hand were easier to visualise using the ToF-SIMS camera, therefore choosing the area to analyse was fairly straight forward. As bacteria are extremely small and the ToF-SIMS camera struggles to capture smaller features, larger areas were imaged to ensure some colonies would be present in the field of view.

In addition to this, BCG tends to form colonies, however, one of the objectives was to image a single bacterium this could only be achieved by reducing the number of bacteria that were added to the substrate, resulting in the number of bacteria in a field of view being sparse, which made the selection of the field of view for analysis challenging.

There is a clear difference between the total ion image (smaller image to the side of the compound image) and the compound only image for the unmodified bacteria (EV), some of the material seen in the total ion image is not present in the compound image, this could be due to the fact that for some micro-colonies the amount of compound is below the limit of detection of the instrument. Despite this, when looking at the image for the compound only, it is clear that the shape of the micro-colonies observed is similar in both conditions. This data indicate that uptake of the compound affects the shape/growth of the colonies as those colonies without compound signal (Figure 92 pane B) appear as thin strands while those containing compound appear to have a rounded shape. Furthermore, activation of DpRE1 results in accumulation of the protein in the bacterial cell well, interaction of the compound with the protein could affect the way bacteria associate.

The same series of experiments were performed with GSK2620592A, however the compound signal was only observed at 50x the MIC, which equates to (250 µM). This compound's MIC is higher than that of GSK3338058, which could potentially explain why it could only be visualised at 50x the MIC.

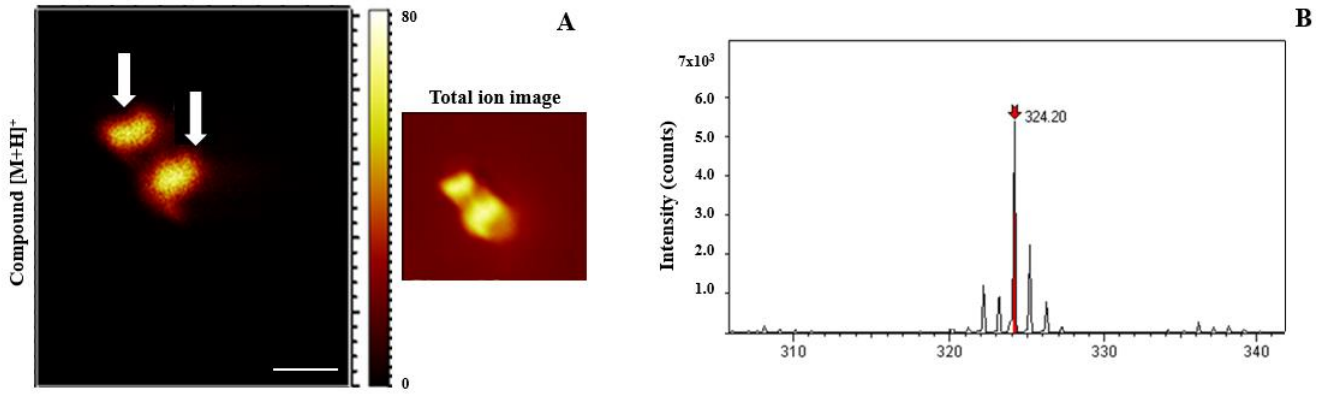


Figure 94: ToF-SIMS DpRE1 mutant BCG incubated with GSK2620592A at 50x the MIC (250 µM). (A) Shows a pictorial representation of the signal for 324 m/z for potentially two bacteria, with the total ion image on the right side. The scale bar is 5 µm. (B) Shows the spectra associated with the compound's molecular weight region showing the $[M+H^+]$ of 324 m/z of the compound.

Figure 94A depicts an image acquired in high spatial resolution mode, the main image relates to the compound's $[M+H^+]$, 324.20 m/z, and the insert shows the total ion image and in Figure 94B is shown

the region of the mass spectrum showing an ion consistent with the compound's $M+H^+$ acquired in high mass resolution mode.

To reiterate, the concentration used for this experiment was fifty times the minimum inhibitory concentration, which equates for this compound to 250 µM and is not representative of a therapeutic concentration. For this reason, the subsequent work was performed using GSK3338058A, as it could be detected at 1x the MIC, a more realistic therapeutic level of 3 µM.

As observed in Figure 95, the spatial resolution of the image generated by the ToF-SIMS measurement was not sufficient to clearly state that the structures seen are single bacteria. For this reason, correlative Atomic Force Microscopy (AFM) experiments were performed prior to the ToF-SIMS experiment in the same bacteria.

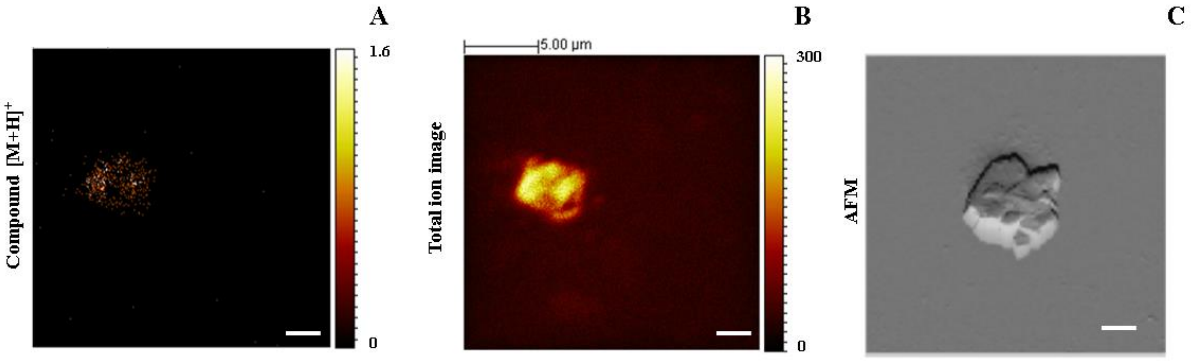


Figure 95: Correlative analysis between ToF-SIMS (A and B) and the same bacteria run on the AFM (C). ToF-SIMS total ion image (B) as well as the compound molecular ion (A). This image shows potentially two bacterial cells side by side, the AFM shows the sample topography, this could be associated to the freeze-drying process these samples have undergone.

Correlative experiments were performed using ToF-SIMS and AFM in which letters (A, B, C) were etched, using the FIB gun of the ToF-SIMS 5, on the slide surface to act as a guiding system to facilitate localisation of the same bacteria on the AFM microscope and then again on the ToF-SIMS. The letters were etched on the glass slide using the FIB gallium beam, a large field of view white light image was acquired using the AFM microscope, after that, a higher spatial resolution image was acquired using AFM, and a spot was placed on the under-side of the slide using a marker pen to facilitate finding the

cell's location. Once the samples were inserted into the ToF-SIMS, the pen mark was located using the instrument camera, the mark A, B or C was then located to analyse the same area that had been analysed using AFM.

Figure 95 shows in C the AFM image and the ToF-SIMS generated images in A and B, in 90B is the total ion image and in 91A is the signal for the compound $M+H^+$ ion. The AFM image indicated that the structures identified as bacteria were extremely angular. This could potentially be due to the salts from the bateria pior to freeze-drying, however it is more likely that is due to the freeze-drying process itself, as seen in chapter 4, the freeze-drying process colapses mammalian cells, therefore, it would be expected the same to occur for bacteria.

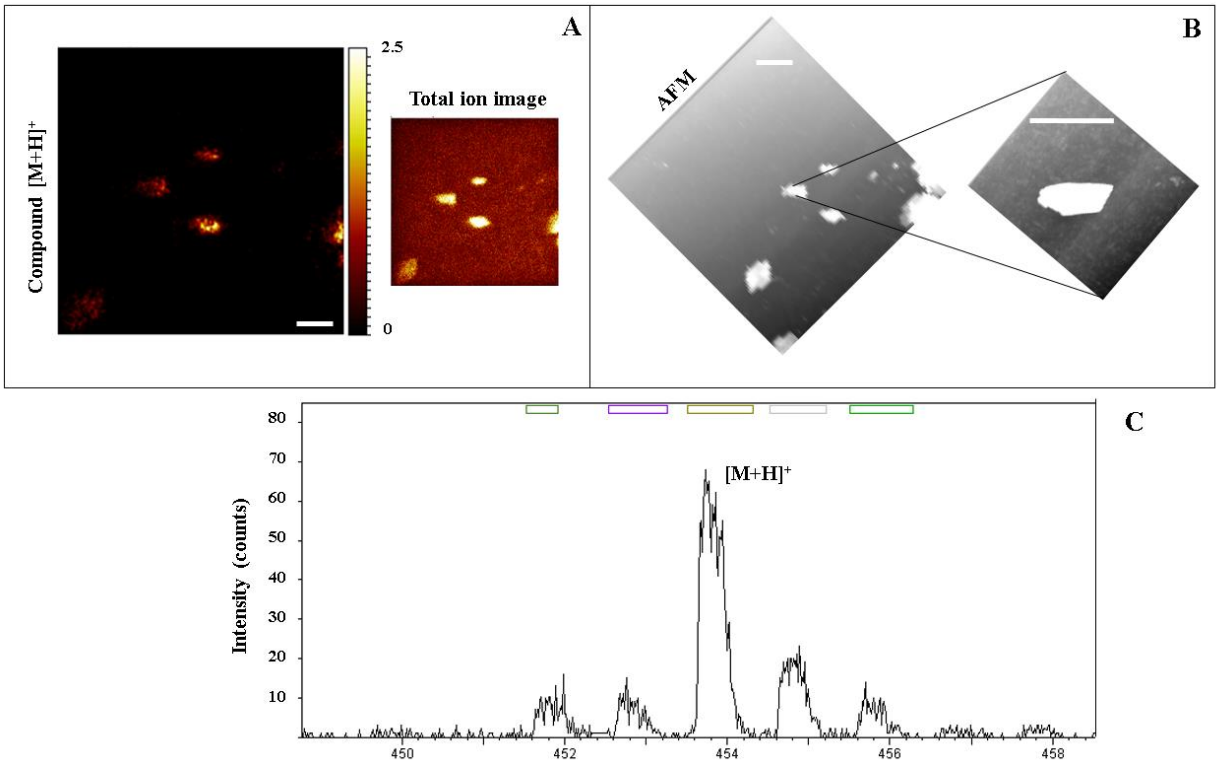


Figure 96: BCG DpRE1 incubated for 48hrs with GSK3338058 at 10x the MIC (30 µM) imaged using ToF-SIMS 5. The image shows in (A) the total ion image obtained by ToF-SIMS and the compound region of the spectra (454 m/z) acquired in the high spatial resolution mode. Scale bar is 2 µm. In (B), the AFM topography image with insert showing detail, the scale bar is also 2 µm. In (C) the compound region of the spectra can be observed (454 m/z). The conditions used for the acquisition of the images on Figure 95 were the same as Figure 96.

The orientation of the sample was different from ToF-SIMS to AFM in some samples, as can be observed in Figure 95. Despite this, there was good correlation between the AFM data and the ToF-SIMS data, especially when looking at the total ion image. As this image was acquired in high lateral resolution mode and as less current was applied the compound signal is low, however it is still detectable and it colocalizes with the bacteria.

Figure 96, provides another example of the correlative analysis using AFM and ToF-SIMS. In this image, with the help of the etch markers, the same bacteria that was previously analysed using AFM was analysed using ToF-SIMS, as explained above. In addition to the AFM generated images, the total ion image and the compound $[M+H]^+$ image are shown together with the region of the mass spectrum showing the $M+H^+$. These data prove unequivocally that label-free drugs can be visualised inside bacteria using ToF-SIMS. There is a slight change in the orientation of the bacteria in the AFM and ToF-SIMS images as once the samples were mounted on the ToF-SIMS holder, it was difficult to replicate the exact position in which the AFM images were acquired. This issue is even more evident on the second biological replicate, shown in Figure 96.

In order to determine unequivocally that the compound mass seen in ToF-SIMS at 454 *m/z* was the compound's molecular ion, and to confirm that the material on the slide was of bacterial origin an experiment with the OrbiSIMS was performed, as the data generated by this instrument is accurate to below 3 ppm mass accuracy. The OrbiSIMS not only provides imaging capabilities on par with the ToF-SIMS 5 but also provides excellent spectral information that results from the superior mass resolution associated to Orbitrap analyser. Therefore, the use of this recently developed system was investigated not only for exogenous but also endogenous molecules within the bacteria.

In Figure 97, an OrbiSIMS mass spectrum for the compound incubated DpRE1 genetically modified BCG is shown. The OrbiSIMS spectrum is rich in information showing the $M+H^+$ of the compound GSK3338058 at m/z 453.2080 compared to a theoretical of 453.19931, a difference of -1.41ppm. The isotopic distribution shown in the insert is also consistent with that expected for the compound.

In addition to the accurate mass of the compound, a large number of masses can also be found in this spectrum, and it can be hypothesized that these masses are bacteria related. Orbitrap data mass accuracy

is often below 3 ppm, with an external calibrant such as the silver clusters used in the OrbiSIMS, and for this reason, all the other species in the spectra could be identified when the masses found were searched against metabolites databases. Some of the species identified might be endogenous metabolites associated with the microorganism or drug related metabolites.

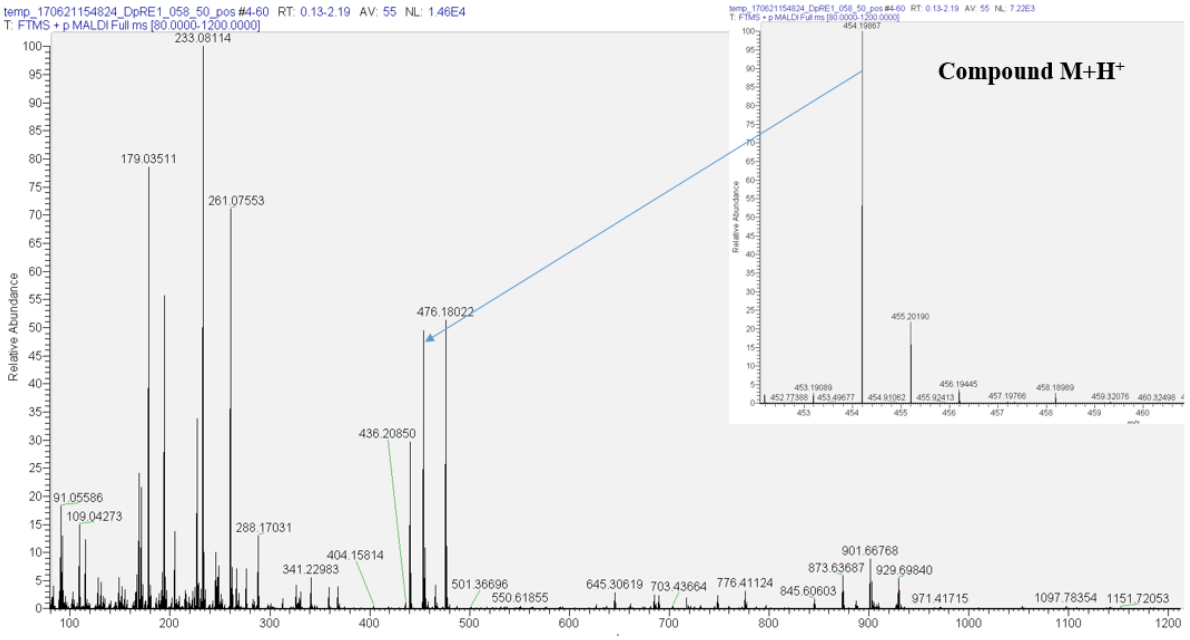


Figure 97: Full scan OrbiSIMS spectrum of BCG incubated with 10x the MIC of GSK3338058. Insert of the compound's pseudo-molecular ion. On the insert, the isotopic pattern matches the expected pattern for this compound.

The data was processed using an R pipeline described in section 3.14.4 which returned 1870 metabolite identifications. The one caveat associated with this type of data is the lack tandem MS, which means the identification of the species was solely based on the accurate mass assignment. The data was further checked for redundancies and the metabolites were grouped in metabolic pathways. As the visual representation of the full KEGG pathway is very complex and unintelligible, the data was filtered based on intensity and a table format was generated with the metabolite groups. Showing all the identified metabolites would make the table too complex (all the identified metabolites are listed in the annex), the table presenting the groups of identified metabolites is shown in Figure 98.

In Figure 98, at least one metabolite was identified in each of the metabolic pathways, 190 metabolites were associated with amino acid metabolism, shown in red and blue, the results associated 70 of the metabolites identified with carbohydrate metabolism, and they can be involved in any of the pathways referenced in yellow in Figure 98. Approximately, 53 of the metabolites identified are involved in the lipid and energy metabolism and those are represented in green. A total of 37 of the metabolites identified belong to the vitamin and co-factor metabolic pathway represented in sky blue and 20 metabolites are involved in nucleotide metabolism shown in purple.

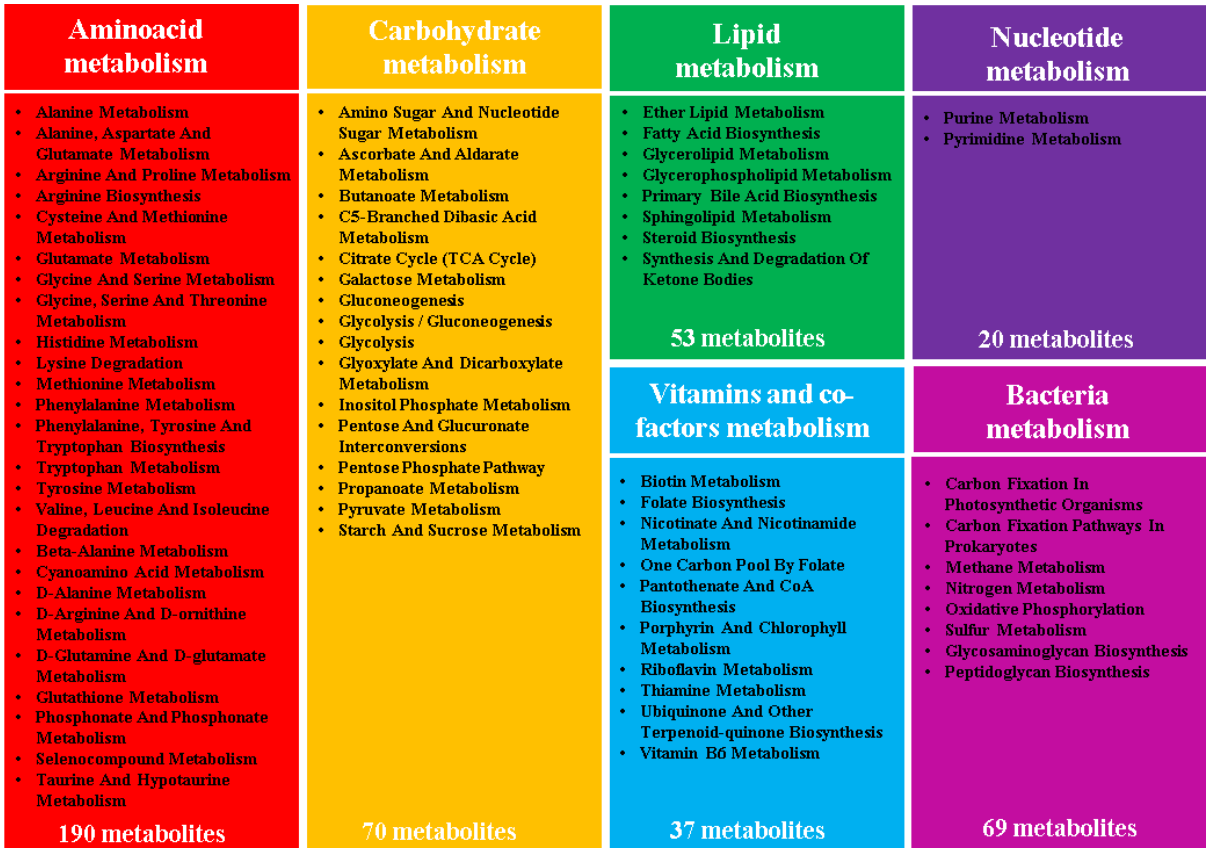


Figure 98: KEGG obtained BCG metabolite pathways in which at least one metabolite was identified. The pathways in the red column relate to aminoacid metabolism, the ones in the yellow column refer to the carbohydrate associated metabolic pathways, in green all the pathways identified associated to lipid metabolism can be identified. The nucleotide metabolism pathways can be found in purple, the vitamin and co-factor pathways can be seen in the blue column, and in the pink column are the metabolic pathways related to bacterial metabolism.

The data shown above (Figure 98), as well as the full metabolomics dataset, could then be used to compare between undosed control and compound treated bacteria. The data shown is solely for DpRE1 overexpressing BCG treated with GSK3338058A at 10 times the MIC.

The pathways identified, as well as the metabolites are mainly from basic metabolic pathways that occur in all cells such as carbohydrates, amino acid metabolism and the Tricarboxylic acid (TCA) cycle, such as fumarate, malate and succinate.

The TCA cycle is the building block of life and is more commonly referred to as a series of chemical reactions mediated by several different enzymes that occur in aerobic organisms to release energy stored through the oxidation of Acetyl-Coenzyme A derived from carbohydrates, proteins and fats.

The study performed in this chapter provides an example of what could be achieved with high resolution OrbiSIMS data, as the mass accuracy and tandem MS capabilities allow us to not only identify the drug related material, but also identify endogenous molecules that might provide data to improve understanding of the mode of action of the drug. This clearly shows how powerful the OrbiSIMS methodology is, and as the data processing capabilities improve so will the confidence on the data reported which in turn leads to a better understanding of the system being studied.

This type of data allows not only the identification of the compound and compound metabolites but the identification of endogenous metabolites, in some instances the compound will have a direct effect on these metabolites, so it useful to determine which metabolites are changing with compound dosing and place that information in the biological context. For example, in this context, the presence of drug should reduce the abundance of most metabolites in the TCA cycle as the compound is toxic to the bacteria.

In summary, ToF-SIMS and OrbiSIMS are valuable in visualizing pharmaceutical compounds in bacteria at therapeutic levels. Both instruments have limited spatial resolution and the images generated do not offer much details regarding the bacteria morphology (cell wall and nucleus cannot be visualized), further correlative work could be performed using EM or NanoSIMS. However, the OrbiSIMS, with its excellent mass resolution and accuracy can potentially provide insight on biological mechanisms that result from compound incubation by detecting compound induced changes in endogenous metabolites.

8. Conclusions

8.1) Summary

The principal aim of this thesis was to determine if SIMS could be used to probe the distribution of pharmaceutical compounds in cells. The ability of SIMS to generate images with cellular resolutions is of particular importance in drug discovery, as for an intracellular drug target, it is fundamental to know if the drug molecule is able to penetrate the cell. The gold standard techniques used for this purpose often need to be used in combination in order to answer this question. MALDI does not have the spatial resolution desired, microscopy often requires labels and bulk LC-MS/MS measurements only offer intracellular information from bulk cell measurements.

Chapter 4 described, to my knowledge, the first published instance where a label-free drug molecule was visualised inside a cell using ToF-SIMS. In order to achieve this, a well-established model was chosen involving rat-derived NR8383 cells. These macrophage-like cells are known to accumulate amiodarone due to the disruption of the lipid metabolism that it causes within a cell via its ability to inhibit phospholipase A2, resulting in phospholipid laden organelles. This, associated with the good ionisation efficiency of amiodarone, meant that this model provided an excellent basis for this proof of concept study. The amiodarone $[M+H]^+$ peak was clearly detected and could be used to reconstruct the images. Also, the phosphatidylcholine head group could be used as a cellular marker to identify the cellular space, while ribose was used as a nuclear marker, due to the fact the nucleus is a ribose rich region.

This model was thoroughly replicated several times and validated using fluorescence microscopy techniques. Despite not being able to visualise the compound using fluorescence microscopy the increase in the size of the lysosomes and increased intensity in the fluorescence of lysotracker red were used as surrogate biomarker of amiodarone accumulation. The 3D ToF-SIMS data had approximately half a micron spatial resolution. Electron microscopy data obtained from freeze-dried cells provided evidence that the structural integrity of the cells was preserved even after the procedure, validating the sample preparation method developed

In chapter 5, the scope of the experiment was expanded to other cell lines that are commonly used in drug discovery, by adding the Hek 293, HepG2 and HeLa cells lines.

The experiments were performed for a high number of cells in the context of ToF-SIMS. To do this, two different sample acquisition modes were applied: high mass resolution mode with a high ion beam current, and high lateral resolution mode with a low ion beam current. The first was faster while the latter produced better quality images. The quality of the images generated in high mass resolution mode was perfectly suitable, as the objective was to obtain the cell associated amiodarone signal for all the cells studied. The first observation to be made from this data is that there is a high degree of cell-to-cell variability, even within the same cell population. Frequency histograms showed a trend towards normal distribution, but this was not expected as the cell lines used were immortalized, which means that they should be similar both genetically and phenotypically, so the incorporation levels should be similar. However, the cells were not synchronised for reasons discussed previously and therefore were at different stages of the cell cycle, which may account for some of the variability seen.

This poses several different questions, for example, if this variability is seen for immortalised cells what would the variability be for patient cells. This can lead to other questions such as the relevance of bulk cell measurements, since they are an average of the population rather than representative of that population. It is interesting that emerging data now appears to support the variation observed, highlighting the intrinsic variation in cells.

The quantitative LC-MS/MS performed on the same samples that were generated for ToF-SIMS showed a good correlation between the ToF-SIMS data and the LC-MS/MS data for all cell lines except HeLa cells. NR8383 cells and HepG2 cells incorporated the most amiodarone, as per the bulk LC-MS/MS results at around 2.5 pg/cell. HeLa and Hek293 cells incorporate approximately ten-fold less than that, as it would be expected as Hek 293 and HeLa display a much-reduced number of membrane transporters when compared with NR8383 and HepG2 cells. When analysing the ToF-SIMS data the cell associated amiodarone signal for HeLa cells is much stronger than the LC-MS/MS results would suggest. This could potentially be explained by the fact that HeLa cells are less complex, due to the absence of some transporters, than the other cells studied. This means that the ToF-SIMS matrix

suppression effects would be less for these cells, which could manifest itself as a relatively high cell associated amiodarone ToF-SIMS signal for this cell line.

In chapter 6, the test of the applicability of ToF-SIMS in drug discovery was extended to the analysis of different drug molecules. A set of twenty compounds, all with very different physical-chemical properties were studied. HepG2 cells were incubated with these compounds at a concentration of 10 µM for 2 hours and then the samples were analysed using ToF-SIMS. Approximately half of the compounds were detected intracellularly in HepG2. To understand the reason why the signal for some compounds could be detected while others could not, the compounds were also tested in different matrices: neat, spotted on tissue, using the models described by Vorng et al., the compound mixed with HepG2 cell lysate and finally in HepG2 cells. Statistical analysis of the data was employed and the signal from the neat compound was identified as having the best correlation with the ToF-SIMS signal obtained from the compounds incubated with cells. Therefore, the usage of this method is recommended in the future when testing compounds for ToF-SIMS prior to cell incubation experiments.

When performing statistical analysis to correlate the different measured and experimental physical-chemical properties of the compounds and their ToF-SIMS signal, the property that produced the best correlation was LogD. This result is in accordance with previous data from Vorng et al., that stated that LogP was the measurement that had best aligned with ToF-SIMS signal for the compounds studied in their liver paste model. Both LogD and LogP are measurements of lipophilicity, however, LogD accounts for pH, which is quite crucial since most drug molecules are weak bases or weak acids.

In chapter 7, the ToF-SIMS spatial resolution was tested by attempting to visualise compound inside bacteria. Bacteria are typically 2 µm by 1 µm, which can pose a challenge to ToF-SIMS analysis.

Using both high mass resolution methods, to confirm the identity of the compound, and high spatial resolution methods, two GSK drugs were detectable in BCG. One of these drugs was even detected at a therapeutic level. Furthermore, by making use of the impressive mass resolution capabilities of the OrbiSIMS, endogenous metabolites were identified using an internal GSK metabolite identification pipeline. This proof of concept study shows that the OrbiSIMS is a powerful tool, and the ability to perform metabolomics and can potentially provide crucial information on the effects the compound is

having on the organism after treatment. Additional work could be performed and expand this approach to mammalian cells.

This thesis demonstrates a wide variety of applications in drug discovery that SIMS is suitable for. Correlative techniques need to be used in additions to this mass spectrometry imaging technique in order to validate the results. I have demonstrated that SIMS is a very useful technique that can be used to inform drug discovery at several stages.

8.2) Future Perspective

The ability to determine if a compound is located intracellularly is of vital importance to drug discovery, it addresses what is known as the first pillar of drug discovery: is the drug reaching the target? Confocal fluorescence microscopy is often used to address this question, however the addition of a fluorescent label to a small molecule, often similar in mass to the drug itself, changes the physical-chemical properties of the drug which can interfere with the drug's behaviour. ToF-SIMS has the advantage of allowing the detection of compounds intracellularly in a label-free way, however there are some drawbacks associated to the technique, such as the limited number of compounds that can be detected intracellularly when the cells are incubated at therapeutic level, the success rate is approximately half. The obvious improvement that can be envisaged is an increase in ionized material, by post-laser ionization or other mechanisms that would increase the number of ionized species, making the instrument more sensitive. Another possible improvement regarding increased ionization could be the development of ion guns that would make the sputter/ ionization process more efficient.

The other major limitation of ToF-SIMS is spatial resolution, despite the sub-µm resolution, the current resolution of the instrument is not sufficient to pin-point the compound localization at an organelle level, that information would be invaluable in drug discovery, as organelle associated toxicity and organelle compound accumulation could easily be detected with improved spatial resolution. Improvements in this field will have to surface as different ion guns are developed, those ion guns would have to be both highly focused at around 10nm and gentle enough not to cause molecular damage to the sample.

The OrbiSIMS is already a great improvement on ToF-SIMS, the hybrid instrument has exceptional mass resolution and accuracy, as well as allowing for fragmentation data to be acquired, however, currently that process is extremely manual, and the ions have to be intense in order to be fragmented. A significant and realistic improvement on this, would be increasing the transmission to the Orbitrap, and allowing the analyser to automatically fragment, for instance the Top10 most intense ions per scan. I believe that if these improvements could be achieved, SIMS would be a very useful technique that could span all stages of drug discovery, from early research, determining in which organelle a drug accumulates, to analysing drug formulations in order to assess if the active pharmaceutical ingredient in the formulation is distributed in the best way to increase its bioavailability. However, SIMS faces strong competition from techniques like MALDI, as the spatial resolution of the technique improves, researchers currently claim it to be 1µm, there only main differences between the techniques are: the reduced sample preparation of SIMS, as a matrix is not required, saving therefore time and reagents; and the fact that SIMS provides 3-dimensional information, while MALDI only provides 2-dimensional information.

Currently, as both techniques are still being developed, I believe them to be complementary and MALDI can be used as a way to quickly interrogate a sample, for instance by determining in which areas of an organ the compound is localized. Then, SIMS can be used to probe the sample further, for instance by determining what cell type within a tissue the compound is associated to.

Presently, the OrbiSIMS is probably the most versatile SIMS instrument, as it possesses all the capabilities of the newest version of a ToF-SIMS associated to the increased mass resolution, accuracy and fragmentation capabilities of the Orbitrap analyser. However, these are significant improvements on the horizon, researchers and manufacturers need to continue to work together in order to keep innovating to deliver instruments that allow researchers to answer the next question sooner.

Bibliography

1. Fernández, B., Costa, J. M., Pereiro, and Sanz-Medel R., A. Inorganic mass spectrometry as a tool for characterisation at the nanoscale. *Anal. Bioanal. Chem*, 2010, 396, 15–29.
2. Fearn, S. Characterisation of biological material with ToF-SIMS: a review. *Mater. Sci. Technol*, 2015, 31, 148–161.
3. Passarelli, M.K., Pirkl, A., Moellers, R., Grinfeld, D., Kollmer, F., Havelund, R., Newman, C.F., Marshall, P.S., Arlinghaus, H., Alexander, M.R., West, A., Horning, S., Niehuis, E., Makarov, A., Dollery, C.T. and Gilmore, I.S. The 3D OrbiSIMS - Label-free metabolic imaging with subcellular lateral resolution and high mass-resolving power. *Nat. Methods*, 2017, 14(12), 1175-1183.
4. Amstalden van Hove, E. R., Smith, D. F. and Heeren, R. M. A. A concise review of mass spectrometry imaging. *J. Chromatogr*, 2010, *A* 1217, 3946-3954.
5. Passarelli, M. K., Newman, C.F., Marshall, P.S., West, A., Gilmore, I.S., Bunch, J., Alexander, M.R. and Dollery, C.T. Single-Cell Analysis: Visualizing Pharmaceutical and Metabolite Uptake in Cells with Label-Free 3D Mass Spectrometry Imaging. *Anal. Chem*, 2015, 87, 6696-6702.
6. Newman, C. F., Havelund, R., Passarelli, M.K., Marshall, P.S., Francis, I., West, A., Alexander, M.R., Gilmore, I.S., Dollery, C.T. Intracellular drug uptake - a comparison of single cell measurements using ToF-SIMS imaging and quantification from cell populations with LC-MS/MS. *Anal. Chem*, 2017, 89 (22), 11944-11953.
7. Lombardino, J. G. and Lowe, J. A. The role of the medicinal chemist in drug discovery- then and now. *Nat. Rev. Drug Discovery*, 2004, 3 (10), 853-862.
8. Mitragotri, S., Burke, P. A. and Langer, R. Overcoming the challenges in administering biopharmaceuticals: formulation and delivery strategies. *Nat. Publ. Gr.*, 2014, 13 (9), 655-672.
9. Castner, D. G. View from the edge. *Nature*, 2003, 422, 129–130.
10. Fonseca, F., Cenard, S. and Passot, S. Freeze-drying of lactic acid bacteria. *Methods Mol. Biol.*, 2015, 1257, 477-488.
11. Piwowar, A., Fletcher, J., Lockyer, N. and Vickerman, J. Investigating the effect of temperature on depth profiles of biological material using ToF-SIMS. *Surf. Interface Anal.* 2011, 43, 207–210.
12. Fletcher, J. S., Henderson, A., Jarvis, R.M., Lockyer, N.P., Vickerman, J.C. and Goodacre, R. Rapid discrimination of the causal agents of urinary tract infection using ToF-SIMS with chemometric cluster analysis. *Appl. Surf. Sci.* 2006, 252, 6869–6874.
13. Chen, R., Zhang, G., Gao, Y., Xiao, L. and Jia, S. Electron transfer-based single molecule fluorescence as a probe for nano-environment dynamics. *Sensors*, 2014, 14(2), 2449–2467.
14. Sanderson, M. J., Smith, I., Parker, I. & Bootman, M. D. Flourescence Microscopy. *Cold Spring Harb Protoc.*, 2014, 36.
15. Chéreau, R., Tønnesen, J. and Nägerl, U. V. STED microscopy for nanoscale imaging in living brain slices. *Methods*, 2015, 88, 57–66.
16. Pollaro, L., Equis, S., Piazza, B. D. and Cotte, Y. Stain-free 3D Nanoscopy of Living Cells. *Optik and photonik*, 2016, 11(1), 38–42.
17. Reimer, Ludwig. *Transmission Electron Microscopy*. Springer-Verlag Berlin Heidelberg, 1993.
18. Palade, G. E. A study of fixation for electron microscopy. *The Rockedler Institute for Medical Research*, 1951, 23.
19. Barattin, R. and Voyer, N. Chemical modifications of AFM tips for the study of molecular recognition events. *Chem. Commun.* 2008, 0, 1513–1532.
20. Ritchie, M. D., Holzinger, E. R., Li, R., Pendergrass, S. A. and Kim, D. Methods of integrating data to uncover genotype-phenotype interactions. *Nat. Rev. Genet.* 2015, 16, 85–97.
21. Altelaar, A. F. M., Munoz, J. and Heck, A. J. R. Next-generation proteomics: Towards an integrative view of proteome dynamics. *Nat. Rev. Genet.* 2013, 14, 35–48.
22. Rustam, Y. H. and Reid, G. E. Analytical Challenges and Recent Advances in Mass Spectrometry Based Lipidomics. *Anal. Chem.* 2017, 90(1) 374-397.
23. Lam, S. M., Tian, H. and Shui, G. Lipidomics, en route to accurate quantitation. *Biochim.*

Biophys. Acta - Mol. Cell Biol. Lipids, 2017, 1862, 752–761.
24. Vasilopoulou, C. G., Margarity, M. and Klapa, M. I. Metabolomic analysis in brain research: Opportunities and challenges. *Front. Physiol.* 2016, 7, 1–8.
25. Kennedy, T. Managing the drug discovery/development interface. *Drug Discov. Today*, 1997, 2, 436–444.
26. Hodgson, J. ADMET - Turning chemicals into drugs. Rapidly resolving the pharmacokinetic and toxicological properties of drug candidates remains a key challenge for drug developers. *Nat. Biotechnol.* 2001, 19, 722–726.
27. Braggio, S., Montanari, D., Rossi, T. and Ratti, E. Drug efficiency: a new concept to guide lead optimization programs towards the selection of better clinical candidates. *Expert Opin. Drug Discov.*, 2010, 5, 609–618.
28. Ritchie, T. J. and Macdonald, S. J. F. The impact of aromatic ring count on compound developability - are too many aromatic rings a liability in drug design? *Drug Discov. Today*, 2009, 14, 1011–1020.
29. Young, R. J., Green, D. V. S., Luscombe, C. N. and Hill, A. P. Getting physical in drug discovery II: The impact of chromatographic hydrophobicity measurements and aromaticity. *Drug Discov. Today*, 2011, 16, 822–830.
30. Leeson, P. D. and Young, R. J. Molecular Property Design: Does Everyone Get It? *ACS Med. Chem. Lett.*, 2015, 6, 722–725.
31. Julian, D. G., Camm, A.J., Frangin, G., Janse, M.J., Munoz, A., Schwartz, P.J. and Simon, P., Randomised trial of effect of amiodarone on mortality in patients with left-ventricular dysfunction after recent myocardial infarction: EMIAT. European Myocardial Infarct Amiodarone Trial Investigators. *Lancet*, 1997, 349, 667–74.
32. Lafuente-Lafuente, C., Alvares, J.C., Leenhardt, A., Mouly, S., Extramiana, F., Caulin, C., Funck-Brentano, C. and Bergmann, J.F. . Amiodarone concentrations in plasma and fat tissue during chronic treatment and related toxicity. *Br. J. Clin. Pharmacol.*, 2009, 67, 511–519.
33. Martino, E., Bartalena, L., Bogazzi, F. and Braverman, L.E., The Effects of Amiodarone on the Thyroid. *Endocr. Rev.* 2001, 22, 240–254.
34. Ammoury, A., Michaud and S., Paul, C., Photodistribution of Blue-Gray Hyperpigmentation After Amiodarone Treatment. *Arch Dermatol*. 2008, 144, 1–5.
35. Nacca, N., Bhamidipati, C. M., Yuhico, L. S., Pinnamaneni, S. and Szombathy, T. Severe amiodarone induced pulmonary toxicity. *J. Thorac. Dis.*, 2012, 4, 667–670.
36. Ahlin, G., Hilgendorf, C., Karlsson, J., Szigyarto, C.A., Uhlen, M. and Artursson, P.. Endogenous gene and protein expression of drug transporting proteins in cell lines routinely used in drug discovery programs. *Drug Metab Dispos*, 2009, 37, 2275–2283.
37. Costantini, S., Di Bernardo, G., Cammarota, M., Castello, G. and Colonna, G. Gene expression signature of human HepG2 cell line. *Gene*, 2013, 518, 335–345.
38. Hunter, R. L., Venkataprasad, N. and Olsen, M. R. The role of trehalose dimycolate (cord factor) on morphology of virulent M. tuberculosis in vitro. *Tuberculosis*, 2006, 86, 349–356.
39. Bacon, J., Alderwick, L.T., Allnutt, J.A., Gabasova, E., Watson, R., Hatch, K.A., Clark, S.O., Jeeves, R.E., Marriott, A., Rayner, E., Tolley, H., Pearson, G., Hall, G., Besra, G.S., Wernisch, L., Williams, A. and Marsh, P.D. Non-replicating Mycobacterium tuberculosis elicits a reduced infectivity profile with corresponding modifications to the cell wall and extracellular matrix. *PLoS One*, 2014, 9(2), e87329.
40. Markova, N., Slavchev, G.and Michailova, L. Unique biological properties of Mycobacterium tuberculosis L-form variants: Impact for survival under stress. *Int. Microbiol.* 2012, 15, 61–68.
41. Kale, S. C., Kale, M. K. and Sarita, S. Mycobacterium Tuberculosis. *Int. Journal of Biom. and Ad. Research*, 2016, 7, 204–207.
42. Lawn, S. D. and Zumla, A. I. Tuberculosis. *Lancet*, 2011, 378, 57–72.
43. Chiaradia, L., Lefebvre, C., Parra, J., Marcoux, J., Burlet-Schiltz, O., Etienne, G., Tropis, M. and Daffe, M. Dissecting the mycobacterial cell envelope and defining the composition of the native mycomembrane. *Sci. Rep.* 2017, 7, 1–12.
44. Bhutani, I., Loharch, S., Gupta, P., Madathil, R. and Parkesh, R. Structure, dynamics, and interaction of Mycobacterium tuberculosis (Mtb) DprE1 and DprE2 examined by molecular

modeling, simulation, and electrostatic studies. *PLoS One*, 2015, 10, 1–31.
45. Dollery, C. T. Lost in Translation (LiT). *Br. J. Pharmacol.* 2014, 171, 2269–2290.
46. Paul, S. M., Mytelka, D.S., Dunwiddie, C.T., Persinger, C.C, Munos, B.H, Lindborg, S.R. and Schacht, A.L. How to improve R&D productivity: the pharmaceutical industry's grand challenge. *Nat. Rev. Drug Discov.* 2010, 9, 203–214.
47. Khanna, I. Drug discovery in pharmaceutical industry: Productivity challenges and trends. *Drug Discov. Today*, 2012, 17, 1088–1102.
48. Lee, J. A., Uhlik, M. T., Moxham, C. M., Tomandl, D. and Sall, D. J. Modern Phenotypic Drug Discovery Is a Viable, Neoclassic Pharma Strategy. *J Med Chem*. 2011, 55(10), 4527-4538. Synthesis and preliminary in vitro biological evaluation of 4-[(4-hydroxyphenyl)sulfanyl]but-3-en-2-one, a 4-mercaptophenol derivative designed as a novel bifunctional antimelanoma agent. *J Med Chem*. 2009, 52(15), 4973-4976.
50. Hann, M. M. Molecular obesity, potency and other addictions in drug discovery. *Med. ChemComm.* 2011, 2, 349-355.
51. Trim, P. J., Henson, C.M., Avery, J.L., McEwen, A., Snel, M.F., Claude, E., Marshall, P.S., West, A., Princivalle, A.P., Clench, M.R., Spectrometry Imaging of Vinblastine in Whole Body Tissue Sections Matrix-Assisted Laser Desorption / Ionization-Ion Mobility Separation-Mass Spectrometry Imaging of Vinblastine in Whole Body Tissue Sections. *Anal. Chem.* 2008, 80, 8628–8634.
52. Van de Plas, R., Yang, J., Spraggins, J. and Caprioli, R. M. Image fusion of mass spectrometry and microscopy: a multimodality paradigm for molecular tissue mapping. *Nat. Methods.* 2015 12, 366–72.
53. Dillard, R. S., Hampton, C.M, Strauss, J.D., and Ke, Z. Biological Applications at the Cutting Edge of Cryo-Electron Microscopy. *Microsc. Microanal.* 2018, 24, 406–419.
54. Scharmann, M., Janning, P., Ziegler, S. and Waldmann, H. Small-Molecule Target Engagement in Cells. *Cell Chem. Biol.* 2016, 23, 435–441.
55. Mateus, A., Matsson, P. and Artursson, P. Rapid measurement of intracellular unbound drug concentrations. *Mol. Pharm.* 2013, 10, 2467–2478.
56. Anderson, A. B., Xiong, G. and Arriaga, E. A. Doxorubicin accumulation in individually electrophoresed organelles. *J. Am. Chem. Soc.* 2004, 126, 9168–9169.
57. 3D-NanoSIMS label free molecular imaging, National Physical Laboratory, 2015, Available from: www.npl.co.uk/news/3d-nanosims-label-free-molecular-imaging.
58. VICKERMAN, John, and David BRIGGS , D. *ToF-SIMS: Materials Analysis by Mass Spectrometry 2nd Edition*. IM Publications LLP, 2013.
59. Briggs, D. and Wootton, B. Analysis of polymer surfaces by SIMS - 1. An investigation of practical problems. *Surf. Interface Anal.* 1982, 4, 109–115.
60. VICKERMAN, John, Ian S. GILMORE. *Surface Analysis – The Principal Techniques 2nd Edition*. Wiley, 2009.
61. Tahallah, N., Brunelle, A., De La Porte, S. and Laprévote, O. Lipid mapping in human dystrophic muscle by cluster-time-of-flight secondary ion mass spectrometry imaging. *J. Lipid Res.* 2008, 49, 438–54.
62. Touboul, D., Roy, S., Germain, D.P, Chaminade, P., Brunelle, A., Laprévote, O. MALDI-TOF and cluster-TOF-SIMS imaging of Fabry disease biomarkers. *Int. J. Mass Spectrom.* 2007, 260, 158–165.
63. MAHONEY, Christine M. An Introduction to Cluster Secondary Ion Mass Spectrometry (Cluster SIMS). *Cluster Secondary Ion Mass Spectrometry: Principles and Applications*, Wiley, 2013.
64. Rabbani, S., Barber, A. M., Fletcher, J. S., Lockyer, N. P. and Vickerman, J. C. TOF-SIMS with argon gas cluster ion beams: A comparison with C60+. *Anal. Chem.* 2011, 83, 3793–3800.
65. Adriens, A., Van Vaeck, L., Adams, F., Static secondary ion mass spectrometry (S-SIMS) Part 2: material science applications. *MassSpectrometryReviews* 1999, 18(1) 48-8.
66. Winograd, N. Gas Cluster Ion Beams for Secondary Ion Mass Spectrometry. *Annu. Rev. Anal. Chem.* 2018, 11 (1), 29-48.
67. Gilmore, I. S. SIMS of organics—Advances in 2D and 3D imaging and future outlook. *J. Vac. Sci. Technol. A Vacuum, Surfaces, Film.* 2013, 31, 050819.

68. Sheraz Née Rabbani, S., Razo, I. B., Kohn, T., Lockyer, N. P. and Vickerman, J. C. Enhancing ion yields in time-of-flight-secondary ion mass spectrometry: A comparative study of argon and water cluster primary beams. *Anal. Chem.* 2015, 87, 2367–2374.
69. Jones, E. A., Lockyer, N. P., Kordys, J. and Vickerman, J. C. Suppression and Enhancement of Secondary Ion Formation Due to the Chemical Environment in Static-Secondary Ion Mass Spectrometry. *J. Am. Soc. Mass Spectrom.* 2007, 18, 1559–1567.
70. Alnajeebi, A. M., Vickerman, J. C. and Lockyer, N. P. Matrix effects in biological SIMS using cluster ion beams of different chemical composition. *Biointerphases.* 2016, 11, 02A317.
71. Arlinghaus, H. F, Kriegeskotte, C., fartmann, M., Witting, A. Mass spectrometric characterization of elements and molecules in cell cultures and tissues. *Appl. Surf. Sci.* 2006, 252, 6941–6948.
72. Fletcher, J. S. Cellular imaging with secondary ion mass spectrometry. *Analyst,* 2009, 134, 2204–2215.
73. Cotter, Robert J. *Time-of-Flight Mass Spectrometry*.American Chemical Society, 1993.
74. Ion-TOF Software help section. ION-TOF.
75. De Souza, R. A., Zehnpfenning, J., Martin, M. and Maier, J. Determining oxygen isotope profiles in oxides with Time-of-Flight SIMS. *Solid State Ionics,* 2005, 176, 1465–1471.
76. Makarov, A. Electrostatic Axially Harmonic Orbital Trapping: A High-Performance Technique of Mass Analysis. *Anal. Chem.*2000, 72, 1156–1162.
77. Chief, E. C. Method of the Year 2012 - Targeted Proteomics. *Nat. Methods* 2012, 10, 2013.
78. Picotti, P., Bodenmiller, B. and Aebersold, R. Proteomics meets the scientific method. *Nat. Methods,* 2013, 10, 24–27.
79. Nagaraj, N., Wisniewski, J.R., geiger, T., Cox, J., Kircher, M., Kelso, J., Paabo, S., Mann, M. Deep proteome and transcriptome mapping of a human cancer cell line. *Mol. Syst. Biol.* 2011, 7, 548.
80. Pachl, F., Ruprecht, B., Lemeer, S. and Kuster, B. Characterization of a high field Orbitrap mass spectrometer for proteome analysis. *Proteomics,* 2013, 13, 2552–2562.
81. Dahl, R., Staehelin, L.A.High pressure for the preservation of biological structure: theory and practice. *J. Electron Microsc. Tech.* 1989, 12, 165–174.
82. Robinson, M. A., Graham, D. J. and Castner, D. G. ToF-SIMS depth profiling of cells: Z-correction, 3D imaging, and sputter rate of individual NIH/3T3 fibroblasts. *Anal. Chem.* 2012, 84, 4880–4885.
83. I, E. C. and Layne, R. S. Annals New York Academy of Sciences. *New York,* 1951, 2931.
84. Litchfield, R. J. Optimal Control of a Freeze Dryer. *Chem. Eng. Sci.* 1979, 34, 975–981.
85. Ostrowski, S. G., Bell, C. T. Van, Winograd, N. and Ewing, A. G. Mass Spectrometry imaging of highly curved membranes during Tetrahymena mating. *Science,* 2004, 305 (5680), 71–73.
86. Roddy, T. P., Ostrowski, S. G., Cannon, D. M. and Ewing, A. G. Mass Spectrometry Imaging of Membrane Lipids in Cryogenically Preserved Single Cells. 2002, ASMS 2–3.
87. Sjovall, P., Johansson, B. and Lausmaa, J. Localization of lipids in freeze-dried mouse brain sections by imaging TOF-SIMS. *Appl. Surf. Sci.* 2006, 252, 6966–6974.
88. Fletcher, J. S., Lockyer, N. P., Vaidyanathan, S. and Vickerman, J. C. TOF-SIMS 3D biomolecular imaging of Xenopus laevis oocytes using buckminsterfullerene (C60) primary ions. *Anal. Chem.* 2007, 79, 2199–2206.
89. Breitenstein, D., Rommel, C. E., Möllers, R., Wegener, J. and Hagenhoff, B. The chemical composition of animal cells and their intracellular compartments reconstructed from 3D mass spectrometry. *Angew. Chemie - Int. Ed.* 2007, 46, 5332–5335.
90. Thompson, C. E., Jungnickel, H., Lockyer, N. P., Stephens, G. M. and Vickerman, J. C. ToF-SIMS studies as a tool to discriminate between spores and vegetative cells of bacteria. *Appl. Surf. Sci.* 2004, 231–232, 420–423.
91. Armitage, E. G., Kotze, H., Fletcher, J.S., Hrnderson, A., Williams, K.J., Lockyer, N.P., Vickerman, J.C. Time-of-flight SIMS as a novel approach to unlocking the hypoxic properties of cancer. *Surf. Interface Anal.* 2013, 45, 282–285.
92. Lockyer, N. P. Bioimaging of elements and small molecules using MS. *Bioanalysis,* 2011, 3, 1047–1051.

93. Nwaneshiudu, A., Kuschal, C., Sakamoto, F.H., Anderson, R.R., Schwazenberger, K., Young, R.C. Introduction to confocal microscopy. *J. Invest. Dermatol.* 2012, 132, 1–5.
94. Murphy, D. B. Fundamentals of light microscopy and electronic imaging. *Imaging*, 2001, 83.
95. Webb, R. H. Confocal optical microscopy. *Reports Prog. Phys.* 1996, 59, 427–471.
96. Suhling, K., French, M. W. and Phillips, D. Time-resolved fluorescence microscopy†. *Photochem. Photobiol. Sci.* 2005, 4, 13–22.
97. Oheim, M., Michael, D. J., Geisbauer, M., Madsen, D. and Chow, R. H. Principles of two-photon excitation fluorescence microscopy and other nonlinear imaging approaches. *Adv. Drug Deliv. Rev.* 2006, 58, 788–808.
98. Thorley, J. A., Pike, J. and Rappoport, J. Z. Super-resolution Microscopy: A Comparison of Commercially Available Options. *Fluoresc. Microsc. Super-Resolution other Nov. Tech.* 2014, 199–212.
99. Jensen, E. C. Use of Fluorescent Probes: Their Effect on Cell Biology and Limitations. *Anat. Rec. Adv. Integr. Anat. Evol. Biol.* 2012, 295, 2031–2036.
100. Galandrin, S., Oligny-Longpré, G. and Bouvier, M. The evasive nature of drug efficacy: implications for drug discovery. *Trends Pharmacol. Sci.* 2007, 28, 423–430.
101. Cotte, Y., Toy, F., Jourdain, P., Pavillon, N., Boss, D., Magistretti, P., Marquet, P., Depeursinge, C. Marker-free phase nanoscopy. *Nat. Photonics*, 2013, 7, 418–418.
102. Pollaro, L., Piazza, B. D. and Cotte, Y. Digital Staining : Microscopy of Live Cells Without Invasive Chemicals. *Microscopy-today*, 2015, 1–6.
103. Claxton, N. S., Fellers, T. J. and Davidson, M. W. Laser Scanning Confocal Microscopy. *Encylopedia Med. Devices Instrum.* 2006, 1979, 4–37.
104. Krzysztof N. and Wojciech K. Confocal Laser Scanning Microscopy for Characterisation of Surface Microdiscontinuities of Vitrified. *Int.J. Mech. Eng. and Rob. Res,* 2012, 1(1), 14-28.
105. Sabatini, D., Bensch, K. and Barrnett, R.J. Cytochemistry and electron microscopy. The preservation of cellular ultrastructure and enzymatic activity by aldehyde fixation. *J. Cell Biol.* 1963, 17, 19–58.
106. Binning, G., Quate C.F., and Gerber, C. Atomic force microscope. *Phys. Rev. Lett.* 1986, 56, 1–7.
107. de Jager, M. & van Noort, J. Atomic Force Microscopy. *eLS*, 2007, 156-159.
108. Geisse, N. A. AFM and combined optical techniques. *Mater. Today* 2009, 12, 40–45.
109. GROSS, H. Jurgen. *Mass Spectrometry*. Springer, 2nd edition, 2004.
110. Rabilloud, T. Two-dimensional gel electrophoresis in proteomics: Old, old fashioned, but it still climbs up the mountains. *Proteomics*, 2002, 2, 3–10.
111. Scigelova, M. and Makarov, A. Orbitrap mass analyzer - Overview and applications in proteomics. *Proteomics*, 2006, 1, 16–21.
112. Wilkins, M. R., Appell, R.D., Van Eyk, J.E., Chung, M.C., Gorg, A., Hecker, M., Huber, L.A., Langen, H., Link, A.J., Paik, Y.K., Patterson, S.D., Pennington, S.R., Rabilloud, T., Simpson, R.J, Weiss and W., Dunn, M.J. Guidelines for the next 10 years of proteomics. *Proteomics*, 2006, 6, 4–8.
113. Martens, L., Hermjakob, H., jones, P., Adamski, M., Taylor, C., States, D., Gevaert, K., Vandekerckhove, J, Apweiler, R. PRIDE: The proteomics identifications database. *Proteomics* 2005, 5, 3537–3545.
114. Aebersold, R. and Mann, M. Mass spectrometry-based proteomics. *Nature*, 2003, 422, 198–207.
115. Michalski, A., damoc, E., Hauschild, J.P., Lange, O., Wishaus, A., Makarov, A., Nagaraj, N., Cox, J., Mann, M., Horning, S. Mass Spectrometry-based Proteomics Using Q Exactive, a High-performance Benchtop Quadrupole Orbitrap Mass Spectrometer. *Mol. Cell. Proteomics* 2011, 10, M111.011015.
116. Lange, V., Picotti, P., Domon, B. and Aebersold, R. Selected reaction monitoring for quantitative proteomics: A tutorial. *Mol. Syst. Biol.* 2008, 4, 222.
117. Mann, M. Functional and quantitative proteomics using SILAC. *NatRevMolCellBio*. 2006, 7(12), 952–958.
118. Rolland, T. *et al.* A proteome-scale map of the human interactome network. *Cell* , 2014,159, 1212–1226.

119. Scheubert, K., Hufsky, F., petras, D., wang, M., Nothis, L.F., Duhrkop, K., bandeira, N., Dorrestein, P.C., Bocker, S. Significance estimation for large scale metabolomics annotations by spectral matching. *Nat. Commun.* 2017, 8, 1494.
120. METZ, Thomas, O. *Metabolomic Profiling*, Humana Press 2011.
121. Köfeler, H. C., Fauland, A., Rechberger, G. N. and Trötzmüller, M. Mass Spectrometry Based Lipidomics: An Overview of Technological Platforms. *Metabolites* 2012, 2, 19–38.
122. Alden, N., Krishnan, S., Porkhin, V., raju, R. McElearney, K., gilbert, A., Lee, K. Biologically Consistent Annotation of Metabolomics Data. *Anal. Chem.* 2017, 89(24), 13097-13104.
123. Shevchenko, A. and Simons, K. Lipidomics: Coming to grips with lipid diversity. *Nat. Rev. Mol. Cell Biol.* 2010, 11, 593–598.
124. Bligh, E. . and Dyer, W. . Canadian Journal of Biochemistry and Physiology. *J. Biochem. Physiol.* 1959, 37, 911–917.
125. Folch, J., Less, M., and Stanley, G.H.S. A Simple method for the isolation and purification of total lipids from animal tissue. *J.Biol.Chem* 1957, 226, 497-509.
126. Matyash, V., Liebisch, G., Kurzchalia, T. V., Shevchenko, A. and Schwudke, D. Lipid extraction by methyl- *tert* -butyl ether for high-throughput lipidomics. *J. Lipid Res.* 2008, 49, 1137–1146.
127. Löfgren, L., Stahlman, M., Forsberg, G.B, saarinem, S., Nilsson, P. Hansson, G.I.. The BUME method: a novel automated chloroform-free 96-well total lipid extraction method for blood plasma. *J. Lipid Res.* 2012, 53, 1690–1700.
128. Villas-Bôas, S. G., Mas, S., Åkesson, M., Smedsgaard, J. and Nielsen, J. Mass spectrometry in metabolome analysis. *Mass Spectrom. Rev.* 2005, 24, 613–646.
129. Scalbert, A., Brennan, L., Fiehn, O., Hankemeier, T., Kristal, B.S., van Ommen, B., Pujos-Guillot, E., verheij, E., Wishart, D., Wopereid, B. Mass-spectrometry-based metabolomics: Limitations and recommendations for future progress with particular focus on nutrition research. *Metabolomics*, 2009, 5, 435–458.
130. Jones, L. H. An industry perspective on drug target validation. *Expert Opin. Drug Discov.* 11, 623–625 (2016).
131. Morgan, P. *et al.* Can the flow of medicines be improved? Fundamental pharmacokinetic and pharmacological principles toward improving Phase II survival. *Drug Discov. Today* 17, 419–424 (2012).
132. Lipinski, C. A. Lead- and drug-like compounds: The rule-of-five revolution. *Drug Discov. Today Technol.* 2004, 1, 337–341.
133. Hann, M. M., Leach, A. R. and Harper, G. Molecular complexity and the impact on fi nding leads for drug discovery. *J. Chem. Inform. Comput. Sci.* 2001, 41, 856–864.
134. Valkó, K., Bevan, C. and Reynolds, D. Chromatographic Hydrophobicity Index by Fast-Gradient RP-HPLC: A High-Throughput Alternative to log P/log D. *Anal. Chem.* 1997, 69, 2022–2029.
135. Wohnsland, F. & Faller, B. High-throughput permeability pH profile and high-throughput alkane/water log P with artificial membranes. *J. Med. Chem.* 2001, 44, 923–930.
136. Hobbs, A. N. and Young, R. J. Practical purification of hydrophilic fragments and lead/drug-like molecules by reverse phase flash chromatography: Tips, tricks and contemporary developments. *Drug Discov. Today*, 2013, 18, 148–154.
137. Wan, H. *et al.* High-throughput screening of pKa values of pharmaceuticals by pressure-assisted capillary electrophoresis and mass spectrometry. *Rapid Commun. Mass Spectrom.* 2003, 17, 2639–2648.
138. Xing, L. and Glen, R. C. Novel methods for the prediction of logP, Pka, and logD. *J. Chem. Inf. Comput. Sci.* 2002, 42, 796–805.
139. Bhattachar, S. N., Wesley, J. A. and Seadeek, C. Evaluation of the chemiluminescent nitrogen detector for solubility determinations to support drug discovery. *J. Pharm. Biomed. Anal.* 2006, 41, 152–157.
140. Yamazaki, K. and Kanaoka, M. Computational prediction of the plasma protein-binding percent of diverse pharmaceutical compounds. *J. Pharm. Sci.* 2004, 93, 1480–1494.
141. Abraham, M. H., Grellier, P.L., Prior, D.V., Duce, P.P., Morris, J.J., Taylor, P.J. Hydrohen bonding- part7 a scale of solute hydrgen-bond acidity based on logK values for complexation in tetrachloromethane. *J. Chem. Soc. Perkin Trans.* 1989, 2, 699–711.

142. Gordon, L. J., Allen, M., Artursson, P., Hann, M.M., Leavens, B.J., Mateus, A., readshaw, S., Valko, K., Wayne, G.J. and West.A. *et al.* Direct Measurement of Intracellular Compound Concentration by RapidFire Mass Spectrometry Offers Insights into Cell Permeability. *J. Biomol. Screen.* 2016, 21, 156–164.
143. Lipinski, C. American Pharmaceutical Review - Poor Aqueous Solubility – an Industry Wide Problem in Drug Discovery American Pharmaceutical Review - Poor Aqueous Solubility – an Industry Wide Problem in Drug Discovery. *Am. Pharm. Rev.* 2009, 38–40.
144. Comer, J. and Box, K. High throughput measurement of drug pKa values for ADME screening. *J. Assoc. Lab. Autom.* 2003, 8, 55–59.
145. Lepont, C. and Poole, C. F. Retention characteristics of an immobilized artificial membrane column in reversed-phase liquid chromatography. *J. Chromatogr.* 2002, 946, 107–124.
146. Marsh, K. N., Boxall, J. A. and Lichtenthaler, R. Room temperature ionic liquids and their mixtures - A review. *Fluid Phase Equilib.* 2004, 219, 93–98.
147. Leo, A., Jow, P. Y. C., Silipo, C. and Hansch, C. Calculation of Hydrophobic Constant (Log P) from π and f constants. *J. Med. Chem.* 1975, 18, 865–868.
148. Alexandrov, A., Ionescu, M. F., Schauser, K. E. and Scheiman, C. LogGP : Incorporating Long Messages into the LogP Model for Parallel Computation. *J.Parallel Distrib. Comput.* 1997, 79, 71–79.
149. Mannhold, R., Poda, G. I., Ostermann, C. and Tetko, I. V. Calculation of Molecular Lipophilicity : State-of-the-Art and Comparison of Log P Methods on More Than 96 , 000 Compounds. *J Pharm.Sci.* 2009, 98, 861–893.
150. SIUZDAK, G. An introduction to mass spectrometry ionization: An excerpt from The Expanding Role of Mass Spectrometry in Biotechnology, 2nd ed.; MCC Press: San Diego, 2005. *J. Assoc. Lab. Autom.* 2004, 9, 50–63.
151. Kruve, A., Künnapas, A., Herodes, K. and Leito, I. Matrix effects in pesticide multi-residue analysis by liquid chromatography-mass spectrometry. *J. Chromatogr.* 2008, 1187, 58–66.
152. Oss, M., Kruve, A., Herodes, K. and Leito, I. Electrospray ionization efficiency scale of organic compound. *Anal. Chem.* 2010, 82, 2865–2872.
153. Vorng, J.-L., Kotowska, A.M., Passarelli, M.K., West, A., Marshall, P.S., Havelund, R., Seah, M.P., Dollery, C.T., Rakowska, P.D., Gilmore, I.S. Semi-empirical rules to determine drug sensitivity and ionization efficiency in SIMS using a model tissue sample. *Anal. Chem.* 2016, 88, 11028–11036.
154. singh, B.N, Williams and E.M.V. The effect of amiodarone, a new anti-anginal drug on cardiac Muscle. Br.J.Pharmac. 1970, 39, 657–667.
155. Rosenbaum, M. B. *et al.* Clinical efficacy of amiodarone as an antiarrhythmic agent. *Am. J. Cardiol.* 1976, 38, 934–944.
156. Hondeghem, L. M. Classification of antiarrhythmic agents and the two laws of pharmacology. *Cardiovasc. Res.* 2000, 45, 57–60.
157. Connolly, S. J. Evidence based analysis of amiodarone efficacy and safety. *Circulation* 1999, 100(19), 2025–2034.
158. Holt, D. W., Tucker, G. T., Jackson, P. R. and Storey, G. C. A. Amiodarone pharmacokinetics. *Am. Heart J.* 1983, 106, 840–847.
159. Siddoway, L.A. Amiodarone: Guidelines for use and monitoring. *AmFamPhysician*. 2003, 68(11), 2189-2197.
160. Rose, E. P. Thyroid dysfunction during chronic amiodarone therapy. *J. Am. Coll. Cardiol.* 1987, 9, 175–183.
161. Rappersberger K., Hönigsmann H., Ortel B., Tanew A., Konrad K. Photosensitivity and Hyperpigmentation in Amiodarone-treated patients: Incidence, Time Course and Recovery. *J.of Inv.Derm*. 1989, 93(2), 201-209.
162. Kounis, N. G., Frangides, C., Papadaki, P. J., Zavras, G. M. and Goudevenos, J. Dose-dependent appearance and disappearance of amiodarone-induced skin pigmentation. *Clin. Cardiol.* 1996, 19, 592–594.
163. Wolkove, N., Baltzan, M. Amiodarone pulmonary toxicity. *CanRespirJ*. 2009, 16(2) 43-48
164. Papiris, S. A., Triantafillidou, C., Kolilekas, L., Markoulaki, D. and Manali, E. D. Amiodarone:

Review of pulmonary effects and toxicity. *Drug Saf.* 2010, 33, 539–558.
165. Latini, R., Tognoni, G. and Kates, R. E. Clinical Pharmacokinetics of Amiodarone. *Clin. Pharmacokinet.* 1984, 9, 136–156.
166. Matsuno, O. Drug-induced interstitial lung disease: Mechanisms and best diagnostic approaches. *Respir. Res.* 2012, 13, 1–9.
167. Schwaiblmair, M. Drug Induced Interstitial Lung Disease. *Open Respir. Med. J.* 2012, 6, 63–74.
168. Lesko, L. J. Pharmacokinetic drug interactions with amiodarone. *Clin.Pharmacokinet.* 1989, 17, 130–140
169. Boutitie, F., Boissel, J.P., Connolly, S.J., Camm, A.J., Cairns, J.A., Julians, D.G., Gent, M., janse, M.J., Dorian, P., Frangin, G. Amiodarone interaction with beta-blockers: analysis of merged EMIAT and CAMIAT databases. *Circulation*, 1999, 99(17), 2268-2275.
170. Abe, A. and Shayman, J. A. The role of negatively charged lipids in lysosomal phospholipase A2 function. *J. Lipid Res.* 2009, 50, 2027–2035.
171. Helmke, R. J., Boyd, R.L., German, V.F., and Mangos J.A. From growth factor dependence to growth factor responsiveness: the genesis of and alveolar macrophage cell line. *InVitroCell&developBio.* 1987, 23(8), 567-574.
172. Patton, G. W., Paciga, J. E. and Shelley, S. A. NR8383 alveolar macrophage toxic growth arrest by hydrogen peroxide associated with induction of growth-arrest and DNA damage-inducible genes GADD45 and GADD153. *Toxicol. Appl. Pharmacol.* 1997, 147, 126–134.
173. Helmke, R. J., German, V. F. & Mangos, J. A. A countinous alveolar macrophage cell line:comparison with freshly derived alveolar macrophages. *InVitroCell&developBio.* 1989, 25(1), 44-48.
174. Wong, L. Y. F., Cheung, B. M. Y., Li, Y.-Y. and Tang, F. Adrenomedullin Is Both Proinflammatory and Antiinflammatory: Its Effects on Gene Expression and Secretion of Cytokines and Macrophage Migration Inhibitory Factor in NR8383 Macrophage Cell Line. *Endocrinology*, 2005, 146, 1321–1327.
175. Lane, K. B., Egan, B., Vick, S., Abdolrasulnia, R. and Shepherd, V. L. Characterization of a rat alveolar macrophage cell line that expresses a functional mannose receptor Abstract : The mannose receptor is a single poly- peptide transmembrane glycoprotein expressed on the surface of macrophages that binds and internal-. *J. Leukoc. Biol.* 1988, 64, 345–350.
176. garn, H., Schmidt, A., Grau, V. Stumpf, S., Kaufmann, A., Becker, M. Gemsa, D. and Siese, A. IL-24 is Expressed by Rat and Human Macrophages. *Immunobiology*, 2002, 205, 321–334.
177. Hino, M., Oda, M., Yoshida, A., Nakata, K., Kohchi, C., Nishizawa, T., Inagawa, H., Hori, H., Makino, K., Terada, H., Soma, G. Establishment of an in vitro model using NR8383 cells and Mycobacterium bovis Calmette-Guerin that mimics a chronic infection of Mycobacterium tuberculosis. *In Vivo* 2005, 19, 821–830.
178. Stump, J. L. Henrietta Lacks and The HeLa Cell: Rights of Patients and Responsibilities of Medical Researchers. *Hist. Teacher* 2014, 48, 127–180.
179. Lucey, B. P., Nelson-Rees, W. A. and Hutchins, G. M. Historical Perspective Henrietta Lacks, HeLa Cells, and Cell Culture Contamination. *Arch Pathol Lab Med.* 2009, 133, 1463–1467.
180. Dumont, J., Euwart, D., Mei, B., Estes, S. and Kshirsagar, R. Human cell lines for biopharmaceutical manufacturing: history, status, and future perspectives. *Crit. Rev. Biotechnol.* 2016, 36, 1110–1122.
181. Thomas, P. and Smart, T. G. HEK293 cell line: A vehicle for the expression of recombinant proteins. *J. Pharmacol. Toxicol. Methods*, 2005, 51, 187–200.
182. Berjukow, S., Doring, F., Froschmayr, M., Grabner, M., Glossmann, H., Hering, S., Endogenous calcium channels in human embryonic kidney (HEK293) cells. *Br. J. Pharmacol.* 1996, 118, 748–54.
183. Lussier, Y.A., Xing, H.R., Salama, J.K., Khodarev, N.N, Huang, Y., Zhang, Q., Yang, X., Hasselle, M.D., Darga, T.E., Malik, R., Fan, H., Perakis, S., Filippo, M., Corbin, K., Lee, Y., Posner, M.C., Chmura, S.J, Hellmann, S and Weichselbaum, R.R. MicroRNA expression characterizing oligometastasis.. *PLOS One*, 2011, 6(12), e28650.
184. Stepanenko, A. A. and Dmitrenko, V. V. HEK293 in cell biology and cancer research: Phenotype, karyotype, tumorigenicity, and stress-induced genome-phenotype evolution. *Gene* 2015, 569,

182–190.
185. Schachter, J. B., Sromek, S. M., Nicholas, R. A. and Harden, T. K. HEK293 human embryonic kidney cells endogenously express the P2Y1 and P2Y2 receptors. *Neuropharmacology* 1997, 36, 1181–1187.
186. Ancolio, K., Alves Da Costa, C., Uéda, K. and Checler, F. α-Synuclein and the Parkinson's disease-related mutant Ala53Thr-α- synuclein do not undergo proteasomal degradation in HEK293 and neuronal cells. *Neurosci. Lett.* 2000, 285, 79–82.
187. Vincent, B., paitel, E., Frobert, Y., Lehmann, S., Grassi, J., Checler, F. . Phorbol ester-regulated cleavage of normal prion protein in HEK293 human cells and murine neurons. *J. Biol. Chem.* 2000, 275, 35612–35616.
188. Dietmair, S., Hodson, M.P., Quek, L.E., Timming, N.E., Gray, P. and Nielsen, L.K. A Multi-Omics Analysis of Recombinant Protein Production in Hek293 Cells. *PLoS One*, 2012, 7(8), e43394.
189. Mateus, A., Matsson, P. and Artursson, P. A high-throughput cell-based method to predict the unbound drug fraction in the brain. *J. Med. Chem.* 2014, 57, 3005–3010.
190. Mateus, A., Treyer, A., wegler, C., Karlgren, M., matsson, P., artursson, P. Intracellular drug bioavailability: a new predictor of system dependent drug disposition. *Sci. Rep.* 2017, 7, 43047.
191. Luckert, C., Schulz, C., Lehmann, N., Thomas, M., Hofmann, U., Hammad, S., Hengstler, J.G., Braeuning, A., Lampen, A., Hessel, S. Comparative analysis of 3D culture methods on human HepG2 cells. *Arch. Toxicol.* 2017, 91, 393–406.
192. Donato, M. T., Tolosa, L. and Gómez-Lechón, M. J. *C*ulture and Functional Characterization of Human Hepatoma HepG2 Cells. *Protocols in In Vitro Hepatocyte Research* 2015, 1250, 77-93.
193. Geiger, T., Wehner, A., Schaab, C., Cox, J. and Mann, M. Comparative Proteomic Analysis of Eleven Common Cell Lines Reveals Ubiquitous but Varying Expression of Most Proteins. *Mol. Cell. Proteomics* 2012, 11(3), M111.014050.
194. RATLEDGE, C. *Mycobacteria, 1st edition*, Wiley-Blackwell, 1999.
195. Gutierrez, M.C., Brisse, S., Brosch, R., Fabre, M., Omais, B., Marmiesse, M., supply, P, Vincent, V. Ancient origin and gene mosaicism of the progenitor of Mycobacterium tuberculosis. *PLoS Pathog.* 2005, 1, 0055–0061.
196. RYAN, Kenneth, and George C. Ray, *Sherris Medical Microbiology 6th edition* McGraw Hill 2004.
197. Daniel, T. M. The history of tuberculosis. *Respir. Med.* 2006, 100, 1862–1870.
198. United States Environment Protection Agency (EPA). *Mycobacteria : Health Advisory*.1999, doi:EPA-822-B-01-007
199. Fogel, N. Tuberculosis: A disease without boundaries. *Tuberculosis*, 2015, 95, 527–531.
200. Gupta, A., Kaul, A., Tsolaki, A. G., Kishore, U. and Bhakta, S. Mycobacterium tuberculosis: Immune evasion, latency and reactivation. *Immunobiology*, 2012, 217, 363–374.
201. Ernst, J. D.Macrophage Receptors for Mycobacterium tuberculosis. *Infect. Immun.* 1998, 66, 1277–1281.
202. Logan, P. M., Primack, S. L., Staples, C., Miller, R. R. and Müller, N. L. Acute Lung Disease in the Immunocompromised Host. *Chest* 1995, 108, 1283–1287.
203. Sester, M. *et al.* Risk assessment of tuberculosis in immunocompromised patients: A TBNET study. *Am. J. Respir. Crit. Care Med.* 2014, 190, 1168–1176.
204. World Health Organization. Treatment of tuberculosis. 2010 Available from https://www.who.int/tb/publications/2010/9789241547833/en/
205. Hazbón, M. H. *et al.* Population genetics study of isoniazid resistance mutations and evolution of multidrug-resistant Mycobacterium tuberculosis. *Antimicrob. Agents Chemother.* 2006, 50, 2640–2649.
206. Ryoo, H. N. J. and S. *First– and Second–Line Drugs and Drug Resistance*. (InTech, 2013).
207. Telenti, A., Imboden, P., Marchesi, F., Matter, L., Schopfer, K., Bodmer, T., Lowrie, D., Colston, M.J., Cole, S. *The Lancet*, 1993, 341(8846), 647-651.
208. Somoskovi, A., Parsons, L. M. and Salfinger, M. The molecular basis of resistance to isoniazid, rifampin, and pyrazinamide in Mycobacterium tuberculosis. *Respir. Res.* 2001, 2, 164–168.
209. Udwadia, Z. F., Amale, R. A., Ajbani, K. K. and Rodrigues, C. Totally Drug-Resistant

Tuberculosis in India T o the E ditor — Three years after ex- losis was first described in 2006 , Velayati et al [1] drew attention to the emergence of totally drug-resistant (TDR) tuberculosis in a cohort of 15 patients from. *Clin. Infect. Dis.* 2006, 54, 579–581.

210. de Sumnienski Rodrigues, V. F. *et al.* Characterization of pncA Mutations in Pyrazinamide-Resistant Mycobacterium tuberculosis in Brazil. *Antimicrob. Agents Chemother.* 2005, 49, 444–446.
211. Leibold, J. E. The ocular toxicity of ethambuutol and its relation to dose. *AnnNYAcadSci.* 1966, 135(2), 904-909
212. Brennan, P. J. Biogenesis of the Mycobacterial Cell Wall and the Site of Action of Ethambutol AND. 1995, 39, 2484–2489.
213. REBROVA, Eva Maria. *Cell wall remodeling proteins in mycibaterium tuberculosis: structure, function and inhibition,* PhD thesis, Karoliska Institute, 2017.
214. Korf, J., Stoltz, A., Verschoor, J., De Baetselier, P. and Grooten, J. The Mycobacterium tuberculosis cell wall component mycolic acid elicits pathogen-associated host innate immune responses. *Eur. J. Immunol.* 2005, 35, 890–900.
215. Brennan, P. J. Structure, function, and biogenesis of the cell wall of Mycobacterium tuberculosis. *Tuberculosis,* 2003, 83, 91–97.
216. Wolfe, L. M., Mahaffey, S. B., Kruh, N. A.and Dobos, K. M. Proteomic definition of the cell wall of *Mycobacterium tuberculosis*. *J. Proteome Res.* 2010, 9, 5816–5826.
217. Abrahams, K. A. and Besra, G. S. Mycobacterial cell wall biosynthesis: a multifaceted antibiotic target. *Parasitology*, 2016, 1–18.
218. Milstien, J. B. and Gibson, J. J. Quality control of BCG vaccine by WHO: a review of factors that may influence vaccine effectiveness and safety. *Bull. World Health Organ.* 1990, 68, 93–108.
219. Langermans, J. A. *et al.* Divergent effect of bacillus Calmette-Guérin (BCG) vaccination on Mycobacterium tuberculosis infection in highly related macaque species: implications for primate models in tuberculosis vaccine research. *Proc. Natl. Acad. Sci. U. S. A.* 2001, 98, 11497–502.
220. Sarhan, M. A. Tuberculosis vaccine. *Saudi Med. J.* 2010, 31, 9–13.
221. Oettinger, T., Jorgensen, M., Laefoged, A., Haslow, K.and Anderson, P.Development of the Mycobacterium bovis BCG vaccine: review of the historical and biochemical evidence for a genealogic tree. 1999, 79(4), 243-250.
222. Hermans, P., vanSoolingen, D., Bik, E.M., de Hass, P.E., Dale, J.W., vanEmbden, J.D. Insertion element IS987 from Mycobacterium bovis BCG is located in a hot-spot integration region for insertion elements in Mycobacterium tuberculosis complex strains. *Infect. Immun.* 1991, 59, 2695–2705.
223. Winder, F.G., Collins, P.B., Whelan, D. Effects of Ethionamide and Isoxyl on Mycolic Acid Synthesis in mycobaterium tuberculosis. *JGenMicrobiol*, 1971, 66(3), 379-380 379–380.
224. Bardarov, S., Bardarov, S.J., Pavelka, M.S.J., Sambandamurthy, V., Larsen, M., Tufariello, J., Chan, J., Hatfull, G., Jacobs, W.J. An efecient method for generating marked and unmarked targeted gene disruptions in. *Microbiology* 2002, 148, 3007–3017.
225. Advisory Committee on Dangerous Pathogens (ACDP). The Approved List of Biological Agents. *Heal. Saf. Exec.* 1–32 ,2013.
226. Herman, P. *et al.* Biosafety Recommendations for the Contained Use of Mycobacterium tuberculosis Complex Isolates in Industrialized Countries . *Div. Biosaf. Biotechnol.* 1–17, 2006.
227. World Heath Organization, TUBERCULOSIS laboratory safety manual,2012.
228. Mahairas, G., Sabo, P.J., Hickey, M.J., Singh, D.C., Stover, C.K., Molecular analysis of genetic differences between Mycobacterium bovis BCG and virulent M . bovis. *JBacteriol*.1996, 178(5), 1274–1282.
229. Pym, A. S., Brodin, P., Brosch, R., Huerre, M. and Cole, S. T. Loss of RD1 contributed to the attenuation of the live tuberculosis vaccines Mycobacterium bovis BCG and Mycobacterium microti. *Mol. Microbiol.* 2002, 46, 709–717.
230. Beckman Coulter Reference Vi-Cell Manual, 2003.
231. Tamase, A. *et al.* Identification of tumor-initiating cells in a highly aggressive brain tumor using

promoter activity of nucleostemin. *Proc. Natl. Acad. Sci. U. S. A.* 2009, 106, 17163–17168.
232. Kuse, M., Sharma, T. and Gupta, S. A classification scheme for lymphocyte segmentation in H&E stained histology images. *Lect. Notes Comput. Sci. 2010*, 6388, 235–243.
233. Healthcare, G. E. IN Cell Analyzer 2000. 28–31, 2000.
234. Eliceiri, K. W. *et al. Biological imaging software tools*. *Nat. Methods* 2012, 9(7), 697-710.
235. Zuba-Surma, E. K., Kucia, M., Abdel-Latif, A., Lillard, J. W. and Ratajczak, M. Z. The ImageStream system: A key step to a new era in imaging. *Folia Histochem. Cytobiol.* 2007, 45, 279–290.
236. Corporation, A. Image Data Exploration and Analysis Software User ' s Manual. *Popul. (English Ed.* 206–374, 2009.
237. Thermofisher. Nanodrop, 2000.
238. López-Ferrer, D., Ramos-Fernández, A., Martínez-Bartolomé, S., García-Ruiz, P. and Vázquez, J. Quantitative proteomics using 16O/18O labeling and linear ion trap mass spectrometry. *Proteomics*, 2006, 6, S4–S11.
239. Rappsilber, J., Ishihama, Y. and Mann, M. Stop And Go Extraction tips for matrix-assisted laser desorption/ionization, nanoelectrospray, and LC/MS sample pretreatment in proteomics. *Anal. Chem.* 2003, 75, 663–670.
240. Hosp, F., Scheltema, R.A., Eberl, H.C., Kulak, N.A., keilhauer, E.C., Mayr, K., mann, M.A Double-Barrel Liquid Chromatography-Tandem Mass Spectrometry (LC-MS/MS) System to Quantify 96 Interactomes per Day. *Mol. Cell. Proteomics*, 2015, 14, 2030–2041.
241. Končarević, S., LoBner, C., Kuhn, K., Prinz, T., Pike, I., Zucht, H.D.. In-depth profiling of the peripheral blood mononuclear cells proteome for clinical blood proteomics. *Int. J. Proteomics* 2014, 129259.
242. Ferreira, J. A. The Benjamini-Hochberg method in the case of discrete test statistics. *Int. J. Biostat.* 2007, 3 (1).
243. Nesvizhskii, A. I., Keller, A., Kolker, E. and Aebersold, R. A Statistical Model for Identifying Proteins by Tandem Mass Spectrometry abilities that proteins are present in a sample on the basis. *Anal. Chem.* 2003, 75, 4646–4658.
244. Gatto, L., Breckels, L. M., Naake, T.and Gibb, S. Visualization of proteomics data using R and Bioconductor. *Proteomics*, 2015, 15, 1375–1389.
245. Li, Y., Andersen, H.-E.and McGaughey, R. A Comparison of Statistical Methods for Estimating Data. *J. Appl. For.* 2008, 23, 223–231.
246. Lever, J., Krzywinski, M.and Altman, N. Points of Significance: Principal component analysis. *Nat. Methods*, 2017, 14, 641–642.
247. Szklarczyk, D. *et al.* STRING v10: Protein-protein interaction networks, integrated over the tree of life. *Nucleic Acids Res.* 2015, 43, D447–D452.
248. Peake, D. A., Kiyonami, R., Yokoi, Y., Fukamachi, Y., Huang, Y.. Processing of a Complex Lipid Dataset for the NIST Inter-laboratory Comparison Exercise for Lipidomics Measurements in Human Serum and Plasma. ThermoFisherScientific Poster Note 64471.
249. Bich, C., havelond, R., Moellers, R., Touboult, D., Kollmer, F., Niehuis, E., Gilmore, I.S., Brunelle, A. Argon cluster ion source evaluation on lipid standards and rat brain tissue samples. *Anal. Chem.* 2013, 85, 7745–7752.
250. Grebe, S. K. G. and Singh, R. J. LC-MS / MS in the Clinical Laboratory – Where to From Here ? *ClinBiochemRev*. 2011, 32(1), 5–31.
251. Franzblau, S. G. *et al.* Rapid, low-technology MIC determination with clinical Mycobacterium tuberculosis isolates by using the microplate Alamar Blue assay. *J. Clin. Microbiol.* 1998, 36, 362–366.
252. Sheldon, R. S., Hill, R. J., Cannon, N. J. and Duff, H. J. Amiodarone: biochemical evidence for binding to a receptor for class I drugs associated with the rat cardiac sodium channel. *Circulation Research*, 1989, 65, 477–483
253. Wang, F., Agnihotri, A., Adabag, S. and Roukoz, H. Clinical Utility of Plasma Amiodarone Level Measurement : A Single Center Experience. *Innov. Card. Rythm Manag.* 2011, 2, 508–511.
254. Hrudikova Vyskocilova, E., Grundmann, M., Duricova, J. and Kacirova, I. Therapeutic monitoring of amiodarone: Pharmacokinetics and evaluation of the relationship between effect

and dose/concentration. *Biomed. Pap.* 2017, 161, 134–143.
255. Bedrossian, C. W. M., Warren, C., Ohar, J. and Bhan, R. Amiodarone Pulmonary Toxicity : cytopathology, ultrastructure and immunocytochemistry. 1997, 1, 47–56.
256. Ott, M. C., Khoor, A., Leventhal, J. P., Paterick, T. E.and Burger, C. D. Pulmonary toxicity in patients receiving low-dose amiodarone. *Chest*, 2003, 123, 646–651.
257. Mosser, D. M. and Edwards, J. P. Exploring the full spectrum of macrophage activation. *NatRev Immunol*, 2008, 8(12), 958–969.
258. Wager, C. M. L.and Wormley, F. L. Classical versus alternative macrophage activation: the Ying and the Yang in host defense against pulmonary fungal infections. *Mucosal Immunol.* 2014, 7, 1–13.
259. Mao, J. S., Liu, H. F., Yin, Y. J. and Yao, K. De. The properties of chitosan-gelatin membranes and scaffolds modified with hyaluronic acid by different methods. *Biomaterials*, 2003, 24, 1621–1629.
260. Ritchie, T. J. and Macdonald, S. J. F. Physicochemical descriptors of aromatic character and their use in drug discovery. *J. Med. Chem.* 2014, 57, 7206–7215.
261. Sieweke, M. H. and Allen, J. E. Beyond stem cells: Self-renewal of differentiated macrophages. *Science*, 2013, 80 342.
262. Bell, C. C. *et al.* Characterization of primary human hepatocyte spheroids as a model system for drug-induced liver injury, liver function and disease. *Sci. Rep.* 2016, 6, 25187.
263. van Summeren, A., Renes, J., Bouwman, F.G., Noben, J.P., van Delft, J.H, kleinjans, J.C., Mariman, E.C., Proteomics investigations of drug-induced hepatotoxicity in HepG2 cells. *Toxicol. Sci.* 2011, 120, 110–122.
264. Love, M. I., Huber, W. and Anders, S. Moderated estimation of fold change and dispersion for RNA-seq data with DESeq2. *Genome Biol.* 2014, 15, 1–21.
265. Langley, S. R. and Mayr, M. Comparative analysis of statistical methods used for detecting differential expression in label-free mass spectrometry proteomics. *J. Proteomics* 2015, 129, 83–92.
266. Facchiano, A. and Facchiano, F. Transglutaminases and their substrates in biology and human diseases: 50 Years of growing. *Amino Acids*, 2009, 36, 599–614.
267. Allam, H., Aoki, K., Benigno, B.B., McDonald, J.F., Mackintosh, S.G., Tiemeyer, M., Abbott, K.L. Glycomic analysis of membrane glycoproteins with bisecting glycosylation from ovarian cancer tissues reveals novel structures and functions. *J. Proteome Res.* 2015, 14, 434–446.
268. Storch, J. and Corsico, B. The Emerging Functions and Mechanisms of Mammalian Fatty Acid – Binding Proteins. *Annu Rev Nutr.* 2008, 28, 73-95.
269. Quindere, A., Benevides, N.M.B., Carbone, F., Mach, F. Update on selective treatments targeting neutrophilic inflammation in atherogenesis and atherothrombosis. *Thrombosis and Haemostasis*, 2014, 111(4), 634–646.
270. He, J., liv, Y., Xie, X., Zhu, T., Soules, M., DiMeco, F., Vescovi, A.L., Fan, X., Lubman, D.M. Identification of Cell Surface Glycoprotein Markers for Glioblastoma-Derived Stem-Like Cells Using a Lectin Microarray and LC - MS / MS Approach. *J Proteome Res*, 2010, 9(5), 2565–2572.
271. Furuhashi, H., Takasaki, T., rechtsteiner, A., Li, T., Kimura, H., Checchi, P.M., Stome, S., Kelly, W.G. trans-generational epigenetic regulation of C.elegans primordian germ cells. *Epigenetics and Chromatin*, 2010, 3(15).
272. Halliwell, W. H. Amphiphilic Drug-Induced Phospholipidosis.*Toxicol Pathol* , 1997, 25(1), 53-60.
273. Anderson, N. & Borlak, J. Drug-induced phospholipidosis. *FEBS Lett.* 580, 5533–5540 (2006).
274. Baronas, E. T., Lee, J. W., Alden, C. and Hsieh, F. Y. Biomarkers to monitor drug-induced phospholipidosis. *Toxicol. Appl. Pharmacol.* 2007, 218, 72–78.
275. Goda, K. *et al.* Evaluation of the Potential Risk of Drugs to Induce Hepatotoxicity in Human—Relationships between Hepatic Steatosis Observed in Non-Clinical Toxicity Study and Hepatotoxicity in Humans-. *Int. J. Mol. Sci.* 2017, 18, 810.
276. Rusinova, R., Koeppe, R. E. and Andersen, O. S. A general mechanism for drug promiscuity: Studies with amiodarone and other antiarrhythmics. *J. Gen. Physiol.* 2015, 146, 463–475.

277. Mortuza, G. B., Neville, W. A., Delaney, J., Waterfield, C. J. and Camilleri, P. Characterisation of a potential biomarker of phospholipidosis from amiodarone-treated rats. *Biochim. Biophys. Acta - Mol. Cell Biol. Lipids*, 2003, 1631, 136–146.
278. Mosser, D. M. The many faces of macrophage activation. *J. Leukoc. Biol.* 2003, 73, 209–212.
279. Irvine, J. D. *et al.* MDCK (Madin − Darby Canine Kidney) Cells: A Tool for Membrane Permeability Screening. *J. Pharm. Sci.* 1999, 88, 28–33.
280. Orlov, S. N., Platonova, A. A., Hamet, P. and Grygorczyk, R. Cell volume and monovalent ion transporters: their role in cell death machinery triggering and progression. *AJP Cell Physiol.* 2013, 305, C361–C372.
281. Passarelli, M. K. *et al.* The 3D OrbiSIMS—label-free metabolic imaging with subcellular lateral resolution and high mass-resolving power. *Nat. Methods* (2017). doi:10.1038/nmeth.4504
282. Nakano, S. *et al.* Evaluation of matrix effects on TOF-SIMS data of leu-enkephalin and 1,2-dioleoyl- *sn - glycero* -3-phosphocholine mixed samples. *Biointerphases, 2018,* 13, 03B403.
283. Goodman, S. N. Toward Evidence-Based Medical Statistics. 1: The P value fallacy. *Ann Intern Med*. 1999, 130(12), 995-1004.
284. Lorenz, M., Shard, A. G., Counsell, J. D. P., Hutton, S. and Gilmore, I. S. Angular Distribution of Molecules Sputtered by Gas Cluster Ion Beams and Implications for Secondary Neutral Mass Spectrometry. *J. Phys. Chem.* 2016, 120, 25317–25327.
285. Avdeef, A. pH-Metric Log-P .2. Refinement of Partition-Coefficients and Ionization-Constants of Multiprotic Substances. *J. Pharm. Sci.* 1993, 82, 183–190.
286. Casey, J. R., Grinstein, S. and Orlowski, J. Sensors and regulators of intracellular pH. *Nat. Rev. Mol. Cell Biol.* 2010, 11, 50–61.
287. Wouters, F. S., Verveer, P. J. and Bastiaens, P. I. H. Imaging biochemistry inside cells. *Trends Cell Biol.* 2001, 11, 203–211.
288. Chacon, E. *et al.* Distribution of electrical potential, pH, free Ca2+, and volume inside cultured adult rabbit cardiac myocytes during chemical hypoxia: a multiparameter digitized confocal microscopic study. *Biophys. J.* 1994, 66, 942–952.
289. Webb, B. A., Chimenti, M., Jacobson, M. P. and Barber, D. L. Dysregulated pH: a perfect storm for cancer progression. *Nat. Rev. Cancer*, 2011, 11, 671–677.
290. Dressman, J.B., Amidon, G.L., Reppas, C., and Shah, V.P. Dissolution testing as a prognostic tool for oral drug adsorption:immediate release dosage form. *Pharm Res*. 1998, 15(1) 11-22.
291. Caulfield, A. J. and Wengenack, N. L. Diagnosis of active tuberculosis disease: From microscopy to molecular techniques. *J. Clin. Tuberc. Other Mycobact. Dis.* 2016, 4, 33–43.

Annex

Reagents list

Reagent/ Media	Reference	Manufacturer	Purpose
F-12K Nutrient Mixture Kaighn's Modification media	21127-022	Gibco	NR8383 cells growth media
Heat inactivated Fetal Bovine Serum (FBS)	10100-147	Gibco	All media supplement
Nunc Lab-Tek II Chamber slide system	C6807	Thermo	Cell growth chambers
Ammonium Formate	70222	Sigma	Cell washing buffer
Amiodarone	A8426-5G	Sigma	Drug
4 % Parafix solution	PRC/R/38	Pioneer Research Chemicals	Fixative agent prior to HE staining
Harris 'modified haematoxylin	HHS32-1L	Sigma	HE reagent
Acid alcohol	56694-100ML-F	Sigma	HE reagent
Eosin	HT110232	Sigma	HE reagent
Ethanol	51976	Sigma	HE reagent
DPX mountant for histology	06522-100ML	Sigma	
Lysotracker red	L7528	Life technologies	Fluorescence microscopy
DAPI with Fluoroshield	F6057	Sigma	Fluorescence microscopy
Greiner 96 well u-clear plate	655090	Greiner Bio-one	Fluorescence microscopy
Hoechst 33342	H3570	Thermo	Fluorescence microscopy
Lysotracker Red DND-99	L7528	Thermo	Fluorescence microscopy

PBS	10010015	Gibco	Cell wash
Cell Tracker Red CMTPX	C34552	Thermo	Fluorescence microscopy
Petri dishes (170 µm bottom	81158	Ibidi	Fluorescence microscopy
Dulbecco's Modified Eagle Medium/Nutrient Mixture F-12	31331	Gibco	HeLa cells growth media
cOmplete™, Mini, EDTA-free Protease Inhibitor Cocktail	000000004693159001	Roche	Proteomics buffer
Urea	U5128	Sigma	Proteomics buffer
Dithiothreitol	D0632	Sigma	Proteomics sample preparation
Iodoacetamide	I1149	Sigma	Proteomics sample preparation
Ammonium Bicarbonate	09830	Sigma	Proteomics sample preparation
LC-MS Water Optima	W61	Thermo	LC-MS/MS
LC-MS acetonitrile Optima	A9551	Thermo	LC-MS/MS
Nunc cell scraper	179707	Thermo	Cell culture
Methanol HPLC grade	494291	Sigma	Lipid preparation
Chloroform	1601383	Sigma	Lipid preparation
ProNet cell lysis buffer Tris pH7.6	NA	ESI Source Solution	Cell lysis
Acquity UPLC BEH C18 1.7 µm 2.1x50 mm	176000863	Waters	LC-MS/MS
Acquity UPLC BEH C18 VanGuard cartridge 1.7 µm 2.1x5 mm	1760003975	Waters	LC-MS/MS
DMSO	276855	Sigma	Solvent
Middlebrook 7H9	M0178	Sigma	BCG media

ADC supplement	M0553	Sigma	BCG media
Tween 80	P8074	Sigma	BCG media
Chloroquine	C6628	Sigma	Compound

LC-MS/MS Lipid method

Method of Q Exactive

Overall method settings

Global Settings		
use lock masses	best	
Lock mass injection	–	
Chrom. peak width (FWHM)	15	s
Time		
Method duration	60.00	min
Customized Tolerances (+/-)		
Lock Masses	–	
Inclusion	–	
Exclusion	–	
Neutral Loss	–	
Mass Tags	–	
Dynamic Exclusion	–	

Experiment

Full MS / dd-MS² (TopN)

General		
Runtime	0 to 60	min
Polarity	Positive	
In-source CID	0.0	eV
Default charge state	2	
Inclusion	–	
Exclusion	–	
Tags	–	
Full MS		
Microscans	1	
Resolution	70,000	
AGC target	1e6	
Maximum IT	200	ms
Number of scan ranges	1	
Scan range	120 to 1800	m/z
Spectrum data type	Profile	
dd-MS² / dd-SIM		
Microscans	1	
Resolution	17,500	
AGC target	1e5	
Maximum IT	70	ms
Loop count	10	
MSX count	1	
TopN	10	
Isolation window	4.0	m/z
Isolation offset	0.0	m/z
Scan range	200 to 2000	m/z
Fixed first mass	50.0	m/z
NCE / stepped NCE	26	
Spectrum data type	Profile	
dd Settings		
Underfill ratio	1.0	%
Intensity threshold	1.4e4	
Apex trigger	3 to 8	s
Charge exclusion	unassigned, 4 - 8, >8	
Peptide match	Off	
Exclude isotopes	on	
Dynamic exclusion	10.0	s
If idle ..	do not pick others	

Setup

Tunefiles

General	
Switch Count	0
Base Tunefile	C:\Thermo\nanoTune.mstune

Mass [m/z]	Polarity	Start [min]	End [min]	Comment
391.28429	Positive			
429.08875	Positive			
445.12003	Positive			

Sample pickup:_

Volume [µl]	: 2.00
Flow [µl / min]	: 20.00

Sample loading:_

Volume [µl]	: 6.00
Flow [µl / min]	: (unspecified)
Max. pressure [Bar]	: 800.00

Gradient:_

Time [mm:ss]	Duration [mm:ss]	Flow [nl/min]	Mixture [%B]
00:00	00:00	300.00	30.00
03:00	03:00	300.00	30.00
08:00	05:00	300.00	45.00
10:00	02:00	300.00	52.00
16:00	06:00	300.00	58.00
22:00	06:00	300.00	66.00
28:00	06:00	300.00	70.00
36:00	08:00	300.00	75.00
42:00	06:00	300.00	97.00
50:00	08:00	300.00	97.00
58:00	08:00	300.00	97.00
60:00	02:00	300.00	30.00

Pre-column equilibration:_

Volume [µl]	: 8.00
Flow [µl / min]	: (unspecified)
Max. pressure [Bar]	: 800.00

Analytical column equilibration:_

Volume [µl]	: 6.00
Flow [µl / min]	: (unspecified)
Max. pressure [Bar]	: 800.00

Auto-sampler wash:_

Flush volume [µl]	: 100.00

Mobile phase A: 10mM ammonium formate, 0.1% formic acid 60% acetonitrile and 40% water

Mobile phase B: 10mM ammonium formate, 0.1% formic acid 90% 2-isopropanol and 10% acetonitrile

Column: Accucore C18, 2.6um, 150A 75umx15 cm (ES811, Thermo)

LipidSearch parameters

Target database: QExactive

Search type: Product

Experiment type: LC-MS

Precursor tolerance: 5ppm

Product tolerance 8 ppm

Intensity threshold of the product ion : 5%

m-score threshold: 3

M/z tolerance: +/-5 ppm

Retention time rande (min):+/-1

Main node filter: Main isomer peak

m-score threshold display: 3

ID quality filter: A, B, C and D

BCG drug resistance

Table: First- and second-line drugs, MICs and mechanisms of drug resistance

Drug	**MIC (mg/L)**	**Gene**	**Role of gene product**
Isoniazid	0.02–0.2 (7H9/7H10)	*katG*	catalase/peroxidase
		inhA	enoyl reductase
		ahpC	alkyl hydroperoxide reductase
Rifampicin	0.05–0.1 (7H9/7H10)	*rpoB*	β-subunit of RNA polymerase
Pyrazinimide	16–50 (LJ)	*pncA*	PZase
Streptomycin	2–8 (7H9/7H10)	*rpsL*	S12 ribosomal protein
		rrs	16S rRNA
		gidB	7-methylguanosine methyltransferase
Ethambutol	1–5 (7H9/7H10)	*embB*	arabinosyl transferase
Fluoroquinolones	0.5–2.0 (7H9/7H10)	*gyrA/gyrB*	DNA gyrase
Kanamycin	2–4 (7H9/7H10)	*rrs*	16S rRNA
		eis	aminoglycoside acetyltransferase
Amikacin	2–4 (7H9/7H10)	*rrs*	16S rRNA
Capreomycin	2-4 (7H9/7H10)	*rrs*	16S rRNA
		tylA	rRNA methyltransferase
Ethionamide	2.5–10 (7H11)	*inhA*	enoyl reductase
p-aminosalicylic acid	0.5 (LJ)	*thyA*	thymidylate synthase A

Positive and negative secondary ions used for Orbitrap MS calibration.

Cluster	m/z $[Ag_n]^+$	m/z $[Ag_n]^-$
^{107}Ag	106.9045	106.9056
^{109}Ag	108.9042	108.9053
$^{107}Ag^{109}Ag$	215.8093	215.8104
$^{107}Ag_2^{109}Ag$	322.7144	322.7155
$^{107}Ag_3^{109}Ag_2$	538,5242	538.5253
$^{107}Ag_4^{109}Ag_3$	754.3341	754.3352
$^{107}Ag_5^{109}Ag_4$	970.1439	970.1450
$^{107}Ag_6^{109}Ag_5$	1185.9538	1185.9549
$^{107}Ag_7^{109}Ag_6$	1401.7636	1401.7647

GSK Measured physical-chemical properties of compounds

CMPD_NUMBER	PHYSCHEM_SUMMARY.LAST_CLND_PID	PHYSCHEM_SUMMARY.CLND_CONC_UM_MEAN	PHYSCHEM_SUMMARY.CLND_CONC_UM_RANGE	PHYSCHEM_SUMMARY.CLND_CONC_UM_N	PHYSCHEM_SUMMARY.CHROM_LOGD_PH74_MEAN	PHYSCHEM_SUMMARY.CHROM_LOGD_PH74_RANGE	PHYSCHEM_SUMMARY.CHROM_LOGD_PH74_N	PHYSCHEM_SUMMARY.CHI_LOGD_PH74_MEAN	PHYSCHEM_SUMMARY.CHI_LOGD_PH74_RANGE	PHYSCHEM_SUMMARY.CHI_LOGD_PH74_N	PHYSCHEM_SUMMARY.CHI_LOGP_MEAN	PHYSCHEM_SUMMARY.CHROM_LOGP	PHYSCHEM_SUMMARY.ACID_OR_BASE
CCI1200	18029	554		3	2.73	2.24 - 6.17	87	1.43	1.13 - 3.54	87	3.3	5.78	Acidic
GR924244X	4890	23.56	13 - 64	9	7.95	7.88 - 8.06	6	4.62	4.58 - 4.69	6	5.03	8.6	Acidic
GW4450144X	17091	95	63 - 127	2	4.54	4.45 - 4.63	2	2.55	2.49 - 2.6	2	2.76	4.9	Basic
GW5597688X	5410	164.22	43 - 385	9	2.61	2.52 - 2.66	13	1.36	1.3 - 1.39	13	1.34	2.58	Weak Base
GW5614436X	17976	11	10 - 12	2	5.95	5.84 - 6.04	5	3.4	3.34 - 3.46	5	3.53	6.16	Weak Base
GW5683266X	17091	24	4 - 44	2	5.85		1	3.34		1	3.59	6.25	Weak Base

GW607117X	17976	13.75	7 - 29	4	5.16	3.59 - 5.47	8	2.92	1.95 - 3.11	8	2.89	5.11	Neutral
GW616030X	17976	75.5	28 - 123	2	6.37		1	3.66		1	4	6.92	Basic
GW807982X	50465	33.33	20 - 53	3	7.73	7.69 - 7.79	3	4.5	4.47 - 4.53	3	4.73	8.11	Neutral
GW817394X	17976	3	2 - 4	2	6.61	6.56 - 6.65	2	3.81	3.78 - 3.83	2	3.89	6.74	Neutral
GW817396X	17976	24.5	7 - 42	2	6.55	6.52 - 6.58	2	3.77	3.75 - 3.79	2	4.04	6.99	Weak Base
GW819077X	17091	16.5	3 - 30	2	8.06	7.97 - 8.14	2	4.69	4.64 - 4.74	2	5.05	8.64	
GW824645A	17976	306		1	3.43	3.32 - 3.59	3	1.86	1.79 - 1.96	3	1.85	3.41	Neutral
GW8	17976	18	14 - 22	2	6.83	6.78 - 6.88	2	3.95	3.91 - 3.98	2	4	6.92	Weak Base

2852 5X													
GW837 3311X	17091	7.5	6 - 9	2	6.37	6.26 - 6.54	3	3.66	3.6 - 3.76	3	3.81	6.61	Neutral
GW869 810X	4061	59.33	34 - 78	3	4.73	3.24 - 5.53	3	2.66	1.74 - 3.15	3			
SB-254 169	17091	204		1	2.23		1	1.12		1	2	3.66	Basic
SB-735 465	17091	12.5	10 - 15	2	4.43	4.43 - 4.43	2	2.47	2.47 - 2.47	2	2.62	4.67	Neutral
SB-675 259M													
SB-686 709A													

CMPD_NUMBER	PHYSCHEM_SUMMARY.PFI	PHYSCHEM_SUMMARY.PCT_CHANCE_LOW_SOL	PHYSCHEM_SUMMARY.PERM_NUM_PH7_4_MEAN	PHYSCHEM_SUMMARY.PERM_NUM_PH7_4_RANGE	PHYSCHEM_SUMMARY.PERM_NUM_PH7_4_N	PHYSCHEM_SUMMARY.HSA_PCT_BIND_MEAN	PHYSCHEM_SUMMARY.HSA_PCT_BIND_RANGE	PHYSCHEM_SUMMARY.HSA_PCT_BIND_N	PHYSCHEM_SUMMARY.LOGK_HSA_MEAN	PHYSCHEM_SUMMARY.AGP_PCT_BIND_MEAN	PHYSCHEM_SUMMARY.AGP_PCT_BIND_RANGE	PHYSCHEM_SUMMARY.AGP_PCT_BIND_N	PHYSCHEM_SUMMARY.LOGK_AGP_MEAN
CCI120	5.73	10	48		1	98.6	94.3 - 99.7	445	1.61112	59.7	23.4 - 88.2	304	0.16
GR92424X	7.95	30	255	200 - 280	4	89.8	82.3 - 95.7	5	0.938	66.1	62.4 - 69	3	0.28
GW445014X	6.54	20	630		1								
GW559768X	5.61	10	79	65 - 93	2	90.5	90 - 90.8	3	0.93333	75	69.8 - 78.2	3	0.46
GW561436X	9.95	70	670	650 - 690	2	96.5		1	1.33				
GW568326X	9.85	70	200		1								
GW607117X	9.16	70	480	460 - 500	2	95.3	93.5 - 97.1	2	1.245				
GW616030X	11.37	85	30		1								
GW807982X	11.73	85	500		1								
GW817394X	10.61	80			0								
GW817396X	10.55	80			0								
GW819077X	13.06	95			0								
GW824645A	6.43	20	33	27 - 39	2	95.8		1	1.27	85.4		1	0.74
GW828525X	11.83	85	340		1								
GW837331X	10.37	80			0	95.7		1	1.26				
GW869810X	8.73	50	10		1	98.1		1	1.52	92.4		1	1.03
SB-254169	6.23	20	13		1								

SB-735465	7.43	30	570		1								
SB-675259M													
SB-686709A													

CMPD_NUMBER	PHYSCHEM_SUMMARY.CHI_IAM_MEAN	PHYSCHEM_SUMMARY.LOGK_IAM	PHYSCHEM_SUMMARY.CAD_LIKENESS	PHYSCHEM_SUMMARY.HPLC_DRUG_EFF_MAX_PCT	PHYSCHEM_SUMMARY.LOGVDSS	PHYSCHEM_SUMMARY.VDSS	PHYSCHEM_SUMMARY.LOGVDUSS	PHYSCHEM_SUMMARY.LOGK_PPB	PHYSCHEM_SUMMARY.PCT_PPB	PHYSCHEM_SUMMARY.HPLC_LOG_K_LTB	PHYSCHEM_SUMMARY.HPLC_PCT_LTB
CCI120	28.51	1.73	0	3.33	-0.877	0.133	1.48	1.73	99.2	1.434	96.453
GR92424X	41.22	2.32	0	3.67	0.357	2.28	1.44	2.6	101	1.074	92.229
GW445014X											
GW559768X	36.93	2.12	0	6.02	0.109	1.29	1.22	1.17	94.6	1.282	95.034
GW561436X	43.27	2.41	0	1.43	0.163	1.46	1.84				
GW568326X			0								
GW607117X	41.62	2.34	0	2.07	0.14	1.38	1.68				
GW616030X											
GW807982X			0								
GW817394X			0								
GW817396X			0								
GW819077X											
GW8246	39.6	2.24	0	2.62	-0.00742	0.983	1.58	1.47	97.7	1.84	98.576

45A											
GW828525X			0								
GW833731X	47.99	2.63	0	0.775	0.589	3.88	2.11				
GW869810X								2.19	100	2.351	99.556
SB-254169											
SB-735465			0								
SB-675259M											
SB-686709A											

Calculated physical-chemical properties of compounds

original	CXN_pKa.a1	CXN_pKa.b1	CXN_pKa.b2	ChromlogD.value	PCv6.fraction_hba	PCv6.fraction_hbd	clogD74_cxn.value	clogp_cxn.value	hERG_RF_v3_NOD2M.pIC50_score
CCI120	3.8			3.25	0.32	0	0.27	3.53	4.89
GW445014X	13.66	3.39		4.57	0.24	0.12	3.38	3.38	4.88
GW559768X	10.04	6.68		2.35	0.44	0.22	2.55	2.62	5.07
GW561436X		2.97	0.86	5.89	0.39	0.1	4.26	4.26	5.13
GW568326X		3.19	0.87	5.82	0.33	0.11	4.52	4.52	4.99
GW607117X	11.04			5.09	0.35	0.09	4.21	4.21	4.9
GW616030X		3.84	2.66	6.35	0.31	0.06	4.56	4.56	5.21
GW807982X	12.4	1.88		7.79	0.38	0.09	4.47	4.47	5.07
GW817394X	12.91	4.94	3.18	6.52	0.39	0.1	3.78	3.93	5.15

GW817396X	13.04	5.01	3.32	6.47	0.39	0.1	3.83	3.93	5.16
GW819077X	12.83	1.88		7.56	0.35	0.09	5.87	5.87	5.12
GW824645A	10.26	3.19		3.4	0.35	0.35	2.59	2.59	4.84
GW828525X	13.28	1.73		6.84	0.32	0.08	5.38	5.38	5.13
GW837331X	11.65	5.47		6.4	0.26	0.09	4.27	4.28	5.2
GW869810X		8.25	1.63	5.26	0.25	0.12	4.57	5.48	5.55
SB-254169		10.13	4.71	2.15	0.46	0.08	0.33	2.95	5.18
SB-675259M	9.69	4.21	0.1	1.33	0.66	0.26	0.89	0.89	4.95
SB-686709A	9.68	8.94		1.92	0.4	0.2	0.78	2.01	5.27
SB-735465	11.37	0.22		4.6	0.24	0.24	3.84	3.84	4.94

original	**profile_cxn.logd_pH20**	**profile_cxn.logd_pH55**	**profile_cxn.logd_pH65**	**profile_cxn.logd_pH74**	**profile_cxn.logd_pH110**	**testCXN.clogp**	**testCXN.ApKa1_modified**	**testCXN.BpKa1_modified**	**testCXN.acidic_ionised_form**
CCI120	3.52	1.83	0.89	0.27	0	3.53	3.8	0	99.97
GW445014X	2.52	3.37	3.38	3.38	3.38	3.38	13.66	3.39	0
GW559768X	1.28	1.64	2.25	2.55	1.64	2.62	10.04	6.68	0.11
GW561436X	3.33	4.26	4.26	4.26	4.26	4.26	14	2.97	0
GW568326X	3.44	4.51	4.52	4.52	4.52	4.52	14	3.19	0
GW607117X	4.21	4.21	4.21	4.21	3.95	4.21	11.04	0	0.02
GW616030X	2.25	4.55	4.56	4.56	4.56	4.56	14	3.84	0
GW807982X	4.24	4.47	4.47	4.47	4.45	4.47	12.4	1.88	0
GW817394X	0.73	3.67	3.77	3.78	3.77	3.93	12.91	4.94	0
GW817396X	0.59	3.71	3.82	3.83	3.83	3.93	13.04	5.01	0
GW819077X	5.63	5.87	5.87	5.87	5.86	5.87	12.83	1.88	0
GW824645A	1.37	2.59	2.59	2.59	1.98	2.59	10.26	3.19	0.13
GW828525X	5.2	5.38	5.38	5.38	5.38	5.38	13.28	1.73	0
GW837331X	2.12	3.99	4.24	4.27	4.19	4.28	11.65	5.47	0
GW869810X	2.08	2.85	3.74	4.57	5.48	5.48	14	8.25	0
SB-254169	-1.35	-0.34	-0.15	0.33	2.89	2.95	14	10.13	0
SB-675259M	-0.07	0.87	0.89	0.89	-0.3	0.89	9.69	4.21	0.48
SB-686709A	-1.04	-0.78	-0.07	0.78	1.17	2.01	9.68	8.94	0.26
SB-735465	3.83	3.84	3.84	3.84	3.69	3.84	11.37	0.22	0.01

	PHYSCHEM_SUMMARY.LAST_CLND_PID	PHYSCHEM_SUMMARY.CLND_CONC_UM_MEAN	PHYSCHEM_SUMMARY.CLND_CONC_UM_RANGE	PHYSCHEM_SUMMARY.CLND_CONC_UM_N	PHYSCHEM_SUMMARY.CHROM_LOGD_PH74_MEAN	PHYSCHEM_SUMMARY.CHROM_LOGD_PH74_RANGE	PHYSCHEM_SUMMARY.CHROM_LOGD_PH74_N	PHYSCHEM_SUMMARY.CHI_LOGD_PH74_MEAN	PHYSCHEM_SUMMARY.CHI_LOGD_PH74_RANGE	PHYSCHEM_SUMMARY.CHI_LOGD_PH74_N	PHYSCHEM_SUMMARY.CHI_LOGP_MEAN	PHYSCHEM_SUMMARY.CHROM_LOGP	PHYSCHEM_SUMMARY.ACID_OR_BASE
CMPD_NUMBER													
CCI120	18029	554		3	2.73	2.24 - 6.17	87	1.43	1.13 - 3.54	87	3.3	5.78	Acidic
GR92424X	4890	23.56	13 - 64	9	7.95	7.88 - 8.06	6	4.62	4.58 - 4.69	6	5.03	8.6	Acidic
GW445014X	17091	95	63 - 127	2	4.54	4.45 - 4.63	2	2.55	2.49 - 2.6	2	2.76	4.9	Basic
GW559768X	5410	164.22	43 - 385	9	2.61	2.52 - 2.66	13	1.36	1.3 - 1.39	13	1.34	2.58	Weak Base
GW561436X	17976	11	10 - 12	2	5.95	5.84 - 6.04	5	3.4	3.34 - 3.46	5	3.53	6.16	Weak Base
GW568326X	17091	24	4 - 44	2	5.85		1	3.34		1	3.59	6.25	Weak Base
GW607117X	17976	13.75	7 - 29	4	5.16	3.59 - 5.47	8	2.92	1.95 - 3.11	8	2.89	5.11	Neutral
GW616030X	17976	75.5	28 - 123	2	6.37		1	3.66		1	4	6.92	Basic
GW807982X	50465	33.33	20 - 53	3	7.73	7.69 - 7.79	3	4.5	4.47 - 4.53	3	4.73	8.11	Neutral
GW817394X	17976	3	2 - 4	2	6.61	6.56 - 6.65	2	3.81	3.78 - 3.83	2	3.89	6.74	Neutral
GW817396X	17976	24.5	7 - 42	2	6.55	6.52 - 6.58	2	3.77	3.75 - 3.79	2	4.04	6.99	Weak Base
GW819077X	17091	16.5	3 - 30	2	8.06	7.97 - 8.14	2	4.69	4.64 - 4.74	2	5.05	8.64	
GW824645A	17976	306		1	3.43	3.32 - 3.59	3	1.86	1.79 - 1.96	3	1.85	3.41	Neutral
GW828525X	17976	18	14 - 22	2	6.83	6.78 - 6.88	2	3.95	3.91 - 3.98	2	4	6.92	Weak Base
GW837331X	17091	7.5	6 - 9	2	6.37	6.26 - 6.54	3	3.66	3.6 - 3.76	3	3.81	6.61	Neutral
GW869810X	4061	59.33	34 - 78	3	4.73	3.24 - 5.53	3	2.66	1.74 - 3.15	3			
SB-254169	17091	204		1	2.23		1	1.12		1	2	3.66	Basic
SB-735465	17091	12.5	10 - 15	2	4.43	4.43 - 4.43	2	2.47	2.47 - 2.47	2	2.62	4.67	Neutral
SB-675259M													
SB-686709A													

List of metabolites identifies in BCG sample using the OrbiSIMS

ion m/z	Metabolite name	Sum formula	KEGG ID	theoretical m/z	delta (amu)	delta (ppm)	Isotopologue pattern MRE
70.0656	1-Pyrroline	C4H7N	C15668	70.06513	0.00048	6.847559	#N/A
72.0812	Pyrrolidine	C4H9N		72.08078	0.000449	6.232964	#N/A
73.0472	Acrylamide	C3H5NO	C01659	73.04774	-0.0005	-6.80703	#N/A
75.0264	2-Propene-1-thiol	C3H6S		75.0263	0.000195	2.604651	0.342343
75.0264	1-Propene-1-thiol	C3H6S		75.0263	0.000195	2.604651	0.342343
77.0421	Ethyl methyl sulfide	C3H8S		77.04195	0.000173	2.241997	#N/A
77.0421	2-Propanethiol	C3H8S	C08391	77.04195	0.000173	2.241997	#N/A
77.0421	1-Propanethiol	C3H8S	C08390	77.04195	0.000173	2.241997	#N/A
77.0421	Glycine	C2H5NO2	C00037	77.04266	-0.00054	-7.00356	#N/A
77.0421	Ethyl nitrite	C2H5NO2		77.04266	-0.00054	-7.00356	#N/A
78.0468	Glycine	C2H5NO2	C00037	78.04601	0.00078	9.994874	#N/A
78.0468	Ethyl nitrite	C2H5NO2		78.04601	0.00078	9.994874	#N/A
81.0001	Chloroacetaldehyde	C2H3ClO		81.00123	-0.00062	-7.64582	#N/A
81.001	Chloroacetaldehyde	C2H3ClO		81.00123	-0.00023	-2.84659	#N/A
81.0451	Pyrimidine	C4H4N2	C00396	81.04472	0.000363	4.478819	0.370229
81.0451	Pyrazine	C4H4N2	C02018	81.04472	0.000363	4.478819	0.370229
82.0484	Pyrimidine	C4H4N2	C00396	82.04808	0.00033	4.024074	0.370229
82.0484	Pyrazine	C4H4N2	C02018	82.04808	0.00033	4.024074	0.370229
82.0655	1-Methylpyrrole	C5H7N		82.06513	0.000344	4.185869	#N/A

82.06547	2-Methylpyrrole	C5H7N		82.06513	0.000344	4.185869	#N/A
83.02949	N-Methylformamide	C2H5NO	C11489	83.02969	-0.00019	-2.31416	#N/A
83.02949	Acetaldehyde oxime	C2H5NO	C02658	83.02969	-0.00019	-2.31416	#N/A
83.02949	Acetamide	C2H5NO	C06244	83.02969	-0.00019	-2.31416	#N/A
83.0369	Acetone	C3H6O	C00207	83.03779	-0.00089	-10.7068	#N/A
83.0369	Propanal	C3H6O	C00479	83.03779	-0.00089	-10.7068	#N/A
83.0369	Methyloxirane	C3H6O	C15508	83.03779	-0.00089	-10.7068	#N/A
83.0369	Allyl alcohol	C3H6O	C02001	83.03779	-0.00089	-10.7068	#N/A
83.04946	2-Methylfuran	C5H6O		83.04914	0.00032	3.856652	#N/A
83.04946	2,4-Pentadienal	C5H6O		83.04914	0.00032	3.856652	#N/A
84.03284	N-Methylformamide	C2H5NO	C11489	84.03304	-0.0002	-2.36822	#N/A
84.03284	Acetaldehyde oxime	C2H5NO	C02658	84.03304	-0.0002	-2.36822	#N/A
84.03284	Acetamide	C2H5NO	C06244	84.03304	-0.0002	-2.36822	#N/A
84.0447	Guanidine	CH5N3	C17349	84.04427	0.000426	5.069549	#N/A
84.05594	5-Aminoimidazole	C3H5N3	C05239	84.05562	0.000315	3.749996	#N/A
84.0811	(+)-2,3-Dihydro-3-methyl-1H-pyrrole	C5H9N		84.08078	0.000327	3.894216	0.347457
84.0811	Pentanenitrile	C5H9N		84.08078	0.000327	3.894216	0.347457
84.96001	Dichloromethane	CH2Cl2	C02271	84.96063	-0.00062	-7.34667	#N/A
84.96001	Carbon dioxide	CO2	C00011	84.9597	0.00031	3.653268	#N/A

85.00759	Dimethylsulfide	C2H6S	C00580	85.00824	-0.00065	-7.67851	#N/A
85.00759	Boric acid (H3BO3)	BH3O3	C12486	85.00674	0.000844	9.925296	326.2509
85.03994	Imidazolone	C3H4N2O	C06195	85.03964	0.0003	3.524469	#N/A
85.08443	(+)-2,3-Dihydro-3-methyl-1H-pyrrole	C5H9N		85.08413	0.000302	3.551844	0.347457
85.08443	Pentanenitrile	C5H9N		85.08413	0.000302	3.551844	0.347457
86.06033	2-Pyrrolidinone	C4H7NO	C11118	86.06004	0.000293	3.404977	#N/A
86.0672	Methyl propenyl ketone	C5H8O		86.06815	-0.00095	-10.9895	#N/A
86.0672	Cyclopentanone	C5H8O	C00557	86.06815	-0.00095	-10.9895	#N/A
86.0672	3-Methyl-3-buten-2-one	C5H8O		86.06815	-0.00095	-10.9895	#N/A
86.0672	2-Pentenal	C5H8O		86.06815	-0.00095	-10.9895	#N/A
86.0672	4-Penten-2-one	C5H8O		86.06815	-0.00095	-10.9895	#N/A
86.0672	1-Penten-3-one	C5H8O		86.06815	-0.00095	-10.9895	#N/A
86.0672	4-Pentenal	C5H8O		86.06815	-0.00095	-10.9895	#N/A
86.0672	xi-2,3-Dihydro-3-methylfuran	C5H8O		86.06815	-0.00095	-10.9895	#N/A
86.0672	2,3-Dihydro-4-methylfuran	C5H8O		86.06815	-0.00095	-10.9895	#N/A
86.09675	Piperidine	C5H11N	C01746	86.09643	0.00032	3.715022	0.474836
87.10005	Piperidine	C5H11N	C01746	87.09978	0.000268	3.081983	0.474836
89.05894	Isobutyric acid	C4H8O2	C02632	89.05971	-0.00077	-8.60118	#N/A
89.05894	Methyl propionate	C4H8O2		89.05971	-0.00077	-8.60118	#N/A

89.05894	Ethyl acetate	C4H8O2	C00849	89.05971	-0.00077	-8.60118	#N/A
89.05894	1-Hydroxy-2-butanone	C4H8O2		89.05971	-0.00077	-8.60118	#N/A
89.05894	Propyl formate	C4H8O2		89.05971	-0.00077	-8.60118	#N/A
89.05894	Isopropyl formate	C4H8O2		89.05971	-0.00077	-8.60118	#N/A
89.05935	Isobutyric acid	C4H8O2	C02632	89.05971	-0.00035	-3.97812	#N/A
89.05935	Methyl propionate	C4H8O2		89.05971	-0.00035	-3.97812	#N/A
89.05935	Ethyl acetate	C4H8O2	C00849	89.05971	-0.00035	-3.97812	#N/A
89.05935	1-Hydroxy-2-butanone	C4H8O2		89.05971	-0.00035	-3.97812	#N/A
89.05935	Propyl formate	C4H8O2		89.05971	-0.00035	-3.97812	#N/A
89.05935	Isopropyl formate	C4H8O2		89.05971	-0.00035	-3.97812	#N/A
89.06012	Isobutyric acid	C4H8O2	C02632	89.05971	0.000416	4.665451	#N/A
89.06012	Methyl propionate	C4H8O2		89.05971	0.000416	4.665451	#N/A
89.06012	Ethyl acetate	C4H8O2	C00849	89.05971	0.000416	4.665451	#N/A
89.06012	1-Hydroxy-2-butanone	C4H8O2		89.05971	0.000416	4.665451	#N/A
89.06012	Propyl formate	C4H8O2		89.05971	0.000416	4.665451	#N/A
89.06012	Isopropyl formate	C4H8O2		89.05971	0.000416	4.665451	#N/A
90.04665	3-Isoxazolidinone	C3H5NO2		90.04601	0.000633	7.031999	#N/A
91.05763	2-Methyl-1-propanethiol	C4H10S		91.0576	3.11E-05	0.341366	0.660131
91.05763	Diethyl sulfide	C4H10S	C02272	91.0576	3.11E-05	0.341366	0.660131
91.05763	2-(Methylthio)propane	C4H10S		91.0576	3.11E-05	0.341366	0.660131

91.05763	Beta-Alanine	C3H7NO2	C00099	91.05831	-0.00068	-7.48111	#N/A
91.05763	L-Alanine	C3H7NO2	C00041	91.05831	-0.00068	-7.48111	#N/A
91.05763	Sarcosine	C3H7NO2	C00213	91.05831	-0.00068	-7.48111	#N/A
91.05763	D-Alanine	C3H7NO2	C00133	91.05831	-0.00068	-7.48111	#N/A
91.05763	Ethyl carbamate	C3H7NO2	C01537	91.05831	-0.00068	-7.48111	#N/A
92.02452	1-Mercapto-2-propanone	C3H6OS		92.02457	-4.7E-05	-0.50615	#N/A
92.02452	S-Methyl thioacetate	C3H6OS		92.02457	-4.7E-05	-0.50615	#N/A
92.02452	(E)-1-Propene-1-sulfenic acid	C3H6OS		92.02457	-4.7E-05	-0.50615	#N/A
92.02452	(Methylthio)acetaldehyde	C3H6OS		92.02457	-4.7E-05	-0.50615	#N/A
92.02452	Thial-1-Propene-1-thiol S-oxide	C3H6OS	C08389	92.02457	-4.7E-05	-0.50615	#N/A
92.03715	3-Butenenitrile	C4H5N		92.03813	-0.00097	-10.5895	#N/A
92.03715	Pyrrole	C4H5N	C19907	92.03813	-0.00097	-10.5895	#N/A
92.06096	2-Methyl-1-propanethiol	C4H10S		92.06095	7.82E-06	0.084998	0.660131
92.06096	Diethyl sulfide	C4H10S	C02272	92.06095	7.82E-06	0.084998	0.660131
92.06096	2-(Methylthio)propane	C4H10S		92.06095	7.82E-06	0.084998	0.660131
92.06096	Beta-Alanine	C3H7NO2	C00099	92.06166	-0.0007	-7.65222	#N/A
92.06096	L-Alanine	C3H7NO2	C00041	92.06166	-0.0007	-7.65222	#N/A

92.06096	Sarcosine	C3H7NO2	C00213	92.06166	-0.0007	-7.65222	#N/A
92.06096	D-Alanine	C3H7NO2	C00133	92.06166	-0.0007	-7.65222	#N/A
92.06096	Ethyl carbamate	C3H7NO2	C01537	92.06166	-0.0007	-7.65222	#N/A
93.03686	Cibulins	C3H8OS		93.03686	-6.5E-06	-0.07028	0.278708
93.03686	2-(Methylthio)ethanol	C3H8OS		93.03686	-6.5E-06	-0.07028	0.278708
93.04494	L-Lactic acid	C3H6O3	C00186	93.04568	-0.00074	-7.97577	#N/A
93.04494	Hydroxypropionic acid	C3H6O3	C01013	93.04568	-0.00074	-7.97577	#N/A
93.04494	Glyceraldehyde	C3H6O3	C02154	93.04568	-0.00074	-7.97577	#N/A
93.04494	D-Lactic acid	C3H6O3	C00256	93.04568	-0.00074	-7.97577	#N/A
93.04494	Dihydroxyacetone	C3H6O3	C00184	93.04568	-0.00074	-7.97577	#N/A
93.04494	Dimethyl carbonate	C3H6O3		93.04568	-0.00074	-7.97577	#N/A
93.04494	Monoethyl carbonate	C3H6O3		93.04568	-0.00074	-7.97577	#N/A
93.04494	Methoxyacetic acid	C3H6O3		93.04568	-0.00074	-7.97577	#N/A
93.05443	Glycerol	C3H8O3	C00116	93.05462	-0.00019	-2.0517	#N/A
94.04016	Cibulins	C3H8OS		94.04022	-6E-05	-0.63728	0.278708
94.04016	2-(Methylthio)ethanol	C3H8OS		94.04022	-6E-05	-0.63728	0.278708
94.06532	Aniline	C6H7N	C00292	94.06513	0.000195	2.077045	#N/A

95.01528	Dimethyl sulfone	C2H6O2S	C11142	95.01613	-0.00084	-8.88341	#N/A
95.01609	Dimethyl sulfone	C2H6O2S	C11142	95.01613	-3.7E-05	-0.38562	0.270718
95.01609	(Chloromethyl)oxirane	C3H5ClO	C14449	95.01688	-0.00079	-8.30041	#N/A
95.04933	Beta-Aminopropionitrile	C3H6N2	C05670	95.04903	0.000305	3.209994	#N/A
95.06053	Methylpyrazine	C5H6N2		95.06037	0.000158	1.667193	0.366803
95.06053	Glycerol	C3H8O3	C00116	95.06133	-0.0008	-8.38524	#N/A
96.04455	2-Hydroxypyridine	C5H5NO	C02502	96.04439	0.000162	1.688637	#N/A
96.04455	1H-Pyrrole-2-carboxaldehyde	C5H5NO		96.04439	0.000162	1.688637	#N/A
96.05266	Methylguanidine	C2H7N3	C02294	96.05322	-0.00056	-5.77886	#N/A
96.06388	Methylpyrazine	C5H6N2		96.06373	0.000148	1.537868	0.366803
96.08094	2,5-Dimethyl-1H-pyrrole	C6H9N		96.08078	0.000166	1.722633	#N/A
96.99532	Silicic acid	H4O4Si		96.99516	0.000157	1.618994	#N/A
96.99532	Chloroacetic acid	C2H3ClO2	C06755	96.99614	-0.00082	-8.50074	#N/A
98.06017	1-Cyano-2-hydroxy-3-butene	C5H7NO		98.06004	0.000135	1.374378	#N/A
98.06017	2,4-Dimethyloxazole	C5H7NO		98.06004	0.000135	1.374378	#N/A
98.06017	2,5-Dimethyloxazole	C5H7NO		98.06004	0.000135	1.374378	#N/A
98.06017	4,5-Dimethyloxazole	C5H7NO		98.06004	0.000135	1.374378	#N/A
98.06017	Methylguanidine	C2H7N3	C02294	98.05992	0.00025	2.546483	#N/A
98.97055	1,2-Dichloroethane	C2H4Cl2	C06752	98.97628	-0.00078	-7.92486	#N/A
98.98356	Phosphoric acid	H3O4P	C00009	98.98417	-0.00061	-6.20797	#N/A

98.98356	Acetic acid	C2H4O2	C00033	98.98429	-0.00073	-7.38265	#N/A
98.98356	Glycolaldehyde	C2H4O2	C00266	98.98429	-0.00073	-7.38265	#N/A
98.98432	Phosphoric acid	H3O4P	C00009	98.98417	0.000145	1.461451	0.208118
98.98432	Acetic acid	C2H4O2	C00033	98.98429	2.84E-05	0.286757	0.083763
98.98432	Glycolaldehyde	C2H4O2	C00266	98.98429	2.84E-05	0.286757	0.083763
99.01096	Acetone	C3H6O	C00207	99.01173	-0.00077	-7.78787	#N/A
99.01096	Propanal	C3H6O	C00479	99.01173	-0.00077	-7.78787	#N/A
99.01096	Methyloxirane	C3H6O	C15508	99.01173	-0.00077	-7.78787	#N/A
99.01096	Allyl alcohol	C3H6O	C02001	99.01173	-0.00077	-7.78787	#N/A
99.02306	Ethyl methyl sulfide	C3H8S		99.02389	-0.00083	-8.34163	#N/A
99.02306	2-Propanethiol	C3H8S	C08391	99.02389	-0.00083	-8.34163	#N/A
99.02306	1-Propanethiol	C3H8S	C08390	99.02389	-0.00083	-8.34163	#N/A
100.0308	Trimethyl sulfonium	C3H9S	C01008	100.0317	-0.00088	-8.83691	#N/A
100.0758	2-Piperidinone	C5H9NO		100.0757	9.44E-05	0.943729	#N/A
100.0758	1-Pyrrolidinecarboxaldehyde	C5H9NO		100.0757	9.44E-05	0.943729	#N/A
100.0758	2,5-Dihydro-2,4-dimethyloxazole	C5H9NO		100.0757	9.44E-05	0.943729	#N/A
101.0063	Thiourea	CH4N2S	C14415	101.0054	0.000873	8.641995	#N/A
101.0387	1,2-Ethanediamine	C2H8N2		101.0386	4.73E-05	0.468286	#N/A
102.0465	(R)-Dihydromaleimide	C4H5NO2		102.046	0.000487	4.76997	#N/A
102.0914	5-Aminopentanal	C5H11NO	C12455	102.0913	7.87E-05	0.77067	#N/A

102.9252	Sulfur dioxide	O2S	C09306	102.9251	0.000132	1.281268	#N/A
102.9257	Sulfur dioxide	O2S	C09306	102.9251	0.000656	6.371287	#N/A
104.0621	L-3-Aminodihydro-2(3H)-furanone	C4H7NO2	C02926	104.0617	0.000428	4.114342	#N/A
104.0621	(S)-2-Azetidinecarboxylic acid	C4H7NO2		104.0617	0.000428	4.114342	#N/A
104.0621	1-Aminocyclopropanecarboxylic acid	C4H7NO2	C01234	104.0617	0.000428	4.114342	#N/A
105.0448	2-Ketobutyric acid	C4H6O3	C00109	105.0457	-0.00091	-8.62012	#N/A
105.0448	Acetoacetic acid	C4H6O3	C00164	105.0457	-0.00091	-8.62012	#N/A
105.0448	2-Methyl-3-oxopropanoic acid	C4H6O3	C00349	105.0457	-0.00091	-8.62012	#N/A
105.0448	(S)-Methylmalonic acid semialdehyde	C4H6O3	C06002	105.0457	-0.00091	-8.62012	#N/A
105.0448	4-Hydroxycrotonic acid	C4H6O3		105.0457	-0.00091	-8.62012	#N/A
105.0448	Acetic anhydride	C4H6O3		105.0457	-0.00091	-8.62012	#N/A
106.04	S-Ethyl thioacetate	C4H8OS		106.0402	-0.00019	-1.77404	#N/A
106.04	S-Methyl propanethioate	C4H8OS		106.0402	-0.00019	-1.77404	#N/A
106.04	3-(Methylthio)propanal	C4H8OS		106.0402	-0.00019	-1.77404	#N/A
106.04	3-Mercapto-2-butanone	C4H8OS		106.0402	-0.00019	-1.77404	#N/A
106.04	(Methylthio)acetone	C4H8OS		106.0402	-0.00019	-1.77404	#N/A
106.04	4-Mercapto-2-butanone	C4H8OS		106.0402	-0.00019	-1.77404	#N/A
106.04	Pyruvatoxime	C3H5NO3		106.0409	-0.0009	-8.49125	#N/A

106.04	3-Oxoalanine	C3H5NO3		106.0409	-0.0009	-8.49125	#N/A
106.9892	3-Butyn-1-al	C4H4O	C06145	106.9894	-0.00022	-2.05895	#N/A
106.9892	Furan	C4H4O	C00089	106.9894	-0.00022	-2.05895	#N/A
107.0473	Methyl propenyl ketone	C5H8O		107.0467	0.000588	5.488977	#N/A
107.0473	Cyclopentanone	C5H8O	C00557	107.0467	0.000588	5.488977	#N/A
107.0473	3-Methyl-3-buten-2-one	C5H8O		107.0467	0.000588	5.488977	#N/A
107.0473	2-Pentenal	C5H8O		107.0467	0.000588	5.488977	#N/A
107.0473	4-Penten-2-one	C5H8O		107.0467	0.000588	5.488977	#N/A
107.0473	1-Penten-3-one	C5H8O		107.0467	0.000588	5.488977	#N/A
107.0473	4-Pentenal	C5H8O		107.0467	0.000588	5.488977	#N/A
107.0473	xi-2,3-Dihydro-3-methylfuran	C5H8O		107.0467	0.000588	5.488977	#N/A
107.0473	2,3-Dihydro-4-methylfuran	C5H8O		107.0467	0.000588	5.488977	#N/A
107.0492	Benzaldehyde	C7H6O	C00193	107.0491	2.89E-05	0.270387	#N/A
107.0604	2-Hydroxybutyric acid	C4H8O3	C05984	107.0613	-0.00094	-8.75791	#N/A
107.0604	(R)-3-Hydroxybutyric acid	C4H8O3	C01089	107.0613	-0.00094	-8.75791	#N/A
107.0604	(S)-3-Hydroxyisobutyric acid	C4H8O3	C06001	107.0613	-0.00094	-8.75791	#N/A
107.0604	(R)-3-Hydroxyisobutyric acid	C4H8O3		107.0613	-0.00094	-8.75791	#N/A
107.0604	3-Hydroxybutyric acid	C4H8O3	C01089	107.0613	-0.00094	-8.75791	#N/A
107.0604	(S)-3-Hydroxybutyric acid	C4H8O3	C03197	107.0613	-0.00094	-8.75791	#N/A
107.0604	4-Hydroxybutyric acid	C4H8O3	C00989	107.0613	-0.00094	-8.75791	#N/A

107.0604	Ethoxyacetic acid	C4H8O3		107.0613	-0.00094	-8.75791	#N/A
107.073	2,3-Diaminopropionic acid	C3H8N2O2	C03401	107.0726	0.000389	3.637149	#N/A
108.0444	5-Aminoimidazole	C3H5N3	C05239	108.0443	9.92E-05	0.918394	#N/A
108.0556	3-(Methylthio)-1-propanol	C4H10OS		108.0559	-0.00026	-2.39284	#N/A
108.0556	3-Mercapto-2-butanol	C4H10OS		108.0559	-0.00026	-2.39284	#N/A
108.0556	4-Mercapto-2-butanol	C4H10OS		108.0559	-0.00026	-2.39284	#N/A
108.0556	L-Serine	C3H7NO3	C00065	108.0566	-0.00097	-8.98475	#N/A
108.0556	D-Serine	C3H7NO3	C00740	108.0566	-0.00097	-8.98475	#N/A
108.0682	N-Nitroethylenediamine	C2H7N3O2		108.0678	0.000413	3.820574	#N/A
108.0808	3-Ethylpyridine	C7H9N		108.0808	1.19E-05	0.110129	#N/A
108.0808	2,4-Dimethylpyridine	C7H9N		108.0808	1.19E-05	0.110129	#N/A
108.0808	2,6-Dimethylpyridine	C7H9N		108.0808	1.19E-05	0.110129	#N/A
108.0808	Benzylamine	C7H9N	C15562	108.0808	1.19E-05	0.110129	#N/A
109.0073	2,3-Dihydrothiophene	C4H6S		109.0082	-0.00091	-8.38895	#N/A
109.0073	Divinyl sulfide	C4H6S		109.0082	-0.00091	-8.38895	#N/A
109.0397	Glyceric acid	C3H6O4	C00258	109.0406	-0.00091	-8.34942	#N/A
109.0397	L-Glyceric acid	C3H6O4		109.0406	-0.00091	-8.34942	#N/A
109.0397	D-2,3-Dihydroxypropanoic acid	C3H6O4		109.0406	-0.00091	-8.34942	#N/A
109.0449	2-Pyrrolidinone	C4H7NO	C11118	109.0453	-0.00046	-4.21133	#N/A

109.0761	2-Ethylpyrazine	C6H8N2		109.076	4.23E-05	0.387823	#N/A
109.0761	2,3-Dimethylpyrazine	C6H8N2		109.076	4.23E-05	0.387823	#N/A
109.0761	2,6-Dimethylpyrazine	C6H8N2		109.076	4.23E-05	0.387823	#N/A
109.0761	2,5-Dimethylpyrazine	C6H8N2		109.076	4.23E-05	0.387823	#N/A
109.0761	(2R*,3R*)-1,2,3-Butanetriol	C4H10O3		109.077	-0.00091	-8.37293	#N/A
110.0601	4-Aminophenol	C6H7NO	C02372	110.06	2.88E-05	0.261287	#N/A
110.0601	2-Acetylpyrrole	C6H7NO		110.06	2.88E-05	0.261287	#N/A
110.0601	1-Methyl-2-pyrrolecarboxaldehyde	C6H7NO		110.06	2.88E-05	0.261287	#N/A
110.0965	1,2,5-Trimethyl-1H-pyrrole	C7H11N		110.0964	4.12E-05	0.374211	#N/A
111.0229	3-(Methylthio)-1-propene	C4H8S		111.0239	-0.00095	-8.59334	#N/A
111.0229	cis-2,3-Dimethylthiirane	C4H8S		111.0239	-0.00095	-8.59334	#N/A
111.0229	Beta-Aminopropionitrile	C3H6N2	C05670	111.023	-3.1E-05	-0.2792	#N/A
111.0553	Imidazole-4-acetaldehyde	C5H6N2O	C05130	111.0553	1.88E-05	0.1696	#N/A
111.0553	Methoxypyrazine	C5H6N2O		111.0553	1.88E-05	0.1696	#N/A
111.0553	2,2-Dihydroperoxypropane	C3H8O4		111.0562	-0.00094	-8.43501	#N/A
112.009	Pyruvic acid	C3H4O3	C00022	112.0086	0.000368	3.288538	#N/A
112.009	Malonic semialdehyde	C3H4O3	C00222	112.0086	0.000368	3.288538	#N/A
112.009	Glucosereductone	C3H4O3		112.0086	0.000368	3.288538	#N/A
112.0757	N-Acetyl-2,3-dihydro-1H-pyrrole	C6H9NO		112.0757	1.11E-05	0.098619	#N/A
112.0757	5-Acetyl-3,4-dihydro-2H-pyrrole	C6H9NO		112.0757	1.11E-05	0.098619	#N/A
112.0757	2-Ethyl-4-methyloxazole	C6H9NO		112.0757	1.11E-05	0.098619	#N/A
112.0757	4-Ethyl-2-methyloxazole	C6H9NO		112.0757	1.11E-05	0.098619	#N/A

112.0757	2-Ethyl-5-methyloxazole	C6H9NO		112.0757	1.11E-05	0.098619	#N/A
112.0757	5-Ethyl-2-methyloxazole	C6H9NO		112.0757	1.11E-05	0.098619	#N/A
112.0757	5-Ethyl-4-methyloxazole	C6H9NO		112.0757	1.11E-05	0.098619	#N/A
112.0757	5-Imino-2-methyl-1-cyclopenten-1-ol	C6H9NO		112.0757	1.11E-05	0.098619	#N/A
112.0757	Trimethyloxazole	C6H9NO		112.0757	1.11E-05	0.098619	#N/A
112.0869	Histamine	C5H9N3	C00388	112.0869	-9.6E-06	-0.08543	#N/A
112.9998	S-Methyl methanesulfinothioate	C2H6OS2		113	-0.00019	-1.67744	#N/A
112.9998	Propionic acid	C3H6O2	C00163	112.9999	-0.00014	-1.19573	#N/A
112.9998	Lactaldehyde	C3H6O2	C00424	112.9999	-0.00014	-1.19573	#N/A
112.9998	3-Hydroxypropanal	C3H6O2	C00969	112.9999	-0.00014	-1.19573	#N/A
112.9998	D-Lactaldehyde	C3H6O2	C00937	112.9999	-0.00014	-1.19573	#N/A
112.9998	Hydroxyacetone	C3H6O2	C05235	112.9999	-0.00014	-1.19573	#N/A
112.9998	Ethyl formate	C3H6O2		112.9999	-0.00014	-1.19573	#N/A
112.9998	Methyl acetate	C3H6O2	C17530	112.9999	-0.00014	-1.19573	#N/A
113.0265	Glycerol alpha-monochlorohydrin	C3H7ClO2	C18676	113.0274	-0.00098	-8.63049	#N/A
113.0265	Tetrahydrofuran	C4H8O		113.0274	-0.00092	-8.09703	#N/A
113.0265	Butanone	C4H8O	C02845	113.0274	-0.00092	-8.09703	#N/A
113.0265	Butanal	C4H8O	C01412	113.0274	-0.00092	-8.09703	#N/A

113.0265	2-Methylpropanal	C4H8O	C03219	113.0274	-0.00092	-8.09703	#N/A
113.0265	3-Buten-1-ol	C4H8O		113.0274	-0.00092	-8.09703	#N/A
113.0265	2-Buten-1-ol	C4H8O		113.0274	-0.00092	-8.09703	#N/A
113.0265	2,2-Dimethyloxirane	C4H8O		113.0274	-0.00092	-8.09703	#N/A
113.0345	Uracil	C4H4N2O2	C00106	113.0346	-5.4E-06	-0.0481	#N/A
113.0386	2-Methyl-1-propanethiol	C4H10S		113.0395	-0.00097	-8.57642	0.329492
113.0386	Diethyl sulfide	C4H10S	C02272	113.0395	-0.00097	-8.57642	0.329492
113.0386	2-(Methylthio)propane	C4H10S		113.0395	-0.00097	-8.57642	0.329492
114.0247	L-Lactic acid	C3H6O3	C00186	114.0243	0.000406	3.560471	#N/A
114.0247	Hydroxypropionic acid	C3H6O3	C01013	114.0243	0.000406	3.560471	#N/A
114.0247	Glyceraldehyde	C3H6O3	C02154	114.0243	0.000406	3.560471	#N/A
114.0247	D-Lactic acid	C3H6O3	C00256	114.0243	0.000406	3.560471	#N/A
114.0247	Dihydroxyacetone	C3H6O3	C00184	114.0243	0.000406	3.560471	#N/A
114.0247	Dimethyl carbonate	C3H6O3		114.0243	0.000406	3.560471	#N/A
114.0247	Monoethyl carbonate	C3H6O3		114.0243	0.000406	3.560471	#N/A
114.0247	Methoxyacetic acid	C3H6O3		114.0243	0.000406	3.560471	#N/A
114.0372	2,4-Dimethylthiazole	C5H7NS		114.0372	4.88E-05	0.427988	#N/A
114.0372	2,5-Dimethylthiazole	C5H7NS		114.0372	4.88E-05	0.427988	#N/A
114.0372	4,5-Dimethylthiazole	C5H7NS		114.0372	4.88E-05	0.427988	#N/A
114.0372	Thiiranepropanenitrile	C5H7NS		114.0372	4.88E-05	0.427988	#N/A
114.0372	2-Ethylthiazole	C5H7NS		114.0372	4.88E-05	0.427988	#N/A

114.0372	Uracil	C4H4N2O2	C00106	114.0379	-0.00066	-5.81819	#N/A
114.042	2-Methyl-1-propanethiol	C4H10S		114.0429	-0.00093	-8.18385	0.329492
114.042	Diethyl sulfide	C4H10S	C02272	114.0429	-0.00093	-8.18385	0.329492
114.042	2-(Methylthio)propane	C4H10S		114.0429	-0.00093	-8.18385	0.329492
114.055	1-Pyrroline-5-carboxylic acid	C5H7NO2	C04322	114.055	3.03E-05	0.265582	427.3529
114.055	1-Pyrroline-2-carboxylic acid	C5H7NO2	C03564	114.055	3.03E-05	0.265582	427.3529
115.0058	Propionic acid	C3H6O2	C00163	115.0066	-0.00089	-7.75697	#N/A
115.0058	Lactaldehyde	C3H6O2	C00424	115.0066	-0.00089	-7.75697	#N/A
115.0058	3-Hydroxypropanal	C3H6O2	C00969	115.0066	-0.00089	-7.75697	#N/A
115.0058	D-Lactaldehyde	C3H6O2	C00937	115.0066	-0.00089	-7.75697	#N/A
115.0058	Hydroxyacetone	C3H6O2	C05235	115.0066	-0.00089	-7.75697	#N/A
115.0058	Ethyl formate	C3H6O2		115.0066	-0.00089	-7.75697	#N/A
115.0058	Methyl acetate	C3H6O2	C17530	115.0066	-0.00089	-7.75697	#N/A
115.0417	Uracil	C4H4N2O2	C00106	115.0413	0.000417	3.626269	#N/A
115.0543	1,3-Diaminopropane	C3H10N2	C00986	115.0543	1.59E-07	0.001381	#N/A
115.0543	1,2 Diaminopropane	C3H10N2		115.0543	1.59E-07	0.001381	#N/A
115.0866	3-Amino-2-piperidone	C5H10N2O		115.0866	7.15E-06	0.062099	#N/A
116.0621	1-Pyrroline-5-carboxylic acid	C5H7NO2	C04322	116.0617	0.000395	3.407138	427.3529
116.0621	1-Pyrroline-2-carboxylic acid	C5H7NO2	C03564	116.0617	0.000395	3.407138	427.3529

116.9859	Glycolic acid	C2H4O3	C00160	116.9859	1.99E-05	0.169925	#N/A
116.9859	Peracetic acid	C2H4O3		116.9859	1.99E-05	0.169925	#N/A
117.0567	xi-2,5-Dihydro-2,4-dimethylthiazole	C5H9NS		117.0562	0.000453	3.871312	51.45486
117.0567	Dihydrouracil	C4H6N2O2	C00429	117.0569	-0.00026	-2.21379	#N/A
117.0567	N-Methylhydantoin	C4H6N2O2	C02565	117.0569	-0.00026	-2.21379	#N/A
117.0573	Dihydrouracil	C4H6N2O2	C00429	117.0569	0.000339	3.335416	#N/A
117.0573	N-Methylhydantoin	C4H6N2O2	C02565	117.0569	0.000339	3.335416	#N/A
118.0399	xI-Dihydro-2-methyl-3(2H)-thiophenone	C5H8OS		118.0402	-0.00028	-2.36054	#N/A
118.0399	Dihydro-5-methyl-2(3H)-thiophenone	C5H8OS		118.0402	-0.00028	-2.36054	#N/A
118.0399	xi-2-Acetylthietane	C5H8OS		118.0402	-0.00028	-2.36054	#N/A
118.0399	Dihydro-2-methyl-3(2H)-furanthione	C5H8OS		118.0402	-0.00028	-2.36054	#N/A
118.0543	3-keto-2-Methylbutyrate	C5H7O3		118.0535	0.000813	6.883335	598.9159
118.0543	Aniline	C6H7N	C00292	118.0538	0.00054	4.578107	#N/A
118.0606	Guanidoacetic acid	C3H7N3O2	C00581	118.0611	-0.0005	-4.1939	#N/A
118.0651	Benzeneacetonitrile	C8H7N	C16074	118.0651	-1.8E-05	-0.15593	0.297864
118.9205	Sulfite	O3S	C00094	118.92	0.000572	4.811693	#N/A
119.0352	Homocysteine thiolactone	C4H7NOS		119.0355	-0.00024	-2.05537	#N/A
119.0491	Methylpyrazine	C5H6N2		119.049	0.000112	0.943199	434.7823
119.0604	7-Azaindolizine	C7H6N2		119.0604	2.31E-05	0.194383	#N/A
119.0604	5H-Cyclopentapyrazine	C7H6N2		119.0604	2.31E-05	0.194383	#N/A

119.0604	Methylacetoacetic acid	C5H8O3		119.0613	-0.00093	-7.8317	#N/A
119.0604	Levulinic acid	C5H8O3		119.0613	-0.00093	-7.8317	#N/A
119.0604	2-Oxovaleric acid	C5H8O3	C06255	119.0613	-0.00093	-7.8317	#N/A
119.0604	Ethyl pyruvate	C5H8O3		119.0613	-0.00093	-7.8317	#N/A
119.0604	Acetoxyacetone	C5H8O3		119.0613	-0.00093	-7.8317	#N/A
119.0685	Benzeneacetonitrile	C8H7N	C16074	119.0685	6.43E-06	0.053973	0.297864
120.0556	S-Methyl butanethioate	C5H10OS		120.0559	-0.00023	-1.94079	#N/A
120.0556	4-(Methylthio)-2-butanone	C5H10OS		120.0559	-0.00023	-1.94079	#N/A
120.0556	4-Mercapto-2-pentanone	C5H10OS		120.0559	-0.00023	-1.94079	#N/A
120.0556	S-Propyl thioacetate	C5H10OS		120.0559	-0.00023	-1.94079	#N/A
120.0556	3-Mercapto-2-pentanone	C5H10OS		120.0559	-0.00023	-1.94079	#N/A
120.0556	2-Mercapto-3-pentanone	C5H10OS		120.0559	-0.00023	-1.94079	#N/A
120.0556	Tetrahydro-2-methylthiophen-3-ol	C5H10OS		120.0559	-0.00023	-1.94079	#N/A
120.0556	Tetrahydro-2-methyl-3-furanthiol	C5H10OS		120.0559	-0.00023	-1.94079	#N/A
120.0556	1-(Methylthio)-2-butanone	C5H10OS		120.0559	-0.00023	-1.94079	#N/A
120.0556	4-(Methylthio)butanal	C5H10OS		120.0559	-0.00023	-1.94079	#N/A
120.0556	xi-2-Methyl-1,3-oxathiane	C5H10OS		120.0559	-0.00023	-1.94079	#N/A

120.0556	3-(Methylthio)butanal	C5H10OS		120.0559	-0.00023	-1.94079	#N/A
120.0556	3-(Methylthio)-2-butanone	C5H10OS		120.0559	-0.00023	-1.94079	#N/A
120.0556	Acetylglycine	C4H7NO3		120.0566	-0.00095	-7.87382	#N/A
120.0556	L-2-Amino-3-oxobutanoic acid	C4H7NO3	C03508	120.0566	-0.00095	-7.87382	#N/A
120.0556	L-Aspartate-semialdehyde	C4H7NO3	C00441	120.0566	-0.00095	-7.87382	#N/A
120.9362	Sulfurous acid	H2O3S	C00094	120.9356	0.00058	4.795583	#N/A
121.0396	Methylmalonic acid	C4H6O4	C02170	121.0406	-0.00097	-8.03246	#N/A
121.0396	Succinic acid	C4H6O4	C00042	121.0406	-0.00097	-8.03246	#N/A
121.0396	Erythrono-1,4-lactone	C4H6O4		121.0406	-0.00097	-8.03246	#N/A
121.0396	Threonolactone	C4H6O4		121.0406	-0.00097	-8.03246	#N/A
121.0396	4-Hydroxy-2-oxobutanoic acid	C4H6O4		121.0406	-0.00097	-8.03246	#N/A
121.0396	xi-3-Hydroxy-2-oxobutanoic acid	C4H6O4		121.0406	-0.00097	-8.03246	#N/A
121.0648	Phenylacetaldehyde	C8H8O	C00601	121.0648	-1.1E-05	-0.09207	482.8672
121.0648	2,3-Dihydrobenzofuran	C8H8O		121.0648	-1.1E-05	-0.09207	482.8672
121.0648	Acetophenone	C8H8O	C07113	121.0648	-1.1E-05	-0.09207	482.8672
121.076	(1-Methylethenyl)pyrazine	C7H8N2		121.076	5.02E-06	0.041428	#N/A
121.076	2-Methyl-5-vinylpyrazine	C7H8N2		121.076	5.02E-06	0.041428	#N/A
121.076	2-Methyl-3-vinylpyrazine	C7H8N2		121.076	5.02E-06	0.041428	#N/A

121.076	1-Propenylpyrazine	C7H8N2		121.076	5.02E-06	0.041428	#N/A
121.076	3-Hydroxy-2-methyl-[R-(R,S)]-butanoic acid	C5H10O3		121.077	-0.00095	-7.85104	#N/A
121.076	2-Methyl-3-hydroxybutyric acid	C5H10O3		121.077	-0.00095	-7.85104	#N/A
121.076	2-Ethylhydracrylic acid	C5H10O3		121.077	-0.00095	-7.85104	#N/A
121.076	3-Hydroxy-2-methyl-[S-(R,R)]-butanoic acid	C5H10O3		121.077	-0.00095	-7.85104	#N/A
121.076	3-Hydroxyvaleric acid	C5H10O3		121.077	-0.00095	-7.85104	#N/A
121.076	Erythronilic acid	C5H10O3		121.077	-0.00095	-7.85104	#N/A
121.076	3-Hydroxyisovaleric acid	C5H10O3		121.077	-0.00095	-7.85104	#N/A
121.076	2-Hydroxyvaleric acid	C5H10O3		121.077	-0.00095	-7.85104	#N/A
121.076	Ethyl lactate	C5H10O3		121.077	-0.00095	-7.85104	#N/A
121.076	Methyl 3-hydroxybutyrate	C5H10O3		121.077	-0.00095	-7.85104	#N/A
122.0297	2-Furanmethanol	C5H6O2		122.0294	0.000318	2.602992	#N/A
122.0297	5-Methyl-2(3H)-furanone	C5H6O2		122.0294	0.000318	2.602992	#N/A
122.0297	5-Hydroxy-4-pentenoic acid d-lactone	C5H6O2		122.0294	0.000318	2.602992	#N/A
122.06	Benzamide	C7H7NO	C09815	122.06	-2.7E-05	-0.21812	#N/A
122.06	3-Acetylpyridine	C7H7NO		122.06	-2.7E-05	-0.21812	#N/A
122.06	2-Acetylpyridine	C7H7NO		122.06	-2.7E-05	-0.21812	#N/A
122.0712	3-Mercapto-2-methyl-1-butanol	C5H12OS		122.0715	-0.00027	-2.22303	#N/A

122.0712	3-Mercapto-3-methyl-1-butanol	C5H12OS		122.0715	-0.00027	-2.22303	#N/A
122.0712	xi-2-Mercapto-3-methyl-1-butanol	C5H12OS		122.0715	-0.00027	-2.22303	#N/A
122.0712	4-(Methylthio)-2-butanol	C5H12OS		122.0715	-0.00027	-2.22303	#N/A
122.0712	4-(Methylthio)-1-butanol	C5H12OS		122.0715	-0.00027	-2.22303	#N/A
122.0712	L-Threonine	C4H9NO3	C00188	122.0722	-0.00098	-8.0581	#N/A
122.0712	L-Homoserine	C4H9NO3	C00263	122.0722	-0.00098	-8.0581	#N/A
122.0712	L-Allothreonine	C4H9NO3	C05519	122.0722	-0.00098	-8.0581	#N/A
122.0964	1-Phenylethylamine	C8H11N	C02455	122.0964	-2.7E-05	-0.22167	#N/A
122.0964	Phenylethylamine	C8H11N	C05332	122.0964	-2.7E-05	-0.22167	#N/A
122.0964	5-Ethyl-2-methylpyridine	C8H11N		122.0964	-2.7E-05	-0.22167	#N/A
123.0117	3-Mercaptolactic acid	C3H6O3S	C05823	123.011	0.000682	5.545943	#N/A
123.0117	2-Methylfuran	C5H6O		123.0117	-9.5E-06	-0.07747	#N/A
123.0117	2,4-Pentadienal	C5H6O		123.0117	-9.5E-06	-0.07747	#N/A
123.0552	Niacinamide	C6H6N2O	C00153	123.0553	-4.3E-05	-0.3479	#N/A
123.0552	2-Acetylpyrazine	C6H6N2O		123.0553	-4.3E-05	-0.3479	#N/A
123.0552	(S)-3,4-Dihydroxybutyric acid	C4H8O4		123.0562	-0.001	-8.11342	#N/A
123.0552	2,4-Dihydroxybutanoic acid	C4H8O4		123.0562	-0.001	-8.11342	#N/A

123.0552	4-Deoxyerythronic acid	C4H8O4		123.0562	-0.001	-8.11342	#N/A
123.0552	4-Deoxythreonic acid	C4H8O4		123.0562	-0.001	-8.11342	#N/A
123.0552	A,b-Dihydroxyisobutyric acid	C4H8O4		123.0562	-0.001	-8.11342	#N/A
123.0552	Erythrose	C4H8O4	C01796	123.0562	-0.001	-8.11342	#N/A
123.0552	L-Erythrulose	C4H8O4	C02045	123.0562	-0.001	-8.11342	#N/A
124.009	Succinic anhydride	C4H4O3	C19524	124.0086	0.000402	3.244131	#N/A
124.0757	p-Anisidine	C7H9NO	C19326	124.0757	2.98E-05	0.24022	#N/A
124.0757	2-Propionylpyrrole	C7H9NO		124.0757	2.98E-05	0.24022	#N/A
124.0757	4-Hydroxybenzylamine	C7H9NO		124.0757	2.98E-05	0.24022	#N/A
124.0757	1-Ethyl-1H-pyrrole-2-carboxaldehyde	C7H9NO		124.0757	2.98E-05	0.24022	#N/A
124.0757	2-Acetyl-1-methylpyrrole	C7H9NO		124.0757	2.98E-05	0.24022	#N/A
124.9998	Gamma-Butyrolactone	C4H6O2	C01770	124.9999	-9.4E-05	-0.74851	0.337826
124.9998	Oxolan-3-one	C4H6O2		124.9999	-9.4E-05	-0.74851	0.337826
124.9998	Diacetyl	C4H6O2	C00741	124.9999	-9.4E-05	-0.74851	0.337826
124.9998	Ethenyl acetate	C4H6O2	C19309	124.9999	-9.4E-05	-0.74851	0.337826
124.9998	Methyl acrylate	C4H6O2	C19443	124.9999	-9.4E-05	-0.74851	0.337826
125.0168	3-Mercaptolactic acid	C3H6O3S	C05823	125.0178	-0.00092	-7.38258	#N/A
125.0709	Methylimidazole acetaldehyde	C6H8N2O	C05827	125.0709	-2.8E-05	-0.2207	#N/A

125.0709	2-Methoxy-3-methylpyrazine	C6H8N2O		125.0709	-2.8E-05	-0.2207	#N/A
125.0709	2-Methoxy-5-methylpyrazine	C6H8N2O		125.0709	-2.8E-05	-0.2207	#N/A
125.0709	2-Methoxy-6-methylpyrazine	C6H8N2O		125.0709	-2.8E-05	-0.2207	#N/A
125.0709	Erythritol	C4H10O4	C00503	125.0719	-0.00098	-7.86107	#N/A
125.0709	D-Threitol	C4H10O4	C16884	125.0719	-0.00098	-7.86107	#N/A
126.0031	Gamma-Butyrolactone	C4H6O2	C01770	126.0033	-0.00015	-1.15077	0.337826
126.0031	Oxolan-3-one	C4H6O2		126.0033	-0.00015	-1.15077	0.337826
126.0031	Diacetyl	C4H6O2	C00741	126.0033	-0.00015	-1.15077	0.337826
126.0031	Ethenyl acetate	C4H6O2	C19309	126.0033	-0.00015	-1.15077	0.337826
126.0031	Methyl acrylate	C4H6O2	C19443	126.0033	-0.00015	-1.15077	0.337826
126.0372	4-Methyl-5-vinylthiazole	C6H7NS		126.0372	2.02E-05	0.160199	#N/A
126.0372	2-Pyridinemethanethiol	C6H7NS		126.0372	2.02E-05	0.160199	#N/A
126.0464	Nicotinic acid	C6H5NO2	C00253	126.046	0.000382	3.027135	#N/A
126.0464	Picolinic acid	C6H5NO2	C10164	126.046	0.000382	3.027135	#N/A
126.0464	2-Hydroxy-4-imino-2,5-cyclohexadienone	C6H5NO2		126.046	0.000382	3.027135	#N/A
126.0914	6-Acetyl-1,2,3,4-tetrahydropyridine	C7H11NO		126.0913	2.43E-05	0.192582	#N/A
126.0914	3,4-Dihydro-5-propanoyl-2H-pyrrole	C7H11NO		126.0913	2.43E-05	0.192582	#N/A
126.0914	2-Methyl-4-propyloxazole	C7H11NO		126.0913	2.43E-05	0.192582	#N/A
126.0914	4-Methyl-2-propyloxazole	C7H11NO		126.0913	2.43E-05	0.192582	#N/A
126.0914	2-Methyl-5-propyloxazole	C7H11NO		126.0913	2.43E-05	0.192582	#N/A

126.0914	5-Methyl-2-propyloxazole	C7H11NO		126.0913	2.43E-05	0.192582	#N/A
126.0914	2-Ethyl-4,5-dimethyloxazole	C7H11NO		126.0913	2.43E-05	0.192582	#N/A
126.0914	4-Ethyl-2,5-dimethyloxazole	C7H11NO		126.0913	2.43E-05	0.192582	#N/A
126.0914	5-Ethyl-2,4-dimethyloxazole	C7H11NO		126.0913	2.43E-05	0.192582	#N/A
126.0914	4-Butyloxazole	C7H11NO		126.0913	2.43E-05	0.192582	#N/A
126.0914	5-Butyloxazole	C7H11NO		126.0913	2.43E-05	0.192582	#N/A
126.0914	2-Ethyl-5-imino-1-cyclopenten-1-ol	C7H11NO		126.0913	2.43E-05	0.192582	#N/A
127.0434	Iso-Valeraldehyde	C5H10O	C07329	127.043	0.00039	3.07038	#N/A
127.0434	Prenol	C5H10O	C01390	127.043	0.00039	3.07038	#N/A
127.0434	Pentanal	C5H10O		127.043	0.00039	3.07038	#N/A
127.0434	(S)-2-Methylbutanal	C5H10O		127.043	0.00039	3.07038	#N/A
127.0434	(Â±)-2-Methylbutanal	C5H10O	C02223	127.043	0.00039	3.07038	#N/A
127.0434	(E)-2-Penten-1-ol	C5H10O		127.043	0.00039	3.07038	#N/A
127.0434	1-Penten-3-ol	C5H10O		127.043	0.00039	3.07038	#N/A
127.0434	Isoprenyl alcohol	C5H10O		127.043	0.00039	3.07038	#N/A
127.0434	2-Pentanone	C5H10O	C01949	127.043	0.00039	3.07038	#N/A
127.0434	2-Methyl-2-buten-1-ol	C5H10O		127.043	0.00039	3.07038	#N/A
127.0434	xi-3-Methyl-3-buten-2-ol	C5H10O		127.043	0.00039	3.07038	#N/A
128.0503	2,3-Diaminopropionic acid	C3H8N2O2	C03401	128.0512	-0.00086	-6.7169	#N/A
128.9859	Pyruvic acid	C3H4O3	C00022	128.9859	-5E-05	-0.38838	#N/A
128.9859	Malonic semialdehyde	C3H4O3	C00222	128.9859	-5E-05	-0.38838	#N/A
128.9859	Glucosereductone	C3H4O3		128.9859	-5E-05	-0.38838	#N/A

129.0044	3-(Methylthio)-1-propene	C4H8S		129.0045	-0.00013	-1.0231	#N/A
129.0044	cis-2,3-Dimethylthiirane	C4H8S		129.0045	-0.00013	-1.0231	#N/A
129.0229	Ethylphosphate	C2H7O4P		129.0222	0.000741	5.744174	#N/A
129.0229	Isobutyric acid	C4H8O2	C02632	129.0223	0.000625	4.84296	#N/A
129.0229	Methyl propionate	C4H8O2		129.0223	0.000625	4.84296	#N/A
129.0229	Ethyl acetate	C4H8O2	C00849	129.0223	0.000625	4.84296	#N/A
129.0229	1-Hydroxy-2-butanone	C4H8O2		129.0223	0.000625	4.84296	#N/A
129.0229	Propyl formate	C4H8O2		129.0223	0.000625	4.84296	#N/A
129.0229	Isopropyl formate	C4H8O2		129.0223	0.000625	4.84296	#N/A
129.0447	1,2,3-Trihydroxybenzene	C6H6O3	C01108	129.0457	-0.00099	-7.68809	#N/A
129.0447	1,3,5-Trihydroxybenzene	C6H6O3	C02183	129.0457	-0.00099	-7.68809	#N/A
129.0447	Methyl 2-furoate	C6H6O3		129.0457	-0.00099	-7.68809	#N/A
129.0447	Maltol	C6H6O3	C11918	129.0457	-0.00099	-7.68809	#N/A
129.0447	4-Hydroxy-2H-pyran-3-carboxaldehyde	C6H6O3		129.0457	-0.00099	-7.68809	#N/A
129.0447	(Z)-Tamarindienal	C6H6O3		129.0457	-0.00099	-7.68809	#N/A
129.0447	5-Hydroxymethyl-2-furancarboxaldehyde	C6H6O3	C11101	129.0457	-0.00099	-7.68809	#N/A
129.0572	Thymine	C5H6N2O2	C00178	129.0569	0.000316	2.450894	#N/A
129.0572	Imidazoleacetic acid	C5H6N2O2	C02835	129.0569	0.000316	2.450894	#N/A
129.0572	1H-Imidazole-1-acetic acid	C5H6N2O2		129.0569	0.000316	2.450894	#N/A
129.0654	Dihydrothymine	C5H8N2O2	C00906	129.0659	-0.00049	-3.78601	#N/A

129.0654	Squamolone	C5H8N2O2		129.0659	-0.00049	-3.78601	#N/A
129.0654	L-Cyclo(alanylglycyl)	C5H8N2O2		129.0659	-0.00049	-3.78601	#N/A
129.0698	Putrescine	C4H12N2	C00134	129.0699	-8.3E-05	-0.64225	#N/A
130.0349	Benzaldehyde	C7H6O	C00193	130.0344	0.000452	3.473069	#N/A
130.0349	2,3-Butanediol	C4H10O2	C00265	130.0346	0.000297	2.282997	11.39715
130.0349	1,1-Dimethoxyethane	C4H10O2		130.0346	0.000297	2.282997	11.39715
130.0349	2-Ethoxyethanol	C4H10O2	C14687	130.0346	0.000297	2.282997	11.39715
130.0349	1,3-Butanediol	C4H10O2		130.0346	0.000297	2.282997	11.39715
130.0349	(2R,3R)-2,3-Butanediol	C4H10O2	C03044	130.0346	0.000297	2.282997	11.39715
130.04	2-(Methylthiomethyl)furan	C6H8OS		130.0402	-0.00026	-1.97053	#N/A
130.04	2-Methyl-3-(methylthio)furan	C6H8OS		130.0402	-0.00026	-1.97053	#N/A
130.04	2-(1-Mercaptoethyl)furan	C6H8OS		130.0402	-0.00026	-1.97053	#N/A
130.04	5-Methyl-2-furanmethanethiol	C6H8OS		130.0402	-0.00026	-1.97053	#N/A
130.04	2,5-Dimethyl-3-furanthiol	C6H8OS		130.0402	-0.00026	-1.97053	#N/A
130.04	Hydroxyminaline	C5H5NO3		130.0409	-0.00097	-7.44803	#N/A
130.0644	Isoquinoline	C9H7N	C06323	130.0651	-0.00074	-5.68344	#N/A
130.0652	Isoquinoline	C9H7N	C06323	130.0651	2.72E-05	0.209224	0.21082
130.0777	D-1-Piperideine-2-carboxylic acid	C6H9NO2	C04092	130.0773	0.000383	2.94247	#N/A
130.0777	(S)-2,3,4,5-Tetrahydropiperidine-2-carboxylate	C6H9NO2		130.0773	0.000383	2.94247	#N/A

130.0777	(Â±)-4-Methylene-2-pyrrolidinecarboxylic acid	C6H9NO2		130.0773	0.000383	2.94247	#N/A
131.0603	Osmundalactone	C6H8O3		131.0613	-0.00098	-7.49394	#N/A
131.0603	3-Hydroxy-4,5-dimethyl-2(5H)-furanone	C6H8O3		131.0613	-0.00098	-7.49394	#N/A
131.0603	2-Ethyl-3,4-dihydroxyfuran	C6H8O3		131.0613	-0.00098	-7.49394	#N/A
131.0603	L-erythro-5-(1-Hydroxyethyl)-2(5H)-furanone	C6H8O3		131.0613	-0.00098	-7.49394	#N/A
131.0603	5,6-Dihydro-4-methoxy-2H-pyran-2-one	C6H8O3		131.0613	-0.00098	-7.49394	#N/A
131.0603	xi-5-Acetyltetrahydro-2(3H)-furanone	C6H8O3		131.0613	-0.00098	-7.49394	#N/A
131.0603	(Â±)-Furaneol	C6H8O3		131.0613	-0.00098	-7.49394	#N/A
131.0603	2,7-Oxepanedione	C6H8O3		131.0613	-0.00098	-7.49394	#N/A
131.0684	Isoquinoline	C9H7N	C06323	131.0685	-5E-05	-0.3777	0.21082
131.0729	Dihydrothymine	C5H8N2O2	C00906	131.0726	0.000343	2.613767	#N/A
131.0729	Squamolone	C5H8N2O2		131.0726	0.000343	2.613767	#N/A
131.0729	L-Cyclo(alanylglycyl)	C5H8N2O2		131.0726	0.000343	2.613767	#N/A
132.0505	Anisole	C7H8O	C01403	132.0501	0.000449	3.403543	12.91345
132.0569	Pyroglutamic acid	C5H7NO3	C01879	132.0566	0.000348	2.633338	#N/A
132.0569	Pyrrolidonecarboxylic acid	C5H7NO3	C02237	132.0566	0.000348	2.633338	#N/A
132.0569	Pyrroline hydroxycarboxylic acid	C5H7NO3	C04281	132.0566	0.000348	2.633338	#N/A
132.0569	N-Acryloylglycine	C5H7NO3		132.0566	0.000348	2.633338	#N/A
132.0569	1-Pyrroline-4-hydroxy-2-carboxylate	C5H7NO3	C04282	132.0566	0.000348	2.633338	#N/A
133.0448	4-Aminophenol	C6H7NO	C02372	133.0453	-0.00054	-4.08541	9.750195

133.0448	2-Acetylpyrrole	C6H7NO		133.04053	-0.00054	-4.08541	9.750195
133.0448	1-Methyl-2-pyrrolecarboxaldehyde	C6H7NO		133.04053	-0.00054	-4.08541	9.750195
133.076	1-Methylpyrrolo[1,2-a]pyrazine	C8H8N2		133.076	-3.2E-05	-0.24282	#N/A
133.076	4-Methylpyrrolo[1,2-a]pyrazine	C8H8N2		133.076	-3.2E-05	-0.24282	#N/A
133.076	2-Ketohexanoic acid	C6H10O3	C00902	133.0777	-0.00099	-7.42359	#N/A
133.076	Mevalonolactone	C6H10O3		133.0777	-0.00099	-7.42359	#N/A
133.076	3-Oxohexanoic acid	C6H10O3	C02122	133.0777	-0.00099	-7.42359	#N/A
133.076	5-Ethoxy-4,5-dihydro-2(3H)furanone	C6H10O3		133.0777	-0.00099	-7.42359	#N/A
133.076	Ethyl acetoacetate	C6H10O3		133.0777	-0.00099	-7.42359	#N/A
133.076	Ethyl 3-oxobutanoate	C6H10O3	C03500	133.0777	-0.00099	-7.42359	#N/A
133.076	Sherry lactone	C6H10O3		133.0777	-0.00099	-7.42359	#N/A
133.076	(4S,6S)-3,4,5,6-Tetrahydro-4-hydroxy-6-methyl-2H-pyran-2-one	C6H10O3		133.0777	-0.00099	-7.42359	#N/A
133.076	Acetoin acetate	C6H10O3		133.0777	-0.00099	-7.42359	#N/A
133.076	Methyl levulinate	C6H10O3		133.0777	-0.00099	-7.42359	#N/A
133.0885	L-cis-3-Amino-2-pyrrolidinecarboxylic acid	C5H10N2O2		133.0882	0.000328	2.463883	#N/A
133.0885	D-1-Amino-2-pyrrolidinecarboxylic acid	C5H10N2O2		133.0882	0.000328	2.463883	#N/A
134.0482	4-Aminophenol	C6H7NO	C02372	134.0487	-0.00052	-3.88302	9.750195

134.0482	2-Acetylpyrrole	C6H7NO		134.04787	-0.00052	-3.88302	9.750195
134.0482	1-Methyl-2-pyrrolecarboxaldehyde	C6H7NO		134.04787	-0.00052	-3.88302	9.750195
134.06	Indoxyl	C8H7NO	C05658	134.06	-8.2E-05	-0.61492	#N/A
134.06	4-Hydroxybenzeneacetonitrile	C8H7NO	C03766	134.06	-8.2E-05	-0.61492	#N/A
134.06	2-Methyl-4,5-benzoxazole	C8H7NO		134.06	-8.2E-05	-0.61492	#N/A
134.06	(Â±)-2-Hydroxy-2-phenylacetonitrile	C8H7NO		134.06	-8.2E-05	-0.61492	#N/A
134.0712	3-Methylpyrrolo[1,2-a]pyrazine	C7H7N3		134.0713	-7E-05	-0.52021	14.48184
134.0712	4-Mercapto-4-methyl-2-pentanone	C6H12OS		134.0715	-0.00031	-2.33487	#N/A
134.0712	2,5-Dimethyl-3-mercaptotetrahydrofuran	C6H12OS		134.0715	-0.00031	-2.33487	#N/A
134.0712	4-(Methylthio)-2-pentanone	C6H12OS		134.0715	-0.00031	-2.33487	#N/A
134.0712	3-Mercapto-2-methylpentanal	C6H12OS		134.0715	-0.00031	-2.33487	#N/A
134.0964	1,2,3,4-Tetrahydroisoquinoline	C9H11N		134.0964	-4.7E-05	-0.35009	#N/A
134.9242	Hydrogen phosphate	HO4P	C01293	134.9244	-0.00023	-1.71269	#N/A
135.0292	L-Malic acid	C4H6O5	C00149	135.0288	0.000353	2.613319	#N/A
135.0292	Malic acid	C4H6O5	C00711	135.0288	0.000353	2.613319	#N/A
135.0292	D-Malic acid	C4H6O5	C00497	135.0288	0.000353	2.613319	#N/A
135.0292	Velcorin	C4H6O5		135.0288	0.000353	2.613319	#N/A
135.0292	3,3-Dimethyl-1,2-dithiolane	C5H10S2		135.0297	-0.00052	-3.81786	#N/A

135.0292	Tetrahydro-2-methyl-2-thiophenethiol	C5H10S2		135.0297	-0.00052	-3.81786	#N/A
135.0292	Tetrahydro-2-methyl-3-thiophenethiol	C5H10S2		135.0297	-0.00052	-3.81786	#N/A
135.0604	N-Acetyl-2,3-dihydro-1H-pyrrole	C6H9NO		135.061	-0.00057	-4.19749	11.2528
135.0604	5-Acetyl-3,4-dihydro-2H-pyrrole	C6H9NO		135.061	-0.00057	-4.19749	11.2528
135.0604	2-Ethyl-4-methyloxazole	C6H9NO		135.061	-0.00057	-4.19749	11.2528
135.0604	4-Ethyl-2-methyloxazole	C6H9NO		135.061	-0.00057	-4.19749	11.2528
135.0604	2-Ethyl-5-methyloxazole	C6H9NO		135.061	-0.00057	-4.19749	11.2528
135.0604	5-Ethyl-2-methyloxazole	C6H9NO		135.061	-0.00057	-4.19749	11.2528
135.0604	5-Ethyl-4-methyloxazole	C6H9NO		135.061	-0.00057	-4.19749	11.2528
135.0604	5-Imino-2-methyl-1-cyclopenten-1-ol	C6H9NO		135.061	-0.00057	-4.19749	11.2528
135.0604	Trimethyloxazole	C6H9NO		135.061	-0.00057	-4.19749	11.2528
135.0678	Ureidopropionic acid	C4H8N2O3	C02642	135.0675	0.000336	2.486334	#N/A
135.0678	L-Asparagine	C4H8N2O3	C00152	135.0675	0.000336	2.486334	#N/A
135.0678	Glycyl-glycine	C4H8N2O3	C02037	135.0675	0.000336	2.486334	#N/A
135.0678	N-Carbamoylsarcosine	C4H8N2O3	C01043	135.0675	0.000336	2.486334	#N/A
135.0678	D-Asparagine	C4H8N2O3	C01905	135.0675	0.000336	2.486334	#N/A
135.0917	5,6,7,8-Tetrahydroquinoxaline	C8H10N2		135.0917	-2.1E-05	-0.15288	#N/A
135.0917	3,5-Dimethyl-2-vinylpyrazine	C8H10N2		135.0917	-2.1E-05	-0.15288	#N/A

135.0917	6,7-Dihydro-2-methyl-5H-cyclopenta[b]pyrazine	C8H10N2		135.0917	-2.1E-05	-0.15288	#N/A
135.0917	6,7-Dihydro-5-methyl-5H-cyclopenta[b]pyrazine	C8H10N2		135.0917	-2.1E-05	-0.15288	#N/A
135.0917	2-Methyl-6-(1-propenyl)pyrazine	C8H10N2		135.0917	-2.1E-05	-0.15288	#N/A
135.0917	2-Methyl-3-(1-propenyl)pyrazine	C8H10N2		135.0917	-2.1E-05	-0.15288	#N/A
135.0917	2-Methyl-6-(2-propenyl)pyrazine	C8H10N2		135.0917	-2.1E-05	-0.15288	#N/A
135.0917	2-Methyl-5-(2-propenyl)pyrazine	C8H10N2		135.0917	-2.1E-05	-0.15288	#N/A
135.0917	2-Methyl-3-(2-propenyl)pyrazine	C8H10N2		135.0917	-2.1E-05	-0.15288	#N/A
135.0917	2-Methyl-5-(1-propenyl)pyrazine	C8H10N2		135.0917	-2.1E-05	-0.15288	#N/A
135.0917	(5R)-5-Hydroxyhexanoic acid	C6H12O3		135.0926	-0.00098	-7.22651	#N/A
135.0917	5-Hydroxyhexanoic acid	C6H12O3		135.0926	-0.00098	-7.22651	#N/A
135.0917	2-Hydroxycaproic acid	C6H12O3		135.0926	-0.00098	-7.22651	#N/A
135.0917	(R)-3-Hydroxyhexanoic acid	C6H12O3		135.0926	-0.00098	-7.22651	#N/A
135.0917	6-Hydroxyhexanoic acid	C6H12O3	C06103	135.0926	-0.00098	-7.22651	#N/A
135.0917	(+/-)-1-Acetoxy-1-ethoxyethane	C6H12O3		135.0926	-0.00098	-7.22651	#N/A
135.0917	Paraldehyde	C6H12O3	C07834	135.0926	-0.00098	-7.22651	#N/A
135.0917	Ethyl (Â±)-3-hydroxybutyrate	C6H12O3		135.0926	-0.00098	-7.22651	#N/A

135.0917	Butoxyacetic acid	C6H12O3		135.0926	-0.00098	-7.22651	#N/A
135.1168	1-Nitrohexane	C6H14NO2		135.1164	0.000334	2.470292	#N/A
136.0455	trans-1,2-Dihydrobenzene-1,2-diol	C6H8O2	C04221	136.045	0.000509	3.74461	#N/A
136.0455	1,2-Cyclohexanedione	C6H8O2	C06105	136.045	0.000509	3.74461	#N/A
136.0455	3-Methyl-1,2-cyclopentanedione	C6H8O2		136.045	0.000509	3.74461	#N/A
136.0455	(E)-4-Oxo-2-hexen-1-al	C6H8O2		136.045	0.000509	3.74461	#N/A
136.0455	2,5-Dimethyl-3(2H)-furanone	C6H8O2		136.045	0.000509	3.74461	#N/A
136.0455	Syoyualdehyde	C6H8O2		136.045	0.000509	3.74461	#N/A
136.0455	2-(Methoxymethyl)furan	C6H8O2		136.045	0.000509	3.74461	#N/A
136.0455	xi-3,5-Dimethyl-2(5H)-furanone	C6H8O2		136.045	0.000509	3.74461	#N/A
136.0455	5,5-Dimethyl-2(5H)-furanone	C6H8O2		136.045	0.000509	3.74461	#N/A
136.0505	Ethyl 2-mercaptopropionate	C5H10O2S		136.0508	-0.00028	-2.09176	#N/A
136.0505	Ethyl 3-mercaptopropanoic acid	C5H10O2S		136.0508	-0.00028	-2.09176	#N/A
136.0505	L-Aspartic acid	C4H7NO4	C00049	136.0515	-0.001	-7.32727	#N/A
136.0505	D-Aspartic acid	C4H7NO4	C00402	136.0515	-0.001	-7.32727	#N/A
136.0505	Iminodiacetic acid	C4H7NO4	C19911	136.0515	-0.001	-7.32727	#N/A
136.0618	Adenine	C5H5N5	C00147	136.0618	-1.4E-05	-0.10172	#N/A
136.0757	N-Acetylarylamine	C8H9NO	C07565	136.0757	-7.8E-06	-0.05701	#N/A
136.0757	2-Phenylacetamide	C8H9NO	C02505	136.0757	-7.8E-06	-0.05701	#N/A
136.0757	2-Aminoacetophenone	C8H9NO		136.0757	-7.8E-06	-0.05701	#N/A

136.0757	2'-Aminoacetophenone	C8H9NO		136.0757	-7.8E-06	-0.05701	#N/A
136.0757	2-Acetyl-4-methylpyridine	C8H9NO		136.0757	-7.8E-06	-0.05701	#N/A
136.0757	2-Acetyl-6-methylpyridine	C8H9NO		136.0757	-7.8E-06	-0.05701	#N/A
136.0757	2,3-Dihydro-1H-pyrrolizine-5-carboxaldehyde	C8H9NO		136.0757	-7.8E-06	-0.05701	#N/A
136.0757	5-(2-Furanyl)-3,4-dihydro-2H-pyrrole	C8H9NO		136.0757	-7.8E-06	-0.05701	#N/A
136.0757	2-Acetyl-5-methylpyridine	C8H9NO		136.0757	-7.8E-06	-0.05701	#N/A
136.0757	4-Acetyl-2-methylpyridine	C8H9NO		136.0757	-7.8E-06	-0.05701	#N/A
136.0757	4-Acetyl-3-methylpyridine	C8H9NO		136.0757	-7.8E-06	-0.05701	#N/A
136.0757	Histamine	C5H9N3	C00388	136.0756	0.000107	0.787639	#N/A
136.0766	N-Acetylarylamine	C8H9NO	C07565	136.0757	0.000899	6.607749	#N/A
136.0766	2-Phenylacetamide	C8H9NO	C02505	136.0757	0.000899	6.607749	#N/A
136.0766	2-Aminoacetophenone	C8H9NO		136.0757	0.000899	6.607749	#N/A
136.0766	2'-Aminoacetophenone	C8H9NO		136.0757	0.000899	6.607749	#N/A
136.0766	2-Acetyl-4-methylpyridine	C8H9NO		136.0757	0.000899	6.607749	#N/A
136.0766	2-Acetyl-6-methylpyridine	C8H9NO		136.0757	0.000899	6.607749	#N/A
136.0766	2,3-Dihydro-1H-pyrrolizine-5-carboxaldehyde	C8H9NO		136.0757	0.000899	6.607749	#N/A
136.0766	5-(2-Furanyl)-3,4-dihydro-2H-pyrrole	C8H9NO		136.0757	0.000899	6.607749	#N/A
136.0766	2-Acetyl-5-methylpyridine	C8H9NO		136.0757	0.000899	6.607749	#N/A
136.0766	4-Acetyl-2-methylpyridine	C8H9NO		136.0757	0.000899	6.607749	#N/A
136.0766	4-Acetyl-3-methylpyridine	C8H9NO		136.0757	0.000899	6.607749	#N/A

136.9998	2-Furanmethanol	C5H6O2		136.9999	-0.00016	-1.1466	#N/A
136.9998	5-Methyl-2(3H)-furanone	C5H6O2		136.9999	-0.00016	-1.1466	#N/A
136.9998	5-Hydroxy-4-pentenoic acid d-lactone	C5H6O2		136.9999	-0.00016	-1.1466	#N/A
137.0085	S-Methyl 2-propene-1-sulfinothioate	C4H8OS2		137.0089	-0.00044	-3.24116	11.50273
137.0085	S-2-Propenyl methanesulfinothioate	C4H8OS2		137.0089	-0.00044	-3.24116	11.50273
137.0085	(Z)-S-Methyl 1-propenesulfinothioate	C4H8OS2		137.0089	-0.00044	-3.24116	11.50273
137.0085	(Z)-S-1-Propenyl methanesulfinothioate	C4H8OS2		137.0089	-0.00044	-3.24116	11.50273
137.0274	2-Methyl-2-cyclopenten-1-one	C6H8O		137.0274	2.39E-05	0.174376	#N/A
137.0274	3-Methyl-2-cyclopenten-1-one	C6H8O		137.0274	2.39E-05	0.174376	#N/A
137.0274	2,4-Dimethylfuran	C6H8O		137.0274	2.39E-05	0.174376	#N/A
137.0274	2,5-Dimethylfuran	C6H8O		137.0274	2.39E-05	0.174376	#N/A
137.0274	(E,E)-2,4-Hexadienal	C6H8O		137.0274	2.39E-05	0.174376	#N/A
137.0274	2-Ethylfuran	C6H8O		137.0274	2.39E-05	0.174376	#N/A
137.0709	N-Methylnicotinamide	C7H8N2O		137.0709	-4.5E-05	-0.32756	#N/A
137.0709	2-Acetyl-3-methylpyrazine	C7H8N2O		137.0709	-4.5E-05	-0.32756	#N/A
137.0709	2-Aminobenzamide	C7H8N2O	C17512	137.0709	-4.5E-05	-0.32756	#N/A
137.0709	4-Acetyl-2-methylpyrimidine	C7H8N2O		137.0709	-4.5E-05	-0.32756	#N/A
137.1073	5-Ethyl-2,3-dimethylpyrazine	C8H12N2		137.1073	-1.8E-05	-0.13438	#N/A

137.1073	2-Ethyl-3,(5 or 6)-dimethylpyrazine	C8H12N2		137.1073	-1.8E-05	-0.13438	#N/A
137.1073	Tetramethylpyrazine	C8H12N2		137.1073	-1.8E-05	-0.13438	#N/A
137.1073	2,5-Diethylpyrazine	C8H12N2		137.1073	-1.8E-05	-0.13438	#N/A
137.1073	2,6-Diethylpyrazine	C8H12N2		137.1073	-1.8E-05	-0.13438	#N/A
137.1073	2-Isopropyl-5-methylpyrazine	C8H12N2		137.1073	-1.8E-05	-0.13438	#N/A
137.1073	2-Methyl-5-propylpyrazine	C8H12N2		137.1073	-1.8E-05	-0.13438	#N/A
137.1073	2-Ethyl-3,5-dimethylpyrazine	C8H12N2		137.1073	-1.8E-05	-0.13438	#N/A
137.1073	2-Methyl-3-propylpyrazine	C8H12N2		137.1073	-1.8E-05	-0.13438	#N/A
137.1073	2,3-Diethylpyrazine	C8H12N2		137.1073	-1.8E-05	-0.13438	#N/A
137.1073	Polypropylene glycol (m w 1,200-3,000)	C6H14O3		137.1083	-0.00097	-7.10402	#N/A
138.0121	S-Methyl 2-propene-1-sulfinothioate	C4H8OS2		138.0123	-0.00022	-1.56941	11.50273
138.0121	S-2-Propenyl methanesulfinothioate	C4H8OS2		138.0123	-0.00022	-1.56941	11.50273
138.0121	(Z)-S-Methyl 1-propenesulfinothioate	C4H8OS2		138.0123	-0.00022	-1.56941	11.50273
138.0121	(Z)-S-1-Propenyl methanesulfinothioate	C4H8OS2		138.0123	-0.00022	-1.56941	11.50273
138.0661	(+)-threo-2-Amino-3,4-dihydroxybutanoic acid	C4H9NO4		138.0671	-0.001	-7.22577	#N/A
138.0913	Tyramine	C8H11NO	C00483	138.0913	-4.1E-05	-0.29575	#N/A

138.0913	2-Hydroxyphenethylamine	C8H11NO	C02735	138.0913	-4.1E-05	-0.29575	#N/A
138.0913	Dimethylaniline-N-oxide	C8H11NO	C01183	138.0913	-4.1E-05	-0.29575	#N/A
138.0913	m-Tyramine	C8H11NO		138.0913	-4.1E-05	-0.29575	#N/A
138.0913	2-Acetyl-1-ethylpyrrole	C8H11NO		138.0913	-4.1E-05	-0.29575	#N/A
138.0913	1,2,3,4,5,6-Hexahydro-7H-cyclopenta[b]pyridin-7-one	C8H11NO		138.0913	-4.1E-05	-0.29575	#N/A
138.0913	(Â±)-2-(2-Furanyl)pyrrolidine	C8H11NO		138.0913	-4.1E-05	-0.29575	#N/A
139.0154	S-Methyl 2-propene-1-sulfinothioate	C4H8OS2		139.0156	-0.00024	-1.76131	11.50273
139.0154	S-2-Propenyl methanesulfinothioate	C4H8OS2		139.0156	-0.00024	-1.76131	11.50273
139.0154	(Z)-S-Methyl 1-propenesulfinothioate	C4H8OS2		139.0156	-0.00024	-1.76131	11.50273
139.0154	(Z)-S-1-Propenyl methanesulfinothioate	C4H8OS2		139.0156	-0.00024	-1.76131	11.50273
139.0154	3-Methylbutyrolactone	C5H8O2		139.0156	-0.00019	-1.36975	406.4895
139.0154	Glutaral	C5H8O2	C12518	139.0156	-0.00019	-1.36975	406.4895
139.0154	Dihydro-2-methyl-3(2H)-furanone	C5H8O2		139.0156	-0.00019	-1.36975	406.4895
139.0154	2,3-Pentanedione	C5H8O2		139.0156	-0.00019	-1.36975	406.4895
139.0154	2,4-Pentanedione	C5H8O2	C15499	139.0156	-0.00019	-1.36975	406.4895
139.0154	Isopropenyl acetate	C5H8O2		139.0156	-0.00019	-1.36975	406.4895

139.0154	Methyl methacrylate	C5H8O2	C14527	139.0156	-0.00019	-1.36975	406.4895
139.0154	Dihydro-5-methyl-2(3H)-furanone	C5H8O2		139.0156	-0.00019	-1.36975	406.4895
139.0154	Ethyl acrylate	C5H8O2	C19238	139.0156	-0.00019	-1.36975	406.4895
139.0154	Dihydro-3-methyl-2(3H)-furanone	C5H8O2		139.0156	-0.00019	-1.36975	406.4895
139.0328	3-keto-2-Methylbutyrate	C5H7O3		139.0321	0.000729	5.244739	#N/A
139.0534	Hypoxanthine	C5H4N4O	C00262	139.0525	0.00093	6.685964	#N/A
139.0534	xi-4,5-Dihydro-2,4(5)-dimethyl-1H-imidazole	C5H10N2		139.0543	-0.00084	-6.0398	#N/A
139.0542	xi-4,5-Dihydro-2,4(5)-dimethyl-1H-imidazole	C5H10N2		139.0543	-5.7E-05	-0.41019	492.1248
139.0866	2-Ethoxy-3-methylpyrazine	C7H10N2O		139.0866	-2E-06	-0.01416	#N/A
139.0866	3-Ethyl-2-methoxypyrazine	C7H10N2O		139.0866	-2E-06	-0.01416	#N/A
139.0866	2-Ethoxy-5-methylpyrazine	C7H10N2O		139.0866	-2E-06	-0.01416	#N/A
139.0866	2-Ethoxy-6-methylpyrazine	C7H10N2O		139.0866	-2E-06	-0.01416	#N/A
139.0866	2-Methoxy-3,5-dimethylpyrimidine	C7H10N2O		139.0866	-2E-06	-0.01416	#N/A
139.0866	2-Methylerythritol	C5H12O4		139.0875	-0.00096	-6.88462	#N/A
139.0866	3-Deoxy-D-arabinitol	C5H12O4		139.0875	-0.00096	-6.88462	#N/A
139.0866	2-Deoxy-D-ribitol	C5H12O4		139.0875	-0.00096	-6.88462	#N/A
139.0866	1-Deoxy-D-ribitol	C5H12O4		139.0875	-0.00096	-6.88462	#N/A

140.062	p-Aminobenzoic acid	C7H7NO2	C00568	140.0617	0.000323	2.309218	#N/A
140.062	3-Pyridylacetic acid	C7H7NO2		140.0617	0.000323	2.309218	#N/A
140.062	Methyl nicotinate	C7H7NO2		140.0617	0.000323	2.309218	#N/A
140.0818	Histidinal	C6H9N3O		140.0818	-7.3E-05	-0.51886	#N/A
140.9797	Mesoxalic acid	C3H2O5	C00830	140.9794	0.000241	1.707889	#N/A
141.0223	3-Methylbutyrolactone	C5H8O2		141.0223	-2.5E-05	-0.17886	406.4895
141.0223	Glutaral	C5H8O2	C12518	141.0223	-2.5E-05	-0.17886	406.4895
141.0223	Dihydro-2-methyl-3(2H)-furanone	C5H8O2		141.0223	-2.5E-05	-0.17886	406.4895
141.0223	2,3-Pentanedione	C5H8O2		141.0223	-2.5E-05	-0.17886	406.4895
141.0223	2,4-Pentanedione	C5H8O2	C15499	141.0223	-2.5E-05	-0.17886	406.4895
141.0223	Isopropenyl acetate	C5H8O2		141.0223	-2.5E-05	-0.17886	406.4895
141.0223	Methyl methacrylate	C5H8O2	C14527	141.0223	-2.5E-05	-0.17886	406.4895
141.0223	Dihydro-5-methyl-2(3H)-furanone	C5H8O2		141.0223	-2.5E-05	-0.17886	406.4895
141.0223	Ethyl acrylate	C5H8O2	C19238	141.0223	-2.5E-05	-0.17886	406.4895
141.0223	Dihydro-3-methyl-2(3H)-furanone	C5H8O2		141.0223	-2.5E-05	-0.17886	406.4895
141.0481	2-Methyl-(3 or 5 or 6)-(methylthio)pyrazine (mixture of isomers)	C6H8N2S		141.0481	-2.3E-05	-0.166	#N/A
141.0481	Pyrazineethanethiol	C6H8N2S		141.0481	-2.3E-05	-0.166	#N/A
141.0481	2-Methyl-5-(methylthio)pyrazine	C6H8N2S		141.0481	-2.3E-05	-0.166	#N/A
141.0481	2-Methyl-6-(methylthio)pyrazine	C6H8N2S		141.0481	-2.3E-05	-0.166	#N/A

141.0481	5-Hydroxypyrazinamide	C5H5N3O2	C01956	141.0488	-0.00074	-5.21603	#N/A
141.0572	2,4-Dimethyl-5-vinylthiazole	C7H9NS		141.0562	0.00099	7.021877	#N/A
141.0572	Urocanic acid	C6H6N2O2	C00785	141.0569	0.000278	1.972101	#N/A
141.0572	Nicotinamide N-oxide	C6H6N2O2		141.0569	0.000278	1.972101	#N/A
141.0572	5-Oxo-2(5H)-isoxazolepropanenitrile	C6H6N2O2		141.0569	0.000278	1.972101	#N/A
141.0572	(E)-Urocanic acid	C6H6N2O2		141.0569	0.000278	1.972101	#N/A
142.0732	Diethylenetriamine	C4H13N3		142.0741	-0.00091	-6.37598	#N/A
142.0777	3,4-Dihydroxybenzylamine	C7H9NO2		142.0773	0.000352	2.480205	#N/A
142.0777	5-Acetyl-2,4-dimethyloxazole	C7H9NO2		142.0773	0.000352	2.480205	#N/A
143.0103	2-Hydroxybutyric acid	C4H8O3	C05984	143.0105	-0.00017	-1.1728	#N/A
143.0103	(R)-3-Hydroxybutyric acid	C4H8O3	C01089	143.0105	-0.00017	-1.1728	#N/A
143.0103	(S)-3-Hydroxyisobutyric acid	C4H8O3	C06001	143.0105	-0.00017	-1.1728	#N/A
143.0103	(R)-3-Hydroxyisobutyric acid	C4H8O3		143.0105	-0.00017	-1.1728	#N/A
143.0103	3-Hydroxybutyric acid	C4H8O3	C01089	143.0105	-0.00017	-1.1728	#N/A
143.0103	(S)-3-Hydroxybutyric acid	C4H8O3	C03197	143.0105	-0.00017	-1.1728	#N/A
143.0103	4-Hydroxybutyric acid	C4H8O3	C00989	143.0105	-0.00017	-1.1728	#N/A
143.0103	Ethoxyacetic acid	C4H8O3		143.0105	-0.00017	-1.1728	#N/A
143.0426	2-Methoxybenzenethiol	C7H8OS		143.0436	-0.001	-6.96891	#N/A
143.0426	Kahweofuran	C7H8OS		143.0436	-0.001	-6.96891	#N/A

143.0426	2-Acetyl-3-methylthiophene	C7H8OS		143.0436	-0.001	-6.96891	#N/A
143.0729	1,3-Dimethyluracil	C6H8N2O2		143.0726	0.000325	2.274308	#N/A
143.0729	Imidazolepropionic acid	C6H8N2O2		143.0726	0.000325	2.274308	#N/A
143.0729	Methylimidazoleacetic acid	C6H8N2O2	C05828	143.0726	0.000325	2.274308	#N/A
143.0729	Pi-Methylimidazoleacetic acid	C6H8N2O2		143.0726	0.000325	2.274308	#N/A
143.0855	Cadaverine	C5H14N2	C01672	143.0856	-8.6E-05	-0.60395	#N/A
143.0855	N-Methylputrescine	C5H14N2	C02723	143.0856	-8.6E-05	-0.60395	#N/A
144.0808	Diethylenetriamine	C4H13N3		144.0808	-4.9E-05	-0.34312	#N/A
145.0172	2-Hydroxybutyric acid	C4H8O3	C05984	145.0172	-2.2E-05	-0.15041	121.4571
145.0172	(R)-3-Hydroxybutyric acid	C4H8O3	C01089	145.0172	-2.2E-05	-0.15041	121.4571
145.0172	(S)-3-Hydroxyisobutyric acid	C4H8O3	C06001	145.0172	-2.2E-05	-0.15041	121.4571
145.0172	(R)-3-Hydroxyisobutyric acid	C4H8O3		145.0172	-2.2E-05	-0.15041	121.4571
145.0172	3-Hydroxybutyric acid	C4H8O3	C01089	145.0172	-2.2E-05	-0.15041	121.4571
145.0172	(S)-3-Hydroxybutyric acid	C4H8O3	C03197	145.0172	-2.2E-05	-0.15041	121.4571
145.0172	4-Hydroxybutyric acid	C4H8O3	C00989	145.0172	-2.2E-05	-0.15041	121.4571
145.0172	Ethoxyacetic acid	C4H8O3		145.0172	-2.2E-05	-0.15041	121.4571
145.0639	(1-Methylethenyl)pyrazine	C7H8N2		145.0647	-0.0008	-5.48594	#N/A
145.0639	2-Methyl-5-vinylpyrazine	C7H8N2		145.0647	-0.0008	-5.48594	#N/A

145.0639	2-Methyl-3-vinylpyrazine	C7H8N2		145.0647	-0.0008	-5.48594	#N/A
145.0639	1-Propenylpyrazine	C7H8N2		145.0647	-0.0008	-5.48594	#N/A
145.0648	(1-Methylethenyl)pyrazine	C7H8N2		145.0647	9.72E-05	0.670137	#N/A
145.0648	2-Methyl-5-vinylpyrazine	C7H8N2		145.0647	9.72E-05	0.670137	#N/A
145.0648	2-Methyl-3-vinylpyrazine	C7H8N2		145.0647	9.72E-05	0.670137	#N/A
145.0648	1-Propenylpyrazine	C7H8N2		145.0647	9.72E-05	0.670137	#N/A
145.076	5-Methylquinoxaline	C9H8N2		145.076	-6.5E-05	-0.44904	#N/A
145.076	2-Aminoquinoline	C9H8N2		145.076	-6.5E-05	-0.44904	#N/A
146.0124	3-(Methylthio)-1-propanol	C4H10OS		146.0117	0.000673	4.611153	#N/A
146.0124	3-Mercapto-2-butanol	C4H10OS		146.0117	0.000673	4.611153	#N/A
146.0124	4-Mercapto-2-butanol	C4H10OS		146.0117	0.000673	4.611153	#N/A
146.0124	L-Serine	C3H7NO3	C00065	146.0125	-3.9E-05	-0.26723	#N/A
146.0124	D-Serine	C3H7NO3	C00740	146.0125	-3.9E-05	-0.26723	#N/A
146.0526	3-Hydroxyadipic acid 3,6-lactone	C6H8O4		146.0529	-0.00025	-1.73827	#N/A
146.0599	1H-Indole-3-carboxaldehyde	C9H7NO	C08493	146.06	-9.7E-05	-0.6625	0.32308
146.0712	S-(3-Methyl-2-butenyl) ethanethioate	C7H12OS		146.0715	-0.00029	-1.97704	7.441033
146.9965	Glyceric acid	C3H6O4	C00258	146.9965	-6.4E-07	-0.00434	#N/A
146.9965	L-Glyceric acid	C3H6O4		146.9965	-6.4E-07	-0.00434	#N/A
146.9965	D-2,3-Dihydroxypropanoic acid	C3H6O4		146.9965	-6.4E-07	-0.00434	#N/A

147.044	Chromone	C9H6O2		147.0441	-8.6E-05	-0.58593	#N/A
147.044	2-Benzofurancarboxaldehyde	C9H6O2		147.0441	-8.6E-05	-0.58593	#N/A
147.044	Niacinamide	C6H6N2O	C00153	147.0439	2.88E-05	0.195713	#N/A
147.044	2-Acetylpyrazine	C6H6N2O		147.0439	2.88E-05	0.195713	#N/A
147.0604	p-Anisidine	C7H9NO	C19326	147.061	-0.00054	-3.67672	31.75792
147.0604	2-Propionylpyrrole	C7H9NO		147.061	-0.00054	-3.67672	31.75792
147.0604	4-Hydroxybenzylamine	C7H9NO		147.061	-0.00054	-3.67672	31.75792
147.0604	1-Ethyl-1H-pyrrole-2-carboxaldehyde	C7H9NO		147.061	-0.00054	-3.67672	31.75792
147.0604	2-Acetyl-1-methylpyrrole	C7H9NO		147.061	-0.00054	-3.67672	31.75792
147.0633	1H-Indole-3-carboxaldehyde	C9H7NO	C08493	147.0634	-9E-05	-0.61474	0.32308
148.0454	4-Methylcatechol	C7H8O2	C06730	148.045	0.000398	2.689276	#N/A
148.0454	Guaiacol	C7H8O2	C01502	148.045	0.000398	2.689276	#N/A
148.0454	4-Hydroxybenzyl alcohol	C7H8O2	C17467	148.045	0.000398	2.689276	#N/A
148.0454	Mequinol	C7H8O2		148.045	0.000398	2.689276	#N/A
148.0454	1-(2-Furanyl)-2-propanone	C7H8O2		148.045	0.000398	2.689276	#N/A
148.0454	2-Acetyl-3-methylfuran	C7H8O2		148.045	0.000398	2.689276	#N/A
148.0454	2-Acetyl-5-methylfuran	C7H8O2		148.045	0.000398	2.689276	#N/A
148.0454	1-(2-Furanyl)-1-propanone	C7H8O2		148.045	0.000398	2.689276	#N/A
148.0683	Adipic acid	C6H10O4	C06104	148.0685	-0.00025	-1.71164	#N/A
148.0683	2,2-Dimethylsuccinic acid	C6H10O4		148.0685	-0.00025	-1.71164	#N/A

148.0683	Dimethyl succinate	C6H10O4		148.0685	-0.00025	-1.71164	#N/A
148.0756	4-(2-Furanylmethylene)-3,4-dihydro-2H-pyrrole	C9H9NO		148.0757	-9.9E-05	-0.66925	#N/A
148.9435	1,2,4-Trithiolane	C2H4S3		148.9434	2.63E-05	0.176339	#N/A
149.0454	3-Hydroxyglutaric acid	C5H8O5		149.0444	0.000921	6.181458	2.983533
149.0454	D-2-Hydroxyglutaric acid	C5H8O5	C01087	149.0444	0.000921	6.181458	2.983533
149.0454	L-2-Hydroxyglutaric acid	C5H8O5	C03196	149.0444	0.000921	6.181458	2.983533
149.0454	Ribonolactone	C5H8O5	C02674	149.0444	0.000921	6.181458	2.983533
149.0454	D-Xylono-1,5-lactone	C5H8O5	C02266	149.0444	0.000921	6.181458	2.983533
149.0709	Adipic acid	C6H10O4	C06104	149.0719	-0.001	-6.70163	380.2344
149.0709	2,2-Dimethylsuccinic acid	C6H10O4		149.0719	-0.001	-6.70163	380.2344
149.0709	Dimethyl succinate	C6H10O4		149.0719	-0.001	-6.70163	380.2344
149.0762	6-Acetyl-1,2,3,4-tetrahydropyridine	C7H11NO		149.0766	-0.00048	-3.20543	#N/A
149.0762	3,4-Dihydro-5-propanoyl-2H-pyrrole	C7H11NO		149.0766	-0.00048	-3.20543	#N/A
149.0762	2-Methyl-4-propyloxazole	C7H11NO		149.0766	-0.00048	-3.20543	#N/A
149.0762	4-Methyl-2-propyloxazole	C7H11NO		149.0766	-0.00048	-3.20543	#N/A
149.0762	2-Methyl-5-propyloxazole	C7H11NO		149.0766	-0.00048	-3.20543	#N/A
149.0762	5-Methyl-2-propyloxazole	C7H11NO		149.0766	-0.00048	-3.20543	#N/A
149.0762	2-Ethyl-4,5-dimethyloxazole	C7H11NO		149.0766	-0.00048	-3.20543	#N/A

149.0762	4-Ethyl-2,5-dimethyloxazole	C7H11NO		149.0766	-0.00048	-3.20543	#N/A
149.0762	5-Ethyl-2,4-dimethyloxazole	C7H11NO		149.0766	-0.00048	-3.20543	#N/A
149.0762	4-Butyloxazole	C7H11NO		149.0766	-0.00048	-3.20543	#N/A
149.0762	5-Butyloxazole	C7H11NO		149.0766	-0.00048	-3.20543	#N/A
149.0762	2-Ethyl-5-imino-1-cyclopenten-1-ol	C7H11NO		149.0766	-0.00048	-3.20543	#N/A
150.0121	Dihydroxyfumaric acid	C4H4O6	C00975	150.0114	0.000657	4.380048	#N/A
150.0121	Dihydro-4-mercapto-5-methyl-3(2H)-thiophenone	C5H8OS2		150.0123	-0.00021	-1.40882	11.12173
150.0121	3-Acetyl-1,2-dithiolane	C5H8OS2		150.0123	-0.00021	-1.40882	11.12173
150.0464	Indole-5,6-quinone	C8H5NO2	C05579	150.046	0.000391	2.607134	152.3044
150.0464	Agrocybin	C8H5NO2		150.046	0.000391	2.607134	152.3044
150.0464	5-Aminoimidazole-4-carboxamide	C4H6N4O	C04051	150.0467	-0.00033	-2.18863	#N/A
150.0611	3-Ethyl-1,2-cyclopentanedione	C7H10O2		150.0607	0.00043	2.867328	#N/A
150.0611	Enol-3-Ethyl-1,2-cyclopentanedione	C7H10O2		150.0607	0.00043	2.867328	#N/A
150.0611	4-Hydroxy-4-methyl-5-hexenoic acid gamma lactone	C7H10O2		150.0607	0.00043	2.867328	#N/A
150.0611	xi-4-Hydroxy-4-methyl-2-cyclohexen-1-one	C7H10O2		150.0607	0.00043	2.867328	#N/A
150.0611	3-Methyl-1,2-cyclohexanedione	C7H10O2		150.0607	0.00043	2.867328	#N/A
150.0611	3-(3-Ethyloxiranyl)-2-propenal	C7H10O2		150.0607	0.00043	2.867328	#N/A
150.0611	3,5-Dimethyl-1,2-cyclopentanedione	C7H10O2		150.0607	0.00043	2.867328	#N/A
150.0611	2-(Ethoxymethyl)furan	C7H10O2		150.0607	0.00043	2.867328	#N/A
150.0611	xi-5-Isopropyl-2(5H)-furanone	C7H10O2		150.0607	0.00043	2.867328	#N/A
150.9391	2,2,2-Trichloroethanol	C2H3Cl3O	C07490	150.9389	0.000183	1.210923	#N/A

150.9391	1,3-Dichloropropene	C3H4Cl2	C06609	150.9389	0.000243	1.610404	#N/A
150.9765	Methyl methanethiosulfonate	C2H6O2S2		150.9768	-0.0004	-2.63659	#N/A
151.0154	Dihydroxyfumaric acid	C4H4O6	C00975	151.0148	0.000645	4.271678	#N/A
151.0154	Dihydro-4-mercapto-5-methyl-3(2H)-thiophenone	C5H8OS2		151.0156	-0.00022	-1.47873	11.12173
151.0154	3-Acetyl-1,2-dithiolane	C5H8OS2		151.0156	-0.00022	-1.47873	11.12173
151.0154	trans-1,2-Dihydrobenzene-1,2-diol	C6H8O2	C04221	151.0156	-0.00017	-1.11828	#N/A
151.0154	1,2-Cyclohexanedione	C6H8O2	C06105	151.0156	-0.00017	-1.11828	#N/A
151.0154	3-Methyl-1,2-cyclopentanedione	C6H8O2		151.0156	-0.00017	-1.11828	#N/A
151.0154	(E)-4-Oxo-2-hexen-1-al	C6H8O2		151.0156	-0.00017	-1.11828	#N/A
151.0154	2,5-Dimethyl-3(2H)-furanone	C6H8O2		151.0156	-0.00017	-1.11828	#N/A
151.0154	Syoyualdehyde	C6H8O2		151.0156	-0.00017	-1.11828	#N/A
151.0154	2-(Methoxymethyl)furan	C6H8O2		151.0156	-0.00017	-1.11828	#N/A
151.0154	xi-3,5-Dimethyl-2(5H)-furanone	C6H8O2		151.0156	-0.00017	-1.11828	#N/A
151.0154	5,5-Dimethyl-2(5H)-furanone	C6H8O2		151.0156	-0.00017	-1.11828	#N/A
151.0231	Tartaric acid	C4H6O6	C00898	151.0237	-0.00059	-3.90388	218.7606
151.0231	D-Tartaric acid	C4H6O6	C02107	151.0237	-0.00059	-3.90388	218.7606
151.0241	Tartaric acid	C4H6O6	C00898	151.0237	0.000433	2.868608	1.207438
151.0241	D-Tartaric acid	C4H6O6	C02107	151.0237	0.000433	2.868608	1.207438

151.0241	2-Methyl-2-(methyldithio)propanal	C5H10OS2		151.0246	-0.00044	-2.88145	0.86595
151.0498	5-Aminoimidazole-4-carboxamide	C4H6N4O	C04051	151.0501	-0.00031	-2.06336	#N/A
152.0277	Tartaric acid	C4H6O6	C00898	152.0271	0.000635	4.179229	1.207438
152.0277	D-Tartaric acid	C4H6O6	C02107	152.0271	0.000635	4.179229	1.207438
152.0277	2-Methyl-2-(methyldithio)propanal	C5H10OS2		152.0279	-0.00023	-1.53289	0.86595
152.062	5,6-Dihydroxyindole	C8H7NO2	C05578	152.0617	0.000369	2.424427	#N/A
152.107	N-Methylphenylethanolamine	C9H13NO	C03711	152.107	1.48E-05	0.097408	#N/A
152.107	N-Methyltyramine	C9H13NO	C02442	152.107	1.48E-05	0.097408	#N/A
152.107	1,2,3,4,5,6-Hexahydro-6-methyl-7H-cyclopenta[b]pyridin-7-one	C9H13NO		152.107	1.48E-05	0.097408	#N/A
152.107	2,3,4,5,6,7-Hexahydrocyclopent[b]azepin-8(1H)-one	C9H13NO		152.107	1.48E-05	0.097408	#N/A
152.107	2-(1-Pyrrolidinyl)-2-cyclopenten-1-one	C9H13NO		152.107	1.48E-05	0.097408	#N/A
152.107	2-(2-Furanyl)piperidine	C9H13NO		152.107	1.48E-05	0.097408	#N/A
152.107	1-Furfurylpyrrolidine	C9H13NO		152.107	1.48E-05	0.097408	#N/A
152.107	2-(5-Methyl-2-furanyl)pyrrolidine	C9H13NO		152.107	1.48E-05	0.097408	#N/A
153.0034	1,4-Dithiane-2,5-diol	C4H8O2S2		153.0038	-0.00041	-2.67239	#N/A
153.0034	Dihydroasparagusic acid	C4H8O2S2	C04371	153.0038	-0.00041	-2.67239	#N/A
153.0071	Dihydrouracil	C4H6N2O2	C00429	153.0061	0.000983	6.424339	0.307788
153.0071	N-Methylhydantoin	C4H6N2O2	C02565	153.0061	0.000983	6.424339	0.307788
153.023	trans-1,2-Dihydrobenzene-1,2-diol	C6H8O2	C04221	153.0223	0.000672	4.390877	#N/A
153.023	1,2-Cyclohexanedione	C6H8O2	C06105	153.0223	0.000672	4.390877	#N/A
153.023	3-Methyl-1,2-cyclopentanedione	C6H8O2		153.0223	0.000672	4.390877	#N/A

153.023	(E)-4-Oxo-2-hexen-1-al	C6H8O2		153.0223	0.000672	4.390877	#N/A
153.023	2,5-Dimethyl-3(2H)-furanone	C6H8O2		153.0223	0.000672	4.390877	#N/A
153.023	Syoyualdehyde	C6H8O2		153.0223	0.000672	4.390877	#N/A
153.023	2-(Methoxymethyl)furan	C6H8O2		153.0223	0.000672	4.390877	#N/A
153.023	xi-3,5-Dimethyl-2(5H)-furanone	C6H8O2		153.0223	0.000672	4.390877	#N/A
153.023	5,5-Dimethyl-2(5H)-furanone	C6H8O2		153.0223	0.000672	4.390877	#N/A
153.0654	N1-Methyl-2-pyridone-5-carboxamide	C7H8N2O2	C05842	153.0659	-0.00046	-2.98156	#N/A
153.0654	N1-Methyl-4-pyridone-3-carboxamide	C7H8N2O2	C05843	153.0659	-0.00046	-2.98156	#N/A
153.0799	1-Methoxy-3-methylene-2-pentanone	C7H12O2		153.0797	0.000285	1.865001	#N/A
153.0799	4-Methyl-5-hexanolide	C7H12O2		153.0797	0.000285	1.865001	#N/A
153.0799	Cyclohexanecarboxylic acid	C7H12O2	C09822	153.0797	0.000285	1.865001	#N/A
153.0799	Cyclohexyl formate	C7H12O2		153.0797	0.000285	1.865001	#N/A
153.0799	2,3-Heptanedione	C7H12O2		153.0797	0.000285	1.865001	#N/A
153.0799	5-Methyl-2,3-hexanedione	C7H12O2		153.0797	0.000285	1.865001	#N/A
153.0799	Dihydro-5-propyl-2(3H)-furanone	C7H12O2		153.0797	0.000285	1.865001	#N/A
153.0799	4-Pentenyl acetate	C7H12O2		153.0797	0.000285	1.865001	#N/A
153.0799	2-Hexenyl formate	C7H12O2		153.0797	0.000285	1.865001	#N/A
153.0799	cis-3-Hexenyl formate	C7H12O2		153.0797	0.000285	1.865001	#N/A
153.1021	2-Methoxy-(3 or 5 or 6)-isopropylpyrazine	C8H12N2O		153.1022	-0.0001	-0.67191	#N/A
153.1021	2-Isopropyl-5-methoxypyrazine	C8H12N2O		153.1022	-0.0001	-0.67191	#N/A
153.1021	2-Isopropyl-6-methoxypyrazine	C8H12N2O		153.1022	-0.0001	-0.67191	#N/A
153.1021	2-Isopropyl-3-methoxypyrazine	C8H12N2O		153.1022	-0.0001	-0.67191	#N/A

154.0651	(Â±)-2-Propylthiazolidine	C6H13NS		154.0661	-0.00099	-6.44674	#N/A
154.0732	FAPy-adenine	C5H7N5O	C06502	154.0723	0.000826	5.358952	#N/A
154.1225	psi-Pelletierine	C9H15NO	C10865	154.1226	-9.2E-05	-0.5958	#N/A
154.1225	2-Butyl-4,5-dimethyloxazole	C9H15NO		154.1226	-9.2E-05	-0.5958	#N/A
154.1225	4-Butyl-2,5-dimethyloxazole	C9H15NO		154.1226	-9.2E-05	-0.5958	#N/A
154.1225	2-Isobutyl-4,5-dimethyloxazole	C9H15NO		154.1226	-9.2E-05	-0.5958	#N/A
154.1225	5-Butyl-2,4-dimethyloxazole	C9H15NO		154.1226	-9.2E-05	-0.5958	#N/A
155.0051	4-Hydroxy-5-methyl-3(2H)-thiophenone	C5H6O2S		155.0048	0.000278	1.794441	#N/A
155.0051	3-keto-2-Methylbutyrate	C5H7O3		155.006	-0.00098	-6.2964	#N/A
155.019	1,4-Dithiothreitol	C4H10O2S2	C00265	155.0195	-0.00047	-3.03093	0.106808
155.0379	Delta-Hexanolactone	C6H10O2		155.0379	-1.4E-05	-0.09264	#N/A
155.0379	Gamma-Caprolactone	C6H10O2		155.0379	-1.4E-05	-0.09264	#N/A
155.0379	Allyl propionate	C6H10O2		155.0379	-1.4E-05	-0.09264	#N/A
155.0379	2,3-Hexanedione	C6H10O2		155.0379	-1.4E-05	-0.09264	#N/A
155.0379	3,4-Hexanedione	C6H10O2		155.0379	-1.4E-05	-0.09264	#N/A
155.0379	4-Methyl-2,3-pentanedione	C6H10O2		155.0379	-1.4E-05	-0.09264	#N/A
155.0379	5-Oxohexanal	C6H10O2		155.0379	-1.4E-05	-0.09264	#N/A

156.0186	1-(2-Thienyl)-1,2-propanedione	C7H6O2S		156.0195	-0.00087	-5.60104	#N/A
156.0186	Iminoaspartic acid	C4H5NO4	C05840	156.0178	0.000822	5.267116	#N/A
156.0505	Diethylphosphate	C4H11O4P	C06608	156.0501	0.000417	2.669144	#N/A
156.0505	(Z)-3-Phenyl-2-propenal	C9H8O		156.0501	0.000455	2.915694	#N/A
156.0505	Isopropyl propionate	C6H12O2		156.0502	0.0003	1.924023	#N/A
156.0505	Propyl propionate	C6H12O2		156.0502	0.0003	1.924023	#N/A
156.0505	2-Methylpropyl acetate	C6H12O2		156.0502	0.0003	1.924023	#N/A
156.0505	Ethyl 2-methylpropanoate	C6H12O2		156.0502	0.0003	1.924023	#N/A
156.0505	n-Butyl acetate	C6H12O2	C12304	156.0502	0.0003	1.924023	#N/A
156.0505	Diacetone alcohol	C6H12O2		156.0502	0.0003	1.924023	#N/A
156.0505	3-Methylbutyl formate	C6H12O2	C12293	156.0502	0.0003	1.924023	#N/A
156.0505	2,2,4-Trimethyl-1,3-dioxolane	C6H12O2		156.0502	0.0003	1.924023	#N/A
156.0505	2,4,5-Trimethyl-1,3-dioxolane	C6H12O2		156.0502	0.0003	1.924023	#N/A
156.0505	Pentyl formate	C6H12O2		156.0502	0.0003	1.924023	#N/A
156.0636	L-2-Amino-5-hydroxypentanoic acid	C5H11NO3		156.0631	0.000519	3.322691	#N/A
156.0636	N-Lactoyl ethanolamine	C5H11NO3		156.0631	0.000519	3.322691	#N/A
156.0636	1,4-Dideoxy-1,4-imino-D-ribitol	C5H11NO3		156.0631	0.000519	3.322691	#N/A
156.9984	S-Propyl thiosulfate	C3H8O3S2		156.9988	-0.00039	-2.48439	#N/A
157.0014	Oxalacetic acid	C4H4O5	C00036	157.0018	-0.00044	-2.82558	#N/A
157.076	3-Indoleacetonitrile	C10H8N2	C02938	157.076	-5.9E-05	-0.37296	#N/A
158.0124	S-Methyl butanethioate	C5H10OS		158.0117	0.00065	4.113563	9.581388
158.0124	4-(Methylthio)-2-butanone	C5H10OS		158.0117	0.00065	4.113563	9.581388
158.0124	4-Mercapto-2-pentanone	C5H10OS		158.0117	0.00065	4.113563	9.581388

158.0124	S-Propyl thioacetate	C5H10OS		158.0117	0.00065	4.113563	9.581388
158.0124	3-Mercapto-2-pentanone	C5H10OS		158.0117	0.00065	4.113563	9.581388
158.0124	2-Mercapto-3-pentanone	C5H10OS		158.0117	0.00065	4.113563	9.581388
158.0124	Tetrahydro-2-methylthiophen-3-ol	C5H10OS		158.0117	0.00065	4.113563	9.581388
158.0124	Tetrahydro-2-methyl-3-furanthiol	C5H10OS		158.0117	0.00065	4.113563	9.581388
158.0124	1-(Methylthio)-2-butanone	C5H10OS		158.0117	0.00065	4.113563	9.581388
158.0124	4-(Methylthio)butanal	C5H10OS		158.0117	0.00065	4.113563	9.581388
158.0124	xi-2-Methyl-1,3-oxathiane	C5H10OS		158.0117	0.00065	4.113563	9.581388
158.0124	3-(Methylthio)butanal	C5H10OS		158.0117	0.00065	4.113563	9.581388
158.0124	3-(Methylthio)-2-butanone	C5H10OS		158.0117	0.00065	4.113563	9.581388
158.0124	Acetylglycine	C4H7NO3		158.0125	-6.2E-05	-0.39433	#N/A
158.0124	L-2-Amino-3-oxobutanoic acid	C4H7NO3	C03508	158.0125	-6.2E-05	-0.39433	#N/A
158.0124	L-Aspartate-semialdehyde	C4H7NO3	C00441	158.0125	-6.2E-05	-0.39433	#N/A
158.06	3-Methylpyrrolo[1,2-a]pyrazine	C7H7N3		158.0599	3.92E-05	0.247892	#N/A
158.9782	Dihydro-4-mercapto-3(2H)-furanone	C4H6O2S		158.9787	-0.00047	-2.9483	#N/A
158.9902	S-Methyl 2-propene-1-sulfinothioate	C4H8OS2		158.9909	-0.0007	-4.40433	#N/A
158.9902	S-2-Propenyl methanesulfinothioate	C4H8OS2		158.9909	-0.0007	-4.40433	#N/A
158.9902	(Z)-S-Methyl 1-propenesulfinothioate	C4H8OS2		158.9909	-0.0007	-4.40433	#N/A
158.9902	(Z)-S-1-Propenyl methanesulfinothioate	C4H8OS2		158.9909	-0.0007	-4.40433	#N/A
159.0076	Purine	C5H4N4	C15587	159.0068	0.000895	5.631566	#N/A
159.0329	Phthalide	C8H6O2	C09921	159.0327	0.000223	1.404419	#N/A

159.0329	3-Hydroxy-2-methyl-[R-(R,S)]-butanoic acid	C5H10O3		159.0329	6.86E-05	0.431348	523.4809
159.0329	2-Methyl-3-hydroxybutyric acid	C5H10O3		159.0329	6.86E-05	0.431348	523.4809
159.0329	2-Ethylhydracrylic acid	C5H10O3		159.0329	6.86E-05	0.431348	523.4809
159.0329	3-Hydroxy-2-methyl-[S-(R,R)]-butanoic acid	C5H10O3		159.0329	6.86E-05	0.431348	523.4809
159.0329	3-Hydroxyvaleric acid	C5H10O3		159.0329	6.86E-05	0.431348	523.4809
159.0329	Erythronilic acid	C5H10O3		159.0329	6.86E-05	0.431348	523.4809
159.0329	3-Hydroxyisovaleric acid	C5H10O3		159.0329	6.86E-05	0.431348	523.4809
159.0329	2-Hydroxyvaleric acid	C5H10O3		159.0329	6.86E-05	0.431348	523.4809
159.0329	Ethyl lactate	C5H10O3		159.0329	6.86E-05	0.431348	523.4809
159.0329	Methyl 3-hydroxybutyrate	C5H10O3		159.0329	6.86E-05	0.431348	523.4809
159.0614	N-Acetylarylamine	C8H9NO	C07565	159.061	0.000396	2.49206	#N/A
159.0614	2-Phenylacetamide	C8H9NO	C02505	159.061	0.000396	2.49206	#N/A
159.0614	2-Aminoacetophenone	C8H9NO		159.061	0.000396	2.49206	#N/A
159.0614	2'-Aminoacetophenone	C8H9NO		159.061	0.000396	2.49206	#N/A
159.0614	2-Acetyl-4-methylpyridine	C8H9NO		159.061	0.000396	2.49206	#N/A
159.0614	2-Acetyl-6-methylpyridine	C8H9NO		159.061	0.000396	2.49206	#N/A
159.0614	2,3-Dihydro-1H-pyrrolizine-5-carboxaldehyde	C8H9NO		159.061	0.000396	2.49206	#N/A
159.0614	5-(2-Furanyl)-3,4-dihydro-2H-pyrrole	C8H9NO		159.061	0.000396	2.49206	#N/A
159.0614	2-Acetyl-5-methylpyridine	C8H9NO		159.061	0.000396	2.49206	#N/A
159.0614	4-Acetyl-2-methylpyridine	C8H9NO		159.061	0.000396	2.49206	#N/A
159.0614	4-Acetyl-3-methylpyridine	C8H9NO		159.061	0.000396	2.49206	#N/A
159.0678	5-Hydroxymethyl-4-methyluracil	C6H8N2O3		159.0675	0.000331	2.079823	#N/A
159.0678	4-Imidazolone-5-propionic acid	C6H8N2O3	C03680	159.0675	0.000331	2.079823	#N/A
159.0678	Imidazolelactic acid	C6H8N2O3	C05132	159.0675	0.000331	2.079823	#N/A
160.028	2-Benzoxazolol	C7H5NO2		160.028	7.77E-05	0.485342	#N/A

160.028	3-Mercapto-2-methyl-1-butanol	C5H12OS		160.0274	0.000635	3.969439	#N/A
160.028	3-Mercapto-3-methyl-1-butanol	C5H12OS		160.0274	0.000635	3.969439	#N/A
160.028	xi-2-Mercapto-3-methyl-1-butanol	C5H12OS		160.0274	0.000635	3.969439	#N/A
160.028	4-(Methylthio)-2-butanol	C5H12OS		160.0274	0.000635	3.969439	#N/A
160.028	4-(Methylthio)-1-butanol	C5H12OS		160.0274	0.000635	3.969439	#N/A
160.028	L-Threonine	C4H9NO3	C00188	160.0281	-7.7E-05	-0.48168	#N/A
160.028	L-Homoserine	C4H9NO3	C00263	160.0281	-7.7E-05	-0.48168	#N/A
160.028	L-Allothreonine	C4H9NO3	C05519	160.0281	-7.7E-05	-0.48168	#N/A
160.0454	Phenylacetic acid	C8H8O2	C07086	160.045	0.000378	2.364871	#N/A
160.0454	4-Hydroxyphenylacetaldehyde	C8H8O2	C03765	160.045	0.000378	2.364871	#N/A
160.0454	4-Methoxybenzaldehyde	C8H8O2	C10761	160.045	0.000378	2.364871	#N/A
160.0454	3-Methoxybenzaldehyde	C8H8O2		160.045	0.000378	2.364871	#N/A
160.0454	3-(5-Methyl-2-furyl)prop-2-enal	C8H8O2		160.045	0.000378	2.364871	#N/A
160.0454	2'-Hydroxyacetophenone	C8H8O2		160.045	0.000378	2.364871	#N/A
160.0454	4-(2-Furanyl)-3-buten-2-one	C8H8O2		160.045	0.000378	2.364871	#N/A
160.0454	2-Methoxybenzaldehyde	C8H8O2		160.045	0.000378	2.364871	#N/A
160.0454	Methyl benzoate	C8H8O2		160.045	0.000378	2.364871	#N/A
160.0454	alpha-Methyl-2-furanacrolein	C8H8O2		160.045	0.000378	2.364871	#N/A
160.0454	3-(3-Furanyl)-2-methyl-2-propenal	C8H8O2		160.045	0.000378	2.364871	#N/A
160.0454	Phenyl acetate	C8H8O2	C00548	160.045	0.000378	2.364871	#N/A
160.0454	Benzyl formate	C8H8O2	C05613	160.045	0.000378	2.364871	#N/A
160.0756	Indoleacetaldehyde	C10H9NO	C00637	160.0757	-1E-04	-0.62245	#N/A

162.0429	p-Aminobenzoic acid	C7H7NO2	C00568	162.0436	-0.00073	-4.53526	#N/A
162.0429	3-Pyridylacetic acid	C7H7NO2		162.0436	-0.00073	-4.53526	#N/A
162.0429	Methyl nicotinate	C7H7NO2		162.0436	-0.00073	-4.53526	#N/A
162.0438	p-Aminobenzoic acid	C7H7NO2	C00568	162.0436	0.000174	1.073065	#N/A
162.0438	3-Pyridylacetic acid	C7H7NO2		162.0436	0.000174	1.073065	#N/A
162.0438	Methyl nicotinate	C7H7NO2		162.0436	0.000174	1.073065	#N/A
162.0548	2-Indolecarboxylic acid	C9H7NO2		162.055	-0.00012	-0.71707	#N/A
162.0548	4,6-Dihydroxyquinoline	C9H7NO2	C05639	162.055	-0.00012	-0.71707	#N/A
162.0548	3-Formyl-6-hydroxyindole	C9H7NO2		162.055	-0.00012	-0.71707	#N/A
162.061	Tyrosol	C8H10O2	C06044	162.0607	0.000344	2.121927	#N/A
162.061	3-Acetyl-2,5-dimethylfuran	C8H10O2		162.0607	0.000344	2.121927	#N/A
162.061	1,4-Dimethoxybenzene	C8H10O2		162.0607	0.000344	2.121927	#N/A
162.061	1,3-Dimethoxybenzene	C8H10O2		162.0607	0.000344	2.121927	#N/A
162.061	4-Ethoxyphenol	C8H10O2		162.0607	0.000344	2.121927	#N/A
162.061	1,2-Dimethoxybenzene	C8H10O2		162.0607	0.000344	2.121927	#N/A
162.061	2-Acetyl-3,5-dimethylfuran	C8H10O2		162.0607	0.000344	2.121927	#N/A
162.061	1-(2-Furyl)butan-3-one	C8H10O2		162.0607	0.000344	2.121927	#N/A
162.061	4-Methoxybenzyl alcohol	C8H10O2		162.0607	0.000344	2.121927	#N/A
162.061	1-(2-Furanyl)-1-butanone	C8H10O2		162.0607	0.000344	2.121927	#N/A
162.061	2-Phenoxyethanol	C8H10O2		162.0607	0.000344	2.121927	#N/A
162.0913	Tryptophanol	C10H11NO	C00955	162.0913	-4E-05	-0.24969	#N/A

162.0913	(R)-Boschniakine	C10H11NO	C09915	162.0913	-4E-05	-0.24969	#N/A
162.0913	1-(2,3-Dihydro-1H-pyrrolizin-5-yl)-2-propen-1-one	C10H11NO		162.0913	-4E-05	-0.24969	#N/A
162.0913	3,4-Dihydro-4-[(5-methyl-2-furanyl)methylene]-2H-pyrrole	C10H11NO		162.0913	-4E-05	-0.24969	#N/A
163.0154	(2-Furanylmethyl) methyl disulfide	C6H8OS2		163.0156	-0.00029	-1.76498	#N/A
163.0154	4-Methylcatechol	C7H8O2	C06730	163.0156	-0.00023	-1.43107	#N/A
163.0154	Guaiacol	C7H8O2	C01502	163.0156	-0.00023	-1.43107	#N/A
163.0154	4-Hydroxybenzyl alcohol	C7H8O2	C17467	163.0156	-0.00023	-1.43107	#N/A
163.0154	Mequinol	C7H8O2		163.0156	-0.00023	-1.43107	#N/A
163.0154	1-(2-Furanyl)-2-propanone	C7H8O2		163.0156	-0.00023	-1.43107	#N/A
163.0154	2-Acetyl-3-methylfuran	C7H8O2		163.0156	-0.00023	-1.43107	#N/A
163.0154	2-Acetyl-5-methylfuran	C7H8O2		163.0156	-0.00023	-1.43107	#N/A
163.0154	1-(2-Furanyl)-1-propanone	C7H8O2		163.0156	-0.00023	-1.43107	#N/A
163.0277	4-Hydroxybenzoic acid	C7H6O3	C00156	163.0276	0.000121	0.744057	#N/A
163.0277	Gentisate aldehyde	C7H6O3	C05585	163.0276	0.000121	0.744057	#N/A
163.0277	2-Methoxy-1,4-benzoquinone	C7H6O3		163.0276	0.000121	0.744057	#N/A
163.0277	alpha-Furyl methyl diketone	C7H6O3		163.0276	0.000121	0.744057	#N/A
163.0277	Sesamol	C7H6O3	C10832	163.0276	0.000121	0.744057	#N/A
163.0277	Methylimidazole acetaldehyde	C6H8N2O	C05827	163.0268	0.000922	5.656415	#N/A
163.0277	2-Methoxy-3-methylpyrazine	C6H8N2O		163.0268	0.000922	5.656415	#N/A

163.0277	2-Methoxy-5-methylpyrazine	C6H8N2O		163.0268	0.000922	5.656415	#N/A
163.0277	2-Methoxy-6-methylpyrazine	C6H8N2O		163.0268	0.000922	5.656415	#N/A
163.0277	Erythritol	C4H10O4	C00503	163.0278	-3.3E-05	-0.20517	#N/A
163.0277	D-Threitol	C4H10O4	C16884	163.0278	-3.3E-05	-0.20517	#N/A
163.0531	Methomyl	C5H10N2O2S	C11196	163.0536	-0.00045	-2.76658	#N/A
163.0542	Methomyl	C5H10N2O2S	C11196	163.0536	0.000604	3.705814	0.292354
163.0542	Trimethylpyrazine	C7H10N2		163.0543	-8.7E-05	-0.53661	#N/A
163.0542	2-Ethyl-3-methylpyrazine, 9CI	C7H10N2		163.0543	-8.7E-05	-0.53661	#N/A
163.0542	2-Ethyl-5-methylpyrazine, 9CI, 8CI	C7H10N2		163.0543	-8.7E-05	-0.53661	#N/A
163.0542	2-Ethyl-6-methylpyrazine	C7H10N2		163.0543	-8.7E-05	-0.53661	#N/A
163.0542	Isopropylpyrazine	C7H10N2		163.0543	-8.7E-05	-0.53661	#N/A
163.0542	Propylpyrazine	C7H10N2		163.0543	-8.7E-05	-0.53661	#N/A
163.0542	2,4-Toluenediamine	C7H10N2	C14401	163.0543	-8.7E-05	-0.53661	#N/A
163.0553	3,4-Dihydroxybenzylamine	C7H9NO2		163.0559	-0.00059	-3.5882	#N/A
163.0553	5-Acetyl-2,4-dimethyloxazole	C7H9NO2		163.0559	-0.00059	-3.5882	#N/A
163.0865	Norcotinine	C9H10N2O		163.0866	-0.00013	-0.81929	#N/A
164.023	2-Methoxybenzenethiol	C7H8OS		164.0222	0.000823	5.016478	#N/A
164.023	Kahweofuran	C7H8OS		164.0222	0.000823	5.016478	#N/A

164.023	2-Acetyl-3-methylthiophene	C7H8OS		164.0222	0.000823	5.016478	#N/A
164.023	4-Nitrophenol	C6H5NO3	C00870	164.0229	0.000111	0.673765	#N/A
164.023	6-Hydroxynicotinic acid	C6H5NO3	C01020	164.0229	0.000111	0.673765	#N/A
164.023	3-Hydroxypicolinic acid	C6H5NO3	C18620	164.0229	0.000111	0.673765	#N/A
164.023	5-Methylcytosine	C5H7N3O	C02376	164.0221	0.000911	5.556316	#N/A
164.023	2-O-Methylcytosine	C5H7N3O		164.0221	0.000911	5.556316	#N/A
164.023	3-Methylcytosine	C5H7N3O		164.0221	0.000911	5.556316	#N/A
164.0574	Pterin	C6H5N5O	C00715	164.0567	0.000758	4.620972	#N/A
164.0574	Methomyl	C5H10N2O2S	C11196	164.0569	0.000515	3.137975	0.292354
164.1071	2,3,6,7-Tetrahydro-7-methylcyclopent[b]azepin-8(1H)-one	C10H13NO		164.107	0.000107	0.651328	#N/A
164.1071	2,3,4,5-Tetrahydro-6-(5-methyl-2-furanyl)pyridine	C10H13NO		164.107	0.000107	0.651328	#N/A
164.1071	2,3-Dihydro-5-propanoyl-1H-pyrrolizine	C10H13NO		164.107	0.000107	0.651328	#N/A
164.1071	5-Acetyl-2,3-dihydro-7-methyl-1H-pyrrolizine	C10H13NO		164.107	0.000107	0.651328	#N/A
164.1071	5-Acetyl-2,3-dihydro-6-methyl-1H-pyrrolizine	C10H13NO		164.107	0.000107	0.651328	#N/A
164.1071	1-(2,3-Dihydro-5-methyl-1H-pyrrolizin-7-yl)ethanone	C10H13NO		164.107	0.000107	0.651328	#N/A
164.1071	2,3-Dihydro-5,6-dimethyl-1H-pyrrolizine-7-carboxaldehyde	C10H13NO		164.107	0.000107	0.651328	#N/A
164.1071	Na,Na-Dimethylhistamine	C7H13N3		164.1069	0.000222	1.351703	#N/A
164.9206	Methylarsonite	CH5AsO2	C07295	164.9204	0.00014	0.847634	#N/A
165.0071	Thymine	C5H6N2O2	C00178	165.0061	0.000977	5.921429	#N/A
165.0071	Imidazoleacetic acid	C5H6N2O2	C02835	165.0061	0.000977	5.921429	#N/A
165.0071	1H-Imidazole-1-acetic acid	C5H6N2O2		165.0061	0.000977	5.921429	#N/A
165.023	3-Methylsulfinylpropyl isothiocyanate	C5H9NOS2		165.0232	-0.00018	-1.09442	16.83897
165.023	N-Nitrosothiazolidine-4-carboxylic acid	C4H6N2O3S		165.0239	-0.00089	-5.41077	#N/A

165.023	4-Methylcatechol	C7H8O2	C06730	165.0223	0.000708	4.292464	#N/A
165.023	Guaiacol	C7H8O2	C01502	165.0223	0.000708	4.292464	#N/A
165.023	4-Hydroxybenzyl alcohol	C7H8O2	C17467	165.0223	0.000708	4.292464	#N/A
165.023	Mequinol	C7H8O2		165.0223	0.000708	4.292464	#N/A
165.023	1-(2-Furanyl)-2-propanone	C7H8O2		165.0223	0.000708	4.292464	#N/A
165.023	2-Acetyl-3-methylfuran	C7H8O2		165.0223	0.000708	4.292464	#N/A
165.023	2-Acetyl-5-methylfuran	C7H8O2		165.0223	0.000708	4.292464	#N/A
165.023	1-(2-Furanyl)-1-propanone	C7H8O2		165.0223	0.000708	4.292464	#N/A
165.0244	N-Nitrosothiazolidine-4-carboxylic acid	C4H6N2O3S		165.0239	0.000519	3.146635	#N/A
165.031	4-Hydroxy-2-oxoglutaric acid	C5H6O6	C01127	165.0304	0.000607	3.67816	#N/A
165.031	Zwiebelane B	C6H10OS2		165.0313	-0.00026	-1.58388	#N/A
165.031	3-Ethyl-1,2-cyclopentanedione	C7H10O2		165.0312	-0.00021	-1.25404	#N/A
165.031	Enol-3-Ethyl-1,2-cyclopentanedione	C7H10O2		165.0312	-0.00021	-1.25404	#N/A
165.031	4-Hydroxy-4-methyl-5-hexenoic acid gamma lactone	C7H10O2		165.0312	-0.00021	-1.25404	#N/A
165.031	xi-4-Hydroxy-4-methyl-2-cyclohexen-1-one	C7H10O2		165.0312	-0.00021	-1.25404	#N/A
165.031	3-Methyl-1,2-cyclohexanedione	C7H10O2		165.0312	-0.00021	-1.25404	#N/A
165.031	3-(3-Ethyloxiranyl)-2-propenal	C7H10O2		165.0312	-0.00021	-1.25404	#N/A
165.031	3,5-Dimethyl-1,2-cyclopentanedione	C7H10O2		165.0312	-0.00021	-1.25404	#N/A
165.031	2-(Ethoxymethyl)furan	C7H10O2		165.0312	-0.00021	-1.25404	#N/A
165.031	xi-5-Isopropyl-2(5H)-furanone	C7H10O2		165.0312	-0.00021	-1.25404	#N/A

165.0356	2-Aminomuconic acid semialdehyde	C6H7NO3	C03824	165.0352	0.00042	2.546419	#N/A
165.0699	S-(2-Aminoethyl)-L-cysteine	C5H12N2O2S		165.0692	0.000664	4.024178	0.072847
165.0709	L-Hypoglycin A	C7H11NO2	C08287	165.0716	-0.00061	-3.71256	#N/A
166.0264	3-Methylsulfinylpropyl isothiocyanate	C5H9NOS2		166.0265	-0.00018	-1.07287	16.83897
166.0264	D-1-Piperideine-2-carboxylic acid	C6H9NO2	C04092	166.0265	-0.00012	-0.74501	#N/A
166.0264	(S)-2,3,4,5-Tetrahydropiperidine-2-carboxylate	C6H9NO2		166.0265	-0.00012	-0.74501	#N/A
166.0264	(Â±)-4-Methylene-2-pyrrolidinecarboxylic acid	C6H9NO2		166.0265	-0.00012	-0.74501	#N/A
166.0308	5-Hydroxymethyluracil	C5H6N2O3	C03088	166.0304	0.00043	2.587339	#N/A
166.0651	1-Methylhistamine	C6H11N3	C05127	166.0652	-8E-05	-0.48391	300.9961
166.0651	3-Methylhistamine	C6H11N3		166.0652	-8E-05	-0.48391	300.9961
166.0732	7-Methylguanine	C6H7N5O	C02242	166.0723	0.000893	5.378093	#N/A
166.0732	3-Methylguanine	C6H7N5O	C02230	166.0723	0.000893	5.378093	#N/A
166.0732	1-Methylguanine	C6H7N5O	C04152	166.0723	0.000893	5.378093	#N/A
166.0732	N2-Methylguanine	C6H7N5O	C04153	166.0723	0.000893	5.378093	#N/A
166.0732	S-(2-Aminoethyl)-L-cysteine	C5H12N2O2S		166.0726	0.00065	3.913095	0.072847
166.1227	Hordenine	C10H15NO	C06199	166.1226	8.05E-05	0.484699	#N/A
166.1227	6-Ethyl-1,2,3,4,5,6-hexahydro-7H-cyclopenta[b]pyridin-7-one	C10H15NO		166.1226	8.05E-05	0.484699	#N/A
166.1227	3-Methyl-2-(1-pyrrolidinyl)-2-cyclopenten-1-one	C10H15NO		166.1226	8.05E-05	0.484699	#N/A
166.1227	5-Methyl-2-(1-pyrrolidinyl)-2-cyclopenten-1-one	C10H15NO		166.1226	8.05E-05	0.484699	#N/A
166.1227	2,3,4,5,6,7-Hexahydro-7-methylcyclopent[b]azepin-8(1H)-one	C10H15NO		166.1226	8.05E-05	0.484699	#N/A
166.1227	2-(5-Methyl-2-furanyl)piperidine	C10H15NO		166.1226	8.05E-05	0.484699	#N/A

166.1227	1-[(5-Methyl-2-furanyl)methyl]pyrrolidine	C10H15NO		166.1226	8.05E-05	0.484699	#N/A
167.0227	Sumiki's acid	C6H6O4		167.0225	0.000209	1.248486	#N/A
167.0227	Kojic acid	C6H6O4	C14516	167.0225	0.000209	1.248486	#N/A
167.0227	5-Hydroxymaltol	C6H6O4		167.0225	0.000209	1.248486	#N/A
167.0386	8-Oxoguanine	C5H3N5O2	C20155	167.0393	-0.00066	-3.95037	#N/A
167.0386	3-Ethyl-1,2-cyclopentanedione	C7H10O2		167.0379	0.000698	4.179262	#N/A
167.0386	Enol-3-Ethyl-1,2-cyclopentanedione	C7H10O2		167.0379	0.000698	4.179262	#N/A
167.0386	4-Hydroxy-4-methyl-5-hexenoic acid gamma lactone	C7H10O2		167.0379	0.000698	4.179262	#N/A
167.0386	xi-4-Hydroxy-4-methyl-2-cyclohexen-1-one	C7H10O2		167.0379	0.000698	4.179262	#N/A
167.0386	3-Methyl-1,2-cyclohexanedione	C7H10O2		167.0379	0.000698	4.179262	#N/A
167.0386	3-(3-Ethyloxiranyl)-2-propenal	C7H10O2		167.0379	0.000698	4.179262	#N/A
167.0386	3,5-Dimethyl-1,2-cyclopentanedione	C7H10O2		167.0379	0.000698	4.179262	#N/A
167.0386	2-(Ethoxymethyl)furan	C7H10O2		167.0379	0.000698	4.179262	#N/A
167.0386	xi-5-Isopropyl-2(5H)-furanone	C7H10O2		167.0379	0.000698	4.179262	#N/A
167.0545	Arabinonic acid	C5H10O6	C00878	167.055	-0.00056	-3.36614	9.244837
167.0545	Ribonic acid	C5H10O6	C01685	167.055	-0.00056	-3.36614	9.244837
167.0545	N,N'-dinitrosopiperazine	C4H8N4O2		167.0539	0.000508	3.042135	11.55629
167.0555	Arabinonic acid	C5H10O6	C00878	167.055	0.000454	2.718054	#N/A
167.0555	Ribonic acid	C5H10O6	C01685	167.055	0.000454	2.718054	#N/A
167.0555	3-Methylxanthine	C6H6N4O2	C16357	167.0564	-0.00088	-5.28767	#N/A
167.0555	7-Methylxanthine	C6H6N4O2	C16353	167.0564	-0.00088	-5.28767	#N/A
167.0555	1-Methylxanthine	C6H6N4O2		167.0564	-0.00088	-5.28767	#N/A

167.0684	4-Hydroxycyclohexylcarboxylic acid	C7H12O3		167.0679	0.00056	3.35042	#N/A
167.0684	Tetrahydrofurfuryl acetate	C7H12O3		167.0679	0.00056	3.35042	#N/A
167.0684	Botryodiplodin	C7H12O3		167.0679	0.00056	3.35042	#N/A
167.0684	Ethyl levulinate	C7H12O3		167.0679	0.00056	3.35042	#N/A
168.0576	Arabinonic acid	C5H10O6	C00878	168.0584	-0.00073	-4.351	9.244837
168.0576	Ribonic acid	C5H10O6	C01685	168.0584	-0.00073	-4.351	9.244837
168.0576	N,N'-dinitrosopiperazine	C4H8N4O2		168.0573	0.000339	2.019017	11.55629
168.0762	(S)-Spinacine	C7H9N3O2		168.0768	-0.00053	-3.1482	#N/A
169.0347	Uric acid	C5H4N4O3	C00366	169.0356	-0.00089	-5.28346	0.481268
169.0648	Noradrenochrome o-semiquinone	C8H8NO3		169.0644	0.000367	2.169087	#N/A
169.0648	4-Methyl-4-(methylthio)-2-pentanone	C7H14OS		169.0658	-0.00098	-5.81574	0.355376
169.0648	3-(Methylthio)hexanal	C7H14OS		169.0658	-0.00098	-5.81574	0.355376
169.0648	5-Methylquinoxaline	C9H8N2		169.0647	9.46E-05	0.55941	#N/A
169.0648	2-Aminoquinoline	C9H8N2		169.0647	9.46E-05	0.55941	#N/A
169.0759	Beta-Carboline	C11H8N2	C20157	169.076	-0.00012	-0.7212	#N/A
170.0125	Cysteic acid	C3H7NO5S	C00506	170.0118	0.000733	4.310209	262.4979
170.0125	2-Ethyldihydro-3(2H)-thiophenone	C6H10OS		170.0117	0.000753	4.431137	#N/A
170.0125	Pyroglutamic acid	C5H7NO3	C01879	170.0125	4.1E-05	0.241421	#N/A
170.0125	Pyrrolidonecarboxylic acid	C5H7NO3	C02237	170.0125	4.1E-05	0.241421	#N/A
170.0125	Pyrroline hydroxycarboxylic acid	C5H7NO3	C04281	170.0125	4.1E-05	0.241421	#N/A
170.0125	N-Acryloylglycine	C5H7NO3		170.0125	4.1E-05	0.241421	#N/A

170.0125	1-Pyrroline-4-hydroxy-2-carboxylate	C5H7NO3	C04282	170.0125	4.1E-05	0.241421	#N/A
170.0299	Chromone	C9H6O2		170.0294	0.000511	3.002764	#N/A
170.0299	2-Benzofurancarboxaldehyde	C9H6O2		170.0294	0.000511	3.002764	#N/A
170.0299	2-Ketohexanoic acid	C6H10O3	C00902	170.0295	0.000356	2.092626	109.1313
170.0299	Mevalonolactone	C6H10O3		170.0295	0.000356	2.092626	109.1313
170.0299	3-Oxohexanoic acid	C6H10O3	C02122	170.0295	0.000356	2.092626	109.1313
170.0299	5-Ethoxy-4,5-dihydro-2(3H)furanone	C6H10O3		170.0295	0.000356	2.092626	109.1313
170.0299	Ethyl acetoacetate	C6H10O3		170.0295	0.000356	2.092626	109.1313
170.0299	Ethyl 3-oxobutanoate	C6H10O3	C03500	170.0295	0.000356	2.092626	109.1313
170.0299	Sherry lactone	C6H10O3		170.0295	0.000356	2.092626	109.1313
170.0299	(4S,6S)-3,4,5,6-Tetrahydro-4-hydroxy-6-methyl-2H-pyran-2-one	C6H10O3		170.0295	0.000356	2.092626	109.1313
170.0299	Acetoin acetate	C6H10O3		170.0295	0.000356	2.092626	109.1313
170.0299	Methyl levulinate	C6H10O3		170.0295	0.000356	2.092626	109.1313
170.038	Uric acid	C5H4N4O3	C00366	170.039	-0.00092	-5.42648	0.481268
171.0153	Cysteic acid	C3H7NO5S	C00506	171.0151	0.000153	0.896361	344.3305
171.0153	2-Ethyldihydro-3(2H)-thiophenone	C6H10OS		171.0151	0.000174	1.01658	#N/A
171.017	Oxoglutaric acid	C5H6O5	C00026	171.0175	-0.00047	-2.76545	#N/A
171.017	3-Oxoglutaric acid	C5H6O5		171.0175	-0.00047	-2.76545	#N/A
171.017	Ureidopropionic acid	C4H8N2O3	C02642	171.0167	0.000328	1.917386	68.15304
171.017	L-Asparagine	C4H8N2O3	C00152	171.0167	0.000328	1.917386	68.15304
171.017	Glycyl-glycine	C4H8N2O3	C02037	171.0167	0.000328	1.917386	68.15304
171.017	N-Carbamoylsarcosine	C4H8N2O3	C01043	171.0167	0.000328	1.917386	68.15304
171.017	D-Asparagine	C4H8N2O3	C01905	171.0167	0.000328	1.917386	68.15304

171.0316	1-Methylpyrrolo[1,2-a]pyrazine	C8H8N2		171.0319	-0.00034	-1.983	#N/A
171.0316	4-Methylpyrrolo[1,2-a]pyrazine	C8H8N2		171.0319	-0.00034	-1.983	#N/A
171.0794	1H-Indole-3-methanamine	C9H10N2		171.0803	-0.00088	-5.14829	#N/A
171.0794	Myosmine	C9H10N2	C10160	171.0803	-0.00088	-5.14829	#N/A
171.0794	1,4-Dimethylpyrrolo[1,2-a]pyrazine	C9H10N2		171.0803	-0.00088	-5.14829	#N/A
171.0794	3,4-Dimethylpyrrolo[1,2-a]pyrazine	C9H10N2		171.0803	-0.00088	-5.14829	#N/A
171.0794	1,3-Dimethylpyrrolo[1,2-a]pyrazine	C9H10N2		171.0803	-0.00088	-5.14829	#N/A
171.0804	R-3-(Methylthio)-1-hexanol	C7H16OS		171.0814	-0.00096	-5.59209	#N/A
171.0804	1H-Indole-3-methanamine	C9H10N2		171.0803	0.000121	0.707951	#N/A
171.0804	Myosmine	C9H10N2	C10160	171.0803	0.000121	0.707951	#N/A
171.0804	1,4-Dimethylpyrrolo[1,2-a]pyrazine	C9H10N2		171.0803	0.000121	0.707951	#N/A
171.0804	3,4-Dimethylpyrrolo[1,2-a]pyrazine	C9H10N2		171.0803	0.000121	0.707951	#N/A
171.0804	1,3-Dimethylpyrrolo[1,2-a]pyrazine	C9H10N2		171.0803	0.000121	0.707951	#N/A
171.0804	N-Acetylputrescine	C6H14N2O	C02714	171.0805	-3.4E-05	-0.1966	175.0374
171.0916	2,6-Dimethoxy-4-methylphenol	C9H12O3		171.0926	-0.001	-5.8218	#N/A
171.0916	4-Ipomeanol	C9H12O3		171.0926	-0.001	-5.8218	#N/A
171.0916	1-Ipomeanol	C9H12O3		171.0926	-0.001	-5.8218	#N/A
171.0916	Epoxyoxophorone	C9H12O3		171.0926	-0.001	-5.8218	#N/A

171.0916	(4-Hydroxy-3-methoxyphenyl)ethanol	C9H12O3		171.0926	-0.001	-5.8218	#N/A
171.0916	Agmatine	C5H14N4	C00179	171.0917	-8E-05	-0.46925	#N/A
172.0281	Diethylthiophosphate	C4H11O3PS	C06607	172.0273	0.000778	4.522216	#N/A
172.0281	2-Amino-3-phosphonopropionic acid	C3H8NO5P	C05672	172.028	6.56E-05	0.381587	#N/A
172.0281	Indole-5,6-quinone	C8H5NO2	C05579	172.028	0.000104	0.605237	#N/A
172.0281	Agrocybin	C8H5NO2		172.028	0.000104	0.605237	#N/A
172.0281	3-Methylpyrrolo[1,2-a]pyrazine	C7H7N3		172.0272	0.000905	5.260584	#N/A
172.0281	4-Mercapto-4-methyl-2-pentanone	C6H12OS		172.0274	0.000662	3.846297	10.73098
172.0281	2,5-Dimethyl-3-mercaptotetrahydrofuran	C6H12OS		172.0274	0.000662	3.846297	10.73098
172.0281	4-(Methylthio)-2-pentanone	C6H12OS		172.0274	0.000662	3.846297	10.73098
172.0281	3-Mercapto-2-methylpentanal	C6H12OS		172.0274	0.000662	3.846297	10.73098
172.0281	4-Hydroxyproline	C5H9NO3	C01157	172.0281	-5.1E-05	-0.29433	393.5419
172.0281	N-Acetyl-L-alanine	C5H9NO3		172.0281	-5.1E-05	-0.29433	393.5419
172.0281	Propionylglycine	C5H9NO3		172.0281	-5.1E-05	-0.29433	393.5419
172.0281	5-Aminolevulinic acid	C5H9NO3	C00430	172.0281	-5.1E-05	-0.29433	393.5419
172.0281	L-Glutamic gamma-semialdehyde	C5H9NO3	C01165	172.0281	-5.1E-05	-0.29433	393.5419
172.0281	3-Hydroxy-L-proline	C5H9NO3	C04397	172.0281	-5.1E-05	-0.29433	393.5419
172.0281	4-Hydroxy-L-proline	C5H9NO3	C01015	172.0281	-5.1E-05	-0.29433	393.5419
172.0281	4-Hydroxy-2-pyrrolidinecarboxylic acid	C5H9NO3		172.0281	-5.1E-05	-0.29433	393.5419

172.0755	N-Carbamoylputrescine	C5H13N3O	C00436	172.0757	-0.00018	-1.0624	#N/A
172.112	Norspermidine	C6H17N3	C03375	172.1121	-0.00016	-0.92425	#N/A
172.9963	Dihydroxyfumaric acid	C4H4O6	C00975	172.9967	-0.00038	-2.2254	#N/A
172.9963	(S)-Ureidoglycolic acid	C3H6N2O4	C00603	172.9959	0.000416	2.403867	0.07349
173.0233	Dihydropteridine	C6H6N4	C05649	173.0224	0.000855	4.93995	#N/A
173.0233	Ureidopropionic acid	C4H8N2O3	C02642	173.0234	-0.0001	-0.58301	68.15304
173.0233	L-Asparagine	C4H8N2O3	C00152	173.0234	-0.0001	-0.58301	68.15304
173.0233	Glycyl-glycine	C4H8N2O3	C02037	173.0234	-0.0001	-0.58301	68.15304
173.0233	N-Carbamoylsarcosine	C4H8N2O3	C01043	173.0234	-0.0001	-0.58301	68.15304
173.0233	D-Asparagine	C4H8N2O3	C01905	173.0234	-0.0001	-0.58301	68.15304
173.0408	5,6-Dihydroxyindole	C8H7NO2	C05578	173.0403	0.000516	2.980449	#N/A
173.0408	L-2-Amino-5-hydroxypentanoic acid	C5H11NO3		173.0404	0.000361	2.086146	#N/A
173.0408	N-Lactoyl ethanolamine	C5H11NO3		173.0404	0.000361	2.086146	#N/A
173.0408	1,4-Dideoxy-1,4-imino-D-ribitol	C5H11NO3		173.0404	0.000361	2.086146	#N/A
173.0485	(E)-3-(2-Hydroxyphenyl)-2-propenal	C9H8O2		173.0484	0.000155	0.898385	#N/A
173.0485	Di-2-furanylmethane	C9H8O2		173.0484	0.000155	0.898385	#N/A
173.0485	1-Phenyl-1,2-propanedione	C9H8O2	C17268	173.0484	0.000155	0.898385	#N/A
173.0485	3,4-Dihydro-2H-1-benzopyran-2-one	C9H8O2	C02274	173.0484	0.000155	0.898385	#N/A
173.0485	(E)-3-(4-Hydroxyphenyl)-2-propenal	C9H8O2	C05608	173.0484	0.000155	0.898385	#N/A
173.0485	5,6,7,8-Tetrahydroquinoxaline	C8H10N2		173.0476	0.000956	5.526283	#N/A
173.0485	3,5-Dimethyl-2-vinylpyrazine	C8H10N2		173.0476	0.000956	5.526283	#N/A

173.0485	6,7-Dihydro-2-methyl-5H-cyclopenta[b]pyrazine	C8H10N2		173.04076	0.000956	5.526283	#N/A
173.0485	6,7-Dihydro-5-methyl-5H-cyclopenta[b]pyrazine	C8H10N2		173.04076	0.000956	5.526283	#N/A
173.0485	2-Methyl-6-(1-propenyl)pyrazine	C8H10N2		173.04076	0.000956	5.526283	#N/A
173.0485	2-Methyl-3-(1-propenyl)pyrazine	C8H10N2		173.04076	0.000956	5.526283	#N/A
173.0485	2-Methyl-6-(2-propenyl)pyrazine	C8H10N2		173.04076	0.000956	5.526283	#N/A
173.0485	2-Methyl-5-(2-propenyl)pyrazine	C8H10N2		173.04076	0.000956	5.526283	#N/A
173.0485	2-Methyl-3-(2-propenyl)pyrazine	C8H10N2		173.04076	0.000956	5.526283	#N/A
173.0485	2-Methyl-5-(1-propenyl)pyrazine	C8H10N2		173.04076	0.000956	5.526283	#N/A
173.0485	(5R)-5-Hydroxyhexanoic acid	C6H12O3		173.04085	7.14E-07	0.004127	#N/A
173.0485	5-Hydroxyhexanoic acid	C6H12O3		173.04085	7.14E-07	0.004127	#N/A
173.0485	2-Hydroxycaproic acid	C6H12O3		173.04085	7.14E-07	0.004127	#N/A
173.0485	(R)-3-Hydroxyhexanoic acid	C6H12O3		173.04085	7.14E-07	0.004127	#N/A
173.0485	6-Hydroxyhexanoic acid	C6H12O3	C06103	173.04085	7.14E-07	0.004127	#N/A
173.0485	(+/-)-1-Acetoxy-1-ethoxyethane	C6H12O3		173.04085	7.14E-07	0.004127	#N/A
173.0485	Paraldehyde	C6H12O3	C07834	173.04085	7.14E-07	0.004127	#N/A
173.0485	Ethyl (Â±)-3-hydroxybutyrate	C6H12O3		173.04085	7.14E-07	0.004127	#N/A
173.0485	Butoxyacetic acid	C6H12O3		173.04085	7.14E-07	0.004127	#N/A
173.996	2-Benzoxazolol	C7H5NO2		173.99952	0.000812	4.668549	#N/A
174.0611	4-Coumaryl alcohol	C9H10O2	C02646	174.06007	0.000411	2.362923	#N/A
174.0611	Benzyl acetate	C9H10O2	C15513	174.06007	0.000411	2.362923	#N/A
174.0611	2'-Methoxyacetophenone	C9H10O2		174.06007	0.000411	2.362923	#N/A
174.0611	4'-Methoxyacetophenone	C9H10O2		174.06007	0.000411	2.362923	#N/A
174.0611	Methyl phenylacetate	C9H10O2		174.06007	0.000411	2.362923	#N/A
174.0611	4-Ethoxybenzaldehyde	C9H10O2		174.06007	0.000411	2.362923	#N/A
174.0611	2-Ethyl-4-(2-furanyl)-2-propenal	C9H10O2		174.06007	0.000411	2.362923	#N/A

174.0611	2-Phenylethyl formate	C9H10O2		174.0607	0.000411	2.362923	#N/A
174.0611	2-(2-Furanyl)-3-methyl-2-butenal	C9H10O2		174.0607	0.000411	2.362923	#N/A
174.0611	Polypropylene glycol (m w 1,200-3,000)	C6H14O3		174.0608	0.000257	1.473864	#N/A
174.9851	1,4-Dithiane-2,5-diol	C4H8O2S2		174.9858	-0.00068	-3.86173	0.013385
174.9851	Dihydroasparagusic acid	C4H8O2S2	C04371	174.9858	-0.00068	-3.86173	0.013385
174.9867	1,4-Dithiane-2,5-diol	C4H8O2S2		174.9858	0.000889	5.080063	22.79009
174.9867	Dihydroasparagusic acid	C4H8O2S2	C04371	174.9858	0.000889	5.080063	22.79009
174.9939	Thiodiacetic acid	C4H6O4S	C14872	174.9946	-0.00073	-4.19131	#N/A
175.9721	3-Methyl-1,2,4-trithiane	C4H8S3		175.9714	0.000719	4.084134	#N/A
176.023	(+)-threo-2-Amino-3,4-dihydroxybutanoic acid	C4H9NO4		176.023	2.48E-06	0.014094	#N/A
176.0608	Quinaldic acid	C10H7NO2	C06325	176.0617	-0.00083	-4.69331	#N/A
176.0608	Ribitol	C5H12O5	C00474	176.061	-0.00021	-1.18422	262.5155
176.0608	D-Arabitol	C5H12O5	C01904	176.061	-0.00021	-1.18422	262.5155
176.0608	L-Arabitol	C5H12O5	C00532	176.061	-0.00021	-1.18422	262.5155
176.0608	L-2-(Hydroxymethyl)-1,2,3,4-butanetetrol	C5H12O5		176.061	-0.00021	-1.18422	262.5155
176.0621	Quinaldic acid	C10H7NO2	C06325	176.0617	0.000403	2.289601	#N/A
176.0818	4,4'-Thiobis-2-butanone	C8H14O2S		176.0821	-0.00032	-1.78977	129.1156
176.9738	B-Sulfinyl pyruvate	C3H4O5S	C05527	176.9739	-3.6E-05	-0.20105	#N/A
176.9738	3-Methyl-1,2,4-trithiane	C4H8S3		176.9747	-0.0009	-5.10795	#N/A

177.0435	p-Hydroxyphenylacetic acid	C8H8O3	C00642	177.0433	0.000204	1.149585	#N/A
177.0435	Ortho-Hydroxyphenylacetic acid	C8H8O3	C05852	177.0433	0.000204	1.149585	#N/A
177.0435	Mandelic acid	C8H8O3	C01984	177.0433	0.000204	1.149585	#N/A
177.0435	p-Anisic acid	C8H8O3	C02519	177.0433	0.000204	1.149585	#N/A
177.0435	3,4-Dihydroxyphenylacetaldehyde	C8H8O3	C04043	177.0433	0.000204	1.149585	#N/A
177.0435	4-Hydroxy-3-methylbenzoic acid	C8H8O3		177.0433	0.000204	1.149585	#N/A
177.0435	Vanillin	C8H8O3	C00755	177.0433	0.000204	1.149585	#N/A
177.0435	2,4'-Dihydroxyacetophenone	C8H8O3	C13635	177.0433	0.000204	1.149585	#N/A
177.0435	2',3'-Dihydroxyacetophenone	C8H8O3		177.0433	0.000204	1.149585	#N/A
177.0435	2',4'-Dihydroxyacetophenone	C8H8O3	C03663	177.0433	0.000204	1.149585	#N/A
177.0435	3',4'-Dihydroxyacetophenone	C8H8O3	C10675	177.0433	0.000204	1.149585	#N/A
177.0435	3',5'-Dihydroxyacetophenone	C8H8O3		177.0433	0.000204	1.149585	#N/A
177.0435	Phenoxyacetic acid	C8H8O3	C02181	177.0433	0.000204	1.149585	#N/A
177.0435	Methylparaben	C8H8O3		177.0433	0.000204	1.149585	#N/A
177.0435	2-(Hydroxymethyl)benzoic acid	C8H8O3	C10804	177.0433	0.000204	1.149585	#N/A
177.0435	2-Methoxybenzoic acid	C8H8O3		177.0433	0.000204	1.149585	#N/A
177.0435	3-Methoxybenzoic acid	C8H8O3		177.0433	0.000204	1.149585	#N/A
177.0435	2',5'-Dihydroxyacetophenone	C8H8O3		177.0433	0.000204	1.149585	#N/A
177.0435	Ethyl 2-furanyl diketone	C8H8O3		177.0433	0.000204	1.149585	#N/A
177.0435	1-(5-Methyl-2-furanyl)-1,2-propanedione	C8H8O3		177.0433	0.000204	1.149585	#N/A
177.0435	2-Propenyl 2-furancarboxylate	C8H8O3		177.0433	0.000204	1.149585	#N/A
177.0435	1-(2-Furanyl)-1,3-butanedione	C8H8O3		177.0433	0.000204	1.149585	#N/A
177.0435	2-Methylerythritol	C5H12O4		177.0434	4.88E-05	0.275505	145.6271
177.0435	3-Deoxy-D-arabinitol	C5H12O4		177.0434	4.88E-05	0.275505	145.6271
177.0435	2-Deoxy-D-ribitol	C5H12O4		177.0434	4.88E-05	0.275505	145.6271

177.0435	1-Deoxy-D-ribitol	C5H12O4		177.0434	4.88E-05	0.275505	145.6271
177.0699	Guanidinosuccinic acid	C5H9N3O4	C03139	177.0699	-4.6E-05	-0.25874	#N/A
177.0699	5-Ethyl-2,3-dimethylpyrazine	C8H12N2		177.0699	-2.5E-05	-0.14263	202.8222
177.0699	2-Ethyl-3,(5 or 6)-dimethylpyrazine	C8H12N2		177.0699	-2.5E-05	-0.14263	202.8222
177.0699	Tetramethylpyrazine	C8H12N2		177.0699	-2.5E-05	-0.14263	202.8222
177.0699	2,5-Diethylpyrazine	C8H12N2		177.0699	-2.5E-05	-0.14263	202.8222
177.0699	2,6-Diethylpyrazine	C8H12N2		177.0699	-2.5E-05	-0.14263	202.8222
177.0699	2-Isopropyl-5-methylpyrazine	C8H12N2		177.0699	-2.5E-05	-0.14263	202.8222
177.0699	2-Methyl-5-propylpyrazine	C8H12N2		177.0699	-2.5E-05	-0.14263	202.8222
177.0699	2-Ethyl-3,5-dimethylpyrazine	C8H12N2		177.0699	-2.5E-05	-0.14263	202.8222
177.0699	2-Methyl-3-propylpyrazine	C8H12N2		177.0699	-2.5E-05	-0.14263	202.8222
177.0699	2,3-Diethylpyrazine	C8H12N2		177.0699	-2.5E-05	-0.14263	202.8222
177.0713	Dopamine	C8H11NO2	C03758	177.0716	-0.00026	-1.47013	136.7395
177.0713	p-Octopamine	C8H11NO2	C04227	177.0716	-0.00026	-1.47013	136.7395
177.0713	Vanillylamine	C8H11NO2	C16666	177.0716	-0.00026	-1.47013	136.7395
178.0386	3-Hydroxyanthranilic acid	C7H7NO3	C00632	178.0385	4.81E-05	0.270254	#N/A
178.0386	Histidinal	C6H9N3O		178.0377	0.000849	4.768435	3.206892
178.0434	Ascorbic acid	C6H8O6	C00072	178.0427	0.000695	3.901721	#N/A

178.0434	D-Glucurono-6,3-lactone	C6H8O6	C02670	178.0427	0.000695	3.901721	#N/A
178.0434	1,2,3-Propanetricarboxylic acid	C6H8O6	C19806	178.0427	0.000695	3.901721	#N/A
178.065	Allantoic acid	C4H8N4O4	C00499	178.0652	-0.00016	-0.90274	#N/A
178.0765	5-Hydroxyindoleacetaldehyde	C10H9NO2	C05634	178.0773	-0.00082	-4.5798	#N/A
178.0765	Hydroxymethyl indol-3-yl ketone	C10H9NO2		178.0773	-0.00082	-4.5798	#N/A
178.0765	1-Methoxy-1H-indole-3-carboxaldehyde	C10H9NO2		178.0773	-0.00082	-4.5798	#N/A
178.0777	5-Hydroxyindoleacetaldehyde	C10H9NO2	C05634	178.0773	0.000391	2.198428	#N/A
178.0777	Hydroxymethyl indol-3-yl ketone	C10H9NO2		178.0773	0.000391	2.198428	#N/A
178.0777	1-Methoxy-1H-indole-3-carboxaldehyde	C10H9NO2		178.0773	0.000391	2.198428	#N/A
178.1227	(S)-Valerianine	C11H15NO	C09991	178.1226	6.72E-05	0.377147	#N/A
178.1227	7-Ethyl-2,3,6,7-tetrahydrocyclopent[b]azepin-8(1H)-one	C11H15NO		178.1226	6.72E-05	0.377147	#N/A
178.1227	1-(2,3-Dihydro-5-ethyl-1H-pyrrolizin-7-yl)ethanone	C11H15NO		178.1226	6.72E-05	0.377147	#N/A
178.1227	1-(2,3-Dihydro-5,6-dimethyl-1H-pyrrolizin-7-yl)ethanone	C11H15NO		178.1226	6.72E-05	0.377147	#N/A
178.9504	Acetylphosphate	C2H5O5P	C00227	178.9506	-0.00024	-1.33735	#N/A
178.9504	Phosphonoacetate	C2H5O5P	C05682	178.9506	-0.00024	-1.33735	#N/A
179.0387	Sulforaphane	C6H11NOS2		179.0388	-0.00015	-0.86354	16.1875
179.0387	Tyrosol	C8H10O2	C06044	179.0379	0.000734	4.101648	152.4787
179.0387	3-Acetyl-2,5-dimethylfuran	C8H10O2		179.0379	0.000734	4.101648	152.4787
179.0387	1,4-Dimethoxybenzene	C8H10O2		179.0379	0.000734	4.101648	152.4787
179.0387	1,3-Dimethoxybenzene	C8H10O2		179.0379	0.000734	4.101648	152.4787
179.0387	4-Ethoxyphenol	C8H10O2		179.0379	0.000734	4.101648	152.4787

179.0387	1,2-Dimethoxybenzene	C8H10O2		179.0379	0.000734	4.101648	152.4787
179.0387	2-Acetyl-3,5-dimethylfuran	C8H10O2		179.0379	0.000734	4.101648	152.4787
179.0387	1-(2-Furyl)butan-3-one	C8H10O2		179.0379	0.000734	4.101648	152.4787
179.0387	4-Methoxybenzyl alcohol	C8H10O2		179.0379	0.000734	4.101648	152.4787
179.0387	1-(2-Furanyl)-1-butanone	C8H10O2		179.0379	0.000734	4.101648	152.4787
179.0387	2-Phenoxyethanol	C8H10O2		179.0379	0.000734	4.101648	152.4787
180.0357	Ascladiol	C7H8O4		180.0348	0.000826	4.585939	#N/A
180.0357	5-Acetyl-2,4-dimethylthiazole	C7H9NOS		180.0364	-0.00076	-4.19399	#N/A
180.042	Sulforaphane	C6H11NOS2		180.0422	-0.00023	-1.26028	16.1875
180.042	L-Hypoglycin A	C7H11NO2	C08287	180.0421	-0.00017	-0.95795	#N/A
180.0432	Sulforaphane	C6H11NOS2		180.0422	0.000966	5.362979	#N/A
180.0807	Na,Na-Dimethylhistamine	C7H13N3		180.0808	-8.8E-05	-0.49049	227.4935
180.9572	Acetylphosphate	C2H5O5P	C00227	180.9573	-0.00013	-0.69291	#N/A
180.9572	Phosphonoacetate	C2H5O5P	C05682	180.9573	-0.00013	-0.69291	#N/A
181.0078	2-[(Ethylthio)methyl]furan	C7H10OS		181.0084	-0.00056	-3.10098	#N/A
181.0332	Allantoin	C4H6N4O3	C01551	181.0332	2.87E-05	0.158669	#N/A
181.0344	2,5-Dimethyl-1,4-dithiane-2,5-diol	C6H12O2S2		181.0351	-0.00074	-4.08752	#N/A
181.0344	Ethyl 2-(methyldithio)propionate	C6H12O2S2		181.0351	-0.00074	-4.08752	#N/A
181.0759	Metenamine	C6H12N4		181.0761	-0.00016	-0.89616	#N/A
181.077	4-Methoxycinnamic acid	C10H10O3		181.077	3.12E-05	0.172163	#N/A

181.077	3-(4-Methylphenyl)oxiranecarboxylic acid	C10H10O3		181.077	3.12E-05	0.172163	#N/A
181.077	(Z)-10-Hydroxy-8-decene-4,6-diynoic acid	C10H10O3		181.077	3.12E-05	0.172163	#N/A
181.077	Di-alpha-furfuryl ether	C10H10O3		181.077	3.12E-05	0.172163	#N/A
181.077	(S)-Isosclerone	C10H10O3		181.077	3.12E-05	0.172163	#N/A
181.077	(E)-10-Hydroxy-2-decene-4,6-diynoic acid	C10H10O3		181.077	3.12E-05	0.172163	#N/A
181.077	3-(4-Hydroxy-2-methoxyphenyl)-2-propenal	C10H10O3		181.077	3.12E-05	0.172163	#N/A
181.077	Metenamine	C6H12N4		181.0761	0.000947	5.229608	#N/A
181.0884	4-Oxo-4-(3-pyridyl)-butanamide	C9H10N2O2		181.0882	0.000236	1.30228	#N/A
181.0884	BOX B	C9H10N2O2		181.0882	0.000236	1.30228	#N/A
181.0884	BOX A	C9H10N2O2		181.0882	0.000236	1.30228	#N/A
182.0838	Acetylisoniazid	C8H9N3O2	C07585	182.0835	0.000349	1.9186	#N/A
182.9903	(2-Furanylmethyl) methyl disulfide	C6H8OS2		182.9909	-0.0006	-3.2942	#N/A
184.0733	8-Hydroxy-7-methylguanine	C6H7N5O2		184.074	-0.00068	-3.69467	#N/A
184.0733	Tryptophanol	C10H11NO	C00955	184.0733	-1.9E-06	-0.01034	0.544329
184.0733	(R)-Boschniakine	C10H11NO	C09915	184.0733	-1.9E-06	-0.01034	0.544329
184.0733	1-(2,3-Dihydro-1H-pyrrolizin-5-yl)-2-propen-1-one	C10H11NO		184.0733	-1.9E-06	-0.01034	0.544329
184.0733	3,4-Dihydro-4-[(5-methyl-2-furanyl)methylene]-2H-pyrrole	C10H11NO		184.0733	-1.9E-06	-0.01034	0.544329
184.0733	3-Dehydroxycarnitine	C7H15NO2	C05543	184.0734	-0.00016	-0.85104	0.166298
185.0766	Tryptophanol	C10H11NO	C00955	185.0766	-8.5E-05	-0.45717	0.544329
185.0766	(R)-Boschniakine	C10H11NO	C09915	185.0766	-8.5E-05	-0.45717	0.544329

185.0766	1-(2,3-Dihydro-1H-pyrrolizin-5-yl)-2-propen-1-one	C10H11NO		185.0766	-8.5E-05	-0.45717	0.544329
185.0766	3,4-Dihydro-4-[(5-methyl-2-furanyl)methylene]-2H-pyrrole	C10H11NO		185.0766	-8.5E-05	-0.45717	0.544329
185.0766	3-Dehydroxycarnitine	C7H15NO2	C05543	185.0768	-0.00024	-1.29331	0.166298
185.1044	Trimethyl-2-propenylpyrazine	C10H14N2		185.1049	-0.00055	-2.96482	#N/A
186.0613	4,5-Dihydro-1-benzoxepin-3(2H)-one	C10H10O2		186.0607	0.000685	3.682227	#N/A
186.0613	3-(4-Methoxyphenyl)-2-propenal	C10H10O2	C10475	186.0607	0.000685	3.682227	#N/A
186.0613	Cassiastearoptene	C10H10O2		186.0607	0.000685	3.682227	#N/A
186.0613	3-Hydroxyisoheptanoic acid	C7H14O3		186.0608	0.00053	2.850506	63.24435
186.0613	Methyl (Â±)-3-hydroxyhexanoate	C7H14O3		186.0608	0.00053	2.850506	63.24435
186.0613	Butyl lactate	C7H14O3		186.0608	0.00053	2.850506	63.24435
186.1276	Spermidine	C7H19N3	C00315	186.1278	-0.00012	-0.63543	#N/A
187.0278	3 Hydroxycoumarin	C9H6O3		187.0276	0.000188	1.003708	#N/A
187.0278	Umbelliferone	C9H6O3	C09315	187.0276	0.000188	1.003708	#N/A
187.0278	Adipic acid	C6H10O4	C06104	187.0278	3.3E-05	0.17629	289.2989
187.0278	2,2-Dimethylsuccinic acid	C6H10O4		187.0278	3.3E-05	0.17629	289.2989
187.0278	Dimethyl succinate	C6H10O4		187.0278	3.3E-05	0.17629	289.2989
187.0542	1H-Indole-3-methanamine	C9H10N2		187.0543	-5.8E-05	-0.31034	#N/A
187.0542	Myosmine	C9H10N2	C10160	187.0543	-5.8E-05	-0.31034	#N/A
187.0542	1,4-Dimethylpyrrolo[1,2-a]pyrazine	C9H10N2		187.0543	-5.8E-05	-0.31034	#N/A
187.0542	3,4-Dimethylpyrrolo[1,2-a]pyrazine	C9H10N2		187.0543	-5.8E-05	-0.31034	#N/A

187.0542	1,3-Dimethylpyrrolo[1,2-a]pyrazine	C9H10N2		187.0543	-5.8E-05	-0.31034	#N/A
188.023	Phosphoserine	C3H8NO6P	C01005	188.0229	0.000137	0.729183	#N/A
188.023	DL-O-Phosphoserine	C3H8NO6P	C01005	188.0229	0.000137	0.729183	#N/A
188.023	3-(Methylthio)propyl acetate	C6H12O2S		188.0223	0.000733	3.899153	#N/A
188.023	Propyl 2-mercaptopropionate	C6H12O2S		188.0223	0.000733	3.899153	#N/A
188.023	3-Mercapto-3-methylbutyl formate	C6H12O2S		188.0223	0.000733	3.899153	#N/A
188.023	2,4,6-Trimethyl-1,3,5-dioxathiane	C6H12O2S		188.0223	0.000733	3.899153	#N/A
188.023	L-Glutamic acid	C5H9NO4	C00025	188.023	2.08E-05	0.110768	#N/A
188.023	N-Acetylserine	C5H9NO4		188.023	2.08E-05	0.110768	#N/A
188.023	O-Acetylserine	C5H9NO4	C00979	188.023	2.08E-05	0.110768	#N/A
188.023	D-Glutamic acid	C5H9NO4	C00217	188.023	2.08E-05	0.110768	#N/A
188.023	L-4-Hydroxyglutamate semialdehyde	C5H9NO4	C05938	188.023	2.08E-05	0.110768	#N/A
188.023	3-(Carboxymethylamino)propanoic acid	C5H9NO4		188.023	2.08E-05	0.110768	#N/A
188.0595	4-(3-Pyridyl)-3-butenoic acid	C9H9NO2		188.0593	0.000241	1.280105	#N/A
188.0595	3-Methyldioxyindole	C9H9NO2	C05834	188.0593	0.000241	1.280105	#N/A
188.0595	R-3-(Methylthio)-1-hexanol	C7H16OS		188.0587	0.000798	4.244879	#N/A
188.0595	(2R,3R,4R)-2-Amino-4-hydroxy-3-methylpentanoic acid	C6H13NO3		188.0594	8.6E-05	0.457226	#N/A
188.0595	Fagomine	C6H13NO3	C10144	188.0594	8.6E-05	0.457226	#N/A
189.0699	S-Methylmethionine	C6H14NO2S		189.0705	-0.00057	-3.0068	#N/A
189.0699	3-Ethyl-5-methyl-2-vinylpyrazine	C9H12N2		189.0699	-3.3E-05	-0.17192	#N/A
189.0699	6,7-Dihydro-2,3-dimethyl-5H-cyclopentapyrazine	C9H12N2		189.0699	-3.3E-05	-0.17192	#N/A

189.0699	6,7-Dihydro-2,5-dimethyl-5H-cyclopentapyrazine	C9H12N2		189.0699	-3.3E-05	-0.17192	#N/A
189.0699	6,7-Dihydro-2,6-dimethyl-5H-cyclopentapyrazine	C9H12N2		189.0699	-3.3E-05	-0.17192	#N/A
189.0699	2,5-Dimethyl-3-(2-propenyl)pyrazine	C9H12N2		189.0699	-3.3E-05	-0.17192	#N/A
189.0699	3,5-Dimethyl-2-(2-propenyl)pyrazine	C9H12N2		189.0699	-3.3E-05	-0.17192	#N/A
189.0699	2,3-Dimethyl-5-(2-propenyl)pyrazine	C9H12N2		189.0699	-3.3E-05	-0.17192	#N/A
189.0699	2,5-Dimethyl-3-(1-propenyl)pyrazine	C9H12N2		189.0699	-3.3E-05	-0.17192	#N/A
189.0699	3,5-Dimethyl-2-(1-propenyl)pyrazine	C9H12N2		189.0699	-3.3E-05	-0.17192	#N/A
189.0699	2,3-Dimethyl-5-(1-propenyl)pyrazine	C9H12N2		189.0699	-3.3E-05	-0.17192	#N/A
190.0386	4-Pyridoxolactone	C8H7NO3	C00971	190.0385	3.32E-05	0.174884	#N/A
190.0386	Formylanthranilic acid	C8H7NO3	C05653	190.0385	3.32E-05	0.174884	#N/A
190.0386	5-Pyridoxolactone	C8H7NO3	C06052	190.0385	3.32E-05	0.174884	#N/A
190.0386	Noradrenochrome	C8H7NO3		190.0385	3.32E-05	0.174884	#N/A
190.0386	6-Methoxy-2(3H)-benzoxazolone	C8H7NO3		190.0385	3.32E-05	0.174884	#N/A
190.0386	(R)-2-Hydroxy-2H-1,4-benzoxazin-3(4H)-one	C8H7NO3	C15769	190.0385	3.32E-05	0.174884	#N/A
190.0434	Tricyclazole	C9H7N3S	C18492	190.0433	9.48E-05	0.498766	#N/A
190.0434	cis-2-Methylaconitate	C7H8O6	C04225	190.0427	0.00072	3.788045	#N/A
190.0434	Noradrenochrome o-semiquinone	C8H8NO3		190.043	0.000448	2.356053	#N/A
190.0777	1-Deoxy-D-glucitol	C6H14O5		190.0767	0.000968	5.091849	#N/A
190.9628	3-Sulfopyruvic acid	C3H4O6S	C05528	190.9621	0.000748	3.918036	0.300729
191.0387	4-Coumaryl alcohol	C9H10O2	C02646	191.0379	0.000705	3.692139	126.4921
191.0387	Benzyl acetate	C9H10O2	C15513	191.0379	0.000705	3.692139	126.4921

191.0387	2'-Methoxyacetophenone	C9H10O2		191.0379	0.000705	3.692139	126.4921
191.0387	4'-Methoxyacetophenone	C9H10O2		191.0379	0.000705	3.692139	126.4921
191.0387	Methyl phenylacetate	C9H10O2		191.0379	0.000705	3.692139	126.4921
191.0387	4-Ethoxybenzaldehyde	C9H10O2		191.0379	0.000705	3.692139	126.4921
191.0387	2-Ethyl-4-(2-furanyl)-2-propenal	C9H10O2		191.0379	0.000705	3.692139	126.4921
191.0387	2-Phenylethyl formate	C9H10O2		191.0379	0.000705	3.692139	126.4921
191.0387	2-(2-Furanyl)-3-methyl-2-butenal	C9H10O2		191.0379	0.000705	3.692139	126.4921
192.0542	Pyridoxal	C8H9NO3	C00250	192.0542	1.62E-06	0.008421	#N/A
192.0542	Isopyridoxal	C8H9NO3	C06051	192.0542	1.62E-06	0.008421	#N/A
192.0542	3alpha,4,5,7alpha-Tetrahydro-5-hydroxy-1H-isoindole-1,3(2H)-dione	C8H9NO3		192.0542	1.62E-06	0.008421	#N/A
192.0542	3alpha,4,7,7alpha-Tetrahydro-4-hydroxy-1H-isoindole-1,3(2H)-dione	C8H9NO3		192.0542	1.62E-06	0.008421	#N/A
192.0542	N-Acetylhistamine	C7H11N3O	C05135	192.0534	0.000802	4.178333	#N/A
192.1172	N-(o)-Hydroxyarginine	C6H14N4O3	C05933	192.1172	4.65E-06	0.024196	291.9997
192.1172	L-erythro-4-Hydroxyarginine	C6H14N4O3	C08284	192.1172	4.65E-06	0.024196	291.9997
192.1253	Homocitrulline	C7H15N3O3	C02427	192.1253	-4.9E-05	-0.25643	#N/A
192.967	1,4-Dithiane-2,5-diol	C4H8O2S2		192.9664	0.000548	2.837318	#N/A
192.967	Dihydroasparagusic acid	C4H8O2S2	C04371	192.9664	0.000548	2.837318	#N/A
193.0544	gamma-Carboxyglutamic acid	C6H9NO6		193.0536	0.000775	4.015318	#N/A
193.0544	3-(4-Hydroxyphenyl)-1-propanol	C9H12O2		193.0536	0.000796	4.121813	119.2856
193.0544	3-(5-Methyl-2-furanyl)butanal	C9H12O2		193.0536	0.000796	4.121813	119.2856
193.0544	4-(Ethoxymethyl)phenol	C9H12O2		193.0536	0.000796	4.121813	119.2856
193.0544	2-(Ethoxymethyl)phenol	C9H12O2		193.0536	0.000796	4.121813	119.2856
194.9556	S-Propyl thiosulfate	C3H8O3S2		194.9546	0.000957	4.906992	#N/A

196.9753	2,5-Furandicarboxylic acid	C6H4O5		196.9757	-0.00039	-1.98734	#N/A
198.0011	(R)-(E)-Sulforaphene	C6H9NOS2		198.0018	-0.00064	-3.24183	57.54916
198.0876	N-Acetylhistidine	C8H11N3O3	C02997	198.0873	0.000244	1.23418	362.1795
198.0888	DL-2-Aminooctanoic acid	C8H17NO2		198.0891	-0.00024	-1.202	#N/A
199.0277	1-Oxo-1H-2-benzopyran-3-carboxaldehyde	C10H6O3		199.0276	8.17E-05	0.410307	#N/A
199.0277	Juglone	C10H6O3	C03840	199.0276	8.17E-05	0.410307	#N/A
199.0277	Succinylacetone	C7H10O4		199.0278	-7.3E-05	-0.36722	#N/A
199.0277	xi-2,3-Dihydro-3,5-dihydroxy-6-methyl-4H-pyran-4-one	C7H10O4		199.0278	-7.3E-05	-0.36722	#N/A
199.0933	DL-2-Aminooctanoic acid	C8H17NO2		199.0924	0.000899	4.51367	#N/A
200.0079	(R)-(E)-Sulforaphene	C6H9NOS2		200.0085	-0.00055	-2.75366	57.54916
200.023	4-Acetylimidazo[4,5-c]pyridine	C8H7N3O		200.0221	0.000977	4.882667	#N/A
200.023	L-2-Amino-4-methylenepentanedioic acid	C6H9NO4	C00651	200.023	2.1E-05	0.105216	#N/A
200.023	L-trans-alpha-Amino-2-carboxycyclopropaneacetic acid	C6H9NO4		200.023	2.1E-05	0.105216	#N/A
201.0008	S,S'-Ethylidene dithioacetate	C6H10O2S2		201.0014	-0.00067	-3.33362	#N/A
201.0008	S-2-Propenyl 2-propene-1-sulfonothioate	C6H10O2S2		201.0014	-0.00067	-3.33362	#N/A
201.0653	2,3-Dimethyl-3-hydroxyglutaric acid	C7H12O5		201.0644	0.000942	4.686478	9.051846
201.0653	3-Isopropylmalate	C7H12O5	C04411	201.0644	0.000942	4.686478	9.051846
201.0653	(Â±)-Glycerol 1,2-diacetate	C7H12O5		201.0644	0.000942	4.686478	9.051846
202.0016	1,2-Dihydroxy-3-keto-5-methylthiopentene	C6H10O3S	C15606	202.0016	7.38E-06	0.036549	#N/A
202.0016	1-(Methylsulfanyl)-1-oxopropan-2-yl acetate	C6H10O3S		202.0016	7.38E-06	0.036549	#N/A

202.0016	4-Hydroxy-L-glutamic acid	C5H7NO5	C03079	202.0023	-0.0007	-3.48965	#N/A
202.0016	A-Ketoglutaric acid oxime	C5H7NO5		202.0023	-0.0007	-3.48965	#N/A
202.0385	O-Phosphohomoserine	C4H10NO6P	C01102	202.0386	-7E-05	-0.34691	#N/A
202.0385	O-Phosphothreonine	C4H10NO6P	C12147	202.0386	-7E-05	-0.34691	#N/A
202.0385	4-Acetyl-2(3H)-benzoxazolone	C9H7NO3		202.0385	-3.2E-05	-0.15648	#N/A
202.0385	3-Mercapto-3-methyl-1-butyl acetate	C7H14O2S		202.038	0.000526	2.603152	#N/A
202.0385	Aminoadipic acid	C6H11NO4	C00956	202.0387	-0.00019	-0.92242	#N/A
202.0385	Acetylhomoserine	C6H11NO4		202.0387	-0.00019	-0.92242	#N/A
202.0385	(Â±)-2,2'-Iminobispropanoic acid	C6H11NO4	C03210	202.0387	-0.00019	-0.92242	#N/A
202.0434	4-Fumarylacetoacetic acid	C8H8O6	C01061	202.0427	0.00073	3.613865	#N/A
202.0434	Maleylacetoacetic acid	C8H8O6	C01036	202.0427	0.00073	3.613865	#N/A
202.0434	Polyvidone	C6H13NOP2		202.0432	0.000284	1.40682	#N/A
202.0777	Nicotine imine	C10H13N2		202.0777	-6.2E-06	-0.03059	#N/A
202.9983	1-Piperazinecarbodithioic acid	C5H10N2S2		202.9984	-7.6E-05	-0.37644	#N/A
203.0387	4-Chloro-3,5-dimethoxybenzaldehyde	C9H9ClO3		203.038	0.000695	3.423639	151.3577
203.0387	4,5-Dihydro-1-benzoxepin-3(2H)-one	C10H10O2		203.0379	0.000755	3.720614	127.612
203.0387	3-(4-Methoxyphenyl)-2-propenal	C10H10O2	C10475	203.0379	0.000755	3.720614	127.612
203.0387	Cassiastearoptene	C10H10O2		203.0379	0.000755	3.720614	127.612
203.0592	Potassium 2-(1'-ethoxy) ethoxypropanoate	C7H13KO4		203.0591	0.00012	0.591325	#N/A
203.0592	4-Methoxycinnamic acid	C10H10O3		203.0589	0.000275	1.352577	#N/A

203.0592	3-(4-Methylphenyl)oxiranecarboxylic acid	C10H10O3		203.0589	0.000275	1.352577	#N/A
203.0592	(Z)-10-Hydroxy-8-decene-4,6-diynoic acid	C10H10O3		203.0589	0.000275	1.352577	#N/A
203.0592	Di-alpha-furfuryl ether	C10H10O3		203.0589	0.000275	1.352577	#N/A
203.0592	(S)-Isosclerone	C10H10O3		203.0589	0.000275	1.352577	#N/A
203.0592	(E)-10-Hydroxy-2-decene-4,6-diynoic acid	C10H10O3		203.0589	0.000275	1.352577	#N/A
203.0592	3-(4-Hydroxy-2-methoxyphenyl)-2-propenal	C10H10O3		203.0589	0.000275	1.352577	#N/A
203.081	2-O-Methyl-L-fucose	C7H14O5		203.0801	0.000905	4.453992	8.870473
203.0857	Trimethyl-2-propenylpyrazine	C10H14N2		203.0856	8.54E-05	0.420435	#N/A
203.0873	2(N)-Methyl-norsalsolinol	C10H13NO2		203.0872	0.000106	0.52091	136.71
203.0873	(R)-Salsolinol	C10H13NO2	C09642	203.0872	0.000106	0.52091	136.71
203.0873	Maltoxazine	C10H13NO2		203.0872	0.000106	0.52091	136.71
203.0873	2,3-Dihydro-5-(3-hydroxypropanoyl)-1H-pyrrolizine	C10H13NO2		203.0872	0.000106	0.52091	136.71
203.0873	Salsolinol	C10H13NO2	C09642	203.0872	0.000106	0.52091	136.71
204.0546	Hippuric acid	C9H9NO3	C01586	204.0542	0.000392	1.920121	#N/A
204.0546	3-Succinoylpyridine	C9H9NO3	C19569	204.0542	0.000392	1.920121	#N/A
204.0546	Adrenochrome	C9H9NO3		204.0542	0.000392	1.920121	#N/A
204.0546	Methyl n-formylanthranilate	C9H9NO3		204.0542	0.000392	1.920121	#N/A
204.0546	1-(4-Methoxyphenyl)-2-nitroethylene	C9H9NO3		204.0542	0.000392	1.920121	#N/A
204.0546	Bicine	C6H13NO4		204.0543	0.000237	1.161743	#N/A
204.0546	2-Amino-4-ethoxy-3-hydroxybutanoic acid	C6H13NO4		204.0543	0.000237	1.161743	#N/A
204.0546	1-Deoxynojirimycin	C6H13NO4	C16843	204.0543	0.000237	1.161743	#N/A
204.0592	Ethyl aconitate	C8H10O6		204.0584	0.000845	4.138645	#N/A
204.0592	Adrenochrome o-semiquinone	C9H10NO3		204.0586	0.000572	2.805008	#N/A
205.0544	4-Chloro-3,5-dimethoxybenzyl alcohol	C9H11ClO3		205.0537	0.000775	3.78072	#N/A

205.0544	3-Hydroxy-4-phenylbutan-2-one	C10H12O2		205.0536	0.000836	4.074776	#N/A
205.0544	3-(4-Methoxyphenyl)-2-propen-1-ol	C10H12O2		205.0536	0.000836	4.074776	#N/A
205.0544	1-(4-Methoxyphenyl)-2-propanone	C10H12O2		205.0536	0.000836	4.074776	#N/A
205.0544	2-Phenylethyl acetate	C10H12O2	C12303	205.0536	0.000836	4.074776	#N/A
205.0544	Epoxyanethole	C10H12O2		205.0536	0.000836	4.074776	#N/A
206.0583	3-Methoxytyramine	C9H13NO2	C05587	206.0578	0.000476	2.308732	#N/A
206.0583	p-Synephrine	C9H13NO2	C04548	206.0578	0.000476	2.308732	#N/A
206.0583	4-Methoxytyramine	C9H13NO2		206.0578	0.000476	2.308732	#N/A
206.0583	4-(beta-Methylaminoethyl)catechol	C9H13NO2	C07453	206.0578	0.000476	2.308732	#N/A
206.0583	Norpandamarilactonine A	C9H13NO2		206.0578	0.000476	2.308732	#N/A
206.0583	2-(2-Furanyl)-3-piperidinol	C9H13NO2		206.0578	0.000476	2.308732	#N/A
206.0583	Epinine	C9H13NO2	C07453	206.0578	0.000476	2.308732	#N/A
206.0623	Cyromazine	C6H10N6	C14147	206.0632	-0.00095	-4.63257	7.701797
206.9846	(Z)-Methyl 3-(methylsulfinyl)-1-propenyl disulfide	C5H10OS3		206.9853	-0.00074	-3.56964	#N/A
207.0054	Homogentisic acid	C8H8O4	C00544	207.0054	-2.7E-05	-0.12912	152.6464
207.0054	Vanillic acid	C8H8O4	C06672	207.0054	-2.7E-05	-0.12912	152.6464
207.0054	3-Hydroxymandelic acid	C8H8O4		207.0054	-2.7E-05	-0.12912	152.6464
207.0054	p-Hydroxymandelic acid	C8H8O4	C11527	207.0054	-2.7E-05	-0.12912	152.6464
207.0054	3,4-Dihydroxybenzeneacetic acid	C8H8O4	C01161	207.0054	-2.7E-05	-0.12912	152.6464
207.0054	3,4-Dihydroxymandelaldehyde	C8H8O4	C05577	207.0054	-2.7E-05	-0.12912	152.6464

207.0054	2',4',6'-Trihydroxyacetophenone	C8H8O4		207.0054	-2.7E-05	-0.12912	152.6464
207.0054	2,6-Dimethoxy-1,4-benzoquinone	C8H8O4	C10331	207.0054	-2.7E-05	-0.12912	152.6464
207.0054	3-Acetyl-4-hydroxy-6-methyl-2H-pyran-2-one	C8H8O4		207.0054	-2.7E-05	-0.12912	152.6464
207.0054	Thermophillin	C8H8O4	C01692	207.0054	-2.7E-05	-0.12912	152.6464
207.0326	Beta-Carboline	C11H8N2	C20157	207.0319	0.000686	3.314231	#N/A
207.0326	D-Phenyllactic acid	C9H10O3	C05607	207.0329	-0.00027	-1.30146	#N/A
207.0326	L-3-Phenyllactic acid	C9H10O3	C05607	207.0329	-0.00027	-1.30146	#N/A
207.0326	Phenyllactic acid	C9H10O3	C01479	207.0329	-0.00027	-1.30146	#N/A
207.0326	4-Methoxyphenylacetic acid	C9H10O3		207.0329	-0.00027	-1.30146	#N/A
207.0326	Desaminotyrosine	C9H10O3	C01744	207.0329	-0.00027	-1.30146	#N/A
207.0326	Homovanillin	C9H10O3	C05581	207.0329	-0.00027	-1.30146	#N/A
207.0326	Ethyl vanillin	C9H10O3		207.0329	-0.00027	-1.30146	#N/A
207.0326	3,4-Dihydroxyphenylacetone	C9H10O3		207.0329	-0.00027	-1.30146	#N/A
207.0326	Guaicyl acetate	C9H10O3		207.0329	-0.00027	-1.30146	#N/A
207.0326	3,4-Dimethoxybenzaldehyde	C9H10O3	C02201	207.0329	-0.00027	-1.30146	#N/A
207.0326	Methyl 2-methoxybenzoate	C9H10O3		207.0329	-0.00027	-1.30146	#N/A
207.0326	Methyl 4-methoxybenzoate	C9H10O3		207.0329	-0.00027	-1.30146	#N/A

207.0326	3-(2-Hydroxyphenyl)propanoic acid	C9H10O3	C01198	207.0329	-0.00027	-1.30146	#N/A
207.0326	Ipomeanine	C9H10O3		207.0329	-0.00027	-1.30146	#N/A
207.0326	4-Methoxybenzyl formate	C9H10O3		207.0329	-0.00027	-1.30146	#N/A
207.0326	3-Hydroxy-1-(4-hydroxyphenyl)-1-propanone	C9H10O3		207.0329	-0.00027	-1.30146	#N/A
207.0326	4-Hydroxyphenyl-2-propionic acid	C9H10O3	C03080	207.0329	-0.00027	-1.30146	#N/A
207.0656	Scoparone	C11H10O4	C09311	207.0652	0.000388	1.872224	#N/A
207.0656	Citropten	C11H10O4		207.0652	0.000388	1.872224	#N/A
207.0656	3-Methoxy-4,5-methylenedioxycinnamaldehyde	C11H10O4		207.0652	0.000388	1.872224	#N/A
207.0656	Cyromazine	C6H10N6	C14147	207.0666	-0.00099	-4.77887	7.701797
208.9733	Phosphohydroxypyruvic acid	C3H5O7P	C03232	208.9732	5.72E-05	0.273833	#N/A
209.0118	(Z)-[3-(Methylsulfinyl)-1-propenyl] 2-propenyl disulfide	C7H12OS3		209.0123	-0.00052	-2.50674	#N/A
209.0118	Homogentisic acid	C8H8O4	C00544	209.0121	-0.00035	-1.66154	152.6464
209.0118	Vanillic acid	C8H8O4	C06672	209.0121	-0.00035	-1.66154	152.6464
209.0118	3-Hydroxymandelic acid	C8H8O4		209.0121	-0.00035	-1.66154	152.6464
209.0118	p-Hydroxymandelic acid	C8H8O4	C11527	209.0121	-0.00035	-1.66154	152.6464
209.0118	3,4-Dihydroxybenzeneacetic acid	C8H8O4	C01161	209.0121	-0.00035	-1.66154	152.6464
209.0118	3,4-Dihydroxymandelaldehyde	C8H8O4	C05577	209.0121	-0.00035	-1.66154	152.6464

209.0118	2',4',6'-Trihydroxyacetophenone	C8H8O4		209.0121	-0.00035	-1.66154	152.6464
209.0118	2,6-Dimethoxy-1,4-benzoquinone	C8H8O4	C10331	209.0121	-0.00035	-1.66154	152.6464
209.0118	3-Acetyl-4-hydroxy-6-methyl-2H-pyran-2-one	C8H8O4		209.0121	-0.00035	-1.66154	152.6464
209.0118	Thermophillin	C8H8O4	C01692	209.0121	-0.00035	-1.66154	152.6464
211.0279	1-(Methylsulfinyl)propyl 1-propenyl disulfide	C7H14OS3		211.028	-5.6E-05	-0.26687	#N/A
211.0279	1-(Methylsulfinyl)propyl 2-propenyl disulfide	C7H14OS3		211.028	-5.6E-05	-0.26687	#N/A
211.0279	Methyl 1-(2-propenylsulfinyl)propyl disulfide	C7H14OS3		211.028	-5.6E-05	-0.26687	#N/A
211.0279	Angelicin	C11H6O3	C09060	211.0276	0.000275	1.30357	#N/A
211.0279	Psoralen	C11H6O3	C09305	211.0276	0.000275	1.30357	#N/A
211.0279	3,4-Dihydroxyphenylglycol	C8H10O4	C05576	211.0278	0.00012	0.570253	#N/A
211.0279	Furaneol acetate	C8H10O4		211.0278	0.00012	0.570253	#N/A
211.0279	Herierin III	C8H10O4		211.0278	0.00012	0.570253	#N/A
211.0279	Herierin IV	C8H10O4		211.0278	0.00012	0.570253	#N/A
211.0649	Cysteinyl-Serine	C6H12N2O4S		211.0658	-0.00082	-3.86971	#N/A
211.0649	Serinyl-Cysteine	C6H12N2O4S		211.0658	-0.00082	-3.86971	#N/A
211.0649	1,4-Ipomeadiol	C9H14O3		211.0642	0.000784	3.716849	#N/A
213.0008	Oxalosuccinic acid	C6H6O7	C05379	213.0006	0.000213	0.998582	#N/A
213.0436	1-(Methylsulfinyl)propyl propyl disulfide	C7H16OS3		213.0436	8.13E-06	0.038139	0.431963
213.0436	Methyl 1-(propylsulfinyl)propyl disulfide	C7H16OS3		213.0436	8.13E-06	0.038139	0.431963
213.0436	Ethyl 2,4-dioxohexanoate	C8H12O4		213.0434	0.000185	0.867343	#N/A

213.07	1,2,3,4-Tetrahydro-beta-carboline	C11H12N2		213.0699	3.64E-05	0.171064	#N/A
213.9759	(R)-(E)-Sulforaphene	C6H9NOS2		213.9757	0.000199	0.930408	#N/A
214.0473	N-Lactoyl ethanolamine phosphate	C5H12NO6P		214.0475	-0.00021	-0.96473	#N/A
214.0473	1-(Methylsulfinyl)propyl propyl disulfide	C7H16OS3		214.047	0.000335	1.565514	0.431963
214.0473	Methyl 1-(propylsulfinyl)propyl disulfide	C7H16OS3		214.047	0.000335	1.565514	0.431963
214.0473	5-Hydroxyindoleacetic acid	C10H9NO3	C05635	214.0475	-0.00017	-0.78498	#N/A
214.0473	xi-2,3-Dihydro-2-oxo-1H-indole-3-acetic acid	C10H9NO3		214.0475	-0.00017	-0.78498	#N/A
214.0473	N-Carboxyethyl-g-aminobutyric acid	C7H13NO4		214.0476	-0.00032	-1.50795	#N/A
214.0473	2-Aminoheptanedioic acid	C7H13NO4		214.0476	-0.00032	-1.50795	#N/A
214.0473	Calystegine B5	C7H13NO4		214.0476	-0.00032	-1.50795	#N/A
214.0473	Calystegine B2	C7H13NO4	C10851	214.0476	-0.00032	-1.50795	#N/A
214.9859	cis-Aconitic acid	C6H6O6	C00417	214.9863	-0.00037	-1.7281	#N/A
214.9859	trans-Aconitic acid	C6H6O6	C02341	214.9863	-0.00037	-1.7281	#N/A
214.9859	Dehydroascorbic acid	C6H6O6	C00425	214.9863	-0.00037	-1.7281	#N/A
215.0489	Demethylated antipyrine	C10H10N2O	C13008	215.0492	-0.00024	-1.1173	#N/A
215.0489	1H-Indole-3-acetamide	C10H10N2O	C02693	215.0492	-0.00024	-1.1173	#N/A
215.0856	Methyl bisnorbiotinyl ketone	C9H14N2O2S		215.0849	0.000743	3.452608	#N/A
216.0807	Debrisoquine	C10H13N3	C13650	216.0808	-7.4E-05	-0.34181	95.34096

217.0307	O-Phospho-4-hydroxy-L-threonine	C4H10NO7P	C06055	217.0301	0.000619	2.849968	#N/A
217.0307	5,6-Dihydroxyindole-2-carboxylic acid	C9H7NO4	C04185	217.0301	0.000657	3.027244	#N/A
217.0307	L-Dopachrome	C9H7NO4	C01693	217.0301	0.000657	3.027244	#N/A
217.0307	D-Dopachrome	C9H7NO4	C15566	217.0301	0.000657	3.027244	#N/A
217.0748	(R)-Shinanolone	C11H12O3		217.0746	0.000257	1.184 97	#N/A
217.0748	Ethyl phenylglycidate	C11H12O3		217.0746	0.000257	1.184 97	#N/A
217.0748	Dehydrozingerone	C11H12O3		217.0746	0.000257	1.184 97	#N/A
217.0748	Ethyl 3-oxo-3-phenylpropanoate	C11H12O3		217.0746	0.000257	1.184 97	#N/A
217.0748	Benzyl acetoacetate	C11H12O3		217.0746	0.000257	1.184 97	#N/A
217.0748	1'-Hydroxychavicol acetate	C11H12O3		217.0746	0.000257	1.184 97	#N/A
218.0385	Dopachrome o-semiquinone	C9H8NO4		218.0379	0.000625	2.864736	#N/A
218.0699	Glycerylphosphorylethanolamine	C5H14NO6P	C01233	218.0699	1.44E-05	0.066057	#N/A
218.0699	Phenylacetylglycine	C10H11NO3	C05598	218.0698	5.29E-05	0.242486	#N/A
218.0699	Methylhippuric acid	C10H11NO3		218.0698	5.29E-05	0.242486	#N/A
218.0699	2-Methylhippuric acid	C10H11NO3	C01586	218.0698	5.29E-05	0.242486	#N/A
218.0699	m-Methylhippuric acid	C10H11NO3		218.0698	5.29E-05	0.242486	#N/A
218.0699	p-Methylhippuric acid	C10H11NO3		218.0698	5.29E-05	0.242486	#N/A
218.0699	Methyl n-acetylanthranilate	C10H11NO3	C06332	218.0698	5.29E-05	0.242486	#N/A
218.0699	Betamipron	C10H11NO3		218.0698	5.29E-05	0.242486	#N/A
218.0699	N-Methyl-1-deoxynojirimycin	C7H15NO4		218.07	-0.0001	-0.46715	#N/A
219.0571	Bergapten	C12H8O4	C01557	219.0562	0.000883	4.028877	#N/A
219.0701	Lycoperdic acid	C8H11NO6		219.0693	0.000848	3.871773	10.15455
220.0735	Lycoperdic acid	C8H11NO6		220.0726	0.000865	3.928933	10.15455
220.0735	beta-O-Methylynephrine	C10H15NO2		220.0734	5.07E-05	0.230315	0.436488

220.0735	2,5-Dimethyl-4-(1-pyrrolidinyl)-3(2H)-furanone	C10H15NO2		220.0734	5.07E-05	0.230315	0.436488
220.0735	2-(5-Methyl-2-furanyl)-3-piperidinol	C10H15NO2		220.0734	5.07E-05	0.230315	0.436488
220.0735	5-(1-Pyrrolidinylmethyl)-2-furanmethanol	C10H15NO2		220.0734	5.07E-05	0.230315	0.436488
220.0735	3,4-Dimethoxyphenylethylamine	C10H15NO2		220.0734	5.07E-05	0.230315	0.436488
220.1135	2-Isopropyl-3,5-dimethoxy-6-methylpyrazine	C10H16N2O2		220.1138	-0.00029	-1.33182	#N/A
220.1135	L-alpha-Amino-1H-pyrrole-1-hexanoic acid	C10H16N2O2		220.1138	-0.00029	-1.33182	#N/A
221.0766	L-beta-aspartyl-L-serine	C7H12N2O6		221.0768	-0.00019	-0.84811	#N/A
221.0766	Aspartyl-Serine	C7H12N2O6		221.0768	-0.00019	-0.84811	#N/A
221.0766	Serinyl-Aspartate	C7H12N2O6		221.0768	-0.00019	-0.84811	#N/A
221.0766	beta-O-Methylynephrine	C10H15NO2		221.0768	-0.00017	-0.75511	0.436488
221.0766	2,5-Dimethyl-4-(1-pyrrolidinyl)-3(2H)-furanone	C10H15NO2		221.0768	-0.00017	-0.75511	0.436488
221.0766	2-(5-Methyl-2-furanyl)-3-piperidinol	C10H15NO2		221.0768	-0.00017	-0.75511	0.436488
221.0766	5-(1-Pyrrolidinylmethyl)-2-furanmethanol	C10H15NO2		221.0768	-0.00017	-0.75511	0.436488
221.0766	3,4-Dimethoxyphenylethylamine	C10H15NO2		221.0768	-0.00017	-0.75511	0.436488
222.0889	1-Isothiocyanato-7-(methylsulfinyl)heptane	C9H17NOS2		222.0891	-0.0002	-0.88234	#N/A
223.0275	3-Dechloroethylifosfamide	C5H12ClN2O2P	C16550	223.0284	-0.00092	-4.13766	#N/A
223.0275	2-Dechloroethylifosfamide	C5H12ClN2O2P	C16555	223.0284	-0.00092	-4.13766	#N/A
223.0275	Homovanillic acid	C9H10O4	C05582	223.0278	-0.00028	-1.25441	#N/A

223.0275	Isohomovanillic acid	C9H10O4		223.0278	-0.00028	-1.25441	#N/A
223.0275	Hydroxyphenyllactic acid	C9H10O4	C03672	223.0278	-0.00028	-1.25441	#N/A
223.0275	3-(3-Hydroxyphenyl)-3-hydroxypropanoic acid	C9H10O4		223.0278	-0.00028	-1.25441	#N/A
223.0275	3-Methoxy-4-hydroxyphenylglycolaldehyde	C9H10O4	C05583	223.0278	-0.00028	-1.25441	#N/A
223.0275	2,6-Dimethoxybenzoic acid	C9H10O4		223.0278	-0.00028	-1.25441	#N/A
223.0275	(Â±)-2-Hydroxy-3-(2-hydroxyphenyl)propanoic acid	C9H10O4		223.0278	-0.00028	-1.25441	#N/A
223.0275	Maltol propionate	C9H10O4		223.0278	-0.00028	-1.25441	#N/A
223.0275	2',4'-Dihydroxy-6'-methoxyacetophenone	C9H10O4		223.0278	-0.00028	-1.25441	#N/A
224.062	2-(4-Methyl-5-thiazolyl)ethyl propionate	C9H13NO2S		224.0626	-0.00062	-2.78572	#N/A
224.1045	N-Acetylgalactosamine	C8H15NO6	C01074	224.1039	0.00057	2.543443	#N/A
224.1045	N-Acetyl-D-glucosamine	C8H15NO6	C00140	224.1039	0.00057	2.543443	#N/A
224.1045	2'-Deoxysepiapterin	C9H11N5O2		224.1053	-0.00077	-3.42432	#N/A
224.1045	Beta-N-Acetylglucosamine	C8H15NO6	C03878	224.1039	0.00057	2.543443	#N/A
224.1045	N-Acetyl-b-D-galactosamine	C8H15NO6	C05021	224.1039	0.00057	2.543443	#N/A
224.1045	N-Acetylmannosamine	C8H15NO6	C00645	224.1039	0.00057	2.543443	#N/A
224.1045	Avenic acid B	C8H15NO6		224.1039	0.00057	2.543443	#N/A
225.0432	1-Methoxy-1H-indole-3-acetonitrile	C11H10N2O		225.0425	0.000682	3.030862	#N/A
225.0432	Vanylglycol	C9H12O4	C05594	225.0434	-0.00027	-1.21542	#N/A
225.0432	Phosphorylcholine	C5H15NO4P	C00588	225.0437	-0.00058	-2.59565	#N/A

225.0432	1-(3-Hydroxy-4-methoxyphenyl)-1,2-ethanediol	C9H12O4		225.0434	-0.00027	-1.21542	#N/A
225.0432	(Â±)-threo-1-(4-Hydroxyphenyl)-1,2,3-propanetriol	C9H12O4		225.0434	-0.00027	-1.21542	#N/A
226.0777	2-Amino-1,6-dimethylfuro[3,2-e]imidazo[4,5-b]pyridine	C10H10N4O		226.078	-0.00029	-1.26615	#N/A
227.0222	Bergaptol	C11H6O4	C00758	227.0225	-0.0003	-1.30969	#N/A
227.0222	(-)-3-Cyanomethyl-3-hydroxy-1H-indol-2(3H)-one	C10H8N2O2		227.0217	0.000504	2.217918	0.625042
227.0222	Erinapyrone C	C8H10O5		227.0227	-0.00045	-1.99134	#N/A
228.0219	Cystathionine ketimine	C7H9NO4S		228.0212	0.000786	3.448189	#N/A
228.0257	(-)-3-Cyanomethyl-3-hydroxy-1H-indol-2(3H)-one	C10H8N2O2		228.0251	0.000626	2.745654	0.625042
228.027	L-Glutamic acid 5-phosphate	C5H10NO7P	C03287	228.0268	0.000244	1.069565	#N/A
228.027	Xanthurenic acid	C10H7NO4	C02470	228.0267	0.000282	1.238291	#N/A
228.027	Zeanic acid	C10H7NO4		228.0267	0.000282	1.238291	#N/A
228.027	4,6-Dihydroxy-2-quinolinecarboxylic acid	C10H7NO4		228.0267	0.000282	1.238291	#N/A
228.027	Glutarylglycine	C7H11NO5		228.0269	0.000128	0.559642	#N/A
228.027	N-Acetylglutamic acid	C7H11NO5	C00624	228.0269	0.000128	0.559642	#N/A
228.027	Pyrrolidino-[1,2E]-4H-2,4-dimethyl-1,3,5-dithiazine	C8H15NS2		228.0277	-0.00074	-3.24866	31.24547
228.1386	N1-Acetylspermidine	C9H21N3O	C00612	228.1383	0.000274	1.201437	#N/A
228.1386	N8-Acetylspermidine	C9H21N3O	C01029	228.1383	0.000274	1.201437	#N/A
229.017	Tricyclazole	C9H7N3S	C18492	229.0026	-0.00088	-3.84026	#N/A
229.017	cis-2-Methylaconitate	C7H8O6	C04225	229.002	-0.00025	-1.11059	#N/A
229.0233	Daucic acid	C7H8O7		229.0229	0.000356	1.552904	#N/A
229.0268	Coixinden A	C11H10O3	C17916	229.0262	0.000638	2.785988	#N/A

230.981	Oxalosuccinic acid	C6H6O7	C05379	230.9812	-0.00025	-1.07039	#N/A
231.0543	Mevalonic acid-5P	C6H13O7P	C01107	231.0539	0.000399	1.727301	#N/A
231.0543	Scoparone	C11H10O4	C09311	231.0538	0.000438	1.893817	#N/A
231.0543	Citropten	C11H10O4		231.0538	0.000438	1.893817	#N/A
231.0543	3-Methoxy-4,5-methylenedioxycinnamaldehyde	C11H10O4		231.0538	0.000438	1.893817	#N/A
231.0543	3-Hydroxysuberic acid	C8H14O5		231.054	0.000283	1.224059	#N/A
231.0543	Diethyl L-malate	C8H14O5		231.054	0.000283	1.224059	#N/A
232.0127	gamma-Carboxyglutamic acid	C6H9NO6		232.0129	-0.00013	-0.54953	#N/A
232.078	L-Kynurenine	C10H12N2O3	C00328	232.0774	0.000613	2.640003	#N/A
232.078	Formyl-5-hydroxykynurenamine	C10H12N2O3	C05647	232.0774	0.000613	2.640003	#N/A
232.9966	Citric acid	C6H8O7	C00158	232.9969	-0.00027	-1.14067	#N/A
232.9966	Isocitric acid	C6H8O7	C00311	232.9969	-0.00027	-1.14067	#N/A
232.9966	D-threo-Isocitric acid	C6H8O7	C00451	232.9969	-0.00027	-1.14067	#N/A
232.9966	Diketogulonic acid	C6H8O7	C04575	232.9969	-0.00027	-1.14067	#N/A
232.9966	2,3-Diketo-L-gulonate	C6H8O7	C04575	232.9969	-0.00027	-1.14067	#N/A
232.9966	(1R,2R)-Isocitric acid	C6H8O7	C04617	232.9969	-0.00027	-1.14067	#N/A
232.9966	D-Glucaro-1,4-lactone	C6H8O7		232.9969	-0.00027	-1.14067	#N/A
233.0858	N2-Succinyl-L-glutamic acid 5-semialdehyde	C9H13NO6	C05932	233.0849	0.000895	3.841435	15.52157
234.0848	Glutamyl-Serine	C8H13N2O6		234.0846	0.000185	0.791529	68.40924
234.0848	Serinyl-Glutamate	C8H13N2O6		234.0846	0.000185	0.791529	68.40924

234.0848	Cassiachromone	C13H12O4		234.0842	0.000633	2.703015	#N/A
234.0891	N2-Succinyl-L-glutamic acid 5-semialdehyde	C9H13NO6	C05932	234.0883	0.000839	3.586217	15.52157
234.9934	p-Chlorobenzene sulfonyl urea	C7H7ClN2O3S		234.9939	-0.00043	-1.84656	#N/A
235.0816	1-Isopropyl citrate	C9H14O7		235.0812	0.000325	1.380822	#N/A
235.0816	2-Isopropyl citrate	C9H14O7		235.0812	0.000325	1.380822	#N/A
235.0836	2-Isopropyl-3,5-dimethoxy-6-methylpyrazine	C10H16N2O2		235.0843	-0.00076	-3.24548	#N/A
235.0836	L-alpha-Amino-1H-pyrrole-1-hexanoic acid	C10H16N2O2		235.0843	-0.00076	-3.24548	#N/A
235.1014	Hirsutin	C10H19NOS2		235.1014	-1.9E-05	-0.08012	#N/A
240.2324	Solamine	C12H29N3		240.2321	0.000347	1.443401	#N/A
243.0702	2,4-Dihydroxy-6,7-dimethoxy-2H-1,4-benzoxazin-3(4H)-one	C10H11NO6		243.0693	0.000904	3.717617	#N/A
243.0702	2,4-Dihydroxy-7,8-dimethoxy-2H-1,4-benzoxazin-3(4H)-one	C10H11NO6		243.0693	0.000904	3.717617	#N/A
244.0859	N-Deschlorobenzoyl indomethacin	C12H13NO3		244.0855	0.000447	1.830055	#N/A
244.0859	Nigellimine N-oxide	C12H13NO3		244.0855	0.000447	1.830055	#N/A
244.0859	alpha-Hydroxy-1-methyl-1H-indole-3-propanoic acid	C12H13NO3		244.0855	0.000447	1.830055	#N/A
244.0859	alpha-Methoxy-1H-indole-3-propanoic acid	C12H13NO3		244.0855	0.000447	1.830055	#N/A
246.1016	Hydrocotarnine	C12H15NO3	C13534	246.1011	0.000476	1.934488	#N/A
246.1016	Pantothenol	C9H19NO4	C05944	246.1013	0.000321	1.305681	#N/A
247.0123	Dimethylallylpyrophosphate	C5H12O7P2	C00235	247.0131	-0.00084	-3.41471	#N/A
247.0123	Isopentenyl pyrophosphate	C5H12O7P2	C00129	247.0131	-0.00084	-3.41471	#N/A
247.0123	2-Methylcitric acid	C7H10O7		247.0125	-0.00026	-1.06094	#N/A
247.0123	Homocitric acid	C7H10O7	C01251	247.0125	-0.00026	-1.06094	#N/A

247.0651	(2RS,5RS)-(E)-2-(2-Phenylethenyl)-1,3-dioxan-5-ol	C12H14O3		247.0642	0.000896	3.626252	#N/A
247.0651	Cuelure	C12H14O3		247.0642	0.000896	3.626252	#N/A
247.0651	2,3-Dihydro-6-methoxy-2,2-dimethyl-4H-1-benzopyran-4-one	C12H14O3		247.0642	0.000896	3.626252	#N/A
247.1015	Biotin	C10H16N2O3S	C00120	247.1021	-0.00067	-2.71706	#N/A
247.1307	Epoxyeremopetasinorol	C13H20O3		247.1305	0.000197	0.795456	#N/A
248.9915	Garcinia acid	C6H8O8		248.9918	-0.00028	-1.11785	#N/A
250.9884	Fluorocitric acid	C6H7FO7		250.9874	0.000974	3.880537	#N/A
250.9905	1-(Methylsulfinyl)propyl 1-propenyl disulfide	C7H14OS3		250.9905	-8.5E-05	-0.33913	300.8673
250.9905	1-(Methylsulfinyl)propyl 2-propenyl disulfide	C7H14OS3		250.9905	-8.5E-05	-0.33913	300.8673
250.9905	Methyl 1-(2-propenylsulfinyl)propyl disulfide	C7H14OS3		250.9905	-8.5E-05	-0.33913	300.8673
254.0194	Glycerylphosphorylethanolamine	C5H14NO6P	C01233	254.019	0.000365	1.438378	#N/A
254.0444	Kinetin	C10H9N5O	C08272	254.0439	0.000493	1.941643	#N/A
254.0444	Methyl bisnorbiotinyl ketone	C9H14N2O2S		254.0441	0.00025	0.983954	#N/A
255.0953	N2-Succinyl-L-ornithine	C9H16N2O5	C03415	255.0951	0.000148	0.579834	#N/A
255.0953	4-(Glutamylamino) butanoate	C9H16N2O5	C15767	255.0951	0.000148	0.579834	#N/A
255.0953	Aspartyl-Valine	C9H16N2O5		255.0951	0.000148	0.579834	#N/A
255.0953	Hydroxyprolyl-Threonine	C9H16N2O5		255.0951	0.000148	0.579834	#N/A
255.0953	Threoninyl-Hydroxyproline	C9H16N2O5		255.0951	0.000148	0.579834	#N/A
255.0953	Valyl-Aspartate	C9H16N2O5		255.0951	0.000148	0.579834	#N/A
255.0953	L-N-(3-Carboxypropyl)glutamine	C9H16N2O5		255.0951	0.000148	0.579834	#N/A
257.0954	Nb-Acetyl-Nb-methyltryptamine	C13H16N2O		257.0961	-0.00075	-2.93248	#N/A

261.0281	6-Phosphonoglucono-D-lactone	C6H11O9P	C01236	261.0281	7.75E-05	0.296745	#N/A
261.0281	2-Keto-3-deoxy-6-phosphogluconic acid	C6H11O9P	C04442	261.0281	7.75E-05	0.296745	#N/A
262.0778	Isopropyl beta-D-glucoside	C9H18O6		262.0769	0.000986	3.762756	#N/A
262.0799	Aspartyl-Glutamate	C9H13N2O7		262.0796	0.000346	1.320341	68.42041
262.0799	Glutamyl-Aspartate	C9H13N2O7		262.0796	0.000346	1.320341	68.42041
262.0799	Pratenol A	C14H12O5		262.0791	0.000793	3.027646	#N/A
262.0799	N-(1-Deoxy-1-fructosyl)glycine	C8H15NO7		262.0808	-0.00088	-3.36423	65.68822
262.082	Sepiapterin	C9H11N5O3	C00835	262.0821	-9.8E-05	-0.37341	83.40015
262.082	Biopterin	C9H11N5O3	C06313	262.0821	-9.8E-05	-0.37341	83.40015
262.082	D-Biopterin	C9H11N5O3		262.0821	-9.8E-05	-0.37341	83.40015
262.082	Orinapterin	C9H11N5O3		262.0821	-9.8E-05	-0.37341	83.40015
262.082	Dyspropterin	C9H11N5O3	C03684	262.0821	-9.8E-05	-0.37341	83.40015
262.082	Primapterin	C9H11N5O3		262.0821	-9.8E-05	-0.37341	83.40015
262.082	Deoxyeritadenine	C9H11N5O3		262.0821	-9.8E-05	-0.37341	83.40015
262.0841	N-Ornithyl-L-taurine	C7H17N3O4S		262.0832	0.000869	3.316615	#N/A
263.0765	Carbadox	C11H10N4O4		263.0775	-0.00096	-3.63799	#N/A
267.9989	5-Phosphoribosylamine	C5H12NO7P	C03090	267.9983	0.000635	2.369164	38.08318
274.956	p-Chlorobenzene sulfonyl urea	C7H7ClN2O3S		274.9565	-0.00047	-1.71546	#N/A
276.0917	Glutamyl-Glutamate	C10H14N2O7		276.0907	0.000991	3.587703	#N/A

276.0917	1-(2,4,6-Trimethoxyphenyl)-1,3-butanedione	C13H16O5		276.0923	-0.00062	-2.26112	#N/A
276.0917	Pandamarilactam 3x	C13H17NO3		276.0907	0.001011	3.662169	#N/A
276.0957	N-(1-Deoxy-1-fructosyl)alanine	C9H17NO7		276.0964	-0.00072	-2.61429	#N/A
277.1669	4-Hydroxycinnamoylagmatine	C14H20N4O2	C04498	277.1659	0.001013	3.653066	#N/A
290.0551	Nitecapone	C12H11NO6		290.0546	0.000552	1.904085	#N/A
290.0551	S-Acetyldihydrolipoamide	C10H19NO2S2	C01136	290.0556	-0.00047	-1.62334	#N/A
290.0551	S-Acetyldihydrolipoamide-E	C10H19NO2S2	C16255	290.0556	-0.00047	-1.62334	#N/A
290.1074	3',4',5'-Trimethoxycinnamyl alcohol acetate	C14H18O5		290.108	-0.00065	-2.2271	#N/A
290.1074	Thiamine	C12H17N4OS	C00378	290.1082	-0.00088	-3.04758	#N/A
290.1074	Isopentyl beta-D-glucoside	C11H22O6		290.1082	-0.0008	-2.76052	#N/A
295.0163	Paraquat dichloride	C12H14Cl2N2	C00225	295.0166	-0.00021	-0.72219	#N/A
297.1971	9-Decenoylcholine	C15H30NO2		297.1975	-0.00038	-1.27458	#N/A
303.1408	Hydroxyvalerylcarnitine	C12H25NO5		303.1398	0.001037	3.420984	#N/A
313.1811	Arginyl-Histidine	C12H21N7O3		313.1812	-0.00014	-0.43941	#N/A
313.1811	Histidinyl-Arginine	C12H21N7O3		313.1812	-0.00014	-0.43941	#N/A
313.1811	N(6)-(Octanoyl)lysine	C14H28N2O3		313.1799	0.001022	3.896641	#N/A
323.9681	[Nitrilotris(methylene)]trisphosphonic acid	C3H12NO9P3		323.9684	-0.00036	-1.10281	#N/A
330.1387	Atropine	C17H23NO3	C01479	330.1377	0.001061	3.212506	#N/A
330.1387	Dihydroferuperine	C17H23NO3		330.1377	0.001061	3.212506	#N/A

331.2192	Arginyl-Arginine	C12H26N8O3		331.2201	-0.00089	-2.68308	17.10672
341.1235	Linocinnamarin	C16H20O8		341.1231	0.000413	1.211309	#N/A
341.1235	Oenanthoside A	C16H20O8		341.1231	0.000413	1.211309	#N/A
341.1235	Neuromedin B (1-3)	C12H22N4O5		341.1222	0.001329	3.895928	#N/A
347.1592	Butyl (S)-3-hydroxybutyrate glucoside	C14H26O8		347.1587	0.000492	1.418149	#N/A
351.1034	Ethylvanillin glucoside	C15H20O8		351.105	-0.00163	-4.63927	#N/A
351.1034	Dihydromelilotoside	C15H20O8		351.105	-0.00163	-4.63927	#N/A
351.1034	Domoic acid	C15H21NO6	C13732	351.1034	6.5E-06	0.018505	#N/A
357.1444	Glutaminyl-Tryptophan	C16H20N4O4		357.1444	-3.3E-05	-0.09139	#N/A
357.1444	Tryptophyl-Glutamine	C16H20N4O4		357.1444	-3.3E-05	-0.09139	#N/A
357.1444	Tryptophyl-Gamma-glutamate	C16H20N4O4		357.1444	-3.3E-05	-0.09139	#N/A
357.1444	Gamma-glutamyl-Tryptophan	C16H20N4O4		357.1444	-3.3E-05	-0.09139	#N/A
367.1474	1-(1,2,3,4,5-Pentahydroxypent-1-yl)-1,2,3,4-tetrahydro-beta-carboline-3-carboxylate	C17H21N2O7		367.1455	0.001845	5.025205	#N/A
367.1474	N1-(2,4-Dimethoxybenzyl)-n2-(2-(pyridin-2-yl) ethyl)oxalamide	C18H21N3O4		367.1458	0.001573	4.283973	#N/A
371.1598	4-Hydroxy-3-prenylbenzoic acid glucoside	C18H24O8		371.1611	-0.00125	-3.38112	#N/A
381.1266	2-Phenylaminoadenosine	C16H18N6O4		381.1282	-0.00153	-4.02512	#N/A
381.1266	4-O-Methylgalactinol	C13H24O11		381.1278	-0.00115	-3.02334	#N/A
381.1266	Galactopinitol B	C13H24O11		381.1278	-0.00115	-3.02334	#N/A

381.1266	Galactopinitol A	C13H24O11		381.1278	-0.00115	-3.02334	#N/A
381.1266	D-Pinitol 2-O-alpha-D-Galactopyranosyl	C13H24O11		381.1278	-0.00115	-3.02334	#N/A
384.142	N-Acetyl-9-O-lactoylneuraminic acid	C14H23NO11		384.1411	0.000916	2.38501	#N/A
386.1556	N-Acetyllactosamine	C14H25NO11	C00611	386.1567	-0.00116	-3.01	#N/A
386.1556	Beta-1,4-mannose-N-acetylglucosamine	C14H25NO11		386.1567	-0.00116	-3.01	#N/A
386.1556	Lacto-N-biose I	C14H25NO11	C06372	386.1567	-0.00116	-3.01	#N/A
386.1556	Poly-N-acetyllactosamine	C14H25NO11		386.1567	-0.00116	-3.01	#N/A
393.1663	(2S)-2-Butanol O-[b-D-Apiofuranosyl-(1->6)-b-D-glucopyranoside]	C15H28O10		393.1642	-0.00117	-2.96869	#N/A
404.1663	Petasitenine	C19H27NO7	C10359	404.168	-0.00167	-4.12648	#N/A
409.1581	2,3-Butanediol apiosylglucoside	C15H28O11		409.1591	-0.001	-2.45478	#N/A
439.197	8-Propanoylneosolaniol	C22H30O9		439.1963	0.000776	1.766536	#N/A
442.1888	18-Carboxy-dinor-LTE4	C21H31NO7S		442.1894	-0.00143	-3.22308	0.254316
442.1888	(E)-Casimiroedine	C21H27N3O6	C10577	442.1859	0.002061	4.659902	52.51494
443.1914	Lusitanicoside	C21H30O10	C10474	443.1912	0.000179	0.404182	#N/A
443.1914	18-Carboxy-dinor-LTE4	C21H31NO7S		443.1928	-0.0014	-3.16244	0.254316
455.2111	Butyl (S)-3-hydroxybutyrate [arabinosyl-(1->6)-glucoside]	C19H34O12		455.2123	-0.00119	-2.61478	0.522734
456.2145	Butyl (S)-3-hydroxybutyrate [arabinosyl-(1->6)-glucoside]	C19H34O12		456.2157	-0.00115	-2.51235	0.522734
468.2038	Biotripyrrin-a	C25H27N3O6		468.204	-0.00022	-0.47213	58.81957

468.2038	Biotripyrrin-b	C25H27N3O6		468.204	-0.00022	-0.47213	58.81957
474.1741	10-Formyltetrahydrofolate	C20H23N7O7	C00234	474.1732	0.000953	2.009725	#N/A
474.1741	N5-Formyl-THF	C20H23N7O7	C03479	474.1732	0.000953	2.009725	#N/A
474.1741	Pteroyl-D-glutamic acid	C20H23N7O7	D01211	474.1732	0.000953	2.009725	#N/A
474.1788	Cadabicine	C25H29N3O4		474.179	-0.00015	-0.31632	#N/A
477.1879	6-Feruloylglucose 2,3,4-trihydroxy-3-methylbutylglycoside	C21H30O12		477.1877	0.000144	0.300 92	37.73708
477.1931	Butyl (S)-3-hydroxybutyrate [arabinosyl-(1->6)-glucoside]	C19H34O12		477.1942	-0.00112	-2.34267	0.289129
478.1966	Butyl (S)-3-hydroxybutyrate [arabinosyl-(1->6)-glucoside]	C19H34O12		478.1976	-0.00105	-2.18601	0.289129
505.1558	6-Caffeoylsucrose	C21H28O14		505.1552	0.000634	1.255897	#N/A
505.1558	Biotripyrrin-a	C25H27N3O6		505.1565	-0.00068	-1.35091	#N/A
505.1558	Biotripyrrin-b	C25H27N3O6		505.1565	-0.00068	-1.35091	#N/A
507.2316	Caffeoylferuloylspermidine	C26H33N3O6		507.2295	0.002046	4.032977	#N/A
507.2316	N1-Caffeoyl-N10-feruloylspermidine	C26H33N3O6		507.2295	0.002046	4.032977	#N/A
511.2265	6-O-Oleuropeoylsucrose	C22H36O13		511.2296	-0.0031	-6.06931	29.91169
521.2425	N1,N10-Diferuloylspermidine	C27H35N3O6		521.2452	-0.00264	-5.06404	#N/A
521.2473	N1,N10-Diferuloylspermidine	C27H35N3O6		521.2452	0.002096	4.020653	#N/A
525.2422	Sarcodon scabrosus Depsipeptide	C23H39N3O8		525.2402	0.00195	3.712153	#N/A
528.1763	Demethyloleuropein	C24H30O13		528.1793	-0.00301	-5.70133	#N/A
528.1763	(S)-Multifidol 2-[apiosyl-(1->6)-glucoside]	C22H32O13		528.1769	-0.0006	-1.1424	#N/A

528.1763	Gravacridonediol glucoside	C25H29NO10		528.1751	0.001187	2.24685	#N/A
535.2629	AFN911	C29H33N7O2		535.2621	0.000757	1.414579	1.494437
536.2662	AFN911	C29H33N7O2		536.2655	0.000685	1.278179	1.494437
537.2816	7,8-Dihydrovomifoliol 9-[rhamnosyl-(1->6)-glucoside]	C25H42O12		537.2816	-4.3E-05	-0.07992	#N/A
537.2816	Postin	C22H40N8O5		537.282	-0.00046	-0.86465	#N/A
538.1606	Salviaflaside methyl ester	C25H28O13		538.1636	-0.00303	-5.62879	#N/A
541.1634	N,N'-Bis(g-glutamyl)-3,3'-(1,2-propylenedithio)dialanine	C19H32N4O10S2		541.1633	9.49E-05	0.175395	#N/A
549.2786	Desmosine	C24H40N5O8		549.2769	0.001734	3.156062	0.374358
549.2786	Isodesmosine	C24H40N5O8		549.2769	0.001734	3.156062	0.374358
550.2823	Desmosine	C24H40N5O8		550.2803	0.002076	3.773275	0.374358
550.2823	Isodesmosine	C24H40N5O8		550.2803	0.002076	3.773275	0.374358
556.1712	Lippioside II	C25H30O14		556.1742	-0.00297	-5.34051	1.491806
556.1712	Alkaloid RC	C26H29NO11		556.17	0.001228	2.207604	15.96382
557.1746	Lippioside II	C25H30O14		557.1775	-0.00299	-5.36046	1.491806
566.0894	dTDP-D-glucose	C16H26N2O16P2	C00842	566.0864	0.003019	5.33348	#N/A
566.0894	dTDP-D-galactose	C16H26N2O16P2	C02097	566.0864	0.003019	5.33348	#N/A
589.0207	UDP-L-rhamnose	C15H24N2O16P2	C02199	589.0233	-0.0026	-4.41433	#N/A
589.025	UDP-L-rhamnose	C15H24N2O16P2	C02199	589.0233	0.001718	2.916243	#N/A
592.2054	Citrusin B	C27H36O13		592.2082	-0.00275	-4.64971	#N/A
776.4146	Angiotensin IV	C40H54N8O8	C15849	776.4171	-0.00251	-3.22931	#N/A
782.2197	Rubrofusarin 6-[glucosyl-(1->3)-glucosyl-(1->6)-glucoside]	C33H42O20		782.2195	0.000178	0.227611	#N/A

782.2197	Pelargonidin 3-sophoroside 5-glucoside	C33H41O20		782.2155	0.004648	5.942401	#N/A